

BULGARIAN CHEMICAL COMMUNICATIONS

2018 Volume 50 / Special Issue G

Selected papers presented on the First International Scientific Conference
Alternative Energy Sources, Materials & Technologies AESMT'18,
Plovdiv, Bulgaria, May 14 -15, 2018

*Journal of the Chemical Institutes
of the Bulgarian Academy of Sciences
and of the Union of Chemists in Bulgaria*

PREFACE

The First International Scientific Conference “Alternative Energy Sources, Materials & Technologies AESMT’18” was held between 14th and 15th May 2018 in Plovdiv, Bulgaria. Representatives of 20 countries (Bulgaria, Kazakhstan, China, Turkey, Russia, Spain, Lithuania, India, United Kingdom, Italy, Germany, Serbia, Romania, Latvia, Malta, USA, Brazil, Iran and Macedonia) sent their works to the conference. Some of the reports (33 works) have been selected and are published after international peer-review in the present Special Issue of the journal “Bulgarian Chemical Communications”.

It is our pleasure to be guest editors of the presented articles, which focus on new international scientific results in the field of Alternative Energy Sources, Materials and Technologies (Solar and Hybrid Thermal Systems, Energy Efficiency, Materials Science, Food Engineering and Technologies, and Biotechnologies).

Prof. Aleksandar Georgiev, PhD (European Polytechnic University, Pernik, Bulgaria)

Assoc. Prof. Daniela Dzhonova-Atanasova (Bulgarian Academy of Sciences, Sofia, Bulgaria)

Guest editors of the present Special Issue

SOLAR AND HYBRID THERMAL SYSTEMS

Numerical heat transfer simulation of solar-geothermal hybrid source heat pump in Kazakhstan climates

G. Saktashova¹, A. Aliuly^{1,2}, Ye. Belyayev^{1,2*}, M. Mohanraj³, Rao Martand Singh⁴

¹Department of Mechanics Al-Farabi Kazakh National University, 71 Al-Farabi Ave., 050040 Almaty, Kazakhstan

² Department of Applied Mechanics and Foundations Designed Machines, Satbayev University, 22a Satbayev Str, 050013 Almaty, Kazakhstan

³ Department of Mechanical Engineering, Hindusthan College of Engineering and Technology, Pollachi Main Road, Coimbatore – 641 032, India

⁴ Department of Civil and Environmental Engineering, Geotechnical Engineering, University of Surrey, 388 Stag Hill, Guildford GU2 7XH, UK

A numerical energy balance model has been proposed in this work for predicting the thermal performances of solar-geothermal hybrid source heat pumps in winter climates of Kazakhstan. The numerical simulation was performed for the year round continental climate conditions. The energy balance model has been developed based on first law of thermodynamics. The proposed heat pump configuration is working in solar mode during sunshine hours and geothermal model during off sunshine hours. Moreover, the system is operating in solar-geothermal hybrid model to meet the evaporator load during insufficient availability of solar and geothermal sources. The energy performance comparison between conventional geothermal source and solar-ground hybrid source heat pump configurations has been made. The influences of solar intensity, ambient temperature, heat pump operating temperatures are discussed.

Keywords: Solar-geothermal source hybrid heat pump; Heat transfer; Numerical simulation.

INTRODUCTION

Heat pump is an energy efficient device due to its capability to deliver more heat output than the work input [1]. The performance of the heat pump systems are improved using renewable energy sources such as, ambient, solar, geo-thermal and its hybrid forms [2]. The continental climate regions are facing with large fluctuations of annual ambient temperature during the day time in winter and drops below -20 °C. The availability of solar radiation and length of sunshine is not sufficient during winter in the continental climatic conditions like, Kazakhstan, Russia, China, Ukraine, Uzbekistan and North America. Hence, it is necessary to integrate the solar and geothermal hybrid sources of energy with the heat pump systems to improve the performance of heat pump systems. Many research and developments have been progressed with solar-geothermal heat pump system in the continental climatic regions, which are summarized in earlier literature reviews [3-5].

From recent studies in the field of solar-geothermal hybrid source heat pumps, it can be noted the following papers [6-14]. In [6] an optimization method for the design and operation of a hybrid solar geothermal source heat pump

was described. The system studied consists of solar thermal collectors, borehole heat exchanger, a heat pump, natural gas boiler and a stratified daily storage tank. In [7] 2000 sets of performance data collected from solar-assisted geothermal source heat pump systems that keep operating over 20 years were simulated. The thermal performance of a solar-geothermal source heat pump system operated in different dual heat source coupling modes were studied experimentally [8]. The average unit COP and collecting efficiency for the solar and geothermal source combination mode are 3.61 and 51.5%. The suitable collector area and geothermal source heat exchangers number are found to be 80 m² and 9, respectively. To eliminate the effect of geothermal thermal imbalance and minimizing system lifetime cost, paper [9] focuses on combining a geothermal source heat pump system with a solar thermal array. Three buildings were investigated for use with the solar-assisted geothermal source heat pump system, which had heating-to-cooling load ratios of 20.4:1, 8.6:1, and 1.2:1. Numerical modelling of transient soil temperature distribution for horizontal geothermal heat exchanger of geothermal source heat pump was presented in [10]. When the system is operated using the geothermal source heat pump at the end of the 10-year heating period, the

* To whom all correspondence should be sent:
yerzhan.belyayev@gmail.com

average soil temperature in solution domain and soil temperature around the pipe are found to decrease by approximately 2.5 °C, 0.7 °C for $Q_{\max}=21$ W/m, respectively. The decrease in these temperatures will increase if the heat drawn from the soil per unit pipe length increases. A solar photovoltaic/thermal-geothermal source heat pump was proposed in [11] to solve the problems of energy shortage and high energy-consuming buildings. According to the results photovoltaic/thermal-geothermal source heat pump system can reduce the temperature of photovoltaic/thermal modules as high as 10 °C, and improve the efficiency of electricity production by 25%, simultaneously with average COP equal to 3. Combined operation of solar thermal and geothermal source heat pump was applied in [12]. According to the results the assistant of solar thermal, heat pump could work temporarily, with a COP of 5.2 in the day. A hybrid solar geothermal source heat pump system was presented in [13]. 32% of the electrical energy consumption in the hybrid solar geothermal source heat pump system could be saved if the load circulation pump was turned off when no fan-coil was running, rather than always keeping it running at all times. Exergy analysis of a hybrid ground-source heat pump system was conducted in [14]. The true exergy performance of the system in heating mode (~30%) is twice as high as for cooling mode (~15%), while the natural exergy performance is considerably better in cooling mode (~26% to~3%).

The cited literature confirmed that, many research and development initiatives have been already progresses on solar-geothermal heat pump systems. However, there is no specific work has been reported on Kazakhstan climatic conditions. Hence, a numerical heat transfer model has been developed for solar-geothermal hybrid heat pump system for the climatic conditions of Almaty in Kazakhstan. In addition, the influence of solar radiation, ambient temperature and heat pump operating temperatures (condenser and evaporator) were discussed.

DESCRIPTION OF THE HYBRID SYSTEM

The schematic illustration of solar-geothermal source hybrid heat pump (SGSHHP) used for space heating and domestic hot water applications is shown in Fig. 1. The SGSHHP consists three circuits namely, solar and geothermal hybrid source circuit I, heat pump circuit II and water heating III. The heat pump circuit II consists of all

the basic components such as, compressor 6, condenser 3', expansion valve 7 and plate type evaporator 3. In addition, the accessories such as, sight glass, liquid receiver, filter-drier have been used to enhance the performance of the system. The pressure and temperature controls have been used to control the system operating parameters. The solar-geothermal circuit I consists of two solar thermal collectors 1, geothermal heat exchangers 4, two centrifugal pumps 5, 5' and solenoid flow control valves 2, 2', 2''. The hot water circuit III consists of pump 5', hot water storage tank 8, plate type heat exchanger 3', room radiators 9 and hot water utilization 9'.

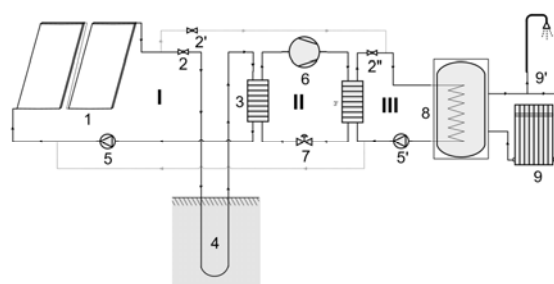


Fig.1. Solar-geothermal hybrid source heat pump

The system is operating in following two modes: (i) solar thermal mode and (ii) solar-geothermal hybrid heat pump mode. In solar thermal mode, the harvested solar energy through the solar collectors is directly transferred and stored in hot water storage tank for domestic water heating and space heating applications using ethylene glycol. In the solar-geothermal hybrid heat pump mode, the harvested solar energy is enhanced with the geothermal source heat exchanger. In heat pump mode, the ethylene glycol is circulated through the solar collectors for harvesting the solar energy and the circulated through the geothermal heat exchangers for extracting the geothermal energy. The combined solar-geothermal hybrid source is used in the evaporator of a heat pump. The compression heat pump absorbs the solar-geothermal heat and enhance to the room space heating requirements.

During peak sunshine hours, the solar energy is harvested by solar collectors and transferred directly to the storage tank. During lean and off sunshine hours, the hybrid forms solar energy (harvested in the solar collectors) and geothermal heat energy (energy extracted by geothermal heat exchangers) are utilized in the evaporator of a heat

pump for further enhancement. The flow of ethylene glycol through the solar collectors and geothermal heat exchangers are controlled by a solenoid direction control valves. In the daytime, when solar radiation is available, the excess heat obtained by the working fluid from solar collectors heats the soil around the ground source heat exchanger, thereby increasing the thermal potential of the soil. At night, in the absence of solar radiation, the working fluid after the evaporator 3 enters the ground source heat exchanger through the solar collectors, where the heat loss due to good insulation of the absorber is insignificant.

MATHEMATICAL MODEL

The mathematical model contains three basic equations: two-dimensional heat transfer equation for a solar thermal collector (1), which includes a main panel and a copper coil; energy conservation equations for the flow of a heat transfer fluid (antifreeze) in a solar collector tube (8) and in a vertical type geothermal source heat exchanger (9).

The two-dimensional heat transfer equation of a thermal collector. The thermal collector consists of two elements: copper coil, copper plate (absorber). By neglecting the thermal resistance at the contact surface, the temperature of these two elements is assumed to be the same on any reference volume. The equation of thermal conductivity of each control volume with a concentrated mass m_c , specific heat C_c and thermal conductivity λ_c is written in the form:

$$\begin{aligned} m_c C_c \frac{\partial T_c}{\partial t} = & G(\tau\beta)_c A_c + \alpha_{a-c} A_c (T_a - T_c) + \\ & + \alpha_{r,a-c} A_c (T_{sky} - T_c) + \alpha_f A_f (T_f - T_c) + \\ & + A_c \frac{T_a - T_c}{R_b} + \lambda_{c,y} l_{c,y} A_c \frac{\partial^2 T_c}{\partial y^2} + \lambda_{c,z} l_{c,z} A_c \frac{\partial^2 T_c}{\partial z^2} \end{aligned} \quad (1)$$

where G is solar radiation; $(\tau\beta)_c$ - effective absorptivity of the thermal collector; α_{a-c} and $\alpha_{r,a-c}$ - coefficients of convective and radiative heat transfer between the collector and the environment; R_b - thermal resistance between the back side of the heat collector and the environment; $l_{c,y}$ and $l_{c,z}$ - effective thickness along the Y and Z directions, respectively.

The above parameters are given by:

$$(\tau\beta)_c = \frac{\tau_c \beta_c}{1 - (1 - \beta_c) \cdot r} \quad (2)$$

$$\alpha_{a-c} = 2.8 + 3.0 \cdot u_{wind} \quad (3)$$

$$\alpha_{r,a-c} = \varepsilon_c \sigma (T_c^2 + T_{sky}^2) (T_c + T_{sky}) \quad (4)$$

where $(\tau\beta)_c$ - absorptivity of the solar collector absorber; τ_c and r - transmissivity and reflective capacity of the absorber; u_{wind} - wind speed; T_{sky} - sky temperature, which defined as

$$T_{sky} = 0.0552 T_a^{1.5} \quad (5)$$

$$\tau_c = \frac{1 - r}{1 + r} \quad (6)$$

$$r = \frac{\sin^2(\theta_1 - \theta_2)}{\sin^2(\theta_1 + \theta_2)} + \frac{\tan^2(\theta_1 - \theta_2)}{\tan^2(\theta_1 + \theta_2)} \quad (7)$$

where θ_1 and θ_2 - the angles of incidence and refraction of sunlight.

Equations of energy conservation for working fluid (antifreeze) flow. The process of transfer of the working fluid in the coil of the evaporator and in the tube of the geothermal heat exchanger can be described by a mathematical system of partial differential equations, which is based on the laws of conservation of energy of the fluid. The following assumptions were made:

- working fluid flow is one-dimensional and incompressible;
- the change of the kinetic and potential energy in the energy equation is neglected.

With the above assumptions, a simplified model of the flow of working fluid can be written as:

Energy conservation equation of working fluid

$$m_f C_f \frac{\partial T_f}{\partial t} + m_f C_f u \frac{\partial T_f}{\partial z} = A_f \alpha_f (T_c - T_f) \quad (8)$$

$$m_f C_f \frac{\partial T_f}{\partial t} + m_f C_f u \frac{\partial T_f}{\partial z} = A_f \frac{(T_g - T_f)}{R_{g-f}} \quad (9)$$

where m_f – fluid mass, C_f – specific heat, α_f – heat transfer coefficient in the solar collector tube, R_{g-f} – thermal resistance between the working fluid and the environment (ground).

$$R_{g-f} = \frac{l_{U-pipe}}{\lambda_{U-pipe}} \quad (10)$$

where l_{U-pipe} – the thickness of pipe wall, λ_{U-pipe} – thermal conductivity of pipe wall. The working fluid and ground temperature change along the U-pipe heat exchanger. Instead of separately calculating the heat balance equation for the pipe wall, the influence of the pipe wall on the heat exchange between the soil and the working fluid was taken into account through the thermal resistance coefficient (10).

METHOD OF SOLUTION

In order to solve the above system of equations (1)-(10) it is necessary to set the initial temperature distribution of the heat collectors. In addition, it is necessary to set the input data for solar insolation, ambient temperature, physical properties of used materials and working fluid flow. In order to investigate the dynamic behavior of the thermal evaporator and working fluid a computer program in C++ has been developed.

The program begins with setting the necessary initial conditions for the physical parameters (Tab.1).

Table 1. System parameters

Density of absorber	ρ_c	8920 kg/m ³
Heat capacity of absorber	C_c	385 J/kg·K
Thermal conductivity of absorber	λ_c	401 W/m·K
Emissivity coefficient of absorber	ε_c	0.05
Absorptivity coefficient of absorber	β_c	0.95
Stefan-Boltzman coefficient	σ	$5.67 \cdot 10^{-8}$ W/m ² ·K ⁴
Heat transfer coefficient of working fluid	α_f	5.6 W/m ² ·K
Density of working fluid	ρ_f	1055 kg/m ³
Heat capacity of working fluid	C_f	3620 J/kg·K
Thermal conductivity of U-pipe material	λ_{U-pipe}	2.5 W/m·K

As the initial conditions for the solar collector temperature T_c , working fluid temperature T_f the ambient temperature was taken. On the ground surface, the temperature of soil is equal to ambient temperature. From the ground surface, the temperature of the soil varies up to 10 meters depth depending on the ambient temperature. After 10 meters of depth, the temperature of the ground is assumed equal to 10 °C.

Then the subprograms for calculating of solar collector absorber and working fluid temperatures distribution, for heat transfer coefficients and physical properties are called. This process is repeated until iteration is established.

RESULTS AND DISCUSSION

Using the above algorithm, the temperature of the heat collector and working fluid was calculated for the climatic conditions of Almaty, Kazakhstan. In the calculations, the corresponding data on solar radiation and ambient temperature were taken into account.

In Fig.2 monthly average solar radiation and ambient temperature are shown. From the data shown in Fig.2, it can observe that the average ambient temperature in Almaty is reached 273.15 K in the month of January and has its maximum value of 303.15 K in July (the dotted line in Fig.2). The average solar irradiance varies from 101.55 W/m² in December to 544.35 W/m² in June (the solid line in Fig.2).

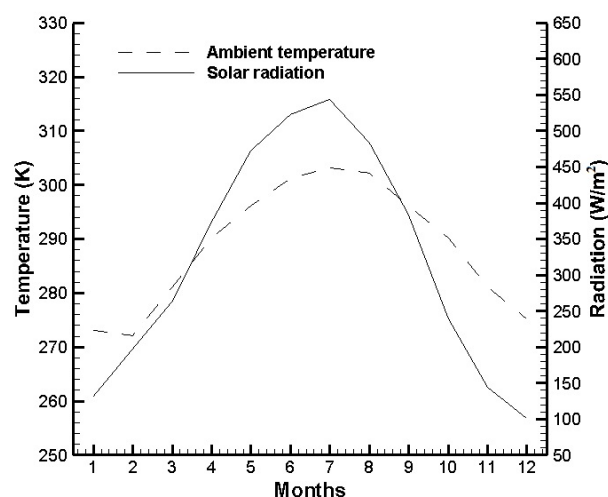


Fig.2. Seasonal solar radiation and ambient temperature data

The authors of the research have installed Vantage Pro2 Plus 6162C weather station, which provide meteorological data (wind speed, wind direction, air temperature, humidity, barometric

pressure, rainfall, rainfall intensity, UV, solar radiation). In Fig.3 the daily solar radiation and ambient temperature variation for different days are shown.

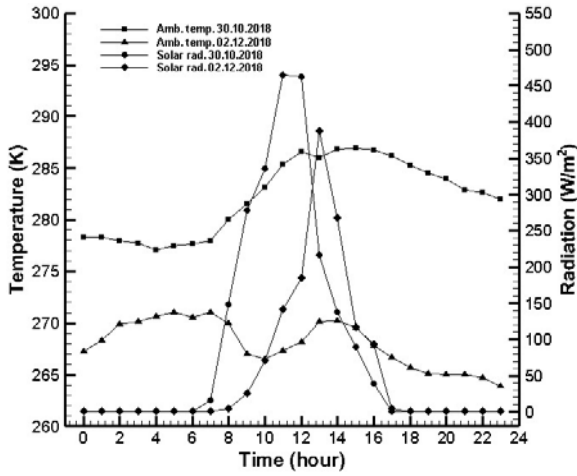


Fig.3. Daily solar radiation and ambient temperature data

Fig.4 shows the temperature variation of the solar collector as a function of the months according to equation (1).

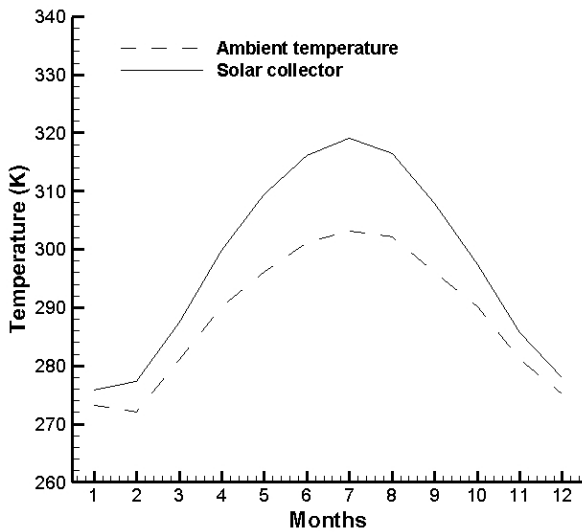


Fig.4. Seasonal temperature variation in the solar collector

From the numerical results presented in Fig.4 the maximum temperature of the solar thermal collector is achieved in the summer season. The behavior of temperature profiles is similar to the behavior of solar radiation, shown in Fig.2. The figure shows that the temperature of the thermal collector increases in summer, reaching a maximum in July 319.06 K. The difference between the temperatures of the absorber and the

environment is 2.77 K in the month of January and 15.91 K in the month of June. This effect is due to the different values of solar radiation in different season.

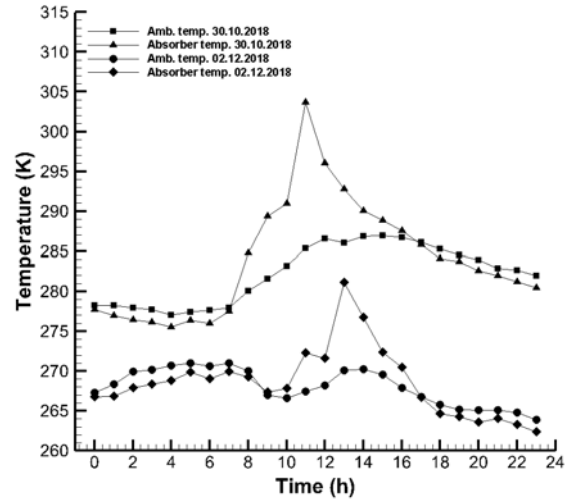


Fig.5. Daily temperature variation in the solar collector

According to the Fig.5 for the daily absorber plate temperature variation same behavior as in seasonal case is observed. During nighttime, without solar radiation and with the cold sky temperature, absorber plate temperature is 1-2% lower, than ambient temperature. This is an indicator that, in the absence of solar radiation, heat losses from the solar collector are small.

Fig.6 shows the daily temperature variation of the working fluid at the outlet of the solar collector tube and the geothermal heat exchanger depending on the hours according to the system of equations (8) - (9) for 30.10.2018.

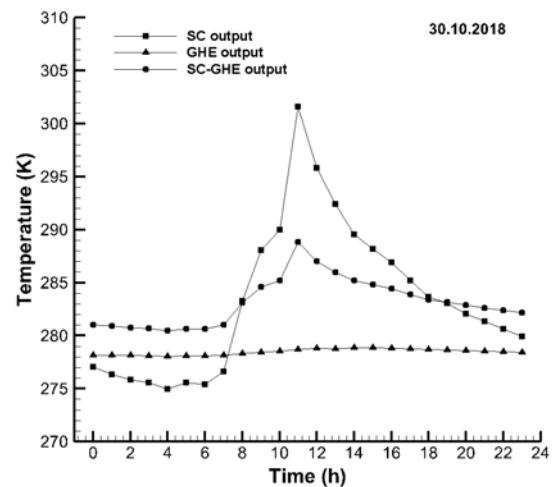


Fig.6. The temperature of working fluid in solar and geothermal collectors (30.10.2018)

Fig.7 shows the same daily temperature variation for 02.12.2018.

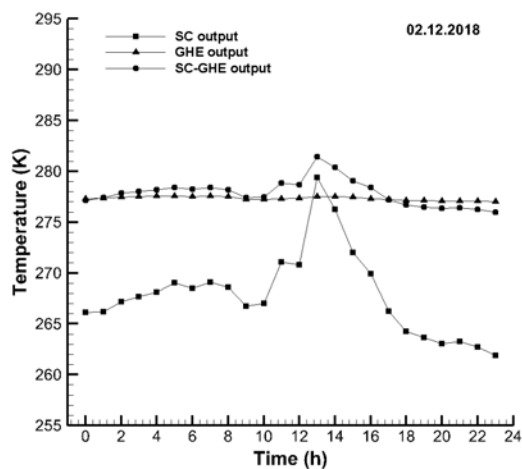


Fig.7. The temperature of working fluid in solar and geothermal collectors (02.12.2018)

From Fig.6-7 it can be seen that the working fluid temperature at the outlet of the solar collector depends on the ambient temperature and solar radiation. At the same time, the temperature of the working fluid at the outlet of the geothermal source heat exchanger is independent of the ambient temperature. During the daytime with the consistent use of a ground collector and solar collector, excessive solar energy is transferred to heat the ground, and in the absence of solar energy (nighttime), this heat from the ground is used for the heat pump evaporator. To obtain high heat pump COP and +50 - +60 °C in heating circuit (space heating and DHW) with a high volumetric compressor efficiency, a positive temperature of +5 - +10 °C is sufficient for the refrigerant evaporation. Therefore, the combined use of two low-potential heat sources – solar and ground collectors is recommended for a heat pump evaporator in continental climatic conditions. In the proposed SGSHP configuration of the heat pump, the ground heat potential is constantly maintained by solar collectors.

Also, according to the SGSHP configuration the system can operate in energy efficient mode, where with sufficient solar radiation, the heat pump circuit can be switched off, and system operate as direct solar water heating.

Two-dimensional results of the temperature distribution in the solar thermal collector absorber

plate were also presented in Fig.8. The grid size is 50x100 (Fig.8a).

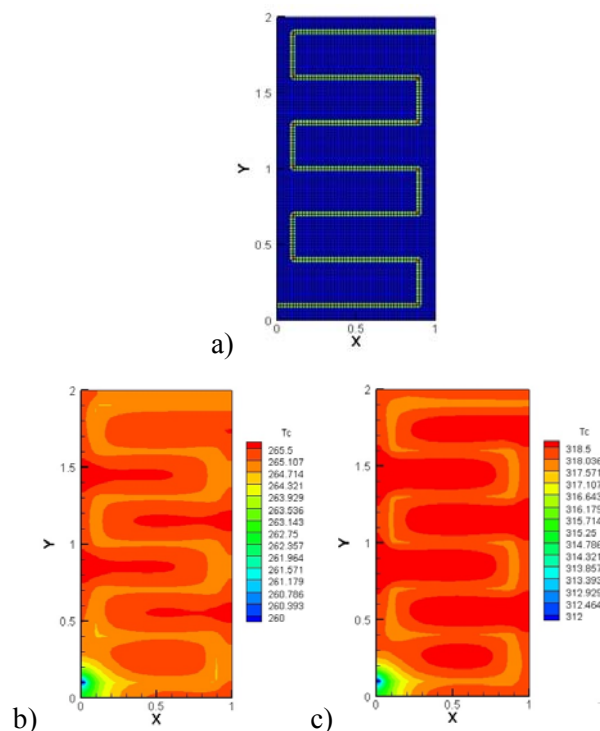


Fig.8. Temperature distribution in the solar thermal collector absorber plate (a – numerical grid, b –January month, c – July month)

CONCLUSIONS

Numerical estimation of hybrid solar-geothermal source heat pump thermal performance in terms of solar thermal collector and geothermal source heat exchanger operation for meteorological conditions of Almaty, Kazakhstan has been conducted. A mathematical model, numerical algorithm and computer program for calculating of solar collector and geothermal source heat exchanger performance parameters has been developed. Numerical calculations showed the efficiency of using a hybrid solar-geothermal heat source for heat pump operation.

ACKNOWLEDGEMENTS

This research is supported by: the Ministry of Education and Science of the Republic of Kazakhstan project “AP05132668 Development of High-Lift Solar Assisted Auto-Cascade Heat Pump for Residential Heating in the Continental Climate” and the Science Committee of the Ministry of Education and Science of the Republic of Kazakhstan and World Bank under

the “Fostering Productive Innovation” Project APP-SSG-17/0280F titled “Cascade Solar Assisted Heat Pump for Space Heating and Domestic Hot Water in Continental Climate Regions”.

NOMENCLATURE

A	-	surface area, m ²
C	-	specific heat, J/(kg K)
G	-	solar irradiance, W/m ²
l	-	effective thickness, m
m	-	mass, kg
R	-	thermal resistance, K/W
r	-	reflectivity, –
T	-	temperature, K
t	-	time, s
u	-	flow velocity, m/s

Subscripts

a	-	air; ambient
b	-	back
c	-	thermal collector
r	-	radiation
f	-	working fluid
g	-	ground

Greek letters

α	-	heat transfer coefficient, W/(m ² K)
β	-	absorptivity, –
ε	-	emissivity, –
θ	-	angle, degree
λ	-	thermal conductivity, W/(m K)
ρ	-	average density, kg/m ³
σ	-	Stefan–Boltzman constant, W/(m ² K ⁴)
($\tau\beta$)	-	effective absorptivity

REFERENCES

- [1] Ito S, Miura N, and Takano Y. Studies of heat pumps using direct expansion type solar collectors. *Journal of Solar Energy Engineering, ASME Transactions* **127**(1), 60-64 (2005).
- [2] Ozgener O and Hepbasli A. Modeling and performance evolution of ground source (geothermal) heat pump systems. *Energy and Buildings* **39**(1), 66-75 (2007).
- [3] Ozgener O., Hepbasli A. Performance analysis of a solar assisted ground-source heat pump system for green house heating: An experimental study. *Building and Environment* **40**(8), 1040-1050 (2005).
- [4] Mohanraj, M., Belyayev, Ye., Jayaraj, S., Kaltayev, A. Research and developments on solar assisted compression heat pump systems - A comprehensive review (Part A: Modeling and modifications). *Renewable and Sustainable Energy Reviews* **83**, 90-123 (2018).
- [5] Mohanraj, M., Belyayev, Ye., Jayaraj, S., Kaltayev, A., Research and developments on solar assisted compression heat pump systems - A comprehensive review (Part-B: Applications). *Renewable and Sustainable Energy Reviews* **83**, 124-155 (2018).
- [6] Miglani, S., Orehousing, K., Carmliet J. Design and optimization of a hybrid solar ground source heat pump with seasonal regeneration. *Energy Procedia* **122**, 1015-1020 (2017).
- [7] Zhuang, Zh., Zhu, Q., Song, J., Zhang, X., Li, H. Study on the methods for predicting the performance of a hybrid solar-assisted ground-source heat pump system. *Procedia Engineering* **205**, 3879–3886 (2017).
- [8] Yang, W., Zhang, H., Liang X. Experimental performance evaluation and parametric study of a solar-ground source heat pump system operated in heating modes. *Energy* **149**, 173-189 (2018).
- [9] Fine, J. P., Nguyen, H. V., Friedman, J., Leong, W. H., Dworkin, S. B. A simplified ground thermal response model for analyzing solar-assisted ground source heat pump systems. *Energy Conversion and Management* **165**, 276-290 (2018).
- [10] Kayaci, N., Demir, H. Numerical modelling of transient soil temperature distribution for horizontal ground heat exchanger of ground source heat pump. *Geothermics* **73**, 33-47 (2018).
- [11] Cai, J., Quan, Zh., Li, T., Hou, L., Zhao, Y., Yao M. Performance study of a novel hybrid solar PV/T ground-source heat pump system. *Procedia Engineering* **205** 1642–1649 (2017).
- [12] Li, H., Xu, W., Yu, Zh., Wu, J., Yu, Zh. Discussion of a combined solar thermal and ground source heat pump system operation strategy for office heating. *Energy and Buildings* **162**, 42-53 (2018).
- [13] Wang, E., Fung, A. S., Qi, Ch., Leong, W. H. Performance prediction of a hybrid solar ground-source heat pump system. *Energy and Buildings* **47**, 600-611 (2012).
- [14] Menberg, K., Heo, Y., Choi, W., Ooka, R., Choudhary, R., Shukuya, M. Exergy analysis of a hybrid ground-source heat pump system. *Applied Energy* **204**, 31-46 (2017).
- [15] Aliuly, A., Mohanraj, M., Belyayev, Ye., Jayaraj, S., Kaltayev, A. Numerical modelling of photovoltaic thermal evaporator for heat pumps. *Bulgarian Chemical Communications* **48E**, 135 - 139 (2016).

Electrical and thermal output characteristics investigation on a solar trough concentrating PV/T system

Jinkang Wang, Xu Ji*, Qiang Wang, Rongkang Fan, Guoliang Li, Ming Li

**Yunnan Normal University, College of Energy and Environmental Science, 768 Juxian Str, Kunming 650500, China*

A solar through concentrating photovoltaic/ thermal system with 1.8m² concentrator was constructed and characterized. The space silicon solar cells were employed as the electricity output unit. The electrical output characteristic and the thermal output characteristic of the system were thoroughly investigated when the PV/T composite receiver was placed ahead of the focal plane at different defocus distances. The effect of the aperture width of the concentrator on the performance of solar cells was also investigated. The maximum output power of solar cells was 22.37W and the solar cells' efficiency was 2.74% when the PV/T composite receiver was 5cm ahead of the focal plane and the aperture width was 157cm. The output power 17.92W and the maximum efficiency 5.71% of solar cells were achieved when the PV/T composite receiver was 3cm ahead of the focal plane and the aperture width was 57cm. The maximum system thermal efficiency of 58.9% was reached when the PV/T composite receiver was 1cm ahead of the focal plane and the aperture width was 157cm. With the condition, the temperature rise of the working medium was 0.68°C and the solar cells' efficiency was 2.2%.

Keywords: solar trough concentrator, PV/T, electrical output characteristic, thermal output characteristic

INTRODUCTION

Photovoltaic power generation has become one of the important ways for the utilization of renewable energy. However, the low energy flux density and uneven distribution of solar irradiation have a negative impact on the performance and cost of photovoltaic power generation. The concentrating technology can significantly increase the energy flux density on the solar cells' surface and the power generation per unit area solar cell, however it makes the solar cells' temperature rise and deteriorates the efficiency. The forced circulation of the cooling working fluid on the back of solar cells can maintain the electrical performance of solar cells, and recover the heat generated under the condition of solar concentration, thus improve the comprehensive utilization of solar energy and realize the combined heat and power generation.

In the late 1970s and early 1980s, Russel [1,2], Florschuetz [3] and Hendrie [4], adopted firstly the forced circulation of the working fluid on the back of the solar panel to cool the solar cell and recover the heat energy. Dupevrat employed a simple 2D model to study some configurations of glazed PV/T collector, and selected the most appropriate concept configuration and suitable material properties [5]. Amrizal proposed a hybrid PV/T dynamic model to predict the power output in any climate [6]. Silva employed the modular environment of Simulink/

Matlab to model individual PV/T system components, and simulated hybrid PV/T systems [7]. Kumar analyzed the life cycle cost of a single slope passive and hybrid photovoltaic (PV/T) active solar stills, and estimated the payback periods [8]. Sok conducted outdoor experiments with a prototype PV/T water-heating system. The annual thermal and electrical performances were analyzed under the climatic conditions of Beijing [9]. Huang introduced the concept of primary-energy saving efficiency to evaluate a PV/T system, and demonstrated a good thermal efficiency of the solar PV/T collector made from a corrugated polycarbonate panel [10]. Bernardo proposed a complete methodology to characterize, simulate and evaluate concentrating PV/T system and experimentally determined the hybrid parameters [11]. Pei presented a heat pipe-type PV/T system and studied the performances of the system with/without glass cover. The glass-covered system had a higher average photothermal efficiency, however a lower photoelectric efficiency [12]. Shan proposed a dynamic performances modeling of a PV/T collector with water heating in buildings and concluded that the less series-connected PV modules, the lower inlet temperature of water and the higher mass flow rate of water resulted in the high photovoltaic efficiency [13]. Chaabane established a low concentrating PV system and a PV/T system, and tested their output performances in spring climatic condition of Tunisia [14]. Jiang established the optical model of a two-stage

* To whom all correspondence should be sent:
lmllldy@126.com

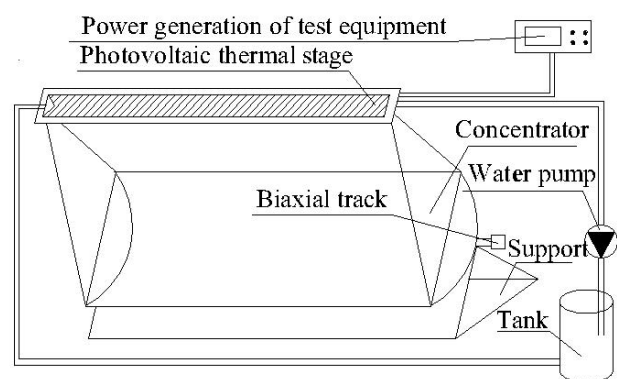
parabolic trough concentrating PV/T system based on spectral beam splitting technology. With the beam splitting filter, the heat load of the cells was reduced by 20.7%, and the overall optical efficiency was about 0.764 [15]. Francesco proposed a finite-volume model for a parabolic trough PV/T receiver, and carried out energetic and exergetic analyses [16,17]. Kalogirou proposed a model for analyzing the thermal performance of parabolic trough collector receiver [18]. Zhai proposed a small scale hybrid solar heating, chilling and power generation system. The evaluation of an annual energy and exergy efficiency under the climate of northwestern China found that the main energy and exergy loss were brought by the parabolic trough collector [19]. Khaled presented a new design of hybrid collectors for domestic air heating and electricity production, which gave good thermal and electric performances compared to the traditional hybrid collectors. Besides the guaranteed supply of electric power, the useful thermal power obtained was about 290 W while thermal efficiency was around 48% [20]. Karima designed different (PV/T) hybrid solar collectors and conducted outdoor test in Iraq climate conditions. The combined efficiency of collector model with double duct and single pass is higher than that of model with single duct and double pass and model with single duct and single pass [21]. Li characterized the electrical and thermal performances of a 2m² TCPV/T system with an energy flux ratio 10.27 and a 10m² TCPV/T system with an energy flux ratio of 20 [22-24]. Ji developed a two-stage PV/T system and studied energy comprehensive utilization of the system [25,26].

The paper developed a solar trough concentrating photovoltaic/thermal system (TCPV/T) with 1.8m² trough concentrator. The composite receiver with solar cells on its surface was placed on the focal plane, ahead of the focal plane to characterize the electrical and thermal output performance of the system. The effect of the aperture width of the trough concentrator on the performance of solar cells was also investigated.

EXPERIMENTAL SETUP

Fig.1 is the schematic diagram and photo of the solar trough concentrating PV/T system. The combined heating and power system is composed of trough concentrator, composite receiver, two axis sun tracking unit, pump for driving working fluid and water storage tank. The composite receiver is made of aluminium with small thermal resistance and good thermal conductivity. The

space single crystal silicon solar cell is adhered on the surface of the composite receiver by employing insulating and heat conduction double-sided tape. The trough concentrator driven by a two-axis sun tracking unit converged solar irradiation on the solar cells. The energy flux density on the solar cells increased significantly (the concentration ratio of the system 10.3). The working fluid - water is driven to flow through the back cavity of the composite receiver by a pump and carries away the produced heat. Therefore, the solar cells work at a relatively low temperature, and their efficiencies are improved. At the same time, the thermal energy at a certain temperature is output.



(a) Schematic view of PV/T system



(b) Picture of Solar trough concentrating PV/T system

Fig.1. Solar trough concentrating PV/T system

The area of the trough concentrator is 1.8m² (length 1.16m, aperture width 1.57m), the focal length is 1.06m, and the mirror optical efficiency is 0.7. The tracking accuracy of the dual axis tracking unit with photoelectric passive sensor, is 0.85. The electrical output unit is composed of 9 space silicon solar cell in series, each of which is 71mm×62mm, with short circuit current 1.45A and open circuit voltage 0.5V. The length of the composite receiver

is 80cm. TRM-2 and TRM-FD1 were respectively employed to record the meteorological data and the working fluid's temperatures in different positions. The solar direct radiation was recorded by direct radiation meter TBS-2-2 with the precision of 2%. The temperatures of the working fluid were sensed by the thermocouples with the precision of 0.2°C. The mass flow rate of the working fluid was measured by the turbine flowmeter with the precision of 1%. The air velocity transducer EC-9S (X) with the precision (0.3+0.03V) was adopted to measure the wind speed and wind direction. The above instruments are all produced by China Jinzhou Sunshine Tech. Co., Ltd. The Fluke infrared thermometer with the accuracy of 1% was used to measure the solar cells' temperature.

RESULTS AND DISCUSSIONS

In our PV/T system, the maximum power(P_m) and efficiency(η_{elec}) of solar cell can be obtained as,

$$P_m = I_{mp} V_{mp} \quad (1)$$

$$\eta_{elec} = \frac{P_m}{\mu A G_D} \quad (2)$$

Where, P_m is the maximum power; I_{mp} is the current corresponding to the maximum power; V_{mp} is the voltage corresponding to the maximum power; η_{elec} is solar cell efficiency; μ is the optical efficiency of the trough concentrator, 0.7; A is the effective area of the trough concentrator; and G_D is the direct solar radiation.

The instantaneous thermal efficiency (η_{th}) is obtained as,

$$\eta_{th} = \frac{\dot{m} c_p (T_o - T_i)}{A G_D} \quad (3)$$

Where, m is the mass flow rate of working fluid, C_p is the specific heat capacity of fluid at constant pressure, T_o is the temperature of water at outlet and T_i is the temperature of water at inlet.

Tab.1 is the output performance of solar cells on different defocus planes with different aperture widths of trough concentrator. On the same defocus plane, with the decrease of the aperture width of the trough concentrator, the efficiency of solar cells increases and the maximum output power decreases.

With the same aperture width of the trough concentrator, the output performance of solar cells enhances with the increase of the distance between solar cells' surface and focal plane. When the aperture width is 157cm, the maximum output

power increases from 20.45W to 22.37W, increased by 9.39% and the solar cells' efficiency increases from 2.20% to 2.74%, increased by 24.55%, with the increase of the defocus distance from 1cm to 5cm. When the aperture width is 117cm, the maximum output power increases from 19.04W to 22.21W, increased by 16.63%, and the solar cells' efficiency increases from 3.07% to 3.43%, increased by 11.73%, with the increase of the defocus distance from 1cm to 5cm. When the aperture width is 97cm, the maximum output power increases from 18.77W to 21.50W, increased by 14.53%, and the solar cells' efficiency increases from 3.29% to 4.12%, increased by 25.23%, with the increase of the defocus distance from 1cm to 5cm. When the aperture width is 77cm, the maximum output power increases from 17.95W to 21.90W, increases by 22.01%, and the solar cells' efficiency increases from 4.01% to 4.98%, increased by 24.19%, with the increase of the defocus distance from 1cm to 5cm. It results from that the larger the defocus distance is, the larger and the closer to the width of the space silicon solar cells the spot width is. The lower the concentration ratio is, the more uniform the energy flux on the solar cells' surface is. Therefore, the better output performance of the solar cells is achieved.

Table 1. Output performance of solar cells on different defocus planes with different aperture widths of trough concentrator

I	II	III	IV	V	VI
cm	cm	°C	w·m ⁻²	W	%
157	1	37	1057.2	20.45	2.20
	3	32	976	21.57	2.51
	5	25	929	22.37	2.74
117	1	53	947.4	19.04	3.07
	3	66	998	20.16	3.08
	5	40	987	22.21	3.43
97	1	46	1051	18.77	3.29
	3	57	1007	19.62	3.59
	5	40	961	21.50	4.12
77	1	39	1038.8	17.95	4.01
	3	58	996	19.41	4.52
	5	33	1019	21.90	4.98
57	1	30	1024.75	16.80	5.13
	3	56	983	17.92	5.71
	5	40	1016	17.03	5.25

I. Aperture width of trough concentrator, II. Distance between solar cells' surface and focal plane, III. Surface temperature of solar cell, IV. Solar direct radiation, V. Maximum power of solar cell, VI. Efficiency of solar cell

When the distance from the focal plane is 5cm and the aperture width is 157cm, the maximum power of solar cell reaches the maximum value of 22.37W, and the solar cells' efficiency is 2.74%.

When the distance from the focal plane is 3cm and the aperture width is 57cm, the solar cells' efficiency reaches the maximum value of 5.71%, and the maximum output power is 17.92W.

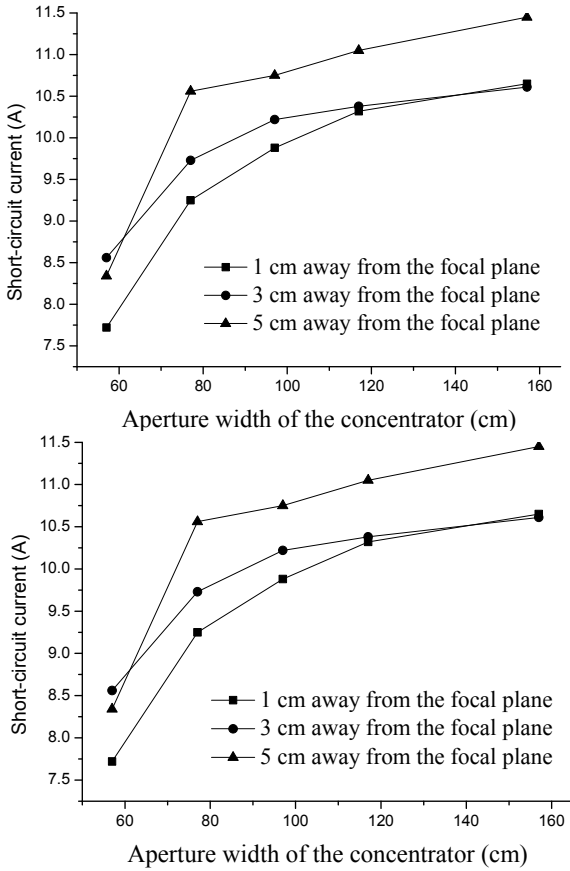


Fig.2. Short circuit current and maximum power

Fig.2 shows the short circuit current and the maximum power under different aperture widths of trough concentrator. The short-circuit current and the maximum power decrease with the decrease of the aperture width. The short-circuit current decrease from 10.65A to 7.72A with the decrease of the aperture width from 157cm to 57cm when the distance between the composite receiver and the focal plane is 1cm, and the maximum power decrease from 20.45W to 16.80W. The short-circuit current decrease from 10.61A to 8.56A with the decrease of the aperture width from 157cm to 57cm when the distance between the composite receiver and the focal plane is 3cm, and the maximum power decrease from 21.57W to 17.92W. The short-circuit current decrease from 11.45A to 8.34A with the decrease of the aperture width from 157cm to 57cm when the distance between the composite receiver and the focal plane is 5cm.

With the decrease of the aperture width of the trough concentrator, the maximum power overall

shows a downward trend, whereas it increases a little bit when the aperture width is 77cm, which is attributed to the influence of solar cells temperature and the irradiance. The drop rate of the maximum power is smaller than that of the short-circuit current. The reason is that the photocurrent decrease with the decrease of the aperture width, and the influence of photocurrent on power is smaller than that of series resistance of solar cells on power loss.

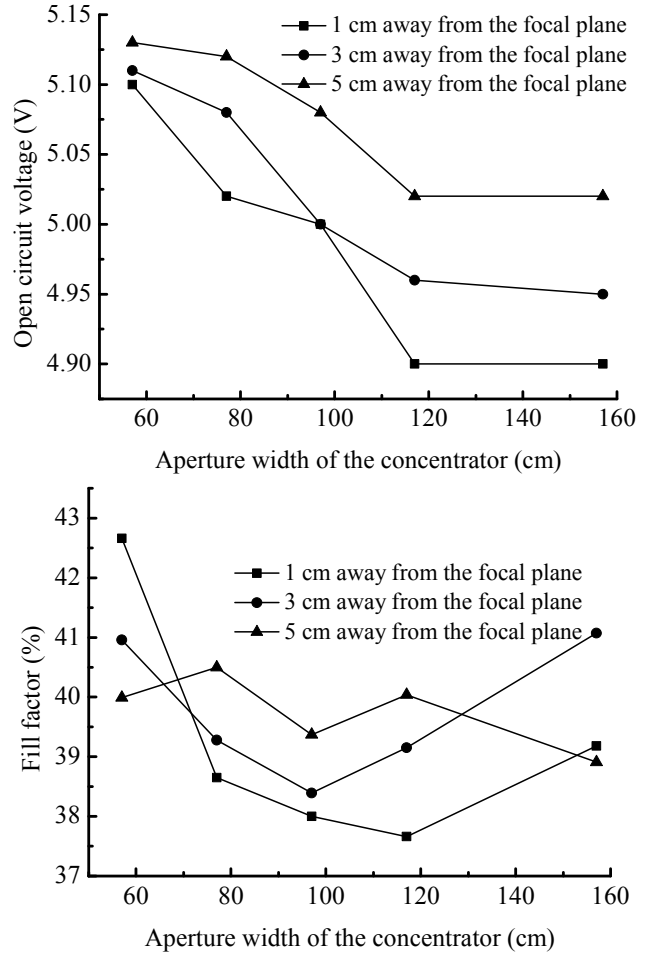


Fig.3. Open circuit voltage and fill factor

Fig.3 shows the open circuit voltage and the fill factor (the ratio of the product of current and voltage at the maximum output power point to the product of open-circuit voltage and short-circuit current can be obtained in the working curve of solar cells, which reflects the changing characteristics of the output power of solar cells with load) under different aperture widths of trough concentrator. When the distance between the composite receiver and the focal plane is 1cm, the open circuit voltage increase by 4.08% from 4.9V to 5.1V with the decrease of the aperture width

from 157cm to 57cm. When the distance between the composite receiver and the focal plane is 3cm, the open circuit voltage increased by 3.23% from 4.95V to 5.11V with the decrease of the aperture width from 157cm to 57cm. When the distance between the composite receiver and the focal plane is 5cm, the open circuit voltage increased by 2.19% from 5.02V to 5.13V with the decrease of the aperture width from 157cm to 57cm.

The maximum fill factor of 42.66% is obtained when the aperture width is 57cm and the distance between the composite receiver and the focal plane is 1cm. When the aperture width decreases from 157cm to 57cm, the open-circuit voltage increases by 4.08%, the short-circuit current decreases by 27.51%, thus the maximum output power decreases by 17.86%.

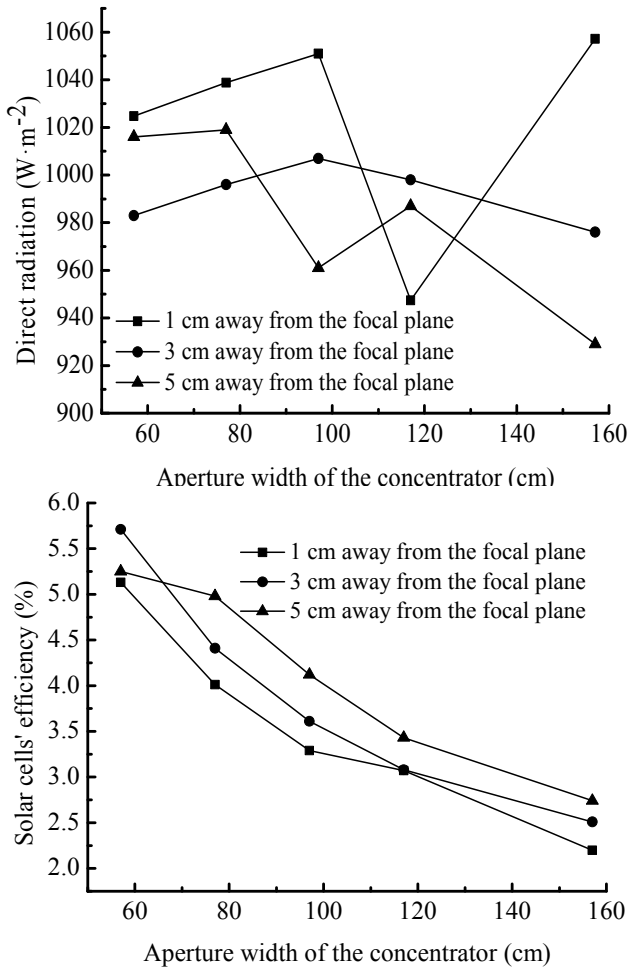


Fig.4. Direct radiation and solar cells' efficiency

Fig.4 shows the direct radiation and the solar cells' efficiency under different aperture widths of trough concentrator. The solar cells' efficiency decreases by 57.12% from 5.13% to 2.2% with the increase of the aperture width from 57cm to 157cm

when the distance between the composite receiver and the focal plane is 1cm. The solar cells' efficiency decreases by 56.04% from 5.71% to 2.51% when the distance between the composite receiver and the focal plane is 3cm. The solar cells' efficiency decreased by 47.81% from 5.25% to 2.74% when the distance between the composite receiver and the focal plane is 5cm.

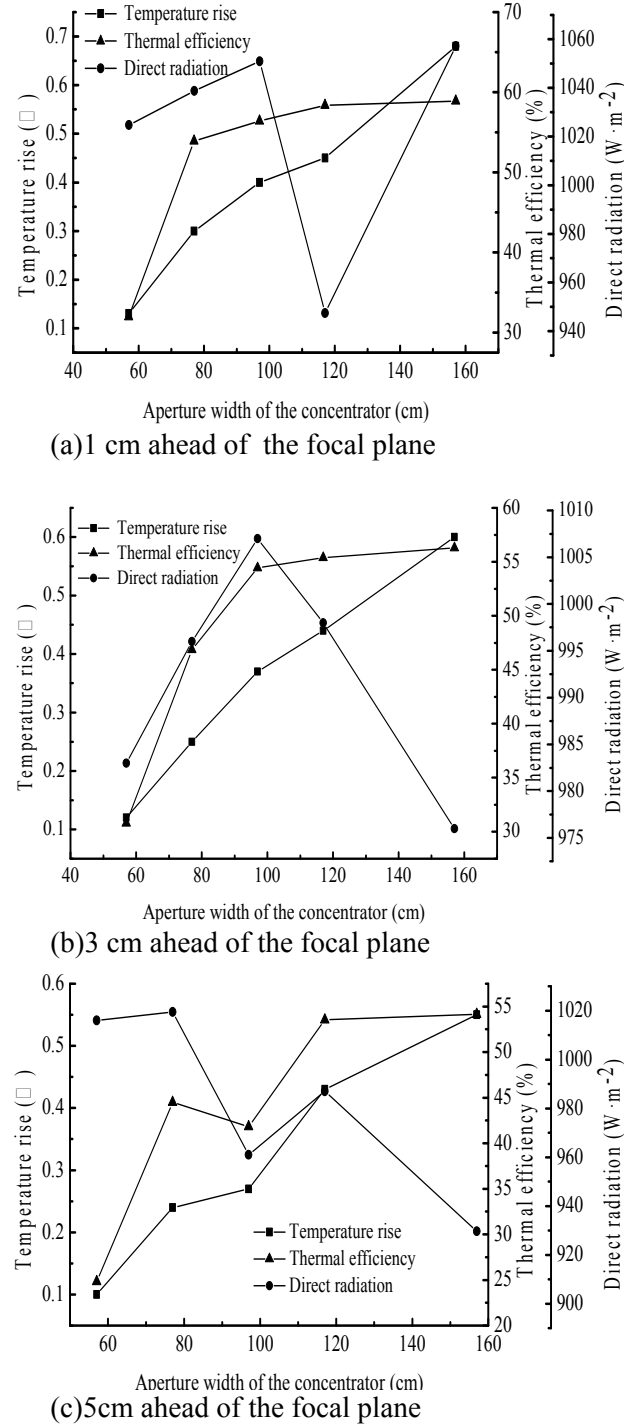


Fig.5. Thermal output characteristic of the PV/T system

The reason is that with the increase of the aperture width, the maximum peak energy flux density increases, the energy flux uniformity decreases and the solar cells' efficiency declines when the distance between the composite receiver and the focal plane is same.

Fig.5 shows the thermal output characteristic of the PV/T system. When the distance between the composite receiver and the focal plane is 1cm, the temperature rise of the cooling working fluid flowing through the back cavity of the composite receiver are 0.68°C, 0.45°C, 0.4°C, 0.3°C and 0.13°C when the aperture width are respectively 157cm, 117cm, 97cm, 77cm and 57cm. The system thermal efficiency of are 58.9%, 58.36%, 56.4%, 53.91% and 32%, respectively as shown in Fig.5(a). The temperature rise and the thermal efficiency decreases by 80.88% and 45.67%, respectively when the aperture width decreases from 157cm to 57cm.

When the distance between the composite receiver and the focal plane is 3cm, the temperature rise of the cooling working fluid are 0.6°C, 0.44°C, 0.37°C, 0.25°C and 0.12°C, respectively when the aperture width of mirror are respectively 157cm, 117cm, 97cm, 77cm and 57cm, and the system thermal efficiency are 56.29%, 55.4%, 54.45%, 46.86% and 30.79%, respectively as shown in Fig.5(b). The temperature rise and the thermal efficiency decreases by 80% and 45.3%, respectively when the aperture width decreases from 157cm to 57cm.

When the distance between the composite receiver and the focal plane is 5cm, the temperature rise of the cooling working fluid are 0.55°C, 0.43°C, 0.27°C, 0.24°C and 0.1°C, respectively when the aperture width are respectively 157cm, 117cm, 97cm, 77cm and 57cm, and the system thermal efficiency are 54.17%, 53.53%, 41.83%, 44.49% and 24.82%, respectively as shown in Fig.5(c). The temperature rise and the thermal efficiency of system decrease by 81.82% and 54.18%, respectively when the aperture width decreases from 157cm to 57cm.

The thermal efficiency decreases with the decrease of the aperture width when the distance between the composite receiver and the focal plane is the same. The reason is that the small aperture width would result in the small solar collection area and the small concentrating ratio of the system, thus both the energy flux density gathered on the surface of solar cells and the system thermal efficiency would decrease. The maximum thermal efficiency of 58.9% could be obtained and the temperature

rise of the cooling working fluid is 0.68°C when the distance between the composite receiver and the focal plane is 1cm and the aperture width is 157cm.

CONCLUSIONS

The trough concentrating photovoltaic/thermal system with 1.8m² concentrator is established with the space silicon solar cells as the electricity output unit, and the experiments are conducted. Experimental results indicate that the maximum output power of solar cells is 22.37W and the solar efficiency is 2.74% when the distance between the composite receiver and the focal plane is 5cm and the aperture width of the trough concentrator is 157cm. The maximum output power of solar cells is 17.92W. The maximum solar cells' efficiency of 5.71% could be obtained when the distance between the composite receiver and the focal plane is 3cm and the aperture width is 57cm. The maximum system thermal efficiency is 58.9%, the temperature rise of the cooling working fluid is 0.68°C and the solar cells' efficiency is 2.2% when the distance between the composite receiver and the focal plane is 1cm and the aperture width is 157cm.

ACKNOWLEDGEMENTS

This work has been supported financially by the National Natural Science Foundation of China (Grant No. 51106134), which is gratefully acknowledged by the author.

REFERENCES

- [1] E.C. Kern and M.C. Russel, Combined photovoltaics and thermal hybrid collector systems. *Proc. 13th IEEE Photovoltaic Specialists, Washington*, 1153-1157 (1978).
- [2] Russell T., Beall J., Loferski J.J. et al., Combined photovoltaic/thermal collector panels of improved design. *Proceedings of IEEE photovoltaic specialists conference*, (1981).
- [3] LW. Florschuetz, Extension of the Hottel-Whillier model to the analysis of combined photovoltaic/thermal flat plate collectors. *Solar Energy*, **22**, 361-366 (1979).
- [4] Hendrie S.D., Photovoltaic/thermal collector development program-Final Report, Report MIT. Lincoln laboratory, 1982.
- [5] Dupevrat P, Menezo C, Rommel M, et al. Efficient single glazed flat plate photovoltaic-thermal hybrid collector for domestic hot water system. *Solar Energy*, **85** (7), 1457-68 (2011).
- [6] Amrizal N, Chemisana D, Rosell JI. Hybrid photovoltaic-thermal solar collectors dynamic modeling. *Applied Energy*, **101**, 797-807 (2013).

- [7] Silva RM, da Fernandes JLM. Hybrid photovoltaic/thermal (PV/T) solar systems simulation with Simulink/Matlab. *Solar Energy*, **84**, 1985-96 (2010).
- [8] Kumar S, Tiwari GN. Life cycle cost analysis of single slope hybrid (PV/T) active solar still. *Applied Energy*, **86**, 1995-2004 (2009).
- [9] E. Sok, Y. Zhuo, and S. Wang, Performance and Economic Evaluation of a Hybrid Photovoltaic/Thermal Solar System in Northern China. *World Academy of Science, Engineering and Technology*, **72**, 176-181 (2010).
- [10] B.J Huang, T.H Lin, W.C Hung, et al. Performance evaluation of solar photovoltaic/thermal systems. *Solar Energy*, **70**, 443-448 (2001).
- [11] L.R. Bernardo, B. Peters, H. Hakansson, et al. Performance evaluation of low concentrating photovoltaic/thermal system: A case study from Sweden. *Solar Energy*, **85**, 1499-1510 (2011).
- [12] Gang Pei, Tao Zhang, Huide Fu, et al. An Experimental study on a Novel Heat Pipe-Type Photovoltaic/Thermal System with and without a Glass Cover. *International Journal of Green Energy*, **10**, 72-89 (2013).
- [13] Feng shan, Lei Cao, Guiyin Fang. Dynamic performances modeling of a photovoltaic-thermal collector with water heating in buildings. *Energy and buildings*, **66**, 485—494 (2013).
- [14] Monia Chaabane, Wael Charfi, Hatem Mhiri, et al. Performance evaluation of concentrating solar photovoltaic and photovoltaic/thermal systems. *Solar Energy*, **98**, 315-321 (2013).
- [15] Shouli Jiang, Peng Hu, Songping Mo, et al. Optical modeling for a two-stage parabolic trough concentrating photovoltaic/thermal system using spectral beam splitting technology. *Solar Energy Materials and Solar Cells*, **94**, 1686-1696 (2010).
- [16] Francesco Calise, Adolfo Palombo, Laura Vanoli. A finite-volume model of a parabolic trough photovoltaic/thermal collector: Energetic and exergetic analyses. *Energy*, **46**, 283-294 (2012).
- [17] Francesco Calise, Laura Vanoli. Parabolic trough photovoltaic/thermal collectors: Design and simulation model. *Energies*, **5**, 4186-4208 (2012).
- [18] Soteris A. Kalogirou. A detailed thermal model of a parabolic trough collector receiver. *Energy*, **48**, 298-306 (2012).
- [19] H. Zhai, Y.J. Dai, J.Y. Wu, et al. Energy and exergy analyses on a novel hybrid solar heating, cooling and power generation system for remote areas. *Applied Energy*, **86** (9), 1395-1404 (2009).
- [20] Khaled Touafek, Mourad Haddadi, Ali Malek. Design and modeling of a photovoltaic thermal collector for domestic air heating and electricity production. *Energy and Buildings*, **59**, 21-28 (2013).
- [21] Karima E. Amori, Mustafa Adil Abd-AllRaheem. Field study of various air based photovoltaic/thermal hybrid solar collectors. *Renewable Energy*, **63**, 402-414 (2014).
- [22] M Li, X Ji, G L Li, et al. Performance investigation and optimization of the Trough Concentrating Photovoltaic/Thermal system. *Solar Energy*, **85** (5), 1028-1034 (2011).
- [23] M Li, G L Li, X Ji, et al. The performance analysis of the Trough Concentrating Solar Photovoltaic/Thermal system. *Energy Conversion and Management*, **52** (6), 2378-2383 (2011).
- [24] Ming Li, Xu Ji, Guoliang Li, et al. Performance study of solar cell arrays based on a Trough Concentrating Photovoltaic/Thermal system. *Applied Energy*, **88**, 3218-3227 (2011).
- [25] Lijun Tan, Xu Ji, Ming Li, Congbin Leng, Xi Luo, Haili Li, The experimental study of a two-stage photovoltaic thermal system based on solar trough concentration, *Energy Conversion and Management*, **86**, 410-417 (2014).
- [26] Xu Ji, Lijun Tan, Ming Li, Runsheng Tang, Yunfeng Wang, Xiangbo Song, Xi Luo, Improvement of Energy Comprehensive Utilization in a Solar Trough Concentrating PV/T System, *Journal of Energy Engineering*, **142** (4), 1-9 (2016).

Investigation of thermal behaviour of innovative Water Flow Glazing modular unit

M. Nikolaeva-Dimitrova*, M. Stoyanova, Pl. Ivanov, K. Tchonkova, R. Stoykov

Central Laboratory of Solar Energy and New Energy Sources, Bulgarian Academy of Sciences, Tzarigradsko chausses, Blvd. 72, 1784 Sofia, Bulgaria

Water Flow Glazing (WFG) modular unit is an innovative system specifically designed under the Horizon 2020 project "Industrial development of water flow glazing systems" (InDeWaG). It is a vertical-shaped module, which consists of a triple glazing sized 1.3 m x 3 m (one water/fluid chamber: 24 mm; one argon chamber: 16 mm). Each separate modular unit has an individual circulator incl. heat exchanger, a micro pump and a control unit. The circulator allows for flow rates up to 8 l/min per window. A novel spacer is specifically designed to assure a laminar flow of the fluid. The glazing and the circulator are enclosed by an aluminium frame. In this paper we investigate the thermal behaviour of WFG by using mathematical models covering all relevant physical processes - heat exchange, fluid flow dynamics, optical and structural behaviour as well as environmental influences. These models and a simulation tools integrated in the IDA ICE program are developed within the InDeWaG project. We obtain the most important parameters such as thermal transmittance of the glazing U , thermal transmittance between water chamber and indoor U_w , and also depending on climatic and operational conditions – the flow rate v_w , solar irradiation I , internal T_i and external temperatures T_e . The climatic and operational conditions for the location of Scientific Campus II of the Bulgarian Academy of Sciences in Sofia, Bulgaria are used.

Keywords: WFG thermal transmittance, solar heat gain coefficient, water flow rate, climatic conditions

INTRODUCTION

In modern life, the energy consumption is constantly rising and buildings are among the main consumers. This huge energy production leads to increasing harmful effects on the environment. This was the reason that in 2016 in Paris, France the Kyoto Protocol (2005) was replaced. The European initiatives have been focused on the energy consumption reduction in the EU 2020 strategy. Moreover, the Directive 2010/31/EU (2010) aims to improve the energy performance of buildings, taking into account outdoor climatic and local conditions, as well as indoor climate requirements and cost-effectiveness.

Energy consumption in buildings is approximately one third of the total energy consumption. This fact motivates architects and engineers to work towards improving energy efficiency and create innovative technologies for nearly Zero Energy Buildings (nZEB).

In modern architecture glazing takes up most of the facade surface and windows increasingly influence the energy efficiency of the buildings. A huge amount of electricity is consumed to provide a comfort room temperature through air conditioning but advance glazing technologies and materials can be used instead to reduce energy demands and improve indoor environment.

Windows are the biggest part of the commercial buildings and provide the light and thermal comfort, health [1], acoustic comfort [2] and photo-protection [3]. Processes in the windows can be divided into optical and thermal, although they are interconnected. The glass is a heat conducting material with a thermal conductivity that does not depend significantly on its composition. Its optical characteristics can be controlled by its appearance and by coating the low-emission [4] anti-reflective [5] or reflective coatings. Polymer films with different spectral properties in foil form are also used. Most often, the thermal insulation effect is achieved by used a closed gas layer between two glasses filled with air, argon, krypton or xenon but the limitations in this case are well known. Insulating materials from aerogels can be placed between the glasses [6, 7], but they are translucent not transparent. In order to eliminate convective and convective loss of windows, the gas between glasses is removed in the case of vacuum glazing [8, 9]. Heat exchange in this case is mainly radiant. For windows filled with Phase change materials, reliance is placed on the creation of an isothermal layer and the accumulation of heat, but they are not transparent [10, 11, 12]. Leakage of light through the windows except through shading devices is controlled by the use of Solar cell glazing or Smart windows. Big advantage of Solar cell glazing or PV glazing is the extraction of electricity from the window. Solar cell glazing products incorporating both transparent and translucent properties of glass

* To whom all correspondence should be sent:
miglena@phys.bas.bg

can be used in windows regulating daylight, solar thermal gain, solar shading, and solar energy gain by converting solar radiation into electricity [13, 14, 15, 16, 17]. Smart windows can be divided into three different categories: (thermo-, photo- and electro-) chromic materials, liquid crystals and suspended particle devices [18]. The electrochromic materials change its colour and optical properties when a small DC voltage is applied to it. Consequently, a change occurs in transmittance of the visible and near infrared spectra. There exists electrochromic glazing based on both inorganic and organic materials that allows user control on daylighting. ChromoGenics has an electrochromic foil that can be applied to existing windows, which shows the retrofit possibilities for smart windows [19]. The use of multilayer glass and the combination of various methods results in a lower U-value in the case of Multilayer glazing [20], Electrochromic vacuum glazing [21,22], Evacuated aerogel glazing. Evacuated aerogel glazing can be produced using monolithic silica aerogel [23] “Air sandwich” [24, 25].

The Water Flow Glazing (WFG) is an innovative system which harvests solar energy for various use at large scale. It could become a necessary element of the nZEB facade increasing the daylight use, variable ventilation/conditioning and individual comfort control. The main goal of the paper is to investigate the thermal behaviour of WFG units and the amount of usable heat transfer. Three different structural combinations of WFG are studied at the climate zone of Sofia, Bulgaria in order to estimate the proper one.

WFG MODULE PROTOTYPES

Based on construction and architectural design trends and due to its unique characteristics the water flow glazing - WFG module is a product of the future. It is a vertical-shaped modular unit which consists of a triple glazing sized 1.3m x 3m (one fluid/water chamber and an argon chamber), a circulator allowing fast flow rates up to 8 l/min per window, and a modular aluminium frame that encloses the glazing and the circulator. WFG is a combination of: Active Facade with integrated Monitoring and Control System, Radiant Panel providing cooling and heating, transparent solar collector, Sunlight protection window and/or an Internal Partition wall. In the paper three different WFG prototypes according to the position of the coating and the water chamber are investigated. Fig.1 presents the three combinations.

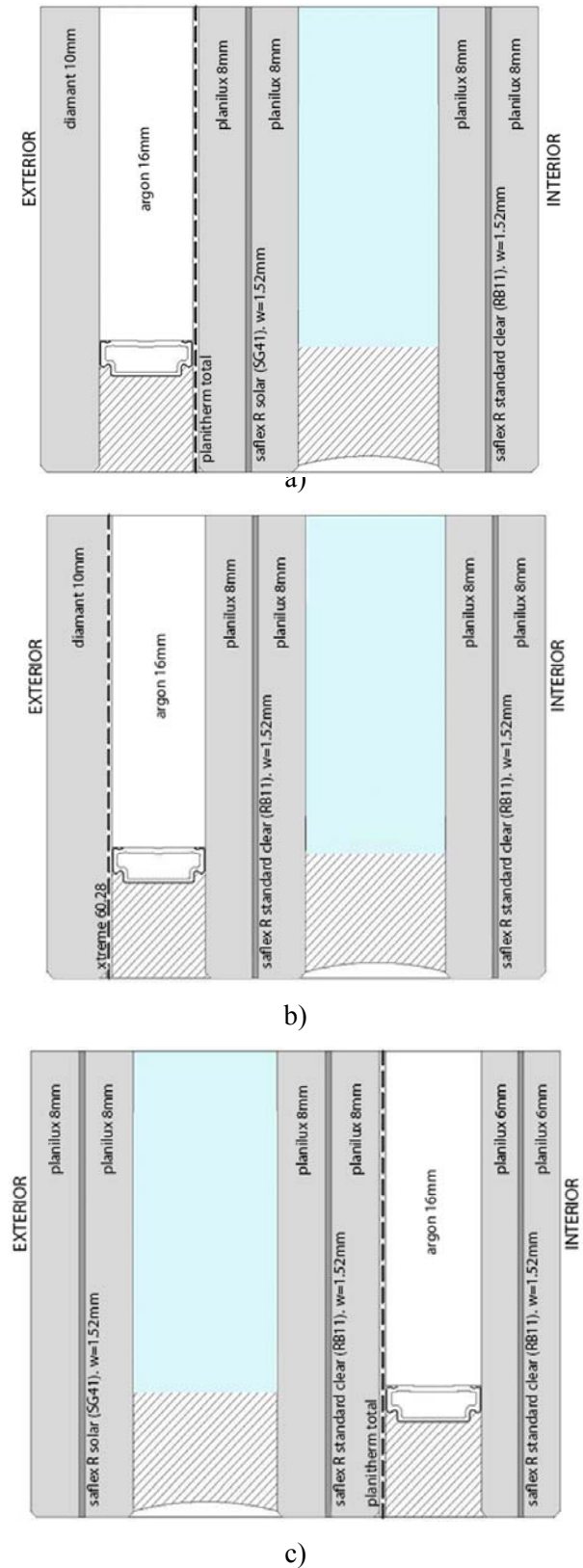


Fig.1. WFG modular units: a) HeatGlass, b) CoolGlass and c) iThermGlass.

HeatGlass and Cool Glass units have the following structure:

- front glass pane - tempered extraclear glass
- 16 mm Argon chamber
- 8 mm float glass
- 1,52 mm PVB Saflex R Solar (SG41)
- 24 mm Water chamber
- 8 mm float glass (Planilux)
- 1,52 mm PVB Saflex R Standard Clear (RB11)
- 8 mm float glass (Planilux)

The only difference between HeatGlass and CoolGlass is the position and the type of the coating layer. In the HeatGlass modular prototype the coating is after the Argon chamber. This is a low-emissivity coating which very effectively reflects long-wave heat radiation back into the water and so the heat loss from the water is minimized. At the same time this coating maximizes natural light transmission. In the CoolGlass module the coating is after the Argon chamber and before the water chamber. The CoolGlass module has a Cool-Lite Xtreme coating which is very transparent with very high light transmission. At the same time, it has low solar factor and blocks energy at the surface.

The iThermGlass layer configuration is different. The water chamber is on the outside and the Argon chamber on the inside. The water chamber is directly exposed to the outside climate conditions and the Argon chamber serves as thermal insulator. The Planitherm Total coating comes after the water chamber and before the Argon chamber. As in the HeatGlass module, it reflects long-wave heat radiation back into the water and it blocks the heat entering the Argon chamber.

SIMULATION MODEL

To predict the performance and behavior of the WFG, as well as to optimize the modular unit and its components, mathematical and simulation models were developed by UPM Spain [26]. These models cover all relevant physical processes – heat exchange, fluid flow dynamics, optical and structural behavior, as well as environmental influences. They are based on thorough research and modern computer simulation methods. The software model is successfully integrated under the existing and widespread software product IDA-ICE and describes the change of the thermal conductivity of the glazing due to varying fluid flow rate (g- and U-values) as well as the energy gain in the WFG. This allows calculations of

different energy management strategies at building level taking into account local meteo data, solar radiation, shading objects, wind speed and direction, type of the building, orientation, insulation and other parameters. Since the demonstrational Pavilion will be built in Sofia (Bulgaria), the assessment of the most appropriate and efficient type of WFG was made using local meteo data in the simulation. The input parameters for the simulations are:

- WFG position – vertical (90 degree).
- Module orientation - south.
- The results are simulated for area of 1 square meter.
- The climate model used in the program is based on real measurement data for the specific location of Sofia.
- Interior temperature is set at 20°C.
- Temperature of the water entering the WFG is set to 20°C for all seasons.
- Water flow rate is set to 2 liters per minute per square meter. Previous investigations [5] found that this is the optimal flow rate.

For only comparing the thermal performance of the different units, the temperature of the inflowing water was set at 20°C, which is the average of the optimal temperatures for each season. Depending on the energy strategy for different buildings with different profiles, this temperature could vary within 3 to 4 degrees above or below that value. The water flow rate is also subject to adjustment for the specific energy requirements of the building. The chosen rate of 2 l/min.m² is the required rate for transporting the absorbed radiation. Depending on the season and the adopted energy strategy, this rate could be reduced to achieve higher internal heat flux.

Based on these inputs, for each module type, the Water Heat Gain (which is measure of the thermal energy absorbed by the water in the water chamber) and Internal Heat Flux (measure of thermal energy transfer from the room to the module) are simulated according to the local weather conditions.

SEASONAL ANALYSIS AND RESULTS

In this section the thermal behaviour of WFG for one month per season is presented. Each month is selected based on the highest fluctuation in the climate model parameters. In the tables below the whole month is taken while the charts show the first 10 days of the month. The performed important simulation parameters are the following: Internal heat flux [W] – gives the room thermal

heat gain; R_{diffus} [W/m^2] – diffuse solar radiation; R_{direct} [W] – direct solar radiation; T_{ext} [$^{\circ}C$] – external temperature; Water heat gain [W] – gives the net energy power of the glazing per unit of the surface.

1. Spring – here the chosen month is May and the table presents the main simulated parameters for the three different WFG units illustrated on fig 1. In HeatGlass the water heat gains is more than 20 times higher than in the other two units and only in the case of iThermGlass it is negative. Also in the HeatGlass the internal heat flux is lowest, which means that we have minimum heat losses. There isn't significant difference between the internal heat fluxes for the investigated units because in the simulations the T_{inlet} is the same as T_{room} .

Table 1. Simulated results for spring month May

May		Internal heat flux	R diffus	R direct	T ext	Water gain,
		W/m^2	W/m^2	W/m^2	$^{\circ}C$	W/m^2
Heat Glass	mean	5.6	60.45	53	15.55	39.88
	min	3.82	41.04	0.21	12.44	10.31
	max	7.34	77.27	140.9	19.87	70.19
Cool Glass	mean	7.52	60.45	53	15.55	2.038
	min	6.96	41.04	0.21	12.44	-4.559
	max	8.08	77.27	140.9	19.87	8.56
iTherm Glass	mean	6.74	60.45	53	15.55	-2.799
	min	5.48	41.04	0.21	12.44	-59.54
	max	7.99	77.27	140.9	19.87	57.1

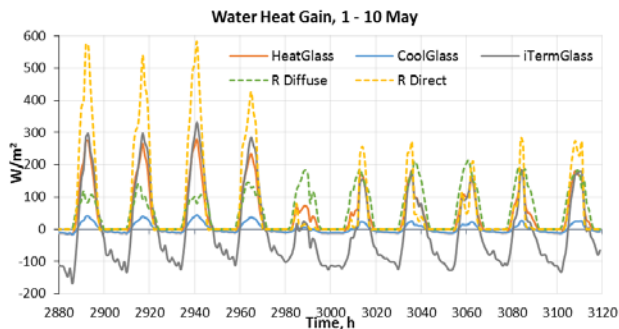


Fig.2. Water heat gain parameter as a function of total solar radiation for the first 10 days in May.

Fig.2 shows the water heat gain for first 10 days in May including the 24 hours solar radiation distribution. As it can be seen the maximum deviation is in the case of iThermGlass because of the configuration of the WFG unit. The water chamber is from the outside of the glazing which means that it is strongly influenced by the environmental conditions. In this modular unit the low-e coating is after the water chamber which keeps the heat in the water. The lowest fluctuations

of the water heat gain are observed in the case of CoolGlass due to the type of coating and the water chamber position. The HeatGlass unit is more efficient due to the low heat losses during the night period and high value of the water heat gain during the day.

2. Summer – the chosen month is July. The water heat gain in all WFG modular units is positive. The highest mean water heat gain is for iThermGlass where it has a negative minimum and the highest positive maximum values. This result confirms that this WFG type is working as effective radiant heating/cooling. The water heat gain for HeatGlass is higher than in the spring time. The internal heat flux for the all WFG is similar to these in May. As it can be seen from the table the investigated parameters for CoolGlass are quite similar to these in the spring time.

Table 2. Simulated results for summer month July

July		Internal heat flux	R diffus	R direct	T ext	Water gain,
		W/m^2	W/m^2	W/m^2	$^{\circ}C$	W/m^2
Heat Glass	mean	4.739	57.26	81.39	20.7	55.07
	min	3.673	33.94	9.544	15.48	22.45
	max	6.633	75.23	145.8	25.93	73.67
Cool Glass	mean	7.069	57.26	81.39	20.7	9.037
	min	6.571	33.94	9.544	15.48	-0.391
	max	7.794	75.23	145.8	25.93	16.27
iTherm Glass	mean	5.848	57.26	81.39	20.7	65.68
	min	4.861	33.94	9.544	15.48	-18.8
	max	7.387	75.23	145.8	25.93	134

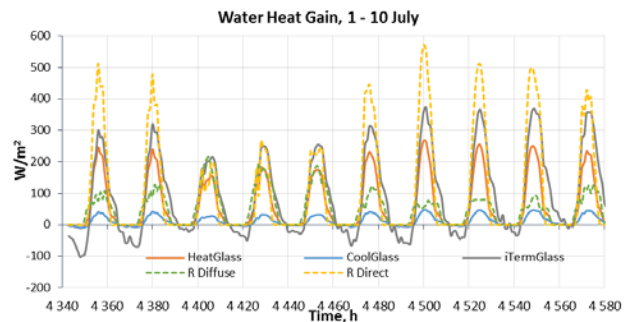


Fig.3. Water heat gain parameter as a function of total solar radiation for the first 10 days in July.

As it can be seen from the Fig.3 in the case of HeatGlass and iThermGlass the water heat gain is highest due to the favourable climate conditions for harvesting of solar energy. Only for CoolGlass we observed very small fluctuations in the internal heat flux.

3. Autumn – the chosen month is October. The water heat gain values are different for all WFG

types compared to the previous investigated months. In case of HeatGlass there is a negative min. value and maximum value is the highest. For the other two units this parameter is negative, which means that we have loss of energy. Only for HeatGlass we still have positive water heat gain, which for the location in Sofia this could be a good solution. The Internal heat flux in all WFG remains approximately the same as in May and July.

Table 3. Simulated results for autumn month October

October		Internal heat flux	R diffus	R direct	T ext	Water gain,
		W/m ²	W/m ²	W/m ²	°C	W/m ²
Heat Glass	mean	5.563	30.05	91.64	11.15	39.85
	min	2.452	18.63	1.665	3.148	-6.914
	max	8.296	43.06	205.4	19.12	93.44
Cool Glass	mean	7.707	30.05	91.64	11.15	-2.1
	min	6.565	18.63	1.665	3.148	-14.63
	max	8.618	43.06	205.4	19.12	12.92
iTherm Glass	mean	7	30.05	91.64	11.15	-48.01
	min	4.492	18.63	1.665	3.148	-166.9
	max	9.072	43.06	205.4	19.12	88.8

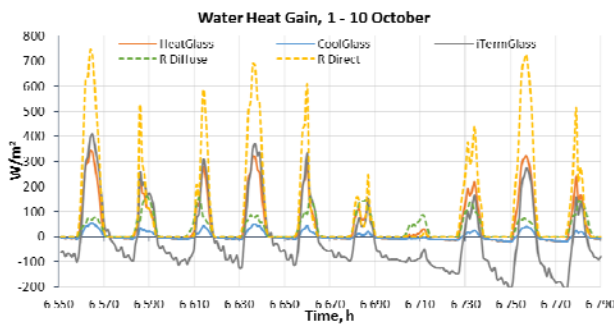


Fig.4. Water heat gain parameter as a function of total solar radiation for the first 10 days in October.

In autumn time (Fig.4) the water heat gain parameter for HeatGlass and CoolGlass follows the solar radiation daily profile. Again due to the coating type and its position in the WFG structure a very low heat losses are observed during the night time. In the case of iThermGlass the effect of the lower T_{ext} dominates and although it has a maximum water heat gain parameter during the sunny days, in the cloudy days it is not so efficient.

4. Winter – the chosen month is January, which for the Bulgarian location is one of the coldest months of the year. During this period, we have positive values for water heat gain only in the case of HeatGlass. The difference in energy harvested between HeatGlass and CoolGlass is approximately 20 times, while compared to iThermGlass it is more than 200 times. For HeatGlass, again the internal heat flux is lowest, which means that we have

minimum heat losses. Fig.5 shows the water heat gain for first 10 days in January. As it can be seen all values in the case of iThermGlass are negative. The position of the water chamber in the glazing and combined effect of low solar radiation levels and low ambient temperatures defines the behavior of the module. Despite the unfavorable weather conditions in this period, only for HeatGlass we obtained positive values for water heat gain.

Table 4. Simulated results for winter month January

January		Internal heat flux	R diffus	R direct	T ext	Water gain,
		W/m ²	W/m ²	W/m ²	°C	W/m ²
Heat Glass	mean	7.757	17.98	42.82	-0.86	1.075
	min	4.402	9.125	0.680	-9.1	-23.85
	max	9.192	26.63	182.8	4.95	57.56
Cool Glass	mean	8.786	17.98	42.82	-0.86	-19.01
	min	7.926	9.125	0.680	-9.1	-27.53
	max	9.378	26.63	182.8	4.96	-10.31
iTherm Glass	mean	9.15	17.98	42.82	-0.86	-209.6
	min	6.994	9.125	0.680	-9.1	-281.2
	max	10.33	26.63	182.8	4.96	-140.1

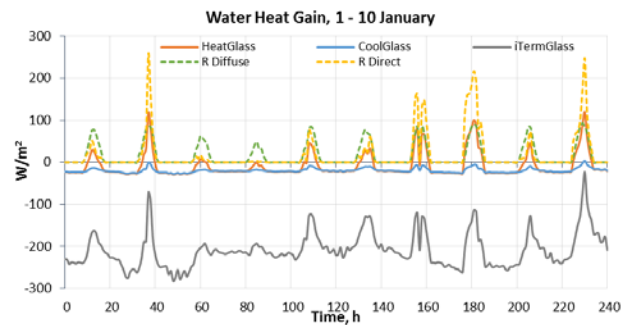


Fig.5. Water heat gain parameter as a function of total solar radiation for the first 10 days in January.

YEARLY BEHAVIOUR OF WFG

In this section the yearly thermal behaviour of WFG is presented. In iThermGlass unit the biggest fluctuation in monthly mean water heat gain parameter (Fig.6) are observed on yearly base. CoolGlass is stable during this period. Only for HeatGlass this mean parameter is positive which means that we are harvesting energy through the whole year.

The yearly variations of the internal heat flux are presented on Fig.7. These variations are strongly related to the annual changes of the T_{ext} and solar radiation. The internal heat flux is an indicator for the energy consumption to insure the indoor comfort. The internal heat flux should be at minimum during the winter and this is when HeatGlass performs best with the lowest reading for this parameter. At the same HeatGlass

underperforms the other units during the summer with lowest internal heat flux, but this performance could be improved through controlling the water flow rate and T inlet.

For a location like Sofia the best performing WFG unit is HeatGlass.

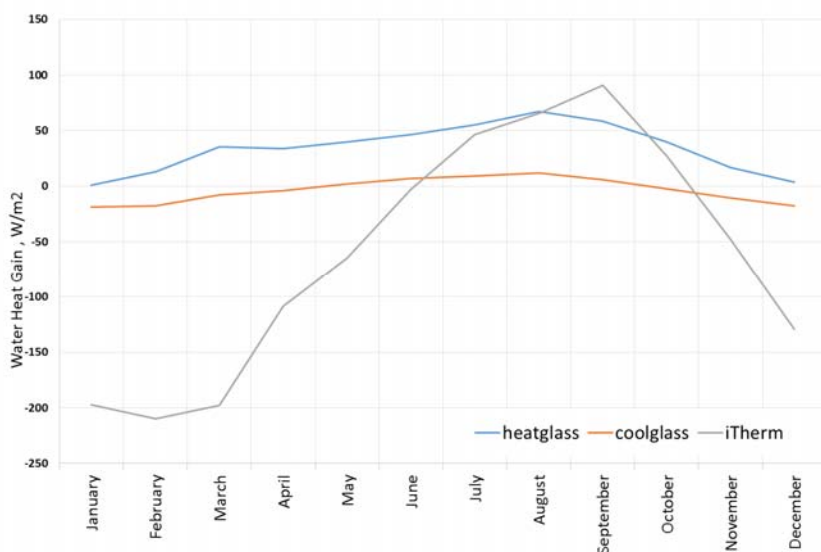


Fig.6. Water heat gain parameter for the whole year of 2017 year in Sofia.

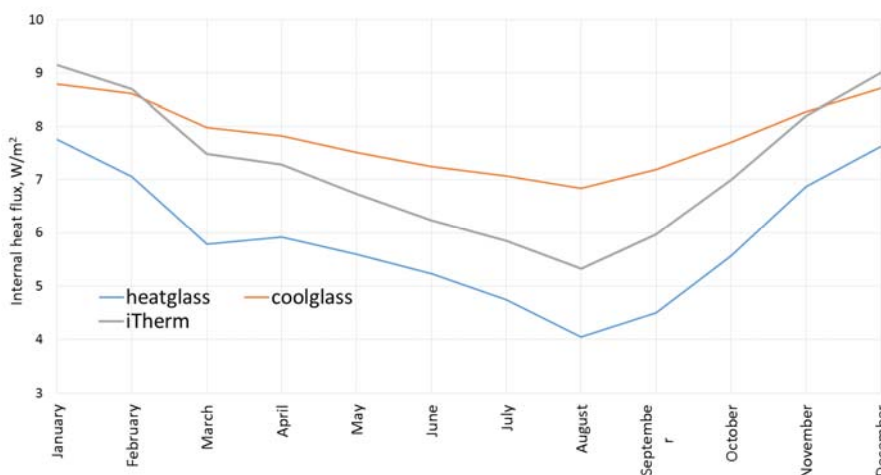


Fig.7. Internal heat flux parameter for the whole year of 2017 year in Sofia.

CONCLUSIONS

This work presents the monthly behaviour of the three investigated WFG units for a specific location in Sofia, Bulgaria. The results show that the structural configuration and the type of coating play important role for the effective work of the units. We can conclude that for all seasons the HeatGlass performed better for this location. Only in this case the water heat gain is positive for the whole

investigated period. This is due to the position of the low-emissivity coating layer and water chamber. The behaviour of the CoolGlass does not change significantly, while in the case of iThermGlass the biggest fluctuations are observed.

With the help of the simulation software developed under the InDeWaG project we can successfully predict the behaviour of the WFG modules and we are able to choose the appropriate configuration of the glazing according to climatic conditions.

ACKNOWLEDGEMENTS

This work was supported by program Horizon 2020 - 'Secure, clean and efficient energy' is split into three focus areas: Energy-efficiency; Low carbon technologies; and Smart Cities & Communities., project ref. 680441 InDeWaG: Industrialized Development of Water Flow Glazing Systems.

REFERENCES

- [1] R. Edlich, K.L. Winters, M.J. Cox, D.G. Becker, J.H. Horowitz, L.S. Nichter, et al., Use of UV-protective windows and window films to aid in the prevention of skin cancer, *J. Long Terms Effects Med. Implants* 14 (2004).
- [2] H.K. Park, H. Kim, Acoustic insulation performance of improved airtight windows, *Constr. Build. Mater.* 93 (2015) 542–550.
- [3] C. Tuchinda, S. Srivannaboon, H.W. Lim, Photoprotection by window glass, automobile glass, and sunglasses, *J. Am. Acad. Dermatology.* 54 (2006) 845–854.
- [4] M. Reidinger, M. Rydzek, C. Scherdel, M. Arduini-Schuster, J. Manara, Low-emitting transparent coatings based on tin doped indiumoxide applied via a sol-gel routine, *Thin Solid Films* 517 (2009) 3096–3099.
- [5] E. Hammarberg, A. Roos, Antireflection treatment of low-emitting glazings for energy efficient windows with high visible transmittance, *Thin Solid Films* 442 (2003) 222–226.
- [6] R. Baetens, B.P. Jelle, A. Gustavsen, Aerogel insulation for building applications: a state-of-the-art review, *En. & Build.* 43 (2011) 711–769.
- [7] J.M. Schultz, K.I. Jensen, F.H. Kristiansen, Super insulating aerogel glazing, *Solar Energy Materials and Solar Cells* 89 (2005) 275–285.
- [8] Y. Fang, P.C. Eames, B. Norton, T.J. Hyde, J. Zhao, J. Wang, Y. Huang, Low emittance coatings and the thermal performance of vacuum glazing, *Solar Energy* 81 (2007) 8–12.
- [9] H. Manz, S. Brunner, L. Wullschleger, Triple vacuum glazing: heat transfer and basic mechanical design constraints, *Solar Energy* 80 (2006) 1632–1642.
- [10] R. Baetens, B.P. Jelle, A. Gustavsen, Phase change materials for building applications: a state-of-the-art review, *Energy and Buildings* 42 (2010) 1311–1368.
- [11] K.A.R. Ismail, J.R. Henriquez, Thermally effective windows with moving phase change material curtains, *Applied Thermal Engineering* 21 (2001) 1909–1923.
- [12] F. Goia, M. Zinzi, E. Carnielo, V. Serra, Spectral and angular solar properties of a PCM-filled double glazing unit, *Energy and Buildings*. 87 (2015) 302–312.
- [13] D.H.W. Li, T.N.T. Lam, W.W.H. Chan, A.H.L. Mak, Energy and cost analysis of semitransparent photovoltaic in office buildings, *Appl. Energy* 86 (2009) 722–729.
- [14] W. Liao, S. Xu, Energy performance comparison among see-through amorphoussilicon PV (photovoltaic) glazings and traditional glazings under different architectural conditions in China, *Energy* 83 (2015) 267–275.
- [15] P.K. Ng, N. Mithraratne, Lifetime performance of semi-transparent building-integrated photovoltaic (BIPV) glazing systems in the tropics, *Renew. Sustain. Energy Rev.* 31 (2014) 736–745.
- [16] S.E. Shaheen, D.S. Ginley, G.E. Jabbour, Organic-based photovoltaics: toward lowcost power generation, *MRS Bull.* 30 (2005) 10–19.
- [17] E. Cuce, Toward multi-functional PV glazing technologies in low/zero carbon buildings: Heat insulation solar glass – Latest developments and future prospects, *Renew. Sustain. Energy Rev.* 60 (2016) 1286–1301, <http://dx.doi.org/10.1016/j.rser.2016.03.009>.
- [18] R. Baetens, B.P. Jelle, A. Gustavsen, Properties, requirements and possibilities of smart windows for dynamic daylight and solar energy control in buildings: a state-of-the-art review, *Solar Energy Materials and Solar Cells* 94 (2010) 87–105.
- [19] ChromoGenics, Smart Windows, retrieved 29 July 2010, [/www.chromogenics.com/smart_eng.htmS](http://www.chromogenics.com/smart_eng.htmS).
- [20] M. Arıcı, H. Karabay, M. Kan, Flow and heat transfer in double, triple and quadruple pane windows, *Energy Build.* 86 (2015) 394–402, <http://dx.doi.org/10.1016/j.enbuild.2014.10.043>.
- [21] S. Papaefthimiou, G. Leftheriotis, P. Yianoulis, T.J. Hyde, P.C. Eames, Y. Fang, P.-Y. Pennarun, P. Jannasch, Development of electrochromic evacuated advanced glazing, *Energy and Buildings* 38 (2006) 1455–1467.
- [22] Y. Fang, T. Hyde, N. Hewitt, P.C. Eames, B. Norton, Thermal performance analysis of an electrochromic vacuum glazing with low emittance coatings, *Sol. En.* 84 (2010) 516–525.
- [23] J.M. Schultz, K.I. Jensen, Evacuated aerogel glazings, *Vacuum* 82 (2008) 723–729.
- [24] Sekisui, Air Sandwich, retrieved 12 August 2010, [/www.sekisui.co.jp/min_ase/airsand/doc/1196214_9172.htmlS](http://www.sekisui.co.jp/min_ase/airsand/doc/1196214_9172.htmlS) (text in Japanese), 2007
- [25] Sekisui, Light-collecting & Insulation Building Materials for Construction Use, retrieved 12 August 2010, [/www.jase-w.eccj.or.jp/technologies/pdf/residence/R-9.pdf](http://www.jase-w.eccj.or.jp/technologies/pdf/residence/R-9.pdf), 2010.
- [26] Pablo Sierra, Juan A. Hernandez, Solara heat gain coefficient of water flow glazings, *Energy and Buildings* 139 (2017) p. 133-145.

Potential of corrosion and/or deposition of solid phases in the thermal waters in the region of Sofia Valley, Bulgaria, depending on their chemical composition

Mila Trayanova^{1*}, Vladimir Hristov¹, Radostina Atanassova¹, Edith Haslinger²,
Otmar Plank², Stefan Wyhlidal², Aleksey Benderev¹

¹Geological Institute, Bulgarian Academy of Sciences, Acad. G. Bonchev St., Block 24, Sofia 1113, Bulgaria

²Austrian Institute of Technology, Center for Energy, Giefinggasse 2, 1210 Vienna, Austria

The thermal waters in the region of Sofia Valley were essential for the emergence and development of the city. There are over 70 water sources with a total flow of 110 l/s and a temperature of 21 °C to 81 °C. They are used for bottling, balneology, as a source of heating energy, spa tourism and others. Waters are formed in rocks with different composition and age, which affect the chemical composition. Therefore, it is essential to evaluate the probability of corrosion of pipes and equipment or the deposition of solid phases in them. The first step is to determine the “Langelier Saturation Index“ and the “Ryznar Stability Index“. To assess the probability of deposition, the saturation indices for different solid phases are determined. The obtained results make it possible to classify the thermal waters in Sofia Valley according to the possibilities of negative processes in their use and to extract conclusions concerning the significance of the geological and hydrogeological factors.

Keywords: thermal water, scaling, corrosion, saturation index, geochemical modelling, Sofia Valley

INTRODUCTION

The emergence and development of the city of Sofia is highly related to the thermal waters. Along with the natural springs located on the territory of the city and its adjacent territories, thermal waters are revealed in different age and composition rocks through many drillings [1-4]. Geological and hydrogeological conditions are the reason for their different composition and temperature. Waters are used for various purposes – drinking and industrial water supply, bottling, heating, prophylaxis and balneology, sports, recreation. By the time water reaches the user, due to a change in the physicochemical conditions (temperature, pressure, redox potential, etc.), after its surface discharge, there are conditions for corrosion processes and solid phase formation on the pipes and equipment used. The purpose of this study is to evaluate the probability of occurrence of these processes for different types of water, according to their diverse chemical composition and temperature.

CHARACTERISTICS OF THERMAL WATERS IN THE SOFIA VALLEY

Sofia Valley is one of the largest geothermal fields in Bulgaria. It is located in the western part of the country and has got a territory of 1180 square kilometres (Fig.1). The length of the graben is of about 60 km and the width is up to 20-25 km.

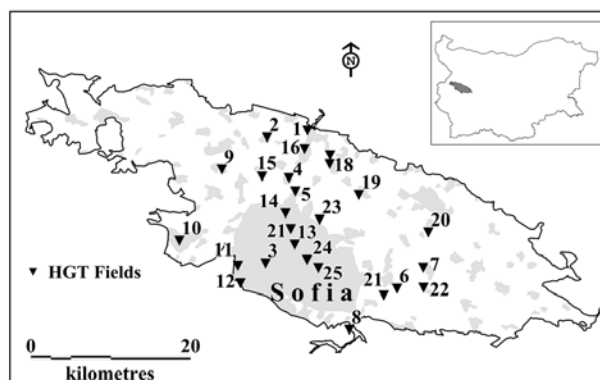


Fig.1. Location of the hydrothermal sources in Sofia Valley (HGT) [1, 2]

The valley represents a tectonic graben structure, striking northwest-southeast [1-2]. The depression is outlined as a closed zone of enhanced thermal potential [1-6]. There are many natural geothermal springs: Sofia-centre (the ancient Thracian settlement was established around it), Ovcha kupel, Knyazhevo, Gorna banya, Ivanyane, Bankya, Pancharevo (nowadays these are quarters of Sofia city or villages at its vicinity) and others (Fig.1, Tab.1). During the period of 1960-1990 a lot of boreholes were drilled and many new geothermal sources were discovered: Kazichene-Ravno pole, Svetovrachene, Novi Iskar, Trebich, Chepintsi and others (Fig.1, Tab.1). The temperature of mineral water currently flowing from geothermal boreholes and natural springs located within the frame of Sofia Valley varies

* To whom all correspondence should be sent:
milat@geology.bas.bg

from 21 °C to maximum 81 °C (borehole P-1 Kazichene). The total approved exploitation resource up to now by the Ministry of Environment and Water, now amounts to approximately 110 l/s (second largest geothermal basin in Bulgaria after Velingrad). Thermal water is partially used only in several areas in Sofia Valley. Bottling of mineral water (Gorna banya, Ivanyane) is a leading application and accounts for about 61% of the total use, followed by treatment and recreation (35% - Ovcha kupel, Bankya) and relaxation and sanitary needs (4% - Pancharevo, Kazichene). Special attention is paid to the further possibilities of geothermal water utilization in the Valley.

Table 1. Characteristics of major hydrothermal sources [1-4]

N on Fig.1	HGT	Rocks	Geolog. index	Flow rate dm ³ /s	T °C
1	Novi Iskar	sandstones	P	0.8	25
2	Dobroslavtsi	sandstones	T ₁	0.8	40-41
3	Ovcha kupel	limestones	T ₂	4.5	32
4	Trebich	limestones	T ₂	1	51
5	Ilientsi	limestones	T ₂	<2	47
6	Kazichene	limestones	T _{2,3}	5.8	80
7	Ravno pole	limestones	T _{2,3}	6.2	50-58
8	Pancharevo	limestones	T ₂	12.5	44-48
9	Kostinbrod Bankya +	limestones	J _{2,3}	~55	25-31
10	Ivanyane	andesites	K ₂	25	24-38
11	Gorna banya	andesites	K ₂	8	19-44
12	Knyazhevo	andesites	K ₂	5.5	23-26
13	Sofia - centre Svoboda distr.	andesites sedim.	K ₂	16	46
14	- Sofia	form.	K ₂	7.2	50
15	Mramor	sands	N ₁	1.5	42.6
16	Kumaritsa	sands	N ₁	1.3	36-41
17	Gnilyane	sands	N ₁	0.9	42
18	Svetovrachene	sands	N ₁	5	45
19	Chepintsi	sands	N ₁	6	50
20	G. Bogrov	sands	N ₁	1.1	44
21	Kazichene	sands	N ₁	1.4	39-60
22	Ravno pole	sands	N ₁	4.4	51-52
23	Birimirtsi Lozenets distr.	sands	N ₁	0.4	30
24	- Sofia	sands	N ₂	2.8	33
25	Sofia 4th km.	sands	N ₂		23

Water is discharged on the surface by springs and boreholes of depth in the range of 200 to 1200 m. Most of the wells have been drilled more than 30 years ago and are in poor technical condition. The majority of the sources are state owned. According to the amendments to the Water Act, after 2011 six hydrothermal sources were granted free of charge for management and exploitation to Sofia Municipality for a period of 25 years - Sofia center, Sofia-Serdica, Sofia-Lozenets, Sofia-Svoboda, Sofia-Ovcha kupel, Pancharevo.

Geological and hydrogeological background

As it was mentioned above, Sofia Valley is a graben structure, bounded by mountains. The graben basement is built of Mesozoic formations. They consist of andesites, volcano-sedimentary and sedimentary rocks of an Upper Cretaceous age in the southwestern part and of carbonate and terrigenous rocks of Triassic, Jurassic and Upper Cretaceous age. The graben is filled of Neogene rocks mainly sands, clay, sandstones and lignite seams at some places. The total thickness of the Neogene complex varies in the range of 100 m to 1142 m. The thickness of the Quaternary cover is mostly between 50 m and 100 m.

The graben structure is complicated by many fault displacements that form internal small horsts and depressions [5]. They provide paths for water circulation and create links between different water bodies. The geological structure is complicated by many faults, some of which are still seismically active.

Three types of reservoirs are presented in the Sofia basin - porous, karstic and fractured. The reservoirs are parts of the basement rocks and of the Neogene and Quaternary formations [6]. They have specific hydrogeological characteristics related to the depth of occurrence, lithological type and structure of the host rocks and the conditions of natural recharge and draining.

The geothermic field of Sofia Valley is strongly disturbed by the mineral water flow. The thermal depression is outlined as a closed zone of enhanced thermal potential on the heat flow map of Bulgaria. The estimated average conductive heat flow is about $80 \times 10^{-3} \text{ W/m}^2$ and the average geothermal gradient is of 4.7 °C/100 m [7]. The highest heat flow density is calculated for Kazichane geothermic anomaly – $140 \times 10^{-3} \text{ W/m}^2$ (south-eastern part of the basin).

Chemical composition of thermal waters

The analysis of the results of water samples taken from different water sources of thermal waters in Sofia Valley [3-4, 8] shows that they are characterized by a different chemical composition. The main reasons for this are the different rocks (Fig.1) in which they are formed as well as the local hydrogeological and geothermal conditions.

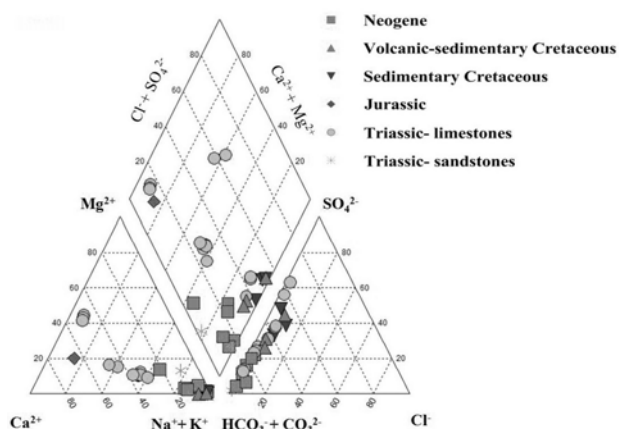


Fig.2. Piper diagram of thermal water sources formed in different rocks

The waters with the highest TDS (total dissolved solids) are formed in the oldest rocks, sandstones, conglomerates, aleurolites and argillites of Permian age – 5 g/dm³. It is hydrocarbonate, sodium-potassium type and is characterized by high content of free CO₂ and increased radioactivity – 226Ra (220 mBq/dm³).

The thermal water in the Lower Triassic sandstones is hydrocarbon, sodium, slightly alkaline (with pH about 8), with TDS ranging from 1 to more than 3 g/dm³. Waters in Triassic limestones and dolomites are reached by boreholes in separate blocks beneath the Neogene deposits, filling Sofia Valley, mainly in the northern part. In addition, there are natural springs in the southern part – Pancharevo, and water conducted by active fault in Ovcha Kupel. In the deep parts, the water is with higher TDS (more than 3 g/dm³ (Trebich). The lowest TDS is in Pancharevo – 0,5 g/dm³. Generally predominant are waters with pH of 7.1-7.6. In some of the water sources, along with nitrogen, CO₂ can also be found. The predominant type of water – hydrocarbonate-sodium and hydrocarbonate-sodium-calcium, the relatively high contents of H₂SiO₃, as well as some microcomponents, are indicative of the deep-water recharge of the thermal waters. The waters with different composition are conducted by an active

fault in Ovcha Kupel. They are sulphate-hydrocarbonate-sodium-calcium.

Kostinbrod heated water (21-30 °C) of Upper Jurassic limestones have a composition of typical karst waters – hydrocarbon-calcium-magnesium with TDS of 0.5 g/dm³, which shows connection with the waters of a large mountain karst region, located in the northern edge of the valley.

The most important for Sofia city are the thermal waters formed in Upper Cretaceous volcanic rocks – mainly andesites. These rocks have a wide area of distribution, mainly in the southern part of the valley and are connected to most of the natural thermal springs by faults. These are waters with nitrogen in their gas composition, with low TDS of 0.1-0.3 g/dm³, relatively high pH values – above 9, and are hydrocarbonate-sulphate-sodium.

Thermal waters are revealed by boreholes in sedimentary rocks of Upper Cretaceous age in the northern part of Sofia (Svoboda district). They have a higher TDS– more than 15 g/dm³, low alkaline (pH about 8), and are hydrocarbon sulphate-sodium.

In the sand layers of the Neogene sediments, filling the Sofia graben, thermal waters are revealed in many places by boreholes. Their chemical composition is mainly formed by mixing waters from the bedrock with the cold waters as a result of surface recharge. This gives a direct relation to the diverse hydrochemical parameters in the different parts of Sofia Valley. In some areas, the presence of CH₄ and CO₂ can be found, which is a result of coal deposits in the Neogene materials and the relatively difficult movement of groundwater.

MATERIALS AND METHODS

The widespread use of thermal waters in Sofia Valley for various purposes necessitates assessment and prediction of the probability of corrosion and solid phase formation in pipes and equipment. The main factors influencing these negative processes are physicochemical: pH, pressure and temperature change, gas and chemical composition. Comparatively simplified approaches have been developed, aiming at the interaction of waters, mainly with metal pipes, and the probability of formation of carbonate and silicate minerals [9-12]. The "Langelier Saturation Index" (LSI) and the "Ryznar Stability Index" (RSI), introduced by Carrier (1965) [13], are also used in this study.

$$LSI = pH - pHs \quad (1)$$

$$RSI = 2 \text{ pHs} - \text{pH} \quad (2)$$

where:

pHs is the pH value of water when it is fully saturated with CaCO₃. It is estimated by the following formula:

$$\text{pHs} = (9,3 + A + B) - (C + D) \quad (3)$$

where:

$$A = (\log(\text{TDS}) - 1) / 10 \quad (4)$$

$$B = (-13.12 \log (\text{T}^\circ\text{C} + 273)) + 34.55 \quad (5)$$

$$C = (\log (\text{calcium hardness})) - 0.4 \quad (6)$$

$$D = \log (\text{alkalinity}) \quad (7)$$

For the purpose of more detailed identification of the various mineral phases that may be formed, the Saturation Index (SI), which is best defined by Garrels, Christ in 1965, is applied. [14] Its determination was made by using the VISUAL MINTEQ software, which is a freeware chemical equilibrium model maintained by Jon Petter Gustafsson at KTH, Sweden. [15] This code allows calculating of saturation indices of a large number of mineral phases as well as the forms of presence of chemical elements in the water.

One of the main problems in the processing of results is the quality of the data from the thermal water analyses. Until now, many samples of thermal waters in Sofia Valley have been taken, some of them were published [5, 8, 16-17]. For the present study only 40 of them, from different water sources, were taken under consideration. The selection requirement was that these samples were analyzed in a comparable manner and that different hydrochemical parameters were analyzed by different methodologies, including field determination of the main changing physicochemical parameters. These conditions are met by some unpublished results, as well as analytical data published by Pentcheva et al. [8] carried out in the laboratory of the University of Antwerp (Belgium).

RESULTS AND DISCUSSION

Using the data from the obtained analyzes and the Eqs.(1-2) for each of the tested water sources, the Langelier Saturation Index (LSI) and the "Ryznar Stability Index" (RSI) were determined. The results are grouped according to the characteristics of the water-bearing rock and are

mapped on Figs.(3, 4). On the same graph, these results are assigned to the relevant water group, as suggested by Carrier [13] LSI and RSI indications.

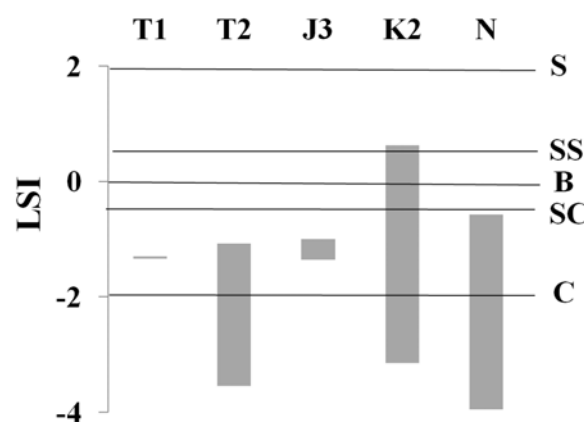


Fig.3. Range of variation of LSI values in different age rocks and their comparison with the suggested by Carrier indications [13] (C - Serious corrosion, SC - Balanced but pitting corrosion possible; SS - Slightly scaling and corrosive; S - Scale forming but not corrosive)

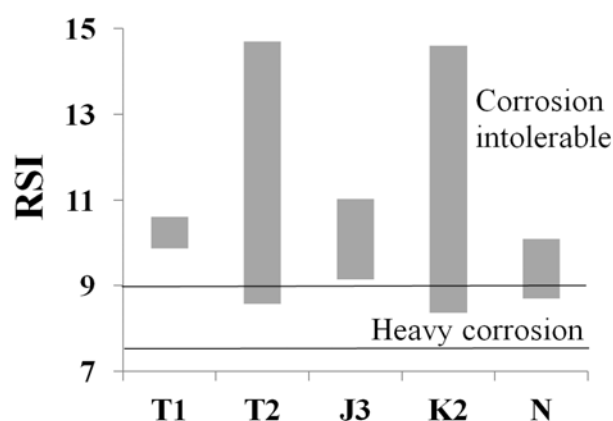


Fig.4. Range of variation of RSI values in different age rocks and their comparison with the suggested by Carrier indications [13]

The obtained results show that in most cases the probability of corrosion of the pipes is higher than the scaling of the carbonate substance. Regarding the LSI prevailing for the whole Sofia Valley, the thermal waters are in the range between Slightly corrosive but non-scale forming and Serious corrosion indications. The waters formed in Triassic carbonate rocks, Upper Cretaceous volcanic rocks and secondary retentive thermal waters in Neogene sediments, which are above Serious Corrosion Index, have a significant presence. Some of the waters formed in the Upper Cretaceous volcanic rocks, which are of major

importance for the users are different in nature. A substantial part of these are related to Balanced but pitting corrosion possible and partly to Slightly corrosive but non-scale forming. According to RSI, most of the thermal waters in the study area are Corrosion intolerable.

It should be noted that the proposed by Carrier method [13] mainly characterizes the probability of deposition of carbonates on the pipes and equipment. The specific chemical composition of each individual water source determines the probability of deposition of other mineral phases. This is evaluated for about 200 mineral phases using the values of the respective water saturation indices calculated with the Visual MINTEQ 3 software. The results obtained with regard to the mineral phases, which according to the past practical experience have the greatest significance for deposits on pipes and equipment (carbonate minerals and forms of SiO_2) show that for the thermal waters in Sofia Valley this probability is small. In most cases, saturation indices indicate that under natural thermodynamic conditions the waters are unsaturated to equilibrium with respect to these mineral phases (Fig.5).

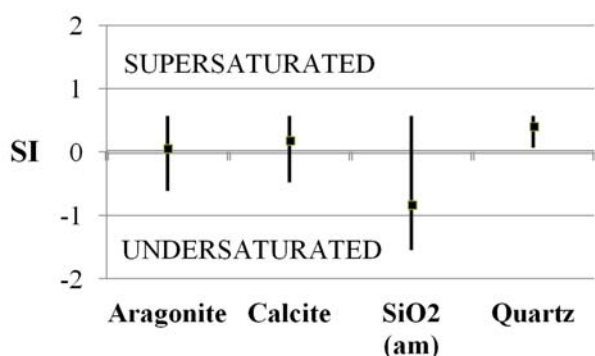


Fig.5. Saturation Index values for thermal waters relative to the major forms of CaCO_3 and SiO_2

Along with the major mineral phases, for which there is a risk of solid phase formation (scaling) on pipes and installations, thermal waters are likely to convert into solid state and other mineral phases. These are mainly compounds and minerals for which higher saturation index values were calculated. For example, in all samples in which phosphorus and fluorine is determined, saturation index values for FCO_3 -Apatite are high – in the range of 3 to 6.5. Elevated saturation index values for some forms of aluminum hydroxides and silicates have been frequently found. Some of the water sources have high values of the saturation

index of phases containing some elements, that are in very low concentrations in thermal waters – Ag, Cr, Cu, Pb, Se, Sn, V, Zn and others. Even if these mineral phases convert into solid state, their amount will be negligible and cannot have a significant effect on the exploitation of the thermal waters.

The evaluation of the probability of deposition of different mineral phases refers to the natural thermodynamic conditions. When the groundwater reaches the surface, so-called geochemical barriers [18] appear – zones in which there is rapid change of the natural conditions leading to a change in the physicochemical conditions. One of the most important factors is the change of thermal water temperature. By simulating such changes for the hottest water source in Sofia Valley – the borehole P1 – Kazichene, it was found that in the case of a sudden drop in the water temperature, the saturation indexes values for carbonate minerals are reduced and they increase in regard to phases containing silicon and aluminum. Another important factor that changes when the thermal water reaches the surface is pH. Considering the type of water in the studied area, its values depend on the state of the CO_2 - HCO_3 - CO_3^{2-} system [19]. As a result of a change in the partial pressure of CO_2 on the surface, pH values may increase. This helps the deposition of carbonate materials at the mouths of the boreholes. These processes are relatively less important for the most significant thermal waters in the region, formed in Upper Cretaceous volcanic rocks, which are sulphate-hydrocarbonated.

CONCLUSIONS

Sofia Valley is one of the most important hydrogeological structures in Bulgaria with regard to the formation of thermal waters. The geological structure predetermines their formation in different by composition and age rocks, and consequently their chemical composition is also different. Taking into account the importance of the thermal waters for the city of Sofia, it is necessary to predict the probability of solid phase formation and corrosion on pipes and equipment. Therefore, the probability of these processes with respect to water formed in different rock collectors has been assessed. It is found that for most of the water sources there is a risk mainly of activating corrosion of metal pipes. Relatively less dangerous in this respect are the facilities through which the thermal waters formed in Upper Cretaceous volcanic sediments, which have the highest flow rates and are most used

(Bankya, Gorna banya, Knyazhevo, Sofia centre, etc.). Solid phase formation can only be expected in the areas of rapid temperature drop and the possibility of releasing CO₂ from the water. The obtained results have an important role for a more complete utilization of the hydrothermal resources in Sofia Valley.

ACKNOWLEDGEMENTS

The research was carried out in the framework of the bilateral cooperation project between Bulgaria and Austria number NTS 01-8 "Scaling and corrosion in hydrogeothermal plants and wells in Austria and Bulgaria - a comparison", financed by the Austrian Federal Ministry of Science, Research and Economy (BMWF) and by the Bulgarian Ministry of Education and Science (Scientific Research Fund).

REFERENCES

- [1] P. Penchev, V. Velichkov. Fields of mineral water in the region of Sofia. Sofia Municipality BAPV, (in Bulgarian), 2011.
- [2] V. Hristov, A. Benderev, K. Bojadgieva. Assessment of hydrogeological conditions and geothermal application in Sofia Municipality (Bulgaria). Proc. 2nd IAH Central European Groundwater Conference "Groundwater risk assesment in urban areas 2015, 36-44 (2016).
- [3] K. Shterev. Mineral waters in Bulgaria, PH Nauka i izkustvo, (in Bulgarian), 1964.
- [4] P. S. Petrov, S. Martinov, K. Limonadov, Y. Straka. Hydrogeological investigations of mineral waters in Bulgaria. Technika, 1970.
- [5] P. Ivanov. Assessment of the Geological Conditions in the Sofia Kettle under Seismic Impact. - Proc. Intern. Symp. on Eng. Geol. and the Env., IAEG, Athens, Greece 23-27 June 1997, Rotterdam, 1265-1270 (1997).
- [6] H. Antonov. D. Danchev. Ground waters in Bulgaria. Technika, (in Bulgarian) 1980.
- [7] K. Bojadgieva, S. Gasharov, Catalogue of geothermal data of Bulgaria, GorexPress, (in Bulgarian), 2001.
- [8] E. Pentcheva, L. Van'tDack, E. Veldeman, V. Hristov, R. Gijbels. Hydrogeochemical characteristics of geothermal systems in South Bulgaria. Universiteit Antwerpen, 1997.
- [9] K. Rafferty. Scaling in geothermal heat pump systems. Contract No. DE-FG07-90ID 13040. Geo-Heat Center, Oregon Institute of Technology, 1999.
- [10] Y. Zhang, H. Shaw, R. Farquhar, R. Dawe. The kinetics of carbonate scaling—application for the prediction of downhole carbonate scaling. Journal of Petroleum Science and Engineering. 29 (2), 85-95 (2001).
- [11] S. Boycheva. Evaluation of scale formation and corrosion potential in geothermal heating systems. Energy forum 13-16 June 2007, Varna. 4.pdf. (in Bulgarian) (2007).
- [12] K. Brown. Thermodynamics and kinetics of silica scaling. Proceedings International Workshop on Mineral Scaling 2011 Manila, Philippines, 25 - 27.pdf (2011).
- [13] Carrier. Air Conditioning Company. Handbook of Air Conditioning System Design. McGraw-Hill Books. New York. 1965.
- [14] R. Garrels, L. Christ. Solution, minerals and equilibria, Harper and Row. 1965.
- [15] <http://hem.bredband.net/b108693/>
- [16] A. Azmanov. Bulgarian mineral springs, State Printing, Sofia (in Bulgarian), 1940.
- [17] B. Kusitaseva, J. Melamed, Composition of the Bulgarian Mineral Waters. Chemical composition studies. Medicine and Physical Education (in Bulgarian), 1958.
- [18] A. Perelman. Geochemistry of Landscape. Vyssh. shkola, Moscow. (in Russian), 1966.
- [19] B. Velikov. Hydrochemistry of Groundwaters. Ministry of Education – Higher Institute of Mining and Geology. Sofia (in Bulgarian), 1986.

In-situ measurements of the soil thermal properties for energy foundation applications in São Paulo, Brazil

T. S. O. Morais¹, C. H. C. Tsuha^{2*}

¹University of São Paulo, Dept. of Geotechnical Engineering, Av. Trabalhador São Carlense, 400,13566-590 São Carlos, Brazil

² University of São Paulo, Dept. of Geotechnical Engineering, Av. Trabalhador São Carlense, 400,13566-590 São Carlos, Brazil

The consumption of electrical energy for air-cooling systems in Brazilian urban areas is very high. Therefore, under this scenario, the use of ground source heat pump (GSHP) systems with geothermal piles seems to be an interesting alternative for energy savings. For an efficient design of geothermal piles (also known as “energy piles”), it is necessary to determine the following parameters: (i) ground thermal conductivity, (ii) pile thermal resistance, and (iii) undisturbed ground temperature. Such parameters can be estimated from Thermal Response Tests (TRTs) on energy piles. In order to investigate the thermal properties of the ground at a site in São Paulo city, Brazil, a TRT was carried out during 10 days on an energy micropile with 15 m length and 350 mm diameter, with a single U-shaped tube. The current paper presents the results of this experimental investigation, which can be used to guide the design of geothermal pile systems in tropical areas of similar ground conditions.

Keywords: Shallow geothermal energy, energy piles, thermal response test, ground thermal properties, sub-tropical climate

INTRODUCTION

São Paulo is the most populous city in South America (12.2 million people), and is also one of the world's largest metropolitan areas. This city has a humid subtropical climate, and air conditioning (cooling) accounts for approximately 20 percent of the total electricity used in commercial buildings. In order to minimize this problem, the use of geothermal energy systems with energy piles could be an interesting alternative to reduce the consumption of electrical energy for air-cooling.

For the design of energy piles it is necessary to determine the ground thermal properties and the thermal performance of the pile. Parameters as undisturbed ground temperature, thermal conductivity, and pile thermal resistance can be estimated from the results of a Thermal Response Test (TRT) carried out on the pile loop.

The current paper describes the test procedure and results of the first TRT test performed in an energy pile installed at a site which represents a typical soil condition in large area of São Paulo. The current work is the first case reported in literature of a TRT conducted in the Brazilian subtropical region.

GROUND CONDITIONS

The TRT test was carried out at the campus of the University of São Paulo at Sao Paulo city,

southeast of Brazil. In this area, the ground is predominantly composed of clayed sand with varied grain diameters, covered by a silt-sand clay layer with a thickness of approximately 2.5 m, and a dark organic-clayey layer with a thickness of 1 m.

Standard penetration tests (SPT) were performed at the test area (boreholes with 20 m depth), for initial soil characterization, according to Brazilian standard [1]. During the test, values of the penetration resistance N_{SPT} (number of blows by a hammer of a standard weight required to drive a standard sampling tube 300 mm into the ground) were measured along the soil depth. The results of average, maximum and minimum N_{SPT} are shown in Fig.1. The depth of the groundwater table varies seasonally from approximately 2 to 3 m at the site. When the current TRT was carried out, the groundwater table was 1.9 m bellow the ground surface.

ENERGY PILE

The use of energy piles is an innovative technology, in which GSHP systems based on energy pile foundations, installed in constant ground temperature, are used for heating and cooling of building.

For the current study, a small diameter (0.35 m) energy micropile of 15 m length was constructed at the test site. The micropile drilling process is illustrated in Fig.2a. Borehole casing pipes were used to ensure the stability of the drilled hole before

* To whom all correspondence should be sent:
chctsuha@sc.usp.br

grout placement (Fig.2b). After the hole has reached the final depth, water was pumped to expel the slurry out (until clean water is obtained in the returns).

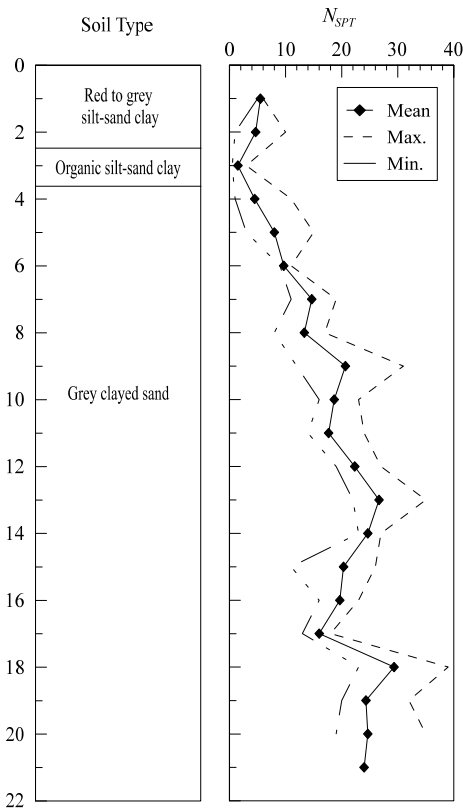


Fig.1. Soil profile at the test site of the University of São Paulo at São Paulo, Brazil

(Fig.3). Details of the tube installation into the energy micropile are presented in Fig.4. The U-loop was installed along the total length of the pile (active pipe length of 15m).



Fig.3. Installation of the U-shaped exchanger tubes in the reinforcement cage of the micropile

After the reinforcement cage installation, the hole was filled with grout, with cement/aggregate ratio of 0.55, and cement/water ratio of 0.5. Grouting was stopped after total removal of water from the borehole. The steps of the construction process of the energy pile are described in Fig.4.



Fig.2. Construction of the energy pile: a) hydraulic drilling rig, and b) drilling process

After a cleaning procedure, high-density polyethylene (HDPE) heat exchanger tubes were installed into the cased hole. A high density polyethylene (HDPE) tube that forms U-shaped pipe (inner diameter of 26 mm and outer diameter of 32 mm) was attached to the reinforcement cage



Fig.4. Construction of the energy pile: installation of the reinforcement cage with a U-shaped heat exchanger tube

THERMAL RESPONSE TESTS

The thermal response testing involves applying a constant heating power to the ground via a heated circulating fluid.

Normally, the TRT interpretation is carried out by a simple analytical technique, based on the line source model. The number of the TRT carried on energy piles has been increasing, although some researchers [2] commented that longer duration tests are necessary for application of the line source model with piles. The test duration usually is set to a minimum of 48 hours; however, based on the recommendation of [2], for the current study the TRT duration was approximately 10 days.

In the present work, the thermal response test was performed based on the procedure described in the European Committee for Standardization document, TC 341 WI 00341067.6 [3], prepared by CEN/TC 341 – ‘Geotechnical Investigation and Testing’ and of few works available in the literature [2, 4 – 6].

Test equipment

The TRT equipment used in this work was constructed for the investigation described partially in [7], performed to evaluate the feasibility of ground source heat pumps systems in Brazilian unsaturated soils. This cited work was carried out in order to evaluate the thermal performance of energy piles installed in unsaturated lateritic soils (typical in Brazil) [7].

The TRT was carried out by injecting a constant heat power into the heat exchanger pile. During the heat injection, the inlet and outlet fluid temperatures in the pile were monitored using two thermistors (PT-100) connected to a data acquisition system with a high temporal resolution (at least 0.1 Hz). The equipment used is composed of: a heater reservoir, a circulation pump, a flowmeter, three PT-100 thermistors sensors and a high resolution data acquisition system [7].

The PT-100 thermistors sensors have an operating range from 273.15 to 523.15 K. These sensors, used for monitoring the inlet (T_{in}) and outlet (T_{out}) temperatures of the heat carrier fluid, were attached to the U-shaped heat exchanger tube (Fig.5). A third PT-100 was used for monitoring the ambient temperature during the test.

The heater reservoir is a conventional electrical water heater with 0.1 m³ capacity and heating rate of 1 kW. For this study, water was used as the heat transfer fluid.

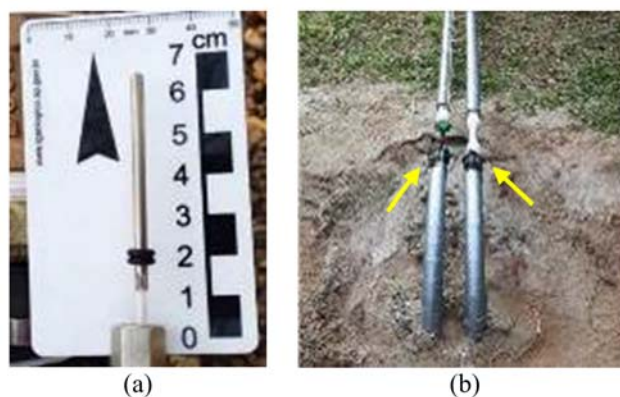


Fig.5. (a) PT-100 resistance temperature sensors; (b) PT-100 installed in the inlet and outlet pipe

The turbine flowmeter used to measure the water flow rate through the U-tube, with a repeatability and straightness of $\pm 0.5\%$ (for liquids), was connected to the data acquisition system during the test.

After installation, the pipes were insulated to minimize heat loss or gain. The temperature sensors were equally insulated. Fig.6 presents a schematic of the experimental system.

The undisturbed ground temperature was recorded before the beginning of the of the thermal response test, according to the recommendations of the European Committee document TC 341 WI 00341067.6 [3]. During this initial step, the inlet and outlet temperatures of the heat carrier fluid were measured when the water was pumped through the tubes (without heat input).

The TRT was carried out with a flow rate of $3.52 \cdot 10^{-4}$ m³/s, to guarantee a turbulent flow inside the pipe. For the test, the applied power was approximately 1.061 Watts, or 70.8 W/m (amount of heat per length of pile).

TRT interpretation

The TRT results were interpreted based on the analytical Kelvin’s linear heat source theory, considering the data corresponding to the steady-state heat transfer within the U-tube. In this case, the energy pile was assumed to be a finite linear heat source, the ground a semi-infinite homogeneous medium, and the heat transfer at the pile-ground interface constant and in radial direction [5, 8, 9]. The equation used to determine the changes in the ground temperature due to the heat flow, based in Kelvin's line source theory, is defined as:

$$\Delta T_g(t, r) = \frac{q_t}{4\pi\lambda} \left[\ln\left(\frac{4\alpha t}{r^2}\right) - \gamma \right] \quad (1)$$

where:
 ΔT_g – ground temperature change, K;
 q_t – heat power injection supply per unit of geothermal exchanger, W/m;
 λ – ground thermal conductivity, W/mK;
 r – radial distance between the heat source and point of interest into ground, m;
 t – TRT duration time, s;

γ – Euler’s constant ($\gamma = 0,5772$)
 α – ground thermal diffusivity, m²/s, Eq.2:

$$\alpha = \lambda / \rho S_c \quad (2)$$

where :
 ρ – mass density of the soil, Kg/m³
 S_c – specific heat capacity, Jkg⁻¹K⁻¹.

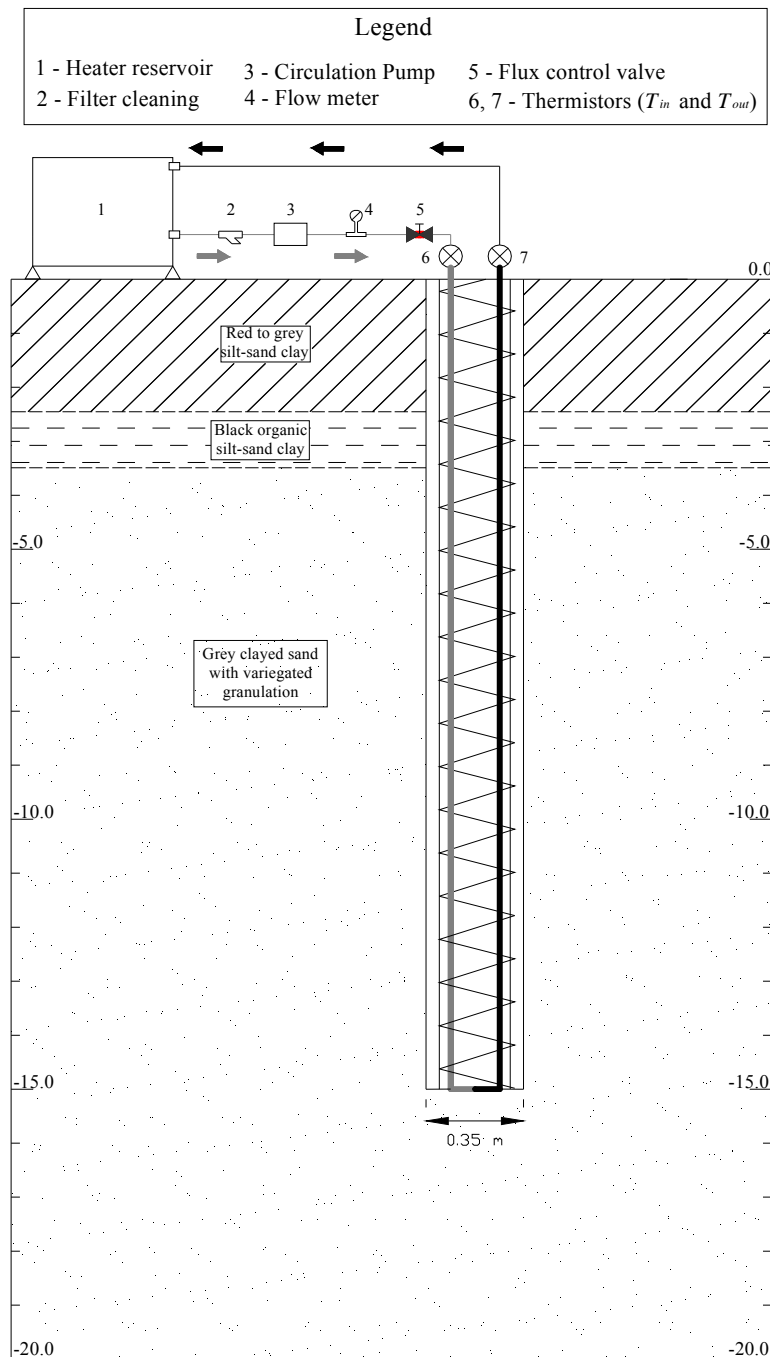


Fig.6. Schematic of the experimental system

The thermal resistance R_b between the heat carrier fluid and the pile wall can be obtained by

the fundamental relation [5, 9] described in the Eq.3:

$$\Delta T_f = q_t R_b + \frac{q_t}{4\pi\lambda} \left[\ln\left(\frac{4\alpha t}{r_b^2}\right) - \gamma \right] \quad (3)$$

where:

ΔT_f – change in mean temperature of the heat carried fluid during TRT tests, K;

R_b – overall thermal resistance of the geothermal heat exchanger, mK/W;

r_b – geothermal heat exchanger (pile) radius, m.

The effective ground thermal conductivity (λ_{eff}) can be determined from the variation of the fluid mean temperature versus logarithmic time recorded during the TRT, and are calculated by the Eq.4:

$$\lambda_{eff} = \frac{q_t}{4\pi k} \quad (4)$$

where:

k – slope of the linear regression of mean fluid temperature versus logarithmic time.

To guarantee that the analysis were done considering the steady-state heat transfer condition, according to the recommendations of some authors [3 – 5, 9], we discarded the early test data before a minimum test period, t_{min} , calculated by the Eq.5.

$$t_{min} = \frac{5 r_b^2}{\alpha} \quad (5)$$

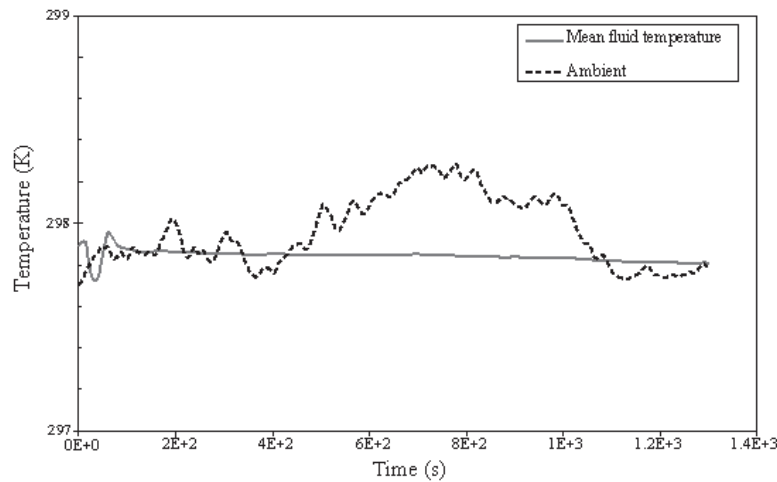


Fig.7. Results of the undisturbed ground temperature during water circulation inside the pile before the TRT

The undisturbed ground temperature of 297.85 K is inside the range observed for tropical climate areas found in the literature [4]. The ground temperature obtained in this study is comparable to the values measured in a site at Sao Carlos city, located in the central-east region of the State of Sao Paulo.

RESULTS

Natural Ground Temperature

The TRT was carried out in February 2017 (Brazilian summer). During the initial water circulation inside the energy pile, undisturbed ground temperature (estimated from the inlet and outlet fluid temperatures) and ambient temperature were determined. Table 1 shows the results of the temperature monitoring before the beginning of the TRT.

Table 1. Results of the mean temperature of the ground along the pile (water circulation test)

Duration time	Groundwater position	Temperature	
		Ambient	Ground*
s	m	K	
1,296	1.90	297.95	297.85

*average ground temperature considering 15 m depth.

Fig.7 illustrates the variation of the ambient temperature the mean inlet and outlet fluid temperatures during the water circulation test.

Heating test: ground thermal response and thermal properties

After the water circulation test, the thermal response test was performed during 246 hours to ensure the steady-state of heat exchange. Fig.8 presents the fluid temperature variation during the test. Tab.2 shows the values of fluid temperature at different times.

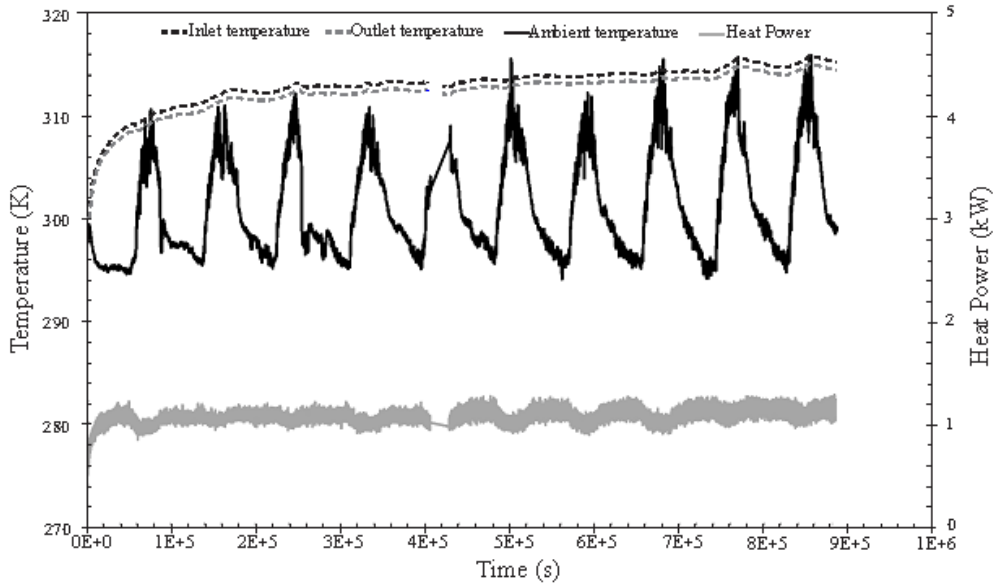


Fig.8. Variation of the fluid and ambient temperatures during the TRT

Table 2. Results of temperature measurements during the TRT.

TRT measurements	Unit	Value
Undisturbed ground temperature		297.85
Average ambient temperature		301.15
Maximum ambient temperature		315.95
Minimum ambient temperature		294.15
Average fluid temperature difference ($T_{in} - T_{out}$)	K	273.87
T_{in} at 50 hours		312.45
T_{out} at 50 hours		311.65
T_{in} at 100 hours		313.25
T_{out} at 100 hours		312.45
T_{in} at 200 hours		314.25
T_{out} at 200 hours		313.55
Flow rate	m/s	0.66
Average Heat power	kW	1.06

Fig.8 highlights the influence of the ambient temperature on the results of heat carrier fluid

temperatures. This figure also illustrates that the heat power injection into the tubes was approximately constant during the period of test.

The parameters as thermal conductivity and pile thermal resistance are essential for the design of geothermal ground energy systems with energy piles. The thermal resistance (R_b) was calculated using Eq.3. Fig.9 presents the variation of the thermal resistance and ambient temperature during the TRT. The average value of the thermal resistance of the energy pile was 0.13 mK/W.

In this work, the Eq.4 was used for the determination of the ground thermal conductivity. The k value was obtained from the curve of mean fluid temperature versus the logarithm of time (t), as indicated in Fig.10.

Table 3 summarizes the main results estimated from the TRT carried out on the energy pile. As shown in this table, the effective ground thermal conductivity found for the soil investigated was 2.82 W/mK.

Table 3. Thermal response test results: thermal conductivity and pile thermal resistance.

	k	R^2	λ_{eff}	R_b
TRT	-	-	W/mK	mK/W
	1.99	0.85	2.82	0.13

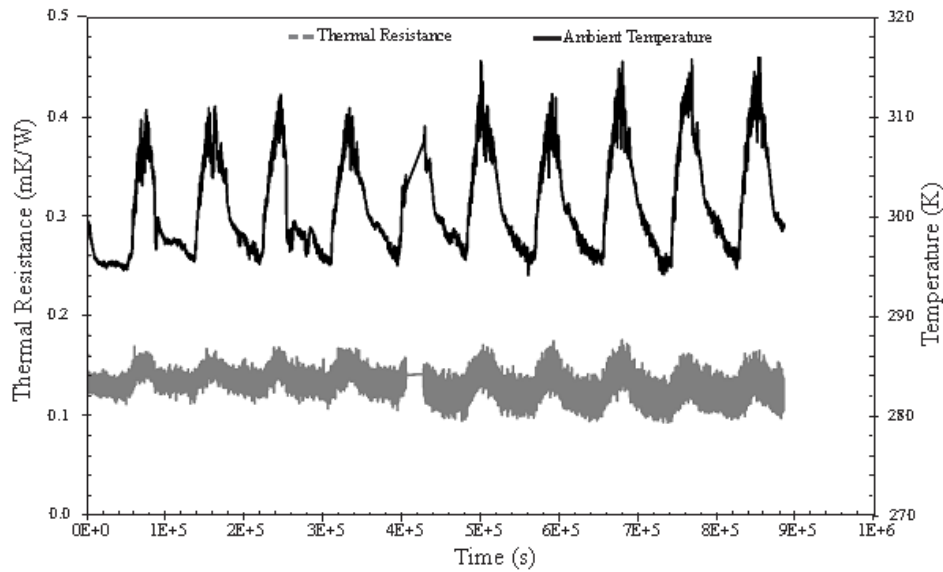


Fig.9. Energy pile thermal resistance during the TRT

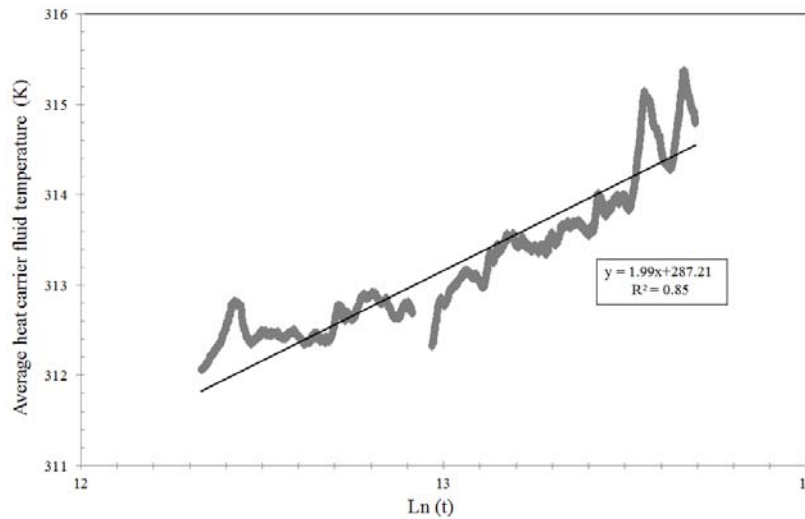


Fig.10. Mean fluid temperature versus the logarithm of time during the TRT

CONCLUSIONS

A thermal response test was conducted during approximately 10 days on an energy pile (micropile) of 15 m length with a U-shaped heat exchanger tube. The aim of the current investigation was to determine the ground thermal conductivity and the pile-thermal resistance of an energy pile installed in the campus of the University of São Paulo at São Paulo city (Brazilian subtropical region).

For analysing the TRT data, the line source model was used, and provided results of thermal parameters that are comparable to previous researches. Additionally, the undisturbed ground temperature of 297.85 K is similar to the results found from measurements in São Carlos city, located in the central-east region of the State of São Paulo.

ACKNOWLEDGEMENTS

The authors are thankful to the São Paulo Research Foundation (Fundação de Amparo à Pesquisa do Estado de São Paulo – FAPESP), for financial support by project N°. 2014/14496-0. The first author also thanks the national Council for Scientific and Technological Development (Conselho nacional de Desenvolvimento Científico e Tecnológico – CNPq) for the scholarship.

REFERENCES

- [1] Associação Brasileira de Normas Técnicas. NBR 6484 (2001). *Standard Penetration Test (SPT)*, Rio de Janeiro, 17 p. (in Portuguese).
- [2] F. Loveridge, W. Powrie & D. Nicholson. Comparison of two different models for pile thermal response test interpretation. *Acta Geotechnica* **9**(3), 367-384 (2014).

- [3] European Standardization Committee: TC 341 WI 00341067.6 (2011) Ground Investigation and testing, *N 525 – Geothermal Testing – Determination of Thermal Conductivity of Soil and Rock using a Borehole Heat Exchanger*. Submitted to the CEN Enquiry.
- [4] H. Brandl. Energy foundations and other thermo-active ground structures. *Géotechnique* **56(2)**, 81 – 122 (2006).
- [5] F. Loveridge. Thermal performance of foundations piles used as heat exchangers in ground energy systems. PhD Thesis 2012: 179E. Southampton: University of Southampton. Faculty of Engineering and The Environment. Civil, Maritime, Environmental Engineering & Science, 2012.
- [6] S. You, X. Cheng, H. Guo, Z. Yao. In-situ experimental study of heat Exchange capacity of CFG pile geothermal exchangers. *Energy and Buildings* **79**, 23-31 (2014).
- [7] T. S. O. Morais, C.H.C. Tsuha,. Energy Pile and Ground Temperature Response to Heating Test: A Case Study in Brazil. *Bulgarian Chemical Communications*, **48**, p. 115-119 (2016).
- [8] S. Gehlin. Thermal response test – method development and evaluation. PhD Thesis 2002: 191 E. Sweden: Luleå University of Technology, Department of Environmental Engineering, Division of Water Resources Engineering, 2002.
- [9] N. Mattson S.; G. Steinmann; L. Laloui. Advanced compact device for the in situ determination of geothermal characteristics of soils. *Energy and Buildings* **40**, 1344 – 1352 (2008).

ENERGY EFFICIENCY

An investigation of the ammonia adsorption performance on different adsorbents for cooling applications

A.F. Altun, M. Kılıç*

Bursa Uludağ University, Engineering Faculty, Dept. of Mechanical Engineering, Bursa, Turkey

Ammonia (NH₃) is a common gas and has been widely investigated on adsorption for numerous purposes. Ammonia is commonly employed as a refrigerant in the refrigeration systems to obtain temperatures below 263 K. Adsorption systems powered by low-temperature heat sources that utilize ammonia as working fluid work at positive pressures, therefore, their manufacturing and usage are much easier, and they require less maintenance, comparing with vacuum systems. In this study, ammonia adsorption performance of various adsorbents is investigated numerically for cooling applications. The adsorbents considered in this study are zeolite, alumina, silica gel and activated carbon. The adsorption performance of each adsorbent-adsorbate pair under various operating conditions is compared. Among the adsorbate-adsorbent pairs investigated in this study, ammonia and activated carbon gave the best performance values in all cases. According to the results of the study, most important parameters that effects COP, Q_r and SCP of an adsorption cooling system are the adsorbent type, cooling source temperature, heating source temperature and evaporation temperature at the evaporator, respectively. It is shown that increasing evaporator temperature and heating source temperature results an increase in COP, Q_r and SCP values of the adsorption system, whereas, for the case of cooling source temperature, highest values of COP, SCP and Q_r are obtained at the lowest cooling fluid inlet temperature.

Keywords: Ammonia, adsorption cooling, adsorbate-adsorbent pair, positive pressure, COP, SCP

INTRODUCTION

Global energy demand is growing rapidly. Cooling and refrigeration demand constitutes a large part of global energy consumption. For this reason, especially during the summer season, a rapid increase can be observed in the amount of electricity consumption. Thermally driven cooling technologies such as absorption and adsorption refrigeration technologies can serve as an alternative to conventional refrigeration cycles [1]. Adsorption refrigeration systems can be considered as environmentally friendly since they require low-grade heat sources such as solar energy or waste heat [2]. In comparison with absorption cooling systems, an adsorption system can be driven by heat sources in a large temperature range, while absorption systems require heat sources with higher temperatures [3],[4]. And last but not least, an adsorption system can be designed and manufactured simply when compared with an absorption system [5]. In addition to their numerous advantages, adsorption cooling systems also have some drawbacks including (a) lower COP when compared with absorption technology and conventional cooling cycles, (b) they have relatively high initial investment costs, as a result, they cannot compete with other cooling technologies

commercially [6]. Many researchers have conducted works on developing adsorption cooling technology in order to overcome the drawbacks that restrict them from being competitive in the related market [7].

Adsorption is a reversible physical phenomenon, realised with an interaction between adsorbent (solid) surfaces and an adsorbate (fluid vapour), driven by cohesive forces [7]. The physical adsorption process of the gas occurs mainly within the pores and surface of the solid adsorbent [8]. The adsorbed amount and concentration of refrigerant in the pores are strongly dependent on pressure and temperature variations as well as the operating conditions of the system [9]. The design of an adsorption refrigeration system requires the knowledge of adsorption characteristics of the employed adsorbent-adsorbate pair when the temperature and pressure are varying [10].

The isosteric heat of adsorption is a combined specific property of an adsorbent/adsorbate pair. The equilibrium adsorption properties at several adsorbent temperatures and adsorption chamber adsorbate pressures were studied for a wide range of pairs by several researchers [5-11].

The adsorption characteristics of every adsorbent-adsorbate pair are usually quite different than each other. Detailed specification about the adsorption isotherms of the assorted

* To whom all correspondence should be sent:
mkilic@uludag.edu.tr

adsorbent/adsorbate pair as well as the isosteric heat of adsorption must be known in order to design an adsorption based cooling system. Detailed literature reviews on adsorption working pairs for refrigeration/cooling applications can be found in the references [1, 3, 4, 5, 14].

Basic adsorption cooling system consists of one adsorption bed, expansion valve, evaporator and condenser. Impermanent cooling production nature of a one-bed system is not convenient as cooling cannot be produced when the bed is undergoing desorption [12]. Multiple bed systems which have at least two adsorber beds are more convenient and practical to use. Using more beds increase COP values, however, the system becomes more complex, as a result of adding more installation elements such as pipes and valves [13].

Adsorption pair which is a vital part of the adsorption refrigeration cycle consists of adsorbent and refrigerant [14]. Refrigerant or adsorbate should have the following properties: [1, 2, 10, 14].

- Small molecular size to allow it to be adsorbed by the adsorbent.
- Non-toxic, non-corrosive and non-flammable.
- Large latent heat per volume
- Good thermal stability

Unfortunately, none of the fluids fulfils completely these requirements. Among the fluids appropriate to use in the adsorption systems, ammonia, methanol and water all have relatively high latent heats, however water cannot be used for freezing purposes as its freezing temperature is 273.15 K and methanol is flammable [1, 14]. Although, ammonia is toxic, it has advantages to other two as it can be used at positive pressures. In addition to that, it has no effect to ozone layer as well as no global warming potential. This makes ammonia a suitable and favoured adsorbate for adsorption cooling cycles.

Ammonia is a colourless, diffusive gas at atmospheric conditions. The ammonia molecule is basic and polar in nature, as a result, several types of adsorbents can be utilized to examine their ammonia adsorption efficiencies, including zeolites, alumina, activated carbon, silica [15]. Ammonia has a relatively high latent heat, about 1365 kJ/kg at 243 K.

In order to choose an appropriate adsorbent some of the important considerations are: [10, 14]

- Low cost, widely available
- Non-toxic and non-corrosive.
- Desorption of most of the adsorbate when exposed to thermal energy

- The ability to change capacity with the variation of temperature

- Excellent compatibility with the refrigerant.

Since adsorbent used for adsorption system affects the system performance significantly, it is very important to understand the characteristics of an adsorbent. Silica gel, zeolite, alumina and activated carbon are the most common adsorbents that are used in adsorption cooling cycles. These are appropriate to the adsorption of the ammonia vapour.

Silica gel is a natural mineral purified and processed into the granular or beaded, vitreous, porous form of silicon dioxide (SiO_2) produced synthetically from silicate and sulfuric acid [5]. Silica gel can be considered as one of the widely used low temperature working adsorbent, which can be employed in the cooling systems driven by the relatively low-temperature heat sources in which the temperature is lower than 373 K [10, 14, 15].

Zeolite is a type of alumina silicate crystal composed of alkali or alkali soil [4]. Due to their low cost and availability, zeolites gained a significant interest as an adsorbent. Natural zeolites also gained a remarkable interest due to their valuable properties such as ion-exchange capability [1]. About 150 types of zeolites can be artificially synthesized, and they are named by one letter or a group of letters, such as type A, type X, type Y, type ZSM, etc. [1, 4].

Activated alumina is aluminium oxide in the form of very porous spheres. Since it is a highly porous material, it is a great adsorbent for adsorption cycles.

Activated carbons are made by pyrolyzing and carbonising source materials, such as coal, lignite, wood, nut shells and synthetic polymers, at high temperatures (1000 to 1100 K) [1, 4, 13, 14]. Activated carbons can be found in many different forms such as powders, granulated, microporous, molecular sieves and carbon fibres. It is widely used for adsorption applications.

Due to its zero global warming and ozone depletion potential, ammonia has been considered as being one of the most efficient refrigerants. However, there are not enough studies in the literature concerning adsorption of ammonia. A number of studies such as refs. [13-17] have been performed on the adsorption cooling systems employing the pair of activated carbon and ammonia. Only a few study considered silica gel-ammonia pair as an adsorbent-adsorbate pair [16, 17]. On the other hand, to the best of our knowledge, there is not any published research subject to a comparative evaluation of the adsorption cooling system with ammonia as adsorbate fluid onto the

adsorbent solid including the silica gel, zeolite, alumina and activated carbon.

Since conducting experimental investigation of adsorption systems is complicated and expensive, it is much easier and convenient to simulate the process numerically. As a result, in this study, a mathematical modelling method for adsorption cooling systems proposed by Kilic [18] is used, validated and applied for ammonia and four different adsorbent pairs. With the used mathematical method, adsorption cooling cycle characteristics of any adsorbent-refrigerant pair can be easily estimated.

In this study, silica gel, zeolite, alumina and activated carbon are chosen as adsorbents and ammonia is considered as the adsorbate. Then, the performance of these four different adsorbent-adsorbate pairs for an adsorption refrigeration / cooling application with different working conditions are investigated and compared with each other. Main contributions of the present study into the current literature can be explained with two-fold as: firstly, it presents a more realistic modelling approach by the use of real fluid properties in the calculations, and secondly, four different adsorbents are used for the adsorption cooling and refrigeration system with the ammonia employed as working fluid. The presented results can be used on the design of an adsorption based cooling cycle systems in which ammonia is employed as adsorbate with the one of the adsorbents among silica gel, zeolite, alumina and activated carbon.

MATHEMATICAL MODELLING

The adsorption cooling systems are similar to the known mechanical vapour compression systems and the system components such as the evaporator, condenser and expansion valve are the same. The main difference is that the thermal compressor takes the place of the mechanical compressor. Therefore, an adsorption cooling/refrigeration system can be driven only by heat energy so it does not need electrical energy to perform. Details of the working principle of the thermal compressor operating according to the adsorption refrigeration cycle are given in the other study by Kilic [18]. In that study, the mathematical model of the two-bed adsorption cooling system and the calculation procedure were given in details. Therefore, the important equations and parameters related to the present work is introduced in this section.

Adsorption isotherms

It has become a common approach that the use of Dubinin–Astakhov (D–A) model for the calculation of the adsorbate uptake value on the adsorbent as a function of temperature and pressure in the adsorption bed [19]. Dubinin–Astakhov (D–A) equation may be written in the form given as follow:

$$W = W_0 \exp \left\{ - \left[\frac{RT}{E} \ln \left(\frac{p_s}{p} \right) \right]^n \right\} \quad (1)$$

with

$$W = Xv_a \text{ and } W_0 = X_0v_0 \quad (2)$$

In Eq.(1), E may be expressed as the specific characteristic energy of the assorted adsorbent-adsorbate pair which may be evaluated from the experimental measurements. R is the gas constant. Pressure is represented by p , and suffix s is referring to the saturation state. Temperature is represented by T . The parameter n is a power constant which results the best fitting of the experimental isotherms. The quantity X represents the specific adsorbed mass of adsorbate (kg of adsorbate per kg of adsorbent), and v_a is the specific volume of the adsorbed phase, which is given by

$$v_a = v_b \exp(\Omega(T - T_b)) \quad (3)$$

where v_b is the saturated liquid specific volume at the normal boiling point, b represents the van der Waals volume, and Ω is given as:

$$\Omega = \ln(b/v_b) / (T_c - T_b) \quad (4)$$

T is the temperature. The critical and normal boiling point temperatures of the refrigerant are represented by suffixes c and b , respectively. The parameter v_0 can be obtained by using Eq.(2) at $T = 273.15$ K. Table 1 shows the properties and parameters of the adsorbates used in the present study.

Table 1. Properties and parameters of the adsorbents used in this study [16, 17]

	Unit	Zeolite13X	Alumina	Silicagel	AC-LM127
ρ	kg/m ³	647	735	445	750
c_p	kJ/kgK	0.96	0.880	0.920	0.900
$^*\Delta H_{ads}$	kJ/kg	1901	1741	1731	1676
W_0	m ³ /kg	0.000399	0.000159	0.000235	0.000577
X_0	kg/kg	0.251	0.100	0.148	0.363
E	kJ/kg	804.0	587.2	558.9	487.1
n		0.98	0.844	1.04	0.95
E_a	kJ/kg	2466	2466	2466	2466

*Calculated values at $T=303.15$ K in the present study.

Adsorption kinetics

Adsorption and desorption rates of the adsorbate onto adsorbent can be calculated by the use of Linear Driving Force (LDF) approach. Adsorption kinetics (dX/dt) equation is given in Eq.(5).

$$\frac{dX}{dt} = F_o \frac{D_o}{r_p^2} \exp\left(-\frac{E_a}{RT}\right) (X_{eq} - X) \quad (5)$$

where X_{eq} is the equilibrium concentration at the given pressure and temperature; F_o is a constant characteristic of adsorbent's shape. The equilibrium concentration is calculated using the Dubinin-Astakhov equation given in Equation 1. X is the instantaneous concentration of the adsorbent bed. The values of the adsorption kinetic parameters are given in Table 1 and Table 2.

Adsorption heat

For adsorption of fluids below their thermodynamic critical point, its magnitude is larger than the heat of vaporization of the adsorbate, which has a strong temperature dependence. As a result, the difference between the adsorption heat and the vaporization heat is a property of relevance in the design of adsorption refrigeration systems. Moreover, the gas phase of the adsorbent is not ideal, during the adsorption of the adsorbate molecules onto the assorted adsorbent is affected by the pressure and temperature changes. Therefore, the heat of adsorption is calculated by using the following Eq.(6) as suggested by El-Sharkawy et al. [20].

$$\Delta H_{ads} = h_{fg} + (E)[\ln(W_0/W)]^{1/n} + (ET\Omega/n)[\ln(W_0/W)]^{((1-n)/n)} \quad (6)$$

Table 2. Properties of the ammonia and the parameters used in the present study

Properties	Values	Unit
MW	17.03	kg/kmol
T_b	239.8	K
T_c	405.4	K
R	0.4882	kJ/kg K
P_c	11333	kPa
ρ_c	225.00	kg/m ³
b	0.002183	m ³
v_b	0.001467	m ³ /kg
v_0	0.001589	m ³ /kg
Ω	0.002402	
$^*h_{fg}$	1145	kJ/kg
D_o	2.54E-4	m ² /s
F_o	15	
R_p	1.7E-4	m
$M_{bm}c_{p,bm}$	14	kJ/K
M_s	10	kg

*Values at $T=303.15$ K.

System performance parameters

Adsorption cooling system performance is commonly defined by its specific cooling power (SCP) in W/kg adsorbent and the coefficient of performance (COP). The two parameters are the most important data among the technical specifications of such products. COP and SCP are expressed by Eq. (7) and Eq. (8) respectively.

$$COP = \frac{Q_{eva}}{Q_{heat}} \quad (7)$$

$$SCP = \frac{Q_{eva}}{t_{cycle}M_s} \quad (8)$$

Where cooling capacity of the evaporator (Q_{eva}) and heat load of the system (Q_{heat}) in a cycle can be calculated by Eq.9 and Eq.10, respectively.

$$Q_{eva} = \oint_0^{t_{cycle}} \frac{dm_{eva,out}}{dt} (h_{exv,o} - h_{eva,sv}) dt \quad (9)$$

$$Q_{heat} = \oint_0^{t_{cycle}} \dot{Q}_{heat} dt \quad (10)$$

It should be mentioned that the electrical power consumption of chilled water, cold water and hot water pumps are relatively small so can be neglected.

Validation of the mathematical model

Several studies have been already reported about the adsorption cooling systems for the use of ammonia-activated carbon pair. Tamainot-Telto et al. [17] conducted a theoretical simulation work by the use of ammonia-activated carbon pair. In order to validate present mathematical model computations performed according to their parameters and working conditions used in their study. LM127 type activated carbon is chosen as the adsorbent. The mass of the metal bed material (M_{bm}) used in adsorption bed is ignored in this calculations. The cooling water inlet temperature ($T_{cool,in}$) to the bed and the condenser temperature (T_{cond}) is equal to 308.15 K. Two different evaporator temperature (T_{eva}) are considered as 268.15 K and 283.15 K. Fig.1 shows the comparisons between the present predicted results and the findings of Tamainot-Telto et al. [17] for the heating fluid inlet temperature in the range of 355.15 to 403.15 K.

It can be seen that the predicted COP values are mainly in a good agreement with the data of Tamainot-Telto et al. [17]. As the temperature increases from 355.15 to 403.15 K, there is a slight increase at COP values for both evaporator temperatures.

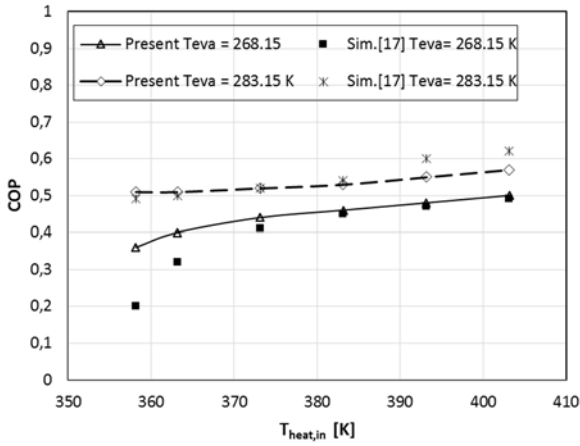


Fig.1. Comparisons of the predicted COP values of ammonia-activated carbon (LM127) pair with the simulation of Ref.[17] for the different heating fluid inlet temperatures. ($T_{cool,in}=T_{cond}=308.15K$)

Increasing evaporator temperature considerably increases COP values in both sets of results. The maximum differences of the predicted COP values appear at lower heating temperature values for the case of low evaporator temperature. Although there is a very good agreement for the case of high evaporator temperature. This is probably resulted by the difference between their model and the present model. Main differences between the models are the form of D-A equation for the pair adsorption heat calculations and fluid properties calculations. In the present model, the properties of the fluid are obtained for real fluid properties, the adsorption heat is not constant. Even though there are differences between the models, the results show very good agreements. Hence, the mathematical model can be accepted as validated.

RESULTS AND DISCUSSION

The aim of the present study is to perform a comparative work on the adsorption cooling system using ammonia with different adsorbents. Four different widely used adsorbents (silica gel, zeolite (13X), alumina and activated carbon (LM127)) are chosen. Two-bed adsorption cooling system as described in previous sections are used in the calculations. The mass of the adsorbent (M_s) used in each bed is taken as 10 kg in the calculations. In the computations, adsorption/desorption time is taken as 600 seconds, precooling/preheating time is taken as 50 seconds. Therefore, the cycle time is taken as 1300 seconds. Computations are performed at the same working conditions for the four different adsorbent-adsorbate pairs. Properties and

parameters of the adsorbents and adsorbate used in this study are given in Tab.1 and Tab.2, respectively.

Table 3. Working conditions used in the calculations

Case	T_{eva} [K]	$T_{heat,in}$ [K]	$T_{cool,in}$ [K]	$T_{chill,in}$ [K]
1	268.15	343.15 – 403.15	303.15	287.15
2	253.15-283.15	363.15	303.15	287.15
3	268.15	363.15	293.15-313.15	287.15

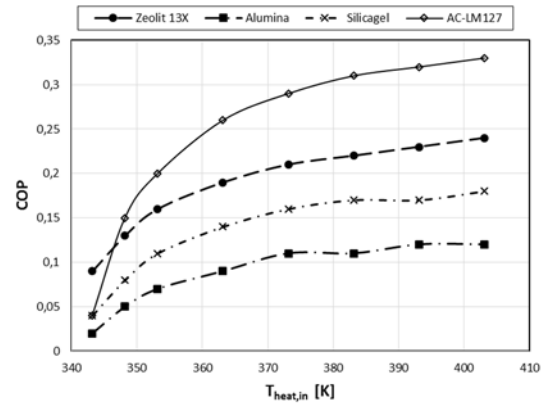


Fig.2. Comparisons of COP for the different heating and cooling fluid inlet temperatures. ($T_{eva}=268.15 K$; $T_{cool,in} = 303.15 K$)

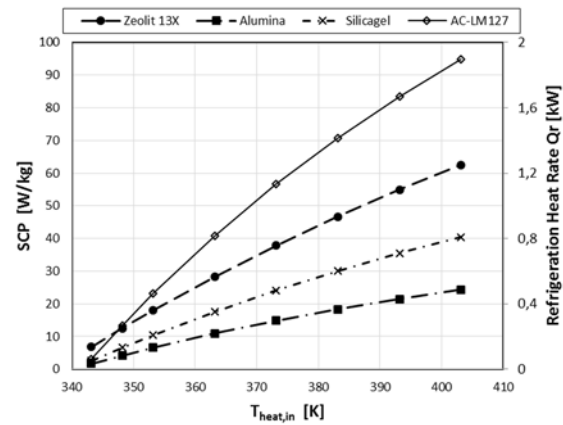


Fig.3. Comparisons of SCP and refrigeration heat rate for the different heating fluid inlet temperatures. ($T_{eva}=268.15 K$; $T_{cool,in} = 303.15 K$)

Other temperature settings are applied as follow:
 Condenser temperature $T_{cond} = T_{cool,in} + 3 K$;
 Evaporator temperature $T_{eva} = T_{chill, o} - 3 K$;
 Bed maximum temperature $T_{bed,max} = T_{heat,in} - 2 K$;
 Bed minimum temperature $T_{bed,min} = T_{cool,in} + 2 K$.

Computations are performed for three different set of working conditions as given in Tab.3. Fig.2 shows the computed results of the coefficient of performance (COP) for Case 1. It can be seen that COP increases with rising heating source temperature for all the pairs. This may be explained

as when the heating temperature rises, more adsorbate circulating in the system with increasing desorption rate from the bed. Active carbon and alumina shows the best and worst COP values, respectively, among the pairs. For all of the pairs, there is a significant drop in the COP under the heating source temperature of 363 K.

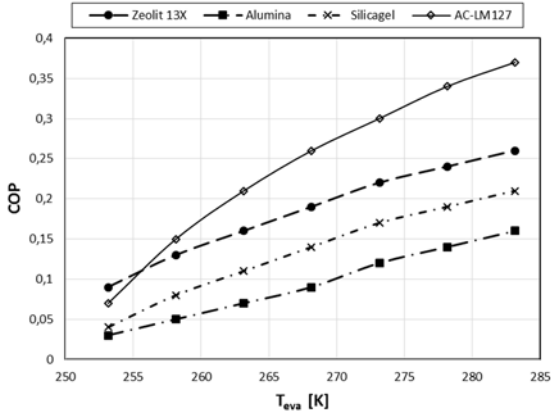


Fig. 4. Comparisons of COP for the different evaporator temperatures. ($T_{\text{heat}}=363 \text{ K}$; $T_{\text{cool,in}}=303 \text{ K}$)

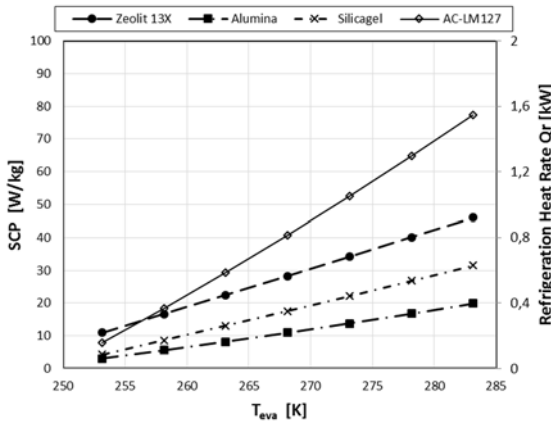


Fig. 5. Comparisons of SCP and refrigeration heat rate for the different evaporator temperatures. ($T_{\text{heat}}=363 \text{ K}$; $T_{\text{cool,in}}=303 \text{ K}$)

Fig. 3 shows the computed results of the specific cooling power (SCP) and refrigeration heat rate (Q_r). For the all working fluids, SCP and Q_r values rise almost linearly with the heating temperature. Active carbon pair has the highest values of SCP and Q_r , 95 W/kg and 1.9 kW, respectively, at the heating temperature of 403.15 K. It may be explained as more fluid mass is desorbed from the bed with rising heating source temperature, due to this more working fluid circulates in the system, and the cooling power rises accordingly. Zeolite, silica gel and alumina pairs show less performance compared to the active carbon in descending order respectively.

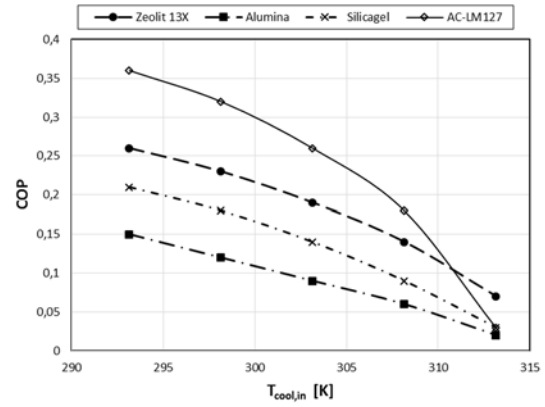


Fig. 6. Comparisons of COP for the different cooling fluid inlet temperatures. ($T_{\text{heat}}=363 \text{ K}$; $T_{\text{eva}}=268 \text{ K}$)

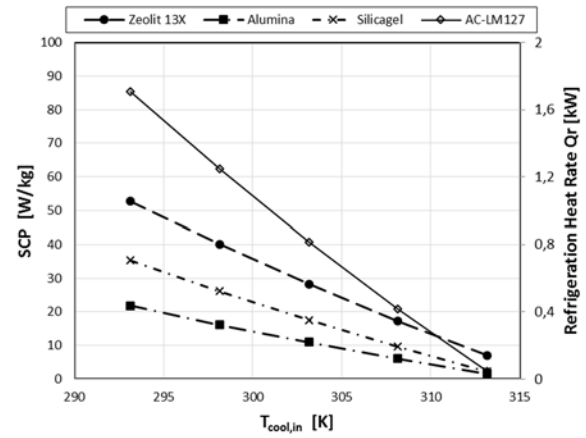


Fig. 7. Comparisons of SCP and refrigeration heat rate for the different cooling fluid inlet temperatures. ($T_{\text{heat}}=363 \text{ K}$; $T_{\text{eva}}=268 \text{ K}$)

Comparing COP and SCP for the working fluids when the evaporator temperature changing as Case 2, it can be seen at Figs. (4, 5) that the highest COP (=0.38) and SCP (=95 W/kg) are obtained for the activated carbon at $T_{\text{eva}} = 283.15 \text{ K}$, and the lowest ones are found for the alumina (as 0.03 and 3 W/kg, respectively) at $T_{\text{eva}} = 253.15$. Refrigeration heat rate also shows a similar trend, and its maximum values are 1.58, 0.92, 0.51 and 0.4 at $T_{\text{eva}} = 283.15 \text{ K}$ for active carbon, zeolite, silica gel and alumina, respectively. In general, increasing evaporator temperature result an increase in COP, SCP and Q_r values.

The results for Case 3 presented in Figs. (6, 7). The change of the cooling fluid inlet temperature on the performance parameters shows a reverse effect with the evaporator temperature. Highest values of COP, SCP and Q_r are obtained at the lowest cooling fluid inlet temperature, $T_{\text{cool,in}} = 293.15 \text{ K}$. This may be explained as decreasing cooling fluid temperature drops the minimum bed temperature and also

decrease condensation temperature and pressure at the condenser. Therefore, more adsorbate can be adsorbed at the bed with a lower adsorption temperature, and more adsorbate can be desorbed at the bed with lower condenser pressure. The performance parameters order is similar to the Case 1 and 2.

Considering the adsorption heat values (at 303.15K) given at Tab.1, zeolite 13X has the largest one (1901 kJ/kg), alumina and silica gel have almost same (1741 and 1731 kJ/kg, respectively), activated carbon has the smallest value (as 1676 kJ/kg).

CONCLUSIONS

This study presents a comparative study on a two bed adsorption cooling system with a working fluid ammonia as adsorbate and four different widely used adsorbents as zeolite 13X, alumina, silica gel and activated carbon (LM127). These four adsorbent-adsorbate pairs and various cycle operating conditions are investigated at the heating source temperature range from 343.15 to 403.15 K.

The effects of the different evaporator and cooling source temperatures are also evaluated and compared. The performance indicators of COP, SCP and refrigeration heat rate (Q_r) are investigated and compared for the same working conditions. Among the adsorbent-adsorbate pairs considered in this study, the best performance values are obtained for the activated carbon and ammonia pair. In the investigated range of working conditions, the maximum values of COP, SCP and Q_r for the pair with activated carbon are 0.38, 88 W/kg and 1.8 kW, respectively. The zeolite-ammonia pair shows similar behaviour to the activated carbon pair with about 28% and 34% less performance in terms of COP and SCP, respectively.

It is shown that the parameters that have the largest effect on COP and SCP are, in decreasing order, adsorbent type, cooling source temperature, heating source temperature and evaporation temperature at the evaporator. These results are valid for all working pairs. In general, increasing evaporation temperature and decreasing adsorption bed temperature during the adsorption process increases COP, SCP and Q_r for all working pairs.

It should be noted that the calculations are performed based on a basic adsorption cycle with a two-bed system. The selection of the adsorbent type has a great effect on the performance of the system. Hence, higher performances may be obtained with the selection of more efficient adsorbent for ammonia. Moreover, the system performances may

be increased by the use of more advanced cycles in which new or advanced techniques, such as heat and mass recovery, applied.

NOMENCLATURE

b -	the van der Waals volume, m^3 ;
c_p -	specific heat, kJ/kgK;
COP	- coefficient of performance, - ;
D_0	- surface diffusion coefficient, m^2/s ;
E	- characteristic energy, kJ/kg;
E_a	- activation energy, kJ/kg;
F_o	- a constant characteristic of adsorbent's shape.
h_{fg} -	vaporization enthalpy, kJ/kg;
ΔH_{ads} -	adsorption heat, kJ/kg;
M	- mass, kg;
MW -	molecular weight of fluid, kg/kmol;
n -	exponential constant, -.
p -	pressure, kPa;
p_s -	saturation pressure, kPa;
R	- gas constant, kJ/kgK;
SCP	- specific cooling power, W/kg;
Q	- heat, kJ;
Q_r	- refrigeration heat rate, kW;
\dot{Q}	- heat rate, kW;
t	- time, s;
t_{cycle} -	total cycle time, s;
T	- temperature, K;
X	- adsorption capacity on mass basis, kg/kg;
v_a	- adsorbed phase specific volume, m^3/kg ;
v_b	- saturated liquid specific volume at normal boiling temperature, m^3/kg ;

Subscripts

a-	adsorbed phase;
ad-	adsorption;
b-	boiling point;
bed-	adsorber bed;
bm-	bed material;
c-	critical point;
cyc-	cycle;
cond-	condenser;
eva-	evaporator;
f-	fluid;
fg-	phase change from liquid to gas;
in-	inlet;
out-	outlet;
min-	minimum;
max-	maximum;
s-	sorbent;
s-	saturation;
l-	liquid phase;
v-	vapour phase.

REFERENCES

- [1] A.A. Askalany, M. Salem, I.M. Ismael, A.H.H. Ali, M.G. Morsy, B.B. Saha. An overview on adsorption pairs for cooling. *Renewable and Sustainable Energy Reviews* **19**, 565–572 (2013).
- [2] D.C. Wang, Y.H. Li, D. Li, Y.Z. Xia, J.P. Zhang. A review on adsorption refrigeration technology and adsorption deterioration in physical adsorption systems. *Renewable and Sustainable Energy Reviews* **14**, 344–353 (2010).
- [3] M.M. Younes, I. El-Sharkawy, A.E. Kabeel, B.B. Saha. A review on adsorbent-adsorbate pairs for cooling applications. *Applied Thermal Engineering* **114**, 394–414 (2016).
- [4] A. Allouhi, T. Kousksou, A. Jamil, T. El Rhafiki, Y. Mourad, Y. Zeaouli. Optimal working pairs for solar adsorption cooling applications, *Energy* **79**, 235–247 (2015).
- [5] L.W. Wang, R.Z. Wang, R.G. Oliveira. A review on adsorption working pairs for refrigeration. *Renewable and Sustainable Energy Reviews* **13**, 518–534 (2009).
- [6] R.Z. Wang, R.G. Oliveria. Adsorption refrigeration - An efficient way to make good use of waste heat and solar energy. *Progress in Energy and Combustion Science* **32**, 424–458 (2006).
- [7] B.B. Saha, S. Koyama, I.I. El-Sharkawy, K. Habib, K. Srinivasan, P. Dutta. Evaluation of adsorption parameters and heats of adsorption through desorption measurements. *Journal of Chemical and Engineering Data* **52(6)**, 2419–2424 (2007).
- [8] M. Kılıç, E. Gönül. Adsorption characteristics evaluation of R134A and R404A on different adsorbents. *Bulgarian Chemical Communications* **48(E)**, 306–311 (2016).
- [9] B.B. Saha, K. Habib, I.I. El-Sharkawy, S. Koyama. Adsorption characteristics and heat of adsorption measurements of R-134a on activated carbon. *International Journal of Refrigeration* **32**, 1563–1569 (2009).
- [10] K. Habib, B.B. Saha, S. Koyama. Study of various adsorbent-refrigerant pairs for the application of solar driven adsorption cooling in tropical climates. *Applied Thermal Engineering* **72**, 266–274 (2014).
- [11] M. Kılıç, E. Gönül. An experimental study on adsorption characteristics of R134A and R404A onto silicagel adsorbents. *Proc. of HEFAT 2017, 13th International Conference on Heat Transfer, Fluid Mechanics and Thermodynamics, Portoroz, Slovenia*, 52–58 (2017).
- [12] W.S. Teng, K.C. Leong, A. Chakraborty. Revisiting adsorption cooling cycle from mathematical modelling to system development. *Renewable and Sustainable Reviews* **63**, 315–332 (2016).
- [13] S.J. Metcalf, R.E. Critoph, Z. Tamainot-Telto. Optimal cycle selection in carbon-ammonia adsorption cycles. *International Journal of Refrigeration* **35**, 571–580 (2012).
- [14] M.M. Younes, I. El-Sharkawy, A.E. Kabeel, B.B. Saha. A review on adsorbent-adsorbate pairs for cooling applications. *Applied Thermal Engineering* **114**, 394–414 (2016).
- [15] R.P. Sah, B. Choudhury, R.N. Das. A review on adsorption cooling systems with silica gel and carbon as adsorbents. *Renewable and Sustainable Energy Reviews* **45**, 123–134 (2015).
- [16] J. Helminen, J. Helenius, E. Paatero, I. Turunen. Comparisons of sorbents and isotherm models for NH₃ – gas separation by adsorption. *AIChE Journal* **46(8)**, 1541–1555 (2000).
- [17] Z. Tamainot-Telto, S.J. Metcalf, R.E. Critoph, Y. Zhong, R. Thorpe. Carbon-ammonia pairs for adsorption refrigeration applications: ice making, air conditioning and heat pumping. *International Journal of Refrigeration* **32**, 1212–1229 (2009).
- [18] M. Kılıç. Comparative performance analysis of a two-bed adsorption cooling system with adsorption of different adsorbates on silica-gel. *Bulgarian Chemical Communications* **50(G)**, (2018).
- [19] M. Kılıç, E. Gönül. Adsorption characteristics evaluation of R134A and R404A on different adsorbents. *Bulgarian Chemical Communications* **48(E)**, 306–311 (2016).
- [20] I.I. El-Sharkawy, K. Kuwahara, B.B. Saha, S. Koyama, K.C. Ng. Experimental investigation of activated carbon fibers/ethanol pairs for adsorption cooling system application. *Applied Thermal Engineering* **26**, 859–865 (2006).

The use of a new “clean” technology for burning low-grade coal in on boilers of Kazakhstan TPPs

A. S. Askarova¹, S. A. Bolegenova¹, A. Georgiev³, S. A. Bolegenova², V. Yu. Maximov²,
R.K. Manatbayev¹, A. B. Yergaliyeva^{2*}, A. O. Nugymanova¹, Zh.T. Baizhuma¹

¹Al-Farabi Kazakh National University, Dept. of Physics and Technology, 71a, Al-Farabi ave, 050040 Almaty, Kazakhstan

²Scientific Research Institute of Experimental and Theoretical Physics, 71a, Al-Farabi ave, 050040 Almaty, Kazakhstan

³Technical University of Sofia, Plovdiv Branch, Dept. of Mechanics, 25 Tsanko Diustabanov Str, 4000 Plovdiv, Bulgaria

The combustion of low-grade coals is associated with the difficulties of their inflammation and burn-out, an increase of harmful dusty and gaseous emissions (ash, nitrogen and sulphur oxides). The use of low-grade coals leads to an increase in the fuel oil and natural gas expenses for the furnace kindling, capturing and stabilization of the pulverized coal torch combustion, and the environmental situation worsens. In this work the research on the torch combustion of the coal dust prepared by a plasma-thermochemical treatment for combustion have been done using the method of three-dimensional simulation. The authors have obtained that the plasma preparation of coal for combustion enables one to optimize the process, improve the conditions for inflammation and combustion and minimize the emissions of harmful substances.

Keywords: Combustion, plasma preparation, simulation, harmful substances, plasma-fuel system

INTRODUCTION

At present, in Kazakhstan, it is necessary to increase energy production processes efficiency in strict compliance with emission standards harmful substances and effective utilization of the equipment.

A promising solution in this area is the new effective technology of combustion processes during the thermal activation of low-grade coal to create efficient methods of "clean" energy production in real combustion chambers of Kazakhstan TPP [1-2]. This is a technology of preliminary preparation for the burning of low-grade coal (high-ash content), which use the plasma-fuel system (PFS). As follows from the very definition of the system, the PFS generally represents a burner device with a plasmatorch. The processes of the plasma thermochemical preparation of solid fuels for combustion are realized in the PFS.

This technology recommended itself quite well on powerful energy units in a number of foreign countries, and has a high economic and ecological potential.

At the use of a plasma activation of the pulverized coal flow the input parameters employed in computations differ from those existing in

practice at a conventional arrangement of the pulverized coal torch combustion. A torch of the reacting fuel mixture enters the combustor, which causes an alteration of the main parameters of the combustion process.

In this connection, a complex investigation of the work process of the furnace chamber with allowance for the influence of the fuel thermochemical preparation, including the numerical simulation of processes occurring within the combustor volume, becomes especially urgent.

The relevance and importance of these researches is that this technology may be implemented on all coal-fired thermal power plants of Kazakhstan.

PLASMA TECHNOLOGY OF LOW-GRADE COAL COMBUSTION

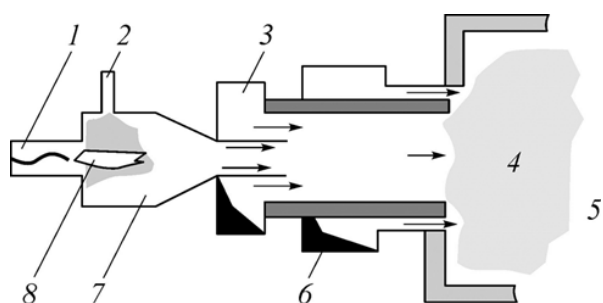
The essence of solid fuel preparation using a plasma technology is that the low-reaction high-ash coal is converted into a high-reaction fuel, heated to the ignition temperature in the volume of burners. The resulting highly reactive fuel by mixing with the secondary air in the combustion chamber intensively ignites and burns rapidly without the "backlight" of the fuel oil (Fig.1).

The plasma thermochemical preparation of coal for combustion consists of the heating by a plasmatorch at an oxygen deficiency in the pulverized coal flow in a special chamber up to a

* To whom all correspondence should be sent:
lmllldy@126.com

temperature exceeding the temperature of the self-inflammation of a given coal.

As a result, the obtained fuel mixture or the highly reactive two-component fuel (HRTF) consisting of the combustible gas and coke rest ignites at its mixing with a secondary air and stably burns without using a pulverized coal torch for stabilization even in a cold furnace of the backup high-reaction fuel (mazut or natural gas).



1 – plasmatron; 2 – a smaller part of the air mixture; 3 – the main part of the air mixture; 4 – the flame of plasma thermochemical preparation products of an air mixture; 5 – furnace space; 6 – secondary air; 7 - the chamber of electrothermochemical preparation of fuel to burning; 8 – plasma flame

Fig.1. Plasmatron in a cylindrical vortex burner [3]

In this case, there occurs a practically complete emission of volatiles and a partial combustion and/or gasification of the coal carbon. The use of various types of burners does not cause the differences in the mechanisms of the process of the plasma thermochemical treatment of coal for combustion. The use of plasma fuel systems enables one to eliminate from the TPS fuel balance the mazut, which is conventionally used for the lighting of boilers.

The method of thermochemical plasma preparation of coal for combustion has been tested successfully on several thermal power stations, which confirms its efficiency. However, one needs the development of special techniques for computing the burner devices for a wide introduction of plasma technology of the coals fuel oil-free inflammation, which will make it possible to estimate prior to experiment the main parameters of the processes occurring in the volume of a burner supplied with a plasmatorch, obtain the fuel mixture composition at the furnace inlet, and compute the characteristics of the heat and mass transfer within the combustor of the TPS boiler. The use of new computer technologies for simulation has enabled one to carry out the computations of these processes [4–12, 25].

OBJECT OF RESEARCH

The present paper deals with the numerical investigation of the plasma source influence on thermochemical conversions of the aeromixture and its combustion by the example of the combustion of the high-ash coal in the furnace of the BKZ-420 boiler of the Almaty TPS-2. Thus, the investigation task included the computation of combustion processes in the furnace of a boiler supplied with the conventional pulverized coal burners with a fuel oil sprayer and the PFS. Three regimes of the boiler operation: 1) the conventional (using six pulverized coal burners); 2-3) plasma activation of combustion (with a replacement of three and six pulverized coal burners with the PFS's) were chosen for numerical investigations.

When carrying out computational experiments for plasma activation of combustion, the authors used the program FLOREAN, which accounts for the furnace actual configuration and the kinetics of the process of the combustion of coal particles by a simplified kinetic scheme. The same code was used also for the computations of the conventional regime of coal combustion in the furnace of boiler BKZ-420.

While replacing the design burners with the vortex PFS's (Fig.1) with a chamber for electrothermochemical fuel preparation 0.73 m in diameter one employs a plasmatorch with 100 kW power. The chamber wall temperature was assumed equal to 700 K. The mean-mass diameter of coal particles was 60 μm ($R_{90} = 14.3\%$), the original aeromixture temperature at the PFS inlet remained the same as at the inlets of the main burners and was equal to 423 K, the coal consumption via the PFS was 7.3 t/h. The thermal efficiency of the PFS based on experimental data was taken to equal 90%. The results of the PFS numerical simulation are summarized in Tab.1. These data taken for the PFS outlet section have been used as the input data for the three-dimensional simulation of the furnace of the power boiler BKZ-420 of the Almaty TPS-2, three and six burners of which were virtually reequipped into the PFS's [13–15].

Table 1. The results of the PFS numerical simulation

CO	H ₂	CH ₄	CO ₂	H ₂ O	N ₂	O ₂
Volumetric, %						
11.04	2.17	0.22	13.53	1.93	70.55	0.13
NO, mg/m ^{3*}		X _C , %	V _g , m/s	T _g , K		τ_g , s
7.5		67.6	42.1	1076		0.016

The table contains the following values:

* Normal cubic meter (under normal conditions: $P = 101325 \text{ Pa}$, $T = 298 \text{ K}$);
 X_C – coal gasification degree;
 V_g – the flow velocity;
 T_g – the temperature of the highly reactive two-component fuel flow;
 τ_g – the time of fuel residence in the plasma-fuel system.

The model presented in to the numerical simulation of BKZ-420 combustion chamber. Its steam capacity equal to 420 t/h. Boiler equipped with six vortex dust burner, arranged in two levels with three burners on the front wall of the boiler as shown in Fig.2.

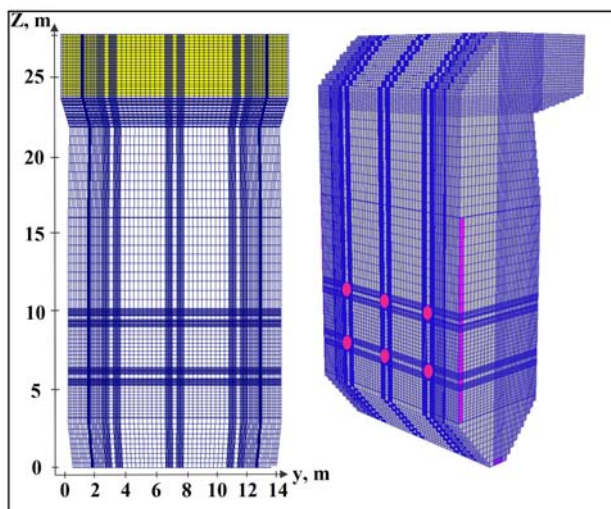


Fig.2. Geometry and finite-difference grid of the boiler furnace BKZ-420 of Almaty TPS-2

Low-grade high-ash coal dust from Ekibastuz has burnt in the boiler, it has ash content of 40 %, volatile – 24 %, moisture content – 5 % and the highest calorific value 16700 kJ/kg. The fineness of coal milling is equal to $R_{90} = 15 \%$. All numerical calculations were performed on above characteristics. The initial parameters required for the three-dimensional calculation of the BKZ-420 boiler of Almaty TPS-2, equipped with plasma-fuel systems, are shown in Tab.2.

Table 2. The initial data of coal and BKZ-420 combustion chamber for numerical calculation

Characteristic	Quantity
Coal type	Ekibstuz
Density of particles, kg/m^3	1300
C_{daf} , %	82.0
H_{daf} , %	5.0
N_{daf} , %	1.5
O_{daf} , %	11.5
Ash, %	40
Humidity, %	5
Volatile, %	24

Coal consumption by the boiler, kg/h	72 000
Coal consumption by the burner, kg/h	12 000
Primary air consumption by the boiler, kg/h	107 035
Secondary air consumption by the boiler, kg/h	402 656
Secondary air temperature, °C	280
Temperature of aeromixture, °C	90
Average particle size of coal, m	60×10^{-6}
The lower heating value of coal, kJ/kg	16 750
The amount of computation (control volume)	$1\,150 \times 10^3$

METHODOLOGY OF THE RESEARCH

Basic equation

Among the methods of modelling the combustion of pulverized fuel most widely used method based on the Euler, an approach to describe the motion and heat transfer of the gas phase. This method uses the spatial balance equations for mass, momentum, the concentrations of gaseous components and energies for the gas mixture. To describe the motion of single particles and heat mass transfer of fuel along their trajectories used Lagrange approach. Turbulent flow structure is described by a two-parameter of $k-\varepsilon$ model of turbulence, where k – the kinetic energy of turbulence, ε – turbulent energy of dissipation [16].

The mathematical description of physical and chemical processes based on the solution of balance equations. In general, these equations contain four terms describing:

- Change in the value of time;
- Convective transfer;
- Diffusive transfer;
- External and internal sources.

To calculate the gas flow solid-phase with the input of all transport quantities in the control volume are determined by the generalized Eq.(1):

$$\frac{\partial(\rho\phi)}{\partial t} = -\frac{\partial(\rho u_1\phi)}{\partial x_1} - \frac{\partial(\rho u_2\phi)}{\partial x_2} - \frac{\partial(\rho u_3\phi)}{\partial x_3} + \frac{\partial}{\partial x_1} \left[\Gamma_\phi \frac{\partial \phi}{\partial x_1} \right] + \frac{\partial}{\partial x_2} \left[\Gamma_\phi \frac{\partial \phi}{\partial x_2} \right] + \frac{\partial}{\partial x_3} \left[\Gamma_\phi \frac{\partial \phi}{\partial x_3} \right] + S_\phi \quad (1)$$

In this equation t – time, ρ – density, $u_1..u_3$ – velocity vector components, $x_1..x_3$ – spatial

coordinates, Γ_ϕ – turbulent exchange coefficient, S_ϕ – describes external and internal sources for the quantity ϕ , other terms describes the variation of ϕ :

$$\frac{\partial(\rho\phi)}{\partial t} - \text{Time component;}$$

$$\frac{\partial(\rho u_j \phi)}{\partial x_j} - \text{Convective transfer;}$$

$$\frac{\partial}{\partial x_1} \left[\Gamma_\phi \frac{\partial \phi}{\partial x_1} \right] - \text{Molecular transfer.}$$

In mathematical model of gas, flow or liquids used equations of conservation of mass and momentum:

$$\frac{\partial \rho}{\partial t} = - \frac{\partial(\rho u_j)}{\partial x_j},$$

here: $\phi=1, \Gamma_\phi=0, S_\phi=0$;

$$\frac{\partial(\rho u_i)}{\partial t} = - \frac{\partial(\rho u_i u_j)}{\partial x_j} + \frac{\partial \tau_{ij}}{\partial x_j} - \frac{\partial p}{\partial x_i} + \rho g_i,$$

$$\phi = u_i; \quad \Gamma_\phi = \mu;$$

here:

$$S_\phi = - \frac{\partial p}{\partial x_i} + \rho g_i + \frac{\partial}{\partial x_j} \left(\mu \cdot \left(\frac{\partial u_j}{\partial x_i} - \frac{2}{3} \cdot \delta_{ij} \frac{\partial u_l}{\partial x_l} \right) \right).$$

For flows in which taken place processes of heat transfer, as well as for compressible media we have to solve the equation of energy conservation:

$$\frac{\partial(\rho h)}{\partial t} = - \frac{\partial(\rho u_i h)}{\partial x_i} + \frac{\partial}{\partial x_i} \left(\frac{\mu}{Pr} \cdot \frac{\partial h}{\partial x_i} \right) + S_h,$$

here: $\phi=h, \Gamma_\phi = \frac{\mu}{Pr}, S_\phi=S_h$, were μ – dynamic viscosity coefficient, Pr – Prandtl number, S_h – source term due to radiant heat transfer.

The six-flow model of De Marco and Lockwood in Cartesian coordinates is used to describe the radiant heat exchange in this work. In this model the distribution of radiant energy flow in corresponding regions is approximated by power series and spherical functions. The distribution of intensity in different directions is approximated by Taylor power series by solid angle.

Source term due to radiant heat transfer in the equation of energy balance is obtained by

integration of total intensity along solid angle $\Omega = 4\pi$.

Thus, we have following:

$$S_h = \frac{4\pi}{3} \cdot K_{abs} (B_1 + B_2 + B_3) - 4 \cdot K_{abs} \cdot \sigma \cdot T^4,$$

here: K_{abs} – integral absorption factor, σ – Stefan-Boltzmann constant.

In flows with the processes of mixing of different components, with the reactions of combustion, etc. must be added the equation of conservation of the mixture components or the conservation equation for mixture fraction and its changes:

$$\frac{\partial(\rho c_\beta)}{\partial t} = - \frac{\partial(\rho c_\beta u_i)}{\partial x_i} + \frac{\partial}{\partial x_i} \left(\rho \cdot D_{c_\beta} \cdot \frac{\partial c_\beta}{\partial x_i} \right) + S_\beta,$$

here: $\phi=c_\beta, \Gamma_\phi=\rho \cdot D_{c_\beta}, S_\phi=S_\beta$, were D_{c_β} – diffusion coefficient, S_β – the formation and decomposition of the components of β as a result of chemical reactions.

For turbulent flow the system of equations is complemented by transport equations for turbulent characteristics.

RESULTS OF COMPUTATIONAL EXPERIMENTS

The present paper provides an overview of the current capabilities of the CFD-computer code FLOREAN (acronym for FLOW and REActioN) developed at the Institute for Fuel and Heat Technology in Technical University of Braunschweig (Germany) [16-23].

Simulation tool FLOREAN allows getting detailed information about furnace performance including velocities, temperature, thermal radiation and concentration distributions, etc. within the furnace and along the walls. The efficient combustion of solid fuel in combustion chambers and the efficient heat transfer to water and steam in steam generators are essential for the economical operation of power plants. This information is useful to evaluate the combustion process and to design optimal furnaces. FLOREAN will also be very useful in improving combustion process of different fuels in industrial boilers, optimizing operation and minimizing pollutant emission [24].

Fig.3 show the full velocity vectors in the combustor cross section for the conventional coal combustion in the burners location plane.

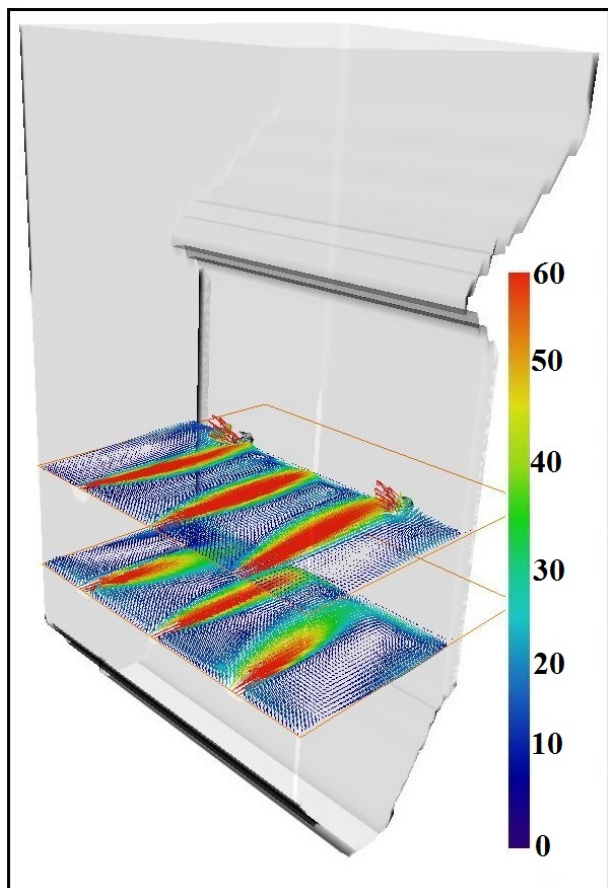


Fig.3. Full velocity vector fields in the combustor cross section at a conventional coal combustion

Fig.4a show the case of a combustor with the same cross section of which is supplied with three PFS's, and Fig.4b show the case of a furnace chamber supplied with all six PFS's.

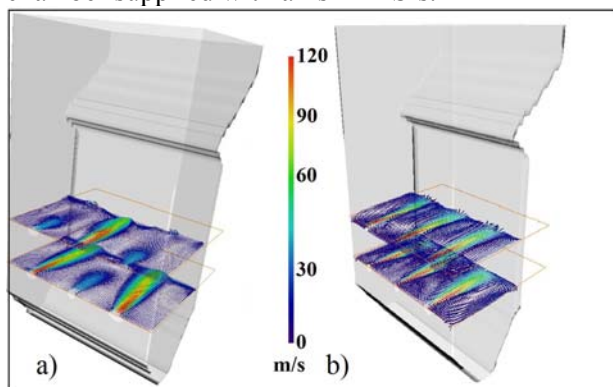


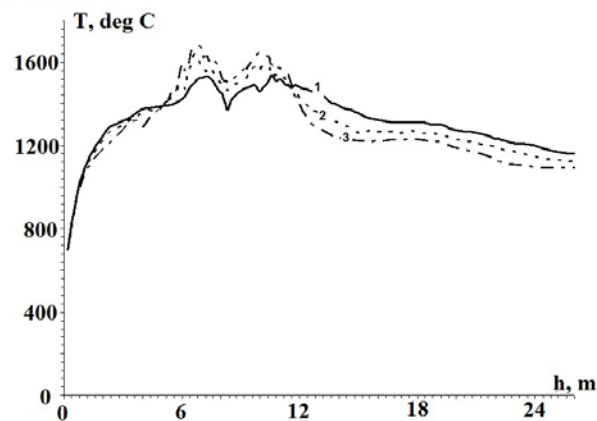
Fig.4. Full velocity vector fields in the combustor cross section at the combustion of a coal activated at three PFS's (a) and at six PFS's (b)

An analysis of the obtained velocity fields has shown that the pulverized coal flow activation affects significantly the flow field, namely the reacting jet propagation in the furnace volume, the admixing processes in the jet, the sizes and shape of

torches. One observes a substantial difference in the distribution of pulverized coal flows entering the furnace through the conventional burners and through the PFS.

The main reason for the alteration in the distribution of velocities in the furnace space is an increase in the velocity of the fuel mixture supplied to the combustor (the two-component high-reaction fuel). With increasing number of the PFS's that is of the thermochemically activated fuel flows, the torch core shifts to the symmetry centre of the furnace chamber, and one observes a clearer pattern of the motion of vortex flows from the PFS.

The mass and heat exchange intensify at a collision of counter torches and tubulisation of flows, and the resulting enhancement of the mixture formation and heating speed up the combustion process. An increase in the velocity along the torch axis increases the intensity of admixing high temperature furnace gases, which in turn leads to a speed-up of the growth of particles temperature and, consequently, to an improvement of the pulverized coal torch inflammation from the burners, which are not supplied with plasma torches. An intense supply of hot furnace gases to the torch root is ensured due to aerodynamic peculiarities of thermochemically activated flows owing to an external and internal recirculation.

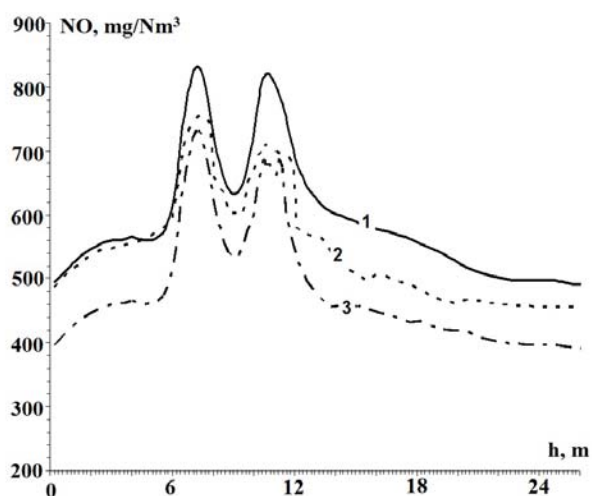


1 - Conventional regime of coal combustion; 2 - Combustion regime of the coal with its plasma activation in three PFS's; 3 - Combustion regime of the coal with its plasma activation in six PFS's

Fig.5. Variation of temperatures over the combustor height

Figs.(5, 6) show the variations of the temperatures and NO concentrations over the combustor height, which were computed for two versions of coal combustion with a preliminary plasma activation of the coal in a PFS and with a conventional one. It is seen that the temperatures over the combustor height, which were computed

for the coal combustion activated by plasma (Fig.5, curves 2 and 3) are mainly below the temperatures calculated for the conventional regime of the coal combustion (Fig.5, curve 1). There is, however, a zone (the combustor lower part up to the level of the upper row of burners), in which the combustion temperature of the coal with plasma activation is above the coal combustion temperature in the conventional regime. This phenomenon may be explained by the PFS influence, which cause an earlier inflammation of the mixture saturated with air and the corresponding shift of the flame front towards the PFS mouth.



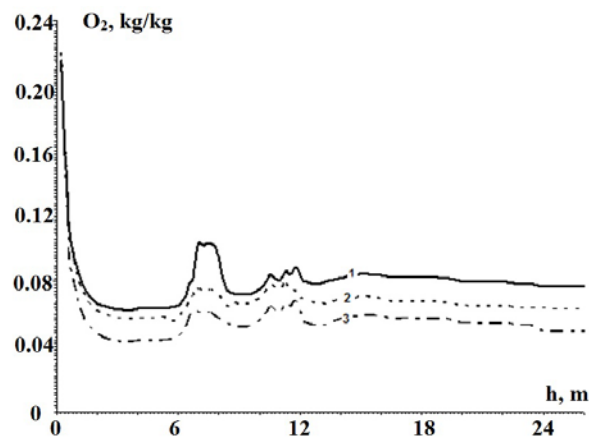
1 - Conventional regime of coal combustion; 2 - Combustion regime of the coal with its plasma activation in three PFS's; 3 - Combustion regime of the coal with its plasma activation in six PFS's

Fig.6. Variation of NO concentrations over the combustor height

One observes also the PFS influence on the formation of NO (Fig.6) over the combustor height. Both the mean values of the NO concentration over the combustor height are much lower in the case of the combustion of the coal with its plasma activation. Note that the use of the PFS reduces the NO concentration (Fig.6, curves 2, and 3) even in the combustor lower part (below the PFS location level). This phenomenon is explained by a suppression of the formation of fuel nitrogen oxides inside the PFS. The fuel nitrogen is released into the gaseous phase at the coal heating together with the volatiles inside the PFS.

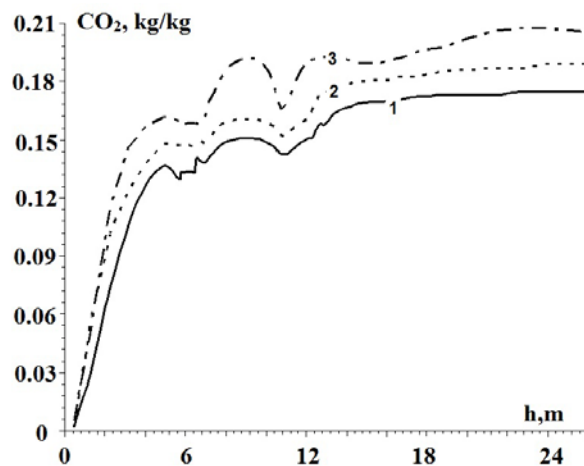
Figs.(7, 8) illustrate the distribution of the concentrations of oxygen and carbon dioxide over the combustor height. The mean values of oxygen concentrations (Fig.7, curves 2 and 3) over the entire combustor height below in the case of the combustion of a coal which has passed a

preliminary thermochemical treatment in the PFS, and the mean values of the carbon dioxide concentrations (Fig.8, curves 2 and 3) are higher.



1 - Conventional regime of coal combustion; 2 - Combustion regime of the coal with its plasma activation in three PFS's; 3 - Combustion regime of the coal with its plasma activation in six PFS's

Fig.7. Variation of oxygen concentrations over the combustor height



1 - Conventional regime of coal combustion; 2 - Combustion regime of the coal with its plasma activation in three PFS's; 3 - Combustion regime of the coal with its plasma activation in six PFS's

Fig.8. Variation of carbon dioxide concentrations over the combustor height

These data confirm the fact that at the use of the PFS for coal combustion stabilization, one observes a more complete coal burn-out and a reduction of the mechanical underburning of the fuel [5].

CONCLUSIONS

A comparative numerical investigation of the conventional coal combustion and the coal combustion in a furnace supplied with a PFS, which has been conducted in the work, shows that the

plasma thermochemical treatment of the coal prior to its combustion enables one to optimize the process, improve the inflammation and combustion conditions, minimize the emissions of harmful substances into atmosphere. The application of the PFS technology will enable a reduction of the equivalent fuel expense per 1 kWh of the generated energy by 10–15 gram of the equivalent fuel, which is equivalent to the 1.5–3 % fuel saving or to an increase in the efficiency of electricity generation by 0.5–1 %. A wide application of the PFS technology carries in itself an important social-economic effect and will make it possible not only to improve the environmental situation in regions near the TPS, optimize the process of the combustion of energy fuels, but also to raise the level of the culture of the TPS workers at the expense of the application of a more progressive and environmentally clean technology of the inflammation and combustion of solid fuels.

ACKNOWLEDGEMENTS

This work has been supported financially by the research project No BR05236730 the call for program-targeted funding for scientific and (or) scientific and technical programs for 2018-2020 of the SRI of Experimental and Theoretical Physics of Al-Farabi Kazakh National University, which is gratefully acknowledged by the authors.

REFERENCES

- [1] A.S. Askarova, E.I. Karpenko, V.E. Messerle, A.B. Ustimenko. Mathematical modelling of the processes of solid fuel ignition and combustion at combustors of the power boilers. *Proc. of the 7th International Fall Seminar on Propellants, Explosives and Pyrotechnics, Xian*, 672-683 (2007).
- [2] S.A. Bolegenova, V.Y. Maximov, A. Bekmukhamet, M.T. Beketayeva, Z.K. Gabitova. Computational method for investigation of solid fuel combustion in combustion chambers of a heat power plant. *High temperature* **5**, 751-757 (2015).
- [3] A. S. Askarova, A. B. Ustimenko, S. A. Bolegenova, V. Yu. Maksimov. Numerical simulation of the coal combustion process initiated by a plasma source. *Thermophysics and aeromechanics* **21**, 747-754 (2014).
- [4] Ye. Heierle, R. Leithner, H. Mueller, A. Askarova. CFD code FLOREAN for industrial boilers simulations. *WSEAS Transactions on Heat and Mass Transfer* **4**, 98-107 (2009).
- [5] F.Ch. Lockwood, V.E. Messerle, K.A. Umbetkaliev, A.B. Ustimenko. Three-dimensional computation of partially gasified solid fuel in the furnace of the PK-39-II boiler of the Reftin regional TPS. *Gorenie i Plasmokhimiya* **6**, 122–130 (2008).
- [6] A.S. Askarova, S.A. Bolegenova, V.Y. Maximov, A. Bekmukhamet, S.S. Ospanova. Numerical research of aerodynamic characteristics of combustion chamber BKZ-75 mining thermal power station. *Procedia Engineering* **42**, 1250-1259 (2012).
- [7] A.S. Askarova, E.I. Karpenko, V.E. Messerle, A.B. Ustimenko. Plasma enhancement of combustion of solid fuels. *High Energy Chemistry* **40**, 111-118 (2006).
- [8] Sh. Ospanova, S. Bolegenova, M. Beketayeva, V. Maximov. Numerical modeling of turbulence characteristics of burning process of the solid fuel in BKZ-420-140-7c combustion chamber. *International Journal of Mechanics* **8**, 112-122 (2014).
- [9] A. Askarova, M.A. Buchmann. Structure of the flame of fluidized-bed burners and combustion processes of high-ash coal. *Proc. 18th Dutch/German Conference on Flames - Combustion and Incineration, Netherlands*, 241-244 (1997).
- [10] S. Vockrodt, R. Leithner, A. Schiller. Firing technique measures for increased efficiency and minimization of toxic emissions in Kasakh coal firing. *Proc. 19th German Conference on Flames, Germany*, 93-97 (1999).
- [11] V.E. Messerle, A.B. Ustimenko, S.A. Bolegenova, V.Yu. Maximov. Reduction of noxious substance emissions at the pulverized fuel combustion in the combustor of the BKZ-160 boiler of the Almaty heat electropower station using the «Overfire Air» technology. *Thermophysics and Aeromechanics* **23**, 125-134 (2016).
- [12] M. Gorokhovski, A. Chtab-Desportes, I. Voloshina. Stochastic simulation of the spray formation assisted by a high pressure. *AIP Conference Proceedings, Xian*, 66-73 (2010).
- [13] S. Bolegenova, M. Beketayeva, Sh. Ospanova, V. Maximov. 3-D Modeling of Heat and Mass Transfer during Combustion of Solid Fuel in Bkz-420-140-7C Combustion Chamber of Kazakhstan. *Journal of Applied Fluid Mechanics* **9**, 699-709 (2016).
- [14] M. Beketayeva, S.A. Bolegenova, S. Bolegenova, A. Bekmukhamet, V. Maximov. Numerical experimenting of combustion in the real boiler of CHP. *International Journal of Mechanics* **7**, 343-352 (2013).
- [15] M. Beketayeva, Sh. Ospanova, Z.K. Gabitova. Investigation of turbulence characteristics of burning process of the solid fuel in BKZ 420 combustion chamber. *WSEAS Transactions on Heat and Mass Transfer* **9**, 40-50 (2014).
- [16] A. Askarova, S. Bolegenova, A. Bekmukhamet, Sh. Ospanova, Z. Gabitova. Using 3D modeling

- technology for investigation of conventional combustion mode of BKZ-420-140-7c combustion chamber. *Journal of Engineering and Applied Sciences* **9**, 24-28 (2014).
- [17] A.S. Askarova, S.A. Bolegenova, A. Bekmuhamet, V.Yu. Maximov. Mathematical simulation of pulverized coal in combustion chamber. *Procedia Engineering* **42**, 1259-1265 (2012).
- [18] A.S. Askarova, Ye. Lavrichsheva, R. Leithner. Combustion of Low-Rank Coals in Furnaces of Kazakhstan Coal-firing Power Plants. *VDI-Berichte* **1988**, 497-505 (2007).
- [19] R. Leithner, A. Askarova, S. Bolegenova, V. Maximov, A.Nugymanova, M. Beketayeva. Computational modeling of heat and mass transfer processes in combustion chamber at power plant of Kazakhstan. *MATEC Web of Conferences* **76**, 06001 (2016).
- [20] A. Askarova, S. Bolegenova, V. Maximov, E. Heierle. CFD study of harmful substances production in coal-fired power plant of Kazakhstan. *Bulgarian Chemical Communications* **48**, 260-265 (2016).
- [21] A. Askarova, S. Bolegenova, V. Maximov. Control of Harmful Emissions Concentration into the Atmosphere of Megacities of Kazakhstan Republic. *IERI Procedia* **10**, 252-258 (2014).
- [22] A. Askarova, S. Bolegenova, S. Bolegenova, V. Maximov. Application of 3D modelling for solving the problem of combustion coal-dust flame. *Bulgarian Chemical Communications* **48**, 236-241 (2016).
- [23] A. Askarova, S. Bolegenova, S. Bolegenova, V. Maximov, R. Manatbayev, Zh. Shortanbayeva. Mathematical modeling of heat and mass transfer in the presence of physical-chemical processes. *Bulgarian Chemical Communications* **48**, 272-277 (2016).
- [24] A.S. Askarova, V.E. Messerle, A.B. Ustimenko. Numerical simulation of pulverized coal combustion in a power boiler furnace. *High temperature* **53**, 445-452 (2015).
- [25] A. Askarova, S. Bolegenova, S. Bolegenova, V. Maximov, R. Manatbayev, Sh. Ospanova. 3D modelling of heat and mass transfer processes during the combustion of liquid fuel. *Bulgarian Chemical Communications* **48**, 229-235 (2016).

The computational study of heat and mass transfer processes at combustion of pulverized Kazakh coal in real conditions of energy objects

A.S. Askarova¹, S. A. Bolegenova¹, V.Yu. Maximov², S. A. Bolegenova²,

A.O. Nugymanova¹, M. T. Beketayeva^{2*}, Sh.S. Ospanova¹, Manatbayev R.K.²

¹*Al-Farabi Kazakh National University, Physics and Technical Physics Department, Al Farabi av. 71, 050038 Almaty, Kazakhstan*

²*Scientific Research Institute of Experimental and Theoretical Physics, Al Farabi av. 71, 050038 Almaty, Kazakhstan*

The article is devoted to the complex research processes of heat and mass transfer occurring during combustion of solid fuel (coal) in the real conditions in the boiler. The methods of numerical 3D modelling were used to describe the aerodynamic and heat-mass transfer processes-characteristics and investigate their exact numerical values. Formation of high-speed flows, its temperature and concentration fields were found during the burning of pulverized low-grade Kazakh coal in the volume of the real combustion chamber. So temperature values increased at core of torch to 1370°C and monotonically decreased to 922°C at the outlet of boiler. Carbon dioxide CO₂ has its maximal values ~ 0.16 kg/kg at the outlet of the chamber, and the nitrous oxides NO_x have their maximal amount of ~ 1200 mg/m³ (at normal conditions) at the burners' zone. Obtained results have great practical importance; it will allow improve the operating energy objects and design new combustion chambers of energy boilers and also-burners, finally optimize the whole process of fossil fuel combustion.

Keywords: aerodynamic, combustion, heat exchange, numerical experiment

INTRODUCTION

Solid fuel combustion is a complex physical and chemical phenomenon, which occurs at high temperatures with rapid and complete oxidation of combustible matter (carbon) by atmospheric oxygen while accompanied by a large amount of heat release [1-2]. Due to the low quality of Kazakh coal deposits the exploitation of its coal has many challenges associated with the growth of scientific and applied research. Conducting in-depth research on coal combustion in real conditions can ensure the efficient technological process [3-5]. Increased interest observed in particular in the study of heat and mass transfer processes at combustion of pulverized Kazakh coal with high ash content [6-10]. Combustion processes take place under conditions of strong turbulence and non-isothermal flow, multiphase medium with a significant impact of nonlinear effects of thermal radiation, interfacial interaction and multistage proceeding with chemical reactions [11-12]. Such phenomena have an important role in studying of the natural phenomenon of low-grade coal combustion. So investigations of turbulent chemically reacting media are extremely important to deepen the knowledge of physical and chemical properties and understanding of possibilities for application.

THE STATE OF THE ART

In the context of depletion of natural energy resources and environmental pollution increasing the efficiency of energy generation and solution of environmental problems are urgent and important task to solve [13-15]. Development of technological processes with economic and ecological advantages are the main purpose for many researches in this area. The complex processes of heat and mass transfer in the presence of combustion are non-stationary, strongly non-isothermal with a constant change in the physical and chemical state of the environment. It greatly complicates their experimental study. In this case, studying of heat and mass transfer in high-reacting media with simulation of physical and chemical processes occur during combustion of pulverized coal is important for the solution of modern power engineering industry and ecology problems. In this regard, a comprehensive study of heat and mass transfer processes at high-temperature media is observed. Research based on the achievements of modern physics using numerical methods of 3D modelling are cost-effective and does not require a lot of manpower and a lot of time as in full-scale studies. Applying of computational technology allow us to describe the actual physical processes that occur during combustion of energy fuel as accurate as possible [16-19]. Finally, the objective of this paper focused on numerical experiments and

* To whom all correspondence should be sent:
Beketayeva.m@gmail.com

studying of heat and mass transfer processes occurring in the areas of real geometry of the combustion chamber during the burning of fuel. A mathematical model of physical-chemical combustion process has been established.

PROBLEM STATEMENT

Study of processes of heat and mass transfer during coal combustion is possible only based on a complete knowledge of combustion physics. It includes a wide range of physical and chemical effects and its formulation of a mathematical model. The fundamental laws of conservation of mass, momentum and energy are used for the simulation of heat and mass transfer in the presence of physical and chemical processes [20-23]. As it known the heat and mass transfer processes in the presence of physical and chemical transformations are the interaction of turbulent flows. Therefore, the chemical processes here should take into account the law of conservation of components of the reacting mixture, multiphase medium, its turbulence degree, heat generation due to the radiation of heated fluid and chemical reactions.

Basic equation

The law of conservation of substance written in the form of the law of conservation of matter as follows:

$$\frac{\partial \rho}{\partial t} + \frac{\partial}{\partial x_i}(\rho u_i) = q_N \quad (1)$$

The law of conservation of momentum and the equation of motion expressed as:

$$\frac{\partial}{\partial t}(\rho u_i) = -\frac{\partial}{\partial x_j}(\rho u_i u_j) + \frac{\partial \tau_{ij}}{\partial x_j} - \frac{\partial P}{\partial x_i} + \rho f_i \quad (2)$$

Law of energy conservation:

$$\frac{\partial}{\partial t}(\rho h) = -\frac{\partial}{\partial x_i}(\rho u_i h) - \frac{\partial q_i^{res}}{\partial x_j} + \frac{\partial P}{\partial t} + u_i \frac{\partial P}{\partial x_i} + \tau_{ij} \frac{\partial u_j}{\partial x_i} + S_h$$

The conservation law for the components of the reaction mixture:

$$\frac{\partial}{\partial t}(\rho C_\beta) = -\frac{\partial}{\partial x_i}(\rho C_\beta u_i) + \frac{\partial j_i}{\partial x_i} + S_\beta \quad (3)$$

For technical flame matter transfer is taken into account only by diffusion. Transfer of substance due to the pressure gradient, the action of external forces (electric and magnetic fields) and thermal diffusion are small and they be neglected. Then the last equation is written as follow:

$$\frac{\partial}{\partial t}(\rho C_\beta) = -\frac{\partial}{\partial x_i}(\rho C_\beta u_i) + \frac{\partial}{\partial x_i} \left(\frac{\mu_{eff}}{\sigma_{\beta eff}} \frac{\partial C_\beta}{\partial x_i} \right) + S_\beta \quad (4)$$

the standard $k-\varepsilon$ turbulence model is used in this paper for modelling of turbulence flows excluding the effect of lift or “twist” of flow, which is represented by the equation of turbulent kinetic energy transfer:

$$\frac{\partial(\overline{\rho k})}{\partial t} = -\frac{\partial(\overline{\rho u_j k})}{\partial x_j} + \frac{\partial}{\partial x_j} \left[\frac{\mu_{eff}}{\sigma_k} \frac{\partial k}{\partial x_j} \right] + P - \overline{\rho \cdot \varepsilon} \quad (5)$$

In addition, the equation of dissipation (turbulent kinetic energy conversion into internal) turbulent kinetic energy ε :

$$\frac{\partial(\overline{\rho \varepsilon})}{\partial t} = -\frac{\partial(\overline{\rho u_j \varepsilon})}{\partial x_j} + \frac{\partial}{\partial x_j} \left[\frac{\mu_{eff}}{\sigma_\varepsilon} \frac{\partial \varepsilon}{\partial x_j} \right] + C_{\varepsilon 1} \cdot \frac{\varepsilon}{k} \cdot P - C_{\varepsilon 2} \cdot \frac{\varepsilon^2}{k} \cdot \overline{\rho} \quad (6)$$

Here the kinetic energy production:

$$P = \left[\mu_{turb} \cdot \left(\frac{\partial \overline{u_i}}{\partial x_j} + \frac{\partial \overline{u_j}}{\partial x_i} \right) - \frac{2}{3} \cdot \overline{\rho} \cdot k \cdot \delta_{ij} \right] \cdot \frac{\partial \overline{u_i}}{\partial x_j} \quad (7)$$

In addition, the rate of dissipation of turbulent energy:

$$\overline{\rho \varepsilon} = \mu_{turb} \cdot \frac{\partial \overline{u_i}}{\partial x_j} \cdot \left(\frac{\partial \overline{u'_i}}{\partial x_j} + \frac{\partial \overline{u'_j}}{\partial x_i} \right) \quad (8)$$

If k and ε are known, the turbulent viscosity determined by the Prandtl-Kolmogorov relationship is:

$$\mu_{turb} = c_\mu \overline{\rho} \frac{k^2}{\varepsilon} \quad (9)$$

Empirical constants like c_μ , σ_k , σ_ε , $C_{\varepsilon 1}$, $C_{\varepsilon 2}$ in previous equations are determined experimentally. For our case, they are taken as $c_\mu = 0.09$; $\sigma_k = 1.00$; $\sigma_\varepsilon = 1.30$; $C_{\varepsilon 1} = 1.44$; $C_{\varepsilon 2} = 1.92$. For the turbulent numbers of Prandtl and Schmidt taken 0.9 [24].

A generalized equation of the transport value in a turbulent flow will then be:

$$\frac{\partial}{\partial t}(\rho \Phi) = -\frac{\partial}{\partial x_j}(\rho u_j \Phi) + \frac{\partial}{\partial x_j} \left[\Gamma_{\phi, eff} \frac{\partial \Phi}{\partial x_j} \right] + S_\phi \quad (10)$$

High-temperature media emits heat during combustion. As a result, this thermal energy is transformed into radiant energy on the surface of the heated body. Thus, the energy equation in the study of heat and mass transfer during combustion considered the heat exchange by radiation. On the heat-exchange by radiation has a major influence of the water vapor and carbon dioxide. Heat exchange by radiation can be treated in modeling of flows at temperatures $500 \text{ K} < T < 2000 \text{ K}$ in the region of the visible and infrared parts of the spectrum. The emissivity of the gas mixture consists of components emissivity, and depends on the partial pressure, temperature and wavelength.

The six-flow model [25] is used to determine the intensity of the radiation in this study.

Physical and chemical processes occurring in the combustion chamber are rapid and complete processes of oxidation of the fuel (in this case high-ash content coal). These processes take place at high temperatures, accompanied by a large release of energy due to chemical reactions and changes in the concentrations of all substances interact. To describe real physical transformations that occur during combustion of fuel, and to avoid mistakes that can lead to a physically meaningless result, an adequate initial and boundary conditions corresponding to real physical process are given, while an adequate numerical model [26-27] of physical process is also chosen. Chemical reactions, which in turn determines the source terms in the equations for energy and the substance components. A chemical model is adopted in this paper it takes into account only the key components of the reaction. A Mitchell-Tarbell model was used [28], which takes into account the rank of coal for modelling nitrogen-containing components (in this case for the Kazakh coal ash content is 35.1%). The Mitchell-Tarbell model demonstrates the formation of nitrogen oxides NO_x by the oxidation of fuel bound nitrogen. The kinetic scheme takes into account the reaction of the primary pyrolysis, homogeneous combustion of hydro carbonaceous compounds, heterogeneous combustion of coke and formation of nitrogen compounds by thermal and fuel NO_x mechanisms.

The Florean software package were used for computational simulations of heat and mass transfer processes during combustion of pulverized coal. And as an object of research was chosen the combustion chamber of the real energy boiler BKZ-75 Shakhtinsk TPC, Kazakhstan). All conditions taken into account describe real processes of solid fuel combustion. Control volume method were used for conducting numerical modelling, where the chamber has been divided into 126 496 cells in computational experiment.

RESULTS OF NUMERICAL MODELLING

The following results show three-dimensional modelling of heat and mass transfer processes during combustion of pulverized low-grade coal in real conditions of combustion chamber of boiler. Aerodynamic pattern of motion of two-phase turbulent flow of pulverized coal combustion causes the heat and mass transfer process in general [29-30]. Fig.1 shows a two-dimensional graph of

the full velocity vector, determined by the relationship:

$$\vec{V} = \sqrt{U^2 + V^2 + W^2}. \quad (11)$$

Flows' speed decreased in the direction of camera output. The peak area values with maximum speed of 20 m/s is clearly visible. The burners were located at 4 m by height of chamber burners, they fed fuel and oxidant mixture into the camera at maximum speed. Distribution character of full velocity vector in Fig.1a depends on the geometrical design of the chamber and due to the vortex transfer of reacting medium. At the outlet region of chamber (Z~16 m, Fig.1b), it is seen that velocity has a maximum value 8.76 m/s, while an average value does not exceed 5 m/s by height.

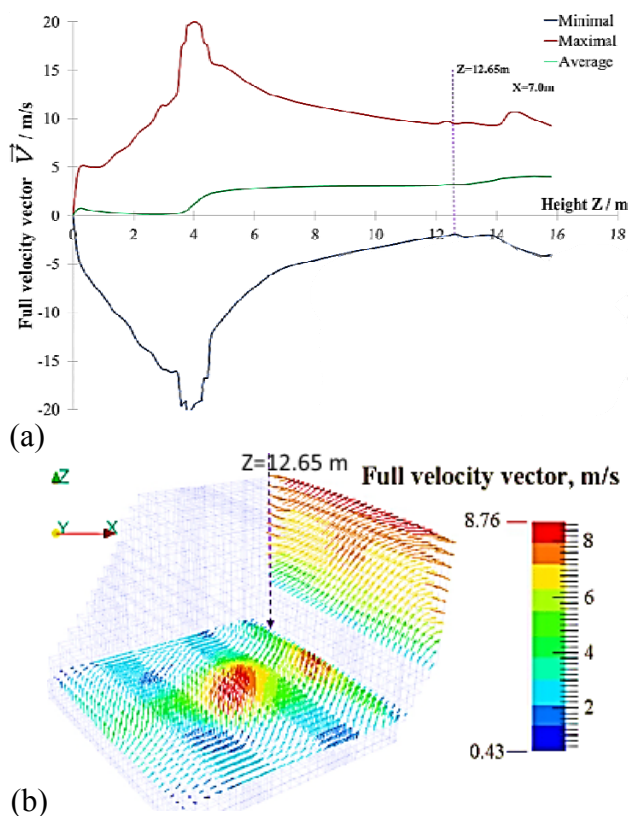


Fig.1. Distribution of full velocity vector

The maximum perturbation of turbulence characteristics notably in the vortex region, this cause the highest change of velocity (Fig.2). The presence of a stream of vortices in the central region of the combustion chamber is advantageous for the combustion of pulverized coal (heat transfer and mass transfer).

Fig.3a shows the distribution of maximum, minimum and average values of the temperature field in the combustion chamber.

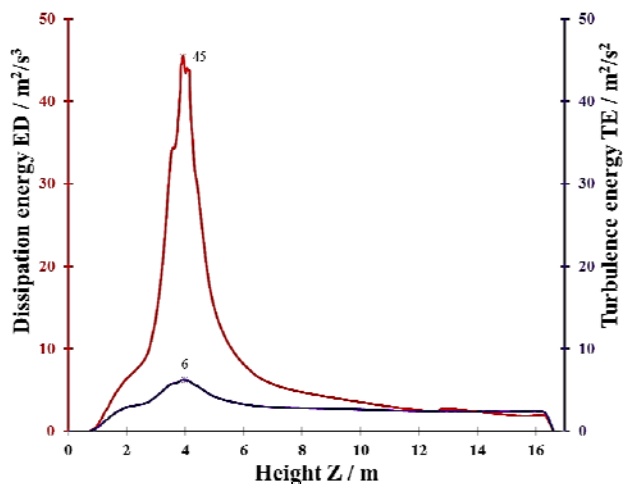
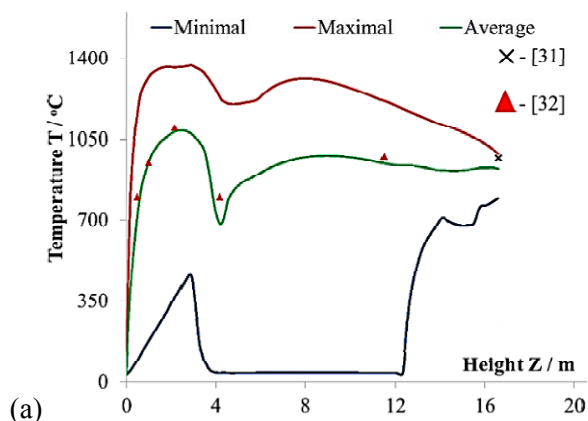
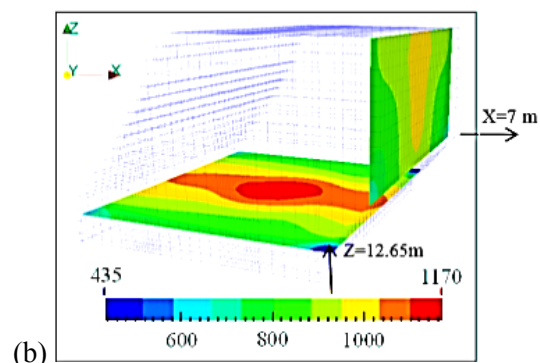


Fig.2. 2D distribution of turbulence characteristics



(a)

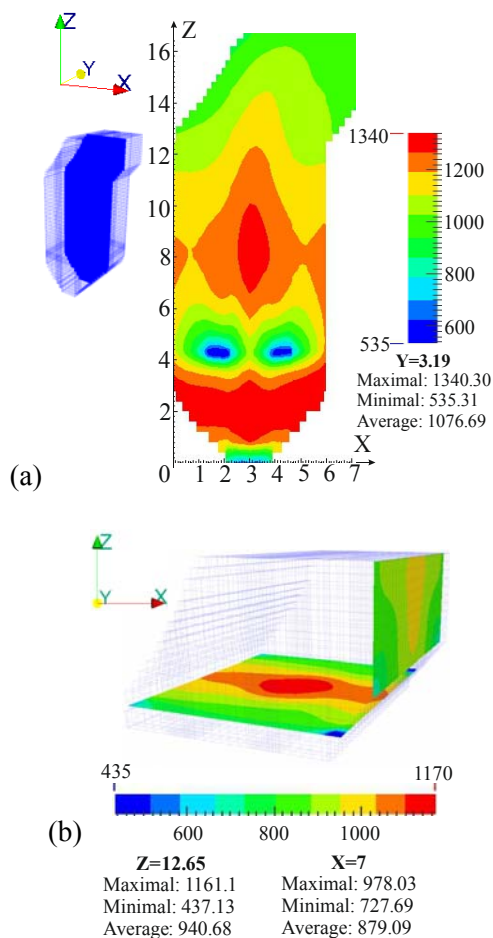


(b)

Fig.3. Distribution of temperature fields and its verification with known data

A sharp decrease in temperature observed at fuel feeding zone—because the fuel supplied there by a lower temperature. It can be seen that temperature values reach their maximum in the area below the burner's zone where torch core is located (approximately at 3 m). This was caused with the eddy currents (from installed four burners: on two burners on two opposite tiers) that have a maximum convective transfer. This increases the residence

time of coal particles here. As a result, the temperature rise to $\sim 1370^{\circ}\text{C}$ in this area. Moreover, maximum value of temperature is about $900\text{--}950^{\circ}\text{C}$ at the output of the chamber. This is clearly seen from the 3D view of temperature in Fig.3b. The point of the theoretically calculated value of the temperature of exhaust gases for this boiler defined according to the normative method of thermal calculation [31] data from the natural experiments held in real TPP of RK [32] are presented in Fig.3a.



(a)

(b)

Fig.4. 3D temperature distribution by the chamber sections

The method of thermal calculation in power engineering is still the most reliable for finding the temperature at the outlet of the combustion chamber. It is seen that the difference between results of numerical calculation and known data is only 4.7%. This proves that the method of 3D modelling gives us a good description of real processes of heat and mass transfer fuel combustion.

The following Fig.4, which shows the 3D temperature distribution by the chamber sections, observed the same character as in the previous

Fig.3. Temperature values are monotonically fall by the height of the combustion chamber.

From 3D view of temperature it is seen that the core of flame is located in the lower part of chamber (section Y=3.19 m, Fig.4a). The maximal value of temperature is equal to 1340°C there and they decreased by the height of camera. So temperature has the value 940°C in average in section Z=12.65 m (Fig.4b), when it has 922°C at the section Z=7 m (the output of chamber, Fig.4b).

Below the results of 3D modeling of carbon dioxide CO₂ and nitrogen oxides NO_x concentration distributions are shown.

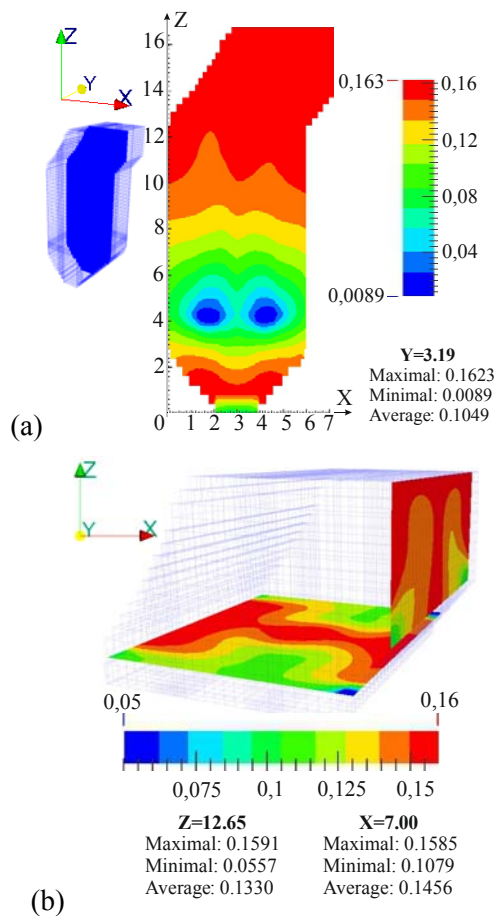


Fig.5. 3D distribution of the carbon dioxide concentrations on sections of the chamber (CO₂, kg/kg)

Carbon monoxide CO completely react with oxygen O₂ and further form carbon dioxide CO₂. Concentrations of carbon dioxide CO₂ have their largest amount at the top areas of chamber (Fig.5a, section Y=3.19 m). In addition, the minimal values are observed at the region, where the burner equipments are set.

Analyzing the Fig.5a it is seen that concentration of carbon dioxide CO₂ has the

minimal value equal to 0.0089 kg/kg at the section Y=3.19 m. In average it is raised to ~ 0.13 kg/kg at the Z=12.65 m section by height and ~ 0.15 kg/kg at the outlet of the chamber (section X=7.0 m, Fig.5b).

Nitrous oxides NO_x are formed by seven main nitrous compounds, but it is considered to negligible others except of nitrous monoxides NO and dioxides NO₂ (in total NO_x). The NO_x formation mechanism is caused mainly with the fuel-N compound. The maximal amount of nitrous oxides NO_x concentration is presented at the burners zone and equal to 0.0109 kg/kg (Fig.6a, see section Y=3.19 m). As it shown in Fig.6 the decreasing of nitrous oxides concentration is observed with height of boiler. It has the average value equal to $5.09 \cdot 10^{-12}$ kg/kg at the output of the combustion volume (section X=7.0 m, Fig.6b).

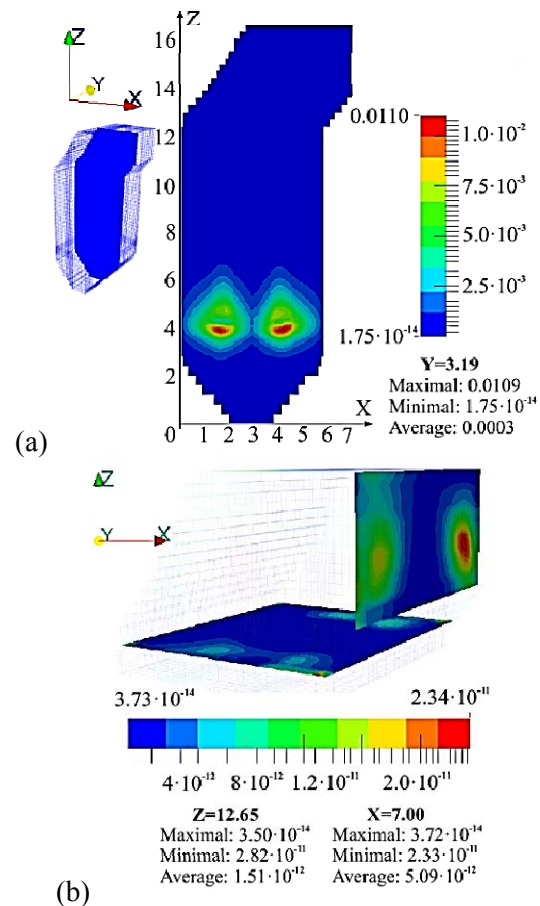


Fig.6. 3D distribution of the nitrogen oxides concentrations on sections of the chamber (NO_x, kg/kg)

Obtained results of computational simulation of carbon dioxide CO₂ and nitrous oxides NO_x concentration distributions were verified with the known data as shown in Fig.7.

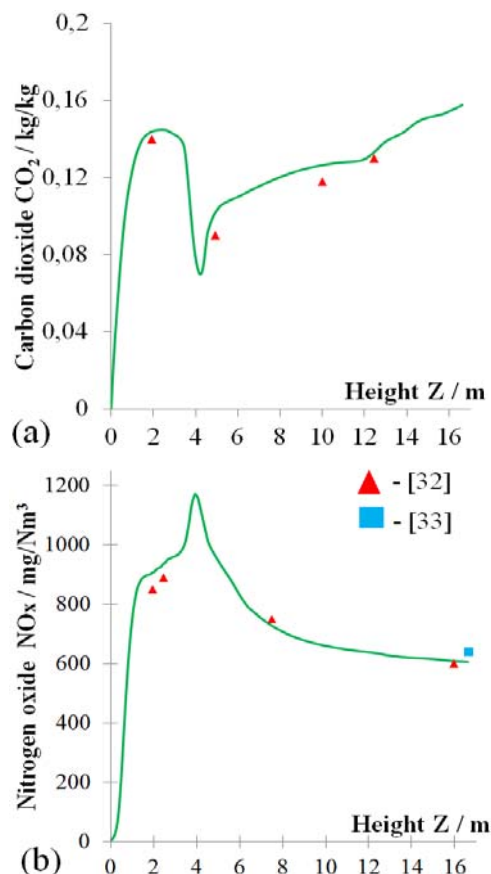


Fig.7. Verification of concentrations of carbon dioxide CO_2 (a) and nitrogen oxides NO_x (b) calculation results with known data [32-33]

Concentrations of carbon dioxide CO_2 (Fig.7a) and nitrous oxides NO_x (Fig.7b) are in a good agreement with experimental data, received from real thermal power plant equipment [32]. Moreover, nitrous oxide NO_x concentrations meet the requirements of limit value for Kazakhstan Republic TPP [33]. By comparison of numerical experiment results held in this work with natural data from TPP, it can be noticed that the difference is for carbon dioxide CO_2 is 4% and for nitrous oxides NO_x is 5%. Finally we can confirm the observed method of research of heat and mass transfer processes is fairly reliable and efficient. Also, the method of computer simulation can be useful in studying the technological processes of low-grade coal combustion in energy objects.

CONCLUSIONS

In conclusion, velocity characteristics of turbulent flows, their turbulent kinetic energy and dissipation energy are determined via computational modelling experiments on heat and mass transfer processes during combustion of Kazakh coal. Aerodynamic characteristics of flow

shows the intensive mixing of fuel and oxidant, which is held in the central part of the chamber. It caused the increasing of temperature values at core of torch to 1370°C and monotonically decreasing to 922°C at the outlet. Formation of hazardous substances as carbon and nitrous oxides (CO_2 , NO_x) are depends on their chemical interaction with oxygen. Carbon dioxide has its maximal values at the outlet of the chamber ($\sim 0.16 \text{ kg/kg}$), and the nitrous oxides have its maximal amount of $\sim 1200 \text{ mg/Nm}^3$ (N means normal conditions) at the burners' zone. Obtained results of numerical experiments have great theoretical and practical importance. It allow to improve design of combustion chambers and burners, to optimize the process of burning of high-ash content energy coal of Kazakhstan Republic.

ACKNOWLEDGEMENTS

This work supported by the Ministry of Education and Science of the Kazakhstan Republic under the International Cooperation of Al Farabi Kazakh National University with China (MT/2013-2015), and within the framework of the Project "Creation of new computer technologies for 3D modeling of heat and mass transfer processes in high-temperature physicochemically reactive media" (AP05133590), which are gratefully acknowledged by the author.

REFERENCES

- [1] S. J. Zarrouk, M. J. O'Sullivan, J. D. St. George. Modelling the spontaneous combustion of coal: the adiabatic testing procedure. *Combustion Theory and Modelling* **10**, 907-926 (2006).
- [2] Ch. K. Law. *Combustion Physics*, Cambridge: Cambridge University Press, 2006.
- [3] A. Bekmukhamet, V. Maximov, M. T. Beketayeva etc. Numerical experimenting of combustion in the real boiler of CHP. *International Journal of Mechanics* **7**, 343-352 (2013).
- [4] M. T. Beketayeva, P. Safarik, A. Nugymanova, etc. Modern computing experiments on pulverized coal combustion processes in boiler furnace of RK. *News of the NAS of the Republic of Kazakhstan. Series phys.-math.* **6**, 5-12 (2018).
- [5] A. S. Askarova, V. E. Messerle, etc. Numerical simulation of pulverized coal combustion in a power boiler furnace. *High temperature* **53**, 445-452 (2015).
- [6] S. A. Bolegenova, V. Yu. Maximov, etc. Control of Harmful Emissions Concentration into the Atmosphere of Megacities of Kazakhstan Republic. *Proc. of the FIE2014, Int. Conf. on Future Inf. Eng., Beijing*, 252. (2014).

- [7] H. Müller, A. Magda, etc. Combustion of low-rank coals in furnaces of Kazakhstan coal-firing power plants. *VDI Berichte* **1988**, 497-502 (2007).
- [8] A. Askarova, M. A. Buchmann. Structure of the flame of fluidized-bed burners and combustion processes of high-ash coal. *VDI Berichte* **1313**, 241-244 (1997).
- [9] V. Ju. Maximov, A. Bekmuhamet, etc. Analysis of formation harmful substances formed as a result of burning the low-grade coal in the combustion chamber of the industrial boiler of Kazakhstan using CFD-code FLOREAN. *Proc. of the PRES 2014, 17th Conference on Process Integration, Modelling and Optimisation for Energy Saving and Pollution Reduction, Prague*, 7.160. (2014).
- [10] M. Beketayeva, A. Ergaliyeva, etc. Three-dimensional modelling of heat and mass transfer during combustion of low-grade Karaganda coal. *Proc. of the PRES 2016, 19th Conference on Process Integration, Modelling and Optimisation for Energy Saving and Pollution Reduction, Prague*, 0734. (2016).
- [11] S. Askarova, Sym. Bolegenova, etc. Mathematical modeling of heat and mass transfer in the presence of physical-chemical processes. *Bulgarian Chem. Comm.* **E**, 272-277 (2016).
- [12] I. Berezovskaya, Zh. Shortanbayeva, etc. Experimental Study of Complex Combustion Processes in Higher Education. *Proc. of the EMSE 2017, 2nd International Conference on Education, Management and Systems Engineering, Beijing*, 377-381. (2017).
- [13] V. E. Messerle, A. B. Ustimenko, etc. Reduction of noxious substance emissions at the pulverized fuel combustion in the combustor of the BKZ-160 boiler of the Almaty heat electropower station using the "Overfire Air" technology. *Thermoph. and aeromechanics* **23**, 125-134 (2016).
- [14] P. Safarik, A. Maksutkhanova, A. Nugimanova, etc. Research of Formation and Destruction of NO_x During Combustion of Low-Grade Coal in CHP. *Proc. of the ECAME 2017, International Conference on Electronic, Control, Automation and Mech. Eng., Sanya*, 731-735. (2017).
- [15] S. Vockrodt, R. Leithner, etc. Firing technique measures for increased efficiency and minimization of toxic emissions in Kazakh coal firing. *VDI Berichte* **1492**, 93 (1999).
- [16] A. S. Askarova, S. A. Bolegenova, etc. Computational method for investigation of solid fuel combustion in combustion chambers of a heat power plant. *High temp.* **5**, 751-757 (2015).
- [17] A. S. Askarova, E. I. Heierle, etc. CFD study of harmful substances production in coal-fired power plant of Kazakhstan. *Bulgarian Chemical Communications* **E**, 260-265 (2016).
- [18] R. Leithner, A. Askarova, etc. Computational modeling of heat and mass transfer processes in combustion chamber at power plant of Kazakhstan. *MATEC Web of Conferences, Corfu*, 5 pdf. (2016).
- [19] H. Muller. Numerische Simulation von Feuerungen, Braunschweig: IWBT, 1997.
- [20] R. Leithner, H. Müller. Investigation of turbulence characteristics of burning process. *Proc. of the Conference on Computational Fluid and Solid Mechanics, Cambridge*, 172. (2003).
- [21] L. El-Mahallawy, S. El-Din Habik. Fundamentals and technology of combustion, Oxford: Elsevier Science: Energy, 2002.
- [22] S. Bolegenova, Sh. Ospanova, etc. 3D modeling of heat and mass transfer during combustion of solid fuel in BKZ-420-140-7c combustion chamber of Kazakhstan. *Journal of Applied Fluid Mechanics* **8**, 699-709 (2016).
- [23] Y. Heierle, R. Leithner, etc. CFD Code Florean for Industrial Boilers Simulations. *WSEAS Trans. on heat and mass transfer* **4**, 98-107 (2009).
- [24] A. Bekmukhamet, Z. K. Gabitova, etc. Numerical modeling of turbulence characteristics of burning process of the solid fuel in BKZ-420-140-7c combustion chamber. *International Journal of Mechanics* **8**, 112-122 (2014).
- [25] F. Lockwood. Combustion and flame, 1977.
- [26] A. Askarova, S. Bolegenova, etc. Influence of boundary conditions to heat and mass transfer processes. *Int. J. of Mechanics* **10**, 320-325 (2016).
- [27] M. T. Beketayeva, V. Maximov, etc. On the effect of the temperature boundary conditions on the walls for the processes of heat and mass transfer. *Int. J. of Mechanics* **10**, 349-355 (2016).
- [28] J. W. Mitchell, J. M. Tarbell. A kinetic model of nitric oxide formation during pulverized coal combustion. *AIChE Journal* **28**, 302-320 (1982).
- [29] V. Y. Maximov, A. Bekmukhamet, etc. Numerical research of aerodynamic characteristics of combustion chamber BKZ-75 mining thermal power station. *Procedia Engineering* **42**, 1250-1259 (2012).
- [30] V. Yu. Maximov, M. T. Beketayeva, etc. Modeling of heat mass transfer in high temperature reacting flows with combustion. *High temperature* **56**, 738-743. (2018).
- [31] Teplovoi raschet kotlov: Normativnyi metod, Spb.: NPO CKTI, 1998.
- [32] B. K. Aliyarov, M. B. Aliyarova. Szhiganiye kazakhstanskikh ugley na TES i na krupnykh kotelnykh: opyt i perspektivy, Almaty, Gylym ordasy, 2011.
- [33] RND 34.02.303-91 Otraselevaya instruktsiya po normirovaniyu vrednykh vybrosov v atmosferu dlya teplovykh elektrostantsiy i kotel'nykh, Astana, MOOS RK, 2004.

Investigation of the different Reynolds numbers influence on the atomization and combustion processes of liquid fuel

A.S. Askarova¹, S.A. Bolegenova^{1*}, V.Yu. Maximov¹, S.A. Bolegenova¹, Sh.S. Ospanova¹,
M.T. Beketayeva¹, A.O. Nugymanova¹, N.V. Pilipenko², Zh.K. Shortanbayeva¹,
K.S. Baktybekov³, A.B. Syzdykov¹

¹ Al-Farabi Kazakh National University, Department of Thermal and Technical Physics, Al-Farabi ave. 71,
Kazakhstan

² Saint-Petersburg national research University of information technologies, mechanics and optics, Saint-Petersburg,
Russia

³ «National Company «Kazakhstan Gharysh Sapary» JSC

The problems of combustion are widely studied now by the scientists of the world. Increasing level of ecological pollution of the environment, reserve depletion of hydrocarbon fuel and economic growth of many countries causing increase of demand for energy - all these factors gave rise to the problem of finding of more economic and ecological way of fuel combustion. In order to solve this problem it is necessary to study thoroughly the combustion process itself and that is why the methods of numerical simulation are getting wide spread in the science. The turbulence plays great role in many devices using combustion process and its study is maybe one of the most complicated sections of hydrodynamics. It is also necessary to take into account additional factors such as various chemical reactions and radiation.

In this article tetradecane's combustion depending on the Reynolds numbers of the gas flow are investigated. Reynolds numbers of the gas flow was ranging from 2300 to 25000. As the result of the conducted numerical experiments it has been determined that at high Reynolds numbers the combustion process occurs intensively. The most effective combustion proceeds at the Reynolds number of the gas flow equal 25000, under these conditions temperature reaches values from 2001 K to 2645 K. With this value of the Reynolds number, the combustion temperature in the combustion chamber reaches maximum values and intensive evaporation of the liquid fuel drops begins. It was shown that when the Reynolds number is 15,000 and 20,000, the concentration of emitted carbon dioxide reaches the average allowable values, which are equal to $0,104823 \cdot 10^{-3}$ kg/kg and $0,104747 \cdot 10^{-3}$ kg/kg respectively.

Keywords: numerical simulation, combustion, two-phase flows, Reynolds number, tetradecane, modeling.

INTRODUCTION

One of the priority tendencies of the scientific and technological development of Kazakhstan is the research of simulation of formation of polluting fog and their dispersion in the atmosphere. This problem has a great value because of the increasing concern for the ecological situation in Kazakhstan as the atmospheric air in the cities of Kazakhstan is daily polluted by different hazardous substances (NO₂, CO, CO₂, soot and so on) [1-5].

For the recent years the dispersion of the liquid sprays in the neutral atmospheric flows has been well studied by means of numerical, laboratory and natural researches. In these researches the main attention has been given to the dispersion of chemically reactive scalar admixture in the free convective flows.

As a matter of urgency, the use of liquid fuels can be said that over the past few years 60 million passenger cars have been produced, that is, 165,000 vehicles are produced per day. The engines of the current generation are significantly different from

those used a few decades ago. The main combustion process in engines remains the same, but the types of injections differ significantly. For example, modern engines with electronically controlled injection systems, along with air compression mechanisms that help improve the combustion process, use only the required amount of fuel. More than 50% of cars are produced in Asia and Oceania, while Europe produces almost a third of the total number of cars in the world. In the last decade, the total number of cars produced per year has increased by 20 million, which leads to a high growth of pollutants that pose a greater threat to the environment [6-11].

The regulations on emissions of pollutants are becoming more and more severe over time, for example, until 2025, due to world-wide established ground rules, it is planned to reduce CO₂ emissions from passenger cars to about 100 mg per km. It is known that the International Energy Agency (IEA) has been tasked to use renewable energy sources as an energy carrier by 2050 and to reduce CO₂ emissions to the atmosphere by half as an indicator of harmful substances [12-14].

Although carbon dioxide is not a toxic gas, it still represents a danger to the environment due to

* To whom all correspondence should be sent:
Saltanat.Bolegenova@kaznu.kz

the greenhouse effect. According to estimates [15], the annual carbon footprint is about 30 billion tons due to various types of human activity around the world. The concentration of carbon dioxide from all sources has increased by 31% since 1750 [16].

The investigation of the formation of polluting fog will allow creating the methods for the decrease of contain of hazardous substances in the atmosphere and for the prevention of formation of such clouds which contain hot liquid particles and these particles are the reasons of the formation of such polluting fog. That kind of problems is one of the significant and insufficiently explored tasks for the present days.

In this region of research the numerical experiments on the combustion of liquid fuel sprays in the burner chamber have been carried out. In this work it has been researched the dependence of maximal temperature of combustion of the liquid fuel from the velocity of the spray by means of the numerical modeling on the basis of the solution of differential two-dimensional equations of the turbulent reactive flows.

MATHEMATICAL MODEL OF THE PROBLEM

Main equations of mathematical model of atomization and combustion of spray of liquid fuel are presented below [17-20].

Continuity equation for component m :

$$\frac{\partial \rho_m}{\partial t} + \vec{\nabla}(\rho_m \vec{u}) = \vec{\nabla} \left[\rho D \vec{\nabla} \left(\frac{\rho_m}{\rho} \right) \right] + \dot{\rho}_m^c + \dot{\rho}_m^s \delta_{m1}. \quad (1)$$

Where ρ_m - mass density of the liquid phase, ρ - total mass density, u - fluid velocity, D - diffusion coefficient, ∇ - Nabla operator, $\dot{\rho}_m^c$ - chemical source term, $\dot{\rho}_m^s$ - source term due to injection, δ - Kronecker symbol.

Momentum equation:

$$\frac{\partial(\rho \vec{u})}{\partial t} + \vec{\nabla}(\rho \vec{u} \vec{u}) = -\frac{1}{a^2} \vec{\nabla} p - A_0 \vec{\nabla} \left(\frac{2}{3} \rho k \right) + \vec{\nabla} \vec{\sigma} + \vec{F}^s + \rho \vec{g}. \quad (2)$$

Where p - fluid pressure, α - immeasurable value used in the PGS method. This is a method that allows one to increase computational efficiency in low Mach number flows, where the pressure is approximately uniform. A_0 is 0 in the case of

laminar flow, and 1, when one of the turbulence models is used. In our studies, we used the method of modeling the turbulent flows of RANS, which is based on the Boussinesq hypothesis and implies a time averaging of the Navier-Stokes equation. Also σ is viscous stress tensor, which depends on the viscosity of the fluid and the specific internal energy. The value \vec{F}^s on the right side of the equation denote external forces that affect the mass and the volume of the fluid.

Energy equation:

$$\frac{\partial(\rho I)}{\partial t} + \vec{\nabla}(\rho \vec{u} I) = -p \vec{\nabla} \vec{u} + (1 - A_0) \sigma \vec{\nabla} \vec{u} - \vec{\nabla} \vec{J} + A_0 \rho \varepsilon + \dot{Q}^c + \dot{Q}^s \quad (3)$$

where heat flux vector consists of electrical conductivity and enthalpy transfer:

$$\vec{J} = -K \nabla T - \rho D \sum_m h_m \nabla \left(\frac{\rho_m}{\rho} \right)$$

and \dot{Q}^c - source term due to heat generated by a chemical reaction, \dot{Q}^s - the heat that brings the injected fuel, ε - dissipation of the kinetic energy of turbulence.

More universal models in engineering calculations of turbulent flows are models with two differential equations. This is a $k - \varepsilon$ model, when two equations are solved for the kinetic energy of turbulence k and its dissipation rate ε . Equations of $k - \varepsilon$ turbulence model [21-26]:

$$\frac{\partial \rho k}{\partial t} + \vec{\nabla}(\rho \vec{u} k) = -\frac{2}{3} \rho k \vec{\nabla} \vec{u} + \vec{\sigma} : \vec{\nabla} \vec{u} + \vec{\nabla} \left[\left(\frac{\mu}{Pr_k} \right) \vec{\nabla} k \right] - \rho \varepsilon + \dot{W}^s. \quad (4)$$

$$\frac{\partial \rho \varepsilon}{\partial t} + \vec{\nabla}(\rho \vec{u} \varepsilon) = -\left(\frac{2}{3} c_{\varepsilon_1} - c_{\varepsilon_3} \right) \rho \varepsilon \vec{\nabla} \vec{u} + \vec{\nabla} \left[\left(\frac{\mu}{Pr_\varepsilon} \right) \vec{\nabla} \varepsilon \right] + \frac{\varepsilon}{k} \left[c_{\varepsilon_1} \vec{\sigma} : \vec{\nabla} \vec{u} - c_{\varepsilon_2} \rho \varepsilon + c_s \dot{W}^s \right] \quad (5)$$

When calculating various flow characteristics, a system of turbulent transfer equations was used, for

closure of which a standard $k-\varepsilon$ model of turbulence was used, since this model exhibits stability, efficiency, and reasonable accuracy in studies of heat and mass transfer processes in turbulent flows of liquid fuels, which makes it most suitable for solving industrial problems.

Initial and boundary conditions of the problem of atomization and combustion of liquid fuels in the combustion chamber

At the initial moment of time, the gas in the combustion chamber is at rest and the initial temperature distribution is constantly:

$$t = 0 : u = 0, v = 0, w = 0, T = T_0, c = c_0.$$

The velocity field at the wall is determined through the turbulent law of the wall, and the velocity component profiles are given by the logarithmic distribution:

$$\frac{v}{u^*} = \begin{cases} 1/k \ln(c_{1\omega} \zeta^{7/8}), & \zeta > R_c \\ \zeta^{1/2}, & \zeta < R_c \end{cases}$$

where $\zeta = \frac{\rho y v}{\mu_{air}(T)}$ - Reynolds number, which is

determined by the relative velocity of the gas to the wall, $v = |\vec{u} - \omega_{wall} \vec{k}|$ - gas velocity relative to the

wall at a distance y from it, u^* - dynamic velocity that is related to the tangential components of the stress tensor as follows:

$$\vec{\sigma}_\omega - (\vec{\sigma}_\omega \cdot \vec{n}) \vec{n} = \rho (u^*)^2 \frac{\vec{v}}{v}, \quad \text{where} \quad \vec{v} = \vec{u} - \omega_{wall} \vec{k},$$

$$k = \sqrt{c_\mu^{1/2} (c_{\varepsilon_2} - c_{\varepsilon_1}) Pr_\varepsilon}. \quad \text{The temperature value on the}$$

wall is fixed, therefore, the above-mentioned law of turbulence is used for it:

$$\frac{J_\omega}{\rho u^* c_p (T - T_\omega)} = \begin{cases} 1 / \left(Pr_\tau \frac{v}{u^*} \right), & \zeta \leq R \\ 1 / \left\{ Pr \left[\frac{v}{u^*} + \left(\frac{Pr_\tau}{Pr} - 1 \right) R_c^{1/2} \right] \right\}, & \zeta > R_c \end{cases}$$

Where Pr - Prandtl number for laminar flow.

For the kinetic energy of turbulence k and its dissipation rate ε , the following boundary conditions are written:

$$\nabla k \cdot \vec{n} = 0, \quad \varepsilon = c_{\mu_\varepsilon} \frac{k^{3/2}}{y}, \quad c_{\mu_\varepsilon} = \left[\frac{c_\mu}{Pr_\varepsilon (c_{\varepsilon_2} - c_{\varepsilon_1})} \right]^{1/2}, \quad \text{where}$$

C_μ is constant and its value is 0.09.

We have studied ($C_{14}H_{30}$) tetradecane's combustion depending on the Reynolds numbers of the gas flow. Tetradecane is the main component of diesel fuel. It's used in passenger, freight and

private vehicles. Liquid fuel is injected into the combustion chamber through a circular nozzle, located in the center of the bottom of the chamber. The overview of the combustion chamber is presented in Fig.1.

The chamber is a cylinder with height equal to 15 cm and diameter is 0,04 m. After the injection there is a rapid evaporation of fuel and the combustion is processing in the gas phase. The burning time of fuel is $4 \cdot 10^{-3}$ s. Time of injection of fuel droplets is $1.4 \cdot 10^{-3}$ s. The temperatures of the walls of the combustion chamber is 353 K. The initial temperature of gas in the chamber is 900 K. The temperature of the injected fuel is 300 K. The initial mean radius of injecting drops is $3 \cdot 10^{-6}$ m. The pressure in the combustion chamber is $4 \cdot 10^6$ Pa.

In the work the dependence of maximum temperature of fuel combustion from Reynolds numbers has been obtained. Reynolds numbers of the gas flow was ranging from 2300 to 25000. It has been known that at low velocities of liquid fuel spray the process of combustion does not occur [27-30].

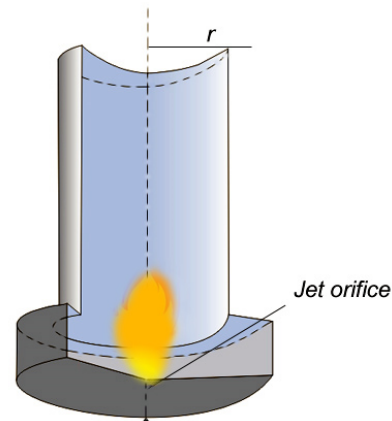
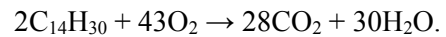


Fig.1. Overview of the combustion chamber

Tetradecane has been an object of research and its chemical formula has the following form as $C_{14}H_{30}$. For this type of fuel the global chemical reaction of combustion leading to the formation of carbon dioxide and water is written in the following way:



This reaction is exothermic, i.e. it proceeds with huge emission of heat.

In this scientific work the KIVA-II computer software package was used as the starting material which was developed by scientists at the Los Alamos National Laboratory (LANL). With this software package can explore the complex

processes of ignition, combustion of fuel and air mixtures, as well as the formation of pollutants released into the atmosphere as a result of the operation of internal combustion engines [18].

In this article, the KIVA-II software package has been optimized to simulate the chemical kinetics of combustion processes in diesel and aircraft engines. This software package was adapted to the task of combustion of liquid fuels in combustion chambers under high turbulence. This made it possible to calculate the aerodynamics of the flow, the injection masses, the oxidant's temperature, pressure, turbulent characteristics, concentrations of combustion products, fuel vapors and other characteristics of the process of liquid fuels' combustion over the entire space of the combustion chamber.

In this paper, the authors carried out simulation of combustion of liquid fuel in a cylindrical combustion chamber at different Reynolds numbers. Also similar computational experiments can be carried out for any kind of fuel. For example, in the following papers the authors carried out simulation of combustion of energy fuel in industrial boilers of Kazakhstan [31-36].

NUMERICAL SIMULATION RESULTS

As the result of the conducted numerical experiments it has been determined that at high Reynolds numbers the combustion process occurs intensively. The most effective combustion proceeds at the Reynolds number of the gas flow equal 25000, under these conditions temperature reaches values from 2001 K to 2645 K (Fig.2).

Analysis of Fig.2 shows that if the Reynolds number of the flow in the combustion chamber takes values above 15000, then the fuel burns more intensively, a large amount of heat is generated and the combustion chamber warms up to 3000 K.

However Fig.3 shows the dependence of the distribution of CO₂ concentration on the Reynolds numbers of the flow, where the highest concentration of CO₂ is equal $0.106303 \cdot 10^{-3}$ kg/kg accounts for the Reynolds number of the flow $Re=25\ 000$.

But at the Reynolds numbers equal to 2300 CO₂ concentration reaches the minimum value to $0.103538 \cdot 10^{-3}$ kg/kg. Also, with a Reynolds numbers of 15 000 and 20 000, the concentrations of emitted carbon dioxide are relatively small, which are equal to $0,104823 \cdot 10^{-3}$ kg/kg and $0,104747 \cdot 10^{-3}$ kg/kg respectively. At these values of the Reynolds number, the fuel quickly reacts

with an oxidizing agent, as a result, the concentration of carbon dioxide formed does not exceed the permissible limits.

Similar studies were conducted by scientists in the field of modeling of heat and mass transfer in the combustion chamber during combustion of solid fuels, especially coal. Many scholars who specialize in the field of computational fluid dynamics and heat power engineering conducted similar researches in the modeling of the combustion of liquid and solid fuels. In their works by the authors was used chemical model of pulverized coal combustion, which takes into account the integral component of the fuel oxidation reaction to the stable final products of the reaction. This model is the formation of the final products of oxidation is also used by us in the research [37-39].

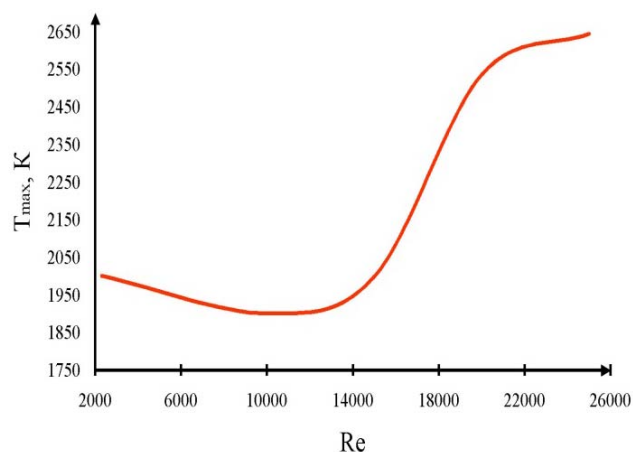


Fig.2. Change of maximum temperature in the burner chamber depending on the Reynolds numbers of the gas flow

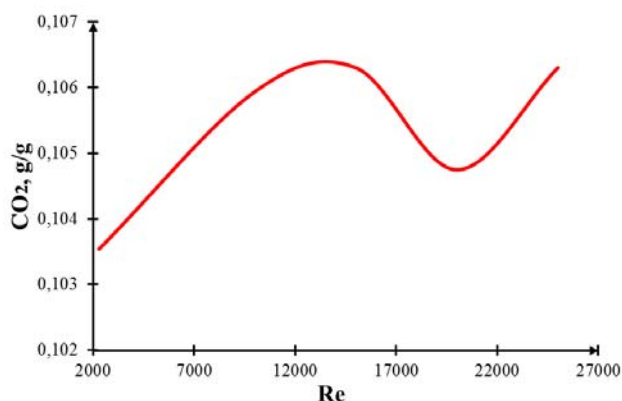


Fig.3. The dependence of the distribution of CO₂ concentration on the Reynolds number

For the optimum and maximum Reynolds number equal to 25000, the plots of the temperature

change in time and of the fuel concentration in the burner chamber have been obtained.

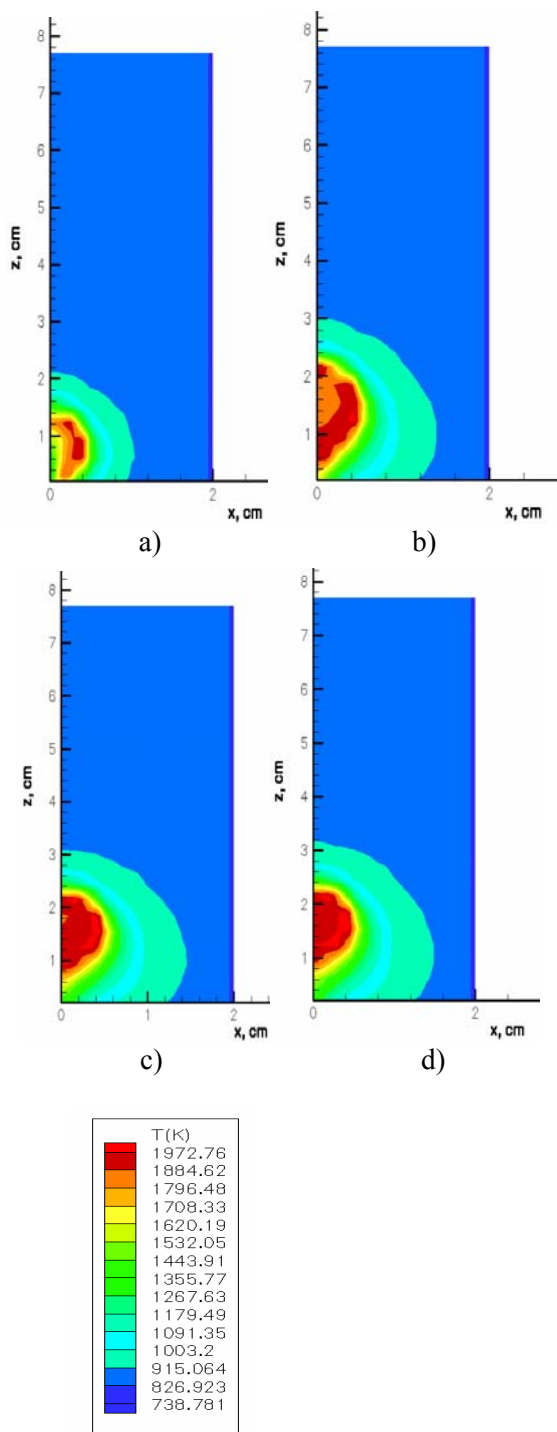


Fig.4. The temperature distribution in the combustion chamber during combustion of tetradecane at various time moments: a) $1.1 \cdot 10^{-3}$ s, b) $1.8 \cdot 10^{-3}$ s; c) $3 \cdot 10^{-3}$ s, d) $4 \cdot 10^{-3}$ s for the $Re=25000$

The following figures show the results of a computational experiment on the influence of the Reynolds number on the processes of atomization

and combustion of liquid fuel (tetradecane). These graphs were obtained at an optimal value of the Reynolds number in the combustion chamber, equal to 25 000.

Fig.4 shows the distribution of the temperature in the space of the burner chamber for the Reynolds numbers equal to 25000 at different times: $1.1 \cdot 10^{-3}$ s, $1.8 \cdot 10^{-3}$ s, $3 \cdot 10^{-3}$ s, $4 \cdot 10^{-3}$ s correspondingly.

From these graphs (Fig.4) it can be seen how the temperature changes in the combustion chamber at different times. As can be seen from Fig.4, during the combustion of the tetradecane, the region of maximum temperatures at time $t=1.8 \cdot 10^{-3}$ s reaches 0,022 m in height of the combustion chamber, the rest of the chamber is heated to 915 K. At this time, the mixture of fuel vapor with the oxidant is ignited, the fuel begins to burn rapidly, a large part of the width of the chamber is covered by thermal flame, where it reaches a value of the order of 1900 K.

At the final time moment the temperature reaches 2645 K and it can be seen that the temperature torch fills up almost all of the space of the chamber.

The distribution of the fuel concentration is presented in Fig.5 for the same time moments as for the temperature and for the Reynolds number 25000. At the initial moment the concentration of fuel has minimal value and then increases because of the fuel injection in the chamber. At high turbulence region occupied by the fuel in the chamber is reduced, a moment of time $t=1.8 \cdot 10^{-3}$ s the fuel vapor of the tetradecane is raised to 0,03 m by the chamber axis.

The fuel quickly vaporizes, the vapors are mixed with the oxidant and the mixture ignites and burns down for $4 \cdot 10^{-3}$ s. At the final moment, the tetradecane burns without residue, the concentrations of fuel are almost zero.

Figs.6-7 show the dynamics of the distribution of reaction products concentration on time for the Reynolds number 25000. Analysis of the Fig.6 shows that with the maximum Reynolds number the maximum amount of carbon dioxide for tetradecane is formed on the axis of the combustion chamber and is equal to $0.114 \cdot 10^{-3}$ kg/kg. At the exit from the combustion chamber, the concentration of carbon dioxide decreases and takes the minimum values for tetradecane $0.008 \cdot 10^{-3}$ kg/kg.

Analysis of Fig.7 shows that at the time point of $4 \cdot 10^{-3}$ s the maximum concentration of water formed as a result of the chemical reaction of tetradecane's combustion is

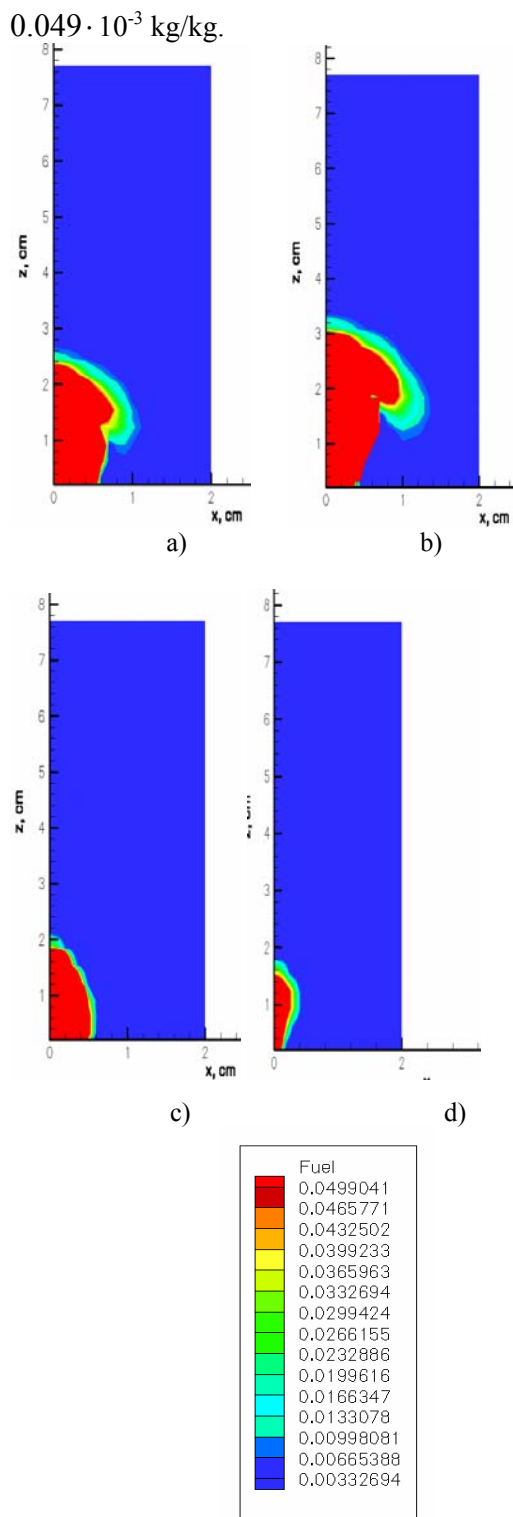


Fig.5. The distribution of fuel vapor concentration in the burner chamber at different time moments: a) $1.1 \cdot 10^{-3}$ s, b) $1.8 \cdot 10^{-3}$ s; c) $3 \cdot 10^{-3}$ s, d) $4 \cdot 10^{-3}$ s for the $Re=25000$

In other parts of the combustion chamber water concentration reaches the lowest value, which amounted to $0.0033 \cdot 10^{-3}$ kg/kg. The values of the concentration of water are especially important in

calculations related to the weight and volume of fuel, wherein the weight ratio of the amount of fuel to the weight of the same volume of water the fuel specific gravity is determined at a given temperature.

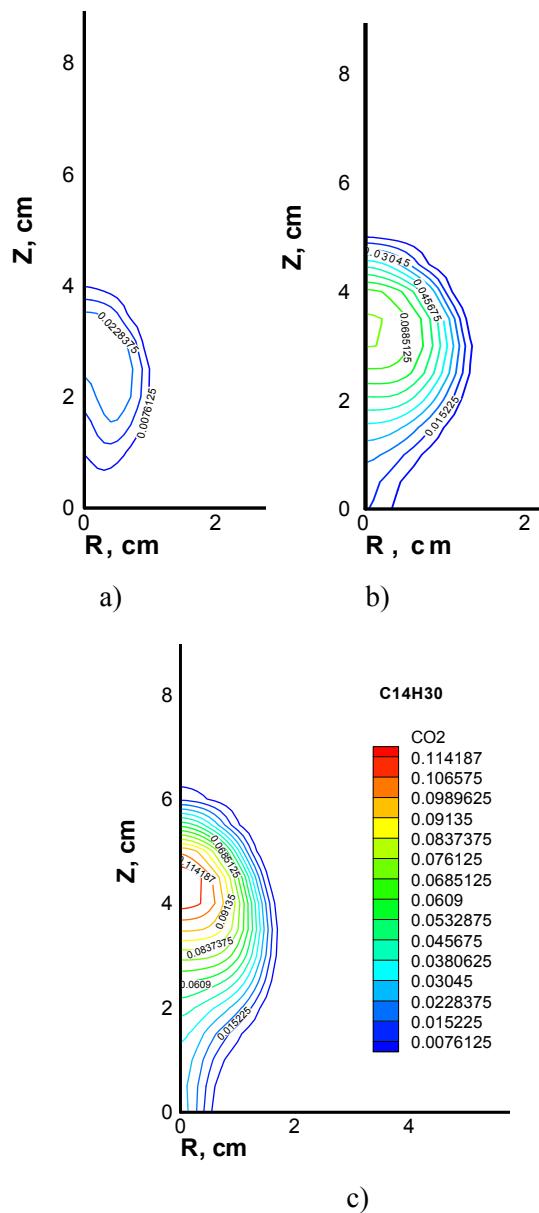


Fig.6. The distribution of CO_2 in the combustion chamber during combustion of tetradecane at various time moments: a) $1.1 \cdot 10^{-3}$ s, b) $1.8 \cdot 10^{-3}$ s; c) $3 \cdot 10^{-3}$ s, d) $4 \cdot 10^{-3}$ s for the $Re=25000$

The following Figs.8-10 show the results of computational experiments on the change in the temporal distributions of the Sauter mean droplet diameter (SMD) of tetradecane with distance from the injector. The Sauter mean diameter is the average volume-surface diameter of the droplets. It

also compares the results obtained with the experimental data presented by the authors *Arcoumanis C., Cutter P., Whitelaw D.* [40]. As can be seen from the figures, the calculated data and experimental data for dodecane are in good agreement.

In [40] studies were performed at various distances from the injector: $10 \cdot 10^{-3}$ m, $20 \cdot 10^{-3}$ m, $30 \cdot 10^{-3}$ m, $40 \cdot 10^{-3}$ m, $50 \cdot 10^{-3}$ m and $60 \cdot 10^{-3}$ m for diesel fuel for $Re=25000$.

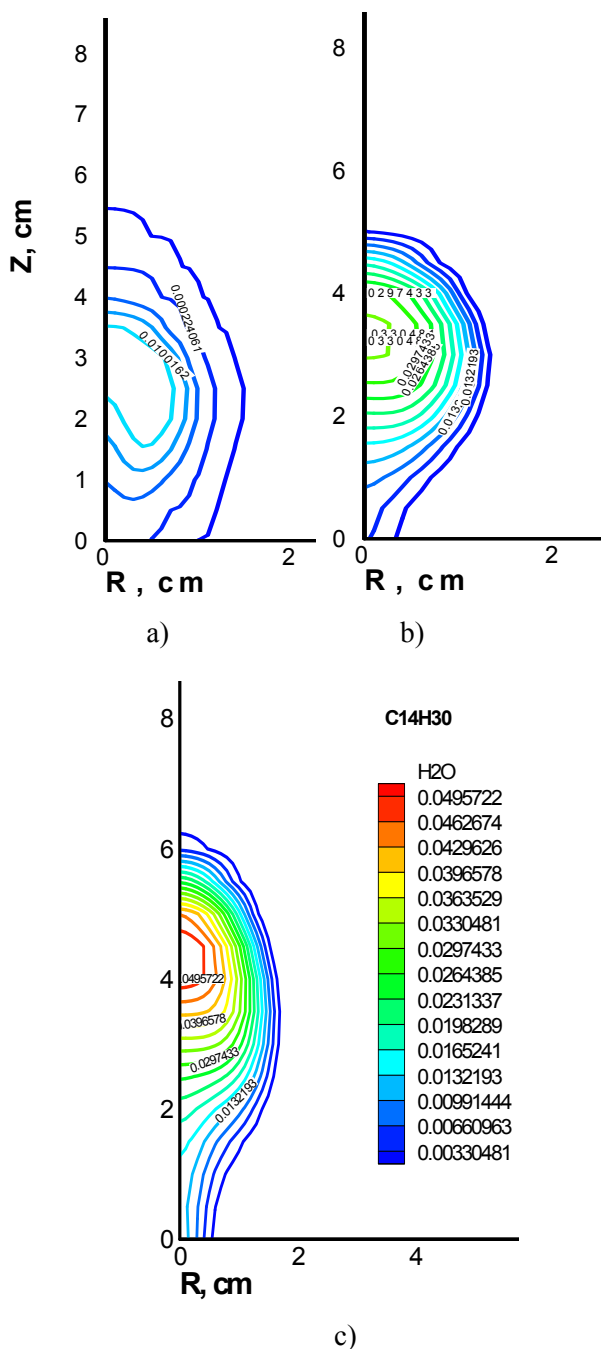


Fig.7. The distribution of concentration of H_2O in the combustion chamber at time moments: a) $1.1 \cdot 10^{-3}$ s, b) $1.8 \cdot 10^{-3}$ s; c) $3 \cdot 10^{-3}$ s, d) $4 \cdot 10^{-3}$ s for the $Re=25000$

In this work a similar study at a distance of $x = 30 \cdot 10^{-3}$ m, $40 \cdot 10^{-3}$ m, $50 \cdot 10^{-3}$ m and $60 \cdot 10^{-3}$ m from the injector for tetradecane and octane are conducted. Octane is the main component of gasoline. As can be seen from Figs.8-10, the coincidence of the data from the field and computer experiments is quite good. Analyzing the data obtained, it can be assumed that the calculated data and experimental data are in good agreement.

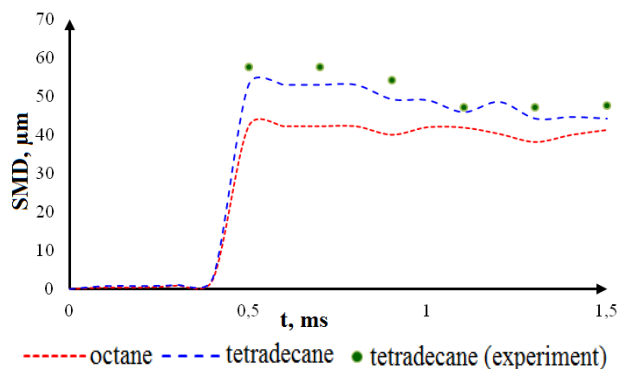


Fig.8. Comparison of the temporal distributions of the Sauter mean diameter of the tetradecane's droplet (SMD) at distances of $40 \cdot 10^{-3}$ m from the injector with experiment for the $Re=25000$

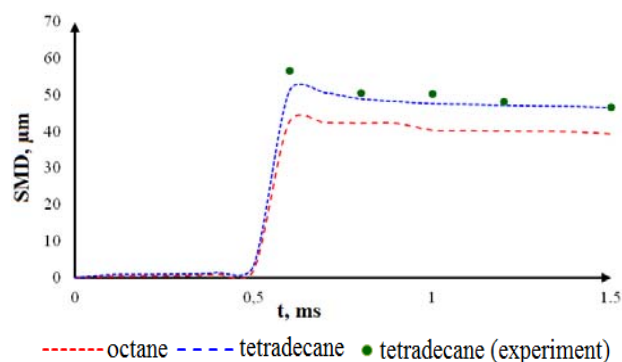


Fig.9. Comparison of the temporal distributions of the Sauter mean diameter of the tetradecane's droplet (SMD) at distances of $50 \cdot 10^{-3}$ m from the injector with experiment for the $Re=25000$

As can be seen from the figures, the results of computer simulation for tetradecane and experimental data for diesel fuel obtained by the authors [40] are in good agreement. The discrepancy in the results for octane can be explained by the fact that this element is found most of all in the composition of gasoline, the surface tension of which is much less than that of diesel fuel.

An analysis of the results presented in Figs.8-10 suggests a good agreement between the numerical

results and the experimental data and allows us to conclude that the numerical model for spraying liquid fuels proposed in the paper adequately describes the actual spray processes and, therefore, the process of burning various types of liquid fuels.

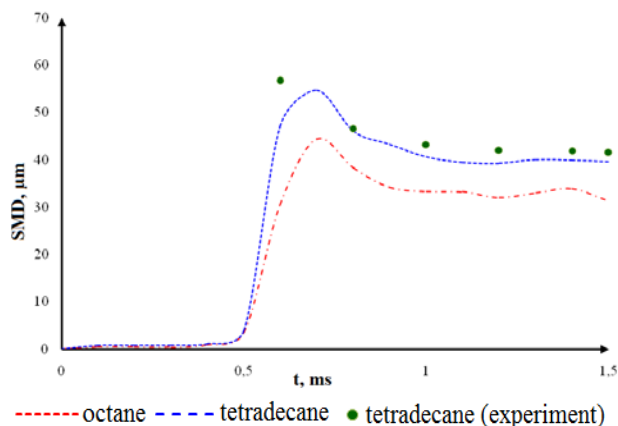


Fig.10. Comparison of the temporal distributions of the Sauter mean diameter of the tetradecane's droplet (SMD) at distances of $60 \cdot 10^{-3}$ m from the injector with experiment for the $Re=25000$

CONCLUSIONS

In this work the influence of the Reynolds number of gas flow on tetradecane's combustion has been studied.

The distributions of maximum temperature and of CO_2 concentration depending on the Reynolds number, time distributions of the fuel, CO_2 , H_2O concentrations and temperature of the gas in the burner chamber for the effective Reynolds number have been obtained. Also the change of maximum temperature in the burner chamber depending on the Reynolds number of the gas flow has been obtained.

As a result of a computer study, the effective mode of the combustion process was determined. The most effective combustion proceeds at the Reynolds number of the gas flow equal 25000, under these conditions temperature reaches high values (from 2001 K to 2645 K).

At this temperature, the fuel is combusted completely, the chamber is warmed to a sufficiently high temperature, and the concentration of formed carbon dioxide takes the smallest value (to $0.104 \cdot 10^{-3}$ kg/kg).

Analyzing the distribution of the fuel vapor it can be concluded that the initial time vapor concentration was $0.05 \cdot 10^{-3}$ kg/kg than then at a final stage of the process of burning fuel vapor at the outlet from the combustion chamber was $0,003 \cdot 10^{-3}$ kg/kg.

Also, the results of numerical simulations were compared with experimental data, obtained by various authors. The temporal distributions of the Sauter mean diameter of the drops at different distances from the injector were obtained. The results of numerical simulation in this case was given a good agreement with experiment. Also for comparison of characteristics of various liquid fuels combustion processes has been studied two types of fuels. Verification of obtained during the computational results of the experiments, a comparison with experimental data and theoretical calculations have revealed good agreement.

The further study of the combustion of liquid sprays will let not only to develop methods for the decrease the contain of harmful substances in the atmosphere and prevention of formation of polluting fog, but also to improve the work of the engines of the internal combustion, of rockets, aviation engines and to make them more efficient and ecologically safer.

REFERENCES

- [1] Messerle, V. E., Ustimenko, A.B., etc. Numerical simulation of pulverized coal combustion in a power boiler furnace. *High temperature* **53** (3) 445-452 (2015).
- [2] Bekmukhamet, A., Beketayeva, M.T. Gabitova, Z. K. etc. Computational method for investigation of solid fuel combustion in combustion chambers of a heat power plant. *High temperature* **5** (5) 751-757 (2015).
- [3] Askarova, A. S., Bolegenova, S.A., Maximov, V.Y., etc. Numerical research of aerodynamic characteristics of combustion chamber BKZ-75 mining thermal power station. *Procedia Engineering* **42** 1250-12-59 (2012).
- [4] Ospanova Sh., Gabitova Z., etc. Using 3D modeling technology for investigation of conventional combustion mode of BKZ-420-140-7c combustion chamber. *J. of Engineering and Applied Sciences* **9** (1) 24-28 (2014).
- [5] Bolegenova S.A., etc. Mathematical simulation of pulverized coal in combustion chamber. *Procedia Engineering* **42**, 1259-1265 (2012).
- [6] Boraiko C., Beardsley T., Wright E. Accident Investigations: one element of an effective safety culture. *Professional Safety* **53(9)**, 26-30 (2008).
- [7] Clarke S. Safety climate in an automobile manufacturing plant: The effects of work environment, job communication and safety attitudes on accidents and unsafe behavior. *Personnel Review* **35(4)**, 413-430 (2004).
- [8] Dawal S.Z., Taha Z. The effects of job organizational factors on job satisfaction in two

- automotive industries in Malaysia. *Journal of Human Ergo logy* **36(2)**, 63-68 (2007).
- [9] Dietl H., Royer S., Stratmann U. Value creation architectures and competitive advantage: lessons from the European automotive industry. *California Management Review* **51**, 24-28 (2009).
- [10] Liang-Hung L., Iuan-Yuan L. Product quality as a determinant of product innovation: an empirical analysis of the global automotive industry. *Total Quality Management and Business Excellence* **14(2)**, 141-147 (2006).
- [11] Oh J., Rhee S.K. Influences of supplier capabilities and collaboration in new car development on competitive advantage of carmakers. *Management Decision* **48(5)**, 756-774 (2010).
- [12] Renard L. The automobile manufacturers' global competitiveness and dimension effects: Differentiation and cost advantages reconciled. *International Journal of Automotive Technology and Management* **2(3,4)**, 280-288 (2002).
- [13] Richardson M., Danford A., Stewart P., Pulignano V. Employee participation and involvement: Experiences of aerospace and automobile workers in the UK and Italy. *European Journal of Industrial Relations* **16(1)**, 21-37 (2006).
- [14] Sako M. The nature and impact of employee «voice» in the European car components industry. *Human Resource Management Journal* **8(2)**, 5-13 (1998).
- [15] Dadach Z.E. Cost Effective Strategies to Reduce CO2 Emissions in the UAE: A Literature Review. *Journal of Industrial Engineering and Management* **2(4)**, 1-9 (2013).
- [16] Smith M., Crotty J. Environmental regulation and innovation driving ecological designing the UK automotive industry. *Business Strategy and the Environment* **17 (6)**, 341-349 (2008).
- [17] Gorokhovski, M., Chtab-Desportes, A., Voloshina, I., Askarova A. Stochastic simulation of the spray formation assisted by a high pressure. *AIP Conference Proceedings Xian*, **1207**, 66-73 (2010).
- [18] Amsden, A.A., O'Rourke, P.J., Butler, T.D. KIVA-II: A computer program for chemically reactive flows with sprays. Los Alamos, 160. 1989.
- [19] R. Manatbayev, Zh. K. Shortanbayeva, A. N. Aldiyarova, etc. Mathematical modeling of heat and mass transfer in the presence of physical-chemical processes. *Bulgarian Chemical Communications* **E**, 272-277 (2016).
- [20] I. Berezovskaya, Sh. Ospanova, A. Nugymanova, etc. 3D modelling of heat and mass transfer processes during the combustion of liquid fuel. *Bulgarian Chemical Communications* **E**, 229-235 (2016).
- [21] Beketayeva M., Ospanova Sh., etc. Investigation of turbulence characteristics of burning process of the solid fuel in BKZ 420 combustion chamber. *WSEAS Transactions on Heat and Mass Transfer* **9**, 39-50 (2014).
- [22] Askarova A.S., Maximov Yu.V., Gabitova Z. K., etc. Numerical modeling of turbulence characteristics of burning process of the solid fuel in BKZ-420-140-7c combustion chamber. *Int. J. of Mechanics* **8**, 112-122 (2014).
- [23] Bolegenova S.A., Beketayeva M.T., etc. Numerical experimenting of combustion in the real boiler of CHP. *Int. J. of Mechanics* **7**, 343-352 (2013).
- [24] Lavrichsheva, Ye.I., Leithner, R., Müller, H., Magda, A., etc. Combustion of low-rank coals in furnaces of Kazakhstan coal-firing power plants. *VDI Berichte*, 497-502 (2007).
- [25] Vockrodt S., Leithner. et al. Firing technique measures for increased efficiency and minimization of toxic emissions in Kasakh coal firing. *VDI, 19th German Conference on Flames, Germany, VDI Gesell Energietechn; Verein Deutsch Ingn., Combustion And Incineration, VDI Berichte* **1492**, 93, (1999).
- [26] Askarowa A, Buchmann M.A. Structure of the flame of fluidized-bed burners and combustion processes of high-ash coal. *Gesell Energietechn, Combustion and incineration - eighteenth dutch-german conference on flames, VDI Berichte*, **1313**, 241-244 (1997).
- [27] Bolegenova, S.A., Bekmukhamet, A, etc. Control of Harmful Emissions Concentration into the Atmosphere of Megacities of Kazakhstan Republic. *Int. Conf. on Future Information Engineering (FIE2014), IERI Procedia, Beijing, China* 252-258 (2014).
- [28] A. Yergaliyeva, A. Boranbayeva, K. Berdikhan, etc. Application of 3D modelling for solving the problem of combustion coal-dust flame. *Bulgarian Chemical Communications* **E**, 236-241 (2016).
- [29] E. I. Heierle, A. B. Ergalieva, etc. CFD study of harmful substances production in coal-fired power plant of Kazakhstan. *Bulgarian Chemical Communications* **E**, 260-265 (2016).
- [30] R. Leithner, Sh. Ospanova, etc. Computational modeling of heat and mass transfer processes in combustion chamber at power plant of Kazakhstan. *MATEC Web of Conferences* DOI:10.1051/ mateconf/ 20167606001, 1–5 (2016).
- [31] Karpenko, E. I., Karpenko, Yu. E., Messerle, V. E., Ustimenko, A. B., etc. Mathematical modelling of the processes of solid fuel ignition and combustion at combustors of the power boilers. *7th Int. Fall Seminar on Propellants, Explosives and Pyrotechnics Xian* **7**, 672-683 (2007).

- [32] Askarova A., Bolegenova Symbat, Ergalieva A., etc. 3D modeling of heat and mass transfer during combustion of solid fuel in BKZ-420-140-7c combustion chamber of Kazakhstan. *J. of Applied Fluid Mechanics* 699-709 (2016).
- [33] Messerle V. E., Ustimenko A.B., etc. Reduction of noxious substance emissions at the pulverized fuel combustion in the combustor of the BKZ-160 boiler of the Almaty heat electropower station using the “Overfire Air” technology. *Thermophysics and aeromechanics* **23** (1) 125-134 (2016).
- [34] Berdikhan, K., etc. Application of numerical methods for calculating the burning problems of coal-dust flame in real scale. *Int. J. of Applied Engineering Research* **11** (8) 5511-5515 (2016).
- [35] Askarova A., Bolegenova S. et al. Influence of boundary conditions to heat and mass transfer processes. *Int. J. of Mechanics* **10**, 320-325 (2016).
- [36] Maximov V. et al. On the effect of the temperature boundary conditions on the walls for the processes of heat and mass transfer. *Int. J. of Mechanics* **10**, 349-355 (2016).
- [37] Askarova, A. S., Maksimov, V. Yu., et. al. Numerical simulation of the coal combustion process initiated by a plasma source. *Thermophysics and aeromechanics* **21**, (6) 747-754 (2014).
- [38] Karpenko E. I., Messerle V.E. et al. Plasma enhancement of combustion of solid fuels. *J. of High Energy Chemistry* **40**, (2) 111-118 (2006).
- [39] Beketayeva, M., Safarik, P., et al. Numerical Modeling of Pulverized Coal Combustion at Thermal Power Plant Boilers. *J. of thermal science* **24** (3) 275-282 (2015).
- [40] Arcoumanis C., Cutter P., Whitelaw D. S. Heat transfer processes in diesel engines. *Institution of Chemical Engineer Trans IChemE* 70, 124-132 (1998).

Atmospheric dispersion modelling and radiological safety analysis for a hypothetical accident of liquid-fuel thorium molten salt reactor (TMSR-LF)

Bo Cao^{1,2,3*}, Weijie Cui^{1,2}, Irsa Rasheed^{1,2}, Yixue Chen^{1,2}

¹School of Nuclear Science and Engineering, North China Electric Power University, Beijing, 102206, China

²Beijing Key Laboratory for Passive Safety Technology of Nuclear Energy, North China Electric Power University, Beijing, 102206, China

³Departments of Atmospheric and Oceanic Sciences, University of California, Los Angeles, CA, 90095, USA

The molten salt reactor (MSR) is one of the six advanced reactor types for future nuclear energy proposed in the Generation IV International Forum (GIF). Because of its potentially favourable economic, fuel utilization, and safety characteristics and nuclear proliferation resistance, the MSR has aroused widespread concern in recent years. Indeed, from 2011, the Shanghai Institute of Applied Physics started the “Thorium Molten Salt Reactor Nuclear Energy System (TMSR)” project in China and aimed to construct a liquid-fuel thorium molten salt reactor (TMSR-LF) and a solid-fuel thorium molten salt reactor (TMSR-SF). An optimized 2 MWth TMSR-LF has been designed and will be built recently in Gansu province. In this study, HotSpot health physics computer code has been used for atmospheric dispersion modelling and radiological safety assessment considering site-specific meteorological conditions. Calculations for total effective dose equivalent (TEDE), ground deposition and the respiratory time-integrated air concentration have been performed, with results indicating maximum value of ground deposition equal to 2.5E+01kBq/m² at a distance of 0.6km from the reactor. Maximum value of TEDE falls below the public dose limit of 1mSv/year proposed by ICRP even for the worst case accident scenario as set in IAEA safety Report Series number 115. The TEDE has three components: inhalation, ground shine and air submersion, the submersion and ground shine doses are insignificant compared to the inhalation doses. It is observed that the highest value of committed effective dose equivalent (CEDE) appears to be the lung, the lower large intestine wall appears to be the second most exposed organ, followed by upper large intestine wall and the red marrow, respectively. The contribution of total 18 selected radionuclides was investigated, three main radionuclides including Sr-90, Sr-89, Cs-137 are the main contributors to the CEDE.

Keywords: atmospheric dispersion modelling, radiological safety analysis, TMSR-LF, TEDE, HotSpot

INTRODUCTION

Generation IV International Forum (GIF) has anticipated molten salt reactor (MSR) as one of the advanced reactors to fulfil the future nuclear energy demands [1], owing to its economic fuel utilization, nuclear proliferation resistance and advanced safety characteristics [2-6].

The MSR was first developed in the Oak Ridge National Laboratory (ORNL) in the late 1940s. The first Molten Salt Reactor Experiment (MSRE) began to construct in 1962 and operated at full power in December 1966 [7]. Several conceptual designs of the MSR have been proposed and have been studied in the past 60 years. Japan, Russia and other countries also paid much attention to the MSR [4, 8-10]. In China, the Shanghai Institute of Applied Physics started the “Thorium Molten Salt Reactor Nuclear Energy System (TMSR)” project in China and aimed to construct a liquid-fuel thorium molten salt reactor (TMSR-LF) and a solid-fuel thorium molten salt reactor (TMSR-SF).

An optimized 2 MWth TMSR-LF has been designed and will be built in Gansu province recent

years. For a MSR, as a fluid fuel reactor, on-line fuel processing can be applied, which helps in removal of gaseous and volatile parts from the source term [7, 11]. The MSR is a more safety advanced reactor and is more resistant to consequences of large accidents in comparison to other reactor types, but there is risk for the source term may be released to the environment [3-5]. It is still necessary to predict the radiological safety analysis of a hypothetical accident with the radionuclides available for release to the environment.

Radiological safety analysis for hypothetical accident provides a major contribution for the safety analysis of nuclear power plant, as far as human health and safety is concerned [12-20].

The total effective dose equivalent (TEDE) attributes to both internal and external dose equivalents for the body resulting from the release of radionuclides during accident. Thus, TEDE is computed by addition of both effective dose equivalent (EDE) and the total committed effective dose equivalent (CEDE). The EDE was caused by the external material such as submersion, ground shine and resuspension, and CEDE was caused by

* To whom all correspondence should be sent:
caobo@ncepu.edu.cn

the internal material such as inhalation. The TEDE is the most complete expression of the combined dose from all applicable delivery pathways [20, 21].

Lawrence Livermore National Laboratory (LLNL) has established a HotSpot computer code for the analysis of personnel health physics near the reactor sites. Gaussian Plume Model (GPM) has been employed for HotSpot code for the calculation of air concentration and TEDE due to release of radionuclides into the atmosphere [21]. In practice, the GPM is one of the most widely validated general dispersion models and has been successfully applied in various dispersion problems [13-20].

In this work, we have performed the atmospheric dispersion modelling and radiological safety analysis of a hypothetical TMSR-LF accident by HotSpot health physics computer code considering site-specific meteorological conditions. The TEDE, the respiratory time-integrated air concentration, and the ground deposition are calculated with source term including 18 radionuclides. These results provide reference for the assessment source term of emergency facility and offsite consequence assessment.

MATERIALS AND METHOD

Site-specific conditions of the TMSR-LF

The TMSR-LF will be in the Wuwei City, Gansu Province, China. It will be built about 2020. Wuwei city has a temperate continental arid climate, where evaporation is larger than precipitation. The local meteorological data indicate a mean year rainfall is about 60~610 mm and a mean year evaporation is about 1400~3040 mm. North-North-West (NNW) and West-South-South (WSS) are the predominant directions, which occurred for about 49.1% and 10.4% with an average speed of 5.0m/s and 2.0m/s, respectively. Stability class D gains predominance as it has percentage occurrence of 61.2%, the second being the stability class E with percentage occurrence of 9.3%, and the remaining 29.5% is taken by other classes.

Source term and accidental release scenario

The TMSR-LF is a graphite moderated reactor. The thermal power is 2 MW, and the fuel salt is LiF-BeF₂-ThF₄-UF₄ (68-28-0.1-3.9 mol %) with 99.95 % abundance of ⁷Li and a coolant salt of LiF-NaF-KF [2, 6].

Although MSR has some inherent features compared with other reactor systems, it still has some safety disadvantage, including the accumulation of fission products in different parts like the primary system, the off-gas system, the fuel storage tanks, and the processing plant. This highlights the significance for proper containment of fission products and removal of decay heat under all anticipated circumstances [11]. According to the research, off-gas system failure accident is generally recognized as the most likely path for radiation release [4, 5]. Base on it, in this paper, the source term is mainly contributed by the off-gas system failure and the radioactivity leak by reactor vessel and pipes. The accident source term during 0~ 1 hour for TMSR-LF is shown in Tab.1 [6].

Table 1: Accident source term for TMSR-LF

Nuclide	Activity released / Bq
H-3	3.30×10 ¹²
Kr-85	8.75×10 ⁴
Kr-85m	1.28×10 ⁶
Kr-87	1.45×10 ⁷
Kr-88	1.03×10 ⁷
Xe-133	2.48×10 ⁴
Xe-135	4.17×10 ⁶
I-131	1.51×10 ⁷
I-132	2.83×10 ⁶
I-133	3.54×10 ⁷
I-134	1.15×10 ⁸
I-135	6.96×10 ⁸
Cs-134	4.21×10 ⁶
Cs-137	1.63×10 ¹⁰
Sr-89	5.29×10 ¹¹
Sr-90	8.46×10 ¹⁰
Ru-103	8.38×10 ⁵
Ru-106	1.89×10 ⁵

The release height was assumed at 40 m and buoyancy and exit momentum effects were neglected. Depending on the site meteorology, a downwind transportation of radionuclides happens after the accident. The annual average wind speed at 10 m is 5 m/s in the predominant direction of NNW. Stability class D gains predominance because of its largest percentage occurrence of 61.2%, a default value of 1.7m for the receptor height and value of 1300m for the inversion layer height has been chosen. A value of 3.33×10⁴ m³ s/l

has been used for the breathing rate of an average human being.

RESULTS AND DISCUSSION

TEDE results and analysis

Based on the site-specific meteorological conditions, an assessment for the calculation of radiation dose calculation was done by HotSpot 3.03 after the hypothetical accident. The TEDE, the ground deposition and the respiratory time-integrated air concentration were generated as a function of downwind distance as presented in Tab.2. It can be seen from Tab.2 that the maximum TEDE is 1.6E-04 Sv at the downwind distance of 0.6 km, which is also shown in Fig.1. It is far below the annual regulatory limits of 1 mSv from public exposure in a year even in the event of worse accident scenario as set in IAEA Safety Report Series number 115, no action related specifically to the public exposure is required.

Meanwhile, the maximum respiratory time-integrated air concentration and the ground deposition value of 5.2E+07 Bq-s/m³ and 2.5E+01

kBq/m² occurred at 0.6 km at an arrival time about one minutes. As is shown in Fig.1 the TEDE first increases with increasing distance downwind, reaches the maximum value and then decreases. The plume centreline ground deposition of radionuclides as a function of downwind distance is shown in Fig.2, which shows a similar tend as TEDE shown in Fig.1. The maximum value of plume centreline ground deposition is 2.5E+01 kBq/m² occurred at about 0.6 km from the reactor, which is accordance with results shown in Tab.2.

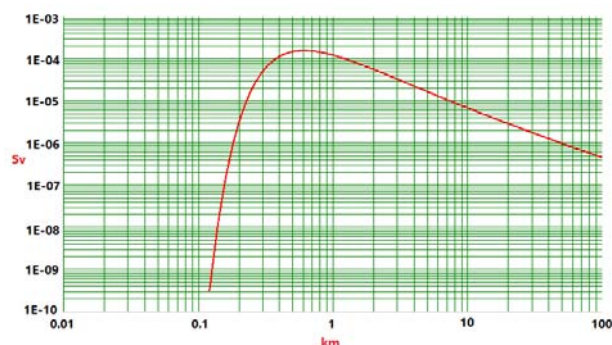


Fig.1. TEDE as a function of downwind distance from the NPP site in D class

Table 2. Downwind distance and other plume parameters at different arrival time intervals

Distance/km	TEDE/Sv	Respirable time-integrated air concentration/ Bq-sm ⁻³	Ground surface deposition/ kBqm ⁻²	Ground shine dose rate/ Sv h ⁻¹	Arrival time /h: min
0.03	0.00E+00	0.00E+00	0.00E+00	0.00E+00	<00:01
0.1	4.7E-13	1.5E-01	1.7E-08	1.2E-18	<00:01
0.2	3.2E-06	1.0E+06	4.3E-01	2.9E-11	<00:01
0.3	5.1E-05	1.7E+07	7.7E+00	5.2E-10	<00:01
0.4	1.1E-04	3.7E+07	1.8E+01	1.2E-09	0:01
0.5	1.5E-04	4.9E+07	2.3E+01	1.6E-09	0:01
0.6	1.6E-04	5.2E+07	2.5E+01	1.7E-09	0:01
0.7	1.5E-04	5.1E+07	2.4E+01	1.6E-09	0:01
0.8	1.4E-04	4.8E+07	2.3E+01	1.5E-09	0:02
0.9	1.3E-04	4.4E+07	2.1E+01	1.4E-09	0:02
1	1.2E-04	4.0E+07	1.0E+01	1.3E-09	0:02
2	5.6E-05	1.9E+07	8.8E+00	6.0E-10	0:05
4	2.2E-05	7.5E+06	3.5E+00	2.4E-10	0:10
6	1.3E-05	4.4E+06	2.1E+00	1.4E-10	0:16
8	9.0E-06	3.0E+06	1.4E+00	9.6E-11	0:21
10	6.8E-06	2.3E+06	1.1E+00	7.2E-11	0:27
20	2.9E-06	9.9E+05	4.5E-01	3.0E-11	0:54
40	1.3E-06	4.5E+05	2.0E-01	1.3E-11	1:48
60	8.0E-07	2.9E+05	1.3E-01	8.3E-12	2:42
80	5.8E-07	2.1E+05	9.2E-02	6.0E-12	03:36

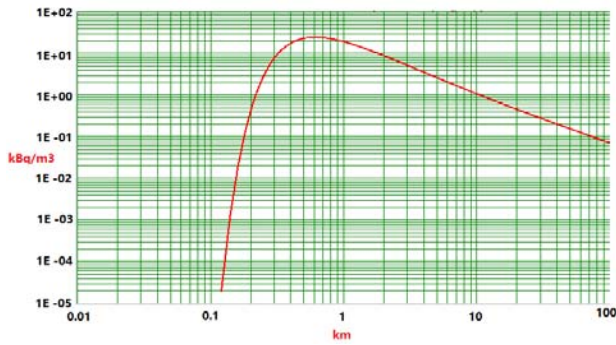


Fig.2. Plume centreline ground deposition of radionuclides as a function of downwind distance in D class

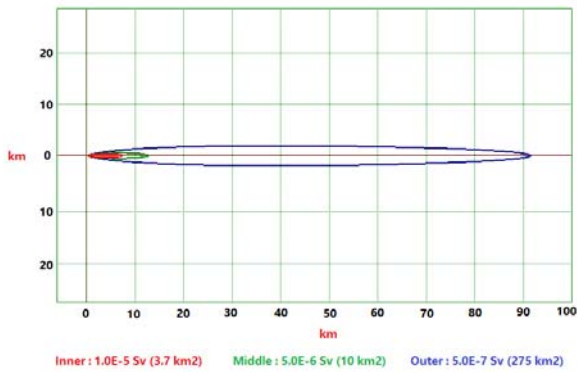


Fig.3. TEDE counter plot for D class



Fig.4. Plume contour ground deposition distribution for D class

Table 3. TEDE including inhalation and submersion and ground shine in different distance

Distance/ km	TEDE/Sv	Inhalation /Sv	Submersion/ Sv	Ground Shine/Sv
0.03	0.00E+00	0	0	0
0.1	4.7E-13	4.69E-13	2.21E-17	2.33E-18
0.2	3.2E-06	3.19E-06	1.50E-10	5.70E-11

0.3	5.1E-05	5.06E-05	2.38E-09	1.03E-09
0.4	1.1E-04	1.14E-04	5.35E-09	2.37E-09
0.5	1.5E-04	1.48E-04	6.95E-09	3.10E-09
0.6	1.6E-04	1.57E-04	7.39E-09	3.30E-09
0.7	1.5E-04	1.53E-04	7.21E-09	3.23E-09
0.8	1.4E-04	1.44 E-04	6.77E-09	3.03E-09
0.9	1.3E-04	1.33E-04	6.25E-09	2.80E-09
1	1.2E-04	1.22E-04	5.73E-09	2.57E-09
2	5.6E-05	5.58E-05	2.62E-09	1.18E-09
4	2.2E-05	2.24E-05	1.05E-09	4.72E-10
6	1.3E-05	1.31E-05	6.13E-10	2.75E-10
8	9.0E-06	9.00E-06	4.21E-10	1.89E-10
10	6.8E-06	6.78E-06	3.16E-10	1.42E-10
20	2.9E-06	2.87E-06	1.33E-10	6.00E-11
40	1.3E-06	1.27E-06	5.84E-11	2.64E-11
60	8.0E-07	8.00E-07	3.64E-11	1.65E-11
80	5.8E-07	5.79E-07	2.61E-11	1.19E-11

In addition, Fig.3 and Fig.4 show TEDE contour plot and plume contour ground deposition distribution under the plume for stability class D and wind speed of 5 m/s, respectively. It can be seen from Fig.3 that three regions with the area of 3.7, 10 and 275 km² has been marked with dose contours of 1.00E-05, 5.00E-06 and 5.00E-07 Sv. Moreover, as is shown in Fig.4, three regions with the area of 0.21, 7.2 and 196 km² has been marked with deposition contours of 10, 1 and 0.1 kBq/m². The TEDE and plume contour ground deposition distribution move away from the source as a function of downwind distance. The red colour area shows higher dose risk for personnel and population, the green and blue area are safer compared with red area. According to the above results and analysis, the calculated TEDE in all distances is below the maximum public dose limit proposed by ICRP, thus reducing the risk for serious hazards for the personnel and population.

Based on the situation, multiple pathways are available for the radiation absorptions, for example TEDE includes the plume passage inhalation and submersion and ground shine which is shown in

Tab.3. It is very obviously that the plume passage inhalation is biggest the donation among them. Moreover, the CEDE is mainly caused by the internal material because of inhalation.

Organ CEDE results and analysis

CEDE specifies the committed dose equivalent, which includes dose equivalents for internal body organ or tissues, which have absorbed radiation over a period of 50 years after the intake of radioactive material. In HotSpot also, CEDE is calculated by the traditional method, that is by integrating the committed dose equivalents throughout 50 years for different tissues and organs of the body, and an appropriate multiplication factor W_T has been used for each committed dose equivalent.

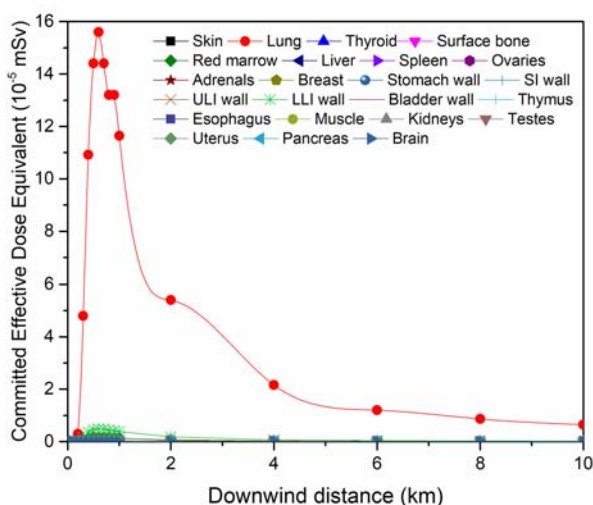


Fig.5. Organ CEDE profile due to 18 selected nuclides versus downwind distance (LLI: lower large intestine; SI: small intestine; ULI: upper large intestine)

Fig.5 and Fig.6 show the distribution of CEDE to different organs as a function of downwind distance. It can be seen from Fig.5 that the biggest value of organ CEDE appears to be the lung. The maximum CEDE of the lungs is about $1.56E-4$ Sv at the downwind distance of 0.6 km. Meanwhile, Fig.6 shows the other organs CEDE as a function of downwind distance except for lungs, because the CEDE of the lungs is far larger than others. From Fig.5 and Fig.6, the lung tops the list, followed by the lower large intestine (LLI) wall, upper large intestine (ULI) wall and red marrow, respectively. It is concluded that these four organs are more radiation sensitive than the others. All the target organ CEDE plots are similar Gaussian trend, as they deplete with as they deplete with distance from receptor location. The maximum CEDE of LLI wall, ULI wall and red marrow are about $4.92E-6$, $1.68E-$

6 and $1.56E-6$ Sv at the downwind distance of 0.6 km, respectively.

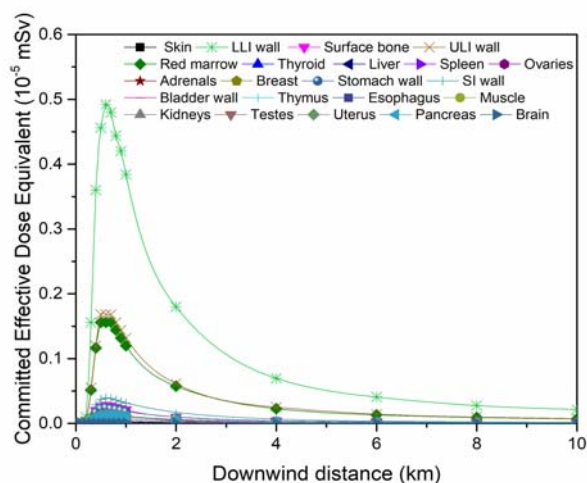


Fig.6. Organ CEDE profile due to 18 selected nuclides versus downwind distance (LLI: lower large intestine; SI: small intestine; ULI: upper large intestine; not include lung)

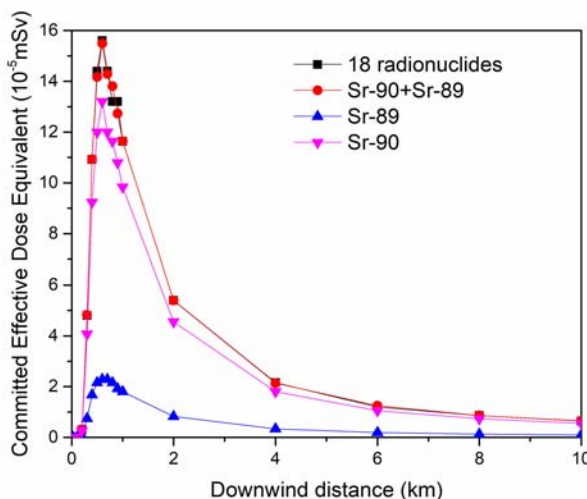


Fig.7. Lung CEDE profile versus downwind distance

The biological properties of the main contributors to the lung CEDE are Sr-90 and Sr-89, which is shown in Fig.7. These two radionuclides are responsible for such a CEDE plot trend, others are very little contributors. Because the lung CEDE contribution percentage of Sr-90 and Sr-89 are about 84.6% and 14.6% at the maximum CEDE. Fig.8 shows the LLI wall CEDE profile as a function of downwind distance. The biological properties of the main contributors to the LLI wall CEDE are Sr-89, Sr-90 and Cs-137, responsible for the dose are about 78%, 19%, and 1.6% at the maximum CEDE, respectively.

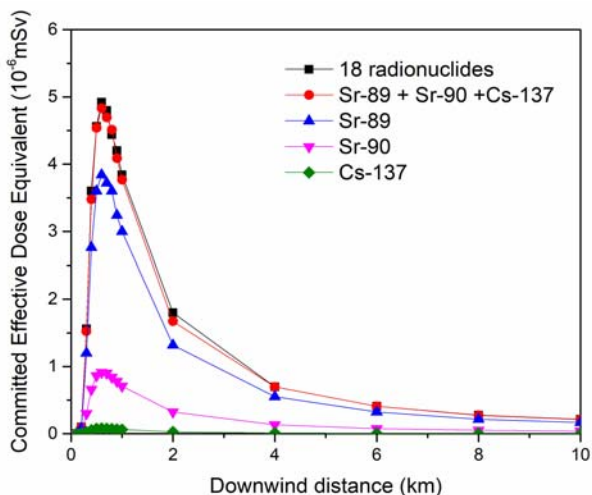


Fig.8. LLI wall CEDE profile versus downwind distance

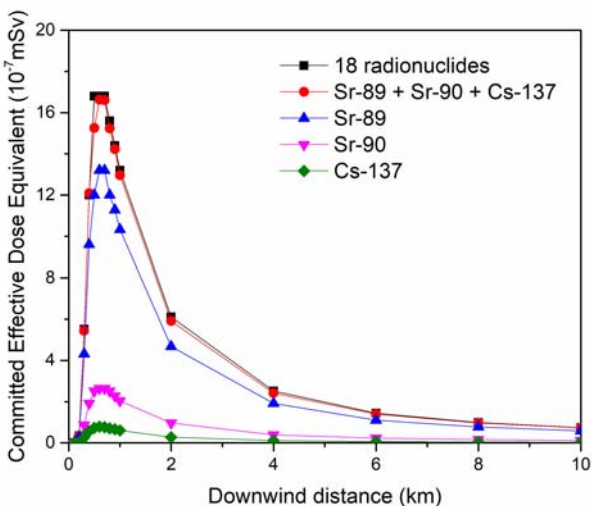


Fig.9. ULI wall CEDE profile versus downwind distance

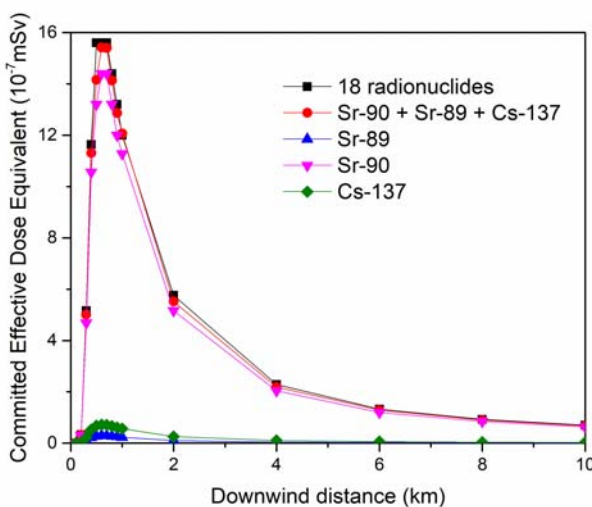


Fig.10. Red Marrow CEDE profile versus downwind distance

Fig.9 and Fig.10 show the ULI wall and red marrow CEDE profile as a function of downwind distance, respectively. The biological properties of the main contributors to the ULI wall and red marrow CEDE are Sr-89, Sr-90 and Cs-137, similar to the LLI wall. For the ULI wall CEDE, Sr-89 is the top contributor, followed by Sr-90 and Cs-137. But for the red marrow CEDE, the biggest contributor is Sr-90 at the maximum CEDE, followed by Cs-137 and Sr-89.

From the above results and analysis, we can conclude that three radionuclides including Sr-90, Sr-89, Cs-137 are the main contributors to the CEDE. Sr-90 is a bone-seeking radionuclide that exhibits biochemical behaviour similar to calcium, the next lighter group 2 elements. It is preferentially incorporated into bones and teeth and will result in long-lasting exposure to ionizing radiation. In addition to this, absorption of rays from radioactive strontium can cause cancers of the bone, bone marrow, and soft tissues around the bone. Cs-137 has gained special attention because of its highest yield percentage, intermediate half-life, high-energy radioactivity, and chemical reactivity. Moreover, it was found as a major health concern in Chernobyl and Fukushima nuclear accident. After penetrating the body, caesium gets uniformly distributed through the body particularly in soft tissues, thus indicating a serious health hazard. It is recommended to take precautionary measures to avoid inhalation and ingestion in case of accidents.

CONCLUSIONS

In this article, the radiation dose calculations and radiological consequences of a hypothetical accident have been performed by considering the TMSR-LF the off-gas system failure and the radioactivity leak by reactor vessel and pipes accident by HotSpot code 3.03. After the hypothetical TMSR-LF accident, TEDE, the respiratory time-integrated air concentration and the ground deposition are calculated. The maximum TEDE value of 1.6×10^{-4} Sv and the maximum plume centreline ground deposition value of 2.5×10^1 kBq/m² occurred at 0.6 km from the reactor, which is below the maximum public dose limit of 1 mSv/year as mentioned in IAEA Safety Report Series No.115. The inhalation doses are significant components of the TEDE compared with the submersion and ground shine doses. It is observed that the highest value of CEDE appears to be the lung, the lower large intestine wall appears to be the second most exposed organ, followed by upper large intestine wall and the red marrow,

respectively. The contribution of total 18 selected radionuclides was investigated, three main radionuclides including Sr-90, Sr-89, Cs-137 are the main contributors to the CEDE.

ACKNOWLEDGEMENTS

This research was financially supported by National Natural Science Foundation of China (11605059), the Fundamental Research Funds for the Central Universities (2018MS042) and China Scholarship Council (CSC).

NOMENCLATURE

MSR - molten salt reactor;
GIF - Generation IV International Forum;
ORNL - Oak Ridge National Laboratory;
MSRE - Molten Salt Reactor Experiment;
TMSR - Thorium Molten Salt Reactor Nuclear Energy System;
TMSR-LF - liquid fuel molten salt reactor;
TMSR-SF - solid fuel molten salt reactor;
TEDE - total effective dose equivalent;
EDE - effective dose equivalent;
CEDE - total committed effective dose equivalent;
LLNL - Lawrence Livermore National Laboratory;
GPM - Gaussian plume model;
NNW - North-North-West;
WSS - West-South-South;
IAEA - International Atomic Energy Agency;
ICRP - International Commission for radiation protection;
WT - weighting factors;
LLI - lower large intestine;
SI - small intestine;
ULI - upper large intestine.

REFERENCES

[1] DoE, U. S., 2002, A technology roadmap for Generation IV Nuclear Energy Systems. *Nuclear Energy Research Advisory Committee and the Generation IV International Forum, United States Department of Energy, Washington, DC*, 42–47 (2002).

[2] X.W. Lyu, X.B. Xia, Z. H. Zhang, J. Cai, C.Q. Chen, Analysis of tritium production in a 2 MW liquid-fueled molten salt experimental reactor and its environmental impact. *Nuclear Science and Techniques* **27**, 78 (2016).

[3] B.M. Elsheikh, Safety assessment of molten salt reactors in comparison with light water reactors. *Journal of Radiation Research and Applied Sciences* **6**, 63-70 (2013).

[4] R. Yoshioka, K. Mitachi, Y. Shimazu, M. Kinoshita, Safety criteria and guidelines for MSR accident analysis. *Proc. Of the international conference on physics of reactors (PHYSOR2014), Kyoto, CD-ROM* (2014).

[5] D.W. Hummel, Source term evaluation for advanced small modular reactor concepts. *Proc. of ITMSR-4, 4th int. conf on Small Reactors, Ottawa*, (2016).

[6] X.W. Lyu, Radiological environmental impact analysis of airborne radioactive effluents from 2 MW thorium molten salt reactor with liquid fuel. Doctor degree, China, (2016).

[7] M.W. Rosenthal, Molten salt reactors—history, status, and potential, *Nuclear Applications and Technology*, **8**, 102-113 (1970).

[8] K Mitachi, Y. Yamana, T. Suzuki, K. Furukawa. Neutronic examination on plutonium transmutation by a small molten-salt fission power station technical report. IAEA-TECDOC–840, 1995.

[9] S. Jérôme, A. Michel, B. Ondřej D. Sylvie F. Olga, G. Véronique, H. Daniel, H. David, I. Victor, L. K. Jan, L. Lelio, M.L. Elsa, U. Jan, Y. Ritsuo, Z.M. Dai. The molten salt reactor (MSR) in generation IV: overview and perspectives. *Progress in Nuclear Energy* **77**, 308-319 (2014).

[10] V. Ignatiev. MOSART fuels and container materials study: case for Na, Li, Be/F solvent system. *Proceedings of the 2003 ANS/ENS International Winter Meeting (GLOBAL 2003), New Orleans, LA*. (2003).

[11] S.E. Beall, P.N. Haubenreich, R.B. Lindauer and J.R. Tallackson, MSRE Design and Operation Report Part V Reactor Safety Analysis Report. Oak Ridge National Laboratory report ORNL-TM-732, 1964.

[12] A. Pirouzmand, P. Dehghani, K. Hadad, M. Nematollahi. Dose assessment of radionuclides dispersion from Bushehr nuclear power plant stack under normal operation and accident conditions. *International Journal of Hydrogen Energy* **40 (44)**, 15198-15205 (2015).

[13] S. S. Raza, M. Iqbal. Atmospheric dispersion modelling for an accidental release from the Pakistan Research Reactor-1 (PARR-1). *Annals of Nuclear Energy* **32**, 1157–1166 (2005).

[14] S.A. Birikorang, R.G. Abrefah, R.B.M. Sogbadji, B.J.B. Nyarko, J.J. Fletcher, E.H.K. Akaho. Ground deposition assessment of radionuclides following a hypothetical release from Ghana Research Reactor-1 (GHARR-1) using atmospheric dispersion model. *Progress in Nuclear Energy* **79**, 96–103 (2015).

[15] N. Sadeghi, M. Sadrnia, S. Khakshournia. Radiation dose calculations for an accidental release from the Tehran Research Reactor. *Nuclear Engineering and Design* **257**, 67–71 (2013).

- [16] J.L. Muswema, G.B. Ekoko, V.M. Lukanda, J.K.-K. Lobo, E.O. Darko, E.K. Boafo. Source term derivation and radiological safety analysis for the TRICO II research reactor in Kinshasa. *Nuclear Engineering and Design* **281**, 51–57 (2015).
- [17] J.L. Muswema, G.B. Ekoko, V.M. Lukanda, J.K.-K. Lobo, V. M. Lukanda, E.K. Boafo. TRICO II Core Inventory Calculation and its Radiological Consequence Analyses. *Journal of Nuclear Engineering and Radiation Science* **2**, 024501 (2016).
- [18] A. Anvar, L. Safarzadeh. Assessment of the total effective dose equivalent for accidental release from the Tehran Research Reactor. *Annals of Nuclear Energy* **50**, 251–255 (2012).
- [19] J.L. Muswema, E.O. Darko. Atmospheric dispersion modelling and radiological safety analysis for a hypothetical accident of Ghana Research Reactor-1 (GHARR-1). *Annals of Nuclear Energy* **68** (3), 239–246 (2014).
- [20] B. Cao, J.X. Zheng, Y.X. Chen. Radiation Dose Calculations for a Hypothetical Accident in Xianning Nuclear Power Plant. *Science and Technology of Nuclear Installations* **2016**, 3105878 (2016).
- [21] S. G. Homann, F. Aluzzi, HotSpot Health Physics Code, Version 3.0, User’s Guide, LLNL-SM-636474. National Atmospheric Release Advisory Center, Lawrence Livermore National Laboratory, Livermore, CA 94550, 2013.

Simulation and thermodynamic analysis of a regenerative and recuperative organic Rankine cycle

E. Ozdemir Kucuk¹, M. Kılıç^{2*}

¹Bursa Uludag University, Yenisehir Ibrahim Orhan of Vocational School, Dept. of Machine, 16900, Bursa, Turkey,

^{2*}Bursa Uludag University, Engineering Faculty, Department of Mechanical Engineering, 16059, Bursa, Turkey

Due to the energy shortage, environmental pollutions and climate change, the issues of energy conversion technologies have become more and more significant. In recent years, organic Rankine cycle has become a leading technology for the conversion of heat into useful work or electricity. This promising technology uses an organic fluid which has high molecular mass hydrocarbon compound, low critical temperature, and pressure as a working fluid. In this paper, energy and exergy analysis of a waste air's heat-driven organic Rankine cycle, which has two turbines, two pumps, an evaporator, a condenser, a recuperator, and a feed fluid heater, is performed using R114, R600, R600a and R245fa organic fluids. The organic Rankine cycle's performance parameters are evaluated depending on various evaporation temperatures and the inlet pressure of the high-pressure turbine. The results indicate that R245fa has the highest thermal efficiency also the highest net power is obtained for the R600 working fluid. Also, the thermal efficiency and the net power increase with the increment of the evaporation temperature and these features raise before and then decreases with the increasing high-pressure turbine inlet pressure in the analysis of ORC.

Keywords: Organic Rankine cycle, working fluid, thermodynamic analysis, high-pressure turbine

INTRODUCTION

In recent years, the energy consumption of countries has increased due to the increment of social and economic factors such as population, industrialization, urbanization, technological development, etc. in a globalizing world. Therefore, providing sustainable energy policies which are the primary input of countries' economic development; ensuring the security of energy supply, and diversifying of energy resources have happened vital issues. As a result, the popularity of the organic Rankine cycle (ORC) has increased recently to convert the low-grade heat sources into power.

The organic Rankine cycle (ORC), which uses an organic fluid instead of water as a working fluid, is a power generation cycle from low-grade waste heat [1, 2] and renewable energy sources, such as solar energy [3, 4], biomass energy [5, 6], geothermal energy [7, 8]. This promising technology consists of four phases: pressure increase in the feed pump; isobaric heating, evaporation and overheating of the working fluid in the evaporator; expansion of the vapor working medium in an expansion machine (e.g. a turbine); isobaric heat release, complete condensation and possible under-cooling of the working medium in the condenser.

The slope of saturation vapor curve of a working fluid in T-s diagram is the most crucial feature to determine the fluid applicability, system efficiency, work output and also the overall structure of the

system in an ORC. Working fluids for ORC's are categorized in three groups based on their slope of saturation vapor curves in T-s diagram. The fluids having positive slope are dry fluids ($ds/dT > 0$). The fluids having negative slope are wet fluids ($ds/dT < 0$). The fluids having nearly infinitely large slopes are isentropic fluids ($ds/dT=0$) [9]. In the ORC, dry or isentropic fluids are more convenient because they do not require superheating in the evaporator to avoid forming moisture in the working fluid during the expansion process [10, 11].

One of the effects to increase the system efficiency of the ORC is the application of different configurations of ORC which are the double stage ORC, regenerative ORC, recuperative ORC and both regenerative and recuperative ORC. Many studies on energy production from low-grade waste heat and renewable energy resources using ORC configurations have been presented in the literature. For example; Shokati et al. [12] compared the basic, dual-pressure and dual-fluid ORCs and Kalina cycle for power generation from the geothermal fluid reservoir utilizing energy, exergy and exergo-economic viewpoints. Their results show that among the considered cycles, dual-pressure ORC has the maximum value of produced electrical power. This is 15.2%, 35.1% and 43.5% more than the corresponding values for the basic ORC, dual-fluid ORC and Kalina cycle, respectively in optimal condition.

Ayachi et al. [13] analysed the exergetic optimization of single and double stage ORCs for

* To whom all correspondence should be sent:
mkilic@uludag.edu.tr

waste heat recovery from the one almost dry heat source and highly moist heat source. They examined different combinations of working fluids, such as R1234yf, R245fa (topping cycle) and R245fa, R125, R41 and CO₂ (bottoming cycle). Their results indicate that global exergy efficiency is strongly linked to the critical temperature of the working fluid. They calculated the highest performances in the supercritical operating conditions and estimated that the addition of a low temperature bottoming cycle for recovering the heat during the condensing process offers an efficiency increase potential of about 33%.

Braimakis and Karellas [14] examined three regenerative ORCs which are including an open pre-heater and two additional configurations with closed-type pre-heater regenerative ORC with backward bleed condensate circulation. In the second configuration, the bleed stream is throttled and conveyed to the condenser. In the third ORC configuration, the bleed stream is re-pressurized via a secondary pump and re-circulates into the evaporator. Their results show that recuperative and regenerative ORCs are mostly suitable for dry fluids. Also, simple recuperative ORC has a higher efficiency than the non-recuperative regenerative cycles. The ORC with closed pre-heater and a secondary pump has the highest efficiency, and it is followed by the ORC with open pre-heater and lastly the ORC with a recuperative and open preheater.

Safarian and Aramoun [15] studied a theoretical framework for energy and exergy evaluation of a basic ORC and modified ORC which consider incorporating turbine bleeding, regeneration and both of them. They concluded that the integrated ORC with recuperation and regeneration has the best thermal and exergy efficiencies, equal to 22.8% and 35.5% respectively.

Xi et al. [16] performed the thermodynamic optimization of different ORC system configurations using six different working fluids for low-grade waste heat. The examined configurations are basic ORC, the single-stage regenerative ORC system and double-stage regenerative ORC system. Their results demonstrate that the double-stage regenerative ORC system gives the best thermal efficiency and exergy efficiency under the optimal operating conditions.

Mago et al. [17] evaluated an analysis of regenerative organic Rankine cycle using dry organic fluids, to convert waste energy to power from low- grade heat sources. They selected four dry organic working fluids which are R113, R245ca, R123 and isobutene. Researchers analyzed basic

ORC and regenerative ORC using a combined first and second law analysis at various reference temperatures and pressures.

Shokati et al. [18] performed a comparative exergo-economic analysis for heat recovery from gas turbine-modular helium reactor (GT-MHR) using simple ORC, ORC with internal heat exchanger and regenerative ORC (RORC) and compared these combined cycles exergo-economically. The results showed that regenerative ORC has the minimum unit cost of power produced by the turbine and this parameter was the maximum for that ORC with an internal heat exchanger. It was also shown that ORC with internal heat exchanger has the maximum exergy destruction cost rate.

Liu et al. [19] analysed the performance of different ORC plant configurations which are a simple cycle, superheated cycle, recuperated cycle and regenerative cycle respectively, with different working fluids for low temperature binary-cycle geothermal plant. Their results illustrate that despite the slightly higher energetic performance of recuperative and regenerative systems, their higher capital costs inhibited their economic competitiveness and suggested that the standard cycles are more cost-efficient.

Bina et al. [20] evaluated four different ORC configurations, including a standard and a recuperative ORC, along with a regenerative cycle including an open-type pre-heater and a double stage system. They designed these cycles to use the geothermal outlet of the Sabalan flash cycle plant, located in Iran. Five different parameters were used to optimize the systems; the energetic efficiency, the exergetic efficiency, the net power output, the production cost, and the total cost. According to their results, the maximum was calculated for the recuperative. However, when considering the energy production cost and the total energy cost, the regenerative and the standard ORC were the best cycles.

Wang et al. [21] modeled a regenerative organic Rankine cycle for utilizing solar energy over a range of low temperatures, considering flat-plate solar collectors and thermal storage systems. They showed that system performance could be improved, under realistic constraints, by increasing turbine inlet pressure and temperature or lowering the turbine backpressure, and by using a higher turbine inlet temperature with a saturated vapor input. Zare [22] investigated and compared the performance of three configurations of ORC for binary geothermal power plants. The considered configurations are simple ORC, regenerative ORC, and ORC with an internal

heat exchanger. His results illustrate that ORC with internal heat exchanger has the best performance from the thermodynamic point of view while simple ORC has the minimum cost among the considered cycles.

Literature summary shows that when a regenerator or a recuperator were separately added the system, the thermal efficiency of system increases. Although many studies have been done in the literature about ORC, there is relatively less research about regenerative and recuperative ORC system. Therefore, in this paper, a new configuration

of regenerative and recuperative ORC is analyzed. The energy and exergy analysis of regenerative and recuperative organic Rankine cycle is performed for dry organic fluids. Hence, R245fa, R600, R114, and R600a are selected as working fluids. The organic Rankine cycle's performance parameters are evaluated to identify suitable working fluid which may yield high thermal and exergy efficiencies and net power production depending on varied evaporation temperatures and the inlet pressure of the low-pressure expander.

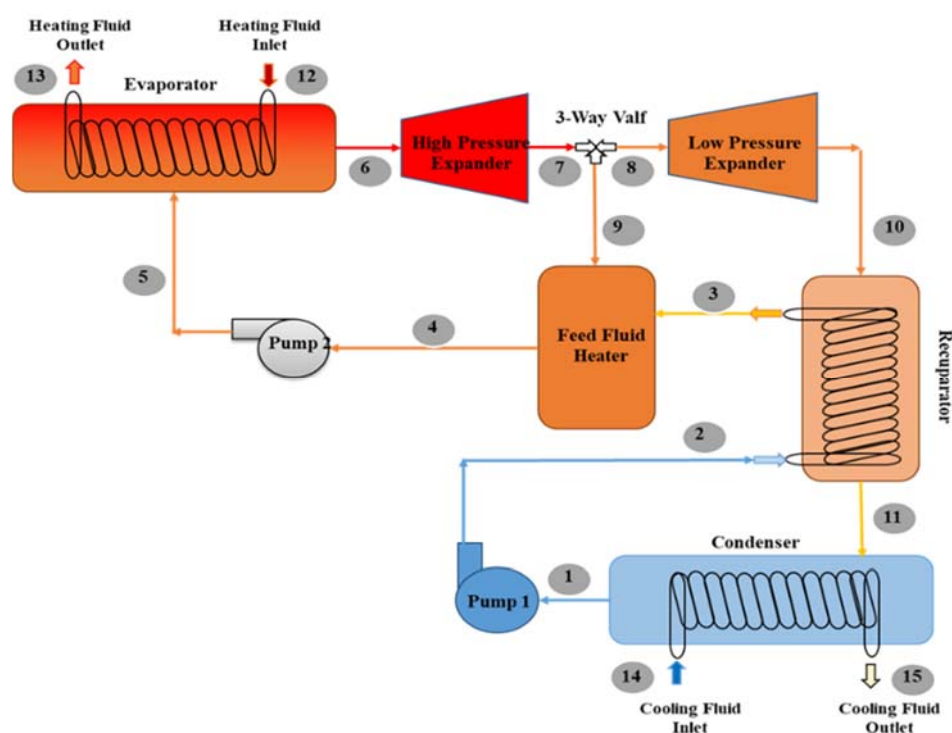


Fig.1. Schematic diagram of the ORC configuration

MATERIAL AND METHOD

The components of the organic Rankine cycle configuration are an evaporator, a high-pressure expander, a low-pressure expander, a recuperator, a feed fluid heater, a condenser, and two pumps system. Fig.1 presents a schematic diagram of the regenerative and recuperative ORC used to obtain energy from waste thermal energy. It is comprised of an evaporator, two expanders, a feed fluid heater (regenerator), a recuperator, a condenser, and two pumps. In the regenerator heat exchanger, heat is transferred between the high-temperature vapor from the high-pressure expander outlet and the low-temperature fluid from the recuperator outlet to avoid energy loss. In a regenerative and recuperative ORC, organic vapor enters the high-pressure expander at the evaporator pressure (6) and expands

isentropically to an intermediate pressure (7). Some vapor is extracted at this state and routed to the feed fluid heater (9), while the remaining vapor (8) continues to expand isentropically to the condenser pressure in the low-pressure expander (10). The expanded vapor enters recuperator, and its heat is transferred to working fluid exiting from pump 1. Partially cooled vapor exits from the recuperator and enters the condenser (11). This vapor leaves the condenser at the condenser pressure (1). The condensed fluid enters to the pump 1, in which the pressure is raised to the recuperator pressure (2) and is routed to recuperator (3), and then working fluid enters feed fluid heater where it mixes with the vapor extracted from the high-pressure expander. The mixture leaves the heater as a saturated liquid at the feed fluid heater pressure (4). The pump 2 raises the pressure of the working fluid to the evaporator

pressure (5). The cycle is completed by evaporating the working fluid in the evaporator (6) [23].

Dry fluids show better thermal efficiencies because they do not condense after the fluid goes through the expander. Therefore, R245fa, R600, R114, and R600a dry organic fluids are selected as the working fluids in this study. Besides, selected fluids have an ozone depletion potential (ODP) value of 0.0-0.7. The working fluids with lower global warming potential (GWP) to the greater one are R600a, R600, R245fa and R114 [24]. Tab.1 shows the thermo-physical properties of the selected fluids. It can be seen that R245fa has the highest value of

critical temperature. It is followed by R600, R114, and R600a respectively.

The analysis of a regenerative and recuperative ORC based on thermodynamic laws and the energy, exergy analyses were performed for the working fluids investigated. For analysed ORC configuration, the considered assumptions and input parameters were made:

- ✓ All processes are operating at steady state.
- ✓ The thermal and friction losses in the pipes are negligible.
- ✓ The kinetic and potential energy changes are negligible.

Table 1. Thermo-physical properties of the selected fluids [25]

Fluids	Molecular mass	Formula	Maximum temperature	Maximum pressure	Critical temperature	Critical pressure	Critical density
	g/mol		K	MPa	K	MPa	kg/m ³
R245fa	134.05	C ₃ F ₅ H ₃	440.00	200.00	427.01	3.65	519.43
R600	58.12	C ₄ H ₁₀	575.00	12.00	425.00	3.80	228.00
R114	170.92	C ₂ Cl ₂ F ₄	507.00	21.00	418.83	3.26	579.97
R600a	58.12	C ₄ H ₁₀	575.00	35.00	407.70	3.63	225.50

- ✓ Pressure drops of working fluid in the evaporator and condenser is neglected.
- ✓ The heat loss from the ORC components is negligible.
- ✓ The isentropic efficiency of expanders η_{exp} and the pumps η_p are 0.80.
- ✓ The effectiveness of recuperator is 0.80.
- ✓ The atmospheric conditions are taken as 100 kPa and 293.15 K.
- ✓ The mass flow rate \dot{m}_{hf} and the pressure P_{hf} of the hot fluid are 10 kg/s and 1 Bar, respectively.
- ✓ The mass flow rate \dot{m}_{cf} and the pressure P_{cf} of the cold fluid are 30 kg/s and 1 Bar, respectively.
- ✓ The overheating in the evaporator and the sub-cooling in the condenser are 5 K.
- ✓ The mass flow rate of working fluid in the low-pressure expander \dot{m}_{lpe} is 1 kg/s.
- ✓ The inlet pressure of low-pressure expander and the inlet pressure of feed fluid heater are equal to the exit pressure of the high-pressure expander in the three-way valve ($P_7 = P_8 = P_9$).
- ✓ The condensing temperature is 30°C.

Engineering Equation Solver software is used to obtain the thermodynamic properties of working fluids and to analyze the regenerative and recuperative ORC system performance. For any steady-state control volume, by neglecting

the potential and kinetic energy changes, the thermodynamic expressions of ORC configuration are given below [12-23].

General expression of mass, energy, and exergy balance equations are that;

Mass balance equation:

$$\sum \dot{m}_{in} = \sum \dot{m}_{out} \quad (1)$$

Energy balance equation:

$$\dot{E}_{in} = \dot{E}_{out} \quad (2)$$

$$\dot{Q} + \dot{W} = \sum \dot{m}_{out} h_{out} - \sum \dot{m}_{in} h_{in} \quad (3)$$

Exergy balance equation:

$$\sum \dot{E}x_{in} - \sum \dot{E}x_{out} - \dot{E}x_d = \Delta \dot{E}x_s \quad (4)$$

Where for a steady-state system, $\Delta \dot{E}x_s$ is zero.

$$\dot{E}x_{in} = \dot{E}x_{out} \quad (5)$$

$$\dot{E}x_{heat} + \dot{W} = \dot{E}x_{out} - \dot{E}x_{in} + \dot{I} \quad (6)$$

$$\dot{E}x = \dot{m}[(h - h_0) - T_0(s - s_0)] \quad (7)$$

Where, subscripts in and out represent the inlet and exit states, \dot{Q} is heat input, \dot{W} is work input, $\dot{E}x$ is exergy rate and \dot{I} is the irreversibility rate.

The passed through the high-pressure turbine working fluid separates two parts in the three-way

valve. The \dot{m}_{ff} amount of the working fluid enters the feed fluid heater and the \dot{m}_{lpe} amount of the working fluid enters the low pressure expander. These processes are showed with the number 7, 8 and 9 in the Fig.1. When practiced the mass balance equation in this section;

$$\dot{m}_{total} = \dot{m}_{ff} + \dot{m}_{lpe} \quad (8)$$

The streams that are mixing inside the feed fluid heater are at the same pressure. Consequently, since the mixing process occurs at an intermediate pressure level between the condensation and the expander inlet pressures, the regenerative and recuperative ORC requires the addition of an additional pump. Hence, it follows:

$$P_2 = P_3 = P_4 = P_7 = P_8 = P_9 \quad (9)$$

The expander power equals the sum of high pressure and low-pressure expander powers, and it can be defined by Eq. (10).

$$\dot{W}_{exp} = \dot{m}_{total}\eta_{exp}(h_6 - h_{7s}) + \dot{m}_{lpe}\eta_{exp}(h_8 - h_{10s}) \quad (10)$$

The inlet power to the pumps and the heat transfer rate to the working fluid in the evaporator can be calculated following equations.

$$\dot{W}_p = \frac{\dot{m}_{lpe}(h_{2s}-h_1)}{\eta_p} + \frac{\dot{m}_{total}(h_{5s}-h_4)}{\eta_p} \quad (11)$$

$$\dot{Q}_e = \dot{m}_{total}(h_6 - h_5) \quad (12)$$

The net output power from the regenerative and recuperative ORC and the thermal efficiency of ORC are expressed by Eq.(13) and Eq.(14) respectively.

$$\dot{W}_{net} = \dot{W}_{exp} - \dot{W}_p \quad (13)$$

$$\eta_{th} = \frac{\dot{W}_{net}}{\dot{Q}_e} = \frac{\dot{W}_{exp}-\dot{W}_p}{\dot{Q}_e} \quad (14)$$

The exergy efficiency of regenerative and recuperative ORC system is given by Eq. (15).

$$\eta_{exe} = \dot{W}_{net}/\dot{E}x_{hf} \quad (15)$$

where, $\dot{E}x_{hf}$ is the exergy supplied to the system in the evaporator from hot fluid and it can be calculated with Eq.(16).

$$\dot{E}x_{hf} = \dot{m}_{hf} \left[(h_{12} - h_{hf_0}) - T_0 (s_{12} - s_{hf_0}) \right] \quad (16)$$

The thermodynamic degree of perfection (TDP) of ORC configuration system and the ratio of the inlet pressure to the outlet pressure in the high-pressure expander and the low-pressure expander are obtained by the following equations.

$$TDP = \eta_{th} \left(1 - \frac{T_L}{T_H} \right)^{-1} \quad (17)$$

$$Rp_{hpe} = \frac{P_6}{P_7} \quad (18)$$

$$Rp_{lpe} = \frac{P_8}{P_{10}} \quad (19)$$

RESULTS AND DISCUSSIONS

In this part, the results of the thermodynamic analysis of regenerative and recuperative ORC system are given using R245fa, R600, R114, and R600a working fluids. Primarily, a comparison of the chosen working fluids utilizing energy and exergy analysis is performed, and the outcomes of calculation are given in Tab.2. The evaporation temperature in the evaporator of ORC configuration is taken as 130°C in the investigation. As seen in Tab.2, R245fa organic fluid has the highest thermal efficiency with approximately 17.4% while the minimum thermal efficiency is calculated for R600a with 16.1% among the all working fluids. R600 and R114 working fluids have a thermal efficiency of about 17.3% and 17.0%, respectively. When this performance parameter is evaluated with the critical temperature of the working fluid, it can be seen that when the critical temperature increases, the thermal efficiency of the regenerative and recuperative ORC improves. In other words, a working fluid with a higher critical temperature exhibits better thermal efficiency.

The highest exergy efficiency values are obtained for R600 and R600a working fluids with about 30.0% and 29.3% respectively. When this result is commented with Eq.(15), R600 working fluid has both the maximum net power and the maximum exergy supplied to the system. The exergy efficiency for R600 is higher because the net power generated is higher than other working fluids. The thermodynamic degree of perfection (TDP) values of the working fluids are obtained with decreasing order as R114, R245fa, R600, and R600a. The maximum value of TDP is calculated for R114 working fluid with about 56.6% at the evaporation temperature of 130°C. This is due to that the

minimum inlet temperature of hot fluid with approximately 144°C is determined for R114 for boiling at 130°C in the evaporator. On the other hand, the lowest the total mass flow is obtained for the R600a.

The highest net power about 77.6 kW value is calculated for R600. The other properties, which are the heat input in the evaporator, recuperator heat and exergy supplied to the system by hot fluid, illustrate same order with the net power. For these properties, the fluids are in the following order from large to small values: R600, R600a, R245fa, and R114. The maximum pressure rate in the high and low-pressure

expanders are computed for R600a and R245fa respectively among the fluid examined.

The evaporation temperature and the inlet pressure of working fluid to expander affect the performance analysis of an ORC. So, a detailed analysis of the effect of two features on system performance are evaluated in the following section of the paper. Firstly, the evaporation temperature is taken as from 90°C to the critical temperature of each working fluid, and its calculation results are presented in the following figures. The inlet pressure of the low-pressure expander is 1 MPa.

Table 2. The comparison of selected fluids for the regenerative and recuperative ORC

Fluids	η_t %	Π_{exe} %	Π_{II} %	m_{total} kg/s	W_{net} kW	Q_{ev} kW	Q_{rec} kW	Ex_{hr} kW	$R_{p_{hpe}}$	$R_{p_{lpe}}$
R245fa	17.35	18.31	56.62	1.384	41.23	237.6	28.58	225.23	2.339	5.644
R600	17.26	30.01	53.42	1.252	77.59	449.7	57.52	258.56	2.632	3.522
R114	17.01	13.25	57.34	1.314	27.47	161.5	26.67	207.35	2.464	4.003
R600a	16.11	29.28	53.35	1.212	63.51	394.2	45.02	216.92	3.430	2.474

Fig.2 illustrates changing thermal efficiency of regenerative and recuperative ORC system for all of working fluids. According to Fig.2, the thermal efficiency increases with the increment of the evaporation temperature. The maximum value of the thermal efficiency is calculated for R245fa working fluid with about 19% at the evaporation temperature of 153°C. In the lower evaporation temperatures, R600 and R600a working fluids show better thermal efficiency than R245fa and R114.

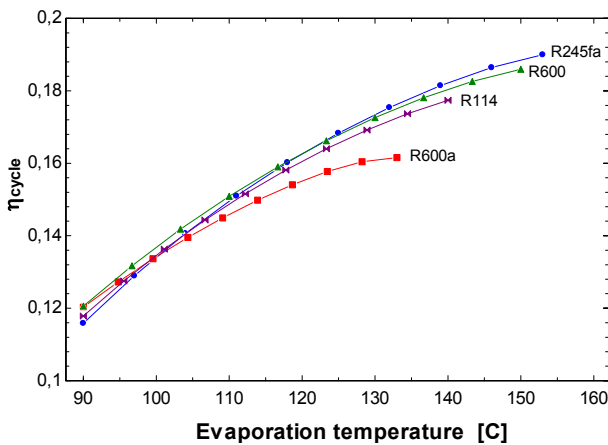


Fig.2. The effect of the evaporator temperature on thermal efficiency of ORC configuration

When examined the effect of the evaporator temperature on the exergy efficiency, which increases before and then decreases with the increase of the evaporation temperature for R245fa, R600 and R600a working fluids (Fig.3). However, this

property decreases with increasing evaporation temperature for R114 fluid. Also, the highest exergy efficiency is obtained for the R600 working fluid with about 30.4% at the evaporation temperature of about 115°C. This is followed by R600a, R245fa, and R114, respectively. When this figure and Eq.(15) are commented, it can be shown that the effect of the exergy supplied to the system by hot fluid on the exergy efficiency is greater than the effect of the increment of the net power on the exergy efficiency. For this reason, the exergy efficiency of ORC configuration reduces despite the increment of the net power and exergy supplied to the system by hot fluid.

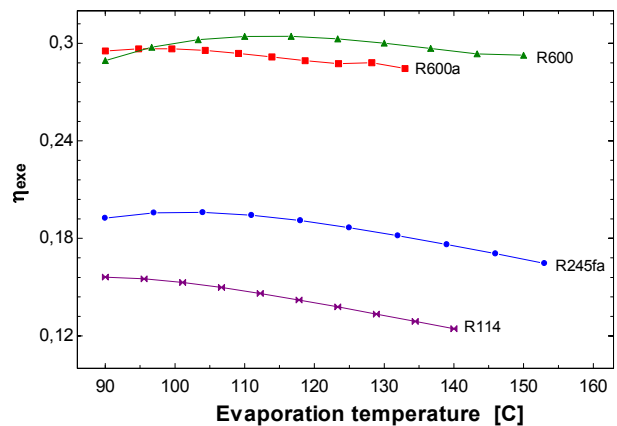


Fig.3. The effect of the evaporator temperature on exergy efficiency of ORC configuration

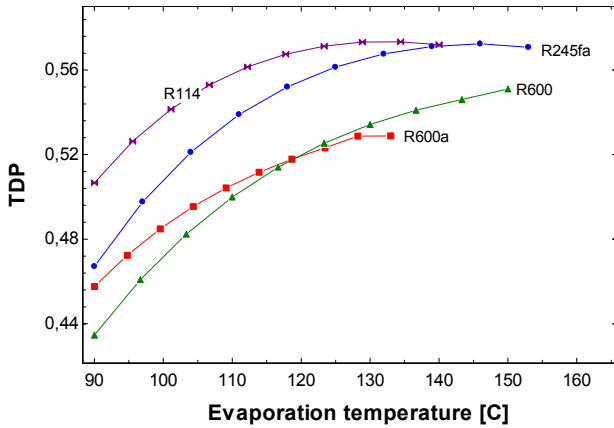


Fig.4. The effect of the evaporator temperature on the thermodynamic degree of perfection (TDP) of ORC configuration

Fig.4 demonstrates the variation of the system the thermodynamic degree of perfection (TDP) with increasing evaporation temperature for selected working fluids in the analysis of regenerative and recuperative ORC. TDP increases and then decreases with the increment of evaporation temperature. The maximum value of this property is calculated for R114 working fluid with about 57.3% at the evaporation temperature of 135°C. As Eq.(17) and Fig.4 are evaluated together, the reason why R114 has the highest TDP value that R114 working fluid requires a lower inlet temperature of hot fluid than the other fluids.

When compared the net power generated of the working fluids investigated in the system, according to Fig.5, the net power rises with the increase of the evaporation temperature, and it exhibits the same trend for all of the working fluids. The maximum net power of regenerative and recuperative ORC is calculated for R600 working fluid with about 85 kW in 150°C and which is followed by R600a, R245fa, and R114.

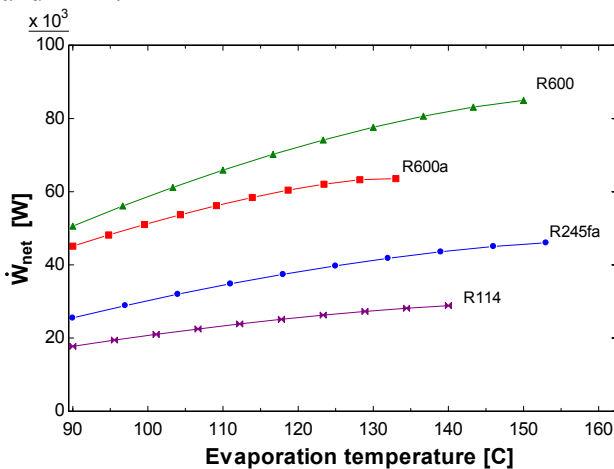


Fig.5. The effect of the evaporator temperature on the net power of ORC configuration

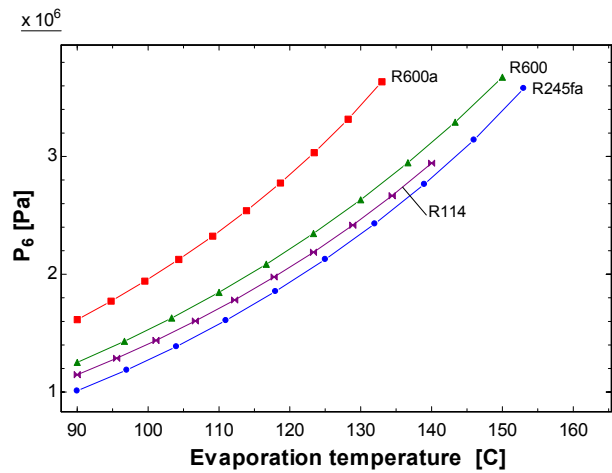


Fig.6. The effect of the evaporator temperature on the P_6 of ORC configuration

The influence of evaporation temperature on the inlet pressure of the high-pressure expander (P_6) are shown in Fig.6. According to the results of ORC configuration's analysis, the inlet pressure of the high-pressure expander rises with the increment of the evaporator temperature because of the increase of saturation pressure for all of the working fluids. It can be seen in the figure; the highest expander pressure value is obtained for R600a working fluid with 3.6 MPa in 133°C evaporation temperature which is followed by R600, R114, and R245fa working fluids. In the same time, rising the inlet pressure of the high-pressure expander will require a larger and more robust expander design.

The increasing evaporation temperature has a considerable effect on the exergy supplied to the system by hot fluid. Therefore, the change of this feature is similar to the net power and inlet pressure of high-pressure expander, raises with the increment of the evaporator temperature. As is seen in Fig.7, maximum exergy entry into the system occurs when R600 working fluid is used in the analyzed system.

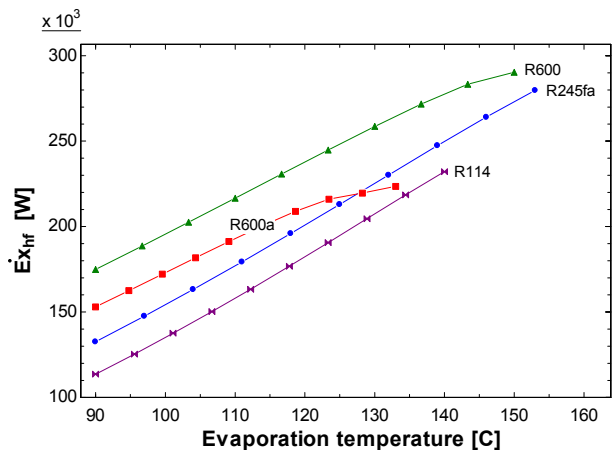


Fig.7. The effect of the evaporator temperature on the exergy supplied of ORC configuration

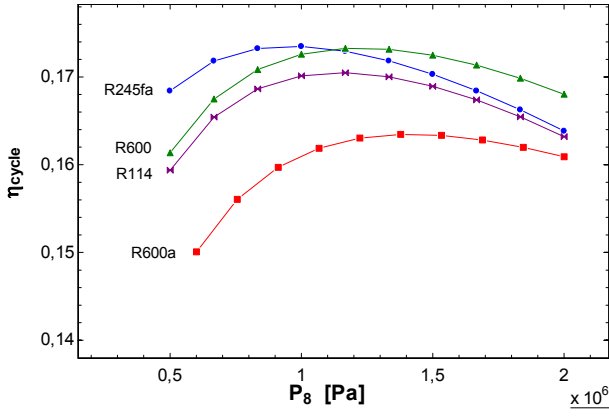


Fig.8. The effect of the inlet pressure of the low pressure expander (P_8) on thermal efficiency ORC configuration

Secondly, the effect of the inlet pressure of the low-pressure expander (P_8) is investigated on the performance parameters of the regenerative and recuperative ORC. The evaporation temperature in the evaporator is assumed as 130°C in the analysis. Moreover, the inlet pressure in the low-pressure expander, which equals to the pressure of feed fluid heater and the outlet pressure of the high-pressure expander, is increased from 0.5 MPa to 2.0 MPa and other performance parameters are calculated.

The Fig.8 presents the change of the thermal efficiency of the system. It can be seen that the thermal efficiency increases up to a maximum value with rising pressure, and then decreases for all of the working fluids in the analysis. Moreover, as the inlet pressure of the low-pressure expander raises, the difference between the calculated thermal efficiency values for the working fluids reduces and approaches each other. The maximum thermal efficiency is performed for R245fa working fluid with 17.4% in the 0.85 MPa of P_8 while the lowest thermal efficiency values belong to R600a.

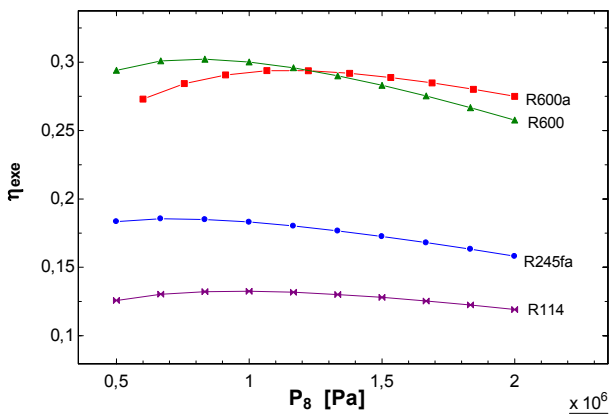


Fig.9. The effect of the P_8 on the exergy efficiency ORC configuration

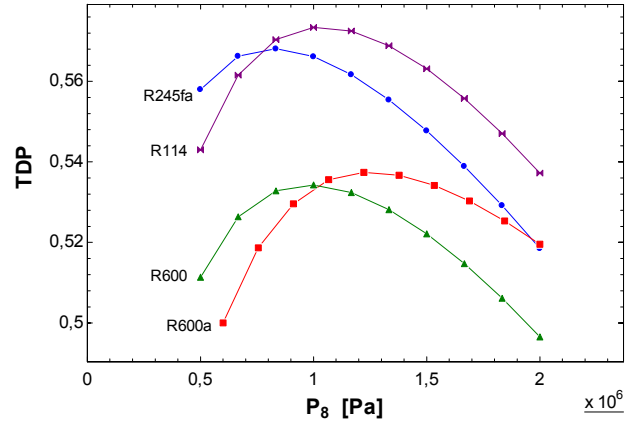


Fig.10. The effect of the (P_8) on the thermodynamic degree of perfection (TDP) ORC configuration

It can be clearly seen from Fig.9 and Fig.10 that the inlet pressure in the low-pressure expander has a positive effect before and then negative effect on exergy and the TDP. The exergy efficiency values of working fluids are calculated with decreasing order as R600a, R600, R245fa, and R114. The maximum value of exergy efficiency is obtained for R600 working fluid with about 30.2% at the 0.83 MPa of P_8 . The reason for the decrease of the exergy efficiency is that the exergy supplied to the system in the evaporator increases with the increasing pressure while the net power of the system drops with a very low amount.

According to Fig.10, the maximum value of the thermodynamic degree of perfection (TDP) is 57.3% obtained about the nearly 1.0 MPa of P_8 for R114.

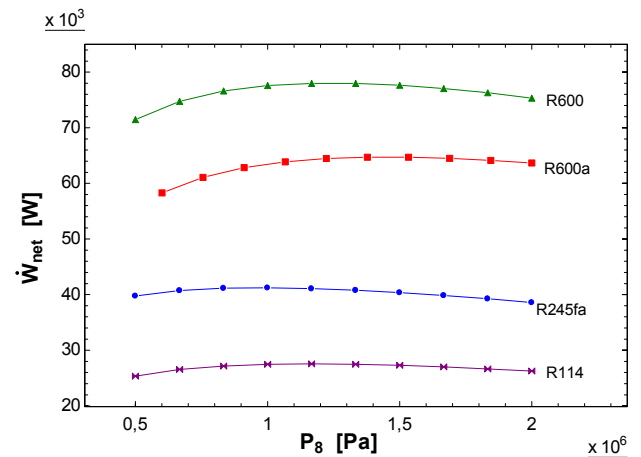


Fig.11. The effect of the (P_8) on the net power ORC configuration

When the effect of the inlet pressure of the low-pressure expander (P_8) on the net power is examined, it is observed that there is very little change in net power with the increment of P_8 (Fig.11). The highest value of the net power is obtained for R600 working fluid. It is calculated as about 78 kW with the inlet

pressure of 1.17 MPa. R600a, R245fa, and R114 follow it with decreasing order.

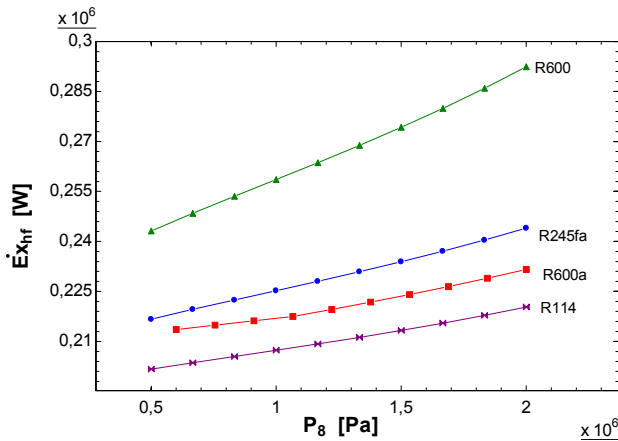


Fig.12. The effect of the (P_8) on the net power ORC configuration

Fig.12 demonstrates the effect of the inlet pressure in the low-pressure expander on the exergy supplied to the system by hot fluid. It can be seen from figure that this property has an inclining trend. Input exergy to the system, which is a measure of how much the hot source has been utilized, has the maximum value with 0.29 MW in the 2.0 MPa of P_8 .

CONCLUSIONS

Thermodynamic analysis of a regenerative and recuperative organic Rankine cycle derived by a low grade heat source for power generation is performed in this study. Four dry organic fluid, namely R600a, R114, R600, and R245fa with critical temperature ranging from 134.6°C to 153.9°C, are chosen as working fluid in the analysis. The effects of the evaporation temperature and the inlet pressure of the low-pressure expander on performance parameters are evaluated, and their results are compared for the working fluid examined by using the Engineering Equation Solver model. Primarily, we have compared the selected dry refrigerants' performance parameters in the admitted conditions. The maximum thermal efficiency and thermodynamic degree of perfection (TDP) values are calculated for R245fa and R114 with %17.35 and %57.34, respectively, at the evaporation temperature of 130 °C. R600 refrigerant has maximum exergy efficiency, net power, evaporator, and recuperator heat rate, exergy supplied to the system by hot fluid properties with %30.01, 77.59 kW, 449.70 kW, 57.52 kW, and 258.56 kW, respectively. After that, we have investigated the influence of evaporation temperature on the performance parameters of the ORC configuration. According to analysis, in

respect to the thermal efficiency, R245fa organic fluid has the best performance with the about 19% at the evaporation temperature of 153 °C. Besides, the thermal efficiency rises with increasing evaporation temperature for all of working fluids. However, when investigated the effects of the maximum power output, exergy efficiency, and the exergy supplied to the system by hot fluid values, R600 working fluid is the optimal fluid. Also, R600 is the more suitable working fluid for ORC configuration concerning expanders expansion ratio. After this analysis, the inlet pressure of the low-pressure expander has been examined, and the obtained results demonstrate that all analysed parameters have similar effects on the performance of the regenerative and recuperative ORC for all working fluids. In the low-pressure values, R245fa represents the best performance features with the thermal efficiency and thermodynamic degree of perfection (TDP). Similarly, R600 organic fluid has the maximum net power and exergy input from a hot source to the analysed system.

NOMENCLATURE

- \dot{E} - energy rate, kW;
- $\dot{E}x$ - exergy rate, kW;
- \dot{I} - irreversibility rate, kW;
- h - specific enthalpy, kJ/kg;
- \dot{m} - mass flow rate, kg/s;
- P - pressure, Pa;
- s - specific entropy, kJ/kgK;
- \dot{Q} - heat rate, kW;
- \dot{W} - power, kW;
- T - temperature, K;
- T_L - low temperature of sink, K;
- T_H - high temperature of source, K;
- η - efficiency;

Subscripts

- cycle* - cycle
- d* - destruction
- e* - evaporator
- exe* - exergetic
- exp* - expander
- ff* - feed fluid
- hf* - hot fluid
- hpe* - high pressure expander
- in* - inlet
- lpe* - low pressure expander
- net* - net
- o* - ambient
- out* - outlet

p - pump
s - system
th - thermal
total - total

Abbreviations

GWP-global warming potential;
ODP- ozone depletion potential;
ORC- organic Rankine cycle;
TDP- the thermodynamic degree of perfection;

REFERENCES

- [1] Y. Chen, P. Lundqvist, A. Johansson, P.A. Platell. Comparative study of the carbondioxide transcritical power cycle compared with an organic Rankine cycle with R123 as working fluid in waste heat recovery. *Applied Thermal Engineering* **26**, 2142-2147 (2006).
- [2] E. Ozdemir, M. Kilic. Energy and exergy analysis of an organic Rankine cycle using different working fluids from waste heat recovery. *Int. J. of Environmental Trends* **1**, 32-45 (2017).
- [3] P. Gang, L. Jing, J. Jie. Analysis of low temperature solar thermal electric generation using regenerative organic Rankine cycle. *Appl. Thermal Engineering* **30**, 998-1004 (2010).
- [4] H. Hajabdollahi, A. Ganjehkaviri, M.N.M. Jaafar. Thermo-economic optimization of regenerative solar organic Rankine cycle considering hourly analysis. *Energy* **87**, 369-380 (2015).
- [5] U. Drescher, D. Bruggemann. Fluid selection for the organic Rankine cycle (ORC) in biomass power and heat plants. *Applied Thermal Engineering* **27**, 223-228 (2007).
- [6] A. Rentizelas, S. Karellas, E. Kakaras, I. Tatsiopoulos. Comparative techno-economic analysis of ORC and gasification for bioenergy applications. *Energy Conversion and Management* **50(3)**, 674-81 (2009).
- [7] O. Arslan, O. Yetik. ANN based optimization of supercritical ORC-binary geothermal power plant: Simav case study. *Applied Thermal Engineering* **31**, 3922-3928 (2011).
- [8] S.J. Zhang, H.X. Wang, T. Guo. Performance comparison and parametric optimization of subcritical organic Rankine cycle and transcritical power cycle system for low-temperature geothermal power generation. *Applied Energy* **88**, 2740-2754 (2011).
- [9] T.C. Hung, T.Y. Shai, S.K. Wang. A review of organic Rankine Cycles (ORCs) for the recovery of low-grade waste heat. *Energy* **22(7)**, 661-667 (1997).
- [10] B.-T. Liu, K.-H. Chien, C.-C. Wang. Effect of working fluids on organic Rankine cycle for waste heat recovery. *Energy* **29(8)**, 1207-1217 (2004).
- [11] D. Wang, X. Ling, H. Peng. Performance analysis of double organic Rankine cycle for discontinuous low temperature waste heat recovery. *Appl. Thermal Eng.* **48**, 63-71 (2012).
- [12] N. Shokati, F. Ranjbar, M. Yari. Exergoeconomic analysis and optimization of basic, dual-pressure and dual-fluid ORCs and Kalina gethermal power plants: A comparative study. *Renewable Energy* **83**, 527-542 (2015).
- [13] F. Ayachi, E. Boulawz Ksayer, A. Zoughaib, P. Neveu. ORC optimization for medium grade heat heat recovery. *Energy* **68**, 47-56 (2014).
- [14] K. Braimakis, S. Karellas. Energetic optimization of regenerative organic Rankine cycle (ORC) configurations. *Energy Conversion and Management* **159**, 353-370 (2018).
- [15] S. Safarian, F. Aramoun. Energy and exergy assessments of modified organic Rankine cycles (ORCs). *Energy Reports* **1**, 1-7 (2015).
- [16] H. Xi, M.J. Li, C. Xu, Y.L. He. Parametric optimization of regenerative organic Rankine cycle (ORC) for low grade waste heat recovery using genetic algorithm. *Energy* **58**, 473-482 (2013).
- [17] P.J. Mago, L.M. Chamra, K. Srinivasan, C. Somayaji. An examination of regenerative organic Rankine cycles using dry fluids. *Applied Thermal Engineering* **28 (8)**, 998-1007 (2008).
- [18] N. Shokati, F. Mohammadkhani, M. Yari, S.M.S. Mahmoudi, M.A. Rosen. A comparative exergoeconomic analysis of waste heat recovery from a gas turbine-modular helium reactor via organic Rankine cycles. *Sustainability* **6**, 2474-2489 (2014).
- [19] X. Liu, M. Wei, L. Yang, X. Wang. Thermo-economic analysis and optimization selection of ORC system configurations for low temperature binary-cycle geothermal plant. *Applied Thermal Engineering* **125**, 153-164 (2017).
- [20] M.S. Bina, S. Jalilinasrabad, H. Fujii. Thermo-economic evaluation of various bottoming ORCs for geothermal power plant, determination of optimum cycle for Sabalan power plant exhaust. *Geothermics* **70**, 181-191 (2017).
- [21] M. Wang, J. Wang, Y. Zhao, Y. Dai. Thermodynamic analysis and optimization of a solar-driven regenerative organic Rankine cycle (ORC) based on flat-plate solar collectors. *Appl. Thermal Engineering* **50**, 816-825 (2013).
- [22] V. Zare. A comparative exergoeconomic analysis of different ORC configurations for binary geothermal power plants. *Energy Conversion and Management* **105**, 127-138 (2015).
- [23] Y.A. Cengel, M.A. Boles. Thermodynamics: An Engineering Approach, 7th ed., New York, USA: McGraw-Hill Inc., 2011.
- [24] https://en.wikipedia.org/wiki/List_of_refrigerants#cite_note-AR4-1, (Date accessed: 05.12.2018)
- [25] http://www.coolprop.org/fluid_properties/PurePseudoPure.html#thermodynamic-properties-of-fluid, (Date accessed: 05.01.2018)

Evaluation of mass flowing with COP for triple effect absorption refrigeration system

Kenan Saka*

Bursa Uludağ University, Vocational School of Yenişehir Ibrahim Orhan, Bursa, Turkey

Triple effect absorption refrigeration system has the highest performance among its counterparts. Coefficient of performance of this system is higher than those single and double effect absorption refrigeration systems but its system design involves more system components which make the thermodynamic cycle more complex. A basic absorption refrigeration system has only an evaporator, a condenser, an absorber and a generator. Adding heat exchanger/s improves the coefficient of performance. Absorption refrigeration systems do not involve a compressor as compared to vapor compression systems due to absorber and generator. The high-pressure generator is the significant components of an absorption refrigeration system which allows to use solar energy and industrial waste heat as a heat source. In this study, a thermodynamic analysis was performed for a lithium bromide-water series flow triple effect absorption refrigeration system including eight different mass flow lines. The variation in coefficient of performance with mass flow rates in the cycle was investigated thoroughly. It was indicated that mass flow rates of the solutions decrease with increasing temperature of the low-pressure generator and this has resulted in a positive impact on the coefficient of performance. Evaporator temperature has the same effect with low pressure generator on the system but the effect of condenser temperature is vice versa.

Keywords: Mass flow rate, coefficient of performance, triple effect absorption refrigeration

INTRODUCTION

The absorption refrigeration systems (ARSs) can have different cycle configurations depending on available source temperature. As the potential source temperature gets higher, the use of multi-effect cycle becomes a reasonable way of increasing coefficient of performance (COP).

In addition, ARSs are able to be run directly from source such as burning of natural gas. Most industrial processes use a lot of thermal energy by burning fossil fuel to produce steam or heat for various purposes. After the processes, an amount of heat is rejected to the surroundings as waste. The waste heat can be converted to useful refrigeration by using a heat powered refrigeration system such as an absorption refrigeration cycle. These systems use particularly waste heat or renewable energy as a primary heating source to drive the cooling operation. They can be alternative to vapor compression systems.

The absorption refrigeration systems use natural refrigerants such as lithium bromide-water solution which plays role in attenuating the negative impacts of greenhouse. To increase the COP of these systems there are available cycle configurations from half to triple effect [1] and even quadruple effect [2] in the literature.

Single effect ARSs are widely used in commercial applications due to low cost and less

system complexity. Nowadays, double effect ARSs have been used rather since many industries have potential high temperature waste heat which has been the driving force for using these systems. It was reported that the maximum COP of a single effect ranges from 0.6–0.75. This value is the range of 1.0–1.28 for a double effect ARS [3].

Alternative solutions instead of lithium bromide-water can be possibly used in ARSs. Using different solutions, the COP of the system can be enhanced [4]. Several research studies on this topic were published in the literature as in [5–9]. With advancing of the system control technologies, more complex thermodynamic systems have been controlled better. In ARSs, increasing the effect number makes the system's control more difficult. Not only controlling an energy system is sufficient but also being less cost is another issue. Similarly, triple effect ARSs are at the starting point from this view. There were several studies about the triple effect ARSs in the literature [10–15] however the number of studies is increasing gradually.

In this study, the thermodynamic analysis of a triple effect series flow lithium bromide-water ARS was performed using the Delphi program, and the obtained simulation results was verified with the literature. Moreover, the effect and effectiveness of heat exchangers on the system performance were shown based on the capacity variations of the system components. In addition, it was investigated the mass flowing of lithium bromide-water solution and water vapor effect on the COP based on the component temperatures.

* To whom all correspondence should be sent:
kenansaka@uludag.edu.tr

Absorption refrigeration cycle

The basic ARS is single effect and very simple according to triple effect ARS. It has only an evaporator, a condenser, an absorber and a generator. Also, a heat exchanger can be added to improve the COP. To have an idea about triple effect ARS it is necessary to start from single effect ARS. Evaporator, condenser and absorber are common components in absorption refrigeration configurations. Evaporator is single component can do cooling in the system. There is heat rejection from the system to environment by condenser and absorber.

The components of a triple effect ARS are shown in Fig.1. ARSs do not involve a compressor as compared to vapor compression systems instead they use absorber and generator. The high-pressure generator (HPG) and the absorber are the significant components of ARS which provides to use solar energy and industrial waste heat as a heat source. Additionally, condenser, evaporator, inter-condenser and generators, expansion valves and pump are the remaining components. Here, the superheated vapor generated by the high-pressure generator is condensed by the high-pressure condenser (HPC) then goes to the condenser at constant flow rate. The resulting heat is rejected to be used by the medium pressure generator (MPG). Similarly, this process is realized between the MPC and the lower pressure generator (LPG), and the remaining vapor is simultaneously transferred to the condenser. The collected vapor which becomes the refrigerant of the vapor cycle enters the expansion valve, evaporator and absorber, respectively. Four different pressure and concentration levels take place during this cycle.

The system has eight different mass flow rate circulating values. One of them is coolant which is water vapor. Also, the lithium bromide-water solution has four different mass flow rates. Finally, water vapor generated by the generators flows in three different mass flow rates. The flow rates in other system components related to heat transfer of the system with environment such as condenser, evaporator, absorber and high-pressure generator (HPG) were not considered in the scope of this study. While the HPG, evaporator and pump involve energy input, heat rejection from the condenser and absorber takes place by the cooling waters. The evaporator removes heat from the cooling media for cooling effect. The heat exchangers provide to heat the weak solution leaving the absorber consequently the thermal capacity of the HPG is reduced, and the system performance is improved.

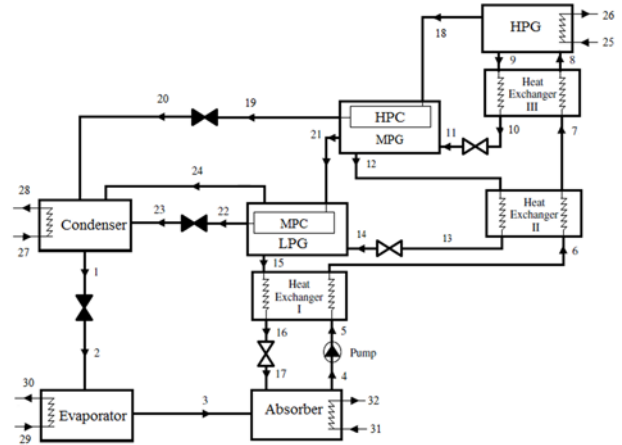


Fig.1. A triple effect series flow ARS and its components

Lithium bromide-water has the possibility of crystallization under different operating conditions thus this case was considered in the system simulation. On the other hand, the energy balances between the integrated condenser-generator system components were satisfied for each loop using iteration algorithm embedded into the simulation algorithm.

TERMODYNAMIC ANALYSIS

For the thermodynamic analysis of the system, mass and energy balances were achieved in the simulation program to calculate the component capacities. The general equations of these balances are as follows:

Mass balance:

$$\sum \dot{m}_i = \sum \dot{m}_e \quad (1)$$

Concentration balance:

$$\dot{m}_i X_i = \dot{m}_e X_e \quad (2)$$

Energy balance:

$$\dot{Q} - \dot{W} = \sum \dot{m}_e h_e - \sum \dot{m}_i h_i \quad (3)$$

Effectiveness:

$$\varepsilon = \frac{h_i - h_e}{h_i - h_e^*} \quad (4)$$

Performance:

$$COP = \frac{\dot{Q}_E}{\dot{Q}_{HPG} + \dot{W}_P} \quad (5)$$

where i : inlet, e : exit, \dot{m} : mass flowrate in kg/s, X : solution concentration in %, h : enthalpy in kJ/kg, \dot{Q} : heat transfer rate in kW and \dot{W} : work rate in kW.

The properties of water and the solutions were obtained from the literature [16-18]. The following assumptions were taken into consideration through the thermodynamic analysis:

- Steady-state conditions exist.
- Evaporator capacity is fixed.
- Pressure losses in heat exchangers and pipelines are negligible.
- Water phase is saturated liquid and saturated vapor at the outlet of the condenser and evaporator, respectively.
- Heat loss from the system components is disregarded.

RESULTS AND DISCUSSION

The component capacities of the triple effect ARS with a 300 kW cooling capacity and its numerical comparison to the literature for the corresponding capacity shown in Tab.1. However, in the present study, the cooling capacity was selected to be 100 kW in order to proportionate heat capacities among the system components. The highest capacity belongs to the absorber whereas the pump has the lowest one.

Table 1. Calculated component capacities

$T_{HPG} = 190\text{ }^{\circ}\text{C}, T_E = 4\text{ }^{\circ}\text{C}, T_A = 33\text{ }^{\circ}\text{C},$		
$T_C = 33\text{ }^{\circ}\text{C}, \varepsilon_{I,II,III} = 0.85$		
Components	Load (kW) Current study	Load (kW) Gomri [13]
HPG, \dot{Q}_{HPG}	170.40	169.68
Condenser, \dot{Q}_C	115.32	112.23
Evaporator, \dot{Q}_E	300.00	300.00
Absorber, \dot{Q}_A	355.39	357.67
Pump, \dot{W}_P	0.23	0.22
COP	1.76	1.76

Tab.2 shows the thermodynamic states, concentration values, and flow rates for the simulated system. As seen, there are variations in the concentration values at various parts of the system. The lithium bromide-water solution undergoes four different concentration levels during system operation. The positive influence of heat exchangers can also be easily seen. At state 4, i.e. outlet of the absorber, the solution leaving the absorber which is weak in concentration is pumped by the pump. The lithium bromide-water solution has two mainly concentration as weak and strong. The weak solution means that the water content of the solution is higher relatively to the strong solution. As the solution passes through the heat exchanger I, its temperature increases to 26 °C. After passing from heat exchanger II and III, the solution reaches 158 °C at

state 8. The use of heat exchangers increases the solution temperature as much as 121 °C instead of entering 33.1 °C to the HPG i.e. without using any heat exchanger. This consequently reduces the thermal capacity of the HPG and improves the system performance.

Table 2. Thermodynamic properties of H₂O-LiBr solution at states

State	Fluid	T (°C)	X (%)	\dot{m} (kg/s)
1	Water	33	0	0.042
2	Water	5	0	0.042
3	Vapor	5	0	0.042
4	Weak sol.	33	54.119	0.358
5	Weak sol.	33.1	54.119	0.358
6	Weak sol.	59.08	54.119	0.358
7	Weak sol.	101.02	54.119	0.358
8	Weak sol.	154.01	54.119	0.358
9	Strong I	185	56.655	0.342
10	Strong I	127.57	56.655	0.342
11	Strong I	127.57	56.655	0.342
12	Strong II	130	59.038	0.328
13	Strong II	81.03	59.038	0.328
14	Strong II	81.03	59.038	0.328
15	Strong III	80	61.352	0.316
16	Strong III	47.43	61.352	0.316
17	Strong III	47.43	61.352	0.316
18	Vapor	185	0	0.016
19	Water	133.35	0	0.016
20	Water	33	0	0.016
21	Vapor	130	0	0.014
22	Water	80.48	0	0.014
23	Water	33	0	0.014
24	Vapor	80	0	0.012
25	Vapor	200	0	0.038
26	Vapor	190	0	0.038
27	Water	23	0	1.933
28	Water	28	0	1.933
29	Water	15	0	4.772
30	Water	10	0	4.772
31	Water	23	0	5.818
32	Water	28	0	5.818

Eight different mass flow rates can be seen in Tab.2. from state 1 to state 24. The mass flow rates after state 24 are related to heat transfer of the system with environment. The water is used for condenser and absorber cooling. The temperature of the cooling water is function of the component temperature. The chilled water is produced by evaporator and high-pressure generator is assisted by vapor.

Tab.3 indicates the component capacities based on a fixed evaporator capacity and two different heat exchanger effectiveness values. The highest capacity component is the absorber which is triple times higher than that of the condenser. As known, the absorber and condensers are the components rejecting heat therefore this feature is significant at the design level of these components. The effectiveness of heat exchangers is quite influential on COP. As the effectiveness value decreases, the capacity of the HPG increases as clearly seen. The COP increases from 1.15 to 1.60 with increasing the heat exchanger effectiveness from 0.3 to 0.7.

Table 3. Component capacities based on heat exchanger effectiveness

Component	Load (kW)	
	$\epsilon_{I,II,III} = 0.3$	$\epsilon_{I,II,III} = 0.7$
HPG, \dot{Q}_{HPG}	86.86	62.31
Condenser, \dot{Q}_C	53.98	40.50
Evaporator, \dot{Q}_E	100.00	100.00
Absorber, \dot{Q}_A	133.02	121.91
Pump, \dot{W}_p	0.0753	0.0702
COP	1.15	1.60

In series flow triple effect absorption refrigeration system, mass flow rate of fluid phases has the possibility of being equal at different states given in Fig.1. Tab.4 shows these equalities.

Table 4. Conditions of flow rates

$\dot{m}_c = \dot{m}_1 = \dot{m}_2 = \dot{m}_3$
$\dot{m}_w = \dot{m}_4 = \dot{m}_5 = \dot{m}_6 = \dot{m}_7 = \dot{m}_8$
$\dot{m}_{s1} = \dot{m}_9 = \dot{m}_{10} = \dot{m}_{11}$
$\dot{m}_{s2} = \dot{m}_{12} = \dot{m}_{13} = \dot{m}_{14}$
$\dot{m}_{s3} = \dot{m}_{15} = \dot{m}_{16} = \dot{m}_{17}$
$\dot{m}_{v1} = \dot{m}_{18} = \dot{m}_{19} = \dot{m}_{20}$
$\dot{m}_{v2} = \dot{m}_{21} = \dot{m}_{22} = \dot{m}_{23}$
$\dot{m}_{v3} = \dot{m}_{24}$

Fig.2 shows the variations in mass flow rates of lithium bromide-water solution and COP depending on the lower pressure generator temperature. Also, the variations in mass flow rates of water vapor are shown in Fig. 3.

Increasing the lower pressure generator temperature has a positive impact on the coefficient of performance. The COP of the system increases from 1.351 to 1.595 with 18% rises depending on the lower pressure generator temperature. The maximum mass flow rate belongs to the weak solution in the system.

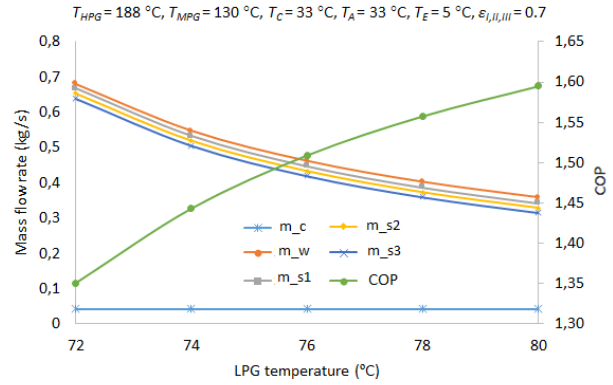


Fig.2. Flow rates of solutions and COP variations with LPG temperature

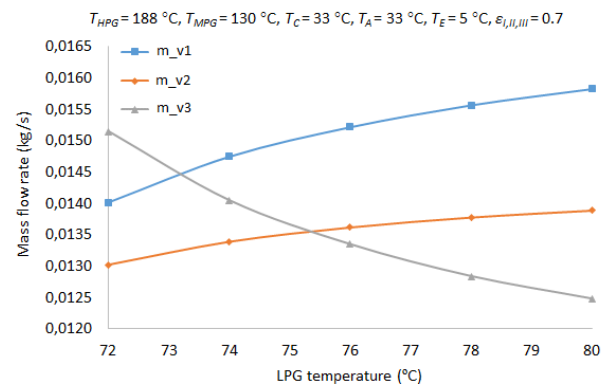


Fig.3. Flow rates of water vapor variations with LPG temperature

Mass flow rate of the weak solution decreases from 0.681 kg/s to 0.358 kg/s as in seen in Fig.2. The decreasing is approximately 47.4 %. The other high mass flow rate belongs to strong solution I, strong solution II and strong solution III respectively. Mass flow rate in evaporator is fixed due to fixed evaporator capacity and it is 0.042 kg/s. Changes for the other three water vapor lines are shown in Fig.3. Based on the LPG temperature rising, there is increasing on mass flow rate of the vapor generated by the HPG and MPG. But there is decreasing on mass flow rate of the vapor generated by the LPG.

Fig.4 shows the variations in mass flow rates of the lithium bromide-water solutions and COP depending on the condenser temperature. The coefficient of performance of the system decreases with increasing condenser temperature. At the 28 °C condenser temperature the COP is 1.661 and it decreases at higher condenser temperatures to 1.528. Mass flow rate in evaporator is 0.042 kg/s

Similarly, in Fig.5, the flow rate in the vapor lines is nearly constant depending on the condenser temperature change. Water vapor mass flow rates are between 0.016-0.012 kg/s approximately.

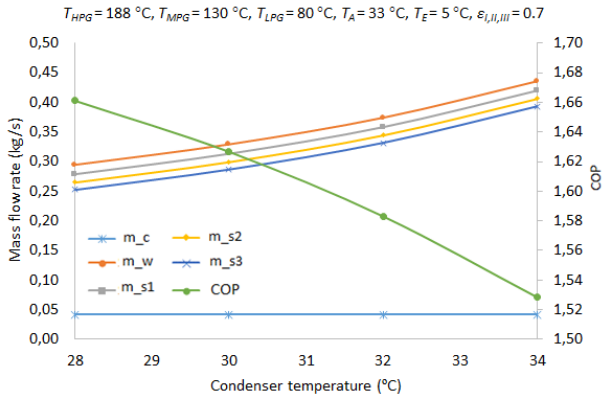


Fig.4. Flow rates of solutions and COP variations with condenser temperature

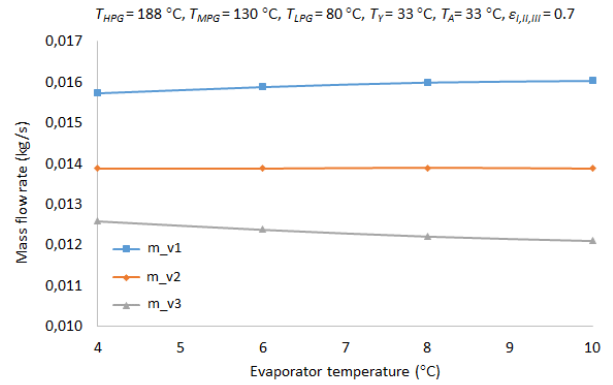


Fig.7. Flow rates and COP variations with evaporator temperature

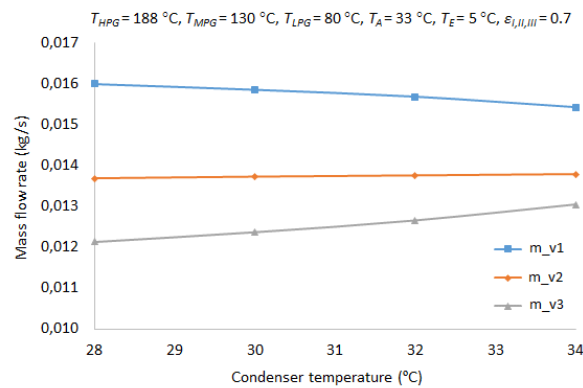


Fig.5. Flow rates of water vapor variations with condenser temperature

It should be noted that the effect of the absorber on the system was not presented in this study since the condenser and the absorber are the heat rejecting system components and they have similar effects on the system.

Fig.6 and Fig. 7. show the variations in mass flow rates of the solution, water vapor and the COP depending on the evaporator temperature. The coefficient of performance increases with evaporating temperature, and there is linear relationship between them.

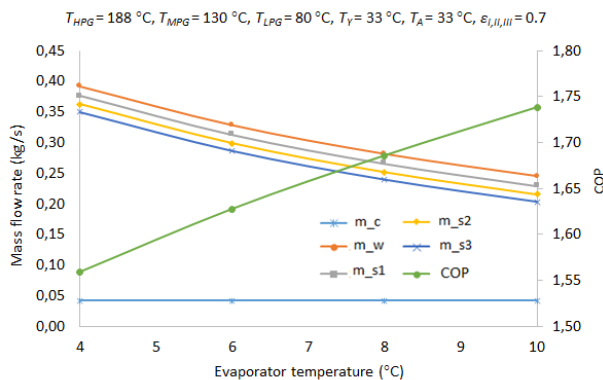


Fig.6. Flow rates and COP variations with evaporator temperature

Results in Fig.4. and Fig.6 are compatible with experimental studies of the absorption refrigerator using aqueous lithium–bromide [19]. According to experimental studies results coefficient of performance of the system decreases with in higher condenser temperature and increases with in higher evaporator temperature.

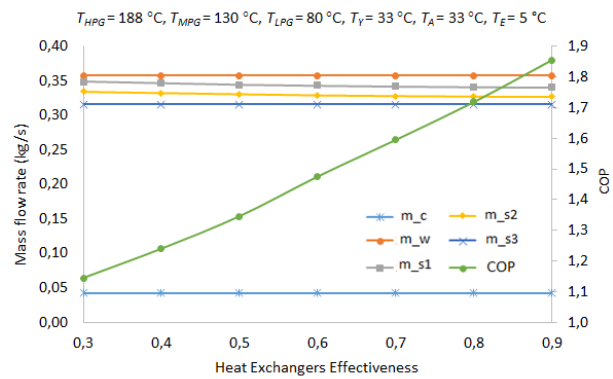


Fig.8. Flow rates of solutions and COP variations with heat exchangers effectiveness

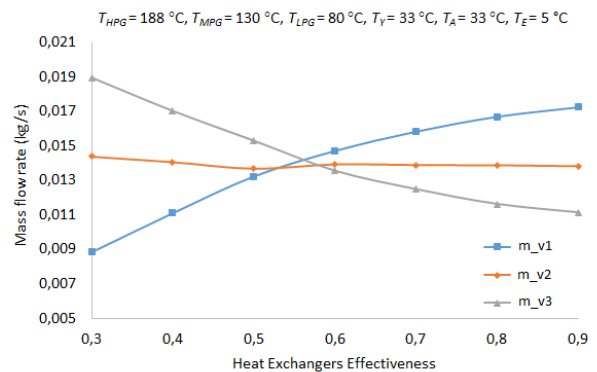


Fig.9. Flow rates variations of water vapor with heat exchangers effectiveness

Flow rates and COP variations according to heat exchangers effectiveness are given in Fig. 8 and Fig. 9. In the system, there are three different heat exchangers. Each heat exchanger can have different

effectiveness but in Fig. 8 and in Fig. 9 they were selected to be equal in each point [20]. Although the positive variation in the heat exchanger effectiveness increases the COP, its effect on the mass flow rate of lithium bromide-water solution changes is insignificant.

CONCLUSIONS

In this study, a thermodynamic analysis of a series flow triple effect ARS working with lithium bromide-water solution was made by simulating it via a prepared Delphi code. It is shown that the COP can be improved with increasing the LPG and evaporator temperatures and lowering the condenser temperature. It is also indicated that there is an inverse relation between the COP and the lithium bromide-water solution mass flow rates. Based on the LPG temperature rising, there is increasing on mass flow rate of the vapor generated by the HPG and MPG. But there is decreasing on mass flow rate of the vapor generated by the LPG. The flow rate in the vapor lines is nearly constant depending on the condenser and evaporator temperature change. Also, COP can be improved by adding heat exchangers in the system. Although the positive variation in the heat exchanger effectiveness increases the COP, its effect on the mass flow rate of lithium bromide-water solution changes is insignificant.

REFERENCES

- [1] P. Srihirin, S. Aphornratana, and S. Chungpaibulpatana, "A review of absorption refrigeration technologies", *Renew Sust Energ Rev* **5**, 343–372 (2001).
- [2] G. Grossman, A. Zaltash, P. W. Adcock, and R. C. Devault, "Simulating a 4-effect absorption chiller", *ASHRAE J*, 45–53 (1995).
- [3] Kaushik S. C., Arora A., "Energy and exergy analysis of single effect and series flow double effect water-lithium bromide absorption refrigeration systems". *International Journal Of Refrigeration* **32**, 1247-1258 (2009).
- [4] Kaynaklı Ö., Saka K., Kaynaklı F., "Absorbsiyonlu soğutma sisteminde farklı eriyiklerin kullanılabilirliği ve performans değerlerinin incelenmesi", (Turkish) 11. *Int. HVAC+R Technology Symposium, İstanbul*, 108-115 (2014).
- [5] Saka K., Yamankaradeniz N., Kaynaklı F., Kaynaklı Ö., "Hava Soğutmalı Çift Kademeli Absorbsiyonlu Soğutma Sisteminin Enerji Ve Ekserji Analizi", (Turkish) 12. *Ulusal Tesisat Mühendisliği Kongresi, İzmir*, 1135-1151, (2015).
- [6] Kaynaklı O., Saka K., Kaynaklı F. Energy and Exergy Analysis of a Double Effect Absorption Refrigeration System Based on Different Heat Sources. *En. Conv. & Man.* **106**, 21-30 (2015).
- [7] Saka, K., Yılmaz, İH., and Kaynaklı O., Investigation on Double Effect Dual-heat Mode Absorption Refrigeration System, in XII. *Int. HVAC+R Techn. Symp., İstanbul* 123-129 (2016).
- [8] Yılmaz, İH., Saka, K., and Kaynaklı O., Influence of the Equilibrium Temperature in the Double Stage of the Absorption Refrigeration System, in *8th International Ege Energy Symposium and Exhibition (IEESE)* 46-51 (2016).
- [9] Yılmaz, İH., Saka, K., and Kaynaklı O., A thermodynamic evaluation on high pressure condenser of double effect absorption refrigeration system. *Energy* **113**, 1031-1041 (2016).
- [10] Gebreslassie B. H., Medrano M., Boer D, "Exergy analysis of multi-effect water–LiBr absorption systems: From half to triple effect". *Renewable Energy* **35**, 1773-1782 (2010).
- [11] Grossman, G., Wilk, M., and DeVault, R. C., Simulation and performance analysis of triple-effect absorption cycles. *ASHRAE Transactions*, **100(2)**, 452-62 (1994).
- [12] Kaita, Y., Simulation results of triple-effect absorption cycles. *International Journal of Refrigeration* **25**, 999-1007 (2002).
- [13] Gomri, R., Thermodynamic evaluation of triple effect absorption chiller. *Thermal Issues in Emerging Techn., ThETA 2, Cairo, Egypt*, (2008).
- [14] Maryami, R. and Dehghan, A.A., An exergy based comparative study between LiBr/water absorption refrigeration systems from half effect to triple effect. *Applied Thermal Engineering*, **124**, 103-123 (2017).
- [15] Saka, K. Yılmaz İH., and Göksu T.T., A Thermodynamic View of Triple-effect Absorption Refrigeration Systems. *Int. Advanced Researches & Eng. Congress, Osmaniye, Turkey* (2017).
- [16] Kaita Y. Thermodynamic properties of lithium bromide-water solutions at high temperatures. *Int J Refrig* **24**, 374-390 (2001).
- [17] Mostafavi M, Agnew B. The impact of ambient temperature on lithium bromide–water absorption machine performance. *Appl Therm Eng* **16**, 515–522 (1996).
- [18] Chua HT, Toh HK, Malek A, Ng KC, Srinivasan K. Improved thermodynamic property field of LiBr–H₂O solution. *Int J Refrig* **23**, 412–429 (2000).
- [19] Aphornratana S, Sriveerakul T. Experimental studies of a single-effect absorption refrigerator using aqueous lithium-bromide: Effect of operating condition to system performance. *Exp Therm Fluid Sci*, **32**: 658-669 (2007).
- [20] Canbolat, A S., Türkan B., Etemoğlu, A. B., Can, M., Avcı, A. Technical and Economical Comparison of Plate, Shell and Tube and Miniature Pipe Type Heat Exchangers. *Uludağ Univ. J. of the Fac. of Eng.* 21:2, 107-122 (2016).

Comparative performance analysis of a two-bed adsorption cooling system with adsorption of different adsorbates on silica-gel

M. Kılıç*

Bursa Uludağ University, Engineering Faculty, Dept. of Mechanical Engineering, Bursa, Turkey

This study presents a comparative performance analysis of a two-bed adsorption cooling system in which various working fluids are used with silica-gel as adsorbent pairs. An adsorption cycle simulation program has been developed to investigate the influence of different operating conditions on the cooling power and COP of the system. For the configuration of the adsorption cycle in the present simulation, two adsorption bed design is used. Different working fluids as adsorbate are considered in this study. These are water, methanol, R134a and R404a. They can be employed in the adsorption refrigeration systems driven by heat sources such as solar energy or waste heat with a temperature lower than 100°C. It is observed that the parameters that have the most significant effect on COP and SCP are, in decreasing order, the adsorption heat of adsorbate-adsorbent pair, cooling source temperature, heating source temperature, condensation temperature at the condenser and evaporation temperature at the evaporator. These results are valid for all working pairs. In general, increasing evaporation temperature and decreasing adsorption bed temperature during the adsorption process increases COP and SCP for all working pairs. In addition to that different design parameter such as specific cooling power, the mass of adsorbent and adsorbate etc. are calculated, compared and discussed for each working pairs.

Keywords: Adsorption cooling, adsorbate-adsorbent pair, silica gel, COP, SCP

INTRODUCTION

Among the thermally driven refrigeration systems, adsorption systems, which can be powered by low-grade renewable energy and waste heat resources, are of great interest and considerable research and development studies have been performed by numerous researchers in recent decades[1]. The primary heat sources for adsorption cooling/refrigeration systems are waste heat and solar energy. The systems in which the physical adsorption working pairs employed are usually preferred when solar energy is used as the heat source [2]. The physical adsorption process of the gas occurs mainly within the pores and surface of the solid adsorbent [3]. The adsorbed amount and concentration of refrigerant in the pores are strongly dependent on pressure and temperature variations as well as the operating conditions of the system [4]. The design of an adsorption refrigeration system requires the knowledge of adsorption characteristics of the employed adsorbent-adsorbate pair when the temperature and pressure are varying.

The isosteric heat of adsorption is a specific combined property of an adsorbent/adsorbate combination. The equilibrium adsorption properties at several adsorbent temperatures and adsorption chamber adsorbate pressures were studied for a wide range of pairs by several researchers [5-9].

Silica gel is a silicon dioxide (SiO_2), an amorphous form of silica which is manufactured from silicate and sulfuric acid. It is a naturally occurring mineral that is purified and processed into beaded or granular form, and is also non-corrosive and chemically inert. Silica gel can be used as a primary desiccant or blended with other desiccants in any application where control of moisture is required.

Silica gel belongs to low temperature working adsorbent, which can be driven by heat source with the temperature lower than 100°C [2]. The silica gel is a type of amorphous synthetic silica. Each kind of silica gel has only one type of pore, which usually is confined in narrow channels. The pore diameters of ordinary silica gel are 2, 3 nm (A type) and 0.7 nm (B type), and the specific surface area is about 100–1000 m^2/g [3, 9].

Sah et al. [10] summarize the performances of the potential adsorption cooling systems which use silica gel and carbon as adsorbents. It is stated that the systems with silica gel as adsorbent have higher COP than the systems with carbon as the adsorbent. However, the applications of both types of systems are different. The system with silica gel has the advantage of relatively low driving temperature. In the adsorption cooling systems, refrigerants like methanol, ammonia, ethanol, carbon dioxide, nitrogen, R134a, R114 are paired with activated carbon. These systems operate with comparatively higher driving temperatures. However, methanol

* To whom all correspondence should be sent:
mkilic@uludag.edu.tr

based adsorption cooling systems cannot operate above 150°C as methanol would decompose and the adsorption power of activated carbon decreases sharply at that high temperature. These methanol systems are used for ice making and air-conditioning purposes [9]. The R134a (tetrafluoroethane CF₃CH₂F) and R404a (CHF₂CF₃ / CH₃CF₃ / CF₃CH₂F) can be employed as a working fluid in the systems operate above atmospheric pressure which ensures that the system leakages are very small and can be used to several cooling applications [7].

The adsorption characteristics of each adsorbent-adsorbate pair are usually entirely different than each other. Detailed specification about the adsorption isotherms of the different adsorbent/adsorbate pair as well as the isosteric heat of adsorption must be known to design the adsorption based cooling cycle system. Detailed literature reviews on adsorption working pairs for refrigeration/cooling applications can be found in the references [3, 4].

Saha et al. [11] studied analytically silica gel-water based advanced adsorption cooling system driven by the low-grade waste heat source of 50°C and cooling source of 30°C. Simulation software was developed to study the effects of operating temperatures, flow rates, and adsorption/desorption cycle times on cooling output, COP and chiller efficiency [12].

A large number of studies such as refs. [13-16] have been published about adsorption cooling systems employing the pair of silica gel and water. Only a few studies such as refs.[17,18] considered silica gel-methanol pair as an adsorbent/adsorbate pair. However, to the best of our knowledge, there is not any published study that has been devoted to studying on the adsorption cooling system with the refrigerants R134A and R404A as adsorbate fluid onto the silica gel as adsorbent solid.

From this mentioned perspective, the present study aims to perform a comparative investigation on the performance of the two-bed adsorption cooling cycle with the adsorbate fluids of water, methanol, R134A and R404A on the commercially available silica gel employed as the adsorbent solid. To realize the aimed research, a cycle simulation program is developed according to the mathematical model proposed in this study to perform realistic simulation and detailed investigation for the design of the adsorption based refrigeration and cooling systems. The presented results can be used on the design of adsorption based cooling cycle systems in which a silica gel is employed as an adsorbent with

the one of the working fluid among water, methanol, R134A and R404A.

MATHEMATICAL MODELLING

The adsorption cooling system is similar to the known mechanical vapour compression systems and the system components such as the evaporator, condenser and expansion valve are the same. The main difference is that the thermal compressor takes the place of the mechanical compressor. This section deals with the operating principle of the thermal compressor operating according to the adsorption refrigeration cycle.

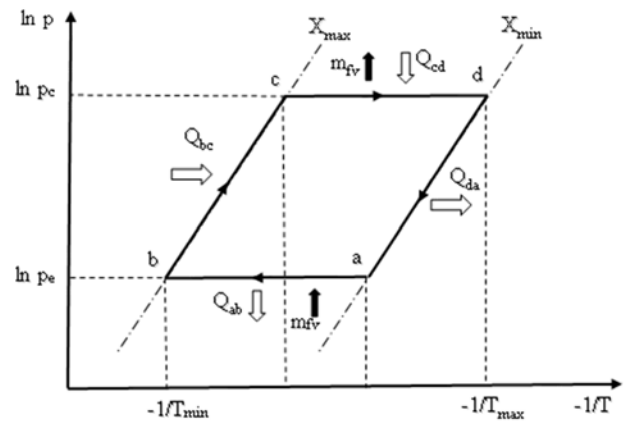


Fig.1. Basic adsorption cycle for an adsorption bed

It is possible to study the system by dividing it into four main sections according to the operating principle of adsorption cooling cycle. According to this, heating and cooling processes in which mass change is not observed are isosteric, whereas adsorption and desorption processes made under constant pressure are isobaric characteristic transports. The $\ln P - 1/T$ diagram of the adsorption refrigeration cycle is given in Fig.1.

Isobaric adsorption, (a-b): In this process, the vapour of the adsorbate supplied from the evaporator is adsorbed by the adsorbent in the bed; meanwhile heat rejection occurs from the bed. The process is completed when the temperature of the bed falls to the value of T_b at constant evaporator pressure.

Isosteric heating process (b-c): Adsorbent bed temperature is increased from T_b to T_c by heat input from the outside (when the evaporator and condenser valves are in the closed position). No desorption occurs during the process, and gas pressure increases in the bed.

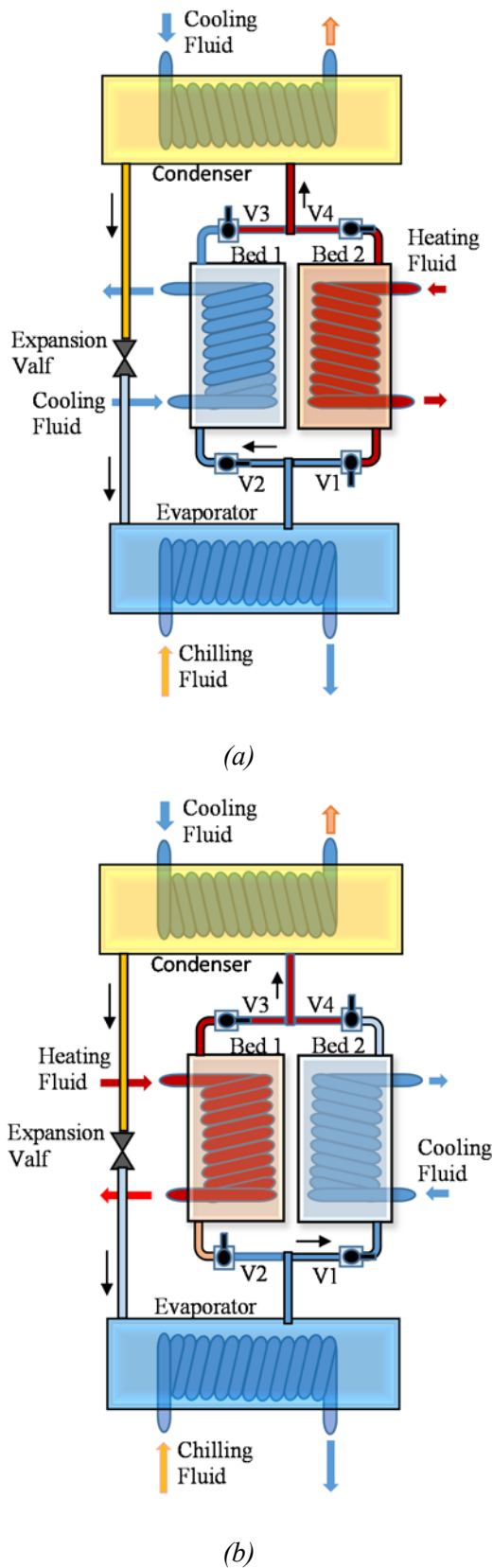


Fig.2. Schematic of the two-bed adsorption cooling cycle: (a) Bed 1 in adsorption phase, Bed 2 in desorption phase ; (b) Bed 1 in desorption phase, Bed 2 in adsorption phase

Isobaric desorption, (c-d): At this stage, the heat input to the adsorbent bed continues. However, the desorption starts and the desorption-induced vapour is condensed in the condenser. The pressure in the adsorbent bed is considered constant at condenser pressure. At the end of the stage, bed temperature reaches the maximum value (T_d).

Isothermic cooling process (d-a): After the desorption process is completed, the adsorbent bed (when the evaporator and condenser valves are in the closed position) is cooled down to T_a temperature, so the pressure is reduced and the adsorption bed is ready for the next cycle.

It can be seen that the cooling effect can be produced during the isobaric adsorption process. In order to provide continuous cooling, it is common to use two (or multiple) adsorption beds in the system. In a working cycle, one of the chambers is used for the adsorption while other for the desorption. The role of each chamber is interchanged in another cycle, to maintain a pseudo-continuous production of the cooling effect. Schematic of the two-bed adsorption cooling cycle system is given in Fig.2.

It is essential to know the isotherms and the adsorption heat of the adsorption pairs used to calculate the yield and the capacity in the cooling cycles. A lumped parameter approach is used in the study. The main assumptions applied in the mathematical model are given as follows:

- (1) The temperature and the pressure are uniform throughout the whole adsorbent bed.
- (2) The refrigerant is adsorbed uniformly in the adsorbent bed and is liquid in the adsorbent.
- (3) The pressure difference between the adsorbent bed and the condenser or the evaporator is neglected.
- (4) The heat conduction of the shell connecting the adsorbent to the condenser or the evaporator is neglected, and the heat exchange between two beds is entirely isolated.
- (5) The system has no heat losses (or refrigerating output loss) to the environment.

Adsorption isotherms

It becomes a common approach that the use of Dubinin–Astakhov (D–A) model for the calculation of the adsorbate uptake value on the adsorbent as a function of temperature and pressure in the adsorption bed [1, 5]. Dubinin–Astakhov (D–A) equation may be written in the form given as follow:

$$W = W_0 \exp \left\{ - \left[\frac{RT}{E} \ln \left(\frac{p_s}{p} \right) \right]^n \right\} \quad (1)$$

with

$$W = Xv_a \text{ and } W_0 = X_0v_0 \quad (2)$$

In Eq.(1), E may be expressed as the specific characteristic energy of the adsorbent-adsorbate pair which may be evaluated from the experimental measurements. R is the gas constant. Pressure is represented by p , and suffix s is referring to the saturation state. Temperature is represented by T . The parameter n is a power constant which results in the best fitting of the experimental isotherms. The quantity X represents the specific adsorbed mass of adsorbate (kg of adsorbate per kg of adsorbent), and v_a is the specific volume of the adsorbed phase, which is given by

$$v_a = v_b \exp(\Omega(T - T_b)) \quad (3)$$

where v_b is the saturated liquid specific volume at the normal boiling point, b represents the van der Waals volume, and Ω is given as:

$$\Omega = \ln(b/v_b) / (T_c - T_b) \quad (4)$$

T is the temperature. The critical and normal boiling point temperatures of the refrigerant are represented by suffixes c and b , respectively. The parameter v_0 can be obtained by using Eq.(2) at $T = 273.15$ K. Tab.1 shows the properties and parameters of the adsorbates used in the present study.

Table 1. Properties and parameters of the adsorbates [19]

	Unit	Water	Methanol	R134A	R404A
MW	kg/kmol	18.02	32.04	102.03	97.60
T_b	K	373.15	338.15	247.09	226.70
T_c	K	647.25	513.40	374.23	345.22
R	kJ/kg K	0.4615	0.2595	0.08149	0.08519
P_c	kPa	22064	8104	4059	3729
ρ_c	kg/m ³	322.00	281.50	515.30	484.50
b	m ³	0.001692	0.002055	0.000939	0.000986
v_b	m ³ /kg	0.001043	0.001337	0.000726	0.000766
v_0	m ³ /kg	0.000875	0.001140	0.000766	0.000845
Ω		0.001764	0.002452	0.002018	0.002125
h_{fg}	kJ/kg	2454	1178	181	146
ΔH_{ads}	kJ/kg	2701	1373	242	262
W_0	m ³ /kg	0.000303	0.000399	0.000402	0.000344
X_0	kg/kg	0.346	0.350	0.525	0.407
E	kJ/kg	227.6	172.84	68.15	83.52
n		1.35	1.7	1.237	1.613
E_a	kJ/kg	2330	1311	412	430

*Values at T=293,15 K

Adsorption kinetics

Adsorption and desorption rates of the adsorbate onto adsorbent can be calculated by the use of Linear Driving Force (LDF) approach. Adsorption kinetics (dX/dt) equation is given in Eq.(5).

$$\frac{dX}{dt} = F_o \frac{D_o}{r_p^2} \exp\left(-\frac{E_a}{RT}\right) (X_{eq} - X) \quad (5)$$

where X_{eq} is the equilibrium concentration at the given pressure and temperature; F_o is a constant characteristic of adsorbent's shape. The equilibrium concentration is calculated using the Dubinin-Astakhov equation given in Eq.(1). X is the instantaneous concentration of the adsorbent bed. The values of the adsorption kinetic parameters used in the present study are given in Table (1, 2).

Table 2. Values of the parameters used in the present study.

Parameter	Values	Unit
D_o	2.54E-4	m ² /s
F_o	15	
R_p	1.7E-4	m
$M_{bmCp,bm}$	78	kJ/K
M_s	47	kg

Adsorption heat

Isosteric heat of adsorption is traditionally expressed as a function of concentration due to its dependence on temperature is relatively weaker. For adsorption of fluids below their thermodynamic critical point, its magnitude is larger than the heat of vaporization of the adsorbate, which has a strong temperature dependence [5, 6]. As a result, the difference between the adsorption heat and the vaporization heat is a property of relevance in the design of adsorption refrigeration systems. By the use of this common evaluation procedure, it has been shown that isosteric heat of adsorption can be approximated as a function of relative adsorption uptake for adsorbent-adsorbate pair combinations which broadly follow the Dubinin's isotherms [5]. However, the gas phase of the adsorbent is not ideal, during the adsorption of the adsorbate molecules onto the assorted adsorbent is affected by the pressure and temperature changes. Therefore, the heat of adsorption may be calculated by using the following Eq.(9) as suggested by El-Sharkawy et al. [20].

$$\Delta H_{ads} = h_{fg} + (E)[\ln(W_0/W)]^{1/n} + (E\Omega/n)[\ln(W_0/W)]^{((1-n)/n)} \quad (9)$$

Energy balance equations

The energy balance equation in the adsorbent bed for the pre-cooling and the adsorption processes can be expressed as given in Eq. (10).

$$\begin{aligned} & \left[(M_{bm}c_{p,bm})_{bed,m} + (M_s c_{p,s})_{bed,s} \right] \frac{dT_{bed}}{dt} + \\ & (M_s X_{ad,f}) \frac{dh_{ad,f}}{dt} + (m_{bed,v}) \frac{dh_{bed,v}}{dt} = \\ & M_s \frac{dX_{ad,f}}{dt} (\Delta H_{ads} + \gamma h_{evap,out} - h_{ad,f}) + \\ & \frac{dm_{bed,v}}{dt} (\gamma h_{bed,in} - h_{bed,v}) - \dot{Q}_{cool} \end{aligned} \quad (10)$$

where the value of $\gamma = 0$ in the pre-cooling process; $\gamma = 1$ in the adsorption process.

The energy balance equation in the adsorbent bed for the pre-heating and the desorption process can be expressed as given in Eq.(11).

$$\begin{aligned} & \left[(M_{bm}c_{p,bm})_{bed,m} + (M_s c_{p,s})_{bed,s} \right] \frac{dT_{bed}}{dt} + \\ & (M_s X_{ad,f}) \frac{dh_{ad,f}}{dt} + (m_{bed,v}) \frac{dh_{bed,v}}{dt} = \\ & M_s \frac{dX_{ad,f}}{dt} (\Delta H_{ads} + \gamma h_{cond,in} - h_{ad,f}) + \\ & \frac{dm_{bed,v}}{dt} (\gamma h_{bed,out} - h_{bed,v}) + \dot{Q}_{heat} \end{aligned} \quad (11)$$

where the value of $\gamma = 0$ in the pre-heating process; $\gamma = 1$ in the desorption process.

Mass balance equations

Amount of adsorbate in the adsorbent bed can be calculated from the following expression (Eq.(12)) at any instant.

$$M_{bed,f} = M_s X_{ad,f} + m_{bed,v} \quad (12)$$

The mass transfer rate between the bed and the evaporator during the adsorption process can be obtained from Eqs.(13) and (14).

$$\frac{dM_{bed,f}}{dt} = M_s \frac{dX_{ad,f}}{dt} + \frac{dm_{bed,v}}{dt} \quad (13)$$

$$\frac{dm_{eva,out}}{dt} = \frac{dm_{bed,in}}{dt} = \frac{dM_{bed,f}}{dt} \quad (14)$$

Similarly, the mass transfer rate between the bed and the condenser during the desorption process can be obtained from Eqs.(13) and (15).

$$\frac{dm_{cond,in}}{dt} = \frac{dm_{bed,out}}{dt} = \frac{dM_{bed,f}}{dt} \quad (15)$$

The cycling mass of the adsorbate in the system can be obtained from Eq.(16) or Eq.(17). The non-cycling mass of the adsorbate in the system can be obtained from Eq.(18).

$$M_{f,cyc} = \int_{des} \frac{dm_{cond,in}}{dt} dt = \int_{ads} \frac{dm_{eva,out}}{dt} dt \quad (16)$$

$$M_{f,cyc} = M_s (X_{max} - X_{min}) + V_{bed,void} (\rho_{v,max} - \rho_{v,min}) \quad (17)$$

$$M_{f,ncyc} = M_s X_{min} + V_{bed,void} \rho_v (P_c, T_{max}) \quad (18)$$

where $V_{bed,void}$ shows the void volume occupied by adsorbate in the vapor phase in the adsorbent bed. $\rho_{v,max}$ represents the maximum vapor density at the condenser pressure (P_{cond}) and the maximum bed temperature (T_{max}); $\rho_{v,min}$ represents the minimum vapor density at the evaporator pressure (P_{eva}) and the minimum bed temperature (T_{min}).

Finally, Eq.(19) gives the total mass of the adsorbate employed in the system.

$$M_{f,sys} = M_{f,cyc} + M_{f,ncyc} \quad (19)$$

System performance parameters

Adsorption cooling system performance is commonly defined by its specific cooling power (SCP) in W/kg adsorbent and the coefficient of performance (COP). The two parameters are the most critical data among the technical specifications of such products. COP and SCP are expressed by Eq.(20) and Eq.(21) respectively.

$$COP = \frac{Q_{eva}}{Q_{heat}} \quad (20)$$

$$SCP = \frac{Q_{eva}}{t_{cycle} M_s} \quad (21)$$

Where cooling capacity of the evaporator (Q_{eva}) and heat load of the system (Q_{heat}) in a cycle can be calculated by Eq.22 and Eq.23, respectively.

$$Q_{eva} = \oint_0^{t_{cycle}} \frac{dm_{eva,out}}{dt} (h_{exv,o} - h_{eva,sv}) dt \quad (22)$$

$$Q_{heat} = \oint_0^{t_{cycle}} \dot{Q}_{heat} dt \quad (23)$$

It should be mentioned that the electrical power consumption of chilled water, cold water and hot water pumps are relatively small so can be neglected.

Calculation procedure of the mathematical model

The home-made-software is written in the RAD Studio 10 environment using the Delphi 10 program language. The thermophysical fluid properties used in the model are obtained as real-fluid properties by including the CoolProp library, which is provided as a high accuracy open-source property package for pure and pseudo-pure fluids, as well as humid air. The CoolProp library, written in the C++ programming language, can calculate properties for 110 different pure and pure fluids, detailed information about the software can be found in Bell et al.[21]. Besides, adsorption heat is calculated as a function of pressure, temperature and concentration when it is not taken as a fixed value as it is in most studies. The equations given in the model are solved by iterative manner.

Validation of the mathematical model

Several studies have been already reported about the adsorption cooling systems for the use of the water-silicagel pair. Di et al. [16] conducted an experimental and theoretical simulation work by the use of the water-silicagel pair. In order to validate present mathematical model computations performed according to their parameters and working conditions used in their study. The mass of the adsorbent (M_s) used in a bed is = 47 kg silica gel. The heat capacity ($M_{bm}c_{p,bm}$) of the adsorption bed metal materials is taken as 78 kJ/K. The cooling water inlet temperature ($T_{cool,in}$) to the bed or the condenser is equal to 30 °C. The chilling water inlet temperature ($T_{chill,in}$) to the evaporator is equal to 20 °C. Evaporation temperature at the evaporator is the function of the cooling power. Other temperature settings are applied as follow:

$$\begin{aligned} \text{Condenser temperature} \quad T_{cond} &= T_{cool,in} + 3 \text{ }^\circ\text{C}; \\ \text{Evaporator temperature} \quad T_{eva} &= T_{chill, o} - 3 \text{ }^\circ\text{C}; \\ \text{Bed maximum temperature} \quad T_{bed,max} &= T_{heat,in} - 2 \text{ }^\circ\text{C}; \\ \text{Bed minimum temperature} \quad T_{bed,min} &= T_{cool,in} + 2 \text{ }^\circ\text{C}. \end{aligned}$$

Tab.4 shows the comparisons between the present predicted results and the findings of Di et al.[16] for the three different heating fluid inlet temperatures as 65, 75 and 85°C. It can be seen that the predicted COP and SCP values are in a good agreement with the experimental and simulation data of Di et al. [16]. As the temperature increases from 65 to 85 °C, there is slight increase at COP values,

whereas, SCP increases sharply with the rising heating fluid temperature. Tab.4 also shows the relative differences between the calculated results and the experimental data. Largest relative difference percentages are 8.1% and 6.5% for COP and SCP, respectively. Considering the experimental uncertainties in the measurements and the assumptions made in the calculations, the agreement of the results is quite well.

Table 3. Physical characteristics of the silicagel used in the present study.

Chemical Composition	SiO ₂ .n(H ₂ O)
SiO ₂ content (%)	99.7
Diameter (mm)	2-5
Density (kg/m ³)	750
Micro Pore Volume(cm ³ /g)	0.343
Specific Surface Area (m ² /g)	693
Pore Diameter (Å)	17.4
Specific Heat (c _p) (kJ/kgK)	0.92
Shape	Spherical
Colour	White

Table 4. Comparisons the present model results with the data given in Di et al.[16] for the silicagel-water pair. ($T_{cool,in} = 30^\circ\text{C}$, $T_{chill, in} = 20^\circ\text{C}$)

$T_{heat,in}$	COP			SCP		
	Exp. [16]	Sim.[16] (RD ¹ %)	Present (RD ¹ %)	Exp. [16] (RD ² %)	Sim.[16] (RD ² %)	Present (RD ² %)
85°C	0.43	0.40(7.5)	0.42(2.3)	99.8	93.3(6.5)	101.0(1.2)
75°C	0.37	0.39(5.4)	0.40(8.1)	80.2	78.8(1.7)	78.2(2.5)
65°C	0.37	0.39(5.4)	0.39(5.4)	63.9	65.1(1.9)	62.4(2.3)

$RD^1 = |COP_{exp} - COP_{sim}| / COP_{exp}$; $RD^2 = |SCP_{exp} - SCP_{sim}| / SCP_{exp}$

RESULTS AND DISCUSSION

The present study aims to perform a corporative work on the adsorption cooling system using silica gel with different working fluids as constitute adsorbent-adsorbate pairs. Four different widely used fluid (water, methanol, R134A and R404A) are chosen as the adsorbate. Two-bed adsorption cooling system as described in previous sections with the conditions described in the validation section are used in the calculations. In the computations, evaporation temperature at the evaporator is set as $T_{eva} = 5^\circ\text{C}$; two different cooling fluid inlet temperature is considered as $T_{cool,in} = 20^\circ\text{C}$ or 30°C ; heating fluid inlet temperature is changing between 60 to 95°C . Adsorption/desorption time is taken as 600

seconds, precooling/preheating time is taken as 50 seconds. Therefore, the cycle time is taken as 1300 second. Computations are performed at the same working conditions for the four different adsorbates.

Fig.3, and Fig.4, show the computed results of the coefficient of performance (COP) and specific cooling power (SCP) respectively. For the all working fluids COP and SCP values at $T_{cool,in} = 20^{\circ}C$ is higher than ones at $T_{cool,in} = 30^{\circ}C$. It is resulted by more adsorbate is adsorbed by the adsorbent at lower temperatures, and the temperature difference between the heating and the cooling is also increased. These results more working fluid circulates in the system, and the cooling power rises considerably.

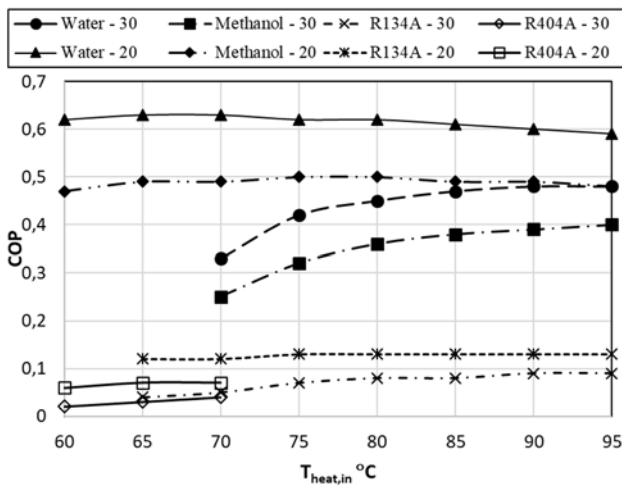


Fig.3. Comparisons of COP for the different heating and cooling fluid inlet temperatures. ($T_{eva}=5^{\circ}C$; $T_{cool,in} = 20$ or $30^{\circ}C$)

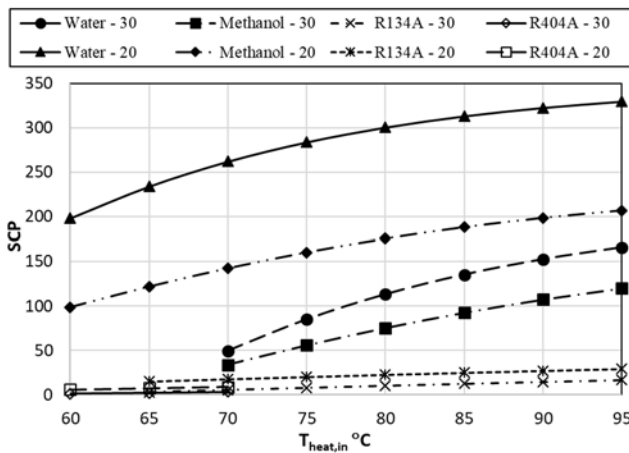


Fig.4. Comparisons of SCP for the different heating and cooling fluid inlet temperatures. ($T_{eva}=5^{\circ}C$; $T_{cool,in} = 20$ or $30^{\circ}C$)

Comparing COP and SCP for the working fluids, it can be seen that the highest COP ($=0.63$) and SCP ($=329$ W/kg) are obtained for the water, and the lowest ones are found for the R404A (as 0.02 and 1.3 W/kg, respectively).

The variations of COP and SCP with hot water inlet temperature shows similar behaviour for water and methanol. It can be seen from Fig.3 that COP values for methanol are about 80% of the value for water at the same operating conditions. COP values of R134A increase slightly with rising hot water inlet temperature, it rises up to 0.13 for $T_{cool,in} = 20^{\circ}C$ and 0.09 for $T_{cool,in} = 30^{\circ}C$. In the meantime, SCP values for water and methanol increase significantly with increasing hot water inlet temperature as well as decreasing cooling water inlet temperatures, as shown in Fig.4. SCP values for methanol are about 70% and 60% of the water's values at $T_{cool,in} = 20^{\circ}C$ and $30^{\circ}C$, respectively. SCP values of R134A increase slightly with rising hot water inlet temperature, it rises up to 30 W/kg for $T_{cool,in} = 20^{\circ}C$ and 17 W/kg for $T_{cool,in} = 30^{\circ}C$.

Considering the adsorption heat values (at $20^{\circ}C$) given at Tab.1, water has the largest one (2751 kJ/kg), methanol has less than half of water's value (as 1373 kJ/kg), R134A and R404 have quite lower than water and methanol values (as 242 and 262 kJ/kg, respectively). When the computed result for COP and SCP are considered together with the adsorption heat values of the adsorbent-adsorbate pairs, it can be seen that the performance parameters show a strong relationship with the adsorption heat magnitude of adsorbate. Therefore, it can be concluded that the adsorption heat has a significant effect on the COP and SCP.

CONCLUSIONS

This study presents a comparative study on a two-bed adsorption cooling system with silica gel as adsorbents and four different working fluids (water, methanol, R134A and R404A) as the adsorbate. These four adsorbent-adsorbate pairs and various cycle operating conditions are investigated at the heating source temperature range from 60 to $95^{\circ}C$. The performance indicators are the COP and the SCP. Among the adsorbent-adsorbate pairs considered in this study, the best performance values are obtained for the silica gel-water pair. The silica gel-methanol pair shows similar behavior to the silica gel-water pair with about 20% and 40% less performance regarding COP and SCP, respectively. However, the silica gel-methanol has the advantage of evaporator temperature can be below $0^{\circ}C$. It

should be mentioned that the adsorption cycles using these two fluids as adsorbate can be operated under atmospheric pressures. On the other hand, positive pressure refrigerants R134 and R404 pairs with silica gel shows shallow performances compared to the water and the methanol ones. The maximum COP and SCP values for the R134A are 0.13 and 30 W/kg respectively. Since the critical temperature is relatively low to the other fluids, R404A can be used the operating temperature less than 72 °C. The maximum COP and SCP values for the R404A are 0.07 and 9 W/kg respectively.

It is shown that the parameters that have the most considerable effect on COP and SCP are, in decreasing order, the adsorption heat of adsorbate-adsorbent pair, cooling source temperature, heating source temperature, condensation temperature at the condenser and evaporation temperature at the evaporator. These results are valid for all working pairs. In general, increasing evaporation temperature and decreasing adsorption bed temperature during the adsorption process increase COP and SCP for all working pairs.

It should be mentioned that the basic adsorption cycle used in this study. The performance of the adsorption cooling systems has been improving by the use of more advanced design optimization and simulation models such as heat recovery, mass recovery, multi-bed and multi-stage technologies as well as improving more efficient adsorbent-adsorbate pairs. It is a promising technology for the use of low-grade renewable energy sources.

NOMENCLATURE

- b - the van der Waals volume, m^3 ;
- c_p - specific heat, kJ/kgK ;
- COP – coefficient of performance, - ;
- D_0 – surface diffusion coefficient, m^2/s ;
- E – characteristic energy of adsorption pair, kJ/kg ;
- E_a – activation energy of adsorption pair, kJ/kg ;
- F_o - a constant characteristic of adsorbent's shape.
- h_{fg} - vaporization enthalpy, kJ/kg ;
- ΔH_{ads} - adsorption heat, kJ/kg ;
- M - mass, kg ;
- MW - molecular weight of fluid, $kg/kmol$;
- n - exponential constant, -.
- p - pressure, kPa ;
- p_s - saturation pressure, kPa ;

- R – gas constant, kJ/kgK ;
- RD - relative difference;
- SCP – specific cooling power, W/kg ;
- Q - heat, kJ ;
- \dot{Q} - heat rate, kW ;
- t - time, s ;
- T - temperature, K ;
- X – adsorption capacity on mass basis, kg/kg ;
- v_a – adsorbed phase specific volume, m^3/kg ;
- v_b – saturated liquid specific volume at normal boiling temperature, m^3/kg ;

Subscripts

- a- adsorbed phase;
- ad- adsorption;
- b- boiling point;
- bed- adsorber bed;
- bm- bed material;
- c- critical point;
- cyc- cycle;
- cond- condenser;
- eva- evaporator;
- f- fluid;
- fg- phase change from liquid to gas;
- in- inlet
- out- outlet
- min- minimum;
- max- maximum;
- s- sorbent;
- s- saturation;
- l- liquid phase;
- v- vapour phase;

REFERENCES

- [1] A.A. Askalany, M. Salem, I.M. Ismael, A.H.H. Ali, M.G. Morsy, B.B. Saha. An overview on adsorption pairs for cooling. *Renewable and Sustainable Energy Reviews* **19**, 565–572 (2013).
- [2] A. Allouhi, T. Kousksou, A. Jamil, T. El Rhafiki, Y. Mourad, Y. Zeaouli. Optimal working pairs for solar adsorption cooling applications, *Energy*, **79**, 235-247 (2015).
- [3] L.W. Wang, R.Z. Wang, R.G. Oliveira. A review on adsorption working pairs for refrigeration. *Renewable and Sustainable Energy Reviews* **13**, 518–534 (2009).
- [4] D.C. Wang, Y.H. Li, D. Li, Y.Z. Xia, J.P. Zhang. A review on adsorption refrigeration technology and adsorption deterioration in physical adsorption systems. *Renewable and Sustainable Energy Reviews* **14**, 344–353 (2010).
- [5] B.B. Saha, S. Koyama, I.I. El-Sharkawy, K. Habib, K. Srinivasan, P. Dutta. Evaluation of adsorption

- parameters and heats of adsorption through desorption measurements. *Journal of Chemical and Engineering Data* **52**(6), 2419–2424 (2007).
- [6] B.B. Saha, K. Habib, I.I. El-Sharkawy, S. Koyama. Adsorption characteristics and heat of adsorption measurements of R-134a on activated carbon. *International Journal of Refrigeration* **32**, 1563–1569 (2009).
- [7] K. Habib, B.B. Saha, S. Koyama. Study of various adsorbent-refrigerant pairs for the application of solar driven adsorption cooling in tropical climates. *Applied Thermal Engineering* **72**, 266–274 (2014).
- [8] M. Kılıç, E. Gönül. Adsorption characteristics evaluation of R134A and R404A on different adsorbents. *Bulgarian Chemical Communications* **48**(E), 306–311 (2016).
- [9] M. Kılıç, E. Gönül. An experimental study on adsorption characteristics of R134A and R404A onto silicagel adsorbents. *Proc. of HEFAT 2017, 13th International Conference on Heat Transfer, Fluid Mechanics and Thermodynamics, Portoroz, Slovenia*, 52–58 (2017).
- [10] R.P. Sah, B.Choudhury, R.N. Das. A review on adsorption cooling systems with silica gel and carbon as adsorbents. *Renewable and Sustainable Energy Reviews* **45**, 123–134 (2015).
- [11] B.B. Saha, E.C. Boelman, T. Kashiwagi. Computer simulation of a silica gel–water adsorption refrigeration cycle the influence of operating conditions on cooling output and COP. *ASHRAE Transactions*. **39**(2), 348–57 (1995).
- [12] B.B. Saha, E.C. Boelman, T. Kashiwagi. Computational analysis of an advanced adsorption-refrigeration cycle. *Energy* **20**(10), 983–994 (1995).
- [13] R.H. Mohammed, O. Mesalhy, M.L. Elsayed, M. Su, L.C. Chow. Revisiting the adsorption equilibrium equations of silica-gel/water for adsorption cooling applications, *International Journal of Refrigeration*, **86**, 40–47 (2018).
- [14] Z.S. Lu, R.Z. Wang, Z.Z. Xia, Q.B. Wu, Y.M. Sun, Z.Y. Chen. An analysis of the performance of a novel solar silica gel-water adsorption air-conditioning, *Applied Thermal Engineering* **31**, 3636–3642 (2011).
- [15] Q.W. Pan, R.Z. Wang, L.W. Wang, D. Liu. Design and experimental study of a silica gel-water adsorption chiller with modular adsorbents. *International Journal of Refrigeration* **67**, 336–344 (2016).
- [16] J. Di, J.Y. Wu, Z.Z. Xia, R.Z. Wang. Theoretical and experimental study on characteristics of a novel silica gel-water chiller under the conditions of variable heat source temperature. *International Journal of Refrigeration* **30**, 515–526 (2007).
- [17] K. Oertel, M. Fische. Adsorption cooling system for cold storage using methanol/silicagel. *Applied Thermal Engineering* **18**, 773–786 (1998).
- [18] M. Ali, S. Ajib. Energy Analysis and Modeling Study of Combined Activated Carbon-Silica Gel/Methanol Adsorption Ice Production System. *Global Journal of Energy Technology Research Updates* **3**, 65–86 (2016).
- [19] ASHRAE Handbook-Fundamentals, American Society of Heating, Refrigeration and Air-Conditioning Engineers, Atlanta, USA, 2009.
- [20] I.I. El-Sharkawy, K. Kuwahara, B.B. Saha, S. Koyama, K.C. Ng. Experimental investigation of activated carbon fibers/ethanol pairs for adsorption cooling system application. *Applied Thermal Engineering*, **26**, 859–865 (2006).
- [21] I.H. Bell, J Wronski, S Quoilin, and V Lemort. Pure and pseudo-pure fluid thermophysical property evaluation and the open-source thermophysical property library CoolProp. *Industrial & Engineering Chemistry Research*, **53** (6), 2498–2508 (2014).

Reducing CO₂ concentration in city centres with green roofs implementation: Case study Belgrade, Serbia

M. Lalošević^{1*}, M. Komatina², B. Živković³, M. Miloš⁴

¹Urban Planning Institute of Belgrade, Palmotićeveva 30, Belgrade, Serbia

^{2,3,4}Faculty of Mechanical Engineering, University of Belgrade, Kraljice Marije 16, Belgrade, Serbia

This paper presents the results on reducing CO₂ concentration with green roofs implementation in a densely populated urban area in Belgrade city centre. The buildings on which green roofs are implemented have an average height of 15 meters. In order to investigate the impact of existing residential urban blocks and potential retrofitting model on CO₂ concentration, base model was designed (the model fully complied with the actual status and real conditions in the location) as well as retrofitting models (which present base model with added elements of extensive and intensive green roofs) and numerical simulations of CO₂ concentrations for all presented models were done. Differences in CO₂ concentrations at height of 1.5 m (pedestrian level), 7.5 m and 17.5 m at 7 am and 7 pm, on a typical summer day in Belgrade were investigated. ENVI-met software was used to perform the simulations. The resultant data of numerical simulation showed that utilizing the green roofs instead of classical flat roofs in Belgrade climatic area could reduce atmospheric concentration of CO₂ around the building up to 11%, average 2.3%. By using proposed strategy, it is demonstrated that applying vegetative roofs could be valuable instrument for noteworthy contribution to environmental protection in Belgrade and for climate change mitigation, both local and global.

Keywords: green roof, CO₂ reduction, urban area, sustainable development, ENVI-met

INTRODUCTION

Green roofs are part of green infrastructure in urban areas. Green infrastructure refers to a strategically planned and managed network of green spaces and other environmental features and technologies necessary for the sustainability of any urban area. Green infrastructure uses vegetation, soils, and natural processes to manage temperature, water, and air quality to create healthier, resilient, and more beautiful urban environments [1].

This study investigates an impact of green roofs implementation on reducing CO₂ concentration in a densely populated urban area in Belgrade city centre.

Green roofs, also known as eco-roofs, roof gardens, vegetative roofs and living roofs can be defined as the roofs with vegetation on the uppermost layer [2]. Green roofs can be split into two categories, "extensive" and "intensive", with respect to weight, substrate layer, maintenance, cost, plant community and irrigation. Intensive green roofs may include shrubs and trees and appear similar to landscaping found in urban parks. The depth of growth media on an intensive green roof usually varies between 20 cm and 1.2 m. Intensive green roofs have intense maintenance needs. Extensive green roofs are planted with low height and slow growing plants and require

insignificant maintenance. The depth of the growth media is less than 15 cm. Due to additional load on building structure, and costs, shallow substrate extensive green roofs are more common than deeper intensive roofs, especially in retrofitting design scenarios when green roofs are installed onto existing buildings.

Green roofs offer multiple benefits. They reduce CO₂ emissions and they have a significant role in the strategies for adapting to high temperatures and reducing the effect of heat islands in urban environments. Establishing green roofs can improve stormwater management, conserve energy, increase longevity of roofing membranes, and improve return on investment compared to traditional roofs. They also contribute to increasing urban biodiversity, reducing noise, offering the possibility for development of urban agriculture, and having positive effects on human health. In addition, green roofs provide a more aesthetically pleasing environment. Reviews of the main environmental benefits of green roofs are available in papers [3, 4].

Green roofs reduce ambient CO₂ concentrations in the vicinities [5-8]. Besides direct amelioration of air pollutants by green roofs, they also reduce emissions indirectly [9]. Green roofs indirectly reduce CO₂ releases from power plants and furnaces by reducing demand for heating and cooling, suggesting long-term economic and environmental benefits of green roofs [6].

Concerning CO₂ sequestration, studies reveal

* To whom all correspondence should be sent:
marija.lalosevic@urbel.com

that green roofs directly sequester substantial amounts of carbon in plants and soils through photosynthesis [10-12]. Photosynthesis removes carbon dioxide from the atmosphere and stores carbon in plant biomass, a process commonly referred to as terrestrial carbon sequestration. Carbon is transferred to the substrate via plant litter and exudates. The time length that this carbon remains in the soil before decomposition has yet to be quantified for green roofs, but if net primary production exceeds decomposition, this man made ecosystem will be a net carbon sink, at least in the short term [10].

The extensive study for Chicago evaluated the impact of green roofs on air pollution control. By using a big-leaf dry deposition model, the air pollutants removed by green roofs in Chicago were quantified. The result showed that the green roofs can remove a large amount of pollutants from air. A total of 1675 kg of air pollutants was removed by 19.8 ha of green roofs in one year with O₃ accounting for 52% of the total, NO₂ (27%), PM₁₀ (14%), and SO₂ (7%). The highest level of air pollution removal occurred in May and the lowest in February. The annual removal per hectare of green roof was 85 kg [13].

Complete review that encompasses published research on how green roofs can help mitigate pollution is given in the paper [14].

Another asset of green roof carbon mitigation is that this urban greening strategy is not in space competition with the surface built environment, which is in contrast to other types of urban greening, e.g. urban parks and green spaces [13].

The green roof can be a solution in the environmental rehabilitation of urban zones since it makes use of rooftops, usually 40–50% of the impermeable area in a city.

To our knowledge, reliable data from the scientific literature are lacking on the impact of green roofs in Belgrade, based on which the impacts of their utilization could be determined. Therefore, for this research, the impact of green roof systems on the urban environment in the Belgrade climatic zone was studied using the software tool, ENVI-met. For research purposes, two scenarios of green roof systems (extensive and intensive) utilized on existing buildings were used and compared with a base (realistic) model as reference, in order to explore the influence on lowering carbon dioxide concentration in atmosphere around buildings, in city centre of Belgrade.

TERRITORY AND DATA

For this research typical residential neighbourhood in Belgrade, was chosen. According to urban structures, number of stories, and percentage of green and asphalt surfaces this area represents typical urban form of the Belgrade city centre. The studied location is part of the territory of the municipality of Vračar.

The model of the urban block fully complied with the actual conditions in the location (shape of the buildings, number of stories, position and type of vegetation, position of roads and pavements). The average building height is 15 m. View of the modelled structures in the location is given in Fig.1 (2D view) and Fig.2 (3D view).

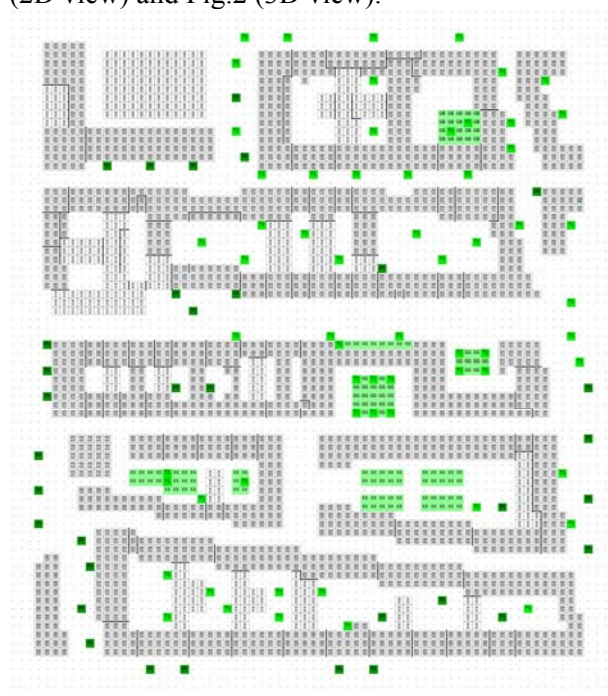


Fig.1. Base model input file – 2D view

Belgrade is located in a moderate continental climate zone, with warm summers, mean summer air temperature from 21 to 25 °C, 30 to 55 tropical days and up to 26 tropical nights annually, with heat waves in July and August. In the current research, statistical data and parameters for a typical summer day in Belgrade were used (Tab.1).

METHODOLOGY

ENVI-met software is one of the most commonly used programs for investigating the microclimate influence of green roofs [15-19]. ENVI-met is a scientifically established prognostic, three-dimensional, high resolution urban

microclimate model [20], which considers physical fundamentals based on the principles of fluid mechanics, thermodynamics and atmospheric physics to calculate three-dimensional wind fields, turbulence, air temperature and humidity, radiative fluxes, and pollutant dispersion. It is designed for microscale with a typical horizontal resolution from 0.5 to 5 metres and a typical time frame of 24 to 48 hours with a time step of 1 to 5 seconds. This resolution allows to analyze small-scale interactions between individual buildings, surfaces and plants.

In the current research, data modelling was performed by ENVI-met Version 4 (Summer17 Release). ENVI-met requires an area input file with 3-dimensional geometry, and a configuration file with the initial parameters.

In the first phase input file for a base (real) model was constructed and investigated.

The dimensions of the studied location were 350x400 meters, divided into a 3-D grid with 5 m gridline divisions. Building heights, the spatial distribution of buildings in the field, position of the vertical greenery, type of trees, and other spatial elements were modelled on real conditions in the location, so the ENVI-met model was properly representative of the urban structures in the location, with spatial relationships reflecting those in real life.

In second phase two models of sustainable retrofitting strategies were modelled and investigated.

The first retrofitting model, extensive green roof model, had all the same characteristics as the baseline model, with added element of extensive green roofs. The second retrofitting model, intensive green roof model, comprised the baseline model with added intensive green roofs.

None of the other characteristics were altered in the research of retrofitting models, so they remained the same as in the baseline model. The green roof structures are treated as an additional layer of insulation. The vegetation used as an element of green roof is of indigenous (native) variety.

In the investigation the base model was used as the reference for comparison with the green roof retrofitting strategies/models, both extensive and intensive.

An area input file with 3-dimensional geometry of the modelled structures for base model is given in Fig.3 (3D view), for green roofs model is given in Fig.4 (extensive green roofs, 3D view) and Fig.5 (intensive green roofs, 3D view).

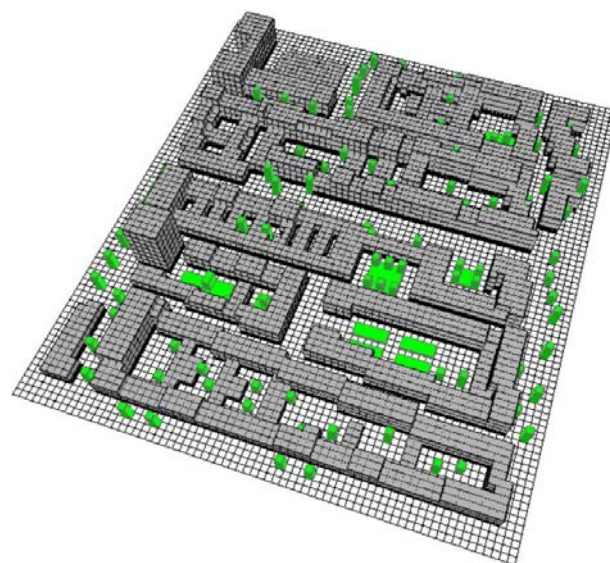


Fig.2. Base model input file – 3D view

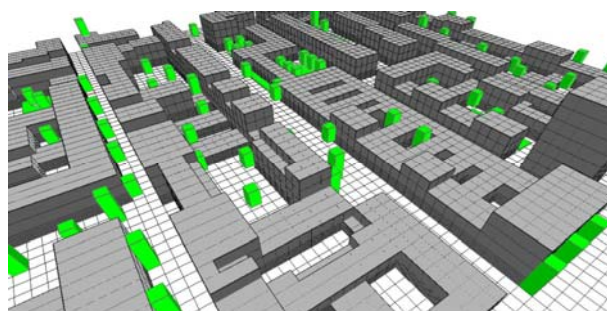


Fig.3. Base model input file, detail – 3D view

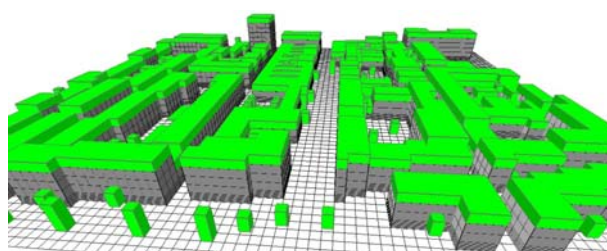


Fig.4. Model with extensive green roofs implemented, input file, detail – 3D view

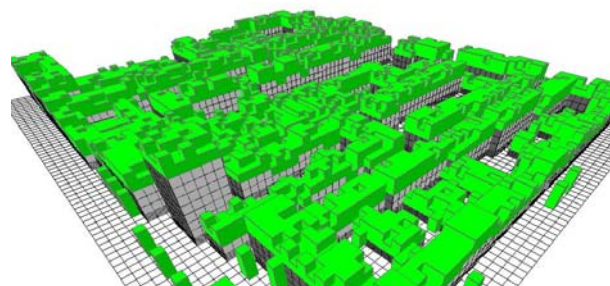


Fig.5. Model with intensive green roofs implemented, input file, detail – 3D view

Simulations were conducted for a 24 h period, for a typical summer day in Belgrade on 23 June. The simulations commenced at 05:00 am.

Table 1. Conditions and details of initial parameters for the simulations used in ENVI-met

<p><u>Start and duration of model run</u> Start Date (Simulation day): 23.06.2017. Start Time: 05:00:00 Total Simulation Time (h): 24</p> <p><u>Initial meteorological conditions</u> Wind speed measured at 10 m height (m/s): 1.9 Wind direction: 150 ° (SSE) Roughness length at measurement site: 0.01 Model rotation out of grid: North was set for the model</p> <p><u>Temperature T</u> Initial air temperature (°C) 16.8 min (°C) 16.8 (05:00 h), max 30.4 (16:00 h)</p> <p><u>Humidity q</u> Relative humidity (%) min 34 (16:00 h), max 62% (21:00 h), average 50%</p> <p><u>Geographic data for Belgrade, Serbia</u> Altitude 132 m Latitude 44°48'N Longitude 20°28'E</p> <p><u>Number and size of grid and nesting properties</u> Main model area: 350x450 m x-Grids:70, y-Grids: 80, z-Grids: 30 Size of grid cell in meters: dx=5.0, dy=5.0, dz=5.0 (base height) Nesting grids around main area: 3 Soil profiles for nesting grids: Default=unsealed soil</p>
--

RESULTS AND DISCUSSION

Fig.6 shows the CO₂ concentration in the atmosphere around buildings at different levels: pedestrian level (1.5 m), 7.5 m and 17.5 m respectfully, for the base model and two models of retrofitting strategies (extensive green roofs and intensive green roofs). The concentration of CO₂ in the atmosphere is shown at 7 in the morning, for a typical summer day in Belgrade, with a mild wind of 1.9 m/s.

Observing the CO₂ concentration, a decreasing trend in reducing concentration in the investigated retrofitting strategies is observed, respectively. A

larger impact on CO₂ reduction has a strategy with intensive green roofs than extensive one.

At all examined cross-cuts, intensive green roofs give a greater contribution than extensive green roofs.

Reduction intensity is directly related from the distance of the green roof. The results of the numerical simulation show that the most intensive impact is at a height of 7.5 meters. This can be explained by the fact that the percentage of buildings with roof tops at 18, 20, 25 and 40 meters is lower than those with roof surfaces at level of 8, 10, 12 and 15 meters, and the result of the impact is expected to be higher at 7.5 meters than 17.5 meters.

Fig.7 and Fig.8 present comparisons for three models – base model with black roofs, model with extensive green roofs and model with intensive green roofs. Minimum and maximum values are displayed for 7 am and 7 pm.

Since the vegetation is more active during the morning hours, decrease in the concentration of CO₂ around objects is observed with the use of vegetative roofs. Intensive green roofs make a greater contribution than the extensive (Fig.7).

Plants absorb CO₂ from the atmosphere for photosynthesis and release CO₂ to the atmosphere during respiration. The rate of photosynthesis depends on the intensity of light. In the daytime with a lot of sunlight, photosynthesis is very active and plants absorb CO₂, resulting in reducing the CO₂ concentration in the surrounding. At night photosynthesis becomes weak and vegetation acts as a source of CO₂ due to respiration, resulting in a higher CO₂ concentration. Because of this process, it is noticeable that there is a small contribution to increasing the concentration of CO₂ in the evening hours, as can be seen in Fig.8.

During periods of direct sunlight intensive green roofs with its denser and higher vegetation contributes to greater impact on improving air quality. Therefore in periods of intense respiration of plants vegetation on intensive green roofs emits more CO₂ than plants on an extensive green roof, which contains only low-growth plants.

In a typical summer sunny day in Belgrade, the CO₂ absorption rate of a green roof vegetation in the daytime is much greater than the CO₂ emission rate at night, as other authors also stated for their location [5].

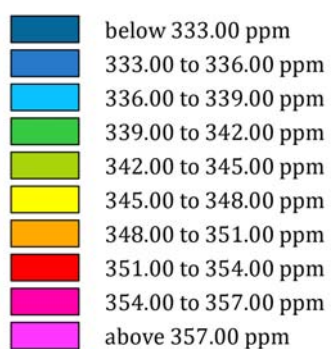
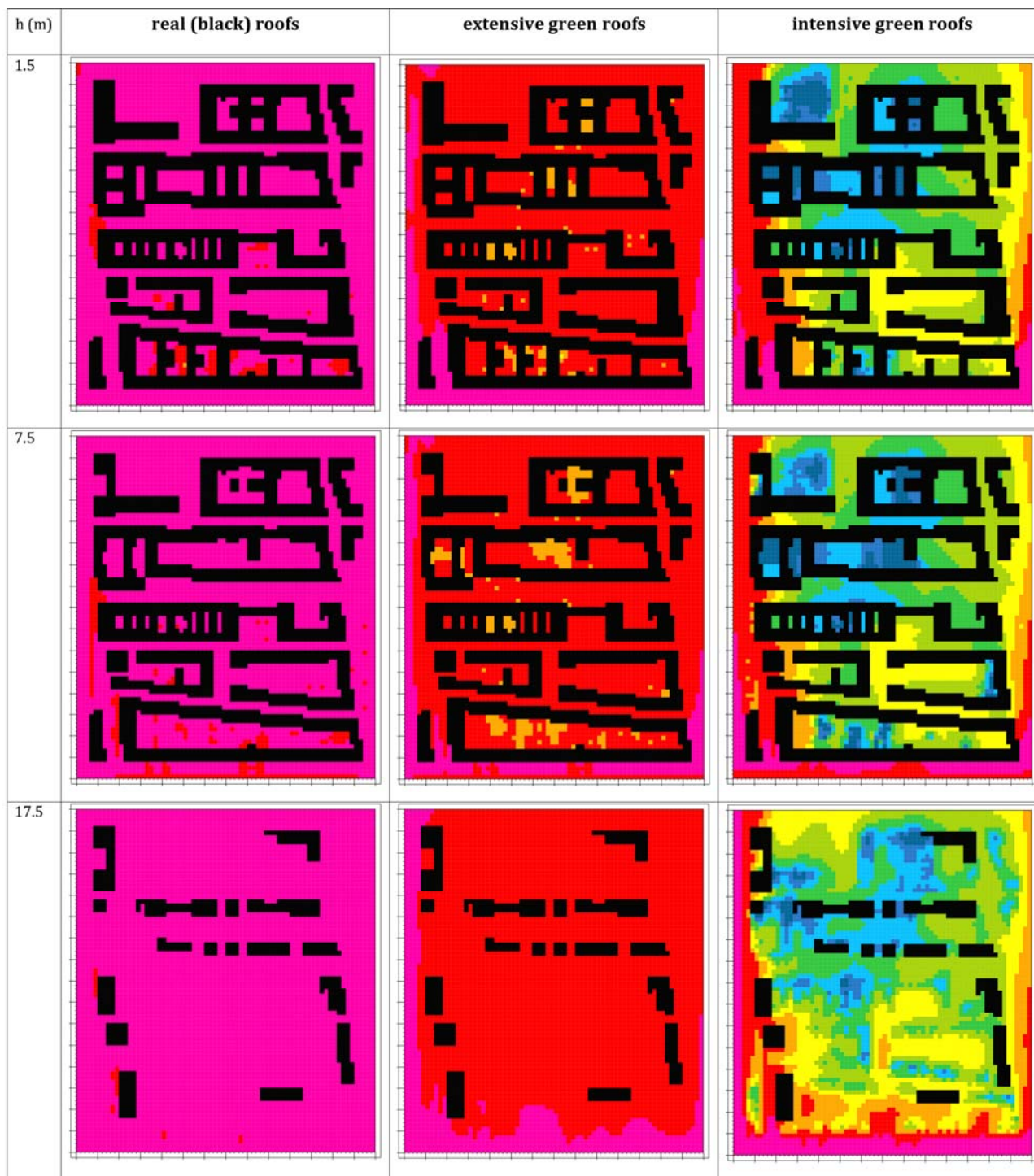


Fig.6. Detailed maps of CO₂ concentration (ppm) for base model, extensive green roofs model and intensive green roofs model, at pedestrian level (1.5 m), 7.5 m and 17.5 m high for typical summer day in Belgrade at 7 am

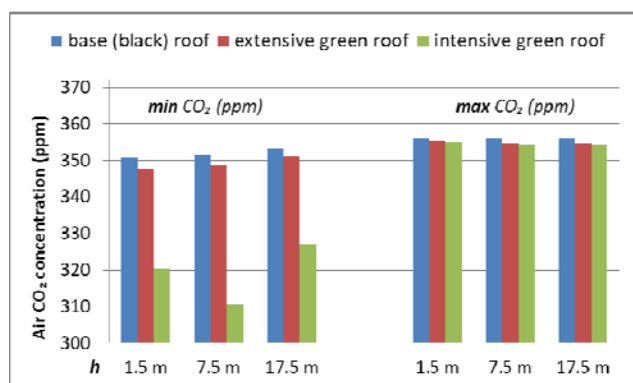


Fig. 7. Minimal and maximal CO₂ concentration (ppm) for base model and two retrofitted models (extensive and intensive green roofs models) at levels of 1.5 m, 7.5 m and 17.5 m on 23 June at 7 am

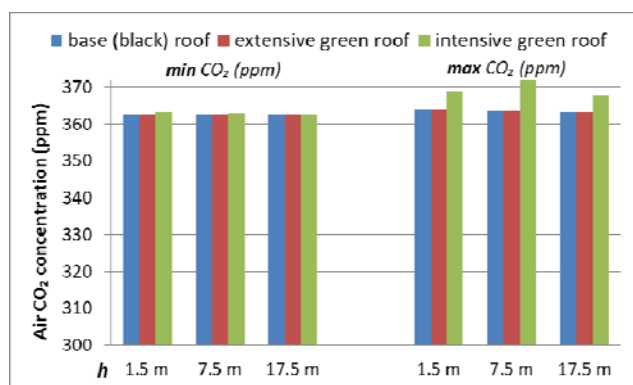


Fig. 8. Minimal and maximal CO₂ concentration (ppm) for base model and two retrofitted models (extensive and intensive green roofs models) at levels of 1.5 m, 7.5 m and 17.5 m on 23 June at 7 pm

At Fig. 9 is shown a potential difference in the CO₂ concentration at a height of 7.5 meters, between the base model with black roof and the models with implemented intensive green roofs.

It is noticeable that the impact of intensive green roofs is significant, especially in the interior of housing blocks. At the observed height of 7.5 meter, it is concluded that impact is smaller in areas where the roof level is 20, 25 or 40 meters. A numerical simulation was run for a typical summer day with a mild wind, so this difference is noticeable. It can be assumed that, in days with strong wind, air mixing is more intense, which would lead to a more unified CO₂ concentration in the air around the objects.

In an explored case with intensive green roofs, the reduction is up to a maximum of 44.81 ppm (up to 11%) compared to the base model. The average decrease in the concentration for the observed comparison of CO₂ is 9.41 ppm (2.3%).

General conclusion is that green roofs contribute to the reduction of the CO₂ concentration to a large extent.

Also, it can be concluded that the closer to the green roof region is, the greater the reduction of CO₂ concentration will be.

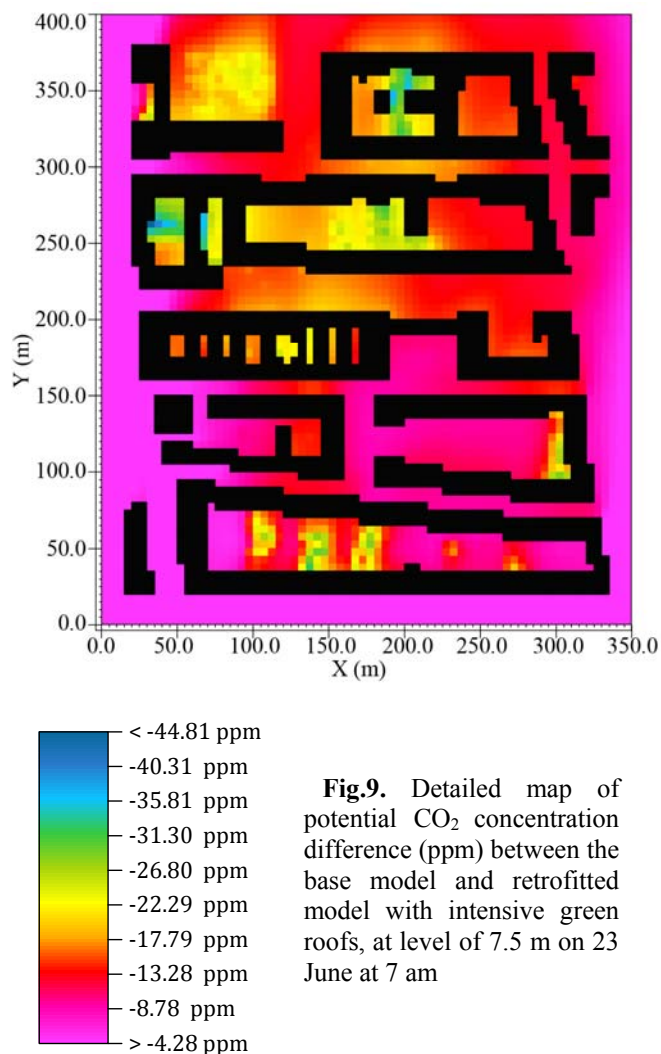


Fig. 9. Detailed map of potential CO₂ concentration difference (ppm) between the base model and retrofitted model with intensive green roofs, at level of 7.5 m on 23 June at 7 am

Result validation of ENVI-met numerical modelling is done by comparing it with verified data from other researches.

In a case study of Hong Kong [5] the authors concluded that the decrease of ambient CO₂ concentration near green roofs is substantial. The paper studied the effect of a green roof on the ambient CO₂ concentration as an example to assess the benefit of urban greening. The study comprises three parts. Firstly, field measurement of the difference of CO₂ concentration at a location in the middle of the plants in a small plot of green roof and one in the surrounding area with bare roof were

done. Data showed that the CO₂ concentration above the green roof, on a typical sunny day with light wind, was 4.3 mg/m³ lower than at the control roof during the day time before 4 pm and slightly higher during the night time. In the second part, in order to further evaluate the effect of green roofs on ambient CO₂ concentration, the authors measured the CO₂ of the green roof in a chamber to construct an absorption/emission velocity curve. In the third part of research, the author modelled the green roof effects in an urban area with a species transport module from commercial computational fluid dynamics software, using absorption/emission velocity curve. Simulation results showed that CO₂ concentration around the green roof fell noticeably. Depending on the amount of wind facilitating the mixing, the reduction of CO₂ concentration in the green roof vicinity reached up to 9.3 %. In Belgrade, the maximum values with the implementation of intensive green roofs are similar (up to 11%). Authors for Hong Kong stated that in a sunny day, a green roof may lower the CO₂ concentration in the nearby region as much as 2%. In our case average difference in CO₂ is 2.3%, which is in a similar range.

The paper [7] that was aimed at evaluating the potentials of extensive green roofs in increasing the ecological function in urban areas compared to impervious surface rooftops by discussing a green roof case study from the South-eastern Tehran is interesting to compare with our results. The main objective of the study was to evaluate the genuine effect of extensive green roofs on microclimatic conditions and air quality parameters. Two buildings with different roof covers (green and bitumen roof) were selected. Air temperature, relative humidity and carbon dioxide concentration data loggers were installed on both of them in two different conditions. For a typical sunny day, results demonstrated that average air CO₂ concentration inside and outside of the screen box above the green roof during the studied period were on average 27.98 and 20.71 ppm lower than the reference roof. In our research we have lower results for extensive green roof case (4.71 ppm), which can be explained by the fact that the concentration of CO₂ in South-eastern Tehran experiment was measured at 1 meter above the roof surface. In such case CO₂ concentration is expected to be lower due to the immediate proximity of the plants that are responsible for carbon sequestration. Also, there is a great difference in the climatic

condition between South-eastern Tehran and Belgrade.

It can be concluded that even low rise vegetation on a roof surface can contribute to the reduction of the CO₂ content in the air, as the other authors concluded [7].

Carbon dioxide is an essential component of the air, and very important for the photosynthesis of vegetation. Plants use photosynthesis to convert the CO₂ from the air into glucose. The higher the biomass of a plant, the higher it absorbs the CO₂. The result of that process is reducing CO₂ concentration in atmosphere around buildings with vegetative roofs on the top. Intensive green roofs have higher biomass than extensive, which results higher lowering CO₂ concentration in case with retrofitting strategy with intensive green roofs model.

The increase of green space in the urban area may potentially contribute to reduce of CO₂ atmospheric concentration.

In densely populated urban units and built-up zones such as investigated one, roof surfaces are almost the only surfaces which could be planted and provide the only chance for some parts of the city to become green oases. Installing green roofs on existing buildings would increase the percentage of planted green surfaces by 43 %.

CONCLUSIONS

This paper uses green roofs systems (extensive and intensive) in densely built urban neighbourhood as an example to quantify their effect on the ambient CO₂ concentration.

After the construction and investigation of the base model, two additional sustainable urban models were constructed. Base model contained all the relevant characteristics of the existing condition – the position, size and shape of buildings, position and type of plants, distribution of surface materials and soil types – representing the current condition for the urban location.

The base model was used as the reference for comparison with the sustainable retrofitting strategies, in which extensive green roofs or intensive green roofs were implemented on all buildings. Except the implementation of green roofs, other parameters of the model were not altered.

The discussion concentrates on how green roofs, both extensive and intensive, influence on reducing

carbon dioxide concentration in atmosphere in urban environment.

It can be concluded from this numerical research that installation of green roof systems on larger urban matrices or in urban neighbourhoods would contribute to CO₂ concentration reductions.

The CO₂ concentration around the green roofs falls noticeably due to the green roof serving as a sink of CO₂.

Atmospheric CO₂ concentration above the base (reference) roof was more than the extensive green roof model and intensive green roof model, due to the effect of vegetation on CO₂ absorption.

This research showed the use of intensive green roofs would produce greater reductions of the CO₂ concentration than did extensive green roofs, at all investigated levels, for a typical sunny day in Belgrade.

The greatest influence of the mitigation of the concentration of CO₂ is felt in the immediate vicinity of the plants.

The paper also refers to green roofs as a new technology and one of the segments of green construction that represent a modern approach to finding sustainable solutions. Green roofs are important for modern architecture and add new value to the role of buildings in urban planning. They are designed not only to return the natural element to the urban environment, but also to provide solutions for important problems such as the effect of urban heat island and high CO₂ concentration.

Innovative and sustainable approaches in urban areas can be adopted to remove existing air pollutants thereby reducing air pollution concentrations. One way to reach that goal is the use of green roofs which can reduce air pollutants through microclimate effects.

While it is desirable to use trees for controlling air pollution, it is not always easy to plant trees in cities, especially in densely populated urban areas. Green roofs can be used to supplement the use of urban vegetation in air pollution improvement and control.

Presented study reports the positive environmental effects of green roofs and provides a scientific basis for understanding the use of green roofs on existing and planned buildings. It also affords evidence for promoting the use of green roofs among the academic community, decision makers, residents and investors.

ACKNOWLEDGEMENTS

Authors are grateful to Ministry of Education, Science and Technological development of the Republic of Serbia for funding this research (in frame of projects III42011 and OI176006). This work has also been supported by the Interreg Danube Transnational Programme through the project Smart Building - Smart Grid - Smart City (3Smart), <http://www.interreg-danube.eu/3smart>, grant DTP1-502-3.2-3Smart.

REFERENCES

- [1] Asian Development Bank. Nature-Based Solutions for Building Resilience in Towns and Cities: Case Studies from the Greater Mekong Subregion. Asian Development Bank, 2016.
- [2] G. Ngan. Green Roof Policies: Tools for Encouraging Sustainable Design. Vancouver, Canada, 2004.
- [3] O. Saadatian, K. Sopian, E. Salleh, C. H. Lim, S. Riffat, E. Saadatian, A. Toudeshki, M. Y. Sulaiman. A review of energy aspects of green roofs. *Renewable and Sustainable Energy Reviews* **23**, 155–168 (2013).
- [4] U. Berardi, A. GhaffarianHoseini, A. GhaffarianHoseini. State-of-the-art analysis of the environmental benefits of green roofs. *Applied Energy* **115**, 411–428 (2014).
- [5] J. Li, O. W. H. Wai, Y. S. Li, J. Zan, Y. Alexander Ho, J. Li, E. Lam. Effect of green roof on ambient CO₂ concentration. *Building and Environment* **45**, 2644–2651 (2010).
- [6] Y. Li, R. W. Babcock. Green roofs against pollution and climate change. A review. *Agronomy for Sustainable Development* **34**, 695–705 (2014).
- [7] M. Moghbel, R. Erfanian Salim. Environmental benefits of green roofs on microclimate of Tehran with specific focus on air temperature, humidity and CO₂ content. *Urban Climate* **20**, 46–58 (2017).
- [8] H. Agra, T. Klein, A. Vasl, G. Kadas, L. Blaustein. Measuring the effect of plant-community composition on carbon fixation on green roofs. *Urban Forestry and Urban Greening* **24**, 1–4 (2017).
- [9] A. H. Rosenfeld, H. Akbari, J. J. Romm, M. Pomerantz. Cool communities: Strategies for heat island mitigation and smog reduction. *Energy and Buildings* **28**, 51–62 (1998).
- [10] D. B. Rowe, G. P. Robertson, B. M. Cregg, J. A. Andresen. Carbon sequestration potential of extensive green roofs. *Environmental Science and Technology* **43**, 7564–7570 (2009).
- [11] J. Heusinger, S. Weber. Extensive green roof CO₂ exchange and its seasonal variation

- quantified by eddy covariance measurements. *Science of the Total Environment* **607–608**, 623–632 (2017).
- [12] L. J. Whittinghill, D. B. Rowe, R. Schutzki, B. M. Cregg. Quantifying carbon sequestration of various green roof and ornamental landscape systems. *Landscape and Urban Planning* **123**, 41–48 (2014).
- [13] J. Yang, Q. Yu, P. Gong. Quantifying air pollution removal by green roofs in Chicago. *Atmospheric Environment* **42**, 7266–7273 (2008).
- [14] D. B. Rowe. Green roofs as a means of pollution abatement. *Environmental Pollution* **159**, 2100–2110 (2011).
- [15] Y. Wang, U. Berardi, H. Akbari. Comparing the effects of urban heat island mitigation strategies for Toronto, Canada. *Energy and Buildings* **114**, 2–19 (2016).
- [16] V. Tsilini, S. Papantoniou, D. D. Kolokotsa, E. A. Maria. Urban gardens as a solution to energy poverty and urban heat island. *Sustainable Cities and Society* **14**, 323–333 (2015).
- [17] M. Taleghani, L. Kleerekoper, M. Tenpierik, A. Van Den Dobbelen. Outdoor thermal comfort within five different urban forms in the Netherlands. *Building and Environment* **83**, 65–78 (2015).
- [18] G. Battista, E. M. Pastore, L. Mauri, C. Basilicata. Green Roof Effects in a Case Study of Rome (Italy). *Energy Procedia* **101**, 1058–1063 (2016).
- [19] T. Shen, D. H. C. Chow, J. Darkwa. Simulating the influence of microclimatic design on mitigating the urban heat island effect in the Hangzhou metropolitan area of China. *International Journal of Low-Carbon Technologies* **11**, 130–139 (2014).
- [20] M. Bruse, H. Fleer. Simulating surface-plant-air interactions inside urban environments with a three dimensional numerical model. *Environmental Modelling and Software* **13**, 373–384 (1998).

Energy efficiency of wind power plants, Case of Lithuania

R. Tamašauskas^{1*}, P. Bruzgevičius², J. Šadauskienė³, D. Nikolic⁴

¹*Kaunas Technical College, Tvirtovės av. 35, LT-50155 Kaunas, Lithuania*

²*JSC „Iraža“ Tunelio str. 60, LT-4440 Kaunas, Lithuania*

³*Kaunas University of Technology, Faculty of Civil Engineering and Architecture, Studentų st. 48, LT - 51367 Kaunas, Lithuania*

⁴*Faculty of engineering at University at Kragujevac, Seste Janic 6, 34000 Kragujevac, Serbia*

The use of energy from wind power plants in a building must be subdivided into renewable and non-renewable energy. Wind power efficiency increases with less auxiliary, i.e. non-renewable energy to produce the same share of electricity. The conditions and circumstances of wind power use are assessed in the calculation of the values of the primary renewable and non-renewable energy factor. The European Standard EN 15603 covers the main principles for calculating primary factors for renewable and non-renewable energy. However, the specific factor values for electricity produced in different wind power plants are determined in accordance with national conditions and requirements. In this article, in accordance with the main regulations of EN 15603, the main factor of non-renewable energy of different power-generating wind power plants was calculated using electricity generation and Lithuanian wind power data and Lithuanian climate conditions in 2007. -2014. Research has shown, that the values of non-renewable primary energy factor for wind turbines operated in Lithuania and calculated according to EN 15603 methodology is 97 % lower than the numeric indicator from the same standard used for calculations.

Keywords: Primary energy, renewable energy, wind power, auxiliary energy, energy efficiency

INTRODUCTION

Declared values of primary energy are used in energy policy making, setting energy saving goals or reporting energy efficiency in the national and international energy statistics, scenarios, environmental impact assessments, European legislation (Directive 2006/32/EB, Directive 2012/27/EU, Directive 2009/28/EC, Directive 2010/31/EU); SEC 2011) and standards (EN 15603:2014; EN 15316-4-5:2007). The demand of primary energy, required to produce one unit of secondary energy, is calculated by means of primary energy factors (PEF). They are called the conversion factors that characterize the entire totally primary energy demand in the energy supply chain to the final consumer. According to the standard EN 15603:2014 totally primary energy is divided into renewable primary energy and non-renewable primary energy.

According to the directive 2010/31/EU it is recommended to use renewable energy sources and to reduce the share of non-renewable energy in the buildings by erecting energy-efficient buildings. Different sources of renewable energy are used in buildings, e.g. sun, wind, hydro, biomass, geothermal, biogenic fraction of waste. They have different PEFs. Energy consumption is one of the areas where PEF values may be meaningful for the

end user when energy source selection decisions are made with the aim to meet the requirements for a nearly zero-energy building (passive house). Literature sources mainly analyse the issues of wind turbine efficiency: wind turbine components (propellers, gear-boxes, generators, transformers) [1–3], accumulation and integration into power grids [4]. Wind parameters receive much attention in the evaluation of renewable energy sources in buildings, however, little information is given about the characteristics of wind energy source. The parameters of wind energy use are not sufficiently analysed too [5]. PEF in production of electricity from wind is calculated by using different methodologies (Tab.1).

The data given in Tab.1 shows that different methodologies render different PEF values for the evaluation of wind energy, therefore it is difficult to compare the values of primary energy or primary energy factors. The primary energy factor for the same source of renewable energy may differ significantly depending on the type of primary energy and applied calculation method [11].

The data are given in Tab.1 also shows that PEF values depend on the energy production and supply chain. Energy production and supply chains differ by countries and subsequently, PEF values are also different. Unfortunately, only a few countries publicly announce this data (Tab.2).

* To whom all correspondence should be sent:
rokas.tamasauskas@edu.ktk.lt

Table 1. Parameters of different methodologies for the evaluation of primary energy produced from the wind

MJ _{primary energy} /MJ _{electricity}	Description of primary energy evaluation	PEF value	PEF value	Literature source
1. Zero equivalent method	Does not evaluate electrical and thermal energy production from renewable energy sources	Total primary energy	0.000	[6]
2a Direct equivalent	Evaluates electrical and thermal energy production from non-fossil renewable energy and nuclear energy sources	Total primary energy	1.000	[7]
2. Amount of physical energy				
2b	Evaluates the primary form of energy obtained in generation process	Total primary energy	1.000	[8]
2c Alternate	Evaluates the primary form of energy that is included into the statistical energy balance prior to conversion to the secondary or tertiary form of energy	Total primary energy	2.500	[9]
3. Only non-renewable primary energy	-	Non-renewable primary energy	0.032	[10]
4a Effectiveness of technical conversion	Evaluates the entire energy production chain by separating the renewable and non-renewable energy	Non-renewable primary energy	0.032	[9,10]
		Renewable primary energy	2.500	
4. Amount of physical energy				
4b	Evaluates the primary form of energy produced in the generation process	Non-renewable primary energy	0.032	[8,10]
		Renewable primary energy	1.000	

The data are given in Tab.1 also shows that PEF values depend on the energy production and supply chain. Energy production and supply chains differ by countries and subsequently, PEF values are also different. Unfortunately, only a few countries publicly announce this data (Tab.2). National standards and norms governing construction work in many EU member states do not include these documents or do not further specify the renewable energy values; therefore it is not clear

whether these values are valid for defining wind energy or are merely politically grounded values not meant for technical or scientific applications.

Table 2. Wind electricity energy values used in construction work standards of EU countries

Country	Primary energy factor	Total primary energy factor	Non-renewable primary energy factor	Renewable primary energy factor	Literature source
Austria	-	-	-	-	[12]
Belgium	-	-	-	-	[13]
Cyprus	-	-	-	-	[14]
Czech-Republic	-	-	-	-	[15]
Denmark	-	-	-	-	[16]
Estonia	-	-	-	-	[17]
Finland	-	-	-	-	[18]
France	1.000	-	-	-	[19]
Germany(1)	-	-	-	-	[20]
Germany(2)	-	1.030	0.030	1.000	[21]
Greece	-	-	-	-	[22]
Hungary	0.000	-	-	-	[23]
Ireland	-	-	-	-	[24]
Italy	-	1.000	0.000	1.000	[25]
Netherlands	-	-	-	-	[26]
Poland	-	1.000	0.000	1.000	[27]
Slovakia	-	-	-	-	[28]
Slovenia	-	-	-	-	[29]
Spain	-	-	-	-	[30]
Sweden	-	0.050	-	-	[31]
United Kingdom	1.000	-	-	-	[32]

Note: - not mentioned.

According to the data presented in Tab.2, presumably, the energy consumed by the wind turbines is not included in the total energy produced from the renewable source, i.e. wind energy. Power to the internal system of wind turbines is supplied from batteries/condensers or from the electrical grid. Various equipment of wind turbines use electric power and its energy consumption may reach up to 0.1% of the total produced energy, in other cases up to 10-20% of the rated power of the wind turbines [33].

MATERIALS AND METHODS

Primary energy calculation methodology

Energy efficiency of a building is calculated as the balance of the used and produced energy. The main aim of constructing energy efficient buildings is to increase the share of renewable energy and decrease the demand for primary energy. PEF of

electrical energy produced on-site or nearby or renewable energy supplied from the electrical grid has a direct influence on the calculation of the total primary energy factor. There are two possibilities: to increase the share of electricity produced from renewable energy sources in electrical grids (Baake found that in 2020 PEF in European electricity grids will drop to 2.500 compared to the current PEF, in 2030 it will drop to 1.650 and in 2050 it will drop to 1.200 [34]) and to use electricity produced on-site or nearby from renewable sources, including wind turbines [35].

In almost all sources of renewable energy part of the energy is non-renewable, therefore the requirement for nearly zero-energy buildings in the Directive 2010/31/EU is to use more than half of the energy produced from renewable sources. It may be related only to the amounts of renewable and non-renewable primary energy, consumed by the building, but not with the energy produced from renewable or non-renewable sources. Therefore, it is not correct to use the methodologies presented in Tab.1 for the calculation of PEF in photovoltaic/wind power systems. In this regard, PEF of wind turbines shall be calculated using the methodology described in EN 15603:2014.

The total primary energy demand of the building is calculated (Eq.1):

$$E_p = \sum (E_{del,i} f_{P,del,i}) - \sum (E_{exp,j} f_{P,exp,j}) \quad (1)$$

where:

E_p – primary energy demand, kW·h;

$E_{del,i}$ – final energy demand by the energy carrier, kW·h;

$f_{P,del,i}$ – primary energy factor depending on the energy carrier, kW·h;

$E_{exp,i}$ – final energy exported by the energy carrier, kW·h;

$f_{P,exp,i}$ – primary energy factor of the exported energy carrier, kW·h.

The total primary energy may be calculated by equation 2:

$$f_{P,tot} = f_{P,nren} + f_{P,ren} \quad (2)$$

where:

$f_{P,tot}$ – total primary energy, kW·h;

$f_{P,nren}$ – non-renewable primary energy, kW·h;

$f_{P,ren}$ – renewable primary energy, kW·h.

Methodology for the evaluation of electrical energy production from wind energy source

Kot method [36] was chosen for the evaluation of electrical energy produced by a wind turbine, taking into consideration the effect of factors on the efficiency. According to this method, electrical

energy produced by a wind turbine is calculated from Eq.3:

$$P_e = \frac{1}{2} \pi R^2 \rho V^3 C_p \eta_g \eta_c \quad (3)$$

where:

ρ is air density, kg/m³;

R is turbine rotor radius, m;

V is wind speed, m/s;

C_p is turbine power factor;

η_g is generator efficiency;

η_c is inverter efficiency.

C_p factor is calculated from Eq.4:

$$C_p = \frac{P_M}{P_W} \quad (4)$$

where:

P_M is mechanical power, W;

P_W is wind power, W.

In theory, C_p value may not exceed the limit expressed by Betz law, Eq.5. In typical turbines this value varies ~0,4 [37]:

$$C_{p,max} = \frac{16}{27} \approx 0,593 \quad (5)$$

Climate data and investigated location of case study

Wind turbines across the entire territory of Lithuania were tested in order to determine the influence of electrical energy cost on the value of wind PEF. Lithuania is situated in the Middle Latitudes. According to Alisov's climate classification, Lithuania is in the zone of a temperate climate and the sub-region of the Atlantic-European continental zone. Only the climate of the Baltic Sea coast is close to the western European climate and can be assigned to a separate South Baltic climate sub-region. South-western and western winds prevail in the major part of Lithuanian territory, with western and south-eastern winds on the coastal zone. The average wind speed at 10-meter height ranges from 4 m/s to 6.5 m/s. The highest wind speed is in the coastal zone, where it reaches 5 – 6.5 m/s and decreases moving away from the coast eastwards [38].

The highest wind speeds in the center of Lithuania are observed in November – January and in October – December in the coastal zone; the lowest wind speeds are in June – July.

Table 3. Basic characteristics of the studied wind turbine

No of tested Wind turbines	Total installed power capacity	Turbine capacity	No of turbine	Turbine type	No of blades	Blade length	Tower height	Turbine location
	MW	MW				m	m	
1A	39.100	2.000	20	horizontal	3	41	85	Šilutė district
2A	34.000	2.000	17	horizontal	3	41	97	Kretinga district
3A	21.400	2.000	10	horizontal	3	41	85	Šilutė district
4A	20.000	2.000	10	horizontal	3	41	85	Tauragė district
5A	16.000	2.750-3.000	6	horizontal	3	41	85	Kretinga district
6A	12.000	2.000	6	horizontal	3	41	78	Šilutė district
1B	0.800	0.800	1	horizontal	3	21	45	Kretinga district
2B	0.800	0.800	1	horizontal	3	21	45	Mažeikiai district
3B	0.600	0.600	1	horizontal	3	20	42	Mažeikiai district
4B	0.250	0.250	1	horizontal	3	15	50	Jurbarkas district
5B	0.250	0.250	1	horizontal	3	15	50	Mažeikiai district
6B	0.250	0.250	1	horizontal	3	15	45	Kaišiadoriai district
7B	0.250	0.250	1	horizontal	3	15	55	Kalvarija district
8B	0.225	0.225	1	horizontal	3	14	50	Tauragė district

In June and July, Lithuanian wind turbines produce about two times less energy compared to December and January. In the summertime, the highest wind speed is between midnight and 6 AM. In the morning it increases until noon and reaches a peak at about 2 PM. The peak speeds last until 6 PM and afterward start dropping to the minimum values that are reached about midnight. In the wintertime, the changes of wind speed are less due to lower fluctuation of air mass temperatures influenced by smaller amounts of solar radiation energy. Wind energy resources in Lithuania were evaluated by measuring data from meteorological stations as well as measurements obtained from various research centers in the regions. The western part of the country is the most suitable for wind turbines because of prevailing wind speeds and more developed transmission networks [39].

Depending on the prevailing wind speeds the efficiency of new wind turbines in Lithuania is 24-25 %, whereas the efficiency of old wind turbines is only 10-18 % [39]. The total capacity of wind turbines operating in Lithuania is 281 MW (the mainland potential is ~1500 MW, and the offshore potential is ~1000 MW). 111 single or group wind turbines are connected to the Lithuanian power grid: 10 small turbines (from 2 to 55 kW) and 101 big turbines (from 160 to 39100 kW) [40].

Research object

Data (Tab. 3) for research (for the period 2007-2014) were collected from 100 wind turbines and 11 wind farms operating in Lithuania. The data were collected by interviewing wind turbine owners/operators and by analyzing the reports of electricity transmission system operators [40].

The analysis of collected data revealed that the majority of wind turbine operators do not collect and systemize any data, do not have accounting instruments or are connected to other electrical energy users. The report of the Lithuanian electricity transmission system operator contains only the amounts of electricity transmitted from all wind turbines to the power grid for certain periods. Therefore, 6 wind farms and 8 wind turbines were selected for the study. The analysis of their results is presented in the following chapter.

RESULTS

The value of the primary non-renewable energy factor depends on the relationship between the amount of non-renewable primary energy and the balance of renewable energy produced by the wind turbine and consumed non-renewable electrical energy (Eq.2). The value of non-renewable energy source factor increases with the increase of consumed non-renewable electrical energy or the

decrease of renewable electrical energy produced by the wind turbine. The methodology provided in EN 15603:2014 gives only one PEF value for wind turbines irrespective of their capacity. The influence of wind turbine capacity on the PEF value is unknown. Therefore, it would be useful to classify wind turbines which were studied into groups of different capacity, to determine their PEFs, and afterward to compare the obtained values with the values provided in EN 15603:2014.

The calculated $f_{P_{nren}}$ factors of the analyzed (>1) MW wind turbines/farms are presented in Fig.1.

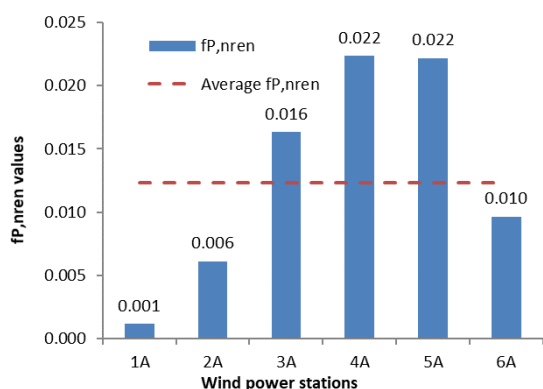


Fig.1. Relationship between $f_{P_{nren}}$ and wind power in (>1) MW wind turbines

The calculated $f_{P_{nren}}$ factors of the analyzed (<1) MW wind turbines/farms are presented in Fig.2.

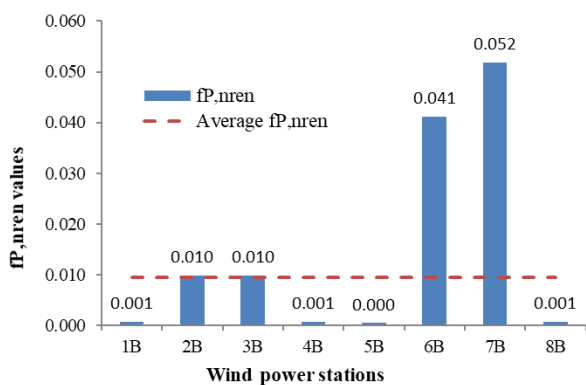


Fig.2. Relationship between $f_{P_{nren}}$ and wind power in (<1) MW wind turbines $f_{P_{nren}}$.

From the data presented in Fig.2, it may be concluded that the average numeric indicator of a $f_{P_{nren}}$ factor in wind turbines/farms of (>1) MW capacity is 0.012 kW·h (the dotted line). The lowest $f_{P_{nren}}$ factor value 0.001 is in wind turbine 1A, the highest factor value 0.022 kW·h is in wind turbines 4A and 5A.

The average numeric indicator of the $f_{P_{nren}}$ factor in wind turbines/farms of (>1) MW capacity illustrated in Fig.2 is 0.009 (the dotted line). Wind turbines 1B, 4B, 5B and 8B have the lowest $f_{P_{nren}}$ factor value 0.001, and wind turbine 7B has the highest factor value 0.052.

The obtained results lead to the conclusion that $f_{P_{nren}}$ factor value is influenced by the capacity of wind turbines. A trend is observed that in wind turbines of (>1) MW capacity this indicator decreases with a higher installed power capacity of wind turbines.

Another test was done by taking into consideration the influence of the average wind speed and the balance of produced and consumed electrical power on $f_{P_{nren}}$ value. The test results are presented in Figs. (3 – 10).

Fig.3 illustrates the average distribution of produced and consumed electric power in (>1) MW wind turbines/farms by months.

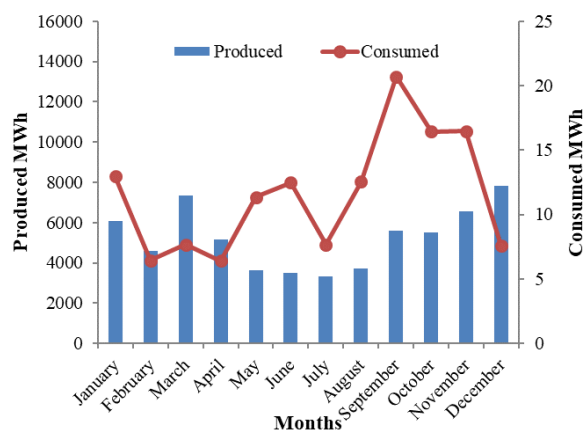


Fig.3. Average performance of (>1) MW capacity wind turbines/farms

Fig.4 illustrates the average distribution of produced and consumed electric power in (<1) MW wind turbines/farms by months.

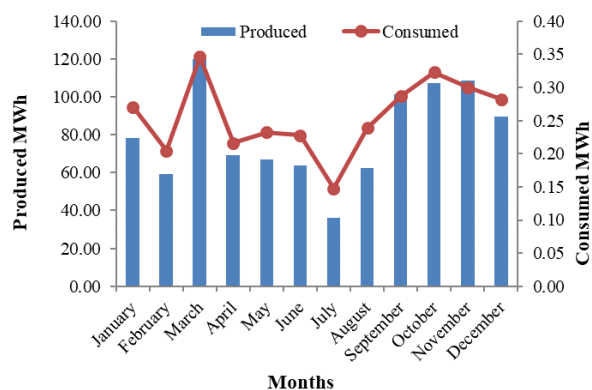


Fig.4. Average performance of (<1) MW capacity wind turbines/farms

The results presented in Fig.3 reveal the inverse relationship between the produced and consumed electric power in (>1) MW capacity wind turbines/farms. According to [33], there are constant turbine-power demand in the production of wind energy. The annual average of turbine-power consumption is up to 0.22 % of the total electric energy production. The consumed amount of electric energy is not constant and changes dynamically within seasons; most often it is higher in the warm season and lower in the cold season, i.e. it may reach 0.10 % in winter and 0.36 % in summer.

Fig.4 reveals a direct relationship between the produced and consumed electric power in (<1) MW capacity wind turbines/farms. The average annual turbine-power consumption is up to 0.32 % of the total produced electric energy. The consumed amount of electric energy is not constant and changes dynamically by seasons, most often it is higher in the warm season and lower in the cold season, i.e. it may reach 0.28 % in winter and 0.41 % in summer.

The obtained results revealed the relationship between the produced and consumed electric energy in wind turbines. The relationship is inverse in high-capacity wind turbines and direct in lower capacity wind turbines.

Figs. (5, 6, 7) illustrates the relationship between analyzed (<1) MW capacity wind turbines/farms power productions, consumption and wind speed.

Comparing data presented in Fig. (5, 7) lead to the conclusions that the amounts of energy produced by (< 1) MW capacity wind turbines/farms increase with higher wind speeds.

Fig.6 compare to Fig.7 reveals that the relationship between the energy consumed by (<1) MW capacity wind turbines/farms and wind speed is difficult to define, because, in 2B, 3B, 6B and 7B wind turbines energy consumption and wind speed is closer to linear, i.e. wind turbines consume more energy at higher wind speeds. Meanwhile, in the rest wind turbines (1B, 4B, 5B and 8B) energy consumption by all analyzed period was stable and it seems wind speed has no influence for energy consumption.

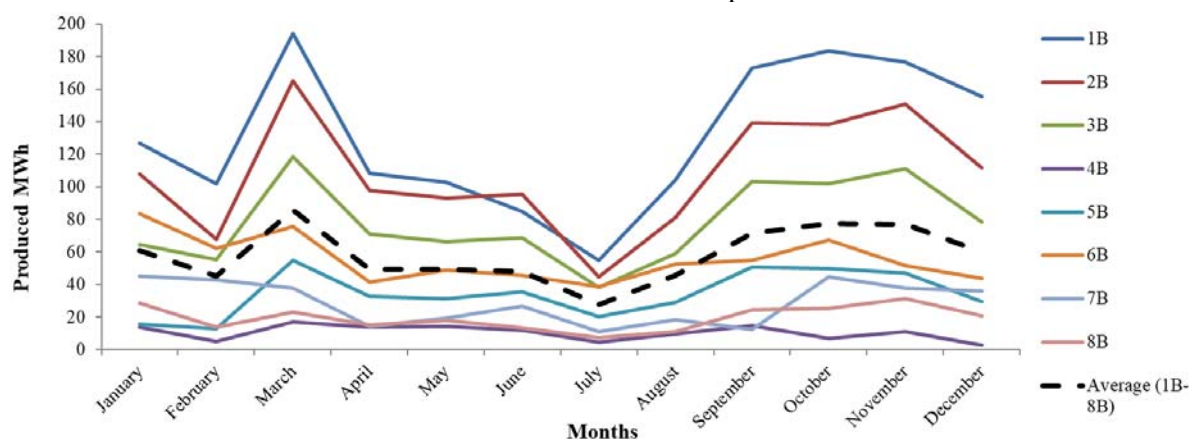


Fig.5 Electricity production performance of (<1) MW capacity wind turbines/farms

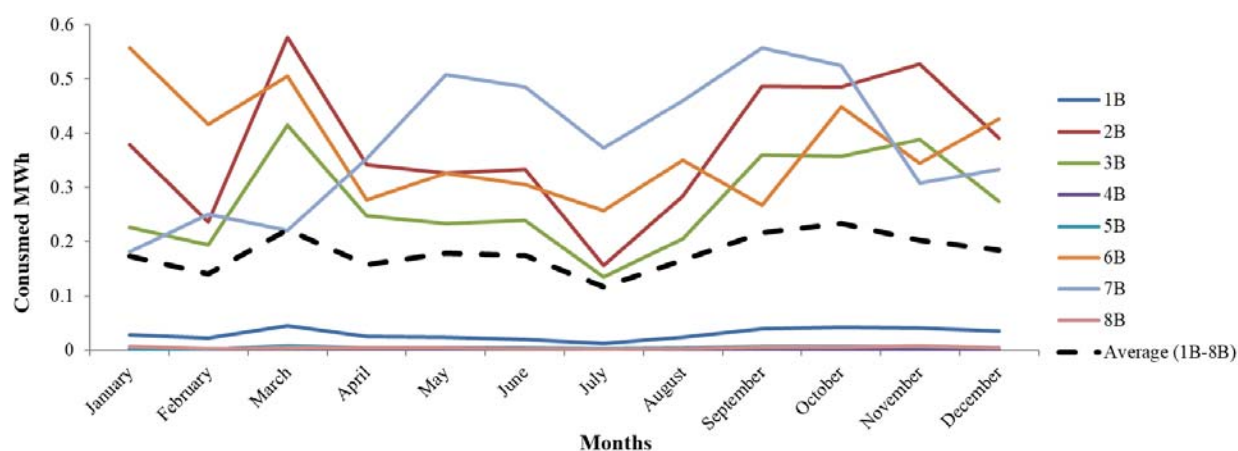


Fig.6. Electricity consumption performance of (<1) MW capacity wind turbines/farms

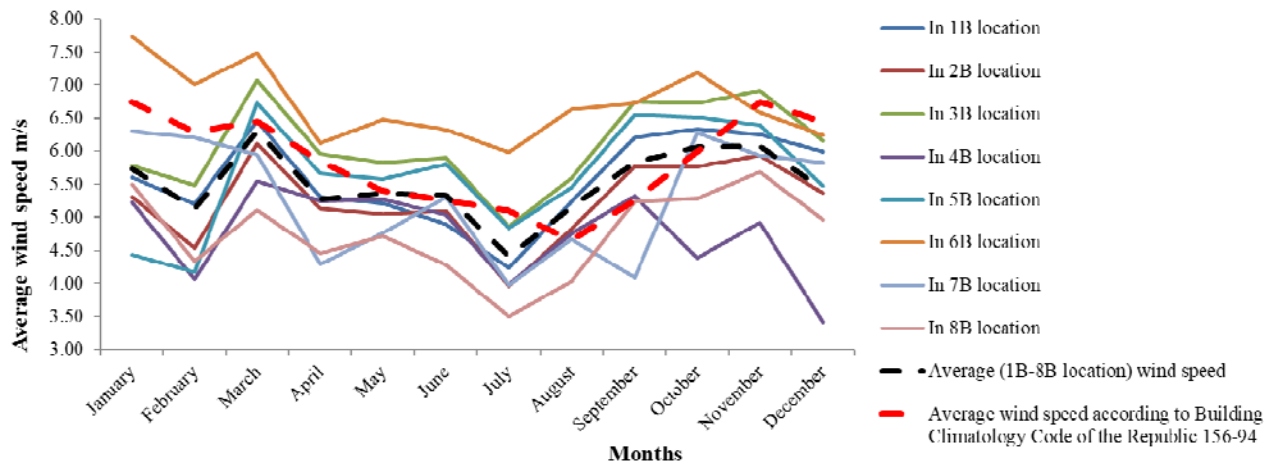


Fig.7. Wind speed in (<1) MW capacity wind turbines/farms

The resulting fluctuations for energy production and consumption may be explained by the efficiency of the wind turbine [1-3, 33] as well actual climate conditions of analysed wind turbines/farms location.

Evaluating according to Building Climatology Building Code of the Republic 156-94 (the dotted red line) in Fig.6 is not enough due to actual wind speed in real time.

Figs. (8, 9, 10) illustrates the relationship between analysed (>1) MW capacity wind turbines/farms power productions, consumption and wind speed.

Comparing the data presented in Figs. (8, 10) which shows that with higher wind speeds the amounts of energy produced by (> 1) MW capacity wind turbines/farms are tend to increase.

Fig.9 compared to Fig.10 reveals that the relationship between the energy consumed by (>1) MW capacity wind turbines/farms and wind speed is closer to linear, i.e. wind turbines consume more energy at higher wind speeds.

The resulting fluctuations for energy production and consumption may be explained by wind turbine efficiency [1-3, 33] as well as actual climate conditions of analyzed wind turbines/farms location.

Evaluating according to Building Climatology Building Code of the Republic 156-94 (the dotted red line) in Fig.10 is not enough due to actual wind speed in real time.

DISCUSSION

In order to meet the requirements, set forth in the Directive 2010/31/EU, the primary energy factor value for wind turbines is calculated following the methodology described in EN 15603:2014.

However, studies of wind turbines operated in Lithuania have shown that $f_{P_{nren}}$ and $f_{P_{tot}}$ values calculated according to the aforementioned methodology are imprecise (Tab.4).

Table 4. Comparison of wind turbine capacities and $f_{P_{nren}}, f_{P_{ren}}, f_{P_{tot}}$ values

Indicators	Values of wind turbines operated in Lithuania, kWh			Values according to EN 15603:2008
	(>1) MW capacity	(<1) MW capacity	Weighted average	
$f_{P_{nren}}$	0.012	0.009	0.010	0.300
$f_{P_{ren}}$	1.000	1.000	1.000	1.000
$f_{P_{tot}}$	1.012	1.009	1.010	1.300

Data presented in the table above shows that the values of non-renewable primary energy factors in (> 1) MW and (< 1) MW capacity wind turbines operated in Lithuania are similar (the average $f_{P_{nren}} = 0.010$). When these values are compared to the values given in EN 15603:2014, the value of non-renewable primary factor for wind turbines operated in Lithuania is 97% lower than the value given in the standard. EN 15603:2014 does not give any reference conditions and criteria used to determine the value of non-renewable primary energy factor.

The calculated total primary energy $f_{P_{tot}}$ of a wind turbine is also imprecise. The test results of wind turbines operated in Lithuania are presented in Tab.4 which show that this imprecision is about 22 % of the rated capacity of a wind turbine.

The test results revealed the importance of declaring precise primary energy values in energy policy making, in defining energy saving

goals or energy consumption efficiency in scenarios, environmental impact assessments, international and national energy statistics, directives and standards.

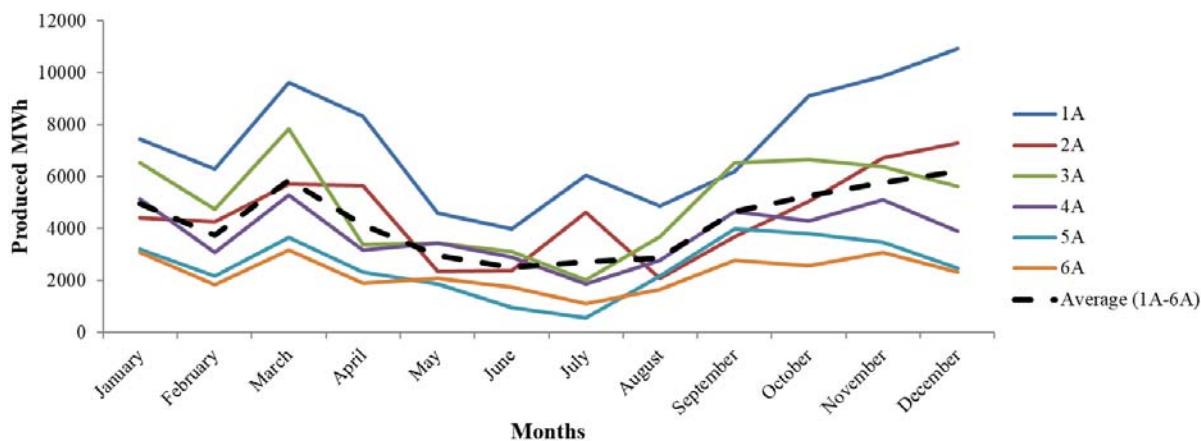


Fig.8. Electricity production performance of (>1) MW capacity wind turbines/farms

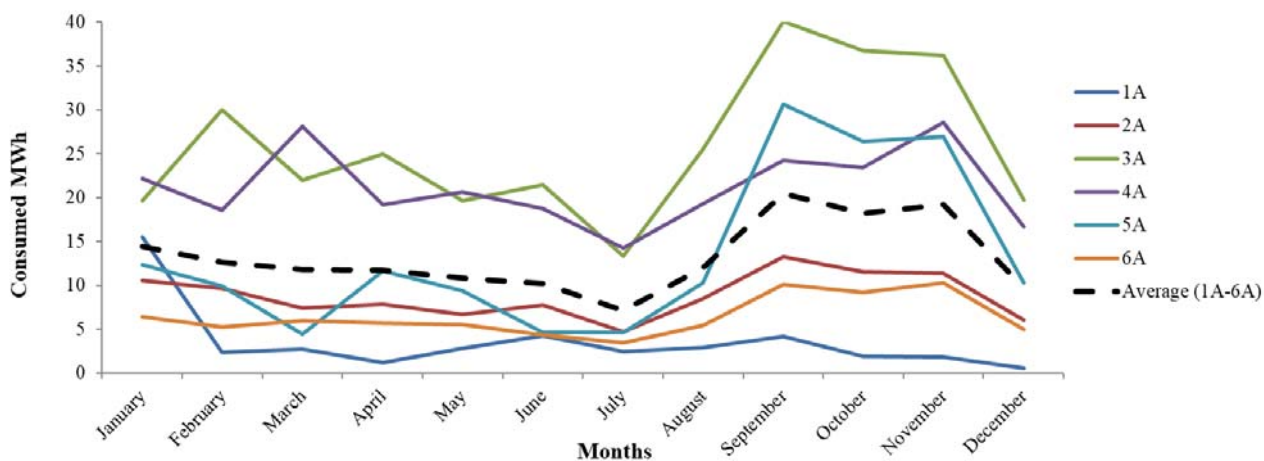


Fig.9. Electricity consumption performance of (>1) MW capacity wind turbines/farms

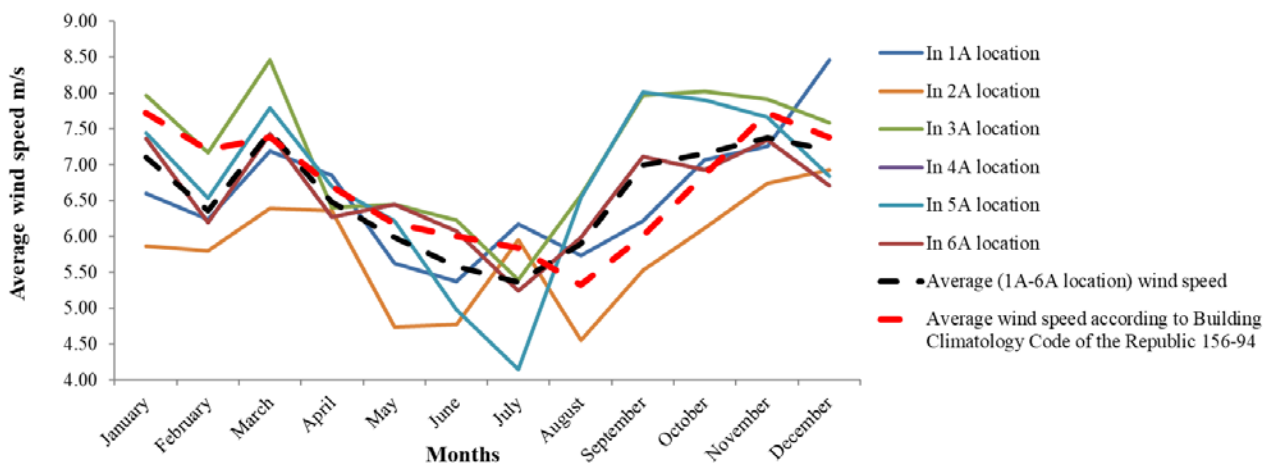


Fig.10. Wind speed in (>1) MW capacity wind turbines/farms

Every European Union member state should define the methodology for the calculation of primary energy in wind turbines as well as the statistical parameters of wind turbines and climate (wind speed, wind turbine capacity, conversion efficiency, turbine-power consumption etc.) for the calculation of PEF value. The progress of wind turbine technologies requires regular recalculation of these values.

The results of this study were used in drafting the national Technical Regulation for Construction Works STR 2.01.09:2012 Certification of Energy Performance of Buildings, which shall ensure the implementation of the provisions and goals of Directive 2010/31/EU in Lithuania.

CONCLUSIONS

The values of non-renewable primary energy factor $f_{P_{nren}}$ for wind turbines operated in Lithuania and calculated according to EN 15603:2014 methodology is 97 % lower than the numeric indicator from the same standard used for calculations.

Calculations of non-renewable energy factor $f_{P_{nren}}$ revealed that wind turbine capacity has no effect on the value of non-renewable energy factor $f_{P_{nren}}$. The value of non-renewable primary energy factor $f_{P_{nren}}$ is 0.010 (kW·h) for (> 1) MW and (< 1) MW capacity wind turbines operated in Lithuania.

The results of the study revealed that in (>1) MW capacity wind turbines the turbine-power consumption increases with lower wind speeds, whereas in (<1) MW capacity wind turbines it is on the contrary, i.e. the turbine-power consumption increases with higher wind speeds.

In order to achieve the goals set forth in EU energy efficiency and renewable energy directives and regulations all EU member states should use the same or very similar methodology for the calculation of primary energy factor of renewable and non-renewable energy sources.

REFERENCES

- [1] Martinez, F.; Herrero, C. L.; Pablo, S. Open loop wind turbine emulator. *Renew. Energy*, 2014, 63, 212-221.
- [2] Yen, J.; Ahmed, A. N. Enhancing vertical axis wind turbine by dynamic stall control using synthetic jets. *J. Wind Eng. Ind. Aerodyn.* 2013, 114, 12-17.
- [3] Islam, R. M.; Mekhilef, S.; Saidur, R. Progress and recent trends of wind energy technology. *Renew. Sustainable Energy Rev.* 2013, 21, 456–468.
- [4] Hasan, S. N.; Hassan, Y. M.; Majid, S. M.; Rahman, A. H. Review of storage schemes for wind energy systems. *Renew. Sustainable Energy Rev.* 2013, 21, 237–247.
- [5] Erhorn, H.; Erhorn-Kluttig, H. Selected examples of Nearly Zero-Energy Buildings detailed report. Available online:http://www.epbd-ca.eu/wp-content/uploads/2011/05/CT5_Report_Selected_examples_of_NZEBs-fina_1.pdf (accessed on 1 December 2017).
- [6] German Energy Efficiency Association for District Heating, Cooling and Combined Heat and Power. AGFW Arbeitsblatt FW 309 Part 1; Frankfurt, Germany, 2010.
- [7] Johannson, T. B.; Patwardhan, A.; Nakicenovic, N.; Gomez-Echeverri, L. *Global Energy Assessment – Towards a Sustainable Future*; Cambridge University Press: Cambridge, United Kingdom, 2012.
- [8] International Energy Agency, Eurostat and the Organization for Economic Cooperation and Development. *Energy Statistics Manual*; IEA Publications: Paris, France, 2004.
- [9] International Energy Agency. *IEA Statistics – Energy balances of non-OECD countries (2012 edition)*; Paris, France, 2012.
- [10] PE INTERNATIONAL AG: GaBi 6 & GaBi databases 2012; Leinfelden-Echterdingen, Germany, 2012.
- [11] Intergovernmental panel on climate change, *Renewable Energy Sources and Climate Change Mitigation*; Cambridge University Press, Cambridge, United Kingdom, 2011.
- [12] Austrian institute of construction engineering. OIB-Richtlinie 6 Energieeinsparung und Wärmeschutz. Available online: <http://www.oib.or.at/de/guidelines/richtlinie-6-1> (accessed on 13 December 2017). (In German)
- [13] VEA 2013. Methodologie. Available online: <http://www.energiesparen.be/node/3476> (accessed on 13 December 2017). (In Belgian)
- [14] The Ministry of Energy, Commerce, Industry and Tourism (MECIT). Infogrend Innovations/BRE (2009), *Methodology for Assessing the Energy Performance of Buildings*. Available online: [http://www.mcit.gov.cy/mcit/mcit.nsf/0/E074577C58AD9EFCC22575B60047BEA8/\\$file/Methodology%20for%20Assesing%20the%20Energy%20Performance%20of%20Buildings.pdf.pdf](http://www.mcit.gov.cy/mcit/mcit.nsf/0/E074577C58AD9EFCC22575B60047BEA8/$file/Methodology%20for%20Assesing%20the%20Energy%20Performance%20of%20Buildings.pdf.pdf) (accessed on 13 December 2017). (In Greek)
- [15] Czech Republic national regulation to implement the EPBD II Directive to the Czech building construction practice. 78/2013 Sb Vyhľadška o energetické náročnosti budov. Available online: <http://www.tzb-info.cz/pravni-predpisy/vyhkladka-c-78-2013-sb-o-energeticke-narocnosti-budov> (accessed on 13 December 2017). (In Czech)

- [16] Denmark building regulations. BR10 2010. Available online: <http://byggningsreglementet.dk/> (accessed on 13 December 2017).
- [17] Estonia building regulations. Vabariigi Valitsuse määrus nr. 68 (30.08.2012). Available online: <https://www.riigiteataja.ee/akt/105092012004> (accessed on 13 December 2017). (In Estonian)
- [18] Finland building regulations. D3 Rakennusten energiatehokkuus. Available online: http://www.finlex.fi/data/normit/37188-D3-2012_Suomi.pdf (accessed on 13 December 2017). (In Finnish)
- [19] France building regulations. Available online: <http://www.legifrance.gouv.fr/affichTexte.do?cidTexte=JORFTEXT000022959397&categorieLien=id> (accessed on 13 December 2017). (In French)
- [20] Germany Standard. DIN V 18599-10:2011-12. Energetische Bewertung von Gebäuden. (In German)
- [21] Großklos, M. Kumulierter Energieaufwand und CO₂-Emissionsfaktoren verschiedener Energieträger und – versorgungen; IWU, Darmstadt, Germany, 2014.
- [22] Greece building regulations. TOTEE 20701-1/2010. Available online: http://portal.tee.gr/portal/page/portal/SCIENTIFIC_WORK/GR_ENERGEIAS/kenak (accessed on 13 December 2017). (In Greek)
- [23] Hungary building regulations. 20/2014 (III.7). Available online: <http://www.kozlonyok.hu/nkonline/MKPDF/hiteles/MK14035.pdf> (accessed on 13 December 2017). (In Hungarian)
- [24] Ireland building regulations. DEAP 2012. Available online: http://www.seai.ie/Your_Building/BER/BER_Assessors/Technical/DEAP/DEAP_2009/DEAP_Manual.pdf (accessed on 13 December 2017).
- [25] Italy building regulations. CTI Raccomandazione 14, 2013. Prestazioni energetiche degli edifici –Determinazione della prestazione energetica per la classificazione dell’edificio. (In Italian)
- [26] Netherlands building regulations. NEN 2904:2004 Energieprestatie van utiliteitsgebouwen – Bepalingsmethode. (In Dutch)
- [27] Poland building regulations. Poz 888 Dz. U. 2014. Available online: <http://isap.sejm.gov.pl/DetailsServlet?id=WDU2014000888> (accessed on 13 December 2017). (In Polish)
- [28] Slovakia building regulations. Vyhláška č. 364/2012 k zákonu č. 555/2005 Z.z. o energetickej hospodárnosti budov. Available online: http://www.sksi.sk/buxus/generate_page.php?page_id=3075 (accessed on 13 December 2017) (In Slovak).
- [29] Slovenia building regulations. TSG-1-004:2010 Učinkovita raba energije. Available online: http://www.arhiv.mop.gov.si/fileadmin/mop.gov.si/pageuploads/zakonodaja/prostor/graditev/TSG-01-004_2010.pdf (accessed on 13 December 2017). (In Slovenian)
- [30] Spain building regulations. LIDER-CALENER unified tool; Madrid, Government of Spain, 2014. (In Spanish)
- [31] Sweden building regulations. IVL 2011. (In Swedish)
- [32] United Kingdom building regulations. The Standard Assessment Procedure for the Energy Rating of Dwellings (SAP 2012). Available online: <http://www.bre.co.uk/sap2012/page.jsp?id=2759> (accessed on 13 December 2017).
- [33] Rosenbloom, E. A problem with wind power. Available online: <http://www.aweo.org/> (accessed on 15 December 2017).
- [34] Baake, E.; Ubbenjans, B. The Scope for Electricity & Carbon Saving in the EU through the use of EPM Technologies, Leibniz University, Hannover, Germany, 2012.
- [35] ECOFYS. Primary energy factors for electricity in buildings. Available online: http://download.dalicloud.com/fis/download/66a8abe211271fa0ec3e2b07/ad5fcc2-4811-434a-8c4f-6a2daa41ad2a/Primary_energy_factors_report_ecofys_29.09.2011.pdf (accessed on 12 December 2017).
- [36] Kot, R.; Rolak, M.; Malinowski, M. Comparison of maximum peak power tracking algorithms for a small wind turbine. *Math. Comput. Simul.* 2013, 91, 29-40.
- [37] Martinez, F.; Herrero, C. L.; Pablo, S. Open loop wind turbine emulator. *Renew. Energy.* 2014, 63, 212-221.
- [38] Deksnys, R. P.; Bačasuskas, A.; Ažubalis, V.; Jonaitis, A.; Slušnys, D.; Staniulis, R.; Radziukynas, V.; Klementavičius, A.; Kadiša, S.; Leonavičius, A.; Rutkauskaitė, N.; Nezvanova, V. Feasibility analysis of wind power development, Part 1; Lithuanian Energy Institute report, Kaunas, Lithuania, 2009 (In Lithuanian)
- [39] Marčiukaitis, M. Wind energy research, modelling and prediction, Dissertation, Lithuanian energy institute, Kaunas, Lithuania, 2009 (In Lithuanian)
- [40] Lithuanian electricity transmission system operator (Litgrid). Available online: <http://www.litgrid.eu/index.php/paslaugos/kilmes-garantiju-suteikimas/ataskaitos/563> (accessed on 5 December 2017). (In Lithuanian)

MATERIALS SCIENCE

Modelling of capillary coatings and heat exchange surfaces of elements of thermal power plants

A. A. Genbach¹, D. Yu. Bondartsev¹, I. K. Iliev^{2*}

¹Almaty University of Power Engineering and Telecommunications, Department of Heat Engineering Installations, 126, A. Baitursynov Str., 050013 Almaty, Kazakhstan

²University of Ruse, Department of Thermotechnics, Hydraulics and Ecology, 8 Studentska Str., 7017, Ruse, Bulgaria

Modelling of the capillary porous structures and similarity of their processes allow to reveal a mechanism of heat transfer during steam generation of liquids, as well as determine zones of rising and developing fatigue cracks in the activation centres of steam seeds, research natural saline deposits and scale deposits and artificial porous coatings applicable on the metal fencing (plates) up to occurrence of the material limit state. Coatings are made of weak heat conductive mineral environment (quartz, granite, teshenite) with low porosity (3÷30%). Heat was initiated from flare of the jet burner and electric current. Stability of heat transfer was maintained by excessive cooler under joint action of capillary and mass forces. Solution related to the thermo elasticity resulted in relation of heat flows, heat stresses and destructive energy from time of heat supply and size of torn particles of coating. The areas of relaxation, breakup micro and macro processes were determined that demonstrate causes of rising and developing fatigue cracks of the heat and power equipment in stress concentrator with further development of erosion processes and relations of limit states of compression and tension to unity. The performed research took place for boiler-and-turbine load switching operations, as well as for establishing capillary porous cooling systems.

Keywords: Porous foam generator, foam generation, foaming, defoaming, heat-mass exchange, capillary-porous structures.

INTRODUCTION

Studies of a porous cooling system for rocket type burners [1,4] was the result of burners development [2,3]. When a mineral weak heat-conducting porous coating is exposed to the thermal action of a burner, after a while a part of the surface heats up to a certain temperature, and other parts of the coating keep the initial temperature. Therefore, a temperature gradient develops inside the porous coating resulted in unequal expansion. The surrounding unheated layers exhibit resistance to this expansion. As a result, thermal stresses occur both in the heated part and in the surrounding unheated part, including the base layer. These stresses can acquire destructive values. The thermoelastic stress problem solutions for idealized processes are given in sources [4]. Normal compressive stresses played the dominant role in destruction process. Porous coating is subjected to destruction as a result of lost stability in a thin layer adjacent to free surface. Therefore, primary focus was on the stressed state of the upper layer, which

thickness depends on heat transfer coefficient and structure of coating and base layer (the metal steam-generating surface).

The vacancy density rapidly increases in the irradiated coating; these vacancies quickly combine with cavity pockets formation due to the fact that the vacancy combining process intensity is proportional to their density square. If the vacancy cavities can transform into dislocations, the irradiated coating acquires plastic properties and does not undergo a destruction process when affected by a burner. This is typical for all metals. Several mineral rocks (tuff, marble, limestone) have the same property.

If no dislocations form in the coating, the growing vacancy cavities concentrate stress at their edges and lead to destruction while the coating thermal stresses are still below the plastic yield point. There is brittle thermal destruction.

As described in the literature, illusory contradictions occur in course of developing a mechanism of the heat exchange process in porous structures for cooling-off the heat exchange surfaces of the power plant elements up to the critical heat fluxes ($\sim 10^6$ W/m²), which happens when the wall medium type - liquid, steam or steam and water mixture - is under discussion. Our works show that

* To whom all correspondence should be sent:
iliev@enconservices.com

all the models do not contradict each other, but describe different boiling regimes [1].

Previously, using the methods of photoelasticity and holography, the destruction mechanism of the porous cooling system of the fire-jet burners' combustion chambers and nozzles was investigated [4]. It is interesting to compare the intensity of heat transfer [5–7] and the surface limit state [8, 9, 12], as well as to evaluate possible mechanisms for the destruction of heating (cooling) surfaces covered with capillary-porous structures [4]. This is in relation to the tasks of increasing the capacity of the thermal power equipment of power plants [10,11]. Such a problem is long overdue in connection with the modernization and extension of the life of gas turbine power plants.

PHYSICAL MODEL OF THE HEAT AND MASS TRANSFER PROCESS

Dynamic models of heat transfer intensification during boiling on porous surface are generated based on experimental and theoretical studies. Developed surfaces contain interconnected internal cavities in the form of rectangular channels and small pores that connect the channels with the liquid pool.

The ratio of latent heat flux ($\frac{\pi}{6} \bar{D}_d^3 \rho_s \bar{n} \bar{f}$) to the total heat flux for a developed surface can be (2...5) times more than that for an ordinary surface with a specific heat flux up to 1×10^4 W/m². That ratio decreased at high heat fluxes. Some data showed deviation of 300% from the calculated ones.

The formula includes the following legend: \bar{D}_d – average steam bubble departure diameter in a porous structure; r – specific evaporation heat; ρ_s – steam density; \bar{n} – average nucleation center density; \bar{f} – average steam bubble generation frequency.

Let us develop a physical model for transferring the specific heat flux “q” through the steam-generating surface (a wall or a base layer) covered with a capillary-porous structure (Fig.1).

The heat and mass transfer processes in the porous coating produce excessive liquid $\tilde{m} = m_l/m_s$ due to the pressure potential activity generated by the capillary and mass forces ΔP_{cap+g} .

The investigated thermal and hydraulic (internal) boiling characteristics [4] allow to show mechanism, to describe nature of the heat and mass transfer process in the investigated mesh porous structures [1,3] exposed to the gravitational force field, and

derive calculated equations for determining the diverted heat flux [3].

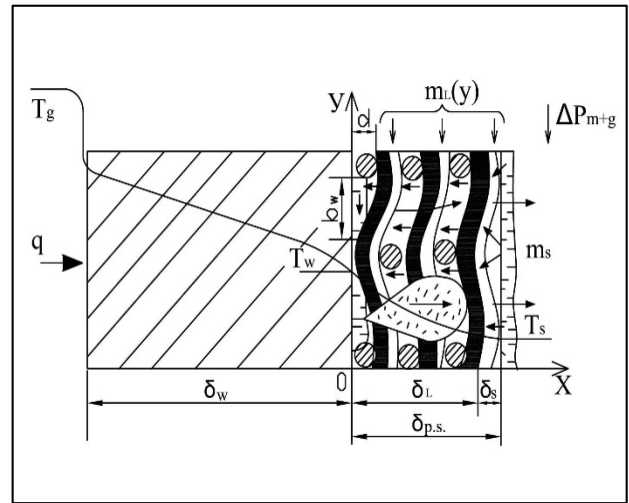


Fig.1. Physical model of the heat and mass transfer process in a real porous coating structure exposed to excessive liquid

The heat in the cooling system under study is transferred at small heat fluxes due to convective heat exchange with the value as higher as greater the effective thermal conductivity of the structure wetted with liquid and the housing thermal conductivity become. The fluid flow is smooth, and no steam bubbles or associated perturbing processes can be observed on the liquid surface. The liquid evaporates intensely from the menisci at low coolant excess; evaporation from the flowing film surface begins with an excessive liquid increase [3].

A certain heat flux, as smaller as lower $\tilde{m} = m_l/m_s$ parameter becomes, causes disturbance of the smooth wavy flow liquid film producing single steam bubbles. Several actively-operating structure meshes represent permanent generation centers. Liquid boiling start $\Delta T_{b.s.}$ depends on many regime and design parameters and can be determined with the equation aimed for this process, $\Delta T_{b.s.}$, which corresponds to the heat flux $q_{b.s.}$ Reduction in the cooling liquid flow rate $m_{l(s)}$, or increase in the heat influx q cause a rapid growth of the evaporation centers.

Each center in the initial boiling regime works with unequal intensity, some heating surface areas are barely affected by the awakening centers which start working. If the circulating coolant rate $m_{l(s)}$ increases, the lifetime of individual steam bubbles increases, and a number of active pores cease operation, long pauses occur between the bubble

nucleation moments, up to excluding such a center from a group of actively-generating ones. Excessive liquid increase “ \tilde{m} ” makes other active generation centers inactive and feeble.

The transition zone to developed bubble boiling is not large due to the high rate of the active steam generation center growth “ \tilde{n} ”. Further growth of the heat load “ q ” results in many steady-operating active bubble formation centers, their uniform distribution throughout the steam generating surface. However, certain critical conditions can lead to a boiling crisis and a burned-out surface. Therefore, the compared deliberate destruction processes applied to fragile materials and the boiling crisis allow to model them and identify mechanism adopted by such processes.

EXPERIMENTAL RESULTS

The destruction process mechanism was studied through experiments which included photoelasticity and holography method application [2]. The model stress state at similar times was evaluated by photographic recording of isochromatic patterns and counting the n-bars order at different points in the studied directions.

The thermoelasticity problem solution makes it possible to determine the medium limit state for a porous coating and a metal steam generating surface [4]. In case weak heat-conducting semi-porous

coatings and a metal wall (a base layer) are subjected to the thermal destruction, it is required to determine the effect produced by the specific heat flux “ q ” applied to the surface and the time of its influence “ τ ” on the destructive stress generation “ σ ”, the husk grain size composition (the detached particle size), and for the metal is the temperature perturbation depth penetration “ δ ”.

As the “ q ” value increases within a short period of time “ τ ”, the dynamic effects become very significant, the compressive stresses “ σ ” reach large values, typically several times higher than the material compressive strength. Therefore, it is necessary to take into account these stresses in the material thermal destruction mechanism. We need to find out what “ σ_i ” stress type reaches its limit values earlier.

Consider a plate $2h$ in thickness. A constant specific heat flux “ q ” is being applied to the surface $z=+h$ starting from $\tau=0$ timepoint. The plate bottom surface $z=-h$ and lateral edges are thermally insulated.

The plate temperature distribution value makes it possible to calculate the thermal stresses of tension and compression arising at a certain timepoint “ τ ” at different depths measured out from the surface δ_i ($h=z_i$) at a given heat flux “ q ”, since the plate with a variable temperature over its thickness is plane-stressed [4].

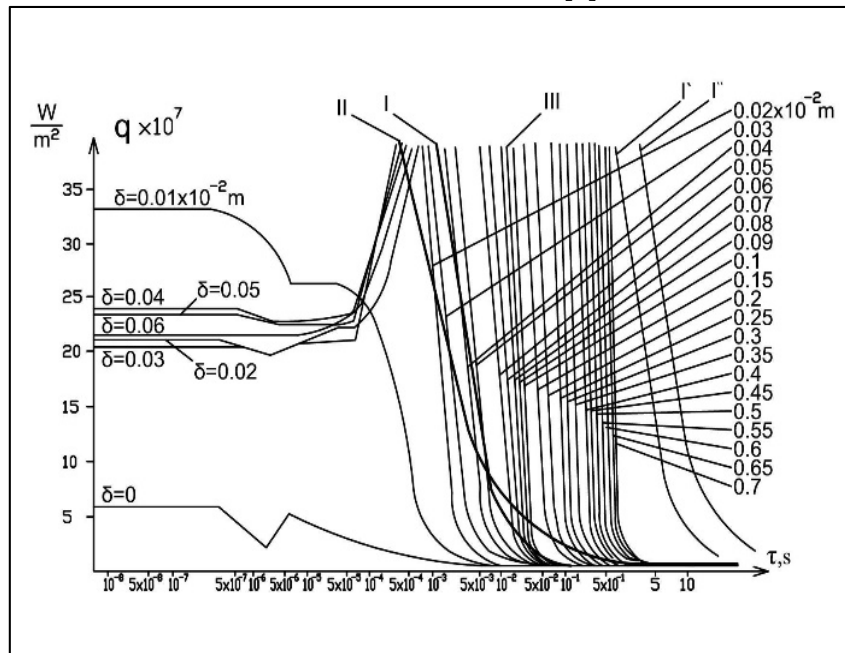


Fig.2. Dependence of heat fluxes “ q_i ” causing the compressive stresses III of the quartz coating in relation to the time “ τ ” for different detached particle thickness “ δ_i ”: I – tensile stresses sufficient for destruction; I’, I¹¹ – copper and stainless steel, $h = 0,1 \cdot 10^{-3}$ m; II – surface fusion

Assume the limit stress values of the compression $\sigma_{lim.compr.}$ and tension $\sigma_{lim.tens.}$ for the coating and metal, this will show us the functional dependence of the heat flux “q” required for the destruction on the delivery time “ τ ” and the penetration depth “ δ ”. In addition, the plate surface temperatures equated to the melting temperature $T_{pl.}$ appropriate for the coating and metal, clarify the specific heat flux values necessary for melting-down the surface layer for a specific period of their action “ q_i ”, i.e. in each

specific case we can trace functional dependences of the heat flux on the time it influences the rock and metal surface [4].

When it comes to a quartz plate (coating), the heat fluxes “ q_i ” have been calculated for a wide time interval of $10^{-8} \dots 10^3$ s. The lower limit of this interval (10^{-8} s) is the relaxation time. Fig. 2 illustrates that the q_1 and q_2 value ratios for the time intervals $10^{-8} \dots 10^3$ s lose their physical significance.

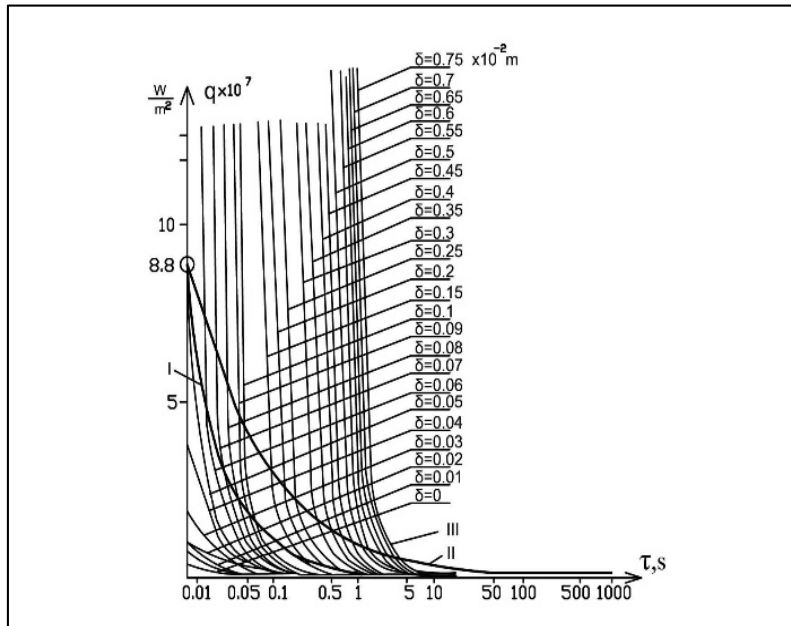


Fig.3. Dependence of heat fluxes “ q_i ” causing the compressive stresses III of the quartz coating in relation to the time “ τ ” for different detached particle thickness δ : I – tensile stresses sufficient for destruction; II – surface fusion; curves II¹ – copper, $\delta = 0.1 \cdot 10^{-3}$ and II¹¹ – stainless steel, $\delta = 0.1 \cdot 10^{-3}$ m, almost coincide with curve I in the region (0.01...0.1) s

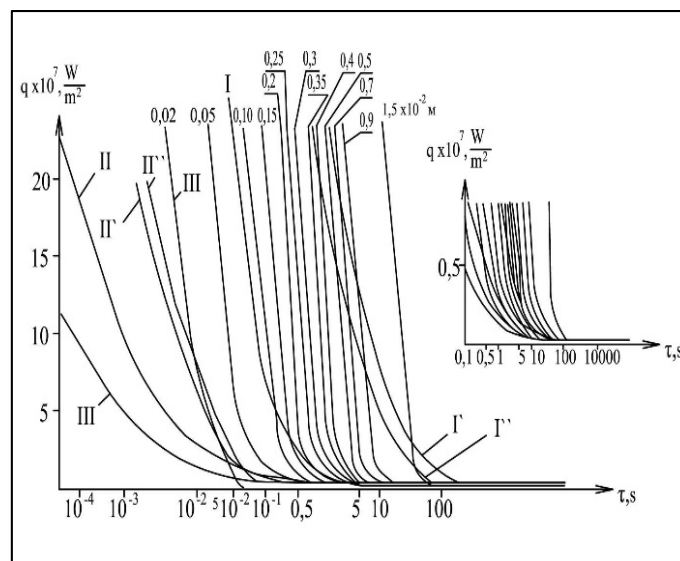


Fig.4. Dependence of heat fluxes “ q_i ” causing the compressive stresses III of the granite coating in relation to the time “ τ ” for different detached particle thickness δ : I – tensile stresses sufficient for destruction (I', I'' - copper and stainless steel, $h = 0.1 \cdot 10^{-3}$ m); II – surface fusion (II', II'' - copper and stainless steel, $h = 0.1 \cdot 10^{-3}$ m)

Since thermal destruction is a macro process, we consider that it lasts $5 \cdot 10^{-3} \dots 10^3$ s. The coating destruction only by compression presents us a number of curves, corresponding to a specific detached particle thickness, which is $(0.25 \dots 0.3) \cdot 10^{-2}$ m for teshenite, as evidenced experimentally through high-speed shooting with a SKS-1M camera.

The compression curve sections, which determine $\delta > 0.3 \cdot 10^{-2}$ m thick particle detachment for the large values “q” and small values “ τ ”, are screened by the melting curve II, and by the tension curve I in the case of small heat fluxes and significant time intervals. The quartz coating surface melting curve is much higher than that of the teshenite coating, which explains its steady brittle destruction (Figs.2, 3).

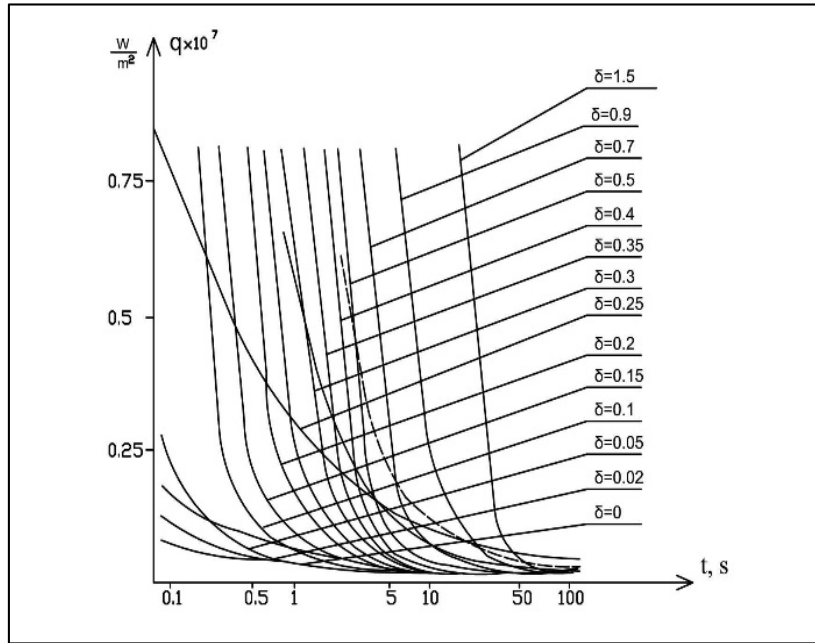


Fig.5. Dependence of $q_i = f(\tau)$ shown in Fig.4 in the range of $q = (0.25 \dots 0.75) \cdot 10^7$ W/m²

Boiler-and-turbine part destruction depends on the background of cracks in the stress concentrator (a relaxation zone) (see Fig.2). An explosive steam center formation (the time interval of 10^{-8} s to 10^{-3} s) represents a starting point for counting. The energy generated due to a steam bubble spontaneous appearance is close to the constant (invariant) value considering the time of its growth. It is spent on sustaining the center with a radius R_c and prevents its collapse (q values reach up to 10^8 W/m²). At this time, a thermodynamic equilibrium is under consideration for transition from a microprocess (microparticles and clusters with radii $(10^{-7} \div 10^{-8})$ m (nano particles) of individual (single) bubbles to processes taking into account the behavior displayed by a large number of bubbles, i.e. with the help of integral characteristics (\bar{q} , $\bar{\alpha}$, $\bar{\Delta T}$, $\bar{\Delta P}$, \bar{w}), where $\bar{\alpha}$, $\bar{\Delta T}$, $\bar{\Delta P}$, \bar{w} is the average value of heat transfer coefficient, temperature and hydro-gas-dynamic head and flux velocity. The presence of stress concentrates, which generate an active steam phase,

significantly reduces the $\sigma_{lim.compr.} / \sigma_{lim.tens.}$ ratio and this value can be of $(1 \div 2)$, in particular, for energy steels. It is also necessary to take into account presence of other stress concentrators, cyclicity produced by loads while the equipment operates in start/shutdown modes leading to fatigue cracks (stresses).

For example, the tensile strength for turbine steels is $\sigma_b \approx (400 \div 1000)$ MPa. The yield point at operating temperature of $-(400 \div 550)^\circ\text{C}$ decreases to $(200 \div 900)$ MPa with deformation of 0,2%. The long-term strength limits decrease to $(70 \div 260)$ MPa with deformation of $(10 \div 20)\%$. The temporary thermal stress value decreases to $(40 \div 120)$ MPa, i.e. by an order of magnitude. The main estimated fatigue stresses amount only up to 0.45 of σ_b .

Therefore, the likelihood is great that the values $\sigma_{lim.tens.} \approx \sigma_{lim.compr.}$, and $\sigma_{lim.tens.}$ values grow to 10 MPa and become of the same magnitude for porous coatings. The bubble “death” processes, as well as nucleation are also explosive ($\tau = 10^{-8} \div 10^{-6}$ s) and

lead to the cumulative event appearance, which destroys the stress concentrator (an active generation center) by erosion along with corrosion and electrical processes and, as a result, its size reaches the critical crack point. In the case of instant steam condensation in a pit (a hole), the steam instantly disappears forming a powerful cumulative effect (cavitation), while shock waves are distributed deep into the parts and cracks develop admitting oxygen inside.

At the very moment a bubble or a drop are “born”, α value is up to $1 \cdot 10^5$ W/m²K at a steam temperature (500÷565)°C the ΔT value reaches 500°C, and q value acting at the bubble bottom (the “dry” spot zone) is up to $5 \cdot 10^7$ W/m². Given that an individual steam bubble generates q value 10 times more than its integral value [1], then the total q value is $5 \cdot 10^8$ W/m², which is represented in the figures $q=q(\tau, \delta)$. The greater the heat wave penetration depth “ δ ” (or that of a particle detached from the porous coating), the longer it will take to destroy the parts (see Figs.2-6 for “ q ”). The interrelation between compressive and tensile stresses is a stress diagram within the plate (coating) for various time intervals calculated from moment the process under consideration begins. At small τ values, 10^{-2} s magnitude, only compressive stresses occur. Starting from $\tau = 10^{-1}$ s, in some region $\Delta(h-z_i)$ the compressive stress turns into a tensile stress, and they are at different depths from the plate surface for different time intervals.

The destruction of the coating and metal subjected to compressive forces happens much earlier than that subjected to the tensile forces. The heat flux intervals, within which such destruction occurs, are as follows: $q_{max}=7 \cdot 10^7$ W/m², $q_{min}=8 \cdot 10^4$ W/m² for quartz coatings, $q_{max}=1 \cdot 10^7$ W/m², $q_{min}=21 \cdot 10^4$ W/m² for granite coating, $q_{max}=2 \cdot 10^6$ W/m² for metal (a base layer) (boiling crisis in a porous system); $q_{min}=1 \cdot 10^4$ W/m² (without cooling).

As q value increases in the heated layer, and therefore, the heating time “ τ ” decreases, the role played by compressive stress becomes more significant. Despite the high resistance to compression, destruction produced by compressive thermal stresses takes place in more favorable conditions instantly and in small volumes. Figs.2-6 displays curves for steam generating heating surfaces at the moment a film regime was established and the surface temperature increased

sharply to a value of T_{pl} . resulting from the boiling regime change. The calculated specific energy Q of a destructed volume unit of quartz, granite and teshenite coatings shows that the curves have expressed minimum values depending on the detached particle thickness “ δ ”.

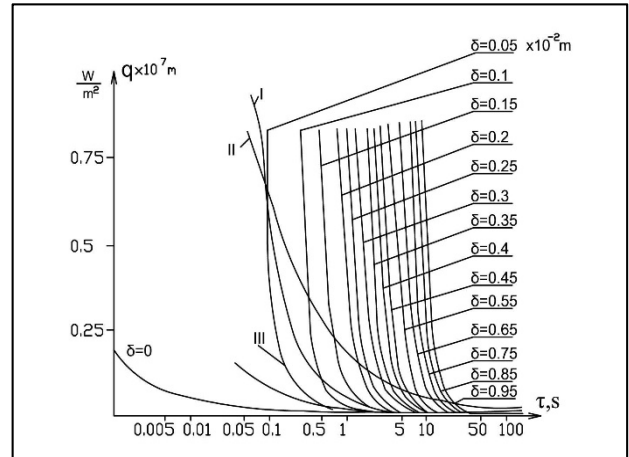


Fig.6. Dependence of heat fluxes “ q_i ” causing the compressive stresses of the teshenite coating in relation to the time “ τ ” for different detached particle thickness δ_i : I – tensile stresses sufficient for destruction; II – surface fusion; III – destructive compressive thermal stresses. Curves II и II’ for copper and steel almost coincide with curve I in the interval $\tau = (0.1 \dots 1)$ s; metal thickness $\delta_{pl} = h = 0.1 \cdot 10^{-3}$ m.

The minimum energy consumption for a quartz coating under destruction conditions is $Q \cong 0.5 \cdot 10^3$ J/m³, where $\tau=(0.1 \div 1)$ s, $\delta_i=(0.1 \div 0.25) \cdot 10^{-2}$ m.

For granite coating: $Q \cong 2.5 \cdot 10^9$ J/m³, where $\tau=(0.1 \div 5)$ s, $\delta_i=(0.1 \div 0.3) \cdot 10^{-2}$ m, where $q \cong 0.1 \cdot 10^7$ W/m² and $\delta=(0.2 \div 1.5) \cdot 10^{-2}$ m, $Q=2.5 \cdot 10^9$ J/m³.

For teshenite coating: $Q \cong 0.5 \cdot 10^9$ J/m³, where $\tau=(0.1 \div 5)$ s, $\delta_i=(0.1 \div 0.4) \cdot 10^{-2}$ m, provided that the ratio of the limit normal compressive and tensile stresses varied from 20 to 30.

CONCLUSIONS

The microcrack presence in the monolith coating reduces its compressive strength in the crack area so that the compressive strength can be only 2 times greater than the tensile strength. The curves $Q=f(q)$ shift their minimum values with grows “ δ_i ” toward decreasing “ q ”, provided that a lower energy consumption “ Q ” is required for the thermally destructed brittle coatings. Thus, the limit thermal stress generation is very likely at the start/shutdown of boiler-and-turbine equipment at power plants.

These stresses arise primarily in the concentrator areas, which are the nucleation centers for the active steam phase, or condensate drop formation. The capillary-porous structure can be of natural origin (salt deposits, film), and produced artificially with usage of well and weak heat-conducting materials over a wide porosity range from 3% to 90% (penetration). The structures can both be a model and act as a high-intensity and forced cooling system. For example, teshenite porous coatings with a linear expansion coefficient 5 times greater, thermal conductivity coefficient 10 times lower and approximately the same melting temperature compared to those of energy steels serve as a modeling material. They demonstrate the highest viscosity with a porosity of up to 30%.

NOMENCLATURE

q – specific heat flux, W/m²;
 T_g, T_w, T_s – gas, wall (base layer) and saturation temperatures, °C;
 $\delta_w, \delta_l, \delta_s, \delta_w$ – wall, liquid, steam, wick thickness, m;
 $m_{l(s)}, m_s$ – liquid and steam flow, kg/s;
 ΔP_{cap+g} – effective driving capillary and mass head, N/m²;
 d – grain size, m;
 b_w – porous material cell width, m.

Subscripts

g – gas;
 w – wall;
 s – saturation;
 l – liquid;
 s – steam;
 w – wick thickness;
 $cap+g$ – capillary and mass.

REFERENCES

- [1] Polyayev V.M., Genbach A.A., Control of Heat Transfer in a Porous Cooling System. Proceedings, 2nd World Conference on Experimental Heat Transfer, Fluid Mechanics and Thermodynamics, Dubrovnik, Yugoslavia, 639-644 (1991).
 [2] Polyayev V.M., Genbach A.N., Genbach A.A. An experimental study of thermal stress in porous materials by methods of holography and photoelasticity // Experimental thermal and fluid science, avenue of the Americas, New York, volume 5, number 6, 697-702, November (1992).
 [3] Polyayev V.M., Genbach A.A., Heat transfer in a porous system operating under the combined action of capillary and gravitational forces. (in Russian), // Thermal Engineering, 7, 55-58, (1993).
 [4] Genbach A.A., Bondartsev D.Yu., Iliev I.K. Investigation of a high-forced cooling system for the

elements of heat power installations. Journal of Machine Engineering, 2018, Vol. 18, №2, 106-117. DOI: 10.5604/01.3001.0012.0937

[5] Shklover E.G. Experimental study of heat transfer from porous surface in pool and forced – convection boiling at low pressures // Phase Change Heat Transfer ASME. 1991. V. 159. P. 75-80. DOI: 10.1080/08916152.2017.1397821

[6] A.S. Surtaev, V.S. Serdyukov, A.N. Pavlenko, D.V. Kozlov, D.S. Selishchev. Characteristics of boiling heat transfer on hydrophilic surface with SiO₂ coating. *Bulgarian Chemical Communications, Vol. 50, Special Issue K (pp. 36 – 44) 2018*

[7] L.L. Tovazhnyansky, P.O. Kapustenko, O.A. Vasilenko, S.K. Kusakov, O.P. Arsenyeva, P.Y. Arsenyev. Mathematical model of a plate heat exchanger for condensation of steam in the presence of non-condensing gas. *Bulgarian Chemical Comm., Vol. 50, Special Issue K (pp. 76 – 82) 2018*

[8] Jamialahmadi M., Müller-Steinhagen H., Abdollahi H., Shariati A. Experimental and theoretical studies on subcooled flow boiling of pure liquids and multicomponent mixtures // Int. J. Heat and Mass Transfer. 2008. V. 51. P. 2482-2493. DOI: 10.1016/j.ijheatmasstransfer.2007.07.052

[9] Krepper E., Koncar B., Egorov Yu. CFD modelling of subcooled boiling - Concept, validation and application to fuel assembly design // Nuclear Engineering and Design. 2007. V. 7. P.716-731. DOI:10.1016/j.nucengdes.2006.10.023

[10] Kupetz M., Jeni Heiew E., Hiss F. Modernization and extension of the life of steam turbine power plants in Eastern Europe and Russia // Heat Power Engineering. 2014. V. 6. P. 35-43. DOI: 10.1134/S0040601514060056

[11] Grin E.A. The possibilities of fracture mechanics in relation to the problems of strength, resource and justification for the safe operation of thermal mechanical equipment // Heat Power Engineering. 2014. V. 1. P. 25-32.

[12] Z.Q. Yu, G.S. Zhou, S.D. Zhu, J.M. Li, L.J. Li. Influence of sensitizing treatment on the corrosion resistance of Incoloy 028 alloy. *Bulgarian Chemical Communications, Vol. 49, Number 4, (pp. 943 – 947) 2017.*

The study of the effect of chromium boron (CrB_2) hardening additive on the developed pg-z40 surfacing powder

B.K. Kenzhaliev¹, V.G. Mironov^{2*}, G.T. Shilov³, Zh.B. Ilmaliyev⁴, D.K. Yermekov⁵

¹«Institute of Metallurgy and Ore Benefication» JSC, general director, 29/133 Schevchenko Str., 050010 Almaty, Kazakhstan

²«KBTU SPLAV» LLP, Head of project, 64A Spasskaya Str., 050028 Almaty, Kazakhstan

³«KBTU SPLAV» LLP, engineer, 64A Spasskaya Str., 050028 Almaty, Kazakhstan

⁴«KBTU Metallum» LLP, director, 59 Tole bi Str, 050000 Almaty, Kazakhstan

⁵«KBTU SPLAV» LLP, engineer, 64A Spasskaya Str., 050028 Almaty, Kazakhstan

Development of a new composite powder alloy to increase wear resistance and impact resistance in gas-powder surfacing of the existing alloy PG-Zh40. Optimization of composition of new composite alloys by an injection 10% of chromium-boron hardening additive and characterization of alloy formation conditions. Phase formation conditions and structure of the new composite surfacing material with boride hardening during mechanical alloying. The following rational part of the new powder filler alloy has been received: Fe = 32-40%; C = 1.1-1.4%; Cr = 14-15%; Si = 2-3%; B = 2-2,9%; Ni = 30-32%, Cu = 2-3% with 0 ÷ 44 HRC hardness.

Keywords: Self-fluxing alloy, gas powder surfacing, durability, mechanochemical technology, attritor, granulation

INTRODUCTION

The world economy annually loses approximately 80 billion USD due to wear and corrosion, but adequate proactive wear protection can help to avoid these losses. This protection involves surfacing of new parts as well as reconditioning and return of worn ones to economic circulation. Surfacing with materials with high performance characteristics is an effective method of machinery parts surfaces hardening. This method is cost-effective, because surfacing is applied only to the surfaces functioning in an aggressive wear environments, and as a rule, the weight of deposited material is very low in comparison with the total weight of a part. Durability of hardened parts is determined by the characteristics of deposited material, and for this reason, the materials or alloys used for surfacing are selected on the basis of the part's operational environment and the surfacing method.

The new self-fluxing surfacing ferrous powder material with hardening additive developed by our team will be used for the reconditioning of components of equipment and machinery operating in abrasion wear, corrosion, high temperature or aggressive environment exposure conditions.

Currently, there are many self-fluxing surfacing powder nickel- and copper-based alloys produced under various methodologies. These alloys have started to take the lead among the materials commercially produced by the world's leading companies such as NACA, JNCO, Battelle, Cabot,

BBC, Vienna, KRUPP etc. Alloys with hardness specified in the range from 35 to 55 HRC (such as PSR-2, PSR-3, PSR-4 etc. (GOST 21.448-75)) were developed to create coating of different hardness. All these alloys are cobalt-, nickel- and copper-based with various carbide-forming additions ensuring required physical and mechanical properties of the surfaced (applied) coating.

The goal of this research is to develop a new alloy technology, based on the previously developed self-fluxing surfacing powder alloy PG-Z40 [1,2], but with the addition of chromium boron hardening additive. The team also studied the formation of structure, phase composition and features of gas-flame coatings. To try out the new alloy technology involving the addition of CrB_2 the team used self-fluxing surfacing powder alloy PG-Z40 with 50-160 μm grading fraction and the following chemical composition: Fe=38%; C=15,1%; Si=3,0%; B=2,9%; Ni=33%.

RESEARCH METHODOLOGY

Fe, Ni, Cr, Si, Cu, B, C powders and CrB_2 hardener were used as initial reagents for the production of the self-fluxing surfacing powder. Copper was added to increase fluidity of the melt and to improve anti-corrosive properties of the alloy. Vanadium was added to increase the alloy's cold resistance; vanadium also forms strengthening phases with carbon, resulting in the improvement of the alloy's wear resistance. The increase of carbon content is necessary for the formation of carbides. Carbides evolve from the liquid solution during gas-powder

* To whom all correspondence should be sent:
kbtu-splav@mail.ru

surfacing, become crystallization centers and contribute to structure refinement resulting in the improvement of the alloy's durability.

The composite material was developed under mechanochemical methodology with the use of attritor [3], and the produced powder was granulated with planetary granulator to create powder of required grain size. The structure of the surfacing alloy, its physical and mechanical performance properties were identified with standard techniques. In particular, the structural analysis in the surface layers of the surfacing ferrous alloy was carried out using metallographic analysis as well as scanning and transmission electron microscopy. X-ray crystallography was used to determine the phase composition of samples. Microhardness was measured with PMT-3 microhardness tester using static indentation method in accordance with GOST 9450-76. Surfacing layer adhesive strength was examined with CDM10/91 strength testing machine. Surfacing layer hardness was determined with TP-7R-1 material and alloy hardness measurement device using Vickers method. Technological properties of produced granulated powder mix were examined with the use of gas-flame surfacing on various steel samples.

Phase composition of the new surfacing alloy was determined with D8 Advance (BRUKER) diffraction meter. Microanalysis of specimen was performed with Neophot-2 metallographic microscope with 200x, 500x and 1000x magnification [4,5,6].

EXPERIMENTAL PART

To try out the new alloy technology involving the addition of CrB₂, the team used self-fluxing surfacing powder alloy PG-Z40 with 50-160 μm grading fraction and the following chemical composition: Fe=38%; Cr=15,0%; Si=3,1%; B=2,9%; Ni=33%; Cu=4%; V=4,0%.

Addition alloy CrB₂ with the following chemical composition: Ti=0,08%; Fe=0,47%; Ni=0,52%; B=15%; Cr=83,43% was used as a hardening additive. CrB₂ hardener was granulated for 5 minutes in a laboratory planetary granulator in alcohol environment with the use of grinding media (5-8 bearing balls with 1:3 powder mix / balls weight ratio). After the granulation average size of CrB₂ particles was 10-30 μm.

2 types of powder mix were prepared for the experiment.

The first type of powder mix was the new surfacing alloy PG-Z40, and the second type was PG-Z40 with CrB₂ hardener. The powder mix was a mechanical mixture of the new PG-Z40 alloy initial state components and CrB₂ hardener subjected to

mechanical alloying in an attritor. Mechanochemical activation of the powder mix was also carried out in attritor. Prior to the mechanochemical activation, 1% of zinc stearate was added to the powder mix to prevent mix material sticking to the balls and the inner surface of the drum. The mix was treated in attritor with the following production conditions:

- Mixer rotation rate – 340 rpm;
- Ball diameter – 5 mm;
- Powder mix weight / ball weight ratio – 1/18;
- Process duration – 2 hours.

Mechanical alloying produced composite powder materials with particle size 10-20 μm [5-8]. To produce glomed powder surfacing material, the initial powder material obtained in the attritor was mixed with an organic bond of 2-3% alcohol solution of phenolic varnish FL-98 with subsequent sintering in a LH15/12 batch furnace at the temperature of 700°C [7,8].

After the sintering, the glomed material was granulated and sieved through a set of sieves to sort out 50-160 μm size particles. The testing of experimental boride-hardened powders for gas powder surfacing was prepared in accordance with GOST 21448-75 «Surfacing alloy powders» taking into account existing methods [9].

Surfacing was performed by oxypropane torch with No.5 tip manufactured under the specification No. 200 of Kaz. SSR 210-84, under the patent №1276 issued by the Republic of Kazakhstan. Compressed gases were used during surfacing: oxygen under GOST 5583-78 and propane under GOST 20448-80. The reference specimen was made of 45 steel under GOST 1050-88, and had dimensions of 30x45x11 (mm). Gas powder surfacing was carried out by the application of 1,2-1,5 mm thick surfacing layer under the following conditions [10]:

- Oxygen pressure at the torch inlet - 9,0 kg/cm²;
- Propane pressure at the torch inlet - 1,2 kg/cm²;
- Oxygen expenditure – 750 l/h;
- Propane expenditure – 700 l/h;
- New surfacing alloy expenditure – 50 g/min;
- Surfacing layer thickness – 2-3 mm.

The surface of the surfacing layer was treated with an abrasive tool made of green silicon carbide. The coating is free of pinholes and slag inclusions.

RESEARCH RESULTS AND DISCUSSION

Fig.1 contains photomicrographs of the produced surfacing powder demonstrating that the particles are globe- and oval-shaped and their size ranges from 50 to 160 μm.

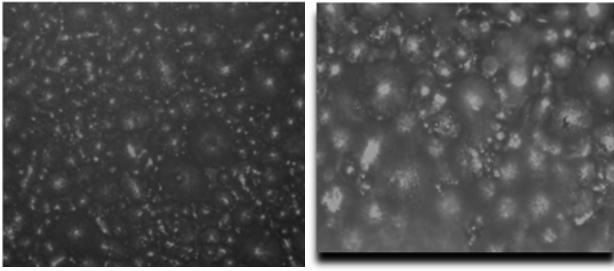


Fig.1. Photomicrographs of the powder with x200 and x500 magnification

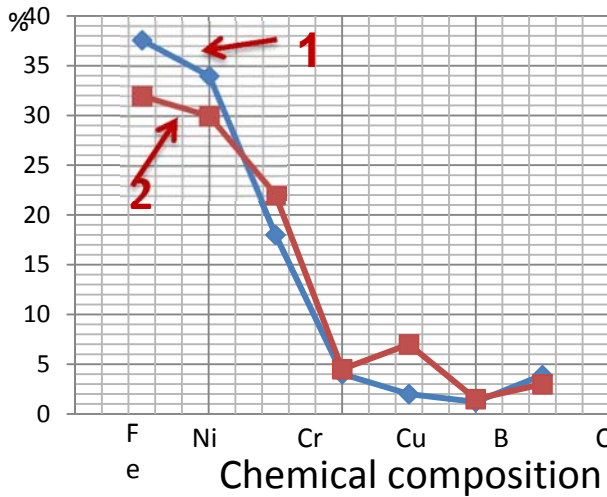


Fig.2. Chemical composition of the surfacing powder

- 1- Powder alloy PG-Z40 – 100%;
- 2- Powder alloy PG-Z40 90% + 10% CrB₂

Chemical composition (Fig.2), powder and composite coating structure was studied with a spectrometer. The used spectrometer had no function of boron, carbon and silicon identification, therefore the initial data on their content in the studied alloys

was put in the graph. The content of other elements in the alloy corresponds to their content in the initial powder. The effect of CrB₂ additive on the changes in the chemical composition of the PG-Z40-based alloy is shown on the graph.

X-ray structure analysis (Fig.3) showed that the alloy's structure is a composition including relatively strong and plastic iron nickel matrix and strengthening phases in the form of carbides and borides such as FeB; Cr₂B; Cr₂B₂; Cr₃C₂; Cr₅B₃; Cr₇C₃; Cr₂₃C₆; Fe₃C; Cr₇BC₄; Fe₃C, silicon nickelide Ni₂Si₅. The produced material is an iron nickel low alloy with a typical two-phase structure. The 12,1% increase of chromium content in the two-phase Fe-Cr structure of the PG-Z40+10% CrB₂ alloy in comparison with the similar PG-Z40 structure should also be noted.

Microhardness on Vickers scale was measured separately for the two alloys and the diffusion zone with the results showing hardness value on the steel baseplate in the diffusion zone and on the surface of the studied glomed powder alloy. The obtained microhardness values for the surfaced coating in the fusion zone of the studied specimen are shown in the Tab.1.

It has to be noted that microhardness increases in the direction towards the surfaced coating of the studied sample.

Coating microhardness values are uniform, there are no apparent hardness variations. The value range from 400 to 500 MPa, implying uniform distribution of carbides and borides, i.e. the structure is homogeneous throughout the entire area of the surfacing coating (Fig.4).

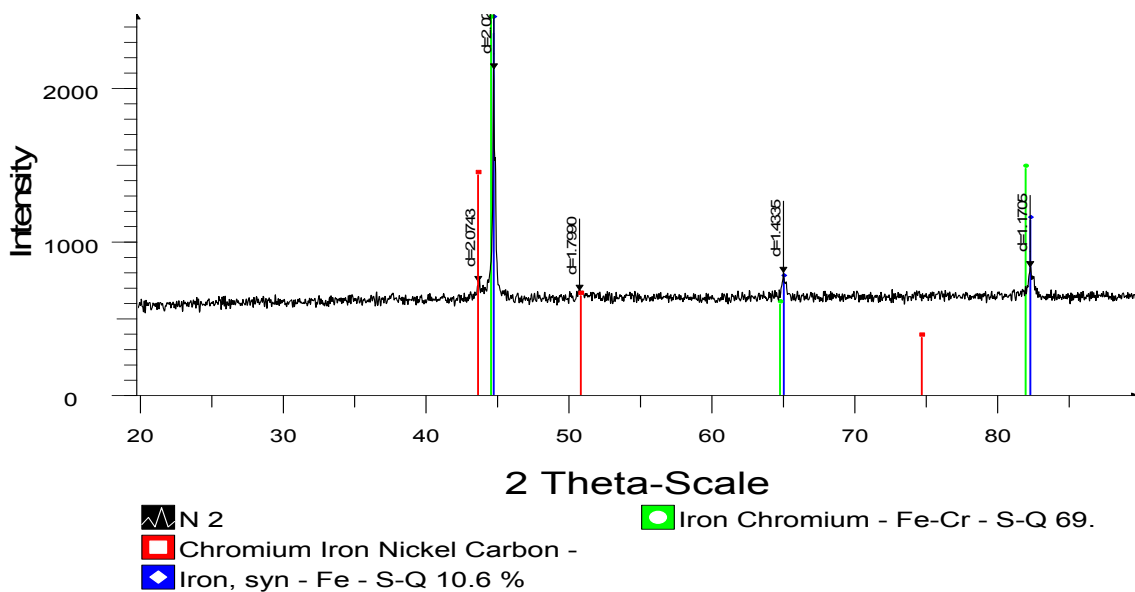


Fig.3. The results of X-ray structure analysis for PG-Z40+10% CrB₂

Table 1.Microhardness measurement results for the studied sample.

Impressions	Vickers hardness, HV 10 kgf		
	Steel baseplate	Diffusion zone	Sample material, 90% PG-Z40+10% CrB ₂
1	382.72	381.40	456.72
2	362.75	426.57	470.63
3	375.41	428.62	530.29
4	359.34	443.42	485.18
Average	HV = 370.34	HV =420.00	HV =546.96

The coating microhardness was measured on the polished specimen №1, №2 having 2 mm thickness in 4-7 measurements of the diagonal of impression.

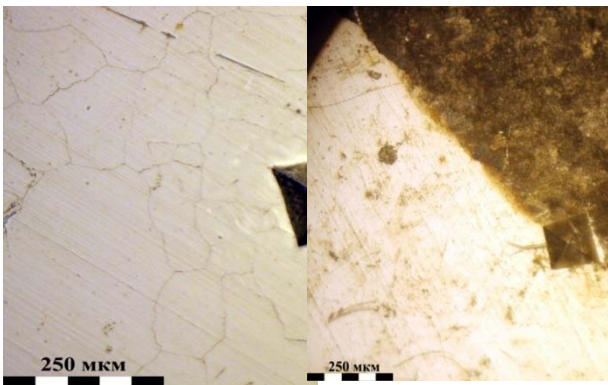


Fig.4.The size of an impression on the polished specimen of the samples: a) PG-Z40; b) PG-Z40+10% CrB₂

The obtained microhardness values for the surfaced coating of the sample are shown in the Tab.2.

Table 2.Microhardness measurement results for the polished specimen of the sample №1 surfaced with PG-Z40 alloy

Impressions	Vickers hardness, HV 10 kgf	
1	482.71	563.64
2	519.13	546.15
3	487.67	542.09
4	492.71	547.96
Average	HV=495.55	HV=549.96

According to microhardness measurement results, the average microhardness value of the sample surfaced with the boride-hardened alloy increases by 54,41 HV in comparison with the initial alloy obtained with the surfacing with PG-Z40 material.

The study of the fusion zone of the new boride-hardened alloy was carried out with the use of metallographic microscope with x200 and x500 magnification. The polished specimen was prepared using a sample surfaced with glomed powder alloy of

the following composition: 90% PG-Z40+10% CrB₂. Fig.5 shows the boundaries of the surfaced alloy's diffusion zone. The formed diffusion zone layers seem to be the result of peritectic reaction, in accordance with the system state diagram: Fe-Ni-Cr-B.

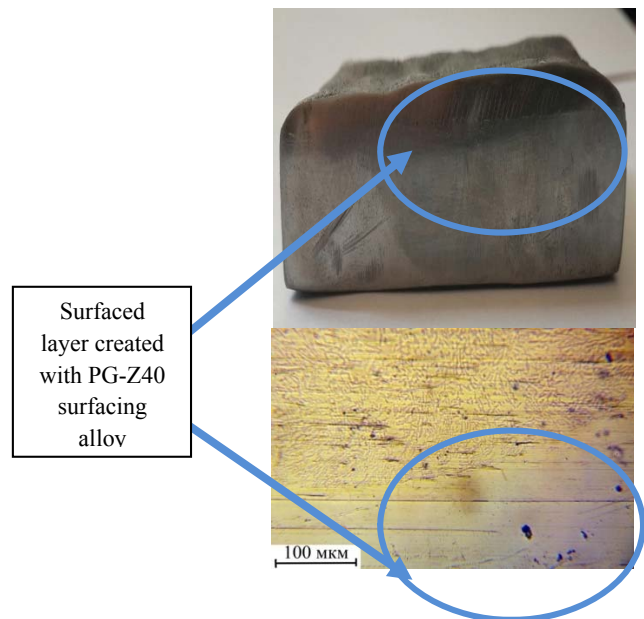


Fig.5. Microstructure of the surfaced metal (PG-Z40+10% CrB₂) with base metal, x500

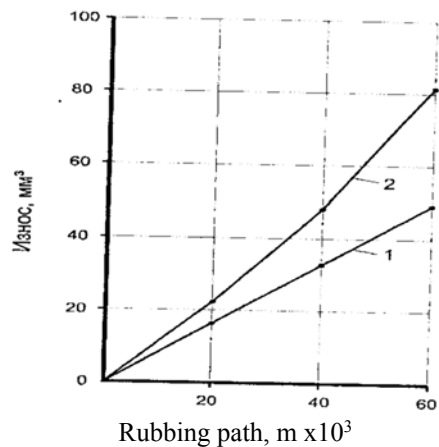


Fig.6. The new alloy and steel wear rates: 1-The new PG-Z40+10% CrB₂ alloy 2-45 steel, 55 HRC hardness

Fig.6 shows the results of wear assessment for the samples with surfaced coating hardened to 55 HRC compared to 20GL steel dressers. We can assume that wear resistance and durability of components of friction units is increased after their reconditioning by PG-Z40 +10% CrB₂ alloy surfacing.

Metallographic analysis was conducted for the sample No.1 surfaced with PG-Z40 alloy and for the sample No.2 surfaced with PG-Z40+10% CrB₂ alloy. Microanalysis was performed with the use of Neophot-32 metallographic microscope with $\times 200$ and $\times 500$ magnification.

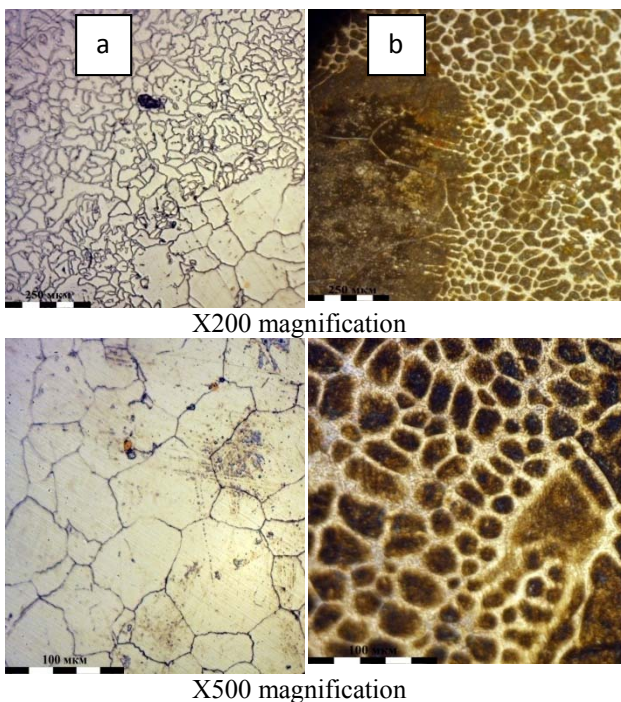


Fig.7. Microstructure of the layer surfaced with PG-Z40 alloy (a) and PG-Z40+10% CrB₂ alloy

Fig.7 shows homogeneous polyhedral, equiaxial block structure with a coarse-grain to fine-grain structure transition zone and localized solid copper solution particles. Chains of multiple proeutectoid constituent precipitations of two types (dark, and sometimes light), which seem to be iron and chromium carbides, can be observed along the grains' boundaries.

Fig.7 also shows large crystals composed of ultrafine-grain sub-crystals in the microstructure of the alloy. Polyhedral ferrite crystals – solid carbon solution in α -iron and perlite – possibly represent eutectoid mix of ferrite and iron and chromium carbide.

The phases mainly formed inside the crystals and along their boundaries in some places are as big as 1 μm and form block structure. From the obtained data we can conclude that the developed boride-hardened

surfacing powder PG-Z40+10% CrB₂ has increased hardness and better properties compared to PG-Z40 surfacing powder [11].

CONCLUSIONS

1. The research helped to determine an optimal composition for CrB₂ hardener added to the new PG-Z40 surfacing alloy. It has been determined that in order to achieve 450-600 HV hardness of surfaced metal, the hardener has to be added in the amount up to 10% of total weight.

2. X-ray structure analysis showed that after mechanical alloying and melting of the compound, the composite surfacing alloy PG-Z40 with the addition of 10% of chromium boron appears as an iron nickel matrix with evenly distributed iron, chromium and nickel borides and carbides, and this observation is confirmed by the surfaced metal microhardness increase from 495,55 to 549,96 HV.

3. Increased hardness coatings can be created on the basis of the self-fluxing PG-Z40 alloy by adding chromium borides to the alloy prior to gas powder surfacing. Chromium borides are genetically bound by the composition of the surfacing material. The obtained structure ensures maximal wear-resistance of the coating and is characterized by even distribution of hardening crystal throughout the entire section achieved by the coating layer surface melting at the temperature of 1000-1100°C. Inadequate temperature during melting does not dissolve the added borides, and it results in non-homogeneity of the surface microstructure.

REFERENCES

- [1] Patent of the Republic of Kazakhstan №27499 dated 09/24/2013. Method of production of surfacing powder alloy for gas thermal surfacing. I.K. Beysembetov, B.K. Kenzhaliev, E.N. Suleimenov, V.G. Mironov, G.T. Shilov. Patent holder: "Kazakhstan-British Technical University" JSC.
- [2] Mironov V.G., Kenzhaliev B.K., Shilov G.T., Mahato M.M., Kalinin V.Yu., Suleimenov E.N. the conditions for producing of new iron-based filler alloy for the reconstruction of varied machines' and equipments' parts by mechanical alloying method. Proceeding of the "International Conference on Science and Technology of Ironmaking and Steelmaking", Section "Chemistry, Microstructure and Properties", Paper #5, 8 pages. Jamshedpur, India, Dec 16-18, 2013.
- [3] Innovation Patent of the Republic of Kazakhstan №27442 dated 09/24/2013. Device for producing surfacing powders "Attritor". B.K. Kenzhaliev, E.N. Suleimenov, G.T. Shilov, V.G. Mironov,

- V.Yu. Kalinin, Zh.B. Ilmaliyev. Patent holder: "Kazakhstan-British Technical University" JSC.
- [4] Hocking M. Metallic and ceramic coatings. Production, high temperature properties and applications. Translation from English edited by G.A. Andrievsky. M.: Mir. 2006. 518 p.
- [5] Mirkin L.I. X-ray diffraction control of engineering materials. M.: Mashinostroyenie, 134 p., 1979.
- [6] Kulik A.Y., Borisov Y.S., Mnukhin A.S., M.D. Nikitin. Gas thermal spraying of composite powders. L.: Mashinostroyenie, - Leningrad branch, p.199, 1985.
- [7] Popov V.A., Zaycev V.A., Prosviryakov A.S. et al. The study of mechanical alloying processes during the production of composite materials with nanoscaled strengthening particles. *Nanostructured materials and functional coatings*, **1**, 48-52, (2010).
- [8] Borisov Y.S., Borisova A.L. et al. Mechanical synthesis and mechanical alloying methods of gas thermal coatings production. «Welding industry», **12**, 18-21 (2010).
- [9] G.F. Lovshenko, F.G. Lovshenko, T.F. Khina. The effect of mechanoactivation on the processes of phase and structure formation during self-propagating high-temperature synthesis. Novosibirsk, Parallel, 168 p., 2008.
- [10] Gorelik S.S. X-ray diffraction and electron optical analysis. M.: Metallurgia, 338 p., 1970.
- [11] Beysembetov I.K., Kenzhaliev B.K., Mironov V.G., Shilov G.T., Ilmaliev Z.B., Omurbekova K.R. Self-Fluxing Surfacing Ferrous Alloy. *J. Chem. Bio. Phy. Sci. Sec. C*, May 2015 – July 2015; Vol.5, No.3; 2780-2787.

Numerical simulation of the coal dust process to the emission of nitrogen oxides

B. Ongar¹, I. K. Iliev²

¹Almaty University of Power Engineering and Telecommunications, Department of Heat Engineering Installations, 126, A. Baitursynov Str., 050013 Almaty, Kazakhstan

²University of Ruse, Department of Thermotechnics, Hydraulics and Ecology, 8 Studentska Str., 7017, Ruse, Bulgaria

In the experiment, the influence of the shift of the oxidant feed on the processes of formation of nitrogen oxides was studied. In order to do so, a vertical tubular furnace with electric heating was used. The flow of dust of Ekibastuz coal in all experiments was kept constant to 0.042 g/s, the grinding factor was 18% and the excess air ratio 1.2. The temperature in the furnace varied from 500°C to 700°C at an 11% oxygen concentration inside.

As a result of the experiments, it is shown that by pyrolysis of coal dust from Ekibastuz coal at temperatures of 500-700°C and the delay of time of air supply to the combustion zone by 0,1 s, under experimental conditions, we were able to reduce the concentration of nitrogen oxides by 3 times, including a 1.25 and 1.9 times reduction due to pyrolysis at temperatures ranging from 500 to 700°C, in addition to a 2.7 and 1.9 times reduction owing to the delay of the air supply introduced.

In the numerical simulation, the effect parameters such as fuel consumption, fuel temperature and air temperature on the nitrogen oxides' formation processes is investigated. Increasing the concentration of oxygen from 16 to 18% significantly increases both the temperature and the formation of thermal nitrogen. The increase in the concentration of coal dust has a complex nature of dependence, for instance at values higher than 40 kg/h, there was a reduction in the formation of nitrogen oxides.

Keywords: Combustion processes, concentration of nitrogen oxides, nitrogen oxides, torch, recombination, burner device

INTRODUCTION

In world energy consumption, coal accounts for about a quarter. For the most part, coal is used to generate electrical and heat energy for the pulverized combustion of large power plants in boilers. Large energy enterprises on coal are the main source of nitrogen oxide emissions into the atmosphere. The use of low-emission burners and step-by-step combustion schemes allows a significant reduction in nitrogen oxide emissions at relatively low costs for the reconstruction of the furnace.

As shown by experiments and data [1], noticeable pyrolysis of coal dust and the formation of nitrogen oxides begin at temperatures above 500° C.

From previous adjustment experiments [1], it is known that pyrolysis of Ekibastuz coal dust occurs without the formation of nitrogen oxides, which confirms the position known from the absence of the influence of fuel oxygen on the formation of nitrogen oxides. During gasification of Ekibastuz coal dust in the air, the concentration of nitric oxide NO increases with increasing temperature. Thus, when the furnace temperature changed from 500 to 900°C, the concentration of nitric oxide changed

from 340 to 670 mg/m³.

However, this is only a simplified scheme. In fact, modernization projects include a full range of changes in the combustion system. First of all, it is necessary to study in detail:

- combustion chamber for calculating heat exchange and residence time of fuel particles in it;
- equipment for air supply;
- elemental composition of fuels, their thermal and physical properties and granulometric characteristics;
- method of burning fuel;
- operating conditions of the boiler, including its load, the composition of the fuel mixture, the distribution of air and gas streams, the boiler control system, etc. All these components are very important and not strongly related to each other. Therefore, they can be modelled separately [2].

Questions of numerical modelling of combustion devices, construction of a mathematical model of the combustion process in the combustion chamber of a boiler unit are relevant.

THE RESULTS OF STUDY AND THEIR DISCUSSION

Suppression of the formation of nitric oxide in the combustion of dust from Ekibastuz coal is mainly dependent on the kinetics of the chemical processes taking place in the mixture. The purpose of this paper is to develop experimental studies on

* To whom all correspondence should be sent:
iiliev@enconservices.com

the determination of effective ways to suppress the formation of nitric oxide, taking into account the concentrations of the components of the mixture. Such studies are carried out using mathematical modelling. The formulation of the problem of mathematical modelling is carried out in the form of a system of algebraic equations, compiled based on the laws of conservation of mass, momentum and energy.

Analysis of the results of well-known experimental studies allow us to draw the following unambiguous conclusions for building a model:

The formation of heat occurs in the initial part of the torch at the stage of ignition and combustion of volatile substances.

The output of fuel NO_x according to this data is in the range of maximum temperature values $T_M = 1200 \div 1800 K$ and is proportional to $(T_M - 1025)^{0,33}$ with oxygen concentration in the reaction zone $\sim O_2^2$.

$$T_M < 1800$$

The type of nitrogen-containing compound and the oxygen content in the fuel do not affect the yield of nitrogen fuel oxides.

The effect of fuel oxides from nitrogen on the total emissions of nitrogen oxides is more significant at low temperatures of the combustion process ($T_M < 1800 K$).

The kinetic mechanism in the formation of fuel oxides of nitrogen has not yet been fully studied, therefore, when building a mathematical model, two trends can be observed. Some researchers [3] are trying to take into account all sorts of elementary combustion reactions and the formation of nitrogen oxides of all kinds, as well as decomposition reactions of nitrogen oxides.

The kinetic constants of reactions, which are taken from literature data [4], as a rule, are very approximate and do not take into account the possible mutual influence of reactions in such a complex system.

In an experimental study of the formation of nitrogen oxides in the pulverized coal flare of Ekibastuz coal, the results of the study are shown in the form of the recombination graphs N_{exit} и N_2 (pic. 1) and experimental points of the experiments, which show the dependence of the concentration of nitrogen oxides on the concentration of molecular oxygen and temperature in a one-dimensional flow. It can be seen that a decrease in the oxygen concentration in the carrier stream leads to a sharp

decrease in NO_x formation and a decrease in the final yield of nitrogen oxides.

Experimental data (Fig. 1) shows that the main formation of nitrogen oxides occurs when volatiles leave the coal. At very low temperatures (less than 900 K), volatiles do not ignite, and fuel oxides of nitrogen are almost not formed.

Figure 1 shows the graphs in the moment of release of atomic nitrogen from the fuel and its recombination into molecular nitrogen at different values of oxygen concentration (curves 1, 2, 3, 4, 5 correspond to oxygen concentrations of 1.3, 7, 10, 14% and process temperature in limits $T = 800 - 1800 K$).

Curve 1 in this figure indicates that in the absence of oxygen, atomic nitrogen fully recombines into molecular nitrogen under temperature conditions corresponding to energetic flue processes. Nitrogen oxides with the highest values of $O_2 = 14\%$ and $T = 1800 K$, are less than 7% from fuel. If, after complete recombination of atomic nitrogen, oxygen is introduced into the molecular nitrogen region of the reaction, nitrogen oxide is not formed. This is the advantage of the proposed method of phase shift processes (MFSP).

Also from curves 2-5 shown in Figure 1, it can be seen that, the greater the oxygen concentration, the less atomic nitrogen recombines into molecular nitrogen at the same temperature values T . This can be explained by the fact that with increasing oxygen concentration, chemically active atomic nitrogen reacts with oxygen to increase the degree of formation of nitric oxide.

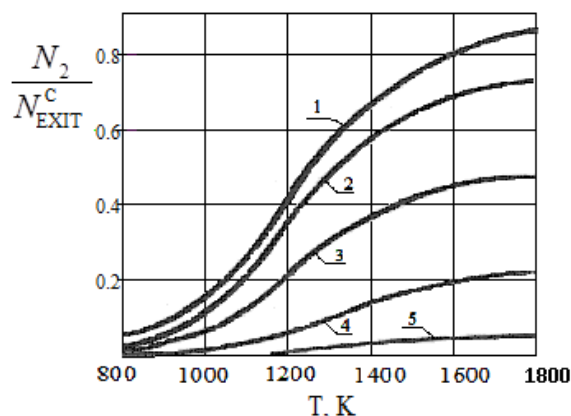


Fig.1. Recombination in for various 1, 2, 3, 4, 5 - ($N_2 = N_{EXIT}$), 1, 3, 7, 14 (%), ($N_{EXIT}^C = 2 \cdot 10^{-4}, kg / nm^3$), 1, 2, 3, 4, 5 - $T = 800, 1000, 1200, 1400, 1600, 1800 K$

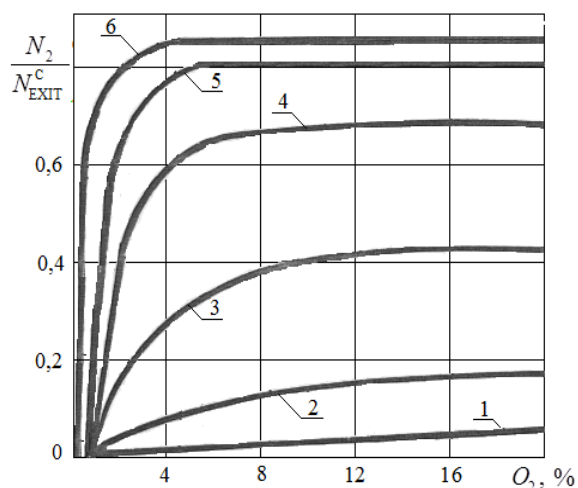


Fig.2. A recombination of N in N₂ depending on the temperature level of process at various values of concentration of oxygen 1 % (1), 2 % (2), 3 % (3), 4 % (4) and 5 % (5) of oxygen

Based on the data presented in Figure 2, it can be seen that the higher the temperature of the gasification process, the faster the release of atomic nitrogen and its recombination into molecular nitrogen. In this case, the indicated recombination ends at lower values of the oxygen concentration.

The recombination of atomic nitrogen into molecular nitrogen occurs, as can be seen from Fig.2, in a very short time and under ordinary energy conditions: $T=1800\div 1600\text{K}$; O_2 no more 3% in flue gases (recirculation to the root of the flare), this recombination ends in a time less than c (see curves 6 in Fig.2). Consequently, the recombination of atomic nitrogen into molecular nitrogen occurs at a distance of at most one meter from the cut-off of the burner. According to Figure 1, the possible recombination of atomic nitrogen into molecular nitrogen occurs in a very short time, less than 0,4s, over a wide range of oxygen concentration changes. For example, if in the gasification of the Ekibastuz coal dust in the environment of the combustion products ($T=1200\text{K}$ and $O_2=3\%$) the degree of this possible recombination is less 20%, then during its pyrolysis at $T=1800\text{K}$ this ratio increases to 74%, that is almost 4 times. The degree of formation (concentration) of nitric oxide decreases so many times.

It is therefore evident, that the realization of such a high pyrolysis temperature of coal dust, close to 1800 K, is most likely possible in the furnace itself due to the powerful radiation of the torch, incendiary belt and lining. Another task is to

provide this gasification temperature of coal dust with possible minimization of oxygen access, at least during the 0,4s.

In order to solve the different tasks, it is proposed to organize furnace processes with a phase shift in the supply of fuel and air to the combustion zone.

Modelling the formation of nitrogen oxides

To predict NO_x emissions, ANSYS Fluent solves the transport equation (equation 1). In cases where fuel nitrogen is specified, ANSYS Fluent solves additional transport equations for intermediate compounds such as HCN, NH₃. The transport equation NO_x is solved on the basis of data on flows and solutions to the equations of the combustion process. In other words, NO_x is processed after solving the combustion equations. Obviously, the accuracy of obtaining data on NO_x emissions are higher the higher the accuracy of the solutions of the combustion equations.

ANSYS Fluent solves the mass transfer equations for NO taking into account convection, diffusion, formation and decomposition of NO and related compounds. This general approach is based on the laws of conservation of mass. The influence of the time of finding on the mechanisms of formation of nitrogen oxides is taken into account through the convection variables in the determining equations. For the equation of the mechanism for the formation of thermal and fast NO_x, only one equation is needed:

$$\frac{\partial}{\partial t}(\rho Y_{NO}) + \nabla \cdot (\rho \bar{v} Y_{NO}) = \nabla \cdot (\rho D Y_{NO}) + S_{NO} \quad (1)$$

where, Y_{NO} is the mass fraction of NO, S_{NO} is a constant set by the user.

The formation of thermal NO_x is determined by a group of chemical equations that depend significantly on temperature, called the extended Zeldovich mechanism.

Influence of the temperature of coal dust on the emission of nitrogen oxides

To calculate the temperature of the particle, taking into account the convective and radiative heat exchange of the particle with the surrounding gas, a mathematical model with a number of empirical expressions was used, which made it possible to correct the heat transfer taking into account the mass exchange processes occurring during the heating and burning of the coal particle [5].

Conducting computational studies, a model of the volume of a fresh charge located in the inlet channels and in the cylinder was created (Fig.3).

The process is a simultaneous flow of interrelated processes: aerodynamic, chemical and thermal.

The pulverized flare in the combustion chamber is a two-phase medium. We use equations for a continuous medium, into which corrections are introduced for the presence of solid dust particles of coal. In such technical flows that occur in combustion chambers, as a rule, the effect of the second phase is neglected and it is believed that the pulverized-coal flare is a two-phase gaseous dispersion medium in which the influence of the solid phase on the flow aerodynamics can be neglected [6-8].

The experience of mathematical modelling of furnace processes is disclosed in an experimental study of the formation of nitrogen oxides in a pulverized-coal flare, so we describe the models used in the study.

For the description of turbulent characteristics, a two-parameter κ - ϵ turbulence model, which has proved itself for developed turbulent flows, is used. This model, as noted in accuracy in conjunction with relatively low requirements for computing facilities. Tab.1 shows the data for the simulation.

Table 1. Initial parameters

Parameter	Unit. Measurement	Digital value
Air consumption	kg/s	0,08
Coal dust consumption	kg/s	0,005
Argon flow rate	kg/s	0,001
Air temperature	K	300
Coal dust temperature	K	300-700
Argon temperature	K	500

During modelling, the temperature of coal dust varied from 500 K to 700 K in steps of one hundred degrees. The isometric view of the simulated area is shown in Fig.3.

In the simulated region, coal was fed from the upper part, and heated argon was fed tangentially. The air was fed by a counter flow to the coal dust.

Heated carrier (argon) is an inert medium in the form of argon that is used to heat the particles to the required temperature before supplying air to the mixing zone and increasing reliability in achieving

adequate conditions for the mixing process and ignition of pulverized coal in physical and numerical experiments.

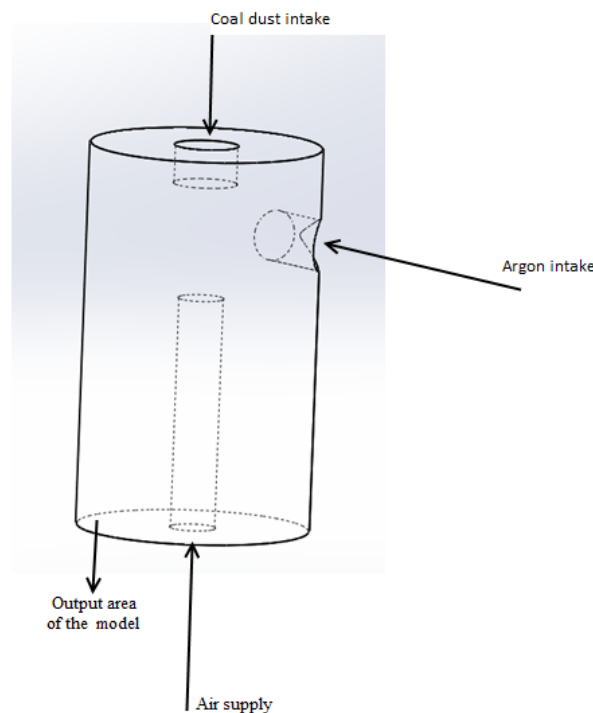


Fig.3. Modelling area

Fig.4 shows the contours of longitudinal velocities at different temperatures of coal dust. As can be seen from the picture, as the temperature increases, the air velocity from the nozzle increases, which indicates a lesser resistance to coal dust.

Second, it can be seen that the tangential velocity component created by argon tends to decrease, which is highlighted by the red circle.

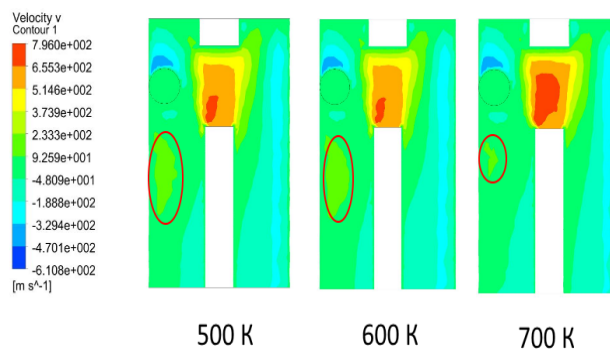


Fig.4. Contours of axial velocities at various temperatures of coal dust

Fig.5 shows the temperature profiles as a function of the temperature of the coal dust. As can be seen from the picture, with an increase in the

temperature of coal dust, the high-temperature zone shifts to the output of the model. This can be explained by the velocity flows shown in Fig.4. Air having a lower resistance pushes out high-temperature gases towards the exit region.

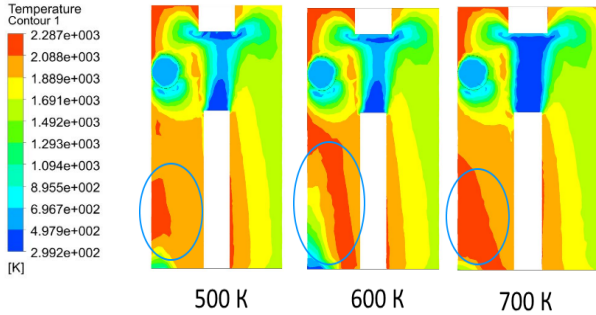


Fig.5. Temperature contours depending on the temperature of coal dust

Fig.6 shows the dependence of the concentrations of nitrogen oxides on the temperature of coal dust. It can be seen from the figure that an increase in the temperature of coal dust leads to an increase in the formation of nitrogen oxides, which is natural, in view of the fact that an increase in the temperature in the combustion zone increases the formation of nitrogen oxides.

An increase in the temperature of coal dust by 100 K leads to a twofold increase in the concentrations of nitrogen oxides, which explains the exponential dependence of the concentrations of nitrogen oxides and temperature.

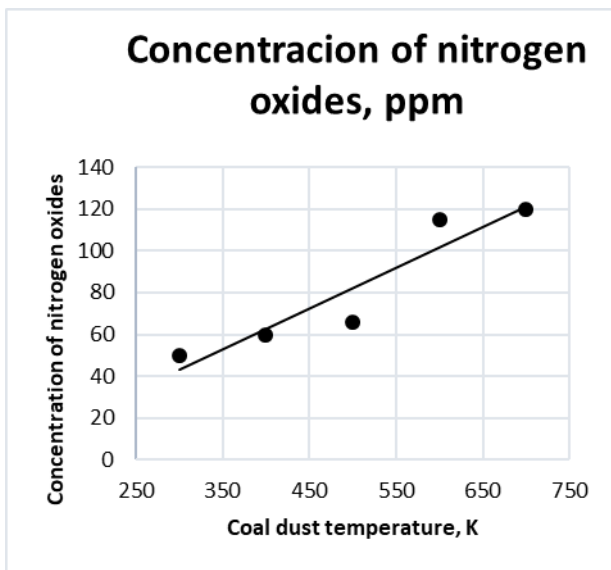


Fig.6. Dependence of concentrations of nitrogen oxides on the temperature of coal dust

Influence of air temperature

In these numerical experiments, the temperature of the initial air varied from 300 to 700 K.

Table 2, Parameters in the study

Parameter	Unit. Measurement	Digital value
Air consumption	kg/s	0,08
Coal dust consumption	kg/s	0,005
Argon flow rate	kg/s	0,001
Air temperature	K	300-700
Coal dust temperature	K	500
Argon temperature	K	500

Fig.7 shows the temperature contours for different initial air temperatures. An increase in air temperature leads to an increase in the temperature in the combustion zone. It is seen that, in comparison with the increase in fuel temperature, an increase in air temperature leads to a significant increase in the emission of nitrogen oxides. This is due to the fact that with an increase in temperature, which in the mass composition is greater than the composition of the fuel.

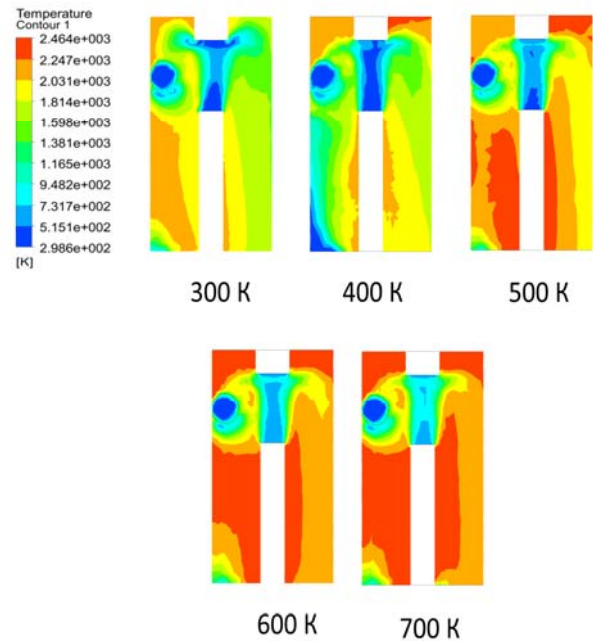


Fig.7. Dependence of temperature on the initial air temperature

Separately, it can be noted that the combustion process starts earlier, which indicates that an increase in temperature leads to an earlier ignition of the fuel.

It should be noted that the high-temperature zone with increasing air temperature approaches asymmetrical form. This is especially noticeable with an initial air of 700 K.

Fig.8 shows the dependence of the concentration of nitrogen oxides on the initial air temperature. An increase in the initial air temperature leads to a sharp increase in the emission of nitrogen oxides. Moreover, an increase in the initial air temperature until leads to an exponential increase in the concentration of nitrogen oxides. When the difference between 600 K and 700 K is almost 150 ppm, which is twice as much.

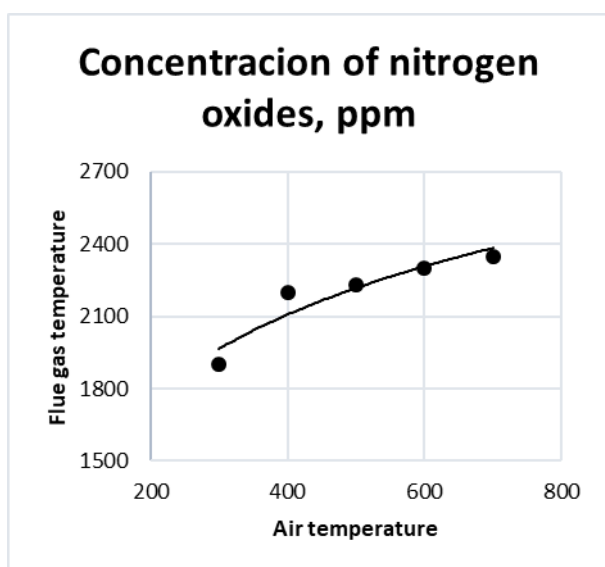


Fig.8. Dependence of the concentration of nitrogen oxides on the initial air temperature

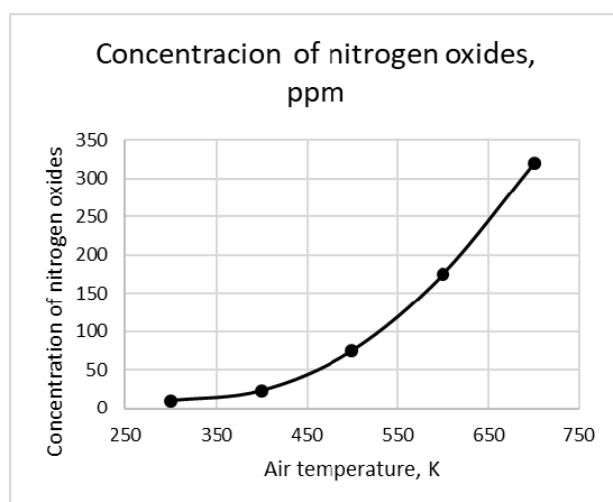


Fig.9. Temperature dependence of outgoing gases as a function of air temperature

An increase in the initial air temperature increases the average temperature at the exit from the experimental zone. Given that most of the nitrogen oxides are thermal, we can assume that despite an insignificant increase in the mean temperature, zones with local concentrations of fuel grow, which ensures a high growth of nitrogen oxide concentrations, as shown in Fig. 9.

CONCLUSIONS

The numerical simulation allowed to draw the following conclusions:

1. The temperature of fuel and air significantly influences the process of emissions of harmful substances. The numerical simulation of the combustion and mixing processes allowed us to determine the optimal combination of fuel consumption.

2. The process of flame stabilization and formation of harmful substances is significantly influenced by the excess air factor, determined in inverse relationship to the concentration of fuel (flow).

3. Numerical modelling of combustion processes, allow more detailed explanation of the combustion processes during the experiments, in view of the fact that the actual combustion processes are short-lived.

4. The optimal parameters for the fuel mass and pressure in the combustion chamber have previously been identified in the works of scientists, specializing in the modelling of two-phase flows [9-12]. Various types of solid fuels are used by these authors, especially coals from Kazakhstan of various grades and ash content, which are burnt in thermal power stations at the different thermal power plants of the country [13-15].

ACKNOWLEDGEMENTS

I express special gratitude to Dr. B.K. Aliyarov, for his encouraging recommendations on research in the field of formation of nitrogen oxides in the combustion of partially gasified coal.

The study was supported by the Almaty University of Energy and Communications, the authors do not state that there is no conflict of interest.

NOMENCLATURE

HHV - Higher heating value of fuel at 273 K, 0.1 MPa basis, MJ/m³;

LHV - Lower heating value of fuel at 273 K, 0.1 MPa basis, MJ/m³;
NO_x - nitrogen oxides;
NO - concentration of an oxide of nitrogen;
N₂ - molecular nitrogen, %;
O₂ - oxygen in air, %;
R - universal gas constant, R=8.314 J/(mol.K);
T - absolute temperature, K.

Subscripts

NO - concentration of an oxide of nitrogen.

REFERENCES

- [1] Khmyrov V. Slyambaeva A. Snezhanova T. Distribution of fuel nitrogen between volatile and coke residues during pyrolysis of coal // *Burner devices of power boilers*. - Almaty.: KazNIIIE. 69-74 (1991).
- [2] Al-Abbas A. CFD modelling of air-fired and oxyfuel combustion of lignite in 100 kWfurnace // *A.H. Al-Abbas, J. Naser, D. Dodds // Fuel*. – 1778–1795 (2011).
- [3] Habib M. Influence of combustion parameters on NO_x production in an industrial boiler [Text] // *M.A. Habib, M. Elshafei, M. Dajani// Compurets and fluids*, **37**: 12-22 (2008).
- [4] Syeda H. Modeling of a turbulent nonpremixed methane flame [Text] // *H. Syeda, D. Cecile// 3rd BSME – ASME International Conference on Thermal Engineering – 20-22 December: 1-7* (2006).
- [5] Chernetsky M., Dekterev A. Mathematical model of the processes of heat exchange and burning of pulverized coal in flaring. The physics of combustion and explosion. **3**, 37-46 (2011).
- [6] Muller H. Numerische Berechnung dreidimensionaler turbulenter Stromungen in Dampferzeugern mit Wärmeübergang und chemischen Reaktionen am Beispiel des SNCR – Verfahrens und der Kohleverbrennung: Fortschritt – Berichte VDI – Verlag. –Reihe 6, 268, 158 (1992).
- [7] Leithner, R. Numerical Simulation. Computational Fluid Dynamics CFD: Course of Lecture. Braunschweig, **52**, (2006).
- [8] Ustimenko B. Dzhakupov K. Krol V. Numerical modeling of aerodynamics and combustion in heating and technological devices. - Alma-Ata: - 224, (1986).
- [9] Gorokhovski M. Chtab-Desporte, A. Voloshina, I. Askarova (AIP Conf. Proc., Xian, 66-73 (2010).
- [10] Askarov, A. Messerle V. Ustimenko A. Bolegenova S. Maksimov V. Thermophysics and aeromechanics, **21**, 747 (2014).
- [11] Askarova A. Bolegenova S. Berezovskaya I. Ospanova Sh. (Proceedings of the 2013 Int. conf. on Applied Mathematics and Computational Methods in engineering, Rhodes Islands, Greece, 155-158 (2013).
- [12] Askarova A. Voloshin, I. Ryspayeva, M. (Abstracts of V-th International conference “Problems of industrial heat engineering”, Kiev, Ukraine, 27-28 (2007).
- [13] Askarova A. Messerle V. Ustimenko A. Bolegenova S. Maximov V. Gabitova, Z. High temperature, **53**, 445 (2015).
- [14] Askarova A. Maximov V. Bolegenova S. Beketayeva M. Safarik, P. Journal of thermal science, **24**, 275 (2015).
- [15] Karpenko E. Messerle V. Askarova A. Journal of High Energy Chemistry, **40**, 111 (2006).

Growth mechanism and photoluminescence property of flower-like ZnO by hydrothermal method

Bo Cao^{1, 2*}, Irsa Rasheed¹

¹*School of Nuclear Science and Engineering, North China Electric Power University, Beijing, 102206, China,*

²*Department of Atmospheric and Oceanic Sciences, University of California, Los Angeles, CA, 90095, USA*

With high stability, good optical characteristics, and unique electrical properties, ZnO nanostructures has been widely used in the vast fields. Because of its good performance in photoluminescence and photocatalysis, the three-dimensional (3D) flower-like nanostructure of ZnO has been paid much attention in recent years. In this paper, flower-like ZnO nanostructures formed by nanorods have been successfully synthesized by hydrothermal method. A number of techniques, including X-ray diffraction (XRD), scanning electron microscopy (SEM), and room temperatures photoluminescence (PL) were used to characterize the structural and optical properties of the obtained flower-like nanostructures of ZnO. The results indicate that the samples are highly crystalline with the wurtzite hexagonal phase, the average crystallite size of the sample was about 44 nm. A uniform flower-like three-dimension (3D) microstructures with diameters in the range of 3-5 μm was assembled by several densely arranged sword-like ZnO nanorods as "petals" with lengths in the range of 400-650 nm and a width in the range of 50-130 nm. The Photoluminescence spectrum (PL) showed that the as-synthesized flower-like ZnO showed ultraviolet emission (UV) at 381 nm and the visible emission band ranging from 450 nm to 750 nm, respectively. In addition, the growth mechanism of the flower-like ZnO was discussed.

Keywords: Zinc oxide, flower-like nanostructures, Photoluminescence spectrum (PL), growth mechanism, hydrothermal method

INTRODUCTION

Zinc oxide (ZnO) is an important n-type semiconductor metal oxide with a wide band gap (3.37 eV) and large exciton binding energy (60 meV) at room temperature. Because of high stability, good optical characteristics, and unique electrical properties [1-3], ZnO nanostructures has been widely used in the enormous fields such as solar cells, nano-lasers, piezoelectric devices, etc. [4-9]. The properties of ZnO nanostructures mainly depended strongly on their morphology, specific surface, crystallize size. Up to date, various morphologies of ZnO nanostructures including nanobelts, nanowires, nanorods, nanotubes, and nanoflowers have been demonstrated via thermal evaporation, chemical-vapor deposition (CVD), thermal evaporation, molecular-beam epitaxy (MBE), pulsed-laser deposition (PLD), electrochemical deposition and spray pyrolysis [10-18].

Because of its good performance in photoluminescence and photocatalysis, the three-dimensional (3D) flower-like nanostructure of ZnO has been paid much attention in recent years [19-22]. The low temperature hydrothermal synthesis has been widely used for the growth of ZnO nanostructures, mainly because of its simplicity,

cost effectiveness and the ability to control the shape and dimensions [23-25]. Till now, although flower-like ZnO have been synthesized by hydrothermal method, the growth mechanism and photoluminescence are also still need to be well exploited.

In the present study, the flower-like nanostructures of ZnO were synthesized by hydrothermal method with zinc acetate dehydrate ($\text{Zn}(\text{CH}_3\text{COO})_2 \cdot 2\text{H}_2\text{O}$) and sodium hydroxide (NaOH). The as-synthesized ZnO nanostructures were characterized by X-ray diffraction (XRD), scanning electron microscopy (SEM), and room temperature photoluminescence (PL) spectra.

EXPERIMENT

In this study, ZnO nanostructures sample has been synthesized using chemical methods. All of the raw materials were of analytical grade. First, about 1.32 mg of zinc acetate dehydrate ($\text{Zn}(\text{CH}_3\text{COO})_2 \cdot 2\text{H}_2\text{O}$) was dissolved in 20 ml of deionized water while stirring at room temperature. Then the 9 ml of sodium hydroxide (NaOH) was added gradually to the above solution under continuous stirring at room temperature. After this step, add distilled water to bring volume to 40 ml. The solution was transferred to a Teflon-lined autoclave. The autoclave was sealed and maintained at 160 °C for 12h, and then cooled to room temperature. The white precipitate was

* To whom all correspondence should be sent:
caobo@ncepu.edu.cn

separated by filtration, washed with deionized water and dried in an oven at 60 °C.

Characterization of samples was performed by X-ray diffraction (XRD) analysis and scanning electron microscopy (SEM) measurement. The powder X-ray patterns were carried out using a Philips X'pert automated diffractometer with monochromated Cu K-Alpha radiation of 1.5406 Å. The X-ray tube was operated at a voltage of 45 kV and a current of 40 mA. The peak position and intensities were obtained between 20 °C and 80 °C with a velocity of 0.02 per second. The surface morphologies and structure of the samples were studied by field emission scanning electron microscope (FE-SEM, JSM 6701-F, JEOL, Japan). Room temperature photoluminescence (RT-PL) spectra were measured using a He-Cd laser with the wavelength of 325 nm as the excitation source.

RESULTS AND DISCUSSION

XRD analysis

The XRD pattern of the as-synthesized product is shown in Fig.1. It can be seen that all of the diffraction peaks are in agreement with the JCPDS file of ZnO (JCPDS No. 36-1451). It is confirmed that the samples show wurtzite structure of ZnO belonging to the space group of P63mc (lattice parameters: $a=0.3249$ nm, $c=0.5206$ nm). No impurities could be observed in these patterns. Moreover, the sharp diffraction peaks manifest the high crystallinity of the sample. By using the Bragg's law and the Debye-Scherrer equation, we calculated the average crystallite size of the sample was about 44 nm.

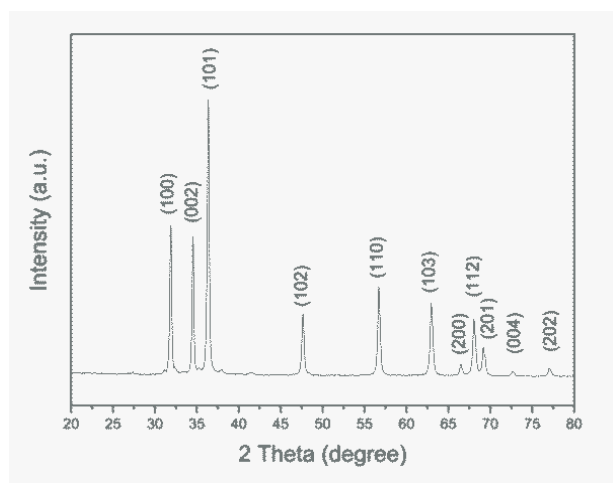


Fig.1. XRD patterns of the synthesized ZnO nanostructures

SEM characterization

Fig.2(a) and Fig.2(b) are the images of flower-like ZnO in low magnification and in high magnification, respectively. It can be seen a uniform flower-like three-dimension (3D) microstructures with diameters in the range of 3-5 μm (Fig.2(a)), assembled by several densely arranged sword-like ZnO nanorods as “petals” with lengths in the range of 400-650 nm (Fig.2(b)); and a width in the range of 50-130 nm.

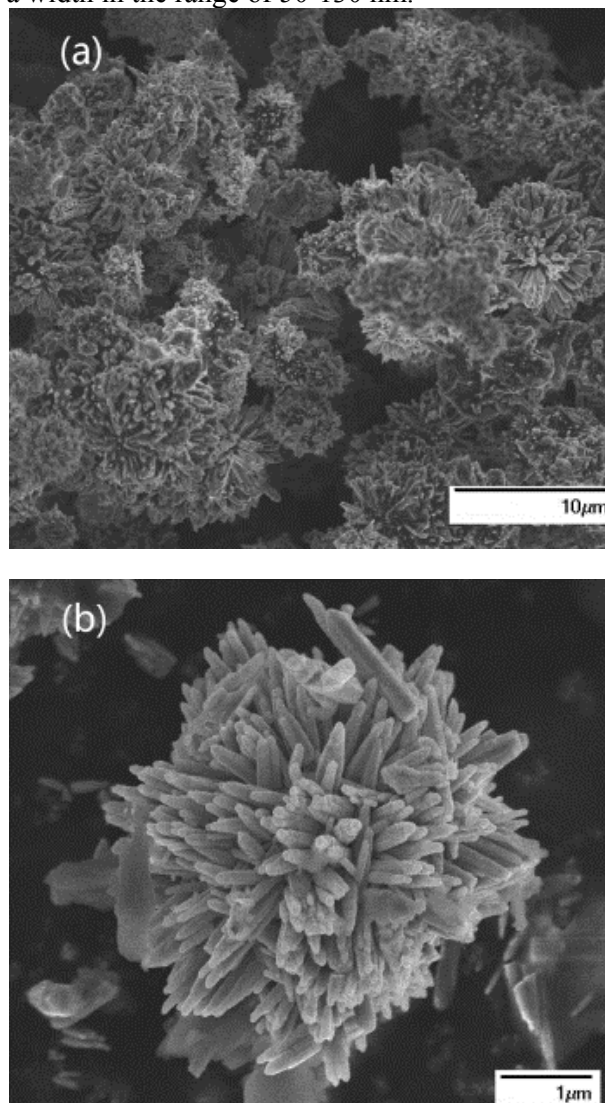


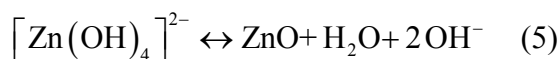
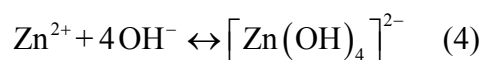
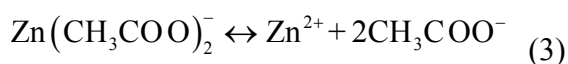
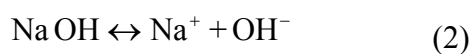
Fig.2. SEM images of synthesized ZnO nanostructures, (a) Low magnification, and (b) high magnification images of ZnO with flower-like morphology

Growth mechanism

Previous reports indicated that the formation process of ZnO nanostructures in alkali medium, the size, dimension and morphology of the final products were affected by external conditions such as temperature, complexing

agent and pH value of the solution during the hydrothermal process [26-27].

The possible formation mechanism of flower-like ZnO is proposed based on the investigation results. Firstly, the formation of primary ions have been shown in Eqs.(1-3). With the increasing of NaOH, the excess OH⁻ ions are in favor of the formation of [Zn(OH)₄]²⁻ ions which further decomposes to give ZnO nanoparticles (Eq.4). A part of [Zn(OH)₄]²⁻ ions will directly transform into ZnO nuclei after the concentration above its critical solubility under hydrothermal conditions (Eq.5) [28].



Based on surface energy minimization, the ZnO crystallites from zinc hydroxyl nucleate are beneficial for lifting the growth rate of ZnO nuclei along the c-axis direction and then grow into 1D nanorods. When the precursor concentration increases, the nucleation of ZnO is so rapid that more ZnO nuclei form in the initial stage. These nuclei may aggregate together due to excess saturation. Each of them individually grows along the c-axis into rod-like crystal, and thus flower-like architectures are finally formed [29]. The possible growth mechanism has been illustrated in Fig.3.

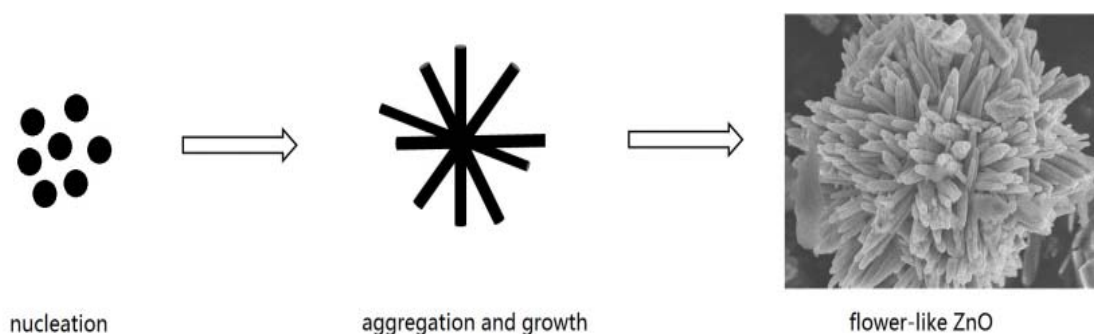


Fig.3. The schematic illustration of the possible growth process for flower-like ZnO nanostructures

Room temperature photoluminescence studies

The room temperature photoluminescence (PL) spectrum of the as-synthesized ZnO nanostructures is shown in Fig.4. It can be seen that the PL spectrum is composed of two emission bands: a weak emission band in violet region (381 nm) and a strong emission band in visible region. In general, the UV peak at room temperature is attributed to the recombination of free excitons [30-32]. The visible emission band of flower-like ZnO microstructures is ranging from 450 nm to 750 nm. This emission is ranging from green to red is quite complicated due to the native and dopant-

induced defects in ZnO, which are sensitively related to the synthesis procedures [33]. The possible intrinsic 'native' deep levels in ZnO are oxygen vacancy (V_O), zinc vacancy (V_{Zn}), oxygen interstitial (O_i), zinc interstitial (Zn_i), oxygen anti-site (O_{Zn}), and zinc anti-site (Zn_o). The green emission at 540 nm (2.30 eV) are attributed to the interstitial oxygen (O_i) [33]. The peak at 600 nm (2.07 eV) are possibly caused by the monovalent vacancies of zinc (V_{Zn}⁺) and oxygen (V_O⁻) in ZnO [33-34]. The result shown that flower-like ZnO possess a high-quality crystal and few oxygen vacancies.

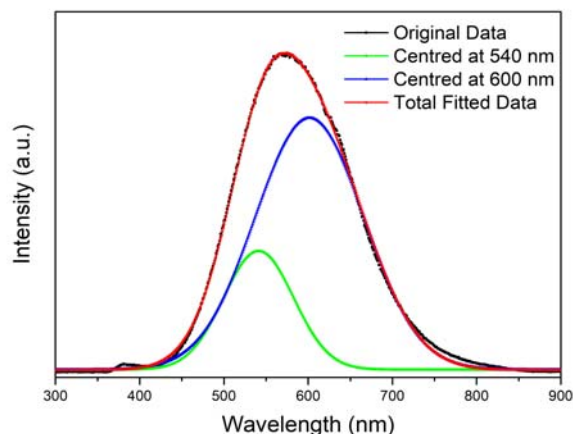


Fig.4. Room temperature photoluminescence spectrum of the as-synthesized ZnO nanostructures

CONCLUSIONS

In summary, flower-like ZnO nanostructures have been successfully synthesized by hydrothermal method with zinc acetate dehydrate ($\text{Zn}(\text{CH}_3\text{COO})_2 \cdot 2\text{H}_2\text{O}$) and sodium hydroxide (NaOH). The as-synthesized ZnO nanostructures were characterized by X-ray diffraction (XRD), scanning electron microscopy (SEM), and room temperature photoluminescence (PL) spectra. The results indicate that the samples are highly crystalline with the wurtzite hexagonal phase. The Photoluminescence spectrum (PL) showed that the as-synthesized flower-like ZnO showed ultraviolet emission (UV) at 381 nm and the visible emission band ranging from 450 nm to 750 nm, respectively. The UV peak at room temperature is attributed to the recombination of free excitons and the visible emission band ranging from green to red is attributed to the interstitial oxygen (O_i) and the monovalent vacancies, respectively.

ACKNOWLEDGEMENTS

This research was financially supported by the Fundamental Research Funds for the Central Universities (2018MS042) and China Scholarship Council (CSC).

NOMENCLATURE

XRD - X-ray diffraction;
SEM - scanning electron microscopy;
PL - photoluminescence;

3D - three-dimension;
UV - ultraviolet emission;
ZnO - Zinc oxide;
CVD - chemical-vapor deposition;
MBE - molecular-beam epitaxy;
PLD - pulsed-laser deposition;
 $\text{Zn}(\text{CH}_3\text{COO})_2 \cdot 2\text{H}_2\text{O}$ - zinc acetate dehydrate;
NaOH - sodium hydroxide;
RT-PL - Room temperature photoluminescence;
 V_O - oxygen vacancy;
 V_Zn - zinc vacancy;
 O_i - oxygen interstitial;
 Zn_i - zinc interstitial;
 O_Zn - oxygen anti-site;
 Zn_O - zinc anti-site.

REFERENCES

- [1] D.C. Look, Doping and Defects in ZnO, 1st ed., Elsevier Ltd., UK, 2006.
- [2] B.A. Buchine, W.L. Hughes, F.L. Degertekin, Z.L. Wang, Bulk acoustic resonator based on piezoelectric ZnO belts. *Nano Letter* **6**, 1155-1159 (2006).
- [3] M. Willander, O. Nur, Q.X. Zhao, L.L. Yang, M. Lorenz, B.Q. Cao, J. Zuniga Perez, C. Czekalla, G. Zimmermann, M. Grundmann, A. Bakin, A. Behrends, M. Al-Suleiman, A. Al-Shaer, A. Che Mofor, B. Postels, A. Waag, N. Boukos, A. Travlos, H.S. Kwack, J. Guinard, D. Le Si Dang, Zinc oxide nanorod based photonic devices: recent progress in growth, light emitting diodes and lasers. *Nanotechnology* **20**, 332001 (2009).
- [4] M. Laurenti, S. Porro, C. Pirri, C. Ricciardi, A. Chiolerio, Zinc oxide thin films for memristive devices: a review. *Critical Reviews in Solid State and Materials Sciences*, **42** (2), 153-172 (2017).
- [5] J.J. Cole, X. Wang, R.J. Knuesel, H.O. Jacobs, Integration of ZnO microcrystals with tailored dimensions forming light emitting diodes and UV PV cells. *Nano Letter* **8**(5), 1477-1481 (2008).
- [6] S. H. Bhang, W. S. Jang, J. Han, J. Yoon, W. La, E. Lee, Y.S. Kim, J. Shin, T. Lee, H.K. Baik, B. Kim. Zinc oxide nanorod-based piezoelectric dermal patch for wound healing. *Advanced Functional Materials*, **27** (1). (2017).
- [7] Q. Zhang, T.P. Chou, B. Russo, S.A. Jenekhe, G. Cao, Aggregation of ZnO nanocrystallites for high conversion efficiency in dye-sensitized solar cells. *Angew. Chemie Int. Ed.* **47**, 2402-6 (2008).
- [8] J.Y. Kim, H. Jeong, D.J. Jang, Hydrothermal fabrication of well-ordered ZnO nanowire arrays on Zn foil: room temperature ultraviolet nanolasers. *Journal of Nanoparticle Research* **13**, 6699-6706 (2011).
- [9] Z.L. Wang, J. Song, Piezoelectric Nanogenerators Based on Zinc Oxide Nanowire Arrays. *Science* **312**, 242-246 (2006).

- [10] T.L. Phan, S.C. Yu, R. Vincent, N.H. Dan, W.S. Shi, Photoluminescence properties of various CVD-grown ZnO nanostructures. *Journal of Luminescence* **130**, 1142-1146 (2010).
- [11] B. Daragh, F.A. Rabie, B. Teresa, G.R. David, T. Brendan, O.H. Martin, M. Enda, Study of Morphological and Related Properties of Aligned Zinc Oxide Nanorods Grown by Vapor Phase Transport on Chemical Bath Deposited Buffer Layers. *Crystal Growth & Design* **11** 5378-5386 (2011).
- [12] I.C. Robin, P. Marotel, A.H. El-Shaer, V. Petukhov, A. Bakin, A. Waag, M. Lafossas, J. Garcia, M. Rosina, A. Ribeaud, S. Brochen, P. Ferret, G. Feuillet, Compared optical properties of ZnO heteroepitaxial, homoepitaxial 2D layers and nanowires. *Journal of Crystal Growth* **311** 2172-2175 (2009).
- [13] Z.Q. Wang, X.D. Liu, J.F. Gong, H.B. Huang, S.L. Gu, S.G. Yang, Epitaxial growth of ZnO nanowires on ZnS nanobelts by metal organic chemical vapor deposition. *Crystal Growth & Design* **8**, 3911-3913 (2008).
- [14] B.A. Taleatu, A.Y. Fasasi, G. Di Santo, S. Bernstorff, A. Goldoni, M. Fanetti, L. Floreano, P. Borghetti, L. Casalis, B. Sanavio, C. Castellarin-Cudia, Electro-chemical deposition of zinc oxide nanostructures by using two electrodes. *AIP Advances* **1**, 032147 (2011).
- [15] M.J. Height, L. Mädler, S.E. Pratsinis, Nanorods of ZnO made by flame spray pyrolysis. *Chemistry of Materials* **18**, 572-578 (2006).
- [16] R.J. Mendelsberg, M. Kerler, S.M. Durbin, R.J. Reeves, Photoluminescence behavior of ZnO nanorods produced by eclipse PLD from a Zn metal target. *Superlattices and Microstructures* **43**, 594-599 (2008).
- [17] J.B. Shen, H.Z. Zhuang, D.X. Wang, C.S. Xue, H. Liu, Growth and Characterization of ZnO Nanoporous Belts. *Crystal Growth & Design* **9**, 2187-2190 (2009).
- [18] L.B. Feng, A.H. Liu, M. Liu, Y. Ma, J. Wei, B.Y. Man, Fabrication and characterization of tetrapod-like ZnO nanostructures prepared by catalyst-free thermal evaporation. *Materials Characterization* **61**, 128-133 (2010).
- [19] H. Zhang, D.R. Yang, X.Y. Ma, Y.J. Ji, J. Xu, D.L. Que, Synthesis of flower-like ZnO nanostructures by an organic-free hydrothermal process. *Nanotechnology* **15**, 622-626 (2004).
- [20] S. Chakraborty, A.K. Kole, P. Kumbhakar, Room temperature chemical synthesis of flower-like ZnO nanostructures. *Materials Letters* **67**, 362-364 (2012).
- [21] X.X. Yang, W. Lei, X.B. Zhang, B.P. Wang, C. Li, K. Hou, Y.K. Cui, Y.S. Di, Electrodeposition for antibacterial nickel-oxide-based coatings. *Thin Solid Films* **517**, 4385-4389 (2009).
- [22] X.T. Su, H. Zhao, F. Xiao, J.K. Jian, J.D. Wang, Synthesis of flower-like 3D ZnO microstructures and their size-dependent ethanol sensing properties. *Ceramics Int.* **38**, 1643-1651 (2012).
- [23] Y.H. Tong, Y.C. Liu, L. Dong, D.X. Zhao, J.Y. Zhang, Y.M. Lu, D.Z. Shen, X.W. Fan, Growth of ZnO nanostructures with different morphologies by using hydrothermal technique. *The J. of Phys. Chemistry B* **110**, 20263-7 (2006).
- [24] S.H. Jung, E. Oh, K.H. Lee, Y. Yang, C.G. Park, W.J. Park, S.H. Jeong, Sonochemical preparation of shape-selective ZnO nanostructures. *Crystal Growth & Design* **8**, 265-269 (2008).
- [25] W.W. Lee, J. Yi, S.B. Kim, Y.H. Kim, H.G. Park, W. Park, Morphology-controlled three-dimensional nanoarchitectures produced by exploiting vertical and in-plane crystallographic orientations in hydrothermal ZnO crystals. *Crystal Growth & Design* **11**, 4927-4932 (2011).
- [26] H. Zhang, D. Yang, S. Li, X.Y. Ma, Y. Ji, J. Xu, D. Que, Controllable growth of ZnO nanostructures by citric acid assisted hydrothermal process. *Materials Letters* **59**, 1696-1700 (2005).
- [27] C. Yan, D. Xue, L. Zou, A solution-phase approach to the chemical synthesis of ZnO nanostructures via a low-temperature route. *J. of Alloys and Compounds* **453**, 87-92 (2008).
- [28] R.X. Shi, P. Yang, X.B. Dong, Q. Ma, A.Y. Zhang, Growth of flower-like ZnO on ZnO nanorod arrays created on zinc substrate through low-temperature hydrothermal synthesis. *Applied Surface Science* **264**, 162-170 (2013).
- [29] W.Q. Peng, S.C. Qu, G.W. Cong, Z.G. Wang, Synthesis and structures of morphology-controlled ZnO nano- and microcrystals. *Crystal Growth & Design* **6**, 1518-1522 (2006).
- [30] J. Zhang, L. Sun, J. Yin, H. Su, C. Liao, C. Yan, Control of ZnO morphology via a simple solution route. *Chemistry of Materials* **14**, 4172-77 (2002).
- [31] M.H. Huang, Y.Y. Wu, H. Feick, N. Tran, E. Weber, and P.D. Yang, Catalytic growth of zinc oxide nanowires by vapor transport. *Advanced Materials* **13**, 113-116 (2001).
- [32] D. Zhang, X. Liu, Xin Wang, Growth and photocatalytic activity of ZnO nanosheets stabilized by Ag nanoparticles. *Journal of Alloys and Compounds* **509**, 4972-4977 (2011).
- [33] Y.W. Zhu, C.H. Sow, T. Yu, Q. Zhao, P.H. Li, Z.X. Shen, D.P. Yu, and Thong, J. T.-L. Thong, Co-synthesis of ZnO-CuO Nanostructures by Directly Heating Brass in Air. *Advanced Functional Materials* **16**, 2415-2422 (2006).
- [34] C. X. Xu, X. W. Sun, X. H. Zhang, L. Ke, and S. J. Chua, Zinc oxide nanowires and nanorods fabricated by vapour-phase transport at low temperature. *Nanotechnology* **15**, 856-861 (2004).

Critical points in solid-state phase transformation of a steel with 0.087% C and 0.511% Mn, determined through dilatometric analyses

C. Dulucleanu, T.L. Severin*, A. Potorac, L. Irimescu

University Stefan cel Mare, Suceava, Faculty of Mechanical Engineering, Mechatronics and Management, Department of Mechanics and Technologies, 13 University Street, 720229 Suceava, Romania, severin.traian@usm.ro

This article contains the results of dilatometric analyses carried out on a hypoeutectoid steel with 0.087% C and 0.511% Mn (Si, Cr, Ni, Mo, Al, Cu, V and W below 0.1%) in order to determine the temperatures that correspond to critical points in solid-state phase transformation, analyses carried out at continuous heating regime with different heating rates (between 1 and 30 °C/min). The eutectoid transformation (the pearlite dissolution into austenite) was carried out in a temperatures interval, ranging between pearlite dissolution start temperature (Ac_1) and pearlite dissolution finish temperature (denoted Ac_{fp} in this article). Increasing the heating rate determined a displacement of the critical points in solid-state phase transformation to higher temperatures; these displacements were more significant for the Ac_{fp} point, than for the critical points Ac_1 and Ac_3 . Raising of the temperatures of the critical points Ac_{fp} and Ac_3 , with the increase of the heating rate led to the decreasing of the temperatures range ($Ac_{fp} - Ac_3$), which is important for the dual-phase steels production technologies. In addition, the authors calculated the temperatures of the critical points Ac_1 and Ac_3 using mathematical models (provided by literature) and determined the differences between the values obtained through dilatometric analyses and those determined with mathematical models.

Keywords: critical point, dilatometric analysis, heating rate, dual-phase steel

INTRODUCTION

According to the Fe-C equilibrium diagram, a hypoeutectoid Fe-C binary alloy has two important critical points in solid-state phase transformation: the point or temperature Ae_1 at which the dissolution of the pearlite (P) in austenite (γ) occurs, process which represents an eutectoid transformation ($P \rightarrow \gamma$) and the point or temperature Ae_3 where the allotropic transformation of proeutectoid ferrite (α) into austenite ends ($\alpha \rightarrow \gamma$); under equilibrium conditions, the pearlite dissolution (the eutectoid transformation, $P \rightarrow \gamma$) takes place at a constant temperature (at 727 °C), and the completion of allotropic transformation ($\alpha \rightarrow \gamma$) occurs at a temperature that decreases progressively with the increase in the percentage of carbon in the alloys. During the heating and cooling cycles of a Fe-C binary alloy a thermal hysteresis appears and for this reason, for the same critical point, three values correspond, namely: Ac for heating, Ar for cooling and Ae for equilibrium conditions; it should be emphasised that the Ac and Ar values are sensitive to the rates of heating and cooling. These critical points in solid-state phase transformation can be easily detected by dilatometric analysis [1-3].

In the case of commercial steels, that are Fe-C

alloys and with other chemical elements in composition (like alloying elements or impurities), the Fe-C equilibrium diagram does not fully apply. The alloying elements and impurities in the chemical composition of commercial steels change the position of critical points (both temperature and carbon composition); in addition, unlike in the case of the binary system, the pearlite dissolution into austenite (eutectoid transformation, $P \rightarrow \gamma$) no longer occurs at constant temperature, but in a temperatures range, namely, between pearlite dissolution start temperature (Ac_1 critical point) and pearlite dissolution finish temperature (denoted Ac_{fp} in this article). The temperature Ac_{fp} indicates the beginning of ferrite and austenite coexistence range during heating (beginning of the allotropic transformation of ferrite into austenite, $\alpha \rightarrow \gamma$), range that stretches up to the temperature of the Ac_3 point, the determination of this range of coexistence of the ferrite and austenite ($Ac_{fp} - Ac_3$) being of great importance for the technologies of manufacturing dual-phase steels [1-5]. These steels are alloys with a low carbon content, which have a structure consisting of a soft and ductile ferrite matrix in which are homogeneously dispersed, martensite (10 to 35 %) and a small amount of residual austenite (1 to 2 %). For dual-phase steels the stress-strain curve is continuous, without yield; they have a low yield strength and a high tensile strength ($R_{p0.2}/R_m$ ratio is about 0.5), and to small stresses their work hardening is very fast. The dual-

* To whom all correspondence should be sent: severin.traian@fim.usv.ro

phase steels products worldwide have, generally, a percentage of carbon less than 0.12 %, a content of manganese between 1.0 % and 3.5 %, whereas elements such as V, Cr, Mo and, Nb, are to be found in chemical composition in proportions situated below 1%; in the last few years there have been carried out studies on steels in which the content of manganese is even less than 1 % (0.5 ÷ 1 % Mn) [6-10]. The main technology of producing these steels consists of quenching at temperatures in the intercritical range ($\alpha + \gamma$); the structure obtained, for a given chemical composition, is the result of combined action of heating temperature and the cooling rate, the influence of these two technical parameters on the structure of the material being directly reflected on its properties. The mechanical properties of a dual-phase steel are fundamentally influenced by the volume fraction of martensite in the structure, by the morphology and the distribution of this phase, structural characteristics which, in their turn, are affected, particularly, by the heating temperature in the range ($\alpha + \gamma$). For this reason, the heating temperature represents an essential technological parameter in the process of making such a steel, determining the volume fraction of austenite and finally, after cooling, the volume fraction of martensite formed into an alloy with a certain chemical composition [6-9]. Therefore, for designing and developing a dual-phase steel production technology, it is necessary to know the temperatures of the critical points Ac_1 , Ac_{fp} and Ac_3 . A quick and convenient method for determining the temperatures of critical points in solid-state phase transformation when heating a steel lies in the use of mathematical models that take into account the chemical composition (equations obtained by statistical processing of experimental results), but these equations can generate severe errors [1, 2, 11]. A high precision in finding these temperatures is obtained by dilatometric analysis; modern dilatometers, connected to computerised systems, collect the signals of change in the length of a specimen as a function of temperature, plot a dilatometric curve, calculate and generate its corresponding derivative and allow the identification of both the critical points Ac_1 and Ac_3 , as well as the pearlite dissolution finish temperature (the Ac_{fp} point) and therefore, the determination of the temperatures range ($Ac_{fp} - Ac_3$) [2, 5, 12, 13].

This article describes some of the researches carried out at "Stefan cel Mare" University of Suceava, Romania, for obtaining and

characterization of dual-phase steels with low manganese content (below 1% Mn). The results of the dilatometric analyses performed on specimens made of a commercial steel, used in industry, mainly, for electrodes and welding wires, are presented. As a result of these researches, the temperatures of the critical points in solid-state phase transformation were identified, the influence of the heating rate on these temperatures was established and a comparison was made between the values determined by dilatometric analyses and those obtained using mathematical models.

EXPERIMENTAL DETAILS

The chemical composition of the investigated steel was determined with a FOUNDRY-MASTER Xpert spectrometer (Oxford Instruments Analytical GmbH, Germania), and led to the next values (weight %): Fe, 0.087 C, 0.511 Mn, 0.091 Si, 0.0036 P, 0.0039 S, 0.029 Cr, 0.005 Mo, 0.049 Ni, 0.003 Al, 0.082 Cu, 0.003 V, 0.003 W; the initial structure was ferrite-pearlite, consisting of 85.30% ferrite and 14.70% pearlite.

The dilatometric analyses were performed with a DIL 402 Expedis-SUPREME Dilatometer (NETZSCH Gerätebau GmbH, Germany), on cylindrical specimens with a diameter of 5 mm and a length of 25 mm, continuous heated in (30 ÷ 980) °C temperature range, in nitrogen atmosphere (100 ml/min N₂), with a load at the specimen of 200 mN and with the following heating rates: 1, 3, 5, 10 and 30 °C/min. Three dilatometric analyses were performed for each heating rate (three specimens for each heating rate); finally, the signals provided by the dilatometer were processed with NETZSCH Proteus® Software 7.1.0.

RESULTS AND DISCUSSION

During austenite formation, the local changes in the crystal structure conducted to a macroscopic volume contraction of the specimen; these changes can be detected and quantified by dilatometric analysis. The volume contraction has two main contributions: I) the difference in specific volume between the phases involved in the transformation (austenite, ferrite and cementite) and II) the variation of the austenite specific volume due to the carbon enrichment or depletion [3, 14]. Thus, at continuous heating of a hypoeutectoid Fe-C binary alloy, the critical points Ac_1 and Ac_3 appear on a dilatometric curve which plots the variation of the relative length of a specimen on temperature, $\Delta L/L_0$.

= $f(T)$, and the two critical points can be determined from changes in the slope of the dilatometric curve (Fig.1). The critical point Ac_1 is defined as the temperature at which the linear thermal expansion (graphically represented by the $\Delta L/L_0=f(T)$ function) has the first deviation from linearity; this behaviour is caused by the volume contraction associated with the austenite formation, which first compensates, and then reverses the normal expansion of the specimen due to the increase in temperature. The location of the point at which the deviation occurs is obtained by extrapolating the linear portion of the dilatometric curve. The critical point Ac_3 is defined as the temperature at which the thermal expansion begins again to depend linearly on temperature; likewise, this point is determined by extrapolating the linear portion of the dilatometric curve after transformation [2-5, 14].

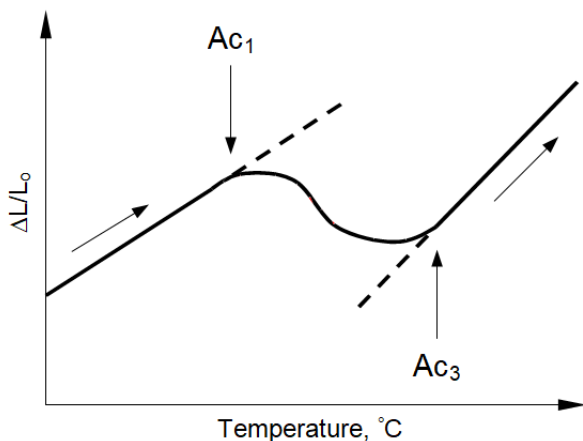


Fig.1. Schematic variation of the relative change of length as a function of temperature during continuous heating of a hypoeutectoid Fe-C binary alloy specimen [4]

The signals of change in the length of the steel specimens characterised by 0.087% C and 0.511% Mn, depending on the temperature, collected during dilatometric analyses with the computerised systems of the DIL 402 Expedis-SUPREME Dilatometer, have led to the plotting of the dilatometric curves, as well as to the calculation and graphic representation of their first derivative. Fig.2 shows the dilatometric curve and its corresponding derivative, for a heating rate of 3 °C/min.

Normally, no difference between the pearlite dissolution process ($P \rightarrow \gamma$) and the allotropic transformation of ferrite into austenite ($\alpha \rightarrow \gamma$) is detected on the continuous heating dilatometric curve obtained for a hypoeutectoid Fe-C binary alloy (Fig.1). However, all the dilatometric curves

drawn for the investigated steel (regardless of the heating rate), present an unusual anomaly at the onset of the austenitization; this obvious anomaly, highlighted by other researchers as well [2-5, 12-

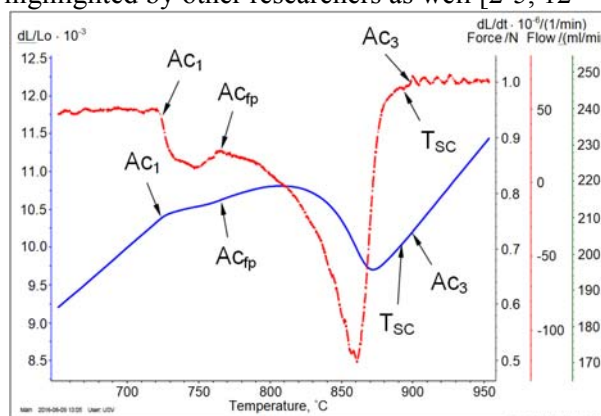


Fig.2. The dilatometric curve (continuous line) and its corresponding derivative, for the heating rate of 3 °C/min

15], is a contraction associated to the pearlite dissolution (Fig.2). The possibility to be able to precisely highlight the two processes that take place when heating a hypoeutectoid steel (the pearlite dissolution into austenite and the allotropic transformation of ferrite into austenite) by means of high resolution dilatometry permits the determination of the Ac_{3p} temperature (the pearlite dissolution finish temperature) as well. Ac_{3p} is the temperature at which the first contraction on the dilatometric curve, due to the pearlite dissolution into austenite ($P \rightarrow \gamma$), finishes; it is also a transition temperature between the two transformations, ($P \rightarrow \gamma$) and ($\alpha \rightarrow \gamma$) [2, 5, 12-15]. This point is less obvious on the dilatometric curve, $\Delta L/L_0 = f(T)$, but easier to determine from the first derivative curve, $d(\Delta L/L_0)/dT = f(T)$. Thus, first derivative curve shows two peaks which indicate the contraction caused by ($P \rightarrow \gamma$) and ($\alpha \rightarrow \gamma$) transformations (Fig.2, dashed line); the critical temperatures Ac_1 and Ac_3 were chosen as points of decrease of first derivative curve below the minimum value found in the section where the derivative is approximately constant, whereas the pearlite dissolution finish temperature, Ac_{3p} , was chosen at the point where the sloping-up part of the first derivative curve starts to bend to the right [2, 12, 13, 16, 17]. Immediately after finishing pearlite dissolution ($P \rightarrow \gamma$), the allotropic transformation of ferrite in austenite ($\alpha \rightarrow \gamma$) begins, transformation which determine also a decrease in the specific volume (a contraction); after achieving a minimum in the changing of the relative length of the specimen, on the dilatometric curves, at a

temperature noted T_{SC} in Fig.2, there is a small contraction which is better highlighted on the first derivative curves, which have a small peak at T_{SC} temperature. This modification of the volume is difficult to explain; perhaps, the phenomenon was caused, either through the formation (almost instantaneously) of austenite from a ferrite that remains untransformed in structure [3, 15], either through a diffusion of carbon from rich-carbon austenite (formed of pearlite) in the less-carbon austenite (formed of ferrite) [17]. Tab.1 shows, depending on the heating rate, the temperatures of the critical points in solid-state phase transformation of a steel with 0.087% C and 0.511% Mn. Results were obtained through processing with NETZSCH Proteus® Software 7.1.0. the signals of change in the length of the specimens provided by the dilatometer, during the tests.

Table 1. Results of the dilatometric analyses

Heating rate °C/min	Ac_1 °C	Ac_{fp} °C	Ac_3 °C	$(Ac_{fp} - Ac_3)$ °C
1	723.40	764.70	898.90	134,20
3	724.00	765.60	899.40	133,80
5	724.90	767.30	901.10	133,80
10	727.60	770.50	904.20	133,70
30	737.30	784.20	908.50	124,30

Data in Tab.1 demonstrate that when increasing the heating rate, the critical points in solid-state phase transformation (Ac_1 , Ac_{fp} and Ac_3) are moving toward higher temperatures (Fig.3). At low heating rates (1 °C/min and 3 °C/min) the differences between temperatures of the same critical points are very low, less than 1 °C (0.60 °C for Ac_1 , 0.90 °C for Ac_{fp} and 0.50 °C for Ac_3). Raising the heating rate has led to an increase in these differences between the temperatures of the critical points; for example, between the temperatures obtained at heating rates of 10 °C/min and 30 °C/min, the differences were 9.70 °C for Ac_1 , 13.70 °C for Ac_{fp} and 4.30 °C for Ac_3 . Increasing the heating rate from 1 to 30 °C/min determined a displacement with 19.50 °C, of the critical point Ac_{fp} toward higher temperatures (from 764.70 to 784.20 °C); the displacement of critical points Ac_1 , and especially the Ac_3 is smaller, that is with 13.90 °C for Ac_1 (from 723.40 °C to 737,30 °C) and with 9.60 °C for Ac_3 (from 898.90 °C to 908.50 °C). The displacements of the critical points in solid-state phase transformation with the increase of the heating rate led to the decreasing of the temperatures range ($Ac_{fp} - Ac_3$), Tab.1. Raising the

heating rate from 1 to 10 °C/min caused an insignificant decrease, of less than 1 °C (from 134.20 °C for 1 °C/min, to 133.80 °C for 3 °C/min and 5 °C/min and at 133.7 °C for 10 °C/min). However, increasing heating rate from 10 to 30 °C/min led to a decrease with 9.40 °C of the temperatures range ($Ac_{fp} - Ac_3$), from 133.70 to 124.30 °C; between the values obtained for this temperature range at heating speeds of 1 and 30 °C/min, the difference is 9.90 °C (from 134,20 to 124,30 °C).

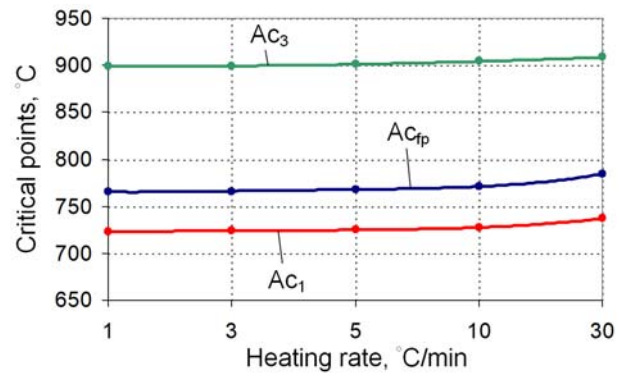


Fig.3. The influence of the heating rate on the temperatures of the critical points

Over the years, many researchers have developed mathematical models, that could estimate, through statistical processing of experimental results, depending on the chemical composition (in mass percent), the temperatures of the critical points in solid-state phase transformation; some of these mathematical models (equations) are listed below (in chronological order):

- R.A. Grange (1961) [1, 11]

$$Ae_1 = 1333 - 25 \cdot Mn + 40 \cdot Si + 42 \cdot Cr - 26 \cdot Ni \quad (1)$$

$$Ae_3 = 1570 - 323 \cdot C - 25 \cdot Mn + 80 \cdot Si - 3 \cdot Cr - 32 \cdot Ni \quad (2)$$

(Ae_1 - lower equilibrium temperature between ferrite and austenite, °F; Ae_3 - upper equilibrium temperature between ferrite and austenite, °F);

- K.W. Andrews (1965) [1, 11]

$$Ae_1 = 723 - 16.9 \cdot Ni + 29.1 \cdot Si + 6.38 \cdot W - 10.7 \cdot Mn + 16.9 \cdot Cr + 290 \cdot As \quad (3)$$

$$Ae_3 = 910 - 203\sqrt{C} + 44.7 \cdot Si - 15.2 \cdot Ni + 31.5 \cdot Mo + 104 \cdot V + 13.1 \cdot W - 30 \cdot Mn + 11 \cdot Cr + 20 \cdot Cu - 700 \cdot P - 400 \cdot Al - 120 \cdot As - 400 \cdot Ti \quad (4)$$

(Ae_1 - lower equilibrium temperature between ferrite and austenite, °C; Ae_3 - upper equilibrium temperature between ferrite and austenite, °C);

- G.T. Eldis (1978) [1, 11]

$$Ae_1 = 712 - 17.8 \cdot Mn - 19.1 \cdot Ni + 20.1 \cdot Si + 11.9 \cdot Cr + 9.8 \cdot Mo \quad (5)$$

$$Ae_3 = 871 - 254.4\sqrt{C} - 14.2 \cdot Ni + 51.7 \cdot Si \quad (6)$$

(Ae_1 - lower equilibrium temperature between ferrite and austenite, °C; Ae_3 - upper equilibrium temperature between ferrite and austenite, °C);

- H.P. Hougardy (1984) [1, 11]

$$Ac_1 = 739 - 22 \cdot C - 7 \cdot Mn + 2 \cdot Si + 14 \cdot Cr + 13 \cdot Mo - 13 \cdot Ni \quad (7)$$

$$Ac_3 = 902 - 255 \cdot C - 11 \cdot Mn + 19 \cdot Si - 5 \cdot Cr + 13 \cdot Mo - 20 \cdot Ni + 55 \cdot V \quad (8)$$

(Ac_1 - lower temperature of the ferrite-austenite field during heating, °C; Ac_3 - upper temperature of the ferrite-austenite field during heating, °C);

- O.G. Kasatkin, B.B. Vinokur (1984) [1, 9, 11]

$$Ac_1 = 723 - 7.08 \cdot Mn + 37.7 \cdot Si + 18.1 \cdot Cr + 44.2 \cdot Mo + 8.95 \cdot Ni + 50.1 \cdot V + 21.7 \cdot Al + 3.18 \cdot W + 297 \cdot S - 830 \cdot N - 11.5 \cdot C \cdot Si - 14 \cdot Mn \cdot Si - 3.1 \cdot Si \cdot Cr - 57.9 \cdot C \cdot Mo - 15.5 \cdot Mn \cdot Mo - 5.28 \cdot C \cdot Ni - 6 \cdot Mn \cdot Ni + 6.77 \cdot Si \cdot Ni - 0.8 \cdot Cr \cdot Ni - 27.4 \cdot C \cdot V + 30.8 \cdot Mo \cdot V - 0.84 \cdot Cr^2 - 3.46 \cdot Mo^2 - 0.46 \cdot Ni^2 - 28 \cdot V^2 \quad (9)$$

$$Ac_3 = 912 - 370 \cdot C - 27.4 \cdot Mn + 27.3 \cdot Si - 6.35 \cdot Cr - 32.7 \cdot Ni + 95.2 \cdot V + 190 \cdot Ti + 72 \cdot Al + 64.5 \cdot Nb + 5.57 \cdot W + 332 \cdot S + 276 \cdot P + 485 \cdot N - 900 \cdot B + 16.2 \cdot C \cdot Mn + 32.3 \cdot C \cdot Si + 15.4 \cdot C \cdot Cr + 48 \cdot C \cdot Ni + 4.32 \cdot Si \cdot Cr - 17.3 \cdot Si \cdot Mo - 18.6 \cdot Si \cdot Ni + 4.8 \cdot Mn \cdot Ni + 40.5 \cdot Mo \cdot V + 174 \cdot C^2 + 2.46 \cdot Mn^2 - 6.86 \cdot Si^2 + 0.322 \cdot Cr^2 + 9.90 \cdot Mo^2 + 1.24 \cdot Ni^2 - 60.2 \cdot V^2 \quad (10)$$

(Ac_1 - lower temperature of the ferrite-austenite field during heating, °C; Ac_3 - upper temperature of the ferrite-austenite field during heating, °C; These equations are valid within these composition limits: C ≤ 0.83%, Mn ≤ 2.0%, Si ≤ 1.0%; Cr ≤ 2.0%, Mo ≤ 1.0%, Ni ≤ 3.0%, V ≤ 0.5%, W ≤ 1.0%, Ti ≤ 0.15%, Al ≤ 0.2%, Cu ≤ 1.0%, Nb ≤ 0.20%, P ≤ 0.040%, S ≤ 0.040%, N ≤ 0.025%, B ≤ 0.010%);

- J. Trzaska, L.A. Dobrzański (2007) [1, 11]

$$Ac_1 = 739 - 22.8 \cdot C - 6.8 \cdot Mn + 18.2 \cdot Si + 11.7 \cdot Cr - 15 \cdot Ni - 6.4 \cdot Mo - 5 \cdot V - 28 \cdot Cu \quad (11)$$

$$Ac_3 = 937.3 - 224.5\sqrt{C} - 17 \cdot Mn + 34 \cdot Si - 14 \cdot Ni + 21.6 \cdot Mo + 41.8 \cdot V - 20 \cdot Cu \quad (12)$$

(Ac_1 - lower temperature of the ferrite-austenite field during heating, °C; Ac_3 - upper temperature of the ferrite-austenite field during heating, °C).

Tab.2 gives the temperatures of critical points of the steel with 0,087% C and 0,511% Mn, obtained using the equations mentioned above.

Table 2. The temperatures of critical points calculated with mathematical models

Mathematical models	Critical points	
	$Ae_1 =$	$Ae_3 =$
R.A. Grange Eq.(1) și (2)	1323.80 °F	1534.70 °F
	or	or
	717.70 °C	834.80 °C
K.W. Andrews Eq.(3) și (4)	$Ae_1 =$	$Ae_3 =$
	719.90 °C	836.90 °C
G.T. Eldis Eq.(5) și (6)	$Ae_1 =$	$Ae_3 =$
	704.20 °C	800.00 °C
H.P. Hougardy Eq.(7) și (8)	$Ac_1 =$	$Ac_3 =$
	733.50 °C	875.00 °C
O.G. Kasatkin, B.B. Vinokur Eq.(9) și (10)	$Ac_1 =$	$Ac_3 =$
	724.40 °C	877.70 °C
J. Trzaska, L.A. Dobrzański Eq.(11) și (12)	$Ac_1 =$	$Ac_3 =$
	732.50 °C	863.40 °C

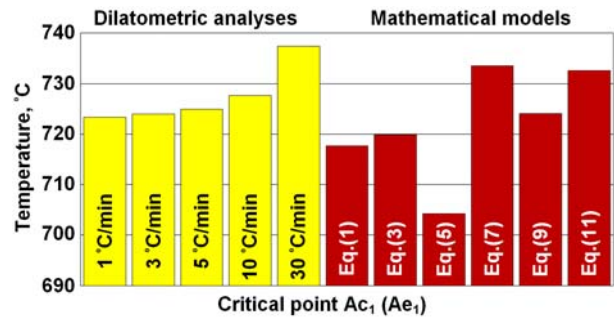


Fig.4. Temperatures of critical point Ac_1 (Ae_1) determined through dilatometric analyses and with mathematical models

The results presented in Tabs.1, 2 show that:

- between the temperatures of critical points determined through dilatometric analyses and those calculated with mathematical models are differences between 0.40 and 33.10 °C for the critical point Ac_1 (Ae_1) and between 21.20 and 108.50 °C for the critical point Ac_3 (Ae_3), Fig.4, 5;

- the lowest errors were generated, for the Ac_1 critical point, by equations of O.G. Kasatkin, B.B. Vinokur (between 0.40 and 12.90 °C), H.P. Hougardy (between 3.80 and 10.10 °C) and J. Trzaska, L.A. Dobrzański (between 4.80 and 9.10

°C), and for the Ac_3 critical point, by equations of O.G. Kasatkin, B.B. Vinokur, (between 21.20 and 30.80 °C) and H.P. Hougardy (between 23.90 and 33.50 °C);

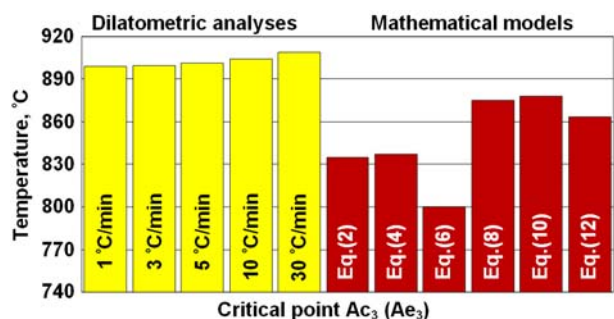


Fig.5. Temperatures of critical point Ac_3 (Ae_3) determined through dilatometric analyses and with mathematical models

- the biggest differences were obtained using the mathematical model developed by G.T. Eldis (between 19.20 and 33.10 °C for the Ac_1 critical point and between 98.90 and 108.50 °C for the Ac_3 critical point);

- unlike the high resolution dilatometry, the mathematical models do not allow the calculation of the pearlite dissolution finish temperature (Ac_{fp}) and hence, the determination of the temperatures range ($Ac_{fp} - Ac_3$).

CONCLUSIONS

The pearlite dissolution into austenite (eutectoid transformation) was carried out in a temperature interval ranging between pearlite dissolution start temperature (critical point Ac_1) and pearlite dissolution finish temperature (denoted Ac_{fp} in this article).

The temperatures of the critical points in solid-state phase transformation were influenced by the heating rate, its increase leading to the displacement of critical points to higher temperatures; raising the heating rate caused a more significant displacement for the Ac_{fp} point, than for the critical points Ac_1 and Ac_3 .

The displacements of the critical points Ac_{fp} and Ac_3 , with the increase of the heating rate, led to the decreasing, up to 9.90 °C, of the temperatures range ($Ac_{fp} - Ac_3$), range which is important for the dual-phase steels production technologies.

The temperatures of the critical points when heating a steel can be determined using mathematical models that take into account the chemical composition; these equations can generate errors and, moreover, do not allow the calculation

of the pearlite dissolution finish temperature (Ac_{fp}) and, consequently, neither the determination of the temperatures range ($Ac_{fp} - Ac_3$).

For the steel with 0.087% C and 0.511% Mn, between the temperatures of critical points determined through dilatometric analyses and those calculated with mathematical models, depending on the heating rate applied to the specimens during the dilatometric analyses and the mathematical model used, were obtained differences between 0.40 and 33.10 °C for the critical point Ac_1 and between 21.20 and 108.50 °C for the critical point Ac_3 .

ACKNOWLEDGEMENTS

This work was partially supported from the project "Integrated Center for research, development and innovation in Advanced Materials, Nanotechnologies, and Distributed Systems for fabrication and control (MANSiD)", Contract No. 671/2015, Sectoral Operational Program for Increase of the Economic Competitiveness co-funded from the European Regional Development Fund.

NOMENCLATURE

Ae_1 - pearlite dissolution temperature (lower equilibrium temperature between ferrite and austenite), °C;

Ae_3 - ferrite to austenite transformation finish temperature (upper equilibrium temperature between ferrite and austenite), °C;

Ac_1 - pearlite dissolution start temperature (lower temperature of the ferrite-austenite field during heating), °C;

Ac_3 - ferrite to austenite transformation finish temperature (upper temperature of the ferrite-austenite field during heating), °C;

Ac_{fp} - pearlite dissolution finish temperature (ferrite to austenite transformation start temperature), °C;

T_{SC} - small contraction temperature, °C;

α - proeutectoid ferrite;

γ - austenite;

P - pearlite.

REFERENCES

- [1] B. Pawlowski, Critical points of hypoeutectoid steel - prediction of the pearlite dissolution finish temperature Ac_{1f} , *Journal of Achievements in Materials and Manufacturing Engineering* **49**, 2, 331-337 (2011).

- [2] B. Pawlowski, Dilatometric examination of continuously heated austenite formation in hypoeutectoid steels, *Journal of Achievements in Materials and Manufacturing Engineering* **54**, 2, 185-193 (2012).
- [3] C. García de Andrés, F.G. Caballero, C. Capdevila, L.F. Álvarez, Application of dilatometric analysis to study of solid-solid phase transformation in steels, *Materials Characterization* **48**, 1, 101-111 (2002).
- [4] C. García de Andrés, F.G. Caballero, C. Capdevila, Dilatometric characterization of pearlite dissolution in 0.1C-0.5Mn low carbon low manganese steel, *Scripta materialia* **38**, 12, 1835-1842 (1998).
- [5] D. San Martin, T. De Cock, A. García-Junceda, F.G. Caballero, C. Capdevila, C. García de Andrés, The effect of heating rate on the reaustenitisation of a low carbon niobium microalloyed steel, *Materials Science and Technology* **24**, 3, 266-272 (2008).
- [6] M.S. Rashid, Dual-phase steels, *Annual Review of Materials Science* **11** 245-266 (1981).
- [7] G.R. Speich, Physical metallurgy of dual-phase steels, *Proc. of Fundamentals of Dual-Phase Steels, 110th AIME Annual Meeting, Chicago*, 3-46 (1981).
- [8] S.A. Golovanenko, N.M. Fonshteyn, Dual-phase alloyed steels, *Metallurgiya*, 1986.
- [9] C. Dulucleanu, Contributions regarding physical, mechanical and technological properties of the ferrite-martensite dual-phase steels, PhD Thesis. Romania: Dunarea de Jos University of Galati, 1999.
- [10] C. Dulucleanu, T. Severin, The influence of ultrasounds on the structure of some low carbon and manganese dual-phase steels, *Proc. of SGEM 2017 Vienna GREEN, 17th International Multidisciplinary Scientific GeoConference SGEM 2017, Vienna* 17/63, 85-92 (2017).
- [11] A.A. Gorni, Steel forming and heat treatment handbook, http://www.gorni.eng.br/e/Gorni_SFHTHandbook.pdf.
- [12] B. Pawlowski, Determination of critical points of hypoeutectoid steels, *Archives of Metallurgy and Materials* **57**, 4, (957-962) 2012.
- [13] F.L.G. Oliveira, M.S. Andrade, A.B. Cota, Kinetics of austenite formation during continuous heating in a low carbon steel, *Materials Characterization* **58**, 256 - 261 (2007).
- [14] D. San Martin, P.E.J. Rivera-Diaz-del-Castillo, C. García de Andrés, In-situ Study of Austenite Formation by Dilatometry in a Low Carbon Microalloyed Steel, *Scripta Materialia* **58**, 926-929 (2008).
- [15] F.G. Caballero, C. Capdevila, C. García de Andrés, Modelling of kinetics of austenite formation in steel with different initial microstructures, *ISIJ International* **41**, 10, 1093-1102 (2001).
- [16] P. Motyčka, M. Kövér, Evaluation methods of dilatometer curves of phase transformations, <http://comat2012.tanger.cz/files/proceedings/11/reports/1237.pdf>.
- [17] B. Pawlowski, P. Bała, J. Krawczyk, Some factors influencing, the determination of eutectoid transformation start and finish temperatures in hypoeutectoid steels, *Metallurgy and Foundry Engineering* **35**, 2, 121-128 (2009).

Influence of reprocessing by melt-mixing and thermo-formation of polyolefin fractions, separated from wastes, on their calorific power

L. Costiuc¹, L. Baltes², S. Patachia^{3*}, M. Tierean², A. Lunguleasa⁴

¹Transilvania University of Brasov, Mechanical Engineering Department, 29 Eroilor Blvd., 500036 Brasov, Romania

²Transilvania University of Brasov, Materials Engineering and Welding Department, 29 Eroilor Blvd., 500036, Brasov, Romania

^{3*}Transilvania University of Brasov, Product Design, Mechatronics and Environmental Protection Department, 29 Eroilor Blvd., 500036, Brasov, Romania, st.patachia@unitbv.ro

⁴Transilvania University of Brasov, Wood Engineering Department, 29 Eroilor Blvd., 500036, Brasov, Romania

Polyolefins recycling is a desideratum, imposed by the actual environmental protection regulations that take into consideration the very high amounts of polyolefin utilization, their non-biodegradability and the rapidly diminishing of the fossil energetic resources. Calorimetric studies, performed on fractions obtained from municipal polymeric waste, from Brasov, Romania, separated by flotation, evidenced that their calorific power is comparable with that of fossil combustibles, meaning that polymeric waste could be incinerated for energy recovery. However, polymers incineration generates environmental concerns, especially for air pollution, remaining one of the last choices in polyolefins recycling. Thermal re-processing of polymeric fractions, by melt-mixing and thermoforming implies thermo-degradation processes that could influence the calorific power of re-used polymers. This paper aims to compare the calorific power of polymeric fractions separated from municipal polymeric waste with that of the re-processed polymers, obtained from the former fractions, by melt-mixing and thermoforming. A critical analysis of the efficiency of polymers recycling versus incineration, in different life cycles, is presented.

Keywords: polyolefin, waste, recycling, calorific power, melt-mixing, thermoforming

INTRODUCTION

Finding of new sources of energy, reducing of energy consumption and energy recovery are some of the most important issues of nowadays society due to the exponentially increase of the energy need.

Plastics are well-known as energy efficient materials considering their whole life-cycle, due to their easiness to be transported, installed and maintained, their high versatility and cost-effectiveness. For example, when comparing with traditional building and construction materials, plastics require 85% less energy to manufacture, generate 95% less CO₂ and use minimal water during production process [1]. However, most of plastics generate, at their end of life cycle, non-biodegradable waste that may have a serious impact on the environment and health. New strategies in the EU countries concerning the plastic products design, their use and recycling have been adopted on the 16th of January, 2018, in Brussels [2]. The use of plastics in circular economy imposes well controlled collection, separation and washing processes [3].

Often, the complexity of the plastic waste composition, due to their contamination during the

use, associated with current low prices of raw materials renders recycling un-economic compared with landfilling [1]. In this context, trying to avoid environmental concerns, the options are: the increase of the plastic biodegradability [1] and energy recovery by pyrolysis [4] or incineration.

One of our former studies showed that fractions separated from Municipal Solid Waste (MSW) from Brasov County, Romania, in 2010, showed a high calorific power that recommend them for recycling by incineration with energy recovery [5-7]. The higher the polyolefin content, the higher the calorific power of the waste is, the last one being comparable with that of the superior coal.

Other studies showed that the re-processing of these fractions by melt-mixing and thermoforming, allows obtaining secondary materials with acceptable mechanical and antimicrobial properties [8-10].

It is well-known that the thermal treatment of polymers as well as their exposure to the ambient conditions (temperature, light, moisture variations) lead to their properties alteration, due to oxidative processes, chain breaking, crosslinking, additives release, phase separation [11].

The aim of the present study is to determine the calorific power of the secondary materials obtained

* To whom all correspondence should be sent:
lmllldy@126.com

from the separated fractions coming from MSW from Brasov in 2010 and processed in the same year by melt-mixing and thermoforming. The influence of the thermal processing and time (assimilated with a second life cycle) on the calorific power of secondary polymers will be discussed in comparison with that of the polymers obtained at the end of the first life cycle. A critical analysis of the efficiency of polymers recycling versus incineration, in different life cycles, is presented.

MATERIALS

Polymeric waste coming from MSW collected in 2010 from Brasov County, Romania, has been separated by flotation in alcohol and alcohol-water solutions, based on density differences, in 13 fractions, described in papers [12-13].

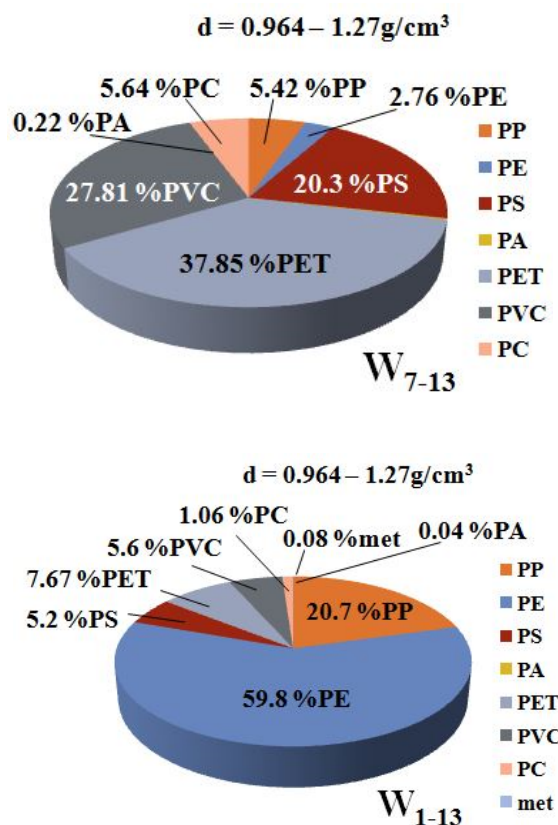
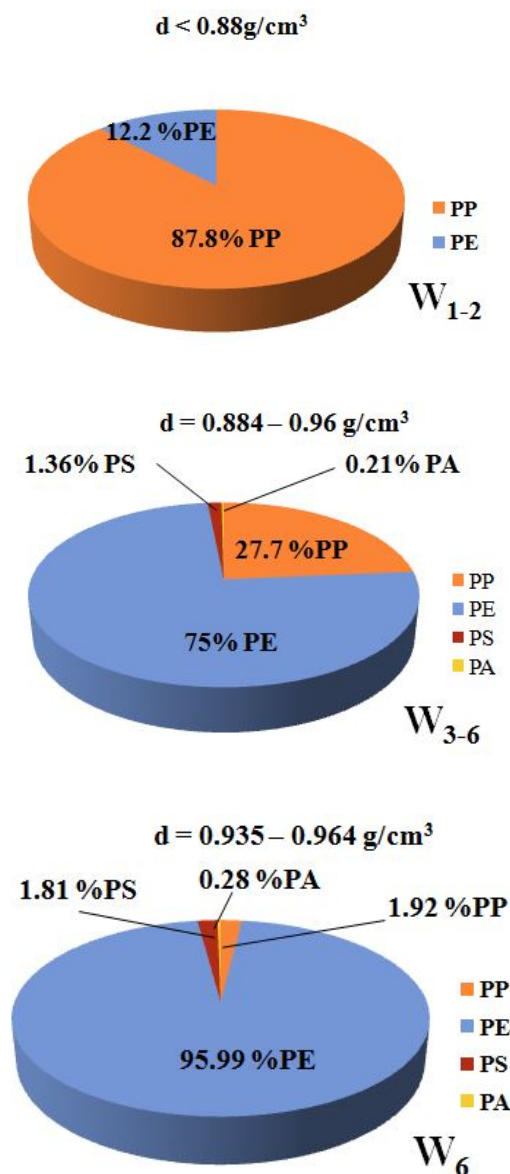


Fig.1. Composition of the fractions under present study, separated from polymeric municipal solid waste (MSW) from Brasov county, Romania in 2010 [12]

The composition of each fraction has been determined by correlating the mass-fraction obtained by FT-IR spectroscopy with the image analysis made by CIELab method [11-12].

Then, different fractions containing similar polymers have been mixed again and coded: W1-2; W3-6; W7-13 and respectively W1-13, where W means waste and the attached number represents the code of mixed density fractions. These narrow fractions were cooled up to -5°C , grinded up to 0.5-1 mm flakes dimensions, by using a centrifugal mill ZM200, melt-mixed by using a Brabender mixer with co-rotating twin screw extruder that allows the setting of the temperature, the mixing speed (60 rpm) and the duration of the mixing (10 minutes). The mixing temperature has been chosen as 10°C higher than the melting temperature of the dominating polymer in the fraction: for fractions with major polyolefin content (PE and PP) the work temperature has been set at 180°C and for fractions containing other polymers than polyolefin, the work temperature has been set at 220°C . The obtained melt mix has been cooled, cut and pressed in a Carver hydraulic press to obtain homogeneous sheets, without air bubbles, having the following

dimensions: L x l x h: 150 x 150 x 1 mm. These samples have been submitted to different analyses to evaluate the opportunity of mechanical polymers recycling.

The composition of the recycled fractions is presented in Fig.1.

The samples have been kept in laboratory conditions for 7 years. Major properties alteration has been noted. The mechanical properties dramatically decreased and the initial bacteriostatic character disappeared (unpublished own results). Considering the storage period as a second life cycle, once the material properties decreased making it unusable for a new life-cycle, another alternative of recycling could be incineration with energy recovery. In this context, the samples were submitted to calorimetric analysis.

METHODS

The obtained waste samples were weighed using the 0.1 mg precision analytical balance (Kern & Sohn ABJ 220-4M). Each weight of the sample was about 1.1 to 1.3 grams to obtain an acceptable temperature increase in calorimeter of 2.0 to 4.0°C for heat value measurements according to standards [14]. The bath temperature was monitored and recorded during the combustion process in a XRY-1C oxygen bomb calorimeter device with data acquisition software (XRY-1C Oxygen Burner Calorimeter, Shanghai Luheng Instrument Co.). Before determination of the heat of combustion, the calorimeter was calibrated using a standardized benzoic acid sample (Parr Instruments Co.). The thermal capacity of the calorimeter was about 12762 J/K. Following the standard procedure [14], the each weighed sample was placed inside the oxygen bomb. On the bottom of the bomb was added 1 ml of deionized water to investigate acid formation. The fuse wire was connected to the electrodes in the vessel and was brought into contact with the sample. The bomb was then assembled, sealed and the air content was removed, by twice pressurizing to 0.5 MPa with pure oxygen. Prior to determination, it is pressurized again with pure oxygen at 3.0 MPa. The increase of bath water temperature was measured by using a precision sensor with a temperature resolution of 1.0 mK. The temperature was recorded, during the test, by the data acquisition system at every 30 seconds.

RESULTS AND DISCUSSIONS

The samples obtained by melt-mixing and thermoforming of fractions coming from separation

of polymeric MSW, collected from Brasov county, Romania, were firstly visually compared, after 7 years of storage in the laboratory conditions, with the same samples evaluated immediately after preparation. The first observation was that they loosed their mechanical resistance, becoming very brittle. The W3-6 initial samples showed a good mechanical resistance, close to that of the virgin PE [15], allowing their application in similar ranges. After 7 years, the samples brittleness makes these materials unusable. Possible ageing processes (oxidation, crosslinking, phase separation) occurred.

In the present study, the heat of combustion was determined for the mentioned samples (2010 samples and 2017 samples) and its value was compared with that obtained for the separated fractions at the end of their first life cycle.

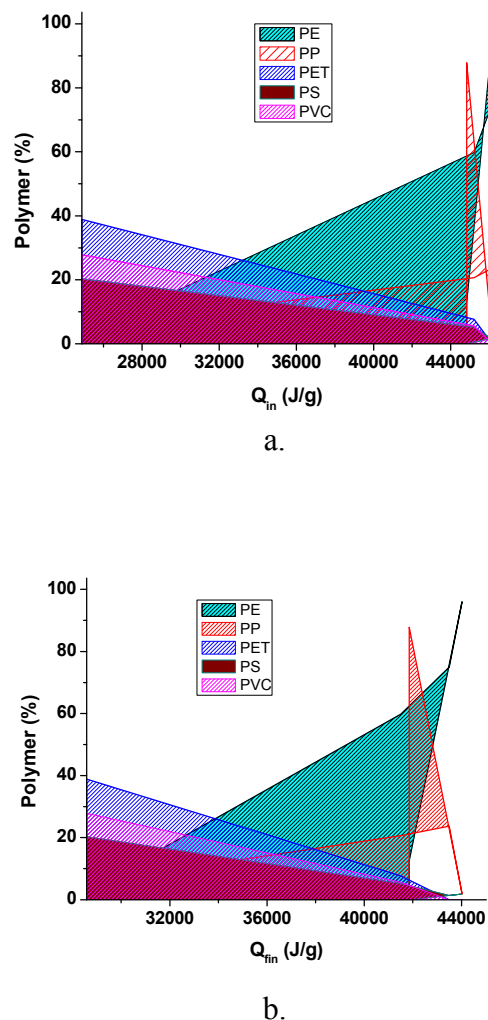


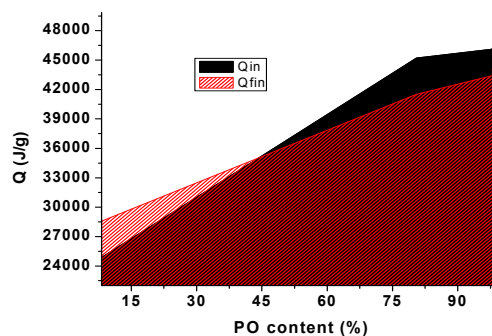
Fig.2. Influence of the composition of the polymeric fractions from MSW on their heat of combustion: (a) initially separated fractions; (b) recycled materials by melt mixing and thermoforming

The differences between the obtained heat of combustion values for the two series of samples will allow us to conclude on the dominating chemical or physical processes that occurred in the tested materials during their thermal treatment and storage for 7 years. Also, these values will give an image on the heat of combustion alteration during a second life cycle of polymeric materials under study, answering to the question: is it better to mechanically recycling polymeric wastes or to incinerate them at the end of the first life cycle?

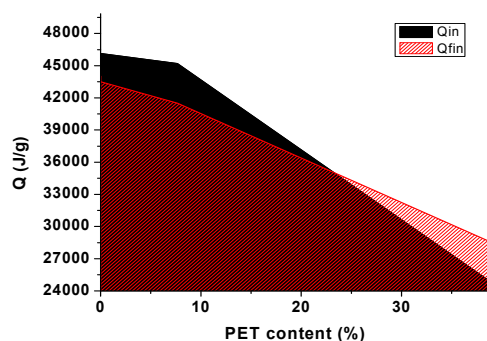
Calorimetric data obtained for both series of samples (initially separated ones and that recycled by melt mixing, thermoforming and kept in the laboratory conditions for 7 years) were compared and graphically represented as function of fractions composition, aiming to evidence the individual influence of each polymer on the energy content of the obtained materials.

Negative influence on the fractions' heat of combustion was recorded for PET, PVC and PS. Higher the PET, PVC and PS content in the polymer fractions, lower the heat of combustion is. This could be explained by the lower Q value of PET (21600 J/g [17]), and of PVC (18000-19000 J/g [16]), and by the low PS content in the MSW fractions, up to 20.7 % in W7-13. PS has a high Q value (41600 J/g) [17], but its low percent in the fractions has the dominating influence on their heat of combustion, as it can be seen in Fig. 2.

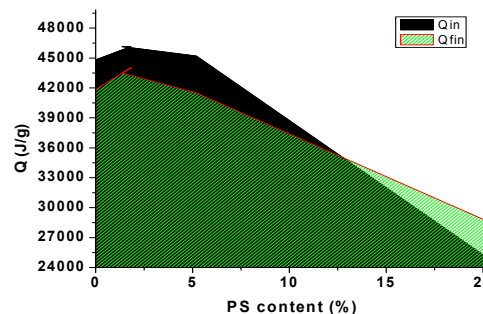
Similar behaviour is revealed in case of recycled fractions by melt mixing, thermoforming and then, stored for 7 years (Fig.2 b). The only differences are: (1) the lower Q values obtained for fraction having higher polyolefin content by comparing to that of fresh separated fractions. This behaviour is normal, taking into account the degradation processes occurring during thermal treatment and storage. Intermediate oxidized compounds have generally lower combustion heat than that of un-oxidized compounds. (2) Higher Q values were obtained for fractions with higher content of PET, PVC and PS by comparing to the same fresh separated fractions. This fact could be explained by PVC degradation during the thermal treatment and storage, releasing HCl. This led to the unsaturated polymeric chains formation. The last ones have higher heat of combustion by comparing to the chlorinated compounds. Also, they could react with thermal degradation compounds coming from PET, PS, PA and contaminants leading to compounds with higher heat of combustion.



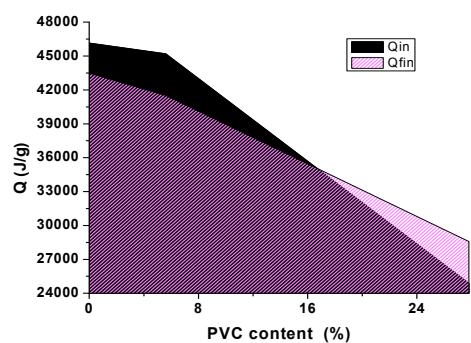
a.



b.



c.



d.

Fig.3. Comparison between the heat of combustion of fractions at the end of first life cycle and at the end of the second life cycle: (a) influence of PO-s content; (b) influence of PET content; (c) influence of PS content; (d) influence of PVC content

From Fig.3 it could be observed also that fresh separated fractions have higher heat of combustion

for higher content of PO-s; the recycled fractions by melt mixing, thermoforming and after storage evidenced lower heat of combustion for fractions with higher PO-s content. For fractions having lower content of PO-s (<45%) the Q-values for recycled fractions increased by comparing to fresh separated fractions (Fig.3.a).

Fig.3.b, 3.c and Fig.3.d show that the increase of the PET, PVC and PS content determines the Q-values decrease in both series of samples, but an increase of the Q-values by comparing the fractions at the end of the second life cycle with the fresh separated ones could be noted for mixtures containing higher PET content than 22% and higher content of PS than 13% and higher PVC content than 17%.

Variations of Q_{fin} by comparing to Q_{in} are presented in Fig.4.

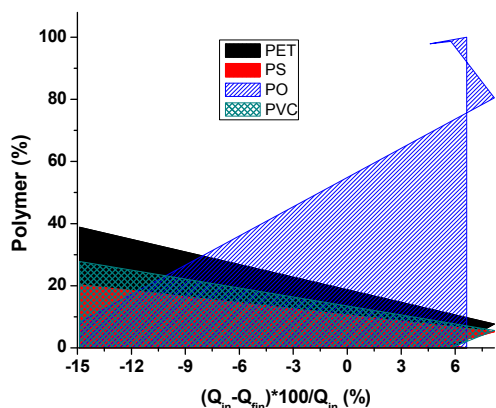


Fig.4. Quantification of abatements of Q_{fin} from Q_{in} as a function of fractions composition

Higher percent of PO-s in fractions increases the mixture instability (PO-s oxidation) and as consequence, decreases the Q_{fin} values and increases the differences ($Q_{in}-Q_{fin}$) up to 6%.

On contrary, the presence of PET, PVC and PS in the mixture, increases the density of the fractions, favoring a better retaining of the degradation products, increasing the Q_{fin} values and making the above mentioned differences negative, up to 15%.

This mechanism is consistent with the ash content measured after samples combustion. Fig.5. shows that the ash content is zero for samples with very high PO-s content while the increase of the PET, PVC and PS determines the increase of the residue. Decreasing PE and PP content will lead to the increase of the ash content. The obtained results are partially consistent with that reported by [18]. Based on the proximate and ultimate analysis results

and heat of combustion values, Zhou H and al. classified plastics from MSW in three clusters: (1) PE, PP and PS; (2) PVC and (3) PET, each containing polymers with similar properties.

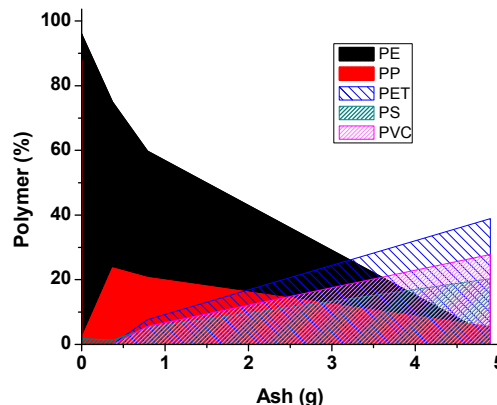


Fig.5. Variation of the ash content obtained after incineration of the polymeric fractions at the end of their second life cycle

1) PE, PP and PS have C+H content nearly 100%, O, N, S, Cl content almost zero, and they are completely volatile plastics, forming no char. Their heat of combustion is high, decreasing in the decreasing sequence: $PP > PE > PS$. [18-19].

2) The second cluster refers to PVC that contains Cl in the range of 50-60% and as consequence the C and H content diminished to 38-42% C and 4-6% H, variable content of ash, probably due to additives, up to 15%, volatiles are in the range of 71-95% and fixed carbon between 4% to 21%. Its heat of combustion is approximately half from that of PP, PE and PS, respectively.

3) The third cluster contains PET. It has approximately 62% C, up to 5% H and a high content of O approximately 33%. Volatiles are around 90-94%, ash very low, 0.09-0.31% and fixed carbon is 5.6-9.45%. The heat of combustion is low, around half from that of the first cluster and close to PVC.

Based on our results, both PVC and PS seems to behave similar to PET, decreasing the fraction's heat of combustion and increasing the ash content, while PE and PP, decrease the ash content and positively contribute to the fraction's heat of combustion.

Negative contribution of PS, PVC and PET content to the heat of combustion of fractions containing them, could be explained by the simultaneous decrease of the PO-s content of those fractions.

In spite of their very low ash content as individual polymers, PS and PET contribute to the increase of

the ash content of waste fractions. This behavior could be explained by PS and PET higher melting temperature (240°C for PS and 212-265°C for PET) when comparing them with PO-s. This characteristic draws near PS to PET, excluding it from the cluster (1), including PE and PP, proposed by using other criteria. PE and PP have lower melting temperature (HDPE: 120-135°C; LDPE: 70-100°C and PP: 130-171°C). This aspect possibly determines the including of PO-s and PVC intermediate combustion products or fillers into a sticky mass of melted PS and PET, finally affecting the waste fractions' combustion mechanism and consequently, the ash content.

Probably, this is the cause for that many researchers reported a higher content of ash for polymeric waste fractions, by comparing to individual polymer ones. For example, analysis of MSW in Piyungan Landfill, Yogyakarta, Indonesia, led to an ash content of plastic fraction of about 10%, while elemental analysis shows a high percent of O, meaning a possibly high percent of PET [20]. Also, analysis of the organic fraction of MSW collected from Hyderabad city of Pakistan, contained a plastic fraction with a high percent of O that generates approximately 5% of ash [21].

Proximate analysis of municipal solid waste in Ado-Ekiti, Ekiti State, Nigeria, shows for polymeric fraction, an ash content about 12% [22].

Pedersen et al. [19] reported a significantly different behavior of PET by comparing to PE and PP, when they were burnt in an electrically heated rotary drum furnace. Almost immediately after the injection, the PET pellets stuck to the drum wall, where they stayed during the devolatilization and char combustion. Van Der Geld et al. evidenced also important differences in combustion regression rate of PS and PE [23].

CONCLUSIONS

All the obtained results led to the following conclusions:

Chemical structure alteration of the polymers, during their second life cycle, is not very high. More important that degradation of individual polymers in the recycling process is the polymers separation effectiveness. This one seems to be the dominating influence both on the energy content and on mechanical properties of the recycled material. The last ones are mainly due to the polymers' incompatibility and as result to phase separation. Calorimetric measurements reveal that chemical degradation during polymeric waste reprocessing by

melt mixing and thermoforming is minor, fact that allows multiple recycling of PO-s. After that, when mechanical properties will no more attain the requested values for specific application, due to the chain scission, oxidation, or contamination, the recycling by incineration could be applied, due to very low decrease of combustion heat during the reprocessing and new life cycles.

Keeping with the actual classification of polymers in wastes, based on proximate and ultimate analysis, our results found similar behaviour for PE and PP (class 1) and PET (class 3) in the complex fraction mixtures. PS, initially included in class 1, behaves different from PE and PP, being closer to PET (which is closer as melting temperature): negatively influencing the fractions Q-values and participating to the increase of the ash content. Incineration of the complex mixture of polymers has to take into consideration the reciprocal influence of the mixture components types and concentration as well as of their T_g and T_m values on the burning mechanism.

NOMENCLATURE

- Q-values - Heat of combustion, J/g;
- Q_{in} - Heat of combustion of freshly separated fractions, J/g;
- Q_{fin} - Heat of combustion of fractions, after processing, J/g;
- T_g - glass transition temperature, °C;
- T_m - melting temperature, °C.

Abbreviations

- HDPE - High density polyethylene
- LDPE - Low density polyethylene
- Met - metal traces
- PA - Polyamide
- PC - Polycarbonate
- PE - Polyethylene
- PET - Poly (ethylene terephthalate)
- PO - Polyolefin
- PP - Polypropylene
- PS - Polystyrene
- PVC - Poly (vinyl chloride)

ACKNOWLEDGEMENTS

This research was funded by FP7 Grant 212782, Magnetic Sorting and Ultrasound Sensor Technologies for Production of High Purity Secondary Polyolefins from Waste, acronym W2Plastics.

REFERENCES

- [1] V.P. Sharma, R.L. Singh, R.P. Singh. Chapter 15 in Degradable Polymers and Plastics of the future: steps toward environmental sustainability, Regulations and Safety aspects Principles and applications of environmental biotechnology for sustainable Future, Applied Environmental Science and Engineering for sustainable future, R.L. Singh (Ed), Springer Science+Bussiness Media Singapore, 2017, 467-487.
- [2] http://ec.europa.eu/environment/waste/plastic_waste.htm.
- [3] C. Ghinea, et.al. Forecasting municipal solid waste generation using prognostic tools and regression analysis. *Journal of Environmental Management*, **182**, 80-93 (2016).
- [4] L. Cafiero, D. Fabbri, E. Trinca, R. Tuffi. Thermal and spectroscopic (TG/DSC_FTIR) characterization of mixed plastics for materials and energy recovery under pyrolytic conditions. *Journal of Thermal analysis and Calorimetry*. **121**, 1111-1119 (2015).
- [5] L. Costiuc, S. Patachia, L. Baltes, M. Tierean. Investigation on Energy Density of Plastic Waste Materials. *Journal of Solid Waste Technology and Management, Philadelphia*, 930-939 (2011).
- [6] L. Costiuc, M. Tierean, L. Baltes, S. Patachia. Experimental investigation on the heat of combustion for solid plastic waste mixtures. *Environmental Engineering and Management Journal*, **14(6)**, 1295-130 (2015).
- [7] G. Ionescu, E.C. Rada, L.I. Cioca. Municipal Solid Waste Sorting and Treatment Schemes for the Maximization of Material and Energy Recovery in a Latest EU Member. *Environmental Engineering and Management Journal*, **14(6)**, 2537-2544 (2015).
- [8] S. Patachia, N. Damian, M.H. Tierean, L. Baltes. Microbial safety of plastic materials obtained from wastes. *Environmental Engineering and Management Journal*, **14(6)**, 1303-1312 (2015).
- [9] L. Baltes, M. Tierean, S. Patachia. Investigation on the friction coefficient of the composite materials obtained from plastics wastes and cellulosic fibers. *Journal of Optoelectronics and Advanced Materials*, **15(7- 8)**, 785- 790 (2013).
- [10] S. Patachia, A. Moldovan, R. Buican, C. Vasile, R. Darie, M. Tierean. Composite materials based on polyolefins wastes, *Proceedings of the 14th European Conference on Composite Materials, Budapest*, 281-ECCM14, (2010).
- [11] A. Moldovan, S. Patachia, R. Buican, M.H. Tierean. Characterization of polyolefins wastes by ftir spectroscopy. *Bulletin of the Transilvania University of Brasov, Series I: Engineering Sciences*, **5(54)**, 65-72 (2012).
- [12] S. Patachia, A. Moldovan, M. Tierean, L. Baltes. Composition Determination Of The Romanian Municipal Plastics Wastes. *Journal of Solid Waste Technology and Management, Philadelphia*, 940-951 (2011).
- [13] B. Vajna, K. Palásti, B. Bodzay, A. Toldy, S. Patachia, R. Buican, C. Catalin, M. Tierean. Complex Analysis of Car Shredder Light Fraction. *The Open Waste Management Journal*, **3**, 46-55 (2010).
- [14] CEN/TS 15400:2006, Solid recovered fuels - Methods for the determination of calorific value, EN 15400:2011, Solid recovered fuels - Determination of calorific value.
- [15] A. Moldovan. Composites materials based on polyolefins and cellulose fibres from secondary raw materials, PhD thesis, Romania, Transilvania University of Brasov, 2012.
- [16] NIST, (2013), National Institute of Standards and Technology, Material Measurement Laboratory, On line at: <http://webbook.nist.gov/cgi/cbook.cgi>.
- [17] M.D. Lechner. Polymers, In: Springer Handbook of Condensed Matter and Materials Data, (Eds.) Martiensen W., Warlimont H., ISBN 978-3-540-44376-6, 477-522, 2005.
- [18] H. Zhou, A. Meng, Y. Long, Q. Li, Y. Zhang. Classification and comparison of municipal solid waste based on thermochemical characteristics. *Journal of the Air & Waste Management Association*, **64**, 597-616 (2014).
- [19] M.N. Pedersen, P.A. Jensen, M. Nielsen, K. Hjuler, K. Dam-Johansen. Agglomeration and Deposition Behaviour of Solid Recovered Fuel. *Proceedings of The Nordic Flame Days*, Technical University of Denmark, (2015).
- [20] H. Sudibyo, A.I. Majid, Y.S. Pradana, W. Budhijanto, Deendarlianto, A. Budiman. Technological Evaluation of Municipal Solid Waste Management System in Indonesia. *Energy Procedia*, **105**, 263 -269 (2017).
- [21] M.S. Korai, R.B. Mahar, M.A. Uqaili. Estimation of Energy Potential from Organic Fractions of Municipal Solid Waste by Using Empirical Models at Hyderabad, Pakistan, *Mehran University Research Journal of Engineering & Technology*, **35(1)**, 129-138 2016.
- [22] O. L. Rominiyi, T. K. Olaniyi , T. M. Azeez, J. F. Eiche S.A. Akinola. Synergetic Effect of Proximate and Ultimate Analysis on the Heating Value of Municipal Solid Waste of Ado – Ekiti, Metropolis, Southwest Nigeria. *Current Journal of Applied Science and Technology*, **22(1)**, 1-12 (2017).
- [23] C.W.M. van der Geld, P.A.O.G. Korting, T. Wijchers. Combustion of PMMA, PE and PS in a ramjet. Delft University of Technology, uid:f0106cdd-97b2-4451-b966-25dce0fc37db (1987).

Multilayer CrN/TiN coatings deposited at low temperatures by unbalanced magnetron sputtering for implant applications

S. N. Rabadzhiyska^{1*}, L. P. Kolaklieva¹, T. M. Cholakova¹, R. D. Kakanakov¹, V. Chitanov¹, P. K. Stefanov², G. B. Atanasova², K. T. Balashev³, B. S. Rangelov⁴, S. B. Atanasova⁴

¹Central Laboratory of Applied Physics, Bulgarian Academy of Sciences, 61 Sankt Petersburg Blvd., Plovdiv 4000, Bulgaria

²Institute of General and Inorganic Chemistry, Bulgarian Academy of Sciences, 11 Academic G. Bonchev St., Sofia 1113, Bulgaria

³Laboratory of Biophysical Chemistry, Department of Physical Chemistry, Faculty of Chemistry and Pharmacy, Sofia University, 1 James Bourchier Ave., Sofia 1164, Bulgaria

⁴Institute of Physical Chemistry, Bulgarian Academy of Sciences, 11 Academic G. Bonchev St., Sofia 1113, Bulgaria

A multilayer CrN/TiN coating was developed and deposited onto high speed steel (HSS) specimens by unbalanced magnetron sputtering in a closed-field magnetron configuration at a temperature lower than 200 °C from Cr (99.99 %) and Ti (99.99%) targets. Multilayers were deposited at different nitrogen partial pressure, a target current ratio ranged from 0.7 to 1 and a bias voltage of -60 V, -70 V and -80 V. The study of mechanical properties indicated that the highest hardness value of 31 GPa and elastic modulus of 378 GPa were achieved at a bias voltage of -80 V and a target current ratio $I_{Cr}/I_{Ti} = 0.7$. The performed scratch tests exhibited good adhesion of the coating to the substrate as no cracks and delamination in the scratch track were observed. The coating thickness varied between 1.2 μm and 1.7 μm . The wear rate of the film was estimated to be $4.8 \times 10^{-6} \text{m}^3 \text{N}^{-1} \text{m}^{-1}$. X-ray photoelectron spectroscopy (XPS) was used to determine binding energies between Cr, Ti and N elements in the coatings. The surface roughness was evaluated to be 16.2 nm by Atomic force microscopy (AFM). The coating surface was characterized by Scanning Electron Microscopy (SEM). Energy-dispersive X-ray spectroscopy (EDX) analysis defined the elemental composition in the multilayer coating layer to be 46.73 at.% chromium, 43.67 at.% nitrogen, 9.61 at.% titanium.

Keywords: Physical Vapour Deposition (PVD), unbalanced magnetron sputtering, low-temperature deposition, CrN/TiN layers, surface morphology, composition

INTRODUCTION

Due to rapid changes in the age structure of the world's population, an increasing number of people need their failed tissues to be replaced by artificial implantable devices. Because of the decreased age that patients are considered for the operation, and a population which is living longer, the need for long lasting implants is becoming a larger concern. The current average life span of 15 years for hip implants is not sufficient in a population that may require 30–40 years of service [1-3].

Over the previous decade there has been a significant impact of metallic implant materials such as stainless steels and titanium (Ti), widely used for surgical prostheses as joint replacements, mechanical heart valves and dental implants [4]. The important disadvantage of the metals is their tendency to corrode in physiological conditions. Although conventional materials technology has resulted in clear improvements in implant performance and longevity, rejection or implant

failures still happen [5]. For this reason, metals and alloys were found unsuitable for implantation as being too reactive in the human body. To solve the problem it is necessary to deposit wear and corrosion resistant coatings.

The most commonly used coatings for biomedical applications are TiN and CrN. These films are well known for their high hardness and wear and corrosion resistance [6, 7], which are not enough for many modern applications. The increase in average life expectancy, as well as rapid advances in modern surgery require new generations coatings with enhanced mechanical, tribological and corrosion properties.

Advances in titanium and chromium manufacturing technologies are expected to play an important role in the development of the next generation wear and corrosion resistant coatings [8, 9]. A multilayer CrN/TiN coating for deposition on implants was elaborated based on the advantages of the alternately deposited single layers. As a sizable part of biomedical materials such as stainless steel, plastics, glass and polymers are unstable at high temperatures; low-temperature technology for achievement of a

* To whom all correspondence should be sent:
s1983@abv.bg

layered structure on the base of the closed-field unbalanced magnetron sputtering was developed.

This study presents the results of mechanical, tribological, morphological and compositional properties of the multilayers CrN/TiN coatings deposited at low-temperatures by unbalanced magnetron sputtering for biomedical applications.

EXPERIMENTAL DETAILS

The multilayer CrN/TiN coatings were deposited onto hardened high-speed steel (HSS) substrates with diameter of 12 mm by unbalanced magnetron sputtering in UDP 850-4 equipment (Teer Coatings Ltd.) from one titanium (99,99 %) and one chromium (99,99%) rectangular targets in a closed-field configuration. Prior to coating deposition, the substrates were ultrasonically cleaned in an alkaline solution at 60 °C for 10 minutes to remove the surface contaminations and subsequently rinsed in de-ionized water. After that, they were dried in a furnace at 100 °C before being loaded into the deposition chamber. Immediately before the deposition, the substrate surface was etched by Ar⁺ plasma for 15 min at a pulsed substrate bias of -500 V with a frequency of 250 kHz and low magnetron power in order to improve the coating adhesion.

Prior to the deposition, the vacuum chamber was evacuated to a base pressure of 1×10^{-3} Pa. After the evacuation, Ar or Ar + N₂ mixture was introduced into the chamber. The Ar flow was controlled by a mass flow controller, while the reactive N₂ gas flow was controlled by an Optical Emission Monochromator (OEM). The distance between the substrates and the targets was 150 mm. In the deposition process, the substrates were rotated biaxial at a speed of 2 rpm in order to obtain homogenous film thickness and composition.

The deposition of the multilayer coating started with an adhesion Cr layer, followed by a gradient CrN layer, in which the nitrogen was gradually increased up to values corresponded to stoichiometric CrN. After that alternate periods of CrN and TiN sublayers were formed. The structure of the multilayer coating is shown in Fig.1.

Two sets of experiments were carried out at different technological parameters. The first set of coatings was made to assess the influence of the nitrogen partial pressure on the mechanical properties of the obtained coatings. For this purpose 12 samples were investigated at different

deposition temperatures and a bias voltage of - 70 V. The second series of coatings was generated to evaluate the effect of the bias voltage and target current ratio I_{Cr}/I_{Ti} on the coatings hardness. That's why the 3 specimens were deposited at a bias voltage of - 60 V, - 70 V and - 80 V, target current ratio from 0.7 to 1 at a temperature of 130 °C. The choice of this deposition temperature was made on the base of literary research for the thermal resistance of the materials. The Ar flow rate was kept a constant (25 sccm) in the all of the experiments. The values of target current ratio were chosen to be between 0.7 and 1 because of the use of different technological regimes and change of targets currents.

Measurements of the coating thickness were performed by a Calotest, which is a suitable method for obtaining quick information about layer configuration, abrasion resistance and thickness. A stainless steel ball with a diameter of 30 mm was used with diamond slurry with particles of 0.25 µm in a diameter. The coating was abraded until the substrate was reached by the ball. The thickness was determined from the crater imaged using an optical microscope with high magnification. The mechanical and tribological properties of the deposited coatings were investigated using Compact Platform CPX (MHT/NHT) CSM Instruments equipment. Nanoindentation was performed by a triangular diamond Berkovich pyramid in the loading interval of 10 - 200 mN. The adhesion of the coating was evaluated by a micro-scratch technique, using a Rockwell diamond indenter with a radius of 200 µm. During the test, the normal load was progressively increased in a linear mode from 1 N to 30 N over the scratch length of 1 mm at a constant scratch speed of 0.5 N/min. Wear tests were accomplished at a load of 5 N in linear mode at scratch length of 3 mm at a constant scratching velocity of 0.2 mm/min.

The Atomic force microscopy (AFM) studies were carried out by NanoScope VAFM (Bruker Inc.) in air in tapping mode. Silicon cantilevers with reflective aluminium coating with a thickness of 30 nm, Tap 300Al-G (Budget Sensors, Innovative solutions Ltd, Bulgaria) were used. All images, taken at a resolution of 512×512 pixels in JPEG format were processed by means of Nanoscope software. Images from three independent locations of the samples were taken for reproducibility purposes. The arithmetic average roughness (Ra) and root mean square

roughness (R_q) were determined from the analysis applied to an image; the statistical values were calculated according to the relative heights of each pixel in the image.

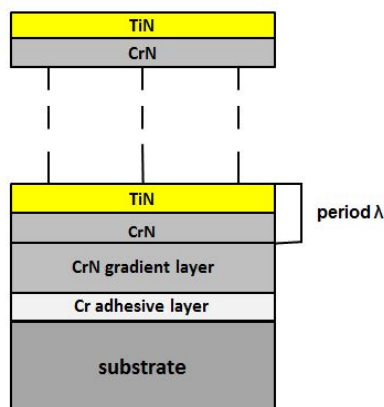


Fig.1. A principal scheme of the multilayer CrN/TiN coating

The XPS spectra were acquired on a Kratos AXIS Supra photoelectron spectrometer using a monochromatic Al K source with energy of 1486.6 eV. The base pressure in the analysis chamber was 5×10^{-8} Pa. The binding energies were corrected relative to the C1s peak at 285.0 eV. The concentration of the elements was derived on the basis of the core level peak areas, corrected by the corresponding relative sensitivity factor values.

Surface observations, morphology and elemental analysis are performed on JEOL JSM 6390 scanning electron microscope, equipped with INCA Oxford EDS energy dispersive detector. Surface images are obtained in secondary electrons (morphology contrast) and back-scattered electrons (density contrast) as well. The elemental analyzer is capable to detect all elements from carbon to uranium.

RESULTS AND DISCUSSION

Coating thickness

The thickness measurements were performed for all 12 coatings deposited at different technological parameters. However, the multilayer CrN/TiN coating obtained at a temperature of 130 °C, a bias voltage of -80 V, target current ratio 0.7 and a nitrogen partial pressure 8×10^{-2} Pa demonstrated better combination of mechanical properties- high coating hardness (32 GPa) and excellent adhesion to the substrate material than

the other coatings properties. For this multilayer, the thickness was estimated to be 1.7 μm and an image of the multilayer CrN/TiN coating surface after performing the calotest is indicated in Fig.2.

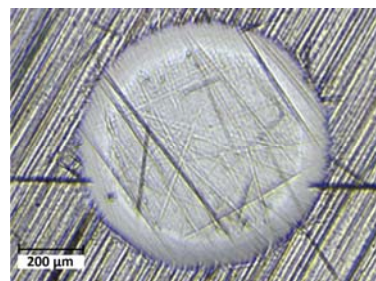


Fig.2. A segment of the optical microscopy image of the multilayer CrN/TiN coating, obtained by ball cratering test

The calculated total thickness for all deposited coatings was in the range of 1.2 –1.7 μm . The thickness of the multilayers depends mainly on the speed of rotation and the applied target currents during the process.

Mechanical properties

The mechanical properties were studied using the Depth Sensing Indentation technique. The nanohardness and elastic modulus were estimated by an Oliver & Pharr method from the load-displacement curve using 10 % of the coating thickness as the indentation depth [10].

The influence of the technological parameters on the mechanical properties of the deposited film was investigated. Dependence of the hardness and elastic modulus of multilayer CrN/TiN coatings on the nitrogen partial pressure is presented in Fig.3. The multilayer CrN/TiN coating hardness varied between 11 GPa and 32 GPa. As it is seen from Fig.3a, maximum hardness value (32 GPa) was achieved at a partial pressure of 8×10^{-2} Pa and a substrate temperature of 130 °C which was created by cathode's power only. The further increase of the nitrogen partial pressure to 11×10^{-2} Pa at a temperature of 200 °C leads to strong decrease of the hardness (11 GPa) probably due to diversion of the stoichiometry in the thin films. A big nitrogen amount introduced in the vacuum chamber to a definite value contributes for the nitride composition formation and the mechanical properties are enhanced. At a relatively high nitrogen flow and high pressure in the chamber stoichiometric structure is not obtained. The latter is due to the poisoned surface of the Ti target with the lower applied current.

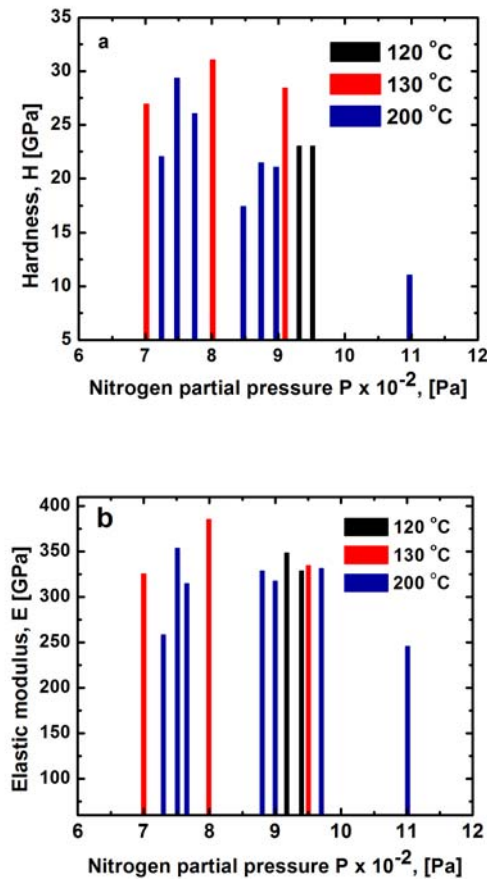


Fig.3. Dependence of the nanohardness (a) and elastic modulus (b) of the CrN/TiN coatings on the N_2 partial pressure at different temperatures

Thus, an increase of the Cr amount in the composition causes decrease of the coating hardness. The low deposition temperature (130 °C) cannot promote the surface kinetics, which results in low density of the films. Increase of the deposition temperature accelerates the particle migration on the surface supporting the dense structure formation and enhancement of the coating hardness, respectively. Despite, the coating deposited at 200 °C possesses almost the same hardness as the one obtained at lower temperature (130 °C). This result is due to the thermal instability of the substrate at temperatures of 200 °C and higher ones. The elastic modulus was found to be relatively insensitive to changes in nitrogen partial pressure at all temperatures (Fig.3b). The elastic modulus is an interesting material property, which depends on the material structure of the deposited coating. The lowest value of the elastic modulus (265 GPa) was

estimated at 200 °C and 11×10^{-2} Pa nitrogen partial pressure.

The substrate bias and target current play an important role determining the mechanical properties of the coatings. The use of ion bombardment allows deposition of adherent coatings at low substrate temperatures. The influence of the substrate bias and targets current ratio on multilayer CrN/TiN coating hardness is depicted in Fig.4.

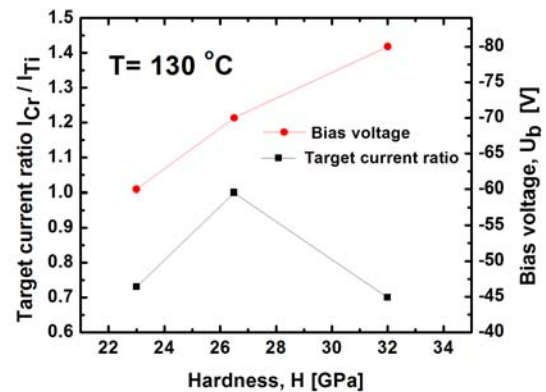


Fig.4. Influence of target current ratio I_{Cr}/I_{Ti} and bias voltage on the nanohardness of the multilayer CrN/TiN coatings

Maximum hardness of 32 GPa was achieved in a film deposited at a bias voltage of - 80 V and target current ratio 0.7. As the bias voltage was diminished to - 60 V, the multilayer hardness decreased to 23 GPa. The most probably reason for lower values of the hardness is the presence of strong tensions and defects in the layer. Moreover, low bias voltage leads to porous structure and not enough dense layer. In general, the hardness increases with the substrate bias up to 100 V, and then decrease significantly at higher bias values (e.g. ≥ 200 V), presumably because of ion beam intermixing effects at the interfaces and interface roughening [11].

The variation of hardness and elastic modulus with indentation depth of the investigated multilayer CrN/TiN coating is given in Fig.5. The highest value 32 GPa of the multilayer hardness is achieved at an indentation depth of 140 nm and a load of 10 mN. The high strength of the multilayer thin film is a result from many interfaces which block dislocation movement [12]. The hardness decreases slowly at indentation depth larger than ~ 200 nm, which was attributed to the substrate effect. It is expected that substrate effect becomes more important with increase of the indentation

depth. It was experimentally proved that the hardness decreases with increasing indentation depth based on the presence of strain gradients in the deformation zone around the indent [13]. With an indentation depth increase to ~ 900 nm, an elastic modulus value slightly decreases. The lower value of the elastic modulus was measured to be 270 GPa.

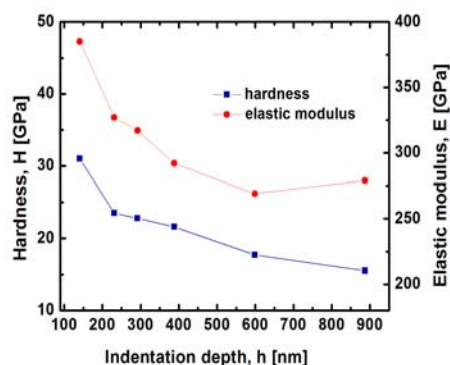


Fig.5. Dependences of the multilayer CrN/TiN coating nanohardness and elastic modulus on the indentation depth

The multilayer adhesion and friction coefficient were studied using a micro-scratch test technique. The results revealed that multilayer thin films possess good adhesion to the substrate (Fig.6). No cracks, track edge chipping and delamination were observed in the scratch track at a load friction force (F_t) from 1 N to 30 N.

The estimated friction coefficient of the coatings was in the range 0.09-0.15.

Surface morphology

The surface morphology of the multilayer CrN/TiN coating was examined by Atomic force microscopy (AFM) and Scanning electron microscopy (SEM). The AFM measurements showed low surface roughness. The 2D and 3D AFM images of the multilayer thin film are shown in Fig.7. They exhibit a smooth surface without hills and vales. The grown film repeats the surface morphology of the substrate.

The measurement revealed an average surface roughness $R_a = 16.2$ nm on an area of $9.51 \mu\text{m}^2$ of the multilayer CrN/TiN coating with the highest nanohardness. The low surface roughness is associated with relatively small grain sizes, typical for the used bias voltages during deposition [14].

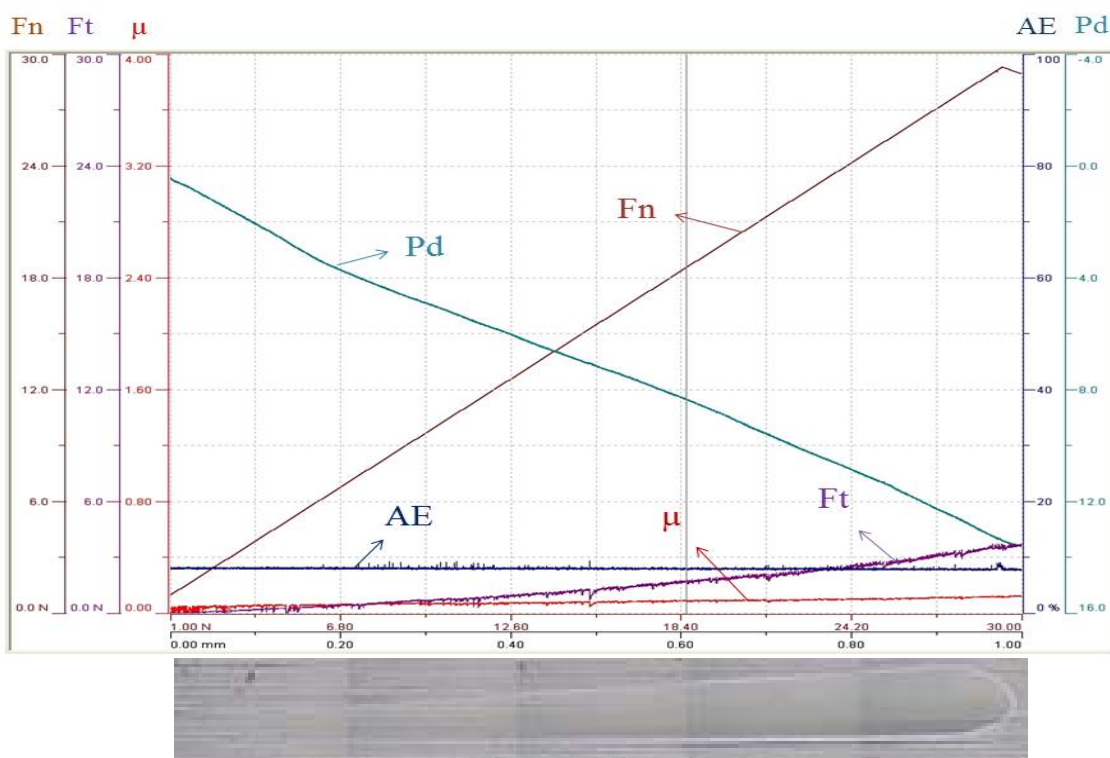


Fig.6. Optical image of the scratch track in the CrN/TiN coating and scratch test results of the normal force (F_n), penetration depth (P_d), acoustic emission (AE), friction force (F_t) and coefficient of friction (μ)

The observed by AFM surface morphology is confirmed by the SEM images. Fig.8. shows the SEM micrograph of the multilayer CrN/TiN coating surface deposited at the same technological parameters as one investigated by AFM measurement.

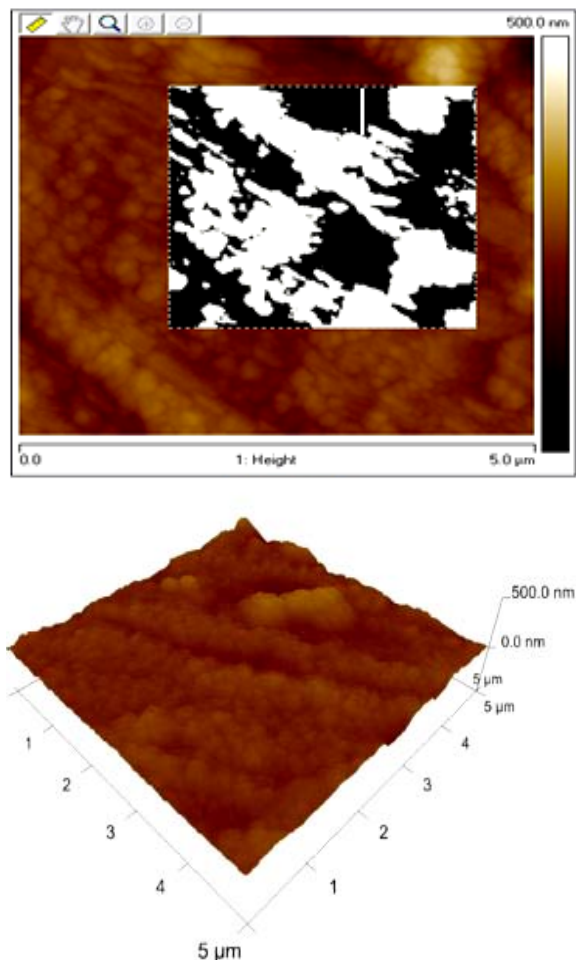


Fig.7. Two-dimensional and three-dimensional AFM images of the CrN/TiN multilayer surface

The results depicted that the coating has dense packed texture, built mainly by grains with an average size of 150- 200 nm. The grains of a higher size 500 nm – 700 nm are very rare. The elemental composition of the multilayer coatings was defined by an Energy-dispersive X-ray spectroscopy (EDX) analysis.

The results indicated that concentrations of chromium, nitrogen, titanium are 46.73 at.%, 43.67 at.% and 9.61 at.%, respectively, supposing formation of CrN and TiN compounds. The CrN part is dominated because of the Cr-based adhesion and transition layers.

XPS analysis

The chemical state and composition of the outermost layers of the Cr/CrN/CrN-TiN coating

were obtained by XPS. From the intensity of the core level Cr2p, N1s, O1s and Ti2p peaks, an element composition was estimated using the atomic sensitivity factors (ASF). It was assumed that carbon belong to a contamination layer and was not taken into account. The element concentrations in atomic [%] are: Ti -10.6, O - 24.9, N- 37.4 and Cr - 27.1. The surface overlayer contains significant oxygen amount. Probably, the air exposure of the coating induced the formation of a thin surface layer, whose composition is a mixture of Cr and Ti oxynitrides and oxides. High-resolution Cr 2p, Ti 2p, N 1s and O1s spectra are shown in Fig.9.

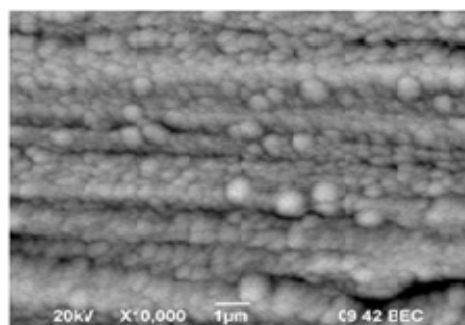


Fig.8. Typical SEM surface image of the multilayer CrN/TiN coating

The spectra are deconvoluted and peaks are assigned to different chemical states according to reference data. The Cr 2p_{3/2} peak on Fig.9a is centred at 574.5 eV and possesses an asymmetric shape. Three main components corresponding to different chemical chromium species could be resolved in the spectrum. The first peak at 574.5 eV was assigned to CrN and the second peak at 576.2 eV to Cr₂N, in accordance with literature findings [15,16]. The contribution of the component assigned to Cr₂N peak could coincide with a contribution from Cr₂O₃ and CrO₂ (usually between 576.1 and 576.6 eV[17]. The third component in the Cr 2p_{3/2} peak is centred at 578.1 eV and it may be related to Cr (VI) species observed in this binding energy range (578.1 - 579.8 eV) or to many body interactions [18].

The deconvolution of the Ti2p peaks gives four features (Fig.9b). These features were assigned to Ti species in different chemical environment. The position of the first component at 455.2 eV and the presence of characteristic shakeup satellite at 456.3 eV confirm the formation of TiN [19]. The peaks at 457.5 eV and 459.1 eV can be associated with Ti–N–O and Ti–O bonds, respectively [20]. These findings also

reveal the formation of an overlayer on the coating containing Ti oxynitride and oxide. The N1s spectrum in Fig.9c. shows a wide peak at 396.7 eV, which can be decomposed into five components. These peaks are assigned to different chemical states formed on the surface of the coating. The first component at 395.7 eV represents nitrogen in nitride bond N-Ti [21], while the next two peaks at 396.7 and 397.5 eV could be assigned to nitrogen in CrN and Cr₂N, correspondingly [22]. The formation of a surface overlayer due to exposure of the coating to air is also reflected in two contributions at 398.6 eV and 399.7 eV, which are ascribed to different chromium and titanium oxynitrides [23, 24].

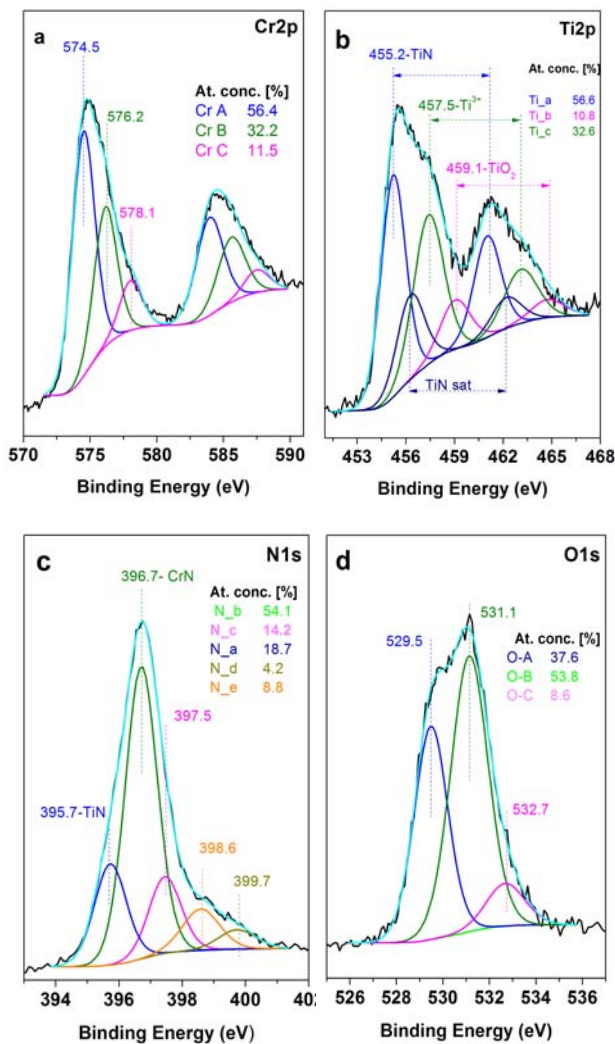


Fig.9. XPS spectra of CrN/TiN multilayer coating (a) Cr2p, (b)- Ti 2p, (c)- N 1s and (d) O 1s

The analysis of the oxygen O1s peak in Fig.9d. presents information about the nature of the oxygen species participating in the surface layer

of the coating. The deconvolution of the oxygen O 1s peak gives three components. The peak at 529.5 eV could be attributed to CrO₂ in accordance with [17]. The most intensive peak at 531.1 eV contains probably a mixture of contributions from different chromium and titanium oxynitrides and oxides.

Tribological behaviour

Wear rate and friction coefficient are of vital significance for the durability of surgical implants, especially for hard tissue replacements like hip and knee joints consisting of mating components. The tribological measurements of the multilayer CrN/TiN coating were performed based on multi pass scratch test (Fig.10). The number of multi passes through the scratch was 10. The multi pass scratch test gave information about the wear resistance at high applied force on a short distance.

The wear and wear rates were investigated for three multilayer structures with the best mechanical parameters. In the scratch wear test, the measurement device registered the friction force, indenter penetration depth and acoustic emission along the scratch track. The observed picks in the acoustic emission (AE) are due to the reciprocal movement of the indenter during the multi pass scratch. The average penetration depth as determined from the plotted curve was found to be 110 nm. The average width of the worn track was determined to be 64 μm. Thus, during the scratch wear test a material volume of 1.06x10⁻⁵mm³ was worn at a force of 5 N applied on a length of 30 mm.

After wear resistance test of the films, no delamination, cracks and critical loads were observed inside and outside the track.

The amount of worn volume (V) is calculated by equation (1) from the cross section area of the worn track and the passed length [25]:

$$V = S \times l \quad (1)$$

where:

S- cross section area of the worn track, mm²;

l- passed length, mm

The wear rate of the coatings is estimated by equation (2) [26]:

$$K = \frac{V}{F_n \times L} \quad (2)$$

where:

K- wear rate, m³/Nm;

V - worn volume, m^3 ;
 F_n - applied normal load, N;
 L - sliding distance, m.

Based on these calculations, the average value of the wear rate of the multilayer CrN/TiN coatings was calculated to be $4.8 \times 10^{-6} m^3/Nm$.

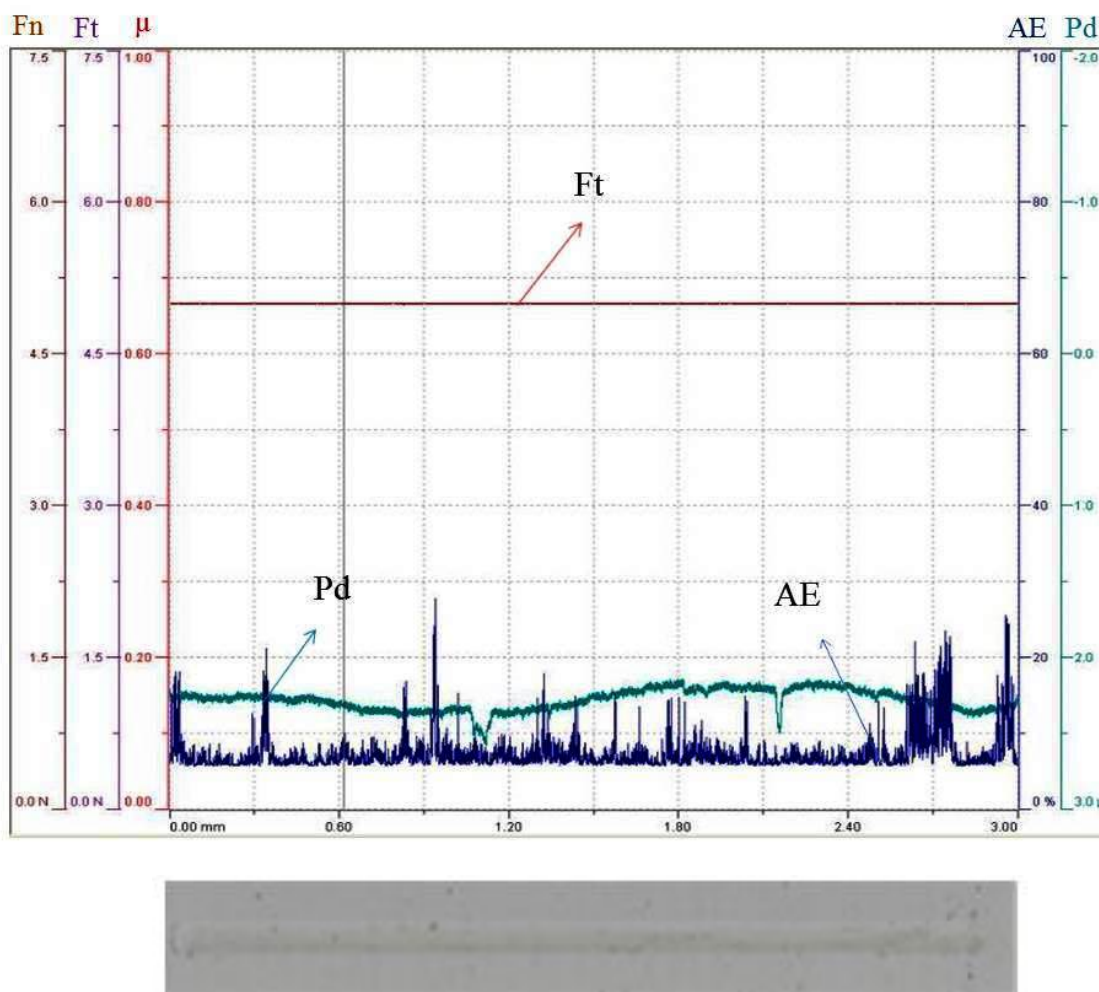


Fig.10. Multi pass scratch test results of the acoustic emission (AE), friction force (Ft) and penetration depth (Pd) and an optical micrograph of the scratch track in the CrN/TiN coating

CONCLUSIONS

Low-temperature technology for deposition of multilayer CrN/TiN films was developed on the base of optimized technologies of CrN and TiN monolayers. Twelve specimens were deposited at different technological conditions. The influence of the bias voltage, target current ratio and nitrogen partial pressure on the coatings properties was evaluated. The mechanical properties of multilayers were studied at temperatures of 120°C, 130 °C and 200 °C. The coating deposited at a bias voltage of – 80 V, at a temperature of 130 °C, 8×10^{-2} Pa partial pressure of nitrogen and target current ratio 0.7 possessed the best combination of mechanical properties - the highest hardness 32 GPa, low friction coefficient 0.1 and excellent

adhesion to the substrate. The enhanced properties of the the developed CrN/TiN coating prove the advantages of the multilayer structure to the single layers. The presence of many interfaces in the coating structure causes crack deflection, dissipation of the defects and crack energy, which results in good tribological properties. AFM and SEM measurements demonstrated a low roughness of the multilayer film surface which is an essential requirement for the implants because it influences directly on the friction. Besides, the low friction coefficient prolong the lifetime of the implants and reduce the pain of the patients. XPS measurements showed that the multilayer CrN/TiN coating consists of CrN and TiN compounds. EDX analysis revealed that the

amount of Cr is predominated due to Cr-based adhesion and transition layers.

The presented results in this work evidence that the developed multilayer CrN/TiN coating is suitable for implant applications.

REFERENCES

- [1] H.Li, Z.Zha. Research progress of the wear particles-induced aseptic prosthesis loosening chin. *Tissue Engineering Research* **16**, 9059–9063 (2012).
- [2] P. Chu, X. Liu. *Biomaterials Fabrication and Processing Handbook*, CRC Press, Taylor& Francis Group, 2008
- [3] M. Driver. *Coatings for Biomedical Applications*, Woodhead Publishing, 2012.
- [4] M. Driver. *Coatings for Biomedical Applications*, Woodhead Publishing, 2012.
- [5] T. Rautray, R. Narayanan, K. Kim. Ion implantation of titanium based biomaterials. *Progress in Materials Science* **56**, 1137–1177 (2011).
- [6] W.D. Sproul. New routes in the preparation of mechanically hard films. *Science* **273**, 889–892 (1996).
- [7] X.Zeng, S. Zhang, C.Sun, Y. Liu. Nanometric-layered CrN/TiN thin films: mechanical strength and thermal stability, *Thin Solid Films* **424**, 99–102 (2003).
- [8] P.Yashar, W.Sproul. Nanometer scale multilayered coatings, *Vacuum* **55**, 179–190 (1999).
- [9] L. Mishnaevsky, E. Levashov. Nanostructured titanium-based materials for medical implants: Modeling and development. *Materials Science and Engineering R* **81**, 1–19 (2014).
- [10] W.Oliver, G. Pharr. An improved technique for determining hardness and elastic modulus using load and displacement sensing indentation experiments. *Journal of Material Research* **7**, 1564-1583 (1992).
- [11] H. Barshiliaa, A. Jainb, K. Rajama. Structure, hardness and thermal stability of nanolayered TiN/CrN multilayer coatings. *Vacuum* **72**, 241–248 (2004).
- [12] J.An, Q. Zhang. Structure, morphology and nanoindentation behavior of multilayered TiN/TaN coatings. *Surface and Coatings Technology* **200**, 2451–2458 (2005).
- [13] W. Poole, M. Ashby, N. Fleck. Micro-hardness of annealed and work-hardened copper polycrystals. *Scripta Materialia* **34**, 559–564 (1996).
- [14] L.Combadiere, J. Machet. Reactive magnetron sputtering deposition of TiN films. I. Influence of the substrate temperature on structure, composition and morphology of the films. *Surface and Coatings Technology* **88**, 17-27 (1997).
- [15] I. Milosev, H.Strehblow, B. Navingek. XPS in the Study of High-Temperature Oxidation of CrN and TiN Hard coatings. *Surface and Coatings Technology* **74-75**, 897-902 (1995).
- [16] A. Conde, A.Cristóbal, G. Fuentes, T. Tate, J. Damborenea. Surface analysis of electrochemically stripped CrN coatings. *Surface and Coatings Technology* **201**, 3588–3595 (2006).
- [17] N. Heinig, H. Jalili, K. Leung. Fabrication of epitaxial CrO₂ nanostructures directly on MgO (100) by pulsed laser deposition. *Applied Physics Letters* **91**, 253102 (2007).
- [18] E. Unveren, E. Kemnitz, S. Hutton, A. Lippitz, W. Unger. Analysis of highly resolved x-ray photoelectron Cr 2p spectra obtained with a Cr₂O₃ powder sample prepared with adhesive tape. *Surface and Interface Analysis* **36**, 92-95 (2004).
- [19] A. Glaser, S. Surnev, F.Netzer, N. Fateh, G.Fontalvo, C. Mitterer. Oxidation of vanadium nitride and titanium nitride coatings. *Surface Science* **601**, 1153–1159 (2007).
- [20] M. Thotiyil, T. Kumar, S. Sampath. Pd Supported on Titanium Nitride for Efficient Ethanol Oxidation. *Journal of Physical Chemistry C* **114**, 17934–17941 (2010).
- [21] D. Duarte, J.Sagás, A. Sobrinho, M. Massi. Modeling the reactive sputter deposition of N-doped TiO₂ for application in dye-sensitized solar cells: Effect of the O₂ flow rate on the substitutional N concentration. *Applied Surface Science* **269**, 55-59 (2013).
- [22] A. Lippitz, T. Hüberr. XPS investigations of chromium nitride thin films. *Surface and Coatings Technology* **200**, 250–253 (2005).
- [23] P. Jouan, M.Peignon, Ch.Cardinaud, G.Lempérière. Characterisation of TiN coatings and of the TiN/Si interface by X-ray photoelectron spectroscopy and Auger electron spectroscopy. *Applied Surface Science* **68**, 595-603 (1993).
- [24] I. Milosev, H.Strehblow, B. Navingek. Electrochemical and Thermal Oxidation of TiN Coatings Studied by XPS. *Surface and Interface Analysis* **23**, 529- 539 (1995).
- [25] M. Nordin, M. Larsson, S. Hogmark. Mechanical and tribological properties of multilayered PVD TiN/CrN. *Wear* **232**, 221-225 (1999).
- [26] M. Nordin, M. Larsson, S. Hogmark. Mechanical and tribological properties of multilayered PVD TiN/CrN, TiN/MoN, TiN/NbN and TiN/TaN coatings on cemented carbide. *Surface and Coatings Technology* **106**, 234–241 (1998).

Wood derived hard carbon anode material for low-cost sodium-ion batteries towards practical application for grid energy storage

Ş. Patat^{1,2*}, A. Ülgen¹, S. Yıldız^{1,2}, A. R. Türkmen¹, T. Öztürk²

¹Erciyes University Faculty of Science, Department of Chemistry, Kayseri/Turkey

²ENDAM, Middle East Technical University, Ankara, Turkey

Electrochemical performance of the hard carbon derived from pine wood pyrolyzed at the temperature of 1600°C for 2 h is investigated as an anode material for sodium ion batteries. The synthesized hard carbon is characterized by X-ray diffraction, field-emission scanning electron microscopy equipped with energy dispersive x-ray spectrometry (EDX), nitrogen adsorption sorptometry, Raman spectroscopy, and conductivity measurements. The yield of hard carbon is 21%, based on the weight of precursor. The hard carbon demonstrates a low irreversible capacity of 26%, the reversible capacity of 234 mA h g⁻¹ at a current density of 30 mA g⁻¹, and a capacity retention of ~96.2% after 134 cycles at 1C.

Keywords: Hard carbon, sodium ion batteries, energy storage systems

INTRODUCTION

Energy storage systems have very important role in the development of portable electronic devices, electric vehicles and large-scale electrical energy storage applications for renewable energy, such as wind and solar power. Lithium ion batteries have dominated the market for portable electronic devices and electric vehicles due to the highest energy density and long cycle life. Sodium ion batteries have attracted great interest recently, especially for grid-scale energy storage because of the cheap, democratic global distribution and abundant of sodium resources [1]. Despite this, the absence of a suitable anode material limits their development. Graphite is the most widely used anode material in commercial lithium ion batteries owing to its abundant resource, excellent electronic conductivity, reasonable reversible capacity (up to 372 mAh g⁻¹), low and flat potential plateaus, high Coulombic efficiency, outstanding cycling stability, and low cost. Unfortunately, graphite demonstrates poor electrochemical performance as an anode material for sodium ion batteries using traditional carbonate electrolytes, mainly attributed to the larger ionic radii of the Na versus Li (102 Å versus 0.76 Å). The candidate anode materials for sodium ion batteries can be classified into carbonaceous materials, alloys, oxides and organic compounds [2, 3]. Among these candidates, hard carbon is one of the most promising anode materials for sodium ion

batteries because of its high specific capacity, low cost, low average potential and facile preparation methods [4]. Therefore, developing a high-performance hard carbon anode is highly desirable. However, hard carbon anodes suffer from the low initial Coulombic efficiency, the poor rate and the poor cycling performance due to side reactions related to larger surface area resulting from the nanostructures. To improve the initial Coulombic efficiency, cycling stability and rate performance, two kinds of methods have been used. One way is the surface modifying to reduce the contact area of carbon anode with electrolyte, which cause low initial Coulombic efficiency [5, 6]. The other one is to optimize the electrolyte [7]. Although some sodium can be trapped in hard carbon anode leading to the initial Coulombic efficiency loss, it is generally considered that hard carbon with a low surface area can give a high initial Coulombic efficiency [6]. It is found that the plateau capacity at the low potential region of voltage profile increases with increasing the carbonization temperature and the insertion process of Na into closed nanovoids limits the rate performance [8]. However, reducing the cost and minimizing the surface area of hard carbon remain a significant challenge. Cellulose is the most abundant and also renewable resource on Earth, which has attracted great interest as a carbon precursor. Various biomasses, such as wood [9-11], mangosteen shell [12], spinifex [13], sucrose [14-16], paper pulp mill sludge[17], banana peel [18], orange peel [19], peat moss [20], and pomelo peels [21] and peanut shell [22] have been used as

* To whom all correspondence should be sent:
patat@erciyes.edu.tr

precursors and the hard carbons derived from them show good performance as anode for sodium ion batteries. In this work, hard carbons derived from pine wood have been successfully developed as anodes for sodium ion batteries.

EXPERIMENTAL SECTION

Hard Carbon Synthesis

The collected pine wood was washed with deionized water, cut into small pieces, and dried at 110°C overnight in an oven. Typically 10 g of wood precursor was loaded in a tube furnace and heated at 1600°C for 2h under an argon atmosphere with the flow rate of 100 sccm. The obtained carbon was ground using ball mill at 350rpm for 1h before use.

Materials Characterization

The crystallinity and the phases of the hard carbon samples were identified by powder X-ray diffraction (XRD) using copper $\text{CuK}\alpha$ radiation ($\lambda=1.5406 \text{ \AA}$) (Bruker AXS D8). The X-ray powder diffraction measurements were made using a Bruker AXS D8 X-ray diffractometer equipped with copper X-ray tube, NaI type scintillation counter detector and graphite monochromator. The diffraction data were collected in 2θ range of 10° - 70° with the step size of 0.02° and a count time of 10 s per step at 40 kV and 40mA.

The Raman spectra were recorded with a confocal microprobe Raman system (Thermo Nicolet Almega XR Raman microscope). The surface morphology of the samples was investigated using a scanning electron microscope (SEM, LEO 440), operated at an accelerating voltage of 20 kV, equipped with energy dispersive X-ray spectrometry (EDX). The samples were laid on carbon tape before being measured and covered with Au-Pd alloy under high vacuum. The elemental composition of the samples was determined by EDX.

The conductivities of the samples were measured at room temperature by linear scanning voltammetry. The powder samples were uniaxially pressed into pellets under a pressure of about 9 tons using a stainless steel die with 13 mm diameter. The prepared pellets were located in a two-electrode Swagelok type cell and the potential versus current values were measured in a potential range of 0-100 mV at a scanning speed of $5 \text{ mV}\cdot\text{s}^{-1}$ with AMETEK Princeton Applied Research VersaSTAT MC model multi-channel galvanostat/potentiostat.

The conductivity is calculated from the slope (V/I) of current versus potential curve given in Eq. (1):

$$\frac{V}{I} = R, \rho = R \cdot \frac{s}{l} \text{ ve } \chi = \frac{1}{\rho} = \frac{l}{sR} \quad (1)$$

Where V, I, R, ρ , s, l, and χ stand for voltage (mV), current (mA), the resistance (ohm), resistivity (ohm.cm), the surface area of pellet (cm^2), thickness of pellet (cm), and conductivity (S/cm), respectively.

Nitrogen adsorption/desorption isotherms of the hard carbon materials were measured using nitrogen gas adsorption on Micromeritic Corporation TriStar II 3020 V1.03. Before measurements, the samples were degassed for 24 hours at 120 °C. Once degassed, the isotherms were measured at 77 K in a p/p^0 (relative pressure) range of 0.001-1, with P^0 being 760 torr. The specific surface area and the pore size distribution were calculated with the Brunauer-Emmett-Teller (BET) and the Barrett-Joyner-Halenda (BJH) methods, respectively.

Electrochemical Characterization

For preparation of the working electrodes, the hard carbon powders (96 wt%) were mixed with sodium alginate (Sigma-Aldrich) as a binder (4 wt%) in *deionized water*. The obtained slurry was pasted onto a piece of Al foil with doctor blade, followed by drying at 60°C in air for 3h, roll pressing, drying at 120°C for 10h in a vacuum oven, and cutting into 13 mm disks, respectively prior to use. The active material mass loading of the electrode ranged from 6 to 8 mg cm^{-2} . A three electrode Swagelok type electrochemical cell with the electrode diameter of 13 mm was used to measure the electrochemical performance. The cell was assembled in an Ar filled glove-box using the hard carbon as a working electrode, pure sodium metal disks (Merck) both as a counter and a reference electrode, a glass fiber filter as a separator and 1M NaPF_6 (Sigma-Aldrich) in 1:1 by weight ethylene carbonate (Merck) and propylene carbonate (Merck) as the electrolyte. The constant current charge/discharge measurements were carried out in the potential range of 0.01-3.0V at different current densities ranging from 0.1C to 1C ($1\text{C}=300 \text{ mA g}^{-1}$) on an AMETEK Princeton Applied Research VersaSTAT MC model multi-channel galvanostat/potentiostat. The cycle life stability was studied by using constant current charge/discharge measurements in the potential

range of 0.01V-3.0V at 1C for 100 cycles. All electrochemical tests were conducted at room temperature.

RESULTS AND DISCUSSION

The elemental content of the hard carbon determined by EDX is found to be 93.73 at % C, 5.39 at%O, 0.40 at% Ca, 0.21 at% Fe and 0.26 at % K. Its conductivity is measured to be 0.73 S cm^{-1} . Its X-ray diffraction (XRD) pattern is given in Fig.1. The XRD pattern demonstrates two broad peaks at $\sim 24^\circ$ (revealing the non-graphitic nature) and $\sim 44^\circ$, which are assigned to the crystallographic planes of (002) and (100) in the carbon structure, respectively. On the basis of the Bragg equation $2d \sin \theta = n\lambda$, the d_{002} value of the hard carbon is 0.371nm, which is much larger than that of graphite ($\sim 0.340\text{nm}$), leading to facile sodium-ion insertion/extraction between the graphene layers. The thickness (L_c) and average width (L_a) of the graphitic domains are calculated using the Scherrer equation with the peak positions and full width at half maximum (FWHM) values of (002) and (100) peaks at $2\theta \approx 24^\circ$ and $2\theta \approx 44^\circ$, respectively. According to the d_{002} and L_c values, the number of layers stacked in the graphitic domains can be roughly estimated. The L_c and d_{002} values of the hard carbon were found to be 0.69 nm and 0.371 nm, respectively, indicating that the graphitic domain of the hard carbon is made up of 3–4 stacked graphene layers ($n = 0.690/0.371 + 1$). L_a value is 2.25nm.

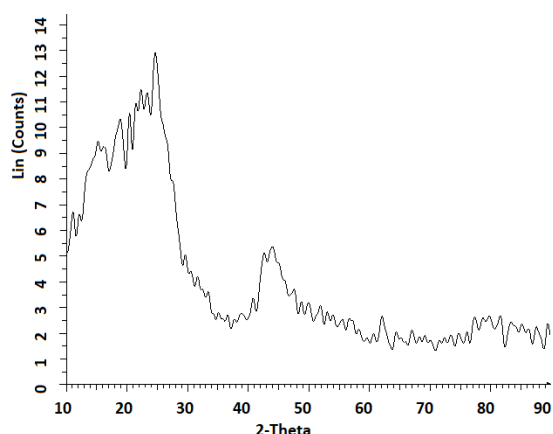


Fig.1. XRD pattern of the hard carbon carbonized at 1600°C

The Raman spectrum of the hard carbon is given in Fig.2. As shown in Fig.2, the spectrum shows two bands located at ~ 1340 and ~ 1584

cm^{-1} corresponding to the defect induced D band representing the sp^3 hybridized carbon atoms and the crystalline graphite G band representing sp^2 hybridized carbon atoms, respectively. The intensity ratio of the D band and G band (I_D/I_G) which is used to quantify the disorder degree of carbon materials was found to be 1.33. An I_D/I_G value greater than 1 implies the disordered nature of the carbon sheets and the associated unrepaired edge defects. The 2D peak at 2657.77 cm^{-1} may also be used as a measure of disorder [19,20].

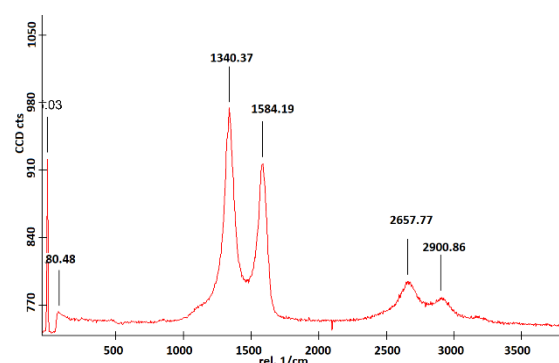


Fig.2. Raman spectrum of the hard carbon

A scanning electron microscope (SEM) image of the hard carbon is given Fig.3. As shown in the SEM image, the hard carbon consists of bulk particles and exhibits porous surface.

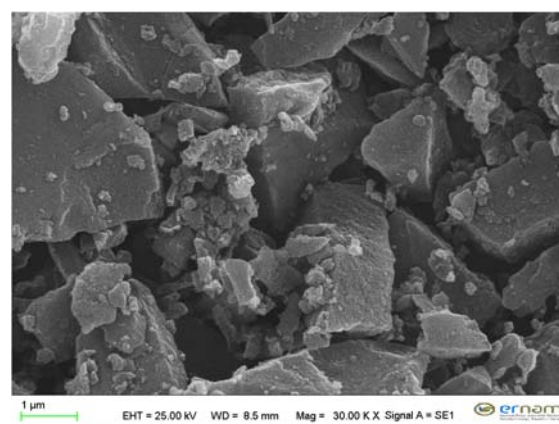


Fig.3. SEM micrograph of the hard carbon

Nitrogen adsorption–desorption isotherm for the hard carbon is given in Fig.4. As shown in Fig.4, the hard carbon demonstrates a typical type IV behavior, and the initial steep region indicates a certain amount of micropores [11] existing in the hard carbon with a Brunauer–Emmett–Teller (BET) surface area of $102 \text{ m}^2 \text{ g}^{-1}$. The inset shows the pore size distribution calculated from the N_2 adsorption–

desorption isotherm using the Barrett–Joyner–Halenda (BJH) method. These distributions indicate the presence of both micropores and mesopores [13].

All the characterization results confirm that the nongraphitizable hard carbon pyrolyzed from the wood was obtained, which have micropores structure to facilitate the electrolyte penetration and provide sites for Na⁺ ion storage.

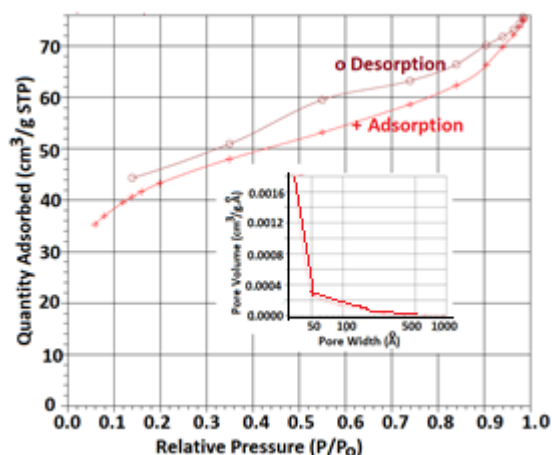


Fig.4. Nitrogen adsorption/desorption isotherm of the hard carbon

Galvanostatic charge/ discharge potential profiles of the hard carbon at different current rates are given in Fig.5. As reported before for hard carbon anodes in sodium ion batteries, the potential profile can be divided into two regions with a slope from 2.0 to ~0.15 V and a plateau close to 0 V. The sloping region corresponds to the insertion of Na⁺ ions intercalation into graphitic nanodomains along with the SEI formation, whereas the plateau region corresponds to the adsorption of Na ions into the hard carbon's nanovoids [23].

The first and second sodiation capacities are 320 and 235 mAh/g, respectively, yielding a high reversible capacity of 74%. This is one of the highest first-cycle reversible capacity value reported for hard carbon anodes in sodium ion batteries (see Table 1). The irreversible capacity loss in the first cycle is mainly due to the decomposition of the electrolyte that leads to the formation of a passivating solid electrolyte interphase (SEI) on the surface of the hard carbon.

The cycling performance of the hard carbon at different current rates is given in Fig.6. As seen from Fig.6, the decreases in specific capacity are observed at higher currents due to

the kinetic limitation of the hard carbon. After 134 cycles at 300 mA g⁻¹, 96.2% of the capacity for the second cycle at 0.1C remained.

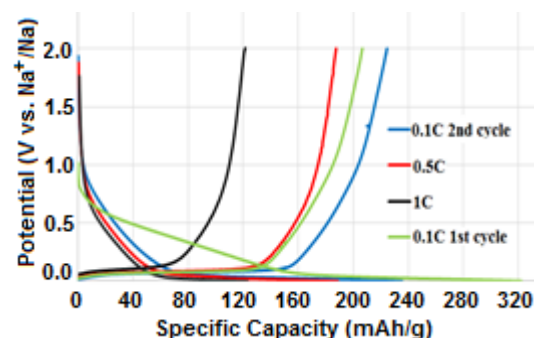


Fig.5. Galvanostatic charge/discharge curves of the hard carbon at 0.1C, 0.5C and 1.0C current densities (1.0C=300 mAh/g)

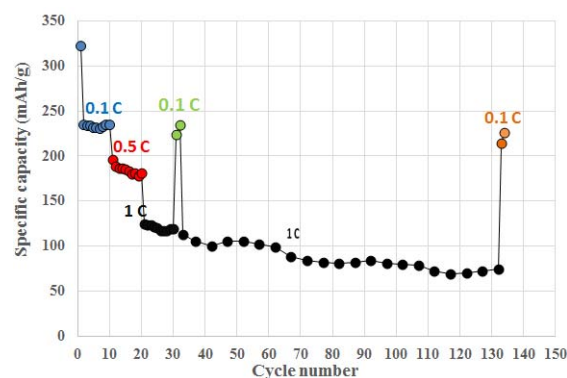


Fig.6. Cycling performance of the hard carbon at different current rates

Table 1. Electrochemical performances of reported carbon anode materials for SIBs.

Materials	nanoporous hard carbon	wood fibre derived carbon	commercially available hard carbon
Initial C.E.	77%	72%	78%
Cyclability (mAh/g)	289 at 0.02 A g ⁻¹ after 100 cycles	196 at 0.1A g ⁻¹ after 200 cycles	225 at 0.025 A g ⁻¹ after 100 cycles
Rate capability (mAh/g)	95 at 0.5 A g ⁻¹		
Reference	[24] 104	[25] 83	[26]

CONCLUSIONS

Hard carbon anode material has been successfully synthesized from pine wood via a simple, one-step pyrolysis process at 1600°C with the yield of 21%. The hard carbon demonstrates low initial irreversible capacity loss of 26%, the high reversible capacity of

~235 mA h g⁻¹ at a current density of 30 mA g⁻¹, and the capacity retention of ~96.2% after 134 cycles. This good performance highlights the potential of the pine wood pyrolyzed hard carbon for practical applications.

ACKNOWLEDGEMENTS

This work has been supported financially by Scientific Research Projects Unit of Erciyes University (with the Project Number FYL-2017-7621 and FBA-12-4031), which is gratefully acknowledged by the authors

REFERENCES

- [1] Yunming Li, Yaxiang Lu, Chenglong Zhao, Yong-Sheng Hu, Maria-Magdalena Titirici, Hong Li, Xuejie Huang, Liquan Chen. Recent advances of electrode materials for low-cost sodium-ion batteries towards practical application for grid energy storage. *Energy Storage Materials*, **7** 130–151 (2017).
- [2] M. Dahbi, N. Yabuuchi, K. Kubota, K. Tokiwa, S. Komaba. Negative electrodes for Na-ion batteries. *Phys. Chem. Chem. Phys.* **16**, 15007–15028 (2014).
- [3] C. Bommier, X.L. Ji. Recent Development on Anodes for Na-Ion Batteries. *Isr. J. Chem.* **55**, 486–507 (2015).
- [4] Hongshuai Hou, Xiaoqing Qiu, Weifeng Wei, Yun Zhang, Xiaobo Ji. Carbon Anode Materials for Advanced Sodium-Ion Batteries. *Adv. Energy Mater.*, 1602898 (2017).
- [5] Clement Bommier, Wei Luo, Wen-Yang Gao, Alex Greaney, Shengqian Ma, Xiulei Ji. Predicting capacity of hard carbon anodes in sodium-ion batteries using porosity measurements. *Carbon* **76**, 165-174 (2014).
- [6] F. Shen, H. Zhu, W. Luo, J. Wan, L. Zhou, J. Dai, B. Zhao, X. Han, K. Fu, L. Hu. Chemically Crushed Wood Cellulose Fiber towards High Performance Sodium-Ion Batteries. *ACS Appl. Mater. Interfaces* **7**, 23291–23296 (2015).
- [7] S. Komaba, W. Murata, T. Ishikawa, N. Yabuuchi, T. Ozeki, T. Nakayama, A. Ogata, K. Gotoh, K. Fujiwara. Electrochemical Na Insertion and Solid Electrolyte Interphase for Hard-Carbon Electrodes and Application to Na-Ion Batteries. *Adv. Funct. Mater.* **21**, 3859–3867 (2011).
- [8] Kun Wang, Yu Jin, Shixiong Sun, Yangyang Huang, Jian Peng, Jiahuan Luo, Qin Zhang, Yuegang Qiu, Chun Fang, Jiantao Han. Low-Cost and High-Performance Hard Carbon Anode Materials for Sodium-Ion Batteries. *ACS Omega* **2**, 1687–1695 (2017).
- [9] Fei Shen, Wei Luo, Jiaqi Dai, Yonggang Yao, Mingwei Zhu, Emily Hitz, Yuefeng Tang, Yanfeng Chen, Vincent L. Sprenkle, Xiaolin Li, Liangbing Hu. Ultra-Thick, Low-Tortuosity, and Mesoporous Wood Carbon Anode for High-Performance Sodium-Ion Batteries. *Adv. Energy Mater.*, **6**, 1600377 (2016).
- [10] Hongli Zhu, Fei Shen, Wei Luo, Shuze Zhu, Minhua Zhao, Bharath Natarajan, Jiaqi Dai, Lihui Zhou, Xiulei Ji, Reza S. Yassar, Teng Li, Liangbing Hu. Low temperature carbonization of cellulose nanocrystals for high performance carbon anode of sodium-ion batteries. *Nano Energy* **33**, 37–44 (2017).
- [11] F. Shen, H. Zhu, W. Luo, J. Wan, L. Zhou, J. Dai, B. Zhao, X. Han, K. Fu, L. Hu. Chemically Crushed Wood Cellulose Fiber towards High Performance Sodium-Ion Batteries. *ACS Appl. Mater. Interfaces* **7**, 23291–23296 (2015).
- [12] Kun Wang, Yu Jin, Shixiong Sun, Yangyang Huang, Jian Peng, Jiahuan Luo, Qin Zhang, Yuegang Qiu, Chun Fang, Jiantao Han. Low-Cost and High-Performance Hard Carbon Anode Materials for Sodium-Ion Batteries. *ACS Omega* **2**, 1687–1695 (2017).
- [13] Rohit Ranganathan Gaddam, Edward Jiang, Nasim Amiralian, Pratheep K. Annamalai, Darren J. Martin, Nanjundan Ashok Kumar X. S. Zhao. Spinifex nanocellulose derived hard carbon anodes for high-performance sodium-ion batteries. *Sustainable Energy Fuels* **1**, 1090–1097 (2017).
- [14] Li, Y. M.; Xu, S. Y.; Wu, X. Y.; Yu, J. Z.; Wang, Y. S.; Hu, Y. S.; Li, H.; Chen, L. Q.; Huang, X. J. Amorphous Monodispersed Hard Carbon Micro-Spherules Derived From Biomass as a High Performance Negative Electrode Material for Sodium-Ion Batteries. *J. Mater. Chem. A* **3**, 71–77 (2015).
- [15] Clement Bommier, Wei Luo, Wen-Yang Gao, Alex Greaney, Shengqian Ma, Xiulei Ji. Predicting capacity of hard carbon anodes in sodium-ion batteries using porosity measurements. *Carbon* **76**, 165-174 (2014).
- [16] Luo, W.; Bommier, C.; Jian, Z.; Li, X.; Carter, R.; Vail, S.; Lu, Y.; Lee, J.-J.; Ji, X. Low-Surface-Area Hard Carbon Anode for Na-Ion Batteries via Graphene Oxide as a Dehydration Agent. *ACS Appl. Mater. Interfaces* **7**, 2626–2631 (2015).
- [17] H. Wang, Z. Li, J.K. Tak, C.M.B. Holt, X. Tan, Z. Xu, B.S. Amirkhiz, D. Harfield, A. Anyia, T. Stephenson, D. Mitlin. Supercapacitors based on carbons with tuned porosity derived from paper pulp mill sludge biowaste. *Carbon* **57**, 317–328 (2013).
- [18] E.M. Lotfabad, J. Ding, K. Cui, A. Kohandehghan, W.P. Kalisvaart, M.

- Hazelton, D. Mitlin. High-Density Sodium and Lithium Ion Battery Anodes from Banana Peels. *ACS Nano* **8**, 7115–7129 (2014).
- [19] Jianyong Xiang, Weiming L, Congpu Mu, Jing Zhao, Bochong Wang. Activated hard carbon from orange peel for lithium/sodium ion battery anode with long cycle life. *Journal of Alloys and Compounds* **701**, 870-874 (2017).
- [20] Jia Ding, Huanlei Wang, Zhi Li, Alireza Kohandehghan, Kai Cui, Zhanwei Xu, Benjamin Zahiri, Xuehai Tan, Elmira Memarzadeh Lotfabad, Brian C. Olsen, David Mitlin. Carbon Nanosheet Frameworks Derived from Peat Moss as High Performance Sodium Ion Battery Anodes. *ACS Nano* **7**, 11004–11015, (2013).
- [21] Kun-lei Hong, Long Qie, Rui Zeng, Zi-qi Yi, Wei Zhang, Duo Wang, Wei Yin, Chao Wu, Qing-jie Fan, Wu-xing Zhang, Yun-hui Huang. Biomass derived hard carbon used as a high performance anode material for sodium ion batteries, *Mater. Chem. A* **2**, 12733-12738 (2014).
- [22] Weiming Lv, Fusheng Wen, Jianyong Xiang, Jing Zhao, Lei Li, Limin Wang, Zhongyuan Liu, Yongjun Tian. Peanut shell derived hard carbon as ultralong cycling anodes for lithium and sodium batteries. *Electrochimica Acta* **176**, 533–541 (2015).
- [23] Stevens, D. A.; Dahn, J. R. High Capacity Anode Materials for Rechargeable Sodium-Ion Batteries. *J. Electrochem. Soc.* **147**, 1271–1273 (2000).
- [24] S.R. Prabakar, J. Jeong, M. Pyo, Nanoporous hard carbon anodes for improved electrochemical performance in sodium ion batteries, *Electrochim. Acta* 2015, 161, 23.
- [25] F. Shen, H. Zhu, W. Luo, J. Wan, L. Zhou, J. Dai, B. Zhao, X. Han, K. Fu, L. Hu, Chemically Crushed Wood Cellulose Fiber towards High-Performance Sodium-Ion Batteries, *ACS Appl. Mater. Interfaces*, 2015, 7(41), 23291
- [26] S. Komaba, W. Murata, T. Ishikawa, N. Yabuuchi, T. Ozeki, T. Nakayama, A. Ogata, K. Gotoh, K. Fujiwara, Electrochemical Na Insertion and Solid Electrolyte Interphase for Hard-Carbon Electrodes and Application to Na-Ion Batteries, *Adv. Funct. Mater.* 2011, 21, 3859.

Mathematical modelling concerning the influence of chemical composition upon hardness of cadmium telluride crystal

- Part 2 -

T. L. Severin*, A. Potorac, C. Dulucceanu, L. Irimescu

University Stefan cel Mare, Suceava, Faculty of Mechanical Engineering, Mechatronics and Management, Department of Mechanics and Technologies, 13 University St., 720229 Suceava, Romania

Cadmium telluride is an alloy with semiconductor properties and is currently the basic material for manufacturing photovoltaic cells. This material has been studied in the literature only in terms of properties defining characteristics of semiconductors, without presenting any data concerning the influence of micro-alloying elements upon hardness values. The mathematical model developed in this paper is aimed to determine hardness of cadmium telluride crystals depending on the chemical composition and expresses the hardness values of cadmium telluride crystal, depending on the micro-alloying elements. In order to establish a link between the micro alloying elements and cadmium telluride crystal hardness, experimental researches were carried out using ablation laser equipment UP213 New Wave Research, coupled to ICP-MS 750 Agilent, respectively Martens method for hardness measuring with hardness testing device Shimadzu DUH-211S. By applying the mathematical model developed, the calculated hardness values correspond within the predetermined limits with the hardness values determined experimentally by the Martens method. From the theoretical and experimental researches, it appears that the hardness of crystals of cadmium tellurium, an important mechanical characteristic in the subsequent mechanical processing of their shape and dimensions, can be predicted with a probability of 95%, using the mathematical model presented in this paper, starting from the concentrations of micro alloying elements.

Keywords: hardness, laser ablation, alloy, hardness tester, cadmium telluride

INTRODUCTION

“Cadmium telluride is an alloy with semiconductor properties, obtained through melting in special furnaces tellurium and cadmium semimetals and is currently the base material for manufacturing photovoltaic cells. Furthermore, through micro-alloying (crystal doping) with mercury, the base material for high performance infrared detectors used in spectrometry and remote sensing is manufactured, whereas through micro-alloying with zinc is obtained the base material for manufacturing Röntgen and Gamma detectors [2,3].

Cadmium telluride is characterized through a crystal, hence fragile structure. In the process of manufacturing large areas solar panels, the cadmium telluride, as base material, should provide corresponding mechanical characteristics depending on operating conditions. That is why a thorough study and an advanced characterization of the mechanical behavior of cadmium telluride crystal could be extremely useful.

The paper proposes a mathematical model which provides the hardness values of cadmium telluride crystal depending on the micro alloying elements. This material has been studied in the literature only in terms of defining the properties

of semiconductor properties [4, 5, 6, 7, 8], without presenting any data concerning the influence of micro-alloying elements upon hardness values. That is why, providing a model and, consequently, having the possibility to predict the mechanical behavior and especially the hardness of cadmium telluride is of the last importance for practical issues depending on operating particularities [1].

EQUIPMENT USED FOR THE ACQUISITION OF EXPERIMENTAL DATA

“LA-ICP-MS technique is particularly useful for in situ samples analyzes, that is, for applications that require understanding of elementary spatial variation for the sample. Laser ablation (LA) coupled to an ICP-MS equipment (mass spectrometry with inductively coupled plasma) may perform direct analysis on almost all materials.

This technology was used in determining the composition of cadmium telluride crystal, by the instrumentality of a LA model UP213 of New Wave Research Company, coupled with a model Agilent 7500 ICP-MS, Agilent Technologies, from the laboratory of Instrumental Analysis of the Faculty of Food Engineering, University of Suceava Romania (Fig.1). The UP 213 (213 nm laser ablation) releases atomic vapors of the material absorbed in the ICP MS to quantitatively determine its elements.

* To whom all correspondence should be sent:
severin.traian@fim.usv.ro

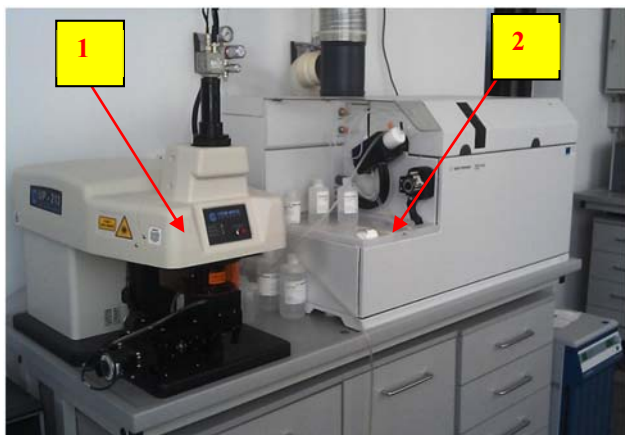


Fig.1. Laser ablation system UP-213 New Wave (1) – ICP-MS Agilent 7500 (2)

The UP series of laser ablation equipment manufactured by New Wave Research Company is specially designed to work with ICP-MS and ICP-OE systems. The YAG laser of UP213 ablation equipment is operating in 213 nm UV region, Fig.2” [1]. The Ablation zone on surface CdTe crystal after a qualitative and quantitative analysis performed with NewWave UP213 spectrometer coupled to an Agilent 7500 ICP-MS; laser continuously 10Hz rate, scan speed 10 μm/s, working energy 0.721 mJ, channel length 1 mm.

Using ICP MS type spectroscopy to study hardness allows highlighting the influence of micro alloying elements traces upon the hardness.

Micro hardness of cadmium telluride crystal was investigated and evaluated using the Shimadzu DUH-211S micro hardness tester, and three micro-indentation were made in each area on the crystal (Fig.2) [1].

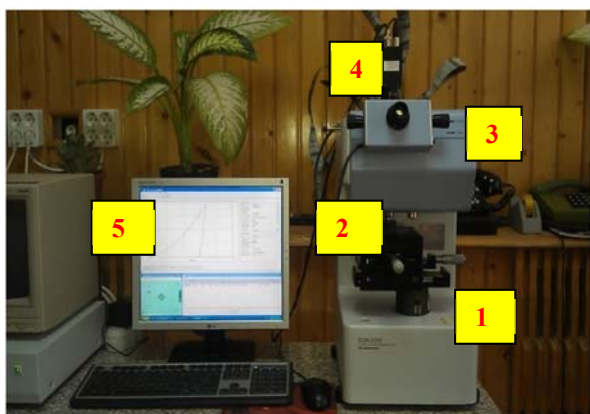


Fig.2. Shimadzu DUH-211S micro hardness tester (1), sample manual positioning system (2), footprint optical viewing system (3) image pickup video system CCD (4), hardness measurement and footprint inspection software (5) [1]

RESULTS

In this experimental research, cadmium telluride single crystal has the composition, concentrations of components and mechanical characteristics consistent with those presented in Tab.1 and determined by ICP-MS-LA technique. Moreover, the research was focused also on the distribution of the segregation of chemical elements of micro alloying with respect to the geometrical position of a point down the axis of the crystal, distribution enabling further correlation of the composition and concentration with the semiconductor, mechanical and thermal properties of cadmium telluride. To this end cadmium telluride crystal was mechanically cut lengthwise and on the symmetry axis have been marked distances of 5 mm on 5 mm (17 areas) [1].

The analysis of the distribution of micro alloying elements of cadmium telluride crystal was extended to all ten chemical elements, whose average concentration (mean concentrations of all the seventeen measurement areas) is shown in Tab. 1. Determination of the crystal hardness (HMV) depending on the micro alloying elements for the 17 analyzed areas was instrumented through the Martens method for determining hardness, using an automatic hardness testing device Shimadzu DUH-211S (Tab.1) [1].

Checking the homogeneity of hardness values variances for cadmium telluride crystal was performed using Bartlett Test and finally verifying χ^2_B which should obey to the law χ^2 with $k-1$ degrees of freedom [1]. The decision according to the results shown in Article part 1 Tab. 3 with respect to checking the homogeneity of variance for hardness values recorded for the CdTe crystal, should be accepted as: $\chi^2_{B-calculated} = (17,68) <$

$\chi^2_{B-table} (27,58)$. Consequently, it was clear that using Bartlett test, the results concerning the influence of micro alloying elements upon the hardness obtained for cadmium telluride crystal is confirmed by 95% confidence level.

Micro alloying elements identified and considered for mathematical model are expressed in parts per billion (ppb): vanadium (ppb) (x_1), chromium (ppb) (x_2), cobalt (ppb) (x_3), nickel (ppb) (x_4), copper (ppb) (x_5), zinc (ppb) (x_6), tin (ppb) (x_7), tungsten (ppb) (x_8), thallium (ppb) (x_9), lead (ppb) (x_{10}), (Tab. 2), for the target function the values of the hardness of the crystal $HMV=Z$ are considered (Tab. 2). In order to elaborate the empirical model of the investigated process we used the programming of the experiment in the factorial space, moving from the real values of the influence factors to the coded equivalent values.

In Tab. 2, after encoding the concentrations of the influence factors used in order to develop the mathematical model, the minimum values of the components are represented with -1 (the lower level of the range), maximum values with +1 (the upper level of the interval), whereas the arithmetic mean of the minimum and maximum values is the 0 level of the interval.

The choice of the mathematical model

In order to obtain the mathematical model of prediction of hardness according to the

microalloying elements, it was started from an order 1 polynomial (rel. 1), explaining the behavior of the studied system, [12].

$$Z = b_0 + \sum_{i=1}^k b_i x_i \tag{1}$$

where Z represents the value of the hardness response for each experiment, b_0 represents the intersection term and b_i represents the terms of the linear coefficient.

Table 1. Influencing factors for developing the mathematical model used for CdTe crystal

No.	Elements Exp. no.	x1 (ppb)	x2 (ppb)	x3 (ppb)	x4 (ppb)	x5 (ppb)	x6 (ppb)	x7 (ppb)	x8 (ppb)	x9 (ppb)	x10 (ppb)	HMV (N/mm ²)
1.	Area 0	120	334	29	37	31	5100	3,4	46	0,21	0,57	697
2.	Area 1	120	250	28	36	30	3800	3,8	33	0,21	0,51	681
3.	Area 2	130	220	27	33	33	2500	3,9	25	0,18	0,35	679
4.	Area 3	150	210	25	25	35	1800	5	19	0,19	0,41	674
5.	Area 4	154	180	24	25	36	1660	9,5	17	0,21	0,37	667
6.	Area 5	154	168	24	24	37	1610	9,4	18	0,22	0,44	663
7.	Area 6	159	165	25	24	38	1590	8,6	20	0,2	0,45	662
8.	Area 7	161	163	24	24	40	1580	9,2	18	0,25	0,43	661
9.	Area 8	161	155	24	23	42	1570	9,6	17	0,17	0,54	660
10.	Area 9	168	148	25	22	44	1550	9,6	20	0,16	0,42	657
11.	Area 10	170	134	26	21	48	1420	9,5	17	0,2	0,41	649
12.	Area 11	171	132	25	20	49	1419	9,5	15	0,15	0,46	649
13.	Area 12	173	129	25	19	50	1411	9,4	13	0,19	0,71	644
14.	Area 13	180	127	24	19	53	1405	9,4	12	0,16	0,57	640
15.	Area 14	220	125	24	19	58	1400	9,3	11	0,18	0,44	639
16.	Area 15	221	125	23	18	60	1398	9,2	11	0,18	0,33	638
17.	Area 16	229	124	22	18	61	1398	9,4	11	0,14	0,47	635

Table 2. Coding the influence factors used to develop the mathematical model for CdTe crystal

Nr crt	Elements Exp. no.	x1	x2	x3	x4	x5	x6	x7	x8	x9	x10	HMV (N/mm ²)
1.	Area 0	-1	1	1	1	-0,935	1	-1	1	0,272	0,263	697
2.	Area 1	-1	0,2	0,714	0,894	-1	0,297	-0,871	0,257	0,272	-0,052	681
3.	Area 2	-0,816	-0,085	0,428	0,578	-0,806	-0,404	-0,838	-0,2	-0,272	-0,894	679
4.	Area 3	-0,449	-0,181	-0,142	-0,263	-0,677	-0,782	-0,483	-0,542	-0,090	-0,578	674
5.	Area 4	-0,376	-0,466	-0,428	-0,263	-0,612	-0,858	0,967	-0,657	0,272	-0,789	667
6.	Area 5	-0,376	-0,581	-0,428	-0,368	-0,548	-0,885	0,935	-0,6	0,454	-0,421	663
7.	Area 6	-0,284	-0,609	-0,142	-0,368	-0,483	-0,896	0,677	-0,485	0,090	-0,368	662
8.	Area 7	-0,247	-0,628	-0,428	-0,368	-0,354	-0,901	0,871	-0,6	1	-0,473	661
9.	Area 8	-0,247	-0,704	-0,428	-0,473	-0,225	-0,907	1	-0,657	-0,454	0,105	660
10.	Area 9	-0,119	-0,771	-0,142	-0,578	-0,096	-0,917	1	-0,485	-0,636	-0,526	657
11.	Area 10	-0,082	-0,904	0,142	-0,684	0,161	-0,988	0,967	-0,657	0,090	-0,578	649
12.	Area 11	-0,064	-0,923	-0,142	-0,789	0,225	-0,988	0,967	-0,771	-0,818	-0,315	649
13.	Area 12	-0,027	-0,952	-0,142	-0,8947	0,290	-0,993	0,935	-0,885	-0,090	1	644
14.	Area 13	0,101	-0,971	-0,428	-0,8947	0,483	-0,996	0,935	-0,942	-0,636	0,263	640
15.	Area 14	0,834	-0,990	-0,428	-0,8947	0,806	-0,998	0,903	-1	-0,272	-0,421	639
16.	Area 15	0,853	-0,990	-0,714	-1	0,935	-1	0,871	-1	-0,272	-1	638
17.	Area 16	1	-1	-1	-1	1	-1	0,935	-1	-1	-0,263	635

The experimental domains and levels of independent variables (x_1, x_2, \dots, x_{11}), used to obtain the prediction model of cadmium tellurium crystals, depending on the micro alloying elements are shown in Tab. 3.

The regression coefficients of the empirical model are calculated using Eq.(2) [12, 13, 14].

$$B = (X^T \cdot X)^{-1} \cdot X^T \cdot Y \quad (2)$$

where B represents matrix regression coefficients, X is the matrix of the encoded variables, X^T is transposed to the matrix X , Y is the matrix of the response values.

Table 3. Experimental domain and levels of independent variables

Independent variable	Code	The level of the variables			Domain
		-1	0	+1	
V, (ppb)	x ₁	120	174,5	229	109
Cr, (ppb)	x ₂	124	229	334	210
Co, (ppb)	x ₃	22	25,5	29	7
Ni, (ppb)	x ₄	18	27,5	37	19
Cu, (ppb)	x ₅	30	45,5	61	31
Zn, (ppb)	x ₆	1398	3249	5100	3702
Sn, (ppb)	x ₇	3,4	6,5	9,6	6,2
W, (ppb)	x ₈	11	28,5	46	35
Tl, (ppb)	x ₉	0,14	0,195	0,25	0,11
Pb, (ppb)	x ₁₀	0,33	0,52	0,71	0,38

For the calculation of the coefficient b_0 , the following equations, that is Eq.(3), (4), (5) are used and where b , b_0 represent intercept term [12, 13]

$$b_0 = b'_0 - \sum_{i=1}^k b_{ii} \left(\frac{\sum_{u=1}^N x_{iu}^2}{N} \right)$$

$$b'_0 = \frac{\sum_{u=1}^N x_{0u} y_u}{\sum_{u=1}^N x_{0u}^2} \quad (3)$$

Calculation of coefficients for simple effects (b_i)

$$b_i = \frac{\sum_{u=1}^N x_{iu} y_u}{\sum_{u=1}^N x_{iu}^2} \quad (4)$$

Calculating coefficients for interaction effects (b_{ij})

$$b_{ij} = \frac{\sum_{u=1}^N x_{iu} x_{ju} y_u}{\sum_{u=1}^N (x_{iu} x_{ju})} \quad (5)$$

where the total number of experiments is $N = 17$. Thus, the values of polynomial coefficients calculated with the above equations are presented in Tab. 4.

Table 4. Polynomial coefficient values

b_0	b_1	b_2	b_3	b_4	b_5
665,6381	-9,1569	3,9332	-9,7158	-0,0005	-8,1460
b_6	b_7	b_8	b_9	b_{10}	
-6,0448	-4,5125	21,0411	-0,1321	-2,1940	

Therefore, the mathematical model has the expression according to the Eq.(1), where the response function Z has the form:

$$Z = 665,6380 - 9,1568x_1 + 3,9331x_2 - 9,7158x_3 + 0,0005x_4 - 8,14603x_5 - 6,0448x_6 - 4,5124x_7 + 21,0410x_8 - 0,1321x_9 - 2,1939x_{10} \quad (6)$$

Testing the significance of the mathematical model

The significance of coefficients of the regression model is tested by comparing the absolute value of the coefficients b_i with the confidence interval calculated with the Eq.7 (Student test).

Coefficients have significant effects if the condition presented in equation 8 is met:

$$\Delta b_i = t_{\alpha;N} \cdot S_{bi} \quad (7)$$

$$|b_i| \geq |\Delta b_i| \quad (8)$$

The calculation of the Student test for the mathematical model presented in Eq.7 used the following parameters:

$$N = 17 \text{ (number of degrees of freedom - experiences)} \quad (9)$$

$$\alpha = 0,05 \text{ (threshold of significance)} \quad (10)$$

$$t_{0,05;17} = 2,110 \text{ (Student test value) [13]} \quad (11)$$

$$S^2 = 7,5294 \text{ (data reproducibility dispersion)} \quad (12)$$

S_{bi} - average square deviation for the coefficient b_{ij}

The confidence intervals of the coefficients are shown in Tab. 5.

Table 5. Confidence intervals for the mathematical model

Δb_0	Δb_1	Δb_2	Δb_3	Δb_4	Δb_5
0,312	0,312	0,312	0,312	0,312	0,312
Δb_6	Δb_7	Δb_8	Δb_9	Δb_{10}	
0,312	0,312	0,312	0,312	0,312	

Table 6. Significant coefficients of the mathematical model

b_0	b_1	b_2	b_3	b_4	b_5
665,638	-9,156	3,933	-	0	-
b_6	b_7	b_8	b_9	b_{10}	
-6,044	-4,512	21,041	0	-2,193	

Since the terms x_4 and x_9 do not meet the condition, they were eliminated (Tab. 6), and the predictive mathematical model of prediction of crystal hardness of the analyzed cadmium telluride becomes according to Eq.(13).

$$Z = 665,6380 - 9,1568x_1 + 3,9331x_2 - 9,7158x_3 - 8,14603x_5 - 6,0448x_6 - 4,5124x_7 + 21,0410 x_8 - 2,1939x_{10} \quad (13)$$

Testing the adequacy of the mathematical model

The Fisher test is used to test the adequacy of the model [12,14].

The Fisher test was performed for a confidence level of $\alpha=0,05$ and for the degrees of freedom $v_1 = 8$ and $v_2 = 10$. The value of the Fisher test calculated ($F_c=0,8068$) was compared to the Fischer tabulated score ($F_{T(v_1, v_2)}= 2,42$).

Because $F_c < F_T$, the mathematical model obtained is appropriate and can be used in optimization processes.

The following chart shows a comparison of analysed crystal hardness values obtained experimentally (blue columns) with those calculated using the regression model (red columns) Eq.(13).

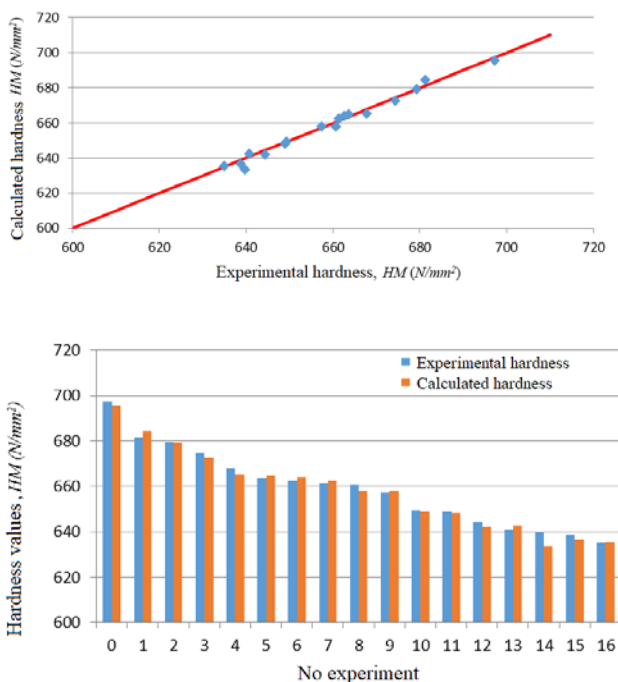


Fig.3. Comparison of the hardness values of the crystal of cadmium telluride obtained experimentally with those calculated using the regression model

Analysing the graphs from Fig.3, one can see a deviation below 5% of the hardness values obtained with the experimental mathematical model against

the values obtained by experimental measurements with the *DUH-211S* Shimadzu.

These small differences demonstrate that the mathematical model can be used to predict the hardness of crystals of cadmium tellurium with the concentrations of the micro-alloying elements contained in the fields presented in Tab. 3.

Micro-alloying elements influence on cadmium telluride crystal hardness using a mathematical model proposed

In this subchapter are presented some of the graphs that represent the influence of the alloying elements on the crystal hardness of the cadmium tellurium.

Fig.4 shows the influences of vanadium and chromium concentrations on the hardness of cadmium telluride crystal. The value +1 of hardness on graph is the maximum encoded value of hardness 678,73 HM for the cadmium tellurium crystal, whose V composition has been modified between 120 ppb and 229 ppb and Cr in the range 124-334 ppb.

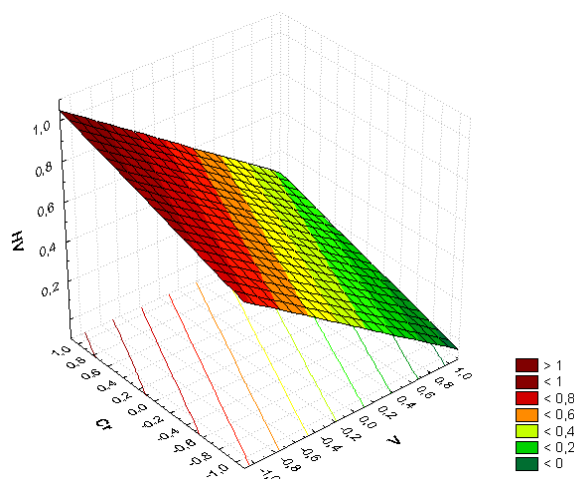


Fig.4. Variation of Cd-Te crystal hardness obtained using regression model based on the interaction of V and Cr

The value 0 of hardness is the minimum encoded value of hardness 652,55 HM for the cadmium tellurium crystal, whose V composition has been modified between 120 ppb and 229 ppb and the Cr in the range 124-334 ppb.

The graph of variation of crystal hardness was represented by coding with -1 V content of 120 ppb (minimum interval value), and with +1 V content of 229 ppb (maximum interval value), for the Cr content the value of -1 is corresponding to 124 ppb (minimum interval value) and +1 to 334 ppb (maximum interval value).

According to the graph in Fig.4 the crystal hardness increases linearly with the increase of the

content of *Cr* and decreases when increasing concentration of *V*. Maximum hardness values are obtained for the maximum content of *Cr* (334 ppb) and to minimum content of *V* (120 ppb).

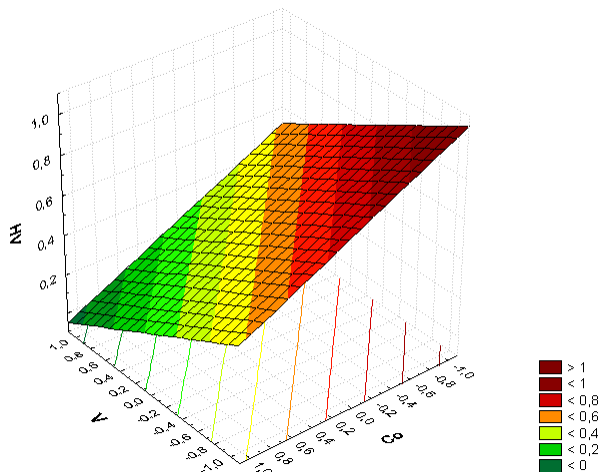


Fig.5. Variation of *Cd-Te* crystal hardness obtained using regression model based on the interaction of *V* and *Co*

By graphical representation of the regression model (Fig.5), the hardness of the crystal decreases with the increase of the content of *V* and *Co*. Maximum values of crystal hardness are obtained for the minimum content of *V* (120 ppb) and *Co* (22 ppb).

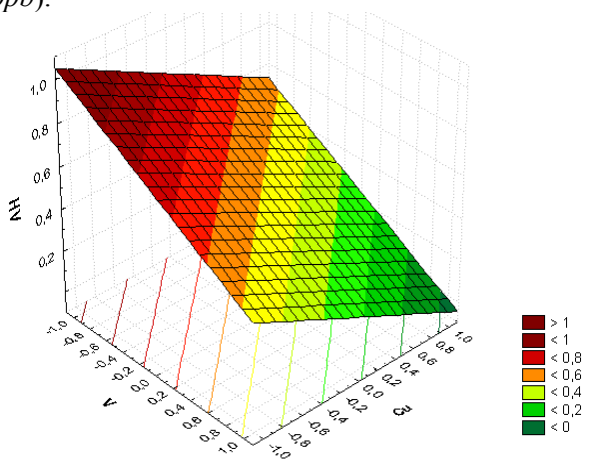


Fig.6. Variation of *Cd-Te* crystal hardness obtained using regression model based on the interaction of *V* and *Cu*

In the representation of Fig.6, the hardness of the crystal is negatively influenced by the increase of the *V* content, respectively, of *Cu*. The maximum values of the crystal hardness are obtained for the minimum values of the *V* content (120 ppb) and *Cu* (30 ppb).

According to the graph in Fig.7, the hardness of the crystal decreases when increasing *Zn* and *V* concentration. The maximum values of the crystal hardness are obtained for the minimum *Zn* content (1398 ppb) and *V* (120 ppb).

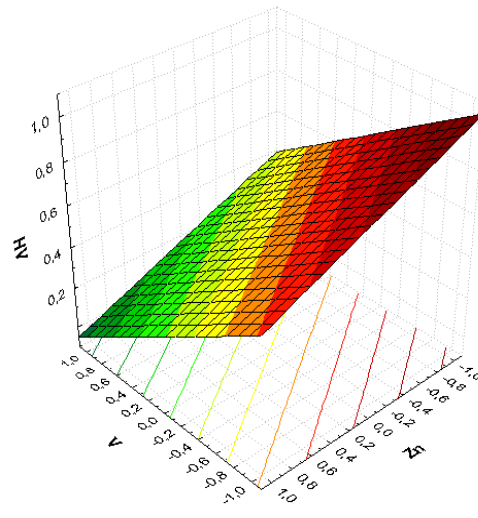


Fig.7. Variation of *Cd-Te* crystal hardness obtained using regression model based on the interaction of *V* and *Zn*

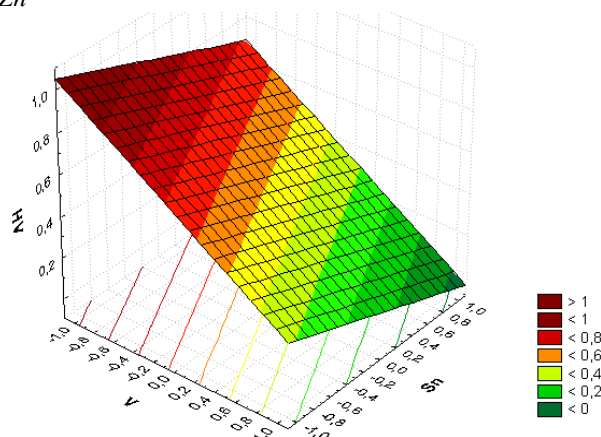


Fig.8. Variation of *Cd-Te* crystal hardness obtained using regression model based on the interaction of *V* and *Sn*

In the situation presented in Fig.8, the hardness of the crystal increases less significantly when decreasing the concentration of *Sn* and more pronounced when increasing concentration of *V*. The maximum values of the crystal hardness are obtained for the minimum values of the *Sn* content (3,4 ppb) respectively of the *V* content (120 ppb).

In Fig.9 the value of crystal hardness increases sharply as the percentage of tungsten increases and decreases when increasing concentration of *V*. Maximum crystalline hardness values are obtained for the minimum content of *V* (120 ppb) and maximum *W* values (46 ppb).

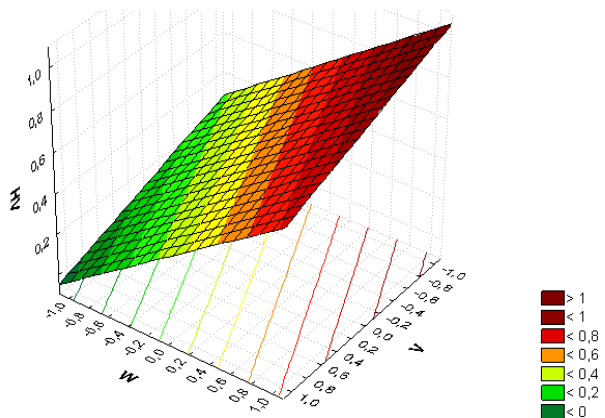


Fig.9. Variation of Cd-Te crystal hardness obtained using regression model based on the interaction of V and W

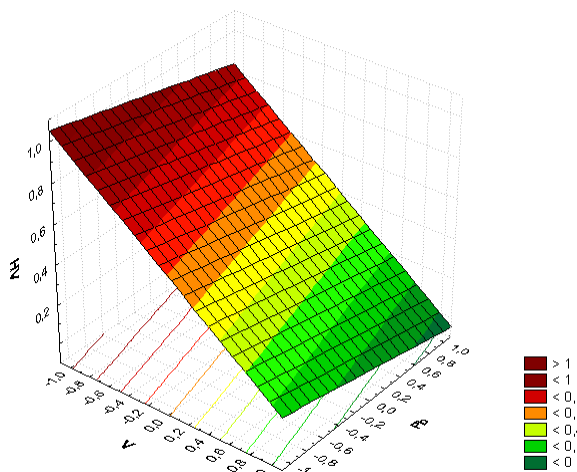


Fig.10. Variation of Cd-Te crystal hardness obtained using regression model based on the interaction of V and Pb

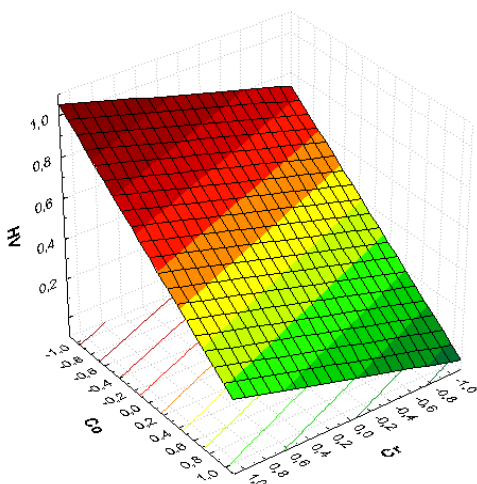


Fig.11. Variation of Cd-Te crystal hardness obtained using regression model based on the interaction of Cr and Co.

Not the same situation is presented in Fig.10 where maximum crystal hardness values are obtained at the minimum contents of V (120 ppb) respectively of Pb (0,33 ppb).

By graphical representation of the regression model Fig.11, the hardness of the crystal increases with the increase in the content of Cr and decreases more pronouncedly when increasing concentration of Co. The maximum values of the crystal hardness are obtained for the maximum values of the Cr content (334 ppb) and minimum Co values (22 ppb).

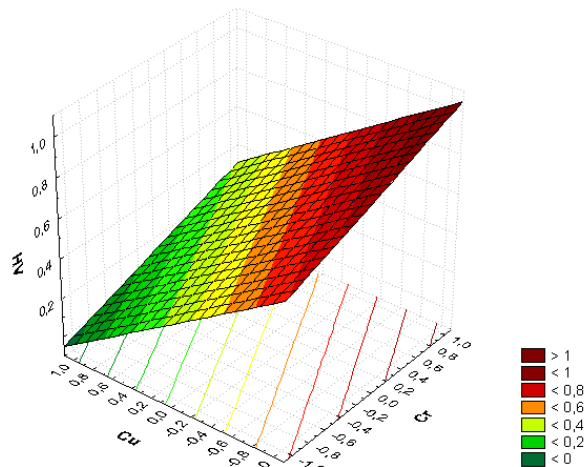


Fig.12. Variation of Cd-Te crystal hardness obtained using regression model based on the interaction of Cr and Cu.

In Fig.12 the hardness of the crystal increases with the increase of Cr content and decreases sharply with the increase of Cu concentration. Maximum crystalline hardness values are obtained for the maximum Cr content (334 ppb) and at minimum Cu values (30 ppb).

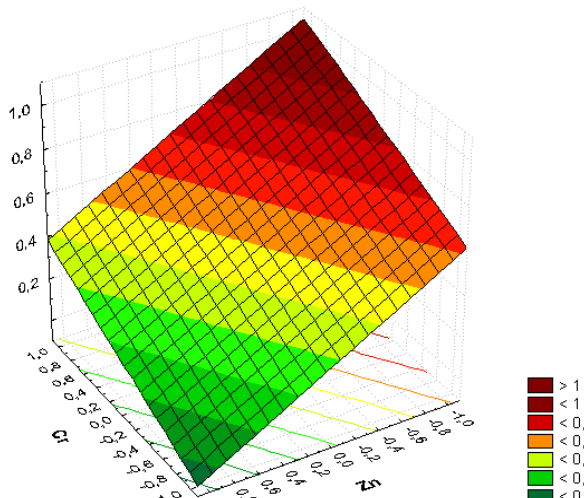


Fig.13. Variation of Cd-Te crystal hardness obtained using regression model based on the interaction of Cr and Zn.

According to the graphical representation in Fig.13, the hardness of the crystal increases with the increase of the *Cr* concentration and decreases with the increase of the *Zn* content. Maximum crystalline hardness values are obtained at the maximum *Cr* content (334 ppb) and at low *Zn* concentrations (1398 ppb).

In Fig.14, the hardness of the crystal increases with the increase of *Cr* concentration and increases sharply with the increase of the percentage of *W*.

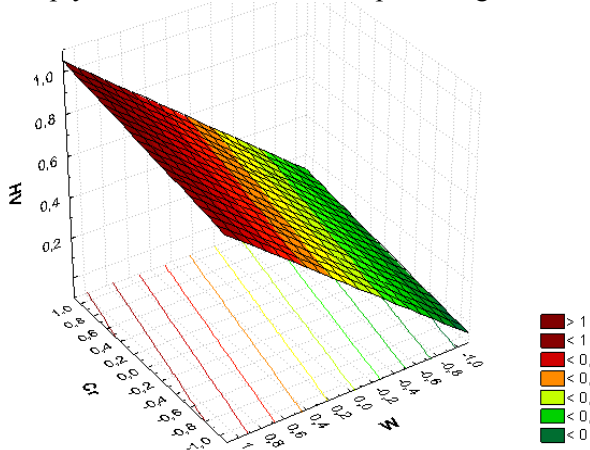


Fig.14. Variation of *Cd-Te* crystal hardness obtained using regression model based on the interaction of *Cr* and *W*

Maximum crystalline hardness values are obtained at the maximum *Cr* content (334 ppb) and *W* (46 ppb).

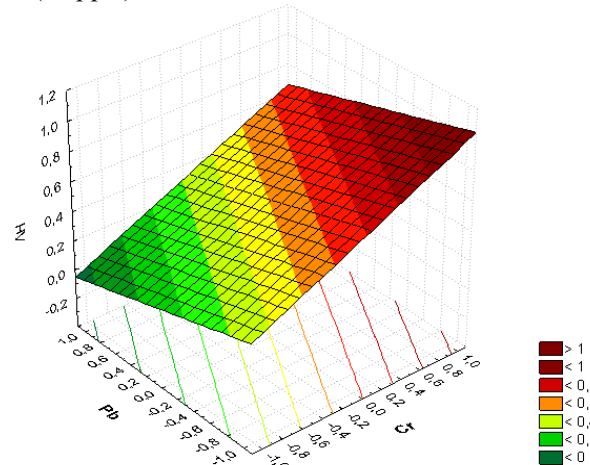


Fig.15. Variation of *Cd-Te* crystal hardness obtained using regression model based on the interaction of *Cr* and *Pb*

The hardness of the crystal of cadmium tellurium increases with the increase in *Cr* content and decreases with the growth of *Pb*. Maximum hardness values are obtained at the maximum *Cr* content (334 ppb) and at minimum *Pb* values (0,33 ppb) (Fig.15).

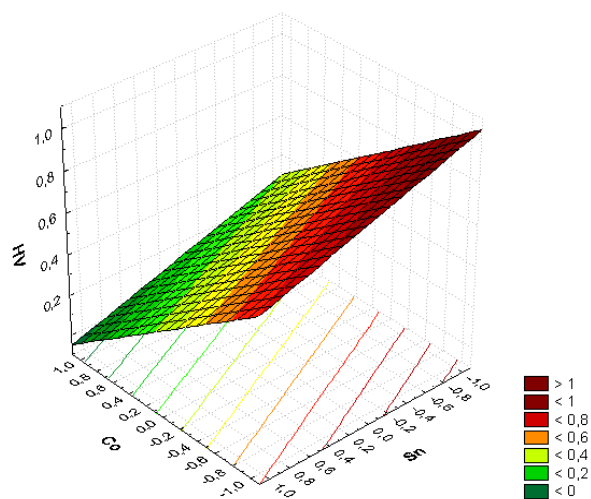


Fig.16. Variation of *Cd-Te* crystal hardness obtained using regression model based on the interaction of *Co* and *Sn*

Fig.16 shows the decrease of the crystal hardness value with the increase of the content of *Co* and *Sn*. Maximum crystalline hardness values are obtained at the minimum *Co* content (22 ppb) and *Sn* (3,4 ppb).

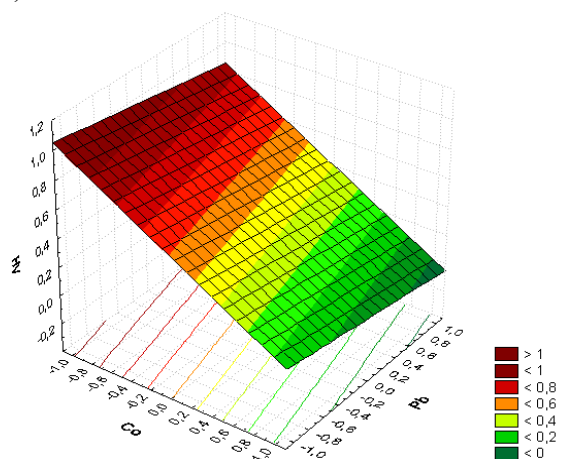


Fig.17. Variation of *Cd-Te* crystal hardness obtained using regression model based on the interaction of *Co* and *Pb*

The hardness of the crystal of cadmium is decreasing with the increase in *Pb* content and even more pronouncedly with the increase of the percentage of *Co*. Maximum crystalline hardness values are obtained at the minimum *Co* content (22 ppb) and *Pb* (0,33 ppb) (Fig.17).

According to the representation in Fig.18, the hardness of the crystal decreases with the increase of *Cu* and *Zn* concentration. Maximum crystalline hardness values are obtained at the minimum content of *Cu* (30 ppb) respectively of *Zn* (1398 ppb).

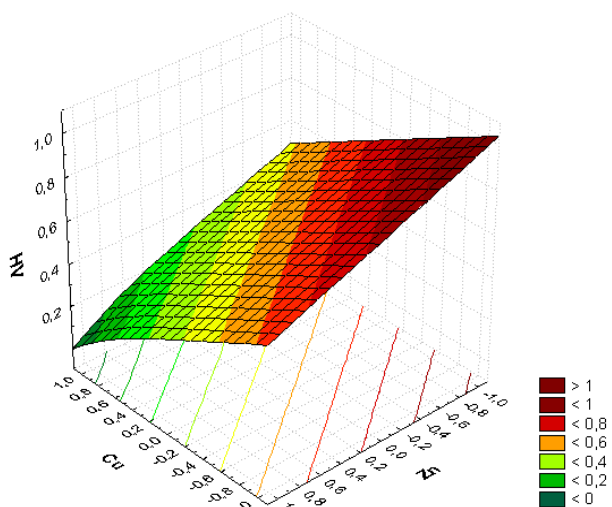


Fig.18. Variation of Cd-Te crystal hardness obtained using regression model based on the interaction of Cu and Zn.

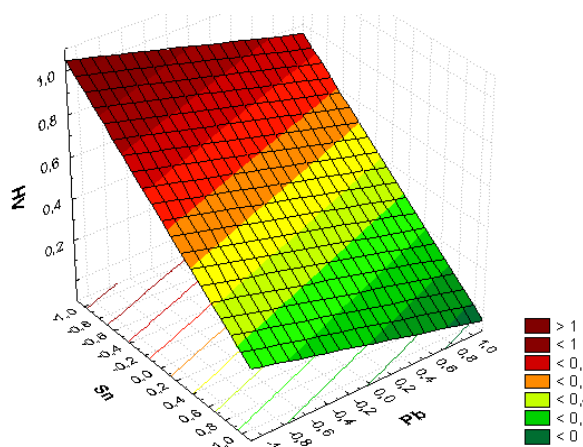


Fig.19. Variation of Cd-Te crystal hardness obtained using regression model based on the interaction of Sn and Pb.

From the analysis of the obtained graph Fig. 19, it turns out that the crystal hardness decreases when increasing the Sn content and decreases less sensitively with the Pb. The maximum values of the crystal hardness are obtained at the minimum values of the Sn content (3,4 ppb) respectively Pb (0,33 ppb).

The Fig. 20 highlights the sharp increase in crystal hardness with increased tungsten concentration and a less sensitive decrease in hardness when increasing lead percentage. Thus, the maximum hardness of the crystal is recorded at the maximum value of the tungsten concentration (46 ppb) and minimal of the lead (0,33 ppb).

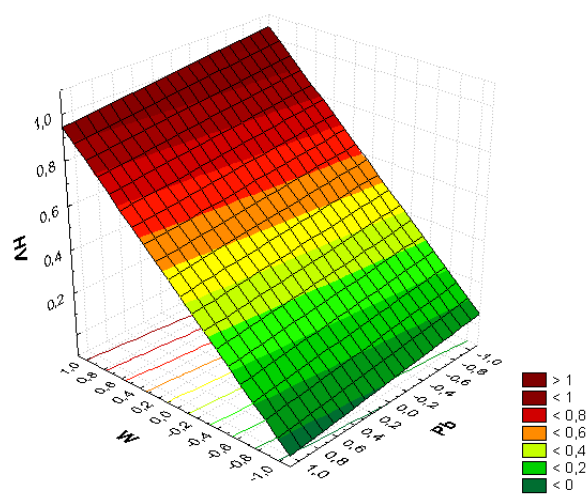


Fig.20. Variation of Cd-Te crystal hardness obtained using regression model based on the interaction of W and Pb.

CONCLUSIONS

In order to establish a link between the micro alloying elements and cadmium telluride crystal hardness experimental researches were carried out using ablation laser equipment UP213 New Wave Research, coupled to ICP-MS 750 Agilent, respectively Martens method for hardness measuring with hardness testing device Shimadzu DUH-211S. The significance of mathematical model coefficients was determined using the Student test, whereas mathematical model adequacy testing was performed using the Fisher test.

The mathematical model for the expression of hardness by micro alloying elements is a linear linkage.

By applying the mathematical model obtained, the calculated hardness values correspond within the predetermined limits with the hardness values determined experimentally by the Martens method.

The micro alloying elements that influence the hardness of the cadmium tellurium crystal are V, Cr, Co, Cu, Zn, Sn, W, Pb, whereas Ni, Tl does not significantly affect hardness.

The results obtained from the theoretical research on cadmium tellurium crystal hardness using the developed mathematical model were plotted according to the concentration of micro alloying elements. The analysis of these surfaces highlights the sharp increase in crystal hardness with the increase in Cr and W content and drops with V, Co, Cu, Zn, Sn, Pb.

From the theoretical and experimental researches, it appears that the hardness of crystals of cadmium tellurium, an important mechanical

characteristic in the subsequent mechanical processing of their shape and dimensions, can be predicted with a probability of 95% using the mathematical model presented in this paper, starting from the concentrations of micro alloying elements.

ACKNOWLEDGEMENTS

Financial support from the POSCCE project “Centru integrat de cercetare, dezvoltare si inovare pentru materiale Avansate, Nanotehnologii si Sisteme distribuite de fabricatie si control (MANSiD)”, Contract No. 671/09.04.2015 is acknowledged.

REFERENCES

- [1] **Severin, T.L., Potorac A.** Mathematical modelling concerning the influence of chemical composition upon hardness of cadmium telluride crystal - Part 1. *Bulgarian Chemical Communications*, **48 E**, 378-383 (2016).
- [2] **Capper, P.** Properties of narrow gap cadmium-based compounds, IET. p. 39-40, ISBN 978-0-85296-880-2, (2012).
- [3] **Brewer, P.D., Zinck, J.J., Olson, G.L.**, Surface composition changes and ablation dynamics in excimer laser irradiated CdTe Laser ablation for materials synthesis, *Book Series, Materials Research Society Symposium Proceedings*, 68-70, (1990).
- [4] **Fochuk, P.; Nykonyuk, Ye, Verzhak, Ye, Dopant** content and thermal treatment of CdZnTe in effects on point-defect structures, *IEEE Nuclear Science Symposium and Medical Imaging Conference (2008 NSS/MIC)*, **1-9**, 4880-4882, (2009).
- [5] **Fochuk, P., Grill, R. Kopach, O.**, Elimination of Te inclusions in Cd_{1-x}Zn_xTe crystals by short-term thermal annealing, *IEEE Transactions on Nuclear Science*, **59** (2), 258-260 (2012).
- [6] **Rzeszutek, J., Oszmaldowski, M., Savchuk, V.** Ablation of CdTe with 100 pulses from Nd:YAG laser: Velocity distribution of emitted particles, *Nuclear Instruments & Methods in Physics Research Section B-beam Interactions with Materials and Atoms*, **266**, Issue 21, 4766-4774, (2008).
- [7] **Savchuk, Victor K.; Kotlyarchuk, Bohdan K.; Zaginey, Apollinary O.** Ablation species generated by high power laser pulses from Cd-Te target, 70091M, *Proceedings of the Society of Photo-Optical Instrumentation Engineers (SPIE)* **7009**, M91-M91 (2008).
- [8] **Semaltianos, N. G., Logothetidis, S., Perrie, W.**, CdTe nanoparticles synthesized by laser ablation, *Applied Physics Letters*, **95** (3), no. 033302 (2009).
- [9] **Gutt, S., Gutt, G., Severin, T. L., Vasilache, V., Poroch, M.**, Contribution to design and carry out an universal dynamic hardness tester for metallic materials testing, *Annals of DAAAM for 2010 & Proc. of 21st International Symposium*, ISBN 978-3-901509-73-5, ISSN 1726-9679, 0506, Vienna, Austria, (2010).
- [10] **Iacob, D.**, Statistica, Ed. Universitatii Stefan cel Mare Suceava, ISBN 973-9408-57-5, p.114-132, (2000).
- [11] **Bulgaru, M., Bolboaca, L.**, Ingineria calitatii. Managementul calitatii, statistica si control, masurari în 3D, Ed. Alma Mater, ISBN 973-85153-0-0, Cluj-Napoca, p.188-209, (2001).
- [12] **Macoveanu, M., Nicu V., Curievici I.**, Bazele tehnologiei chimice, metodologia elaborarii modelelor matematice din industria chimica, Ed. IPI, Iasi, România, (1991).
- [13] **Cuceriu, I.**, Optimizari in industria chimica, Ed. Didactica si Pedagogica, Bucuresti, p. 67-82, (1990).
- [14] **Severin T. L.**, Cercetari si contributii la realizarea si promovarea de noi metode si aparate pentru încercarea de duritate, teza de doctorat, Research and contributions to the development and promotion of new methods and devices for hardness testing, (2012).

Effect of the heat treatment on mechanical and structural properties of CrTiAlN coatings deposited at low temperature

T.M. Cholakova^{1*}, L.P. Kolaklieva¹, R.D. Kakanakov¹, V.A. Chitanov¹, B. S. Rangelov², S. Atanasova-Vladimirova², P. K. Stefanov³, G. B. Atanasova³, K. T. Balashev⁴

¹Central Laboratory of Applied Physics, Bulgarian Academy of Sciences, Plovdiv, Bulgaria,

²Institute of Physical Chemistry, Bulgarian Academy of Sciences, Sofia, Bulgaria

³Institute of General and Inorganic Chemistry, Bulgarian Academy of Sciences, Sofia, Bulgaria

⁴Laboratory of Biophysical Chemistry, Department of Physical Chemistry, Sofia, Bulgaria

The present article investigates the mechanical properties and microstructure of the CrTiAlN thin coatings obtained at a low deposition temperature (150°C) using Closed Field Unbalanced Magnetron Sputtering (CFUBMS) technique onto different substrates. In order to determine the effect of heat treatment on mechanical and structural properties, the as-deposited CrTiAlN coatings were annealed in an argon atmosphere and air at different temperatures (400-800°C) for 2 hours. The alteration of the morphology, microstructure, chemical composition, hardness and adhesion strength after the treatment was analysed by atomic force microscopy (AFM), scanning electron microscopy (SEM) complemented with an energy dispersive x-ray spectroscopy analysis, X-ray photoelectron spectroscopy (XPS), a Nanoindentation Tester and a Micro Scratch Tester. After an annealing to the temperature of 600°C the coatings demonstrated higher hardness and elastic modulus of 29 ± 2 GPa and 365 ± 20 GPa, respectively. Further increase of the treatment temperature caused decrease of the coating hardness and elastic modulus and rise of the surface roughness and coefficient of friction.

Keywords: UBMS, hard coatings, CrTiAlN, thermal resistivity

INTRODUCTION

Thin films deposition has undergone huge advance in the last decades and it is now possible to obtain multilayered, functionally gradient, and nanocomposite coatings that have very good properties, such as high hardness, good adhesion and high wear- and oxidation resistance. Thermal stability of the coatings at high temperatures is a concern not only for applications in hot environments, but also in cutting and drilling operations, where locally temperatures of up to 800 °C can be reached.

A wide range of PVD hard coatings are now available for a variety of applications. TiN is the first generation of PVD hard coating (about 24 GPa) and is still being used as protective hard coatings for bearings, gears, cutting and forming tools. However, the fracture toughness and low oxidation resistance (< 550 °C) of the TiN coatings are not satisfactory for many engineering applications [1,2]. In the advance of hard coating development, TiAlN has been successfully commercialised particularly for high-speed cutting because of its significantly improved oxidation resistance (>700 °C) and hardness over TiN [3-6].

Nevertheless, the oxidation resistance at elevated temperatures of the Ti-based coatings is limited although it has been improved with aluminium incorporation. These drawbacks of the Ti-based coatings have strongly limited their practical applications. Similar to TiN, chromium nitride, CrTiN and AlCrN coatings have been successfully applied to the metal forming and plastic moulding dies and wear components, which is known to be superior to TiN in wear resistance, friction behaviour, and toughness [7-9]. Further improvements in nitride coatings have been found to have promising performance compared to that of ternary films. Cr-Ti-Al-N system offers a high variability ranging from Cr rich to Al rich [10-13] coatings with improved hardness and thermal stability, oxidation and wear resistance and lower coefficient of friction.

The present article investigates the effect of heat treatment in air and argon environment on mechanical properties, microstructure and phase composition of CrTiAlN coatings with a small amount of Al, obtained at a low deposition temperature.

EXPERIMENTAL DETAILS

Coatings deposition conditions

Cr-Al-Ti-N coatings with different thickness

* To whom all correspondence should be sent:
ipfban-dve@mbox.digsys.bg

were prepared using a Teer Coatings UDP 850 closed-field unbalanced magnetron sputtering (CFUBMS) system. The system was equipped with four unbalanced magnetrons uniformly arranged at 90° intervals around the vertical stainless steel vacuum chamber. Each magnetron was fitted with a target: Cr, Ti and two Al. The coatings were deposited onto substrates of high-speed steel (EN: 1.3343), stainless steel (EN: 1.4436) and carbon tool steel (EN: CT105) with low temperature resistance ($\leq 200^{\circ}\text{C}$). The high-speed steel (HSS) and carbon tool steel substrates were preliminary hardened. The substrate holder comprised a rotating vertical rod, supporting a pair of horizontal plates on which the substrates were fixed. The vacuum chamber was pumped down into a high vacuum condition with a background pressure less than 2.0×10^{-3} Pa. In order to remove the top oxide layer the substrates were plasma cleaned in argon atmosphere (2.0×10^{-1} Pa) for 30 minutes at negative pulse substrate bias voltage of 500 V and frequency of 250 kHz. A mixture of argon and nitrogen gases was introduced into the chamber during the process. The ratio of argon was kept a constant (25 sccm) and the nitrogen content was controlled by plasma optical emission monitor (OEM) with a feedback control. The information on the variation of the OEM signal (the plasma characteristics) with changes in the process parameters and the correlations between the signal and the deposition rate, morphology and structure of the coatings, are very important for optimization of the deposition process.

In the current experiments, a substrates temperature of 150°C for deposition of the coating was used. During the deposition substrates were biased with a pulse power source to induce proper ion bombardment on the growing surface to assist the formation of coatings with a dense structure. The experiments were conducted at bias voltage of -70 V and frequency of 150 kHz in DC work regime of the Ti and Cr cathodes and pulsed regime of the Al cathodes. The deposition started with sputtering of a Cr adhesion layer and after that a Cr-N interlayer with thickness of 200 nm was deposited reactively. Following these two layers, the fractions of Ti and Al increased to form a compositionally graded Cr-Ti-Al-N film, and finally Cr-Al-Ti-N with constant composition was obtained. The relative concentration of Cr, Ti and Al in the coatings was adjusted through the sputtering power, applied to the targets during

deposition: $P_{\text{Cr}} = 1.5$ kW; $P_{\text{Ti}} = 2.4$ kW; $P_{\text{Al}} = 0.6$ kW.

Characterization techniques

The mechanical properties such as nanohardness and adhesion of the as-deposited and annealed CrTiAlN coatings were investigated using Compact Platform CPX (MHT/NHT) CSM Instruments equipment which includes a Nanoindentation module (NHT), a Micro Scratch module (MST) and an Optical video microscope with CCD camera, installed together on the same platform. Nanoindentation was performed by a triangular diamond Berkovich pyramid. The adhesion strength of the coating to the substrate was evaluated using MST equipped with a spherical Rockwell indenter with a radius of 200 μm under progressively increasing pressing force in a range of 1-30 N.

The studies of the coating morphology were carried out by Atomic force microscopy (AFM) using NanoScope VAFM (Bruker Inc.) equipment in air in tapping mode. Silicon cantilevers with reflective aluminium coating with thickness of 30 nm, Tap 300Al-G (Budget Sensors, Innovative solutions Ltd, Bulgaria) were used.

Surface observation and composition analysis was performed on JEOL JSM 6390 electron microscope equipped with INCA Oxford EDS energy dispersive detector. Surface images were also obtained in secondary electrons (morphology contrast) and back-scattered electrons (density contrast).

The chemical bonding of the coatings was studied by X-ray photoelectron spectrometry. XPS spectra were acquired on a Kratos AXIS Supra photoelectron spectrometer using a monochromatic Al Ka source with energy of 1486.6 eV. The binding energies were corrected relative to the C1s peak at 285.0 eV. The concentration of the elements was derived on the basis of the core level peak areas, corrected by the corresponding relative sensitivity factor values.

RESULTS AND DISCUSSION

The mechanical properties stability is of a main importance when the ceramic materials are used for industrial applications. Their structure contributes to this stability as it will be discussed in the following sections. In order to evaluate the thermal stability of the designed multicomponent CrTiAlN coatings, annealing tests were performed in circulating argon and atmosphere using a thermal furnace with a maximum temperature of 1100°C .

The coated specimens were carefully degreased using suitable solvents and annealed at different temperatures (400°C, 600°C, 700°C and 800°C) for 2 h at each temperature, and after that were naturally cooled down to room temperature in the furnace. The alteration of the morphology, microstructure, chemical composition, hardness and adhesion strength after the treatment was analyzed.

Mechanical properties

Mechanical and tribological properties of the same as-deposited multicomponent coatings with a composition $\text{Cr}_{0.68}\text{Ti}_{0.19}\text{Al}_{0.13}\text{N}$ and a thickness of 2,1 μm were reported in our previous work [14]. So far no one has reported in the literature high-temperature mechanical properties for such coatings obtained at a low deposition temperature.

1. Hardness and Elastic modulus

Hardness and Elastic modulus of the as-deposited and annealed CrTiAlN/HSS coatings were characterized by dynamical nanoindentation in the loading interval of 10-100 mN and calculated from the load-penetration depth curve using the Oliver and Pharr method [15]. The maximum indentation depth was set at 200 mN which is less than 10% of the coating thickness, to avoid the influence of the substrate. An influence of the annealing temperature on the evolution of hardness and elastic modulus of the CrTiAlN coatings is presented in Fig.1.

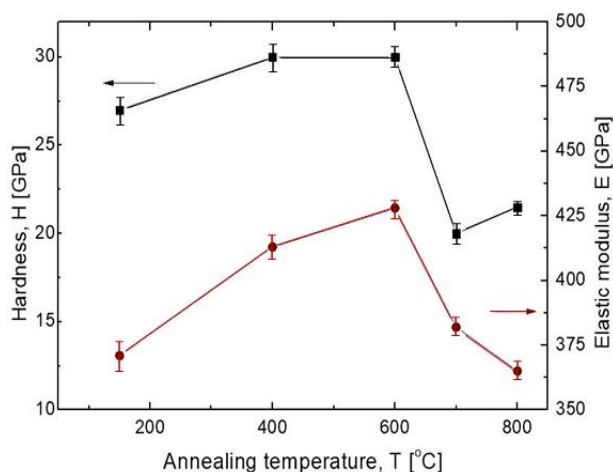


Fig.1. Experimental data of Hardness and Elastic modulus of the CrTiAlN/HSS coating as a function of annealing temperature

The nanohardness of HSS substrate in as-deposited state and after annealing at the 700°C was determined to be 11.0 GPa and 7.0 GPa, respectively. From the above experimental results it can be seen, that the hardness and elastic modulus

show a similar behaviour. After annealing at 400°C and 600°C the hardness and elastic modulus increased from 27 to 31 GPa and from 396 to 426 GPa, respectively. However, as the annealing temperature increased to 700°C, significant change in the coating hardness and elastic modulus (Fig.1) was observed [16, 17]. This could be related to defect annihilation and stress relaxation. As a result the hardness and elastic modulus decrease. The change in mechanical properties is accompanied by a sharp change in morphology of the coating (see Fig.6) accompanied with grain enlargement and drastically increase of the surface roughness as compared to its smooth surface in as-deposited state. Reverse trend was observed for the effect of the annealing temperature of 800 °C on the hardness that was slight higher than for the samples treated at the temperature of 700°C.

2. Scratch resistance

A Rockwell diamond indenter (cone apex angle 120°, tip radius $R=200 \mu\text{m}$) was used to perform scratch tests. The applied load was linearly increased from 1 N up to 30 N with a constant scratch speed of 0.5 N/min. Series of scratch tests were performed before and after thermal treatment on coatings to obtain a load where the coating exhibits failure termed as the critical load (L_c). The critical load values were determined after the test by optical microscopy observation of the damages formed in the scratch tracks and from the recorded acoustic emission (AE) and friction force (F_t) signals. Penetration of the indenter into the surface causes bending of the coating where both compressive and tensional stresses appear. The friction force between surface and sliding tip causes compressive stress in front of the moving tip and tensile stress behind it.

Excellent adhesion results without failures within loading range of 1-30 N were demonstrated by the as-deposited CrTiAlN/HSS coatings. A typical scratch graph and optical micrograph of the main scratch track part ($F_n=25\div 30\text{N}$) of the coating and scratch test results of the acoustic emission (AE), friction force (F_t) and coefficient of friction (μ) are shown in Fig.2. As can be seen, no picks of AE and no changes of F_t were observed. The coefficient of friction of the coating against diamond indenter was measured to be $\mu=0.09$. No visible changes in the coating adhesion were observed after annealing up to 400°C. After annealing at 600°C, it was observed that with increase of the scratch length and the normal load respectively, the values of the friction force and

coefficient of friction change. Very slight semi-circular tensile cracks were observed at the normal load > 20 N within the track. The friction force increased from 2.6 N to 3.4N, and the coefficient of friction from 0.09 to 0.12.

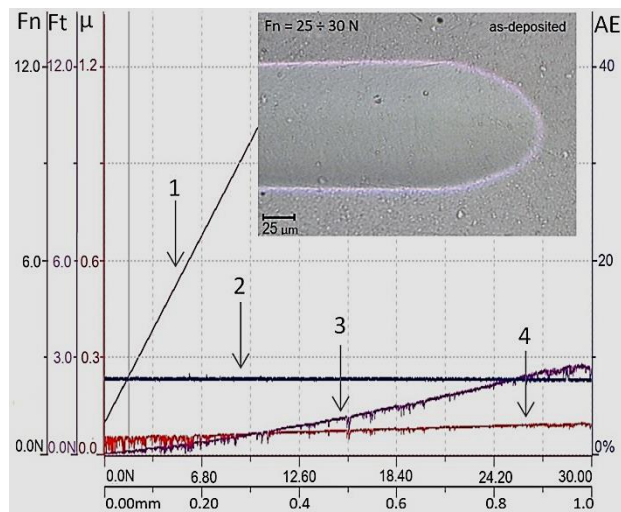


Fig.2. Scratch graph of the as-deposited CrTiAlN/HSS coating and optical micrograph of the main part of the scratch track: 1) Normal load; 2) Acoustic emission; 3) Friction force; 4) Coefficient of friction

After the annealing at a temperature of 700°C the coatings kept good adhesion properties. Only slight brittle tensile and micro-chevron cracks within and outside the track without chipping and spallation were observed (Fig.3). As a result, the friction force increased to 3.7 N and the coefficient of friction to 0.13. This change may be due to an increase of the stress between the substrate and the coating on as well as the formation of a thin, brittle oxide layer on the coating surface.

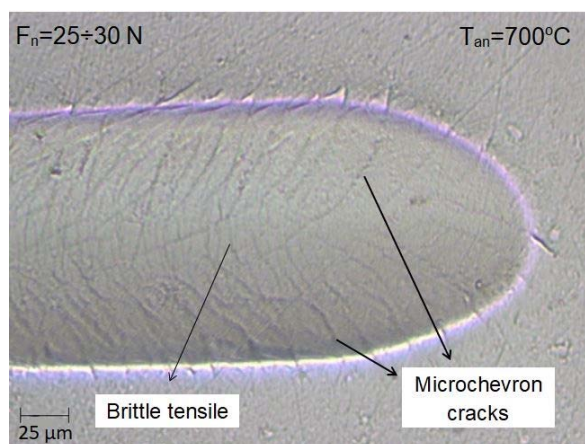


Fig.3. Optical micrograph of the main part of the scratch track obtained after annealing of the CrTiAlN coating at 700°C

After the next annealing of the coating at a temperature of 800°C no failures in the scratch track were observed. However, the brittle tensile and micro-chevron cracks are more pronounced. In this case, a noise in the acoustic emission signal was registered. As a result, an increase in the friction force up to 5.0 N and the coefficient of friction up to 0.18 was determined.

Coating morphology

1. AFM and SEM surface analyses

Effect of the thermal treatment on the CrTiAlN/SS coating morphology was studied by AFM. The AFM data (Fig.4) revealed that the as-deposited coating exhibited a low roughness and densely packed structure [14], consisting of well separated grains with apparently spherical form and predominantly equal sizes. Sporadic small defects were observed on the coating surface which leads to an increase of the roughness. The average roughness (Ra) and root mean square (Rq) roughness were obtained on a scanned area of 10 μm x 10 μm as follows: Ra = 20 nm and Rq = 26 nm.

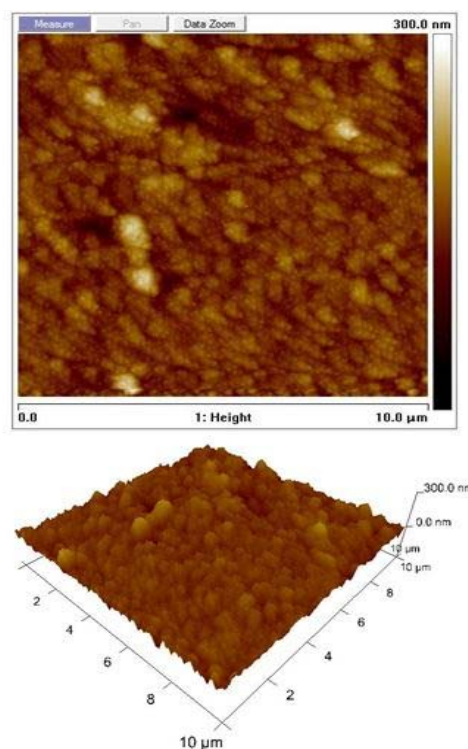


Fig.4. 2D and 3D AFM images of surface topography of the as-deposited CrTiAlN coating

SEM observation of the same as-deposited coatings revealed a similar feature (Fig.5). The coating surface showed columnar boundaries and the average columnar diameter was scattered

between 150 to 300 nm. The coatings are dense and no cracks on the surface were disclosed which indicates a good compactness. No visible differences after the coatings treatment at 400°C and 600°C were observed.

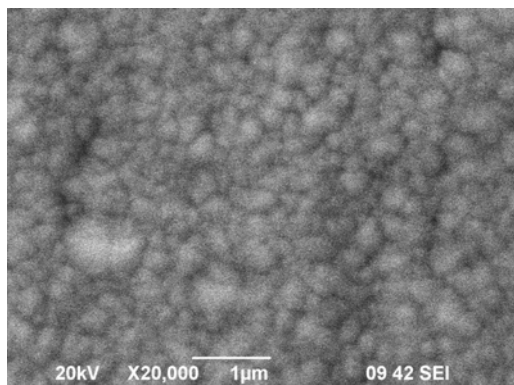


Fig.5. Surface SEM micrograph of the as-deposited CrTiAlN coatings

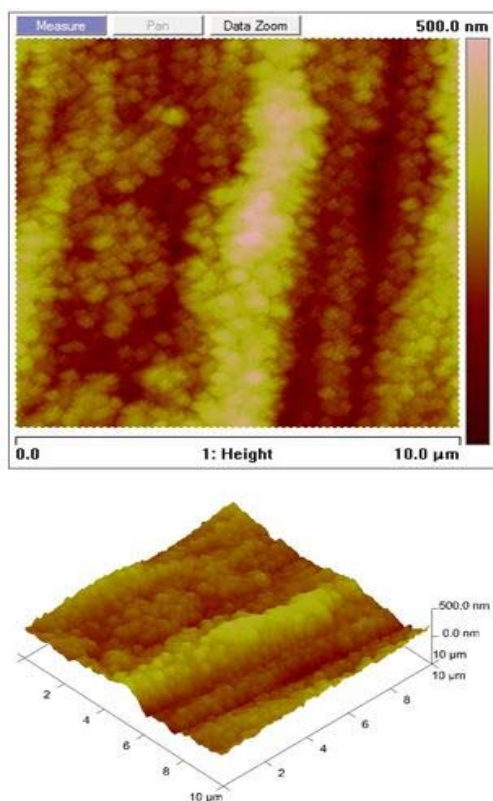


Fig.6. 2D and 3D AFM images of the surface topography of the CrTiAlN coating after annealing at 700°C

As Fig.6 (above) shows, after annealing at temperature of 700°C the average roughness and root mean square surface roughness obtained on the same area (10 µm x 10 µm) increase significantly. The calculated values of Ra and Rq in this case were 62 nm and 78 nm, respectively. According to

the results shown in Fig.6, it could be concluded, that after the thermal treatment at 700°C the surface topography changes as a result of the stress, grain enlargement and the formation of the oxide phases on the coating's surface [18-20]. The increased surface roughness causes increase of the coefficient of friction as the scratch test showed.

Coating composition and chemical bonding

The EDS and XPS analyses were carried out to determine the existence of certain elements and amount of each element present. The evaluated elemental composition of the CrTiAlN coatings before and after annealing is presented in Tab.1.

Table1. Composition of the CrTiAlN coating

CrTiAlN coating	Elemental concentration (at. %)				
	Cr	Ti	Al	N	O
as-deposited state					
EDS	30.95	9.06	6.24	53.75	
XPS	24.5	7.0	4.8	40.1	23.6
after annealing at 700°C					
EDS	36.91	10.44	7.14	45.52	
XPS	19.1	5.5	2.7	10	62.7

The EDS and XPS analyses exhibited difference in elemental concentration of the coatings. It is seen that on the surface (XPS data) the concentration of nitrogen decreased four times, while the content of metallic elements is decreased by 20-25%. Besides, after annealing the concentration of oxygen increased three times. As the XPS analysis was performed without surface ion etching, the reduction of metal nitrides concentration is due to the formation of oxides on the coating surface after annealing. Based on the data from EDS and XPS analyses, the coating chemical composition after annealing was determined to be $Cr_{0.68}Ti_{0.19}Al_{0.13}N$ and $Cr_{0.7}Ti_{0.2}Al_{0.1}N$, respectively.

The chemical bonding status of CrTiAlN coatings was determined by XPS analysis. Typical XPS spectra of Cr2p, Ti2p, Al2p, N 1s and O1s energy regions for as-deposited and annealed CrTiAlN samples are shown in Fig.7. In the Cr2p spectrum the peaks centred at 575.1 eV and 585 eV could be attributed to Cr-N bonds for as-deposited coatings [10, 11]. The coating after annealing process shows similar Cr2p3/2 spectrum as that obtained in the as-deposited state. However, the main peak shifted to energy at 576.3 eV and the second one to 586.4 eV. These peaks could be attributed to formation of Cr-nitride and Cr_2O_3 oxides. The peak associated with Ti consists of two peaks centred at 456.0 eV and 462.0 eV. These

peaks originate from Ti 2p_{3/2} and Ti 2p_{1/2} electrons in titanium nitride and oxynitride. After annealing the binding energies of Ti2p peaks are shifted to energies at 457.8 eV and 463.8 eV, corresponding to the TiNO and Ti₂O₃ bonds [18]. The Al2p spectra contribution with maximum binding energy of 73.7 eV is assigned to Al-N chemical bonding state within the coating.

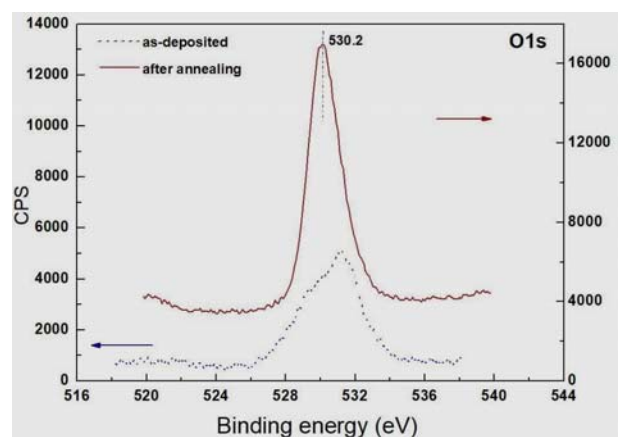
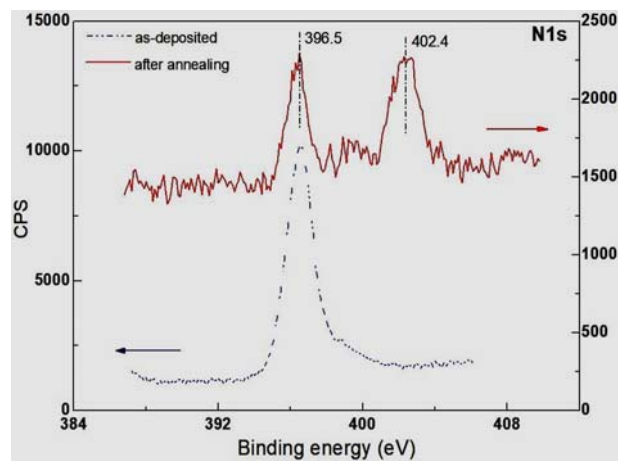
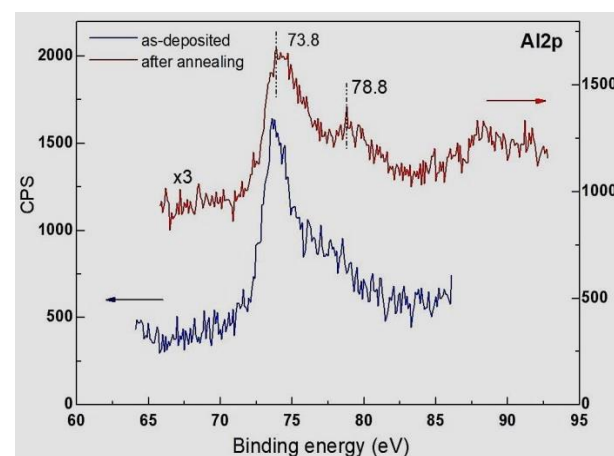
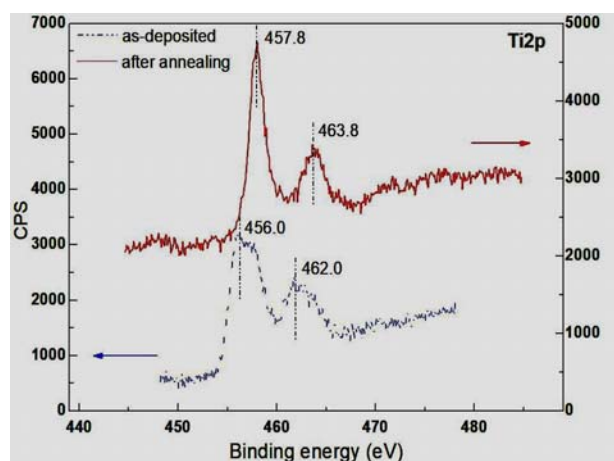
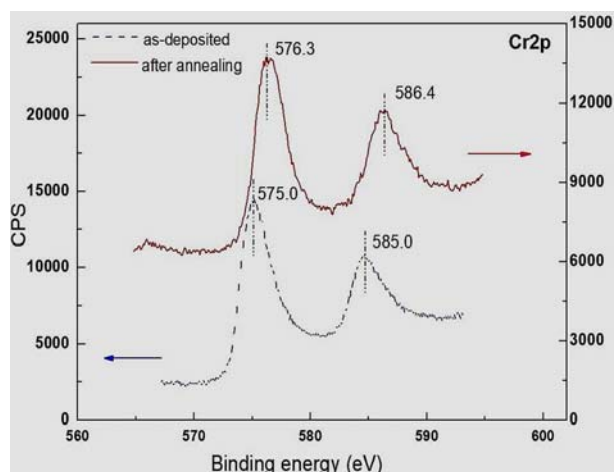


Fig.7. XPS spectra of Cr 2p, Ti 2p, Al 2p, N1s and O 1s on the as-deposited and annealed CrTiAlN coating

The annealing results in appearance of a small second peak with the binding energy at 78.8 eV which origin is not clear. Since the Al2p and Cr3s spectra overlap, the second peak could be attributed to Cr₂O₃ oxides.

The N1s spectrum of the as-deposited coating shows only one lightly asymmetrical peak with binding energy of approximately 396.5 eV which is attributed to the presence of metal nitrides (CrN, TiN and AlN) [19,20,21]. The chemical analysis showed presence of two peaks with low intensity situated at 396.5 eV and 402.4 eV after annealing. A possible explanation is the reduction of the metal nitrides concentration on the coating surface due to the formation of oxy-nitrides [22].

The O1s strong spectrum with a peak at 530.2 eV after annealing showed very high intensity in comparison with the same spectrum of the as-deposited coatings. It can be assigned to formation of oxy-nitride and oxides such as TiNO, CrO₃, Cr₂O₃, and Al₂O₃. The chromium oxide appearance after annealing has been well documented as being an exothermic reaction that normally takes place

above 700 °C as reported in [2, 23, 24]. The above studies show that the mechanisms of Cr-Ti-Al-N thermal stability depend strongly on the elemental concentration. It can be stated that the oxidation process of the CrTiAlN coating is controlled mainly by the outward diffusion of Cr, Al, Ti and N species and by the inward diffusion of oxygen. As the coatings become more Cr-rich the preferential oxide formed might be mainly Cr₂O₃.

CONCLUSIONS

The CrTiAlN coating with a small amount of Al was successfully obtained using the closed-field unbalanced magnetron sputtering technique at the low deposition temperature of 150°C without additional substrate heating. The coating demonstrated good mechanical properties in the as-deposited state: nanohardness value of 27 GPa, an excellent adhesion in the loading interval from 1N to 30N and a low coefficient of friction ($\mu=0.1$) in the as-deposited state.

After annealing at 400°C and 600°C the hardness and elastic modulus increased from 27 GPa to 31 GPa and from 396 GPa to 426 GPa, respectively and then decreased with further increase of the annealing temperature. With the increase of the tested temperature to 800°C, the coating demonstrated a hardness and elastic modulus of 22 GPa and 365 GPa, respectively. The friction coefficient of the coating tends to increase to the value $\mu=0.18$ as no failures in the coating were observed.

The AFM study revealed that the CrTiAlN coating exhibited a higher roughness after annealing. After the thermal treatment at 700°C the surface topography changes as a result of the stress, grains enlargement and the growth mainly of a chromium oxide phase on the coating's surface. The SEM and XPS studies revealed that the mechanisms of the Cr-Ti-Al-N thermal stability depend strongly on the elemental concentration. It was stated that the oxidation process of the coating is mainly controlled by the outward diffusion of Cr, Al, Ti and N species and by the inward diffusion of oxygen. The surface of the coating does not significantly oxidized after continuous heating up to 800°C, implying a better oxidation resistance.

REFERENCES

[1] J.Paulitsch, M. Schenkel, Th. Zufraß, P.H. Mayrhofer, W.-D. Munz. Structure and properties of high power impulse magnetron sputtering and DC magnetron sputtering CrN and

- TiN films deposited in an industrial scale unit, *Thin Solid Films* **518**, 5558–5564 (2010).
- [2] Y.C. Chim, X.Z. Ding, X.T. Zeng, S. Zhang. Oxidation resistance of TiN, CrN, TiAlN and CrAlN coatings deposited by lateral rotating cathode arc. *Thin Solid Films* **517**, 4845–4849 (2009).
- [3] G.S. Fox-Rabinovich, A.I. Kovalev, M.H. Aguirre, B.D. Beake, K. Yamamoto, S.C. Veldhuis, J.L. Endrinof, D.L. Wainstein, A.Y. Rashkovskiy. Design and performance of AlTiN and TiAlCrN PVD coatings for machining of hard to cut materials. *Surface and Coatings Technology* **204**, 489–496 (2009).
- [4] S. PalDey, S.C. Deevi. Single layer and multilayer wear resistant coatings of (Ti,Al)N: a review. *Mater. Sci. Eng. A*, **342**, 58-79 (2003).
- [5] P.W. Shum, K.Y. Li, Z.F. Zhou, Y.G. Shen. Structural and mechanical properties of titanium–aluminium–nitride films deposited by reactive close-field unbalanced magnetron sputtering. *Surface and Coatings Technology* **185**, 245-253 (2004).
- [6] H.C. Barshilia, K. Yogesh, K.S. Rajam. Deposition of TiAlN coatings using reactive bipolar-pulsed direct current unbalanced magnetron sputtering. *Vacuum* **83**, 427-434 (2008).
- [7] H. N. Shah and R. Jayaganthan. Influence of Al Contents on the Microstructure, Mechanical, and Wear properties of Magnetron Sputtered CrAlN Coatings. *J. of Materials Engineering and Performance*. **21**, 2002–2009 (2012).
- [8] H. C. Barshilia, N. Selvakumar, B. Deepthi, and K. S. Rajam. A comparative study of reactive direct current magnetron sputtered CrAlN and CrN coatings. *Surface & Coatings Technology* **201**, 193–2201 (2006).
- [9] A. H. Liu, J. X. Deng, H. B. Cui, J. Zhao, and X. Ai. Oxidation Resistance of CrN and CrAlN Coating Tools. *Advance. Mater. Research*. **189–193**, 137–141 (2011).
- [10] P.L. Tam, Z.F. Zhou, P.W. Shum, K.Y. Li. Structural, mechanical, and tribological studies of Cr–Ti–Al–N coating with different chemical compositions. *Thin Solid Films* **516**, 5725–5731 (2008).
- [11] Yongjing Shi, Siyuan Long, Shicai Yang, Fusheng Pan. Structural and tribological properties of CrTiAlN coatings on Mg alloy by closed-field unbalanced magnetron sputtering ion plating. *Applied Surface Science* **254**, 7342–7350 (2008).
- [12] Xiaoying Li, Wenwen Wu, Hanshan Dong. Microstructural characterisation of carbon doped CrAlTiN nanoscale multilayer coatings. *Surface and Coatings Technology* **205**, 3251–3259 (2011).

- [13] Hui Zhou, Jun Zheng, Binhua Gui, Dongseng Geng, Qimin Wang. AlTiCrN coatings deposited by hybrid HIPIMS/DC magnetron co-sputtering. *Vacuum* **136**, 129-136 (2017).
- [14] T. Cholakova, V. Chitanov, L. Kolaklieva, R. Kakanakov, K. Balashev, B. Ranguelov, V. Rupetchov and G. Mishev. Study of the mechanical properties of Ti- and Cr-based multicomponent hard coatings. *MATEC Web of Conferences, 02003, EDP Sciences, France* **145**, 01-09 (2018).
- [15] Oliver, W.C. Pharr, G.M. An improved technique for determining hardness and elastic modulus using load and displacement sensing indentation experiments. *J. Mater. Res.* **7**, 1564-1583 (1992).
- [16] Tomas Polcar, Albano Cavaleiro. High temperature behavior of nanolayered CrAlTiN coating: Thermal stability, oxidation, and tribological properties. *Surface & Coatings Technology* **257**, 70-77 (2014).
- [17] Lijing Bai, Xiaodong Zhu, Jiming Xiao, Jiawen He. Study on thermal stability of CrTiAlN coating for dry drilling. *Surface and Coating Technology* **201**, 5257-5260 (2007).
- [18] J.L. Endrino, G.S. Fox-Rabinovich, A. Reiter, S.V. Veldhuis, R. Escobar Galindo, J.M. Albella, J.F. Marco. Oxidation tuning in AlCrN coatings. *Surface & Coatings Technology* **201**, 4505-4511 (2007).
- [19] T. Polcar and A. Cavaleiro. High temperature properties of CrAlN, CrAlSiN and AlCrSiN coatings – Structure and oxidation. *Mater. Chem. Phys.* **129**, 195-201 (2011).
- [20] Dong Bok Lee, Thuan Dinh Nguyen, Sun Kyu Kim. Air-oxidation of nano-multilayered CrAlSiN thin films between 800 and 1000°C. *Surface & Coatings Technology* **203**, 1199-1204 (2009).
- [21] Hao Zhang, Shuwang Duoa, Xiaoyan Fei, Xiangmin Xu, Tingzhi Liu, Yubin Wang. Effect of CrTiAlN Coatings on High-Temperature Oxidation Behavior of H13 Steel. *Key Engineering Materials* **544**, 343-346 (2013).
- [22] Jianliang Lin, Xuhai Zhang, Yixiang Ou, Ronghua Wei, The structure, oxidation resistance, mechanical and tribological properties of CrTiAlN coatings. *Surface and Coatings Technology* **277**, 58-66 (2015).
- [23] J. Lin, B. Mishra, J. J. Moore, and W. D. Sproul. A study of the oxidation behavior of CrN and CrAlN thin films in air using DSC and TGA analyses. *Surf. & Coat. Technol.* **202**, 3272-3283 (2008).
- [24] J. Lin, N. Zhang, W. D. Sproul, and J. J. Moore. A comparison of the oxidation behavior of CrN films deposited using continuous dc, pulsed dc and modulated pulsed power magnetron sputtering. *Surf. & Coat. Technol.* **206**, 3283-3290 (2012).

Investigation of triple Cr-Ti-based nitride coatings depending on the graded transition layers

V. A. Chitanov*, L. P. Kolaklieva, T. M. Cholakova, R. D. Kakanakov

Central Laboratory of Applied Physics – Bulgarian Academy of Sciences, 61 Sankt Petersburg Bld., 4000 Plovdiv, Bulgaria

The results from investigation of the relation between the structure of the transition layers and nanohardness and adhesion of the triple Cr-Ti-based nitride coatings are presented in this article. The coatings were deposited on tool steel substrates at temperature of 140 °C and a nitrogen flow of 13 and 18 sccm. Two types of the coating composition, Ti/TiN/TiCrN and Cr/CrN/CrTiN were studied. Nanohardness of 21 GPa to 27 GPa and 22 GPa to 24 GPa was measured for Ti-based and Cr-based structures, respectively. The increase of the N₂ flow in the Cr-based samples has shown considerably improved adhesion to the substrates in comparison with the Ti-based ones. In both cases, the increase of reactive gas flow decreases the coefficient of friction to 0.14 for the Ti-based and to 0.10 for Cr-based structures. The optimal combination of nanohardness, adhesion and coefficient of friction was achieved for the Cr/CrN/CrTiN samples deposited at a nitrogen flow of 18 sccm.

Keywords: Hard coatings, Cr-Ti-N, transition layers, nanohardness, adhesion

INTRODUCTION

During the last years, the Cr- and Ti- based triple nitride coatings with graded transition layers deposited by unbalanced magnetron sputtering have attracted interest for implementation in the industry. The improved mechanical and tribological characteristics resulted from their structure are the main advantage ahead of the standard CrN and TiN coatings [1]. The enhanced mechanical properties of CrN based coatings with incorporated other metals allowed their wide application in the machining industry for improvement of the mechanical performance of stamping and machine components, molds and dies, tool holders and other industry tools [2, 3]. The industry interest is also increasing because of their high oxidation resistance [4]. The appropriate adhesion of the hard coatings is very important, feature, since these films are required to endure excessive loads when they are in industrial service, including cyclical, mechanical and thermal influences [5]. Therefore the triple coatings have to be designed in a way to have excellent coating-substrate adhesion, which ensures longer lifetime of the tools in harsh industrial environments. There are many tool materials limiting the coating deposition to temperatures lower than 200 °C. Such as carbon steels are preferred for industrial applications because of their lower price and specific applications. However, with the increase of the working temperature over 200 °C their hardness

decreases [6]. The adhesion of hard coatings on tool steel substrates is improved with increase of the working temperature [7, 8]. The achievement of optimal combination of excellent adhesion and enhanced nanohardness at deposition temperatures below 200 °C is a challenging technology task. The CrTiN hard coatings can be prepared by different techniques such as magnetron sputtering, ion beam assisted deposition, cathodic arc, and electron beam evaporation. Among these methods, the magnetron sputtering is one of the most widely used techniques to prepare films with large area uniformity and strong adhesion [9]. The Unbalanced Magnetron Sputtering is the most appropriate method for coating deposition at temperatures below 200 °C [10]. In the case of low deposition temperatures, the coating adhesion becomes a critical issue. It is assigned by the adhesion between the substrate and the first deposited metal layer as well as the cohesion between the adhesion metal layer and the graded transition layer. The investigation of relation between the structure of the transition layers and nanohardness and adhesion of the triple Cr-Ti-based nitride coatings deposited below 200 °C is presented in this article.

EXPERIMENTAL

The coatings were deposited on HSS substrates at temperature of 140 °C and nitrogen flow of 13 sccm and 18 sccm. Two structures, Ti/TiN/TiCrN and Cr/CrN/CrTiN, named Ti-based and Cr-based, respectively, were deposited by close field unbalanced magnetron sputtering (CFUBMS) in

* To whom all correspondence should be sent:
vchitanov@gmail.com

UDP 800-4 equipment (Teer Coatings, UK).

Fig.1 presents a scheme of the vacuum chamber used for deposition of the coatings. One Cr and one Ti targets arranged in an opposite configuration were used for deposition. The unused targets were protected by a shield or by an application of a low current of 0.5 A.

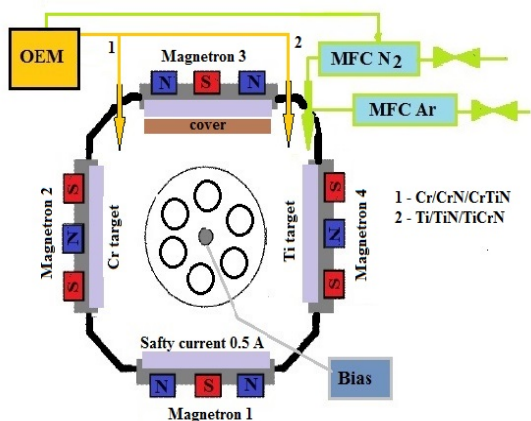


Fig.1. A vacuum chamber scheme of the UDP 800-4 equipment

Before the loading into the chamber, the specimens were ultrasonically cleaned in an alkaline solution, rinsed in deionised water and dried in a furnace. Prior the process start the chamber was evacuated to a base vacuum of 1.5×10^{-5} Torr. Ion cleaning in Ar plasma at a bias voltage of 500 V was performed for 30 min immediately before the coating deposition. The first Ti or Cr adhesion layer was deposited in Ar for 15 minutes. After that a transition layer of TiN or CrN was deposited by a gradually increased N_2 flow. During deposition, the nitrogen flow was controlled by OEM (Optical emission monitoring) with monochromator, tuned to the Ti (501 nm) or Cr peaks (421 nm). Two representative samples of each structure were chosen for investigation of the nitrogen flow effect on the properties of the transition and top layers. One transition layer was deposited at a nitrogen flow rate increased from 2 sccm to 13 sccm and the second one was obtained at a nitrogen flow rate risen from 2 sccm to 18 sccm. The increase was realized in 15 minutes. The internal stress between the transition layer and the active coating layer was reduced with deposition of a thin gradient TiCrN or CrTiN layer, realized by an increase of the Cr or Ti target currents respectively. The power of the Ti and Cr targets were kept a constant during deposition of the top TiCrN and CrTiN coating layers. The sputtering

process was controlled by the Ti and Cr target currents set in a Cr/Ti ratio of 0.7, because of their different reaction activity. The argon (Ar) flow was controlled by a mass-flow controller (MFC) and was kept a constant of 25 sccm during the process. The pulsed bias voltage was maintained at -70 V during deposition. The pressure during deposition varied between 1.6×10^{-3} and 1.9×10^{-3} Torr. The carousel rotated with 5 rpm. Thus, the only factor influenced the mechanical characteristics of coatings was the composition of the transition layers (Ti/TiN or Cr/CrN) and the applied nitrogen flow rate. The total thickness of the Ti-based coating was in the diapason $1.2 - 1.6 \mu\text{m}$, while of the Cr-based was between $1.5 - 2.0 \mu\text{m}$.

A Compact platform CPX- MHT/NHT – CSM Instruments, Anton Paar, Austria was used for characterisation of the mechanical parameters. The nanohardness was measured by a Berkovich indenter in the loading interval 0.01-500 mN. The Oliver and Pharr method was implemented for the calculations. Indentations with loads of 10, 15, 20, 50, 100 and 200 mN were made for the nanohardness study. The adhesion was qualified by a micro scratch test using a spherical Rockwell indenter with a radius of 200 μm . The coefficient of friction against a diamond indenter was also measured. A load progressively increased in the interval of 1 N to 30 N over a length of 1 mm was applied. The scratch velocity was 0.5 N/min.

The coating composition was studied by means of XPS and SEM/EDS analyses. The XPS spectra were acquired on a Kratos AXIS Supra photoelectron spectrometer using a monochromatic Al Ka source with an energy of 1486.6 eV. The base pressure in the analysis chamber was 5×10^{-8} Pa. The binding energies were corrected relative to the C1s peak at 285.0 eV. The elemental analysis was performed on JEOL JSM 6390 electron microscope, equipped with INCA Oxford EDS energy dispersive detector.

RESULTS

The load–displacement curves of the Ti-based coating at indentation loads of 10, 15, 50, 100 and 200 mN for the nitrogen flow rates of 13 and 18 sccm are presented in Fig.2.

The results show that the curves of both samples have the same slope and tendency. However, the curves corresponded to the sample prepared at a higher nitrogen flow are shifted to the bigger penetration depth implying lower nanohardness.

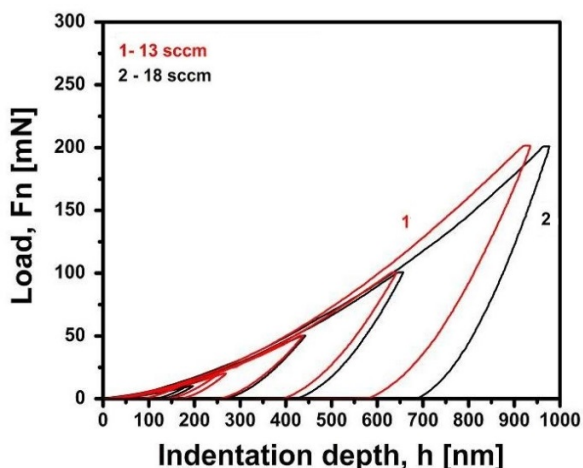


Fig.2. Load-displacement curves for Ti/TiN/TiCrN coating: 1) 13 sccm N₂ flow; 2) 18 sccm N₂ flow

This shift is more pronounced at bigger loads corresponded to penetration higher than 400 nm. Hence, this distinction could be attributed to the substrate than the coating.

The nanohardness H , modulus of elasticity E in dependence on the indentation depth h are presented in Fig.3.

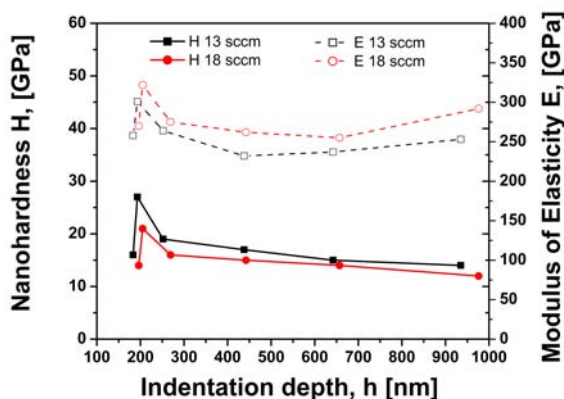


Fig.3. Dependence of the nanohardness and modulus of elasticity on the penetration depth of Ti/TiN/TiCrN coatings

A highest nanohardness of 27 GPa was measured at $h_{max}=193$ nm for the coating deposited at a N₂ flow rate of 13 sccm. The corresponded modulus of elasticity was 301 GPa.

The increase of nitrogen flow leads to decrease of the nanohardness to 21 GPa measured at h_{max} of 205 nm and a corresponding modulus of elasticity of 322 GPa. The nanohardness decrease at loads of 10 mN causes the surface contaminations and roughness [11]. With the indentation depth increase, the nanohardness decreased due to the influence of the substrate.

The load displacement curves as measured at 10, 15, 20, 50, 100 and 200 mN of the Cr-based structure are presented in Fig.4.

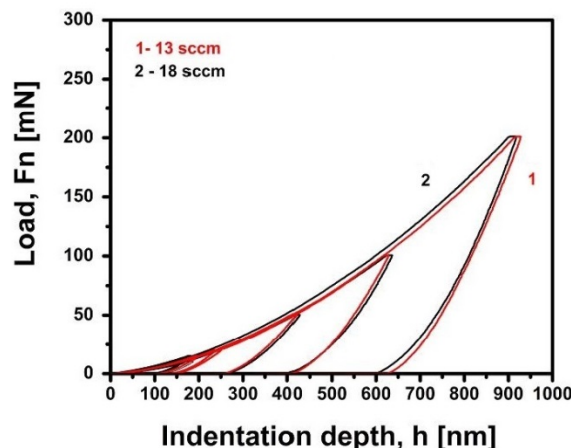


Fig.4. Load-displacement curves for Cr/CrN/CrTiN coating: 1) 13 sccm N₂ flow; 2) 18 sccm N₂ flow

The curves indicated an identical nanohardness for both N₂ flow rates. The maximum nanohardness measured at the indentation depth of 181 nm was 24 GPa and the modulus of elasticity was 380 GPa. The dependences of the nanohardness H and the modulus of elasticity E on the penetration dept, h for this structure are presented in Fig.5.

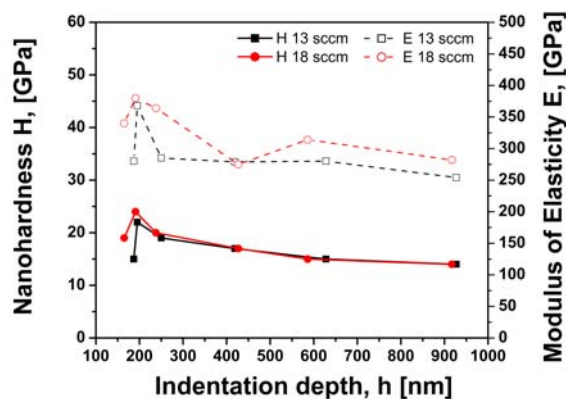


Fig.5. Dependence of the nanohardness and modulus of elasticity on the penetration depth of Cr/CrN/CrTiN coatings

It is seen that there is no difference in the curves corresponded to the both rates of the nitrogen flow. The slight nanohardness difference at a penetration depth of 200 nm is negligible.

Highest nanohardness of 22 GPa and a modulus of elasticity of 368 GPa were measured at a depth of 195 nm for the Cr/CrN/CrTiN coating obtained at 13 sccm nitrogen flow rate.

The study of the nanohardness revealed slight dependence on the nitrogen flow when OEM is tuned to the Ti peak, while the tuning to the Cr

peak does not cause significant dependence of the nanohardness on the nitrogen flow. This effect may relate to the higher titanium affinity to nitrogen than that of Cr atom ($\Delta H_{TiN} = -337.65$ kJ/mol, $\Delta H_{CrN} = -117.15$ kJ/mol). Therefore small changes of the nitrogen flow rate affect more pronounced nanohardness variation as the results for Ti/TiN/TiCrN coatings have shown. The highest nanohardness of 27 GPa and 24 GPa was measured for the Ti/TiN/TiCrN coating deposited at a 13 sccm nitrogen flow and for the Cr/CrN/CrTiN coating deposited at 18 sccm. Because the modulus of elasticity is an intrinsic property of the material, it does not depend essentially on the nitrogen flow rate.

The scratch test results of the Ti based coating with nitrogen flow rate of 13 sccm are shown in Fig.6. Four signals are presented in each graph: the applied normal force F_n , coefficient of friction μ , friction force F_t and acoustic emission AE.

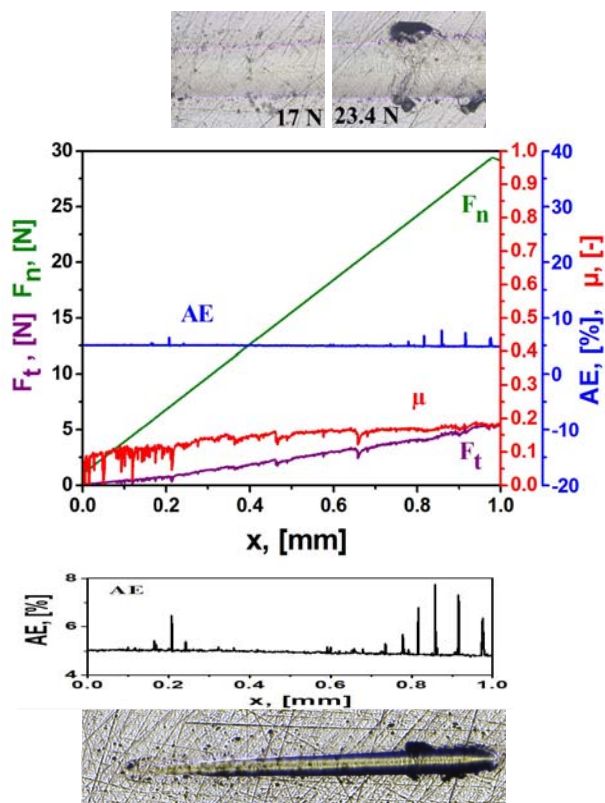


Fig.6. Scratch test results for the Ti/TiN/TiCrN coating at 13 sccm nitrogen flow: F_n - load force; F_t - friction force; μ - coefficient of friction; AE - acoustic emission; and a photo of the scratch test track

As it is seen, the coating exhibits a very good adhesion to the substrate. There was no delamination of the coating. At a load of 17 N a

small single crack was recognised, which related to small changes of the straight trends of F_t and μ . The AE signal has several peaks after 20 N, corresponded to rare small and short angular cracks implying weaker cohesion. Despite that, no chipping and spalling of the coating were appeared at loads up to 30 N. The measured coefficient of friction was 0.18.

The result of the Ti based coating obtained at a nitrogen flow of 18 sccm is presented in Fig.7.

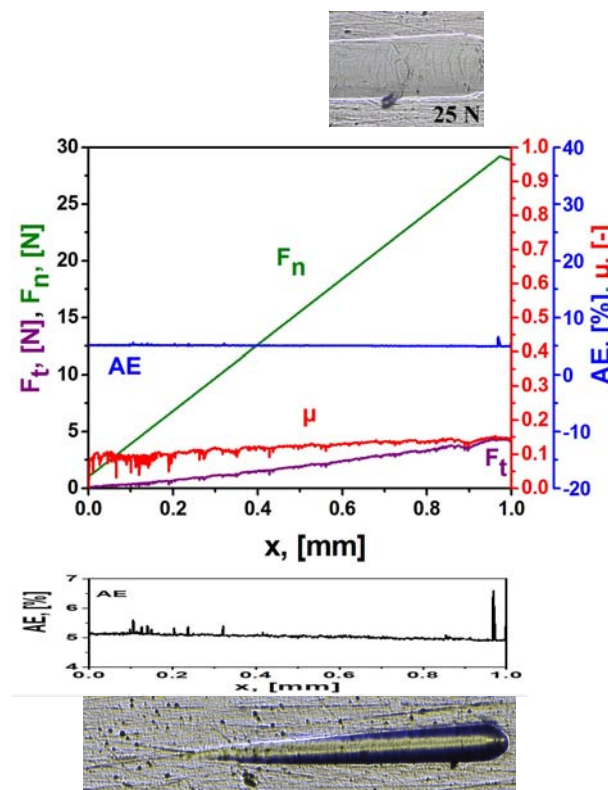


Fig.7. Scratch test results for the Ti/TiN/TiCrN coating at 18 sccm nitrogen flow: F_n - load force, F_t - friction force, μ - coefficient of friction, AE- acoustic emission; and a photo of the scratch test track

Again, a very good adhesion up to a load of 30 N was demonstrated. The improved adhesion up to 25 N could be evident from the scratch track and the trends of the friction force and acoustic emission. The latter was confirmed by the track visualization. A single-angle and several semi-spherical cracks were observed at loads over 25 N indicated with a small drop of the coefficient of friction and friction force. The measured coefficient of friction was 0.14.

The scratch test results of the Cr/CrN/CrTiN coating deposited at a nitrogen flow of 13 sccm are given in Fig.8. This coating also did not delaminate from the substrate. At the small load of 3 N there

was some drop of the coefficient of friction, most probably due to the surface defects. The small picks of the coefficient of friction and friction force signals at 14 N corresponded to thin semi-spherical cracks. The AE signal had not any features during the test. Few short angle cracks at the scratch edge at 27 N were identified. The adhesion of the coating during the scratch was very good. The coefficient of friction was 0.16.

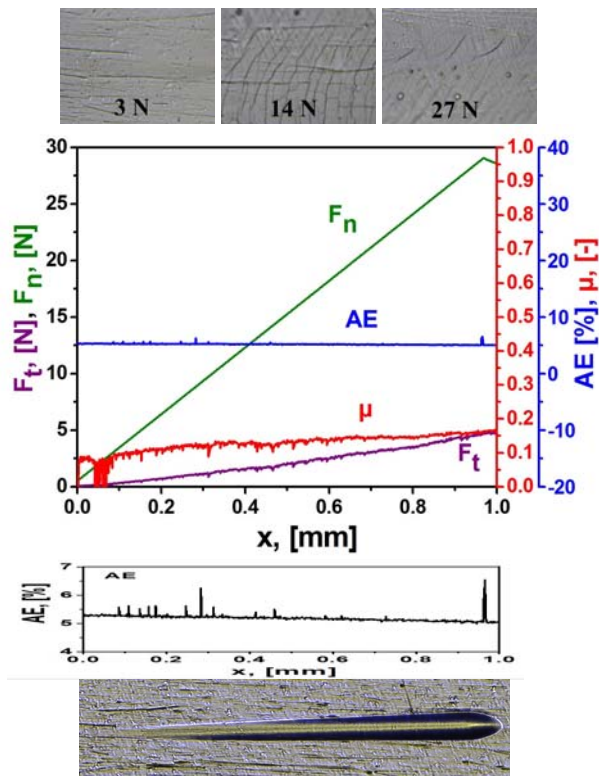


Fig.8. Scratch test results for the Cr/CrN/CrTiN coating at 13 sccm nitrogen flow: F_n - load force, F_t - friction force, μ - coefficient of friction, AE- acoustic emission; and a photo of the scratch test track

Excellent adhesion for loads up to 30 N was obtained for the Cr based coating deposited at an 18 sccm nitrogen flow. The results are presented in Fig.9.

The AE signal is smooth and no cracks were found during the test. The only one pick at the end of the AE signal could be attributed to the unloading process of the indenter and it did not correspond to a crack in the scratch track. There was no change in the trend of the friction force and the coefficient of friction. The measured value of the coefficient of friction was 0.1.

The dependence of the coefficient of friction on the nitrogen flow is presented in Fig.10.

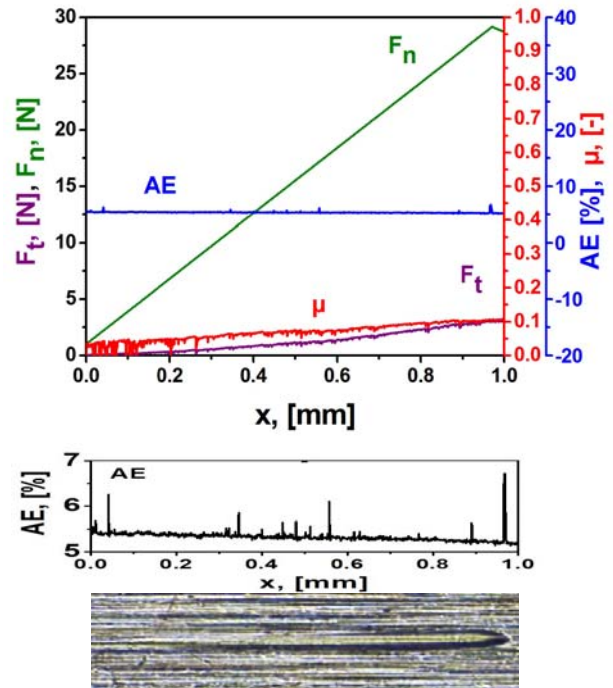


Fig.9. Scratch test results for the Cr/CrN/CrTiN coating at 18 sccm nitrogen flow: F_n - load force, F_t - friction force, μ - coefficient of friction, AE- acoustic emission; and a photo of the scratch test track

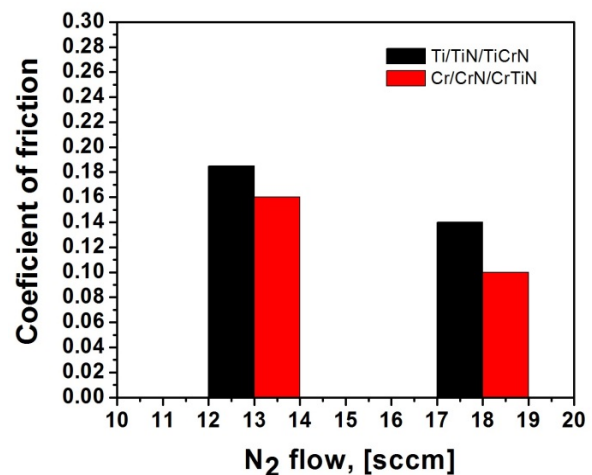


Fig.10. Coefficient of friction in dependence of the N₂ flow

The Cr-based coatings showed a lower coefficient of friction. It was evident that with the increase of the nitrogen flow the coefficient of friction for both structures was decreased. The lowest value of 0.1 had the Cr-based coating deposited at an 18 sccm flow.

The comparative study of the scratch results shown that the scratch resistance was very good with small non-essential cracks of the Ti-based coating. The Cr-based structures had better

scratch resistance because of the better adhesion strength of the CrN layer than the TiN one. This was confirmed by the excellent resistance to the progressive load from 1 to 30 N at 18sccm nitrogen flow.

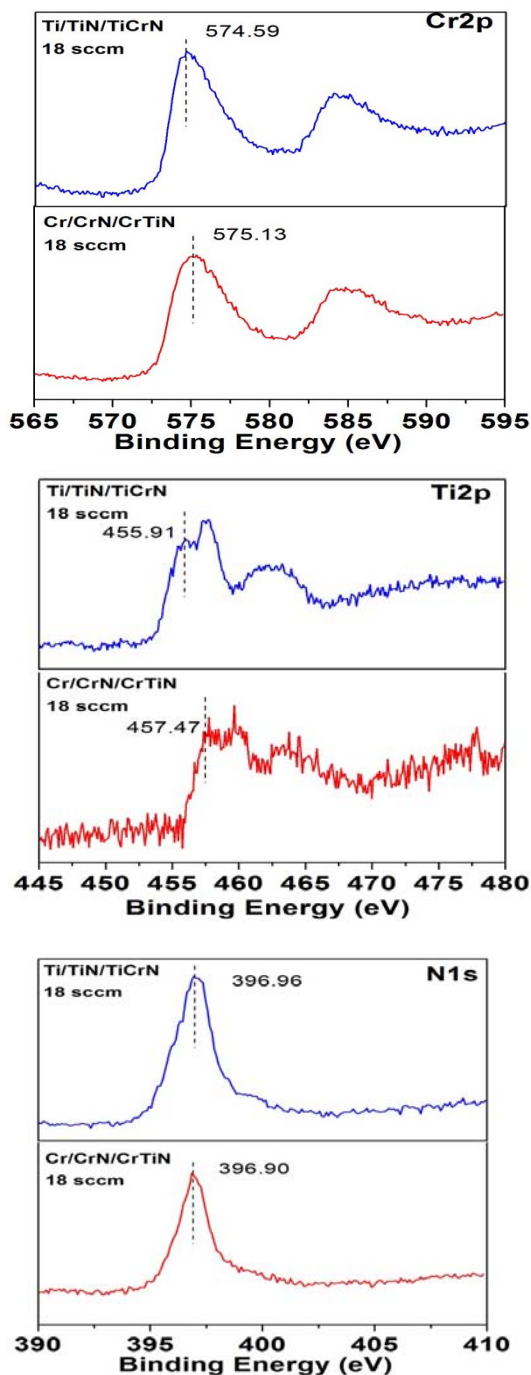


Fig.11. High resolution spectra of the Ti - based and Cr - based coatings

The chemical state and composition were obtained by XPS of the outmost coating layers.

High-resolution Cr (2p), Ti (2p), and N (1s) spectra are presented in Fig. 11. It is seen that the spectra of both coatings do not differ essentially in the shape. The Cr_{2p_{3/2}} peak is centered at 574.59 eV and 575.13 eV for Ti/TiN/TiCrN and Cr/CrN/CrTiN, respectively and possesses an asymmetric shape. The latter allows considering it as overlap of several peaks assigned to different chemical states according to reference data. Two of them could be assigned to CrN (BE 574.5 eV) and Cr₂N (BE 576.2 eV) in accordance with [12, 13]. It should be noted, that to the Cr (2p) peak could be contributed peaks between 576.1 and 576.6 eV assigned to Cr₂O₃ and CrO₂ [12, 14]. The oxygen contamination in a thin surface layer is very likely due to the air exposure of the coating. The third component which could be recognized in the Cr (2p) peak may relate to Cr (VI) state observed in binding energy range (578.1 - 579.8 eV) [15].

The positions of the Ti_{2p} peaks suppose the presence of TiN (BE 455.2 eV) [16] and titanium oxynitride (457.5 eV) and oxide (459.1 eV) [17]. The N_{1s} peak is centered at 396.96 eV in the Ti/TiN/TiCrN coating and at 396.90 eV in the Cr/CrN/CrTiN coating. This peak could be assumed as composed by peaks assigned to TiN at 395.7 eV [18] and two chromium nitrides, CrN (BE 396.7 eV) and Cr₂N (BE 399.7 eV) [19]. The results from the XPS analyses showed that the outermost layers of both coatings, Ti/TiN/TiCrN and Cr/CrN/CrTiN, obtained at the same technological regimes do not differ in a composition. They consist mainly of TiN, CrN and Cr₂N. The presence of oxynitrides and oxides was supposed due to the expose in air, as well. Hence, the difference of the mechanical properties results mostly by the different adhesion and transition layers than the coating composition.

The XPS analyses revealed that the outermost layer is composed by identical compounds when the Ti-based and Cr-based coatings were deposited at the same nitrogen flow.

Table 1. EDS elements analysis

Element	Ti/TiN/TiCrN – 18 sccm	Cr/CrN/CrTiN -18 sccm
	At. c. [%]	At. c. [%]
N	36.81	37.8
Ti	18.91	9.36
Cr	44.28	52.84

The element analysis from EDS investigation are shown in Tab.1. The nitrogen content in both

coatings was almost the same. The Ti was two times more in the Ti - based coating due to the Ti - based adhesion and transition layers. The Cr content was with small percentage higher in the Cr - based coating. It was prevailing over Ti and N in both structures.

CONCLUSIONS

Two coating structures Ti/TiN/TiCrN and Cr/CrN/CrTiN were developed for low temperature applications. The influence of the 13 sccm and 18 sccm nitrogen flow on the mechanical parameters was studied. It was found out that the nitrogen flow influenced mainly the transition layers responsible for the adhesion of the coating. The both structures were composed mainly from TiN, CrN and Cr₂N. The Cr-based coatings demonstrated better adhesion characteristics and lower coefficient of friction. The CrN further improved the mechanical properties of the transition layers. Lightly amended nanohardness was observed for the Ti based coatings deposited at lower N₂ flow. The increased N₂ flow improved the scratch resistance and reduced the coefficient of friction for both compositions. The Cr/CrN/CrTiN coating deposited at 18 sccm had the optimal mechanical characteristics and could be used for deposition on tools for industrial applications limited to temperatures of 200 °C.

REFERENCES

- [1] G. Zhang, P. Yan, P. Wang, Y. Chen, J. Zhang, The structure and tribological behaviors of CrN and Cr-Ti-N coatings, in *Applied Surface Science* **253(18)**, 7353-7359 (2007).
- [2] X. Zeng, S. Zhang, T. Muramatsu, Comparison of three advanced hard coatings for stamping applications, in *Surface and coating technology* **127**, 38-42 (2000).
- [3] S. Yang, K. Cooke, X. Li, F. McIntosh, D. Teer, CrN-based wear resistant hard coatings for machining and forming tools, in *Journal of Physics D: Applied Physics* **42(10)** (2009).
- [4] Y. Otani, S. Hofmann, High temperature oxidation behaviour of (Ti_{1-x}Cr_x)N coatings, in *Thin Solid Films* **281(1-2)**, 188-192 (1996).
- [5] R. Viana, A. Machado, Influence of adhesion between coating and substrate on the performance of coated HSS twist drills, in *Journal of the Brazilian Society of Mechanical Science and Engineering* **31(4)**, 327-332 (2009).
- [6] S. Jaypuria, Heat treatment of low carbon steel, Project report for Bachelor degree, India: Department of mechanical engineering, Nat. Institute of Technology, Rourkela, 2009.
- [7] M. Lufitha, Effect of substrate temperature on coating adhesion, Master thesis Canada: Department of Mechanical and Industrial Engineering, University of Toronto, 2001.
- [8] M. Al-Jaroudi, H. Hentzell, S. Gong, A. Bengston, The influence of titanium nitride reactive magnetron sputtering on hardened tool steel surfaces, in *Thin solid films*, **195(1-2)**, 63-76 (1991).
- [9] C. Paksunchai, S. Denchitcharoen, S. Chaiyakun, P. Limsuwan, Growth and Characterization of Nanostructured TiCrN Films Prepared by DC Magnetron Cosputtering, in *Journal of Nanomaterials*, 1-9 (2014).
- [10] M. Bao, X. Xu, H. Sun, J. He, Microstructure and Properties of Low Temperature Deposit Cr_xN Using Unbalanced Magnetron Sputtering, in *Key engineering materials* **353-358**, 1720 – 1723 (2007).
- [11] N. Demas, O. Ajayi, I. Shareef, Effects of Surface Contamination Layers and Roughness on the Determination of Mechanical Properties of Thins Films Using Nanoindentation, *Proc. of ASME/STLE International Joint Tribology Conference, Los Angeles, California*, 13-15 (2011).
- [12] I. Milosev, H. Strehblow, B. Navingek, XPS in the study of high-temperature oxidation of CrN and TiN hard coatings, in *Surface and coating technologies* **74-75**, 897 – 902 (1995).
- [13] A. Conde, A. Cristobal, G.Fuentes, T. Tate, J. Damborenea, Surface analysis of electrochemically stripped CrN coatings, in *Surf. & coating techn.* **201**, 3588 – 3595 (2006).
- [14] N. Heining, H. Jalili and K. Leung, Fabrication of epitaxial CrO₂ nanostructures directly on MgO(100) by pulsed laser deposition, in *Applied Physics Letters* **91**, 253102 (2007).
- [15] E. Unveren, E. Kemnitz, S. Hutton, A. Lippitz, W. Unger, Analysis of highly resolved x-ray photoelectron Cr2p spectra obtained with a Cr2O3 powder sample prepared with adhesive tape, in *Surf. & interface anal.* **36(1)**, 92 (2004).
- [16] A. Glaser, S. Surnev, F. Netzer, N. Fateh, G. Fontalvo, C. Mitterer, Oxidation of vanadium nitride and titanium nitride coatings, in *Surface Science* **601(4)**, 1153 -1159, (2007).
- [17] M. Thotiyl, T. Kumar and S. Sampath, Pd Supported on Titanium Nitride for Efficient Ethanol Oxidation, in *Journal of Physical Chemistry C* **114(41)**, 17934–17941 (2010).
- [18] D. Duartea, J. Sagasa, A. Sobrinhoa, M. Massi, Modeling the reactive sputter deposition of N-doped TiO₂ for application in dye-sensitized solar cells: Effect of the O₂ flow rate on the substitutional N concentration, in *Applied Surface Science* **269**, 55 -59 (2013).
- [19] A. Lippitz, T. Hubert, XPS investigations of chromium nitride thin films, in *Surface Coating Technologies* **200**, 250 – 253 (2005).

FOOD ENGINEERING AND TECHNOLOGIES

3-D simulation of simultaneous heat and mass transfer of apple

B. Turkan¹, A.S. Canbolat², A.B. Etemoglu^{2*}

¹Bayburt University, Faculty of Engineering, Mechanical Engineering Department, TR-69000, Bayburt, Turkey,

²Uludag University, Faculty of Engineering, Mechanical Engineering Department, TR-16059, Bursa, Turkey

Drying is a complex process associated with the coupled mechanism of heat and mass transfer which plays an important role in almost all industrial sectors. For this reason, the intensive research on drying is carried on specially based on optimisation of energy and process control. The aim of this study is to present a numerical method for drying processes widely used in food industries to provide enhanced product quality and economically advantages at definite production conditions. The governing equations of drying process in a 3-D rectangular object (e.g. apple slices) are solved numerically to predict the temperature and moisture distributions inside the object. Then, statistical tests of agreement between results are performed by determining the coefficient of regression (R^2), chi-square test (χ^2) and standard error of estimate (SEE) values, and it is found that predicted results agree well with the results in literature. Finally, a parametric study is conducted to emphasize the role of parameters on food drying as an important contributor to energy consumption.

Keywords: Heat and mass transfer, drying, numerical modelling

INTRODUCTION

The drying of solids is an operation of widespread importance in the food and pharmaceutical industries, production of textiles, chemical process, and also in the manufacture of paper and plastics. The investigations on the effective drying of foods is becoming increasingly important in the rapidly growing food industry, because the energy and food resources are limited. This is because the practical and easily adaptable drying models should be developed to augment the simultaneous heat and mass transfer consistent with the lowest capital and running costs in the sustainable products policies. Among these, numerical modelling is an essential part of food industry activities which is committed to maximising the process efficiency.

Drying of a food product is one of the oldest preservation methods to reduce microbial deterioration significantly. Nowadays, drying is regarded not only as a preservation process, but also as a method for increasing added value of foods. Therefore, drying process results in a product that is more convenient for final users. According to Avcı and Can [1], the designers of industrial dryers, also, have a need for quite basic heat transfer data to achieve optimum results for drying operations. So, to achieve the desired results for dry foods with defined physical structure, the process should provide the optimum simultaneous heat and mass transfer within the food product.

Numerous papers reported on different aspects and problems of drying for relevant sectors in industry. For example, different authors reported on new numerical and/or experimental models, and, many researchers presented drying characteristics of various solid objects [2-9].

Vega et al. [10] presented a study on maximum surface temperatures of products, which controlled automatically to avoid exceeding the allowable temperature values for convective drying process of fruits and vegetables. Bezerra et al. [11] determined the moisture diffusivity and the moisture transfer coefficient of passion fruit peel during convective drying process. Ateeque et al. [12] developed a 3D numerical model for convective drying of rectangular food material and solved the simultaneous heat and mass transfer equations by a MATLAB code. Lemus-Mondaca et al. [13] investigated the drying characteristics of papaya slices in range of air temperature from 40°C to 80°C both experimentally and numerically.

Understanding the mechanisms during the drying process of solid objects is essential for dryer design, quality control and energy savings. Thus, in literature, numerical investigations are presented for simulating heat and moisture transfer by Hussain and Dincer [14], Kaya et al. [15] and Kim et al. [16]. Similarly, Etemoglu et al. [17, 18] and Harchegani et al. [19] developed mathematical models for drying of thin layers, and validated their results with experimental data.

Aghbashlo et al. [20] stated that drying of wet materials is a complex, dynamic, unsteady, highly nonlinear, strongly interactive, successively interconnected, and multivariable thermal process

* To whom all correspondence should be sent:
aetem@uludag.edu.tr

whose underlying mechanisms are not yet perfectly understood. Therefore, the drying process still needs to be investigated by different perspectives. So, the objective of this study is to simulate the drying process in a 3-D rectangular object, to examine the influence of parameters which affect the heat and mass transfer rates such as temperature, velocity, moisture content, time, effective diffusion coefficient, and to validate the predicted results inside the object with available data in the literature.

MATERIAL AND METHOD

Mathematic modelling

Dried apples are often consumed in daily life because of nutritional values such as vitamin, fibre and low calorie. Thus, the most suitable drying conditions of apples should be determined for quality, hygiene and economical requirements in convective dryers which commonly used in industry. Drying process is a simultaneous heat and mass transfer operation in which the energy and evaporation of a liquid from a solid can be easily characterised and described in terms of the four empirical graphs shown in Fig.1 [1, 18]. A 3-D model is developed to evaluate the simultaneous heat and mass transfer for convective air drying of apple.

Briefly, the liquid inside the apple is transferred to the surface by diffusion and evaporates into the air by transferring heat from air to the food product by convection. Therefore, Fourier's law of heat transfer and Fick's law of mass diffusion are used for the drying process for the energy and water mass balance [14, 21]. The assumptions considered in the numerical model are as follows:

During the drying process, the air velocity, temperature and relative humidity are kept constant [14, 22].

a) During the drying process, the air velocity, temperature and relative humidity are kept constant [14, 22]

b) Gravity effects are negligible [23].

c) The thermophysical properties of the product are kept constant during drying [14, 22-25].

d) Food sample is homogenous [22-24].

e) The heat and mass transfer analogy is applicable [14, 26, 27].

f) There is no heat generation inside product [12, 14, 15, 23].

g) The shrinkage in the product is neglected (12-16, 23, 24, 26).

h) Radiation effects are negligible [13, 15].

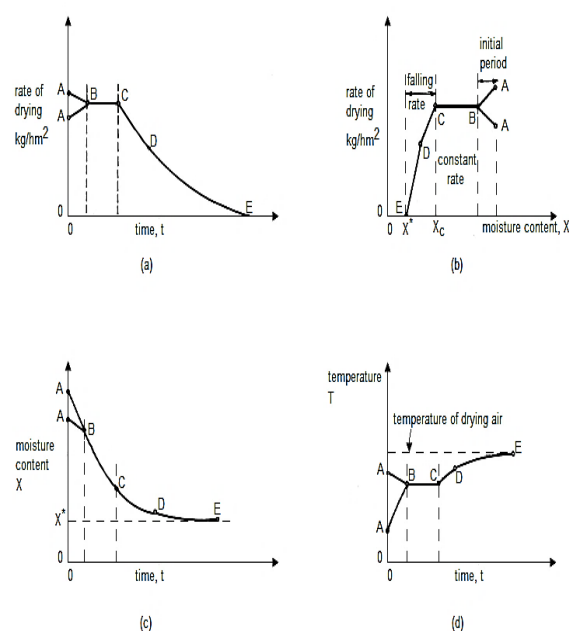


Fig.1. Characteristic drying graphs

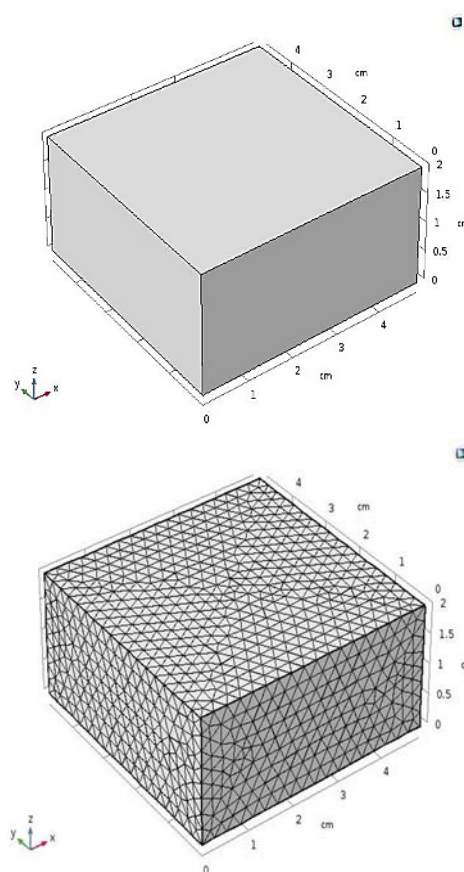


Fig.2. Model and mesh structure of the model

Table 1. Boundary conditions

	Heat Balance	Mass Balance
$x = 0; 0 \leq y \leq B \text{ and } 0 \leq z \leq H$	$-k \frac{\partial T(0,y,z,t)}{\partial x} = h_T(T - T_\infty)$	$-D_{AB} \frac{\partial M(0,y,z,t)}{\partial x} = h_M(M - M_\infty)$
$x = L; 0 \leq y \leq B \text{ and } 0 \leq z \leq H$	$-k \frac{\partial T(L,y,z,t)}{\partial x} = h_T(T - T_\infty)$	$-D_{AB} \frac{\partial M(L,y,z,t)}{\partial x} = h_M(M - M_\infty)$
$y = 0; 0 \leq x \leq L \text{ and } 0 \leq z \leq H$	$-k \frac{\partial T(x,0,z,t)}{\partial y} = h_T(T - T_\infty)$	$-D_{AB} \frac{\partial M(x,0,z,t)}{\partial y} = h_M(M - M_\infty)$
$y = B; 0 \leq x \leq L \text{ and } 0 \leq z \leq H$	$-k \frac{\partial T(x,B,z,t)}{\partial y} = h_T(T - T_\infty)$	$-D_{AB} \frac{\partial M(x,B,z,t)}{\partial y} = h_M(M - M_\infty)$
$z = H; 0 \leq x \leq L \text{ and } 0 \leq y \leq B$	$-k \frac{\partial T(x,y,H,t)}{\partial z} = h_T(T - T_\infty)$	$-D_{AB} \frac{\partial M(x,y,H,t)}{\partial z} = h_M(M - M_\infty)$

These assumptions are widely used because they provide acceptable accuracy and a more practical solution in engineering applications. The dimensions of the material are determined as 4.9 cm×4.8 cm×2 cm. The geometry of the physical model and mesh structure are shown in Fig.2.

Boundary conditions used in the analysis are shown in Tab.1.

Governing equations

The heat and mass transfer equations for moisture diffusion and temperature within food product can be expressed as:

$$\frac{\rho c_p}{k} \left(\frac{\partial T}{\partial t} \right) = \frac{\partial}{\partial x} \left(\frac{\partial T}{\partial x} \right) + \frac{\partial}{\partial y} \left(\frac{\partial T}{\partial y} \right) + \frac{\partial}{\partial z} \left(\frac{\partial T}{\partial z} \right) \quad (1)$$

$$\frac{\partial M}{\partial t} = \frac{\partial}{\partial x} \left(D \frac{\partial M}{\partial x} \right) + \frac{\partial}{\partial y} \left(D \frac{\partial M}{\partial y} \right) + \frac{\partial}{\partial z} \left(D \frac{\partial M}{\partial z} \right) \quad (2)$$

Initial conditions

The boundary conditions for the numerical solution are given as follows:

$$T(x, y, z, 0) = T_0 \quad (3)$$

$$M(x, y, z, 0) = M_0 \quad (4)$$

T_0 and M_0 are the initial temperature and the moisture content of the material, respectively.

Five surfaces of the moist material which has length L, height H and width B are in contact with the hot air; i.e. there is no heat or mass transfer from the base (see Fig.2). The boundary conditions in the x, y and z directions are given in Tab.1.

Heat and mass transfer coefficients (h_T , h_M) can be calculated by well-known semi-empirical correlation equations using the average Nusselt and

Sherwood numbers for laminar flow over flat plates [21].

$$Nu = \frac{h_T L_k}{k} = 0.664 Re^{0.5} Pr^{0.33} \quad (5)$$

$$Sh = \frac{h_M L_k}{D_{AB}} = 0.664 Re^{0.5} Sc^{0.33} \quad (6)$$

Solution methodology

Non-linear simultaneous heat and mass transfer equations are solved numerically by COMSOL Multiphysics using appropriate initial and boundary conditions and assumptions to obtain the temperature and moisture distributions in the apple during drying. The main steps of the solution process are as follows:

- Heat and mass transfer coefficients calculation
- Defining geometry
- Creating mesh structure
- Realizing the physical conditions (initial, boundary conditions etc.)
- Integrating and solving the governing equations [28].

The independence of the solution with respect to the mesh structure in the model geometry was carried out for moisture content and the maximum difference was found 1%. Mesh structure which consists of 12465 tetrahedral, 1468 triangular and 124 edge elements was used for all analysis (Fig.2). The time-dependent problem was solved by an implicit time stepping method. The non-linear coupled heat and mass transfer equations were solved using Newton's method with relative tolerance 0.01 and absolute tolerance 0.001.

Moisture ratio

Apple samples were dried by a convective dryer, so, the dimensionless moisture ratio, MR, is obtained as follows;

$$MR = \frac{M_t - M_e}{M_b - M_e} \quad (7)$$

where MR is the moisture ratio, M_t is the moisture content at time t (kg water/kg dry solid), M_e is the equilibrium moisture content (kg water/kg dry solid), and M_b is the initial moisture content (kg water/kg dry solid). Since the value of M_e is very small compared to the values of M_t and M_b , moisture ratio was calculated as;

$$MR = \frac{M_t}{M_b} \quad (8)$$

Statistical parameters

The non-linear regression analysis was applied for the drying models which are given in Tab.2 by SigmaPlot. The coefficient of regression (R^2), standard error of estimated (SEE) and chi-square test (χ^2) were used to evaluate the accuracies of the data.

Table 2. Considered drying models

Model No	Model Name	Equation	Reference
1	Lewis	$MR = \exp(-kt)$	[2]
2	Henderson and Pabis	$MR = a \exp(-kt)$	[3]
3	Two Term Exponential	$MR = a \exp(-k_0 t) + b \exp(-k_1 t)$	[4]
4	Wang and Singh	$MR = 1 + at + bt^2$	[5]
5	Midilli et al.	$MR = a \exp(-kt^n) + bt$	[7]

$$SEE = \sqrt{\frac{\sum_{i=1}^N (MR_{analysis} - MR_{prediction})^2}{N - z}} \quad (9)$$

$$\chi^2 = \frac{\sum_{i=1}^N (MR_{analysis} - MR_{prediction})^2}{N - z} \quad (10)$$

where $MR_{analysis}$ and $MR_{prediction}$ are estimated dimensionless moisture ratio by numerical analysis and the SigmaPlot program, N is the number of data points, z is the number of parameters in model.

RESULTS AND DISCUSSION

Model verification

The results of the present study is compared with numerical results by Younsi et al [23] and experimental results by Chiang and Petersen [29] under the same drying conditions. Thermophysical properties of material and the drying conditions are given in Tab.3.

The predicted centre temperature and moisture distributions inside the sample object are compared with experimental and numerical data available in the literature and are shown in Fig.3. As seen from Fig.3, considerably high agreement is found between predicted and numerical/experimental results.

Table 3. Thermophysical properties and initial conditions of the sample

Parameter (Unit)	Value
Density (kg/m ³)	856
Air temperature (°C)	81
Moisture content of material (%)	87
Moisture content of air (%)	12
Thermal conductivity (W/mK)	0.577
Heat of molar evaporation (J/kg)	0.25×10^7
Specific heat (J/kgK)	4201.4
Moisture capacity (kg/kg)	0.01
Moisture conductivity (kg/ms)	2.2×10^{-8}
Heat transfer coefficient (W/m ² K)	25
Mass transfer coefficient (kg/m ² s)	0.0001
Water molecular weight (gr/mol)	18

Thin layer drying models commonly used in the literature were also used to verify the drying curves obtained as a function of predicted data (see Tab.2). The statistical results from these models such as regression coefficient (R^2), chi-square (χ^2) and standard error of estimated (SEE) are given in Tab.4.

From the statistical analysis, it is revealed that the Midilli model yielded the highest R^2 and the lowest χ^2 and SEE values. Hence, the Midilli model gave better predictions than the other considered models.

Table 4. Statistical results of the drying models

Model/Coefficient	a	b	k	k_0	k_1	n	R ²	SEE	χ^2
Lewis			6.81×10^{-5}				0.95	0.0751	0.0056
Henderson and Pabis	1.07		7.76×10^{-5}				0.97	0.0622	0.0039
Two Term	3.9×10^{-3}	1.07		1.03×10^{-12}	7.82×10^{-5}		0.97	0.0803	0.0064
Wang and Singh	-6.97×10^{-5}	1.24×10^{-9}					0.98	0.0593	0.0035
Midilli et al.	1.03	3.49×10^{-6}	1.50×10^{-6}			1.43	0.99	0.0480	0.0023

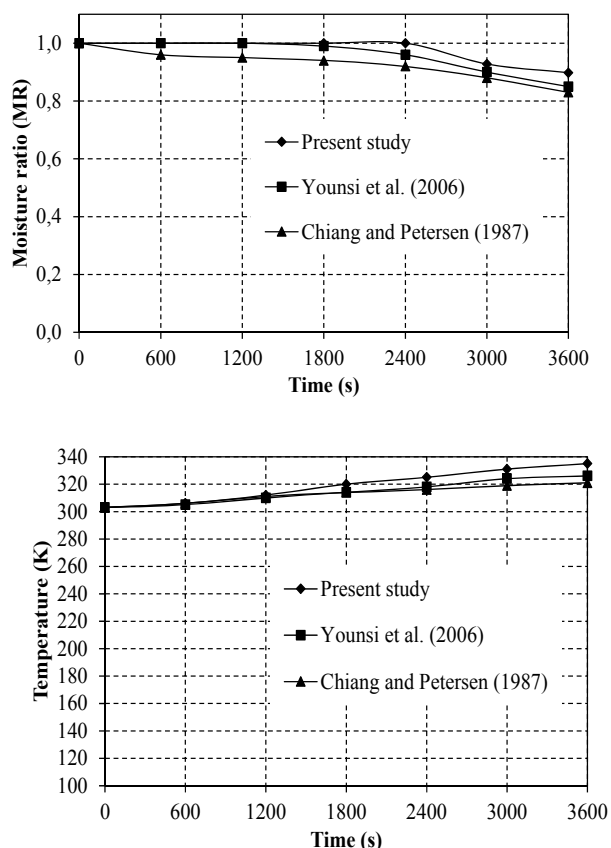


Fig.3. Comparison of the model prediction with the given results in literature

Numerical results

Fig.4 shows that the present numerical model can be used to predict the effects of many parameters on the operation conditions of dryers. The temperature and moisture distribution inside the food products are important knowledge for the producers because of the determination of quality and storage conditions. The moisture variation of the y-axis and z-axis inside the material, and the central temperature change of the y- and z-axes inside the material are shown in Fig.4a, 4b, 4c and Fig.5a, 5b and 5c respectively. The central moisture contents (on wet basis) are calculated for 3 different drying time (1800 s, 3600 s and 7200 s) as 87%, 86% and 80%, respectively. The central moisture content of the product decreases slowly with time.

During initial stage of drying, surface moisture is removed and in later stage, internal moisture movement governs the moisture removal rate. When surface moisture is removed, internal moisture movement starts. This is a slow process due to resistance in flow of moisture from inside to surface. Similarly, the central temperatures of the product after 1800, 3600 and 7200 seconds are 62°C, 75°C and 80°C, respectively. Drying processes lead to changes of foods at microstructural level, consequently it affects their macroscopic characteristics. Loss of water and segregation of components occurring during drying result in rigidity of cell walls. Damage and disruption of the cellular walls may happen, and even collapse of the cellular tissue may occur.

Frequently, during drying processes, the product surface dries much faster than its core, a phenomenon that originates internal stresses that results in very cracked and porous product interior. These changes are associated with volume reduction and colour change of the product.

So, the temperature and moisture values should be known for practical purposes. Tab.5 shows the temperature and the moisture ratios for 1000, 2000 and 4000 seconds for different depths from the surface of the product. The variations of the product temperature and the moisture ratio are presented as a function of drying time in Fig.6.

Table 5. Temperature distribution and moisture ratio of the material through the z-axis

Time (s)	1000	2000	4000
z-axis distance (cm)			
Temperature (°C)			
0	46	63	76
0.5	46.8	63.55	76.65
1	49	64.55	76.92
1.5	52.2	66.5	77.35
2	57	69	78
Moisture ratio (MR)			
0	1	1	1
0.5	1	1	1
1	1	1	0.78
1.5	1	0.56	0.33
2	0.03	0.02	0.02

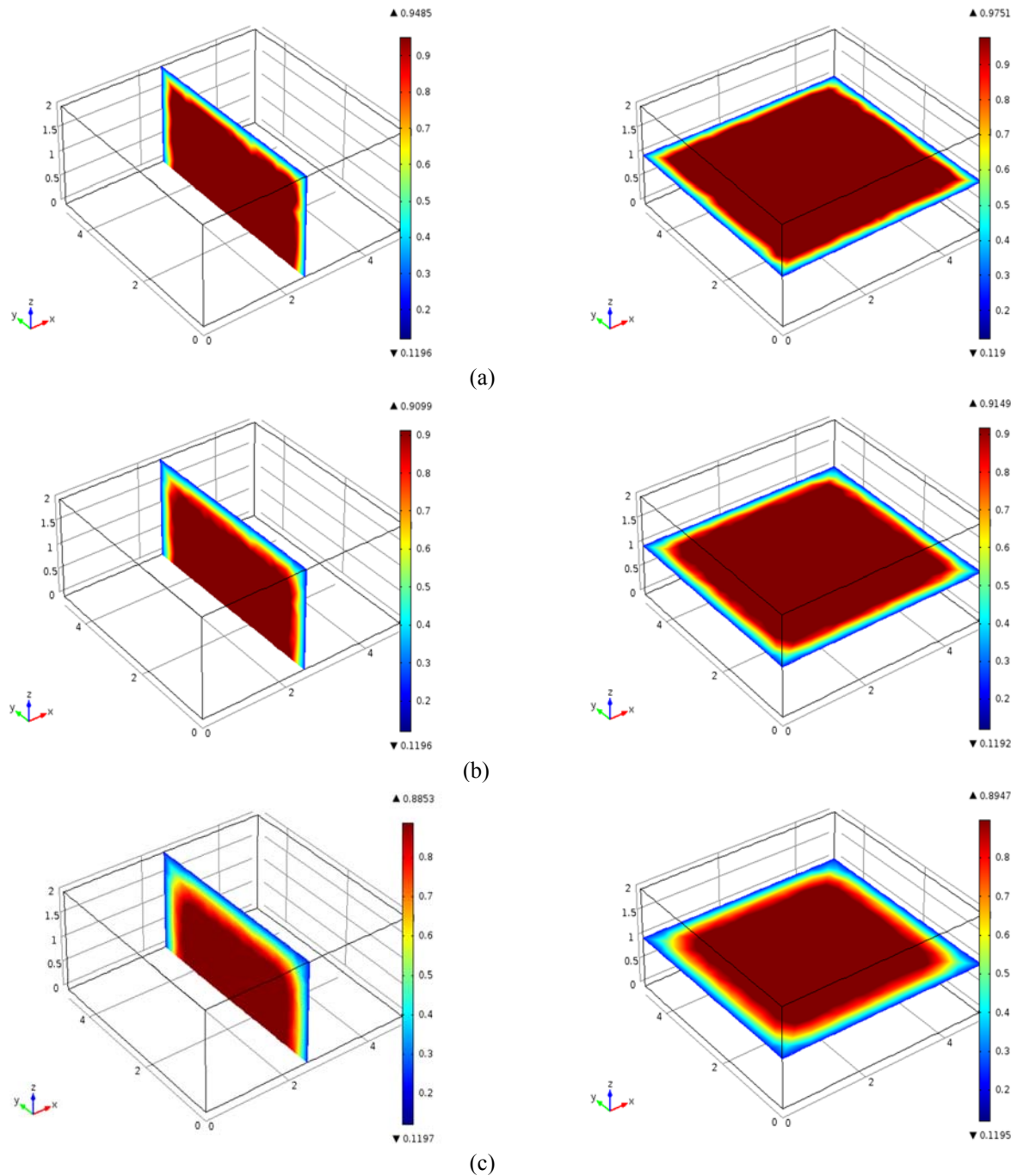


Fig.4. Moisture distribution inside the material (a-1800 s, b-3600 s, c-7200 s)

As can be seen from Fig.6, the central temperature of the product reached quickly 80°C after approximately 8000 seconds and, the total drying process consists of a short constant rate period and then first and second falling rate periods.

If the temperature of the drying air is not too high, the constant rate period can be observed in the drying of fruits containing high amount of moisture. In the constant rate drying period, the

product surface is continuously wet and covered with a moisture layer. As the liquid evaporates from the surface, liquid transfer takes place through diffusion from the product inside to the surface. The constant rate period continues until the first critical point that the liquid layer on the surface is reduced. After which the first falling rate period (between 2400 and 16000 seconds) starts.

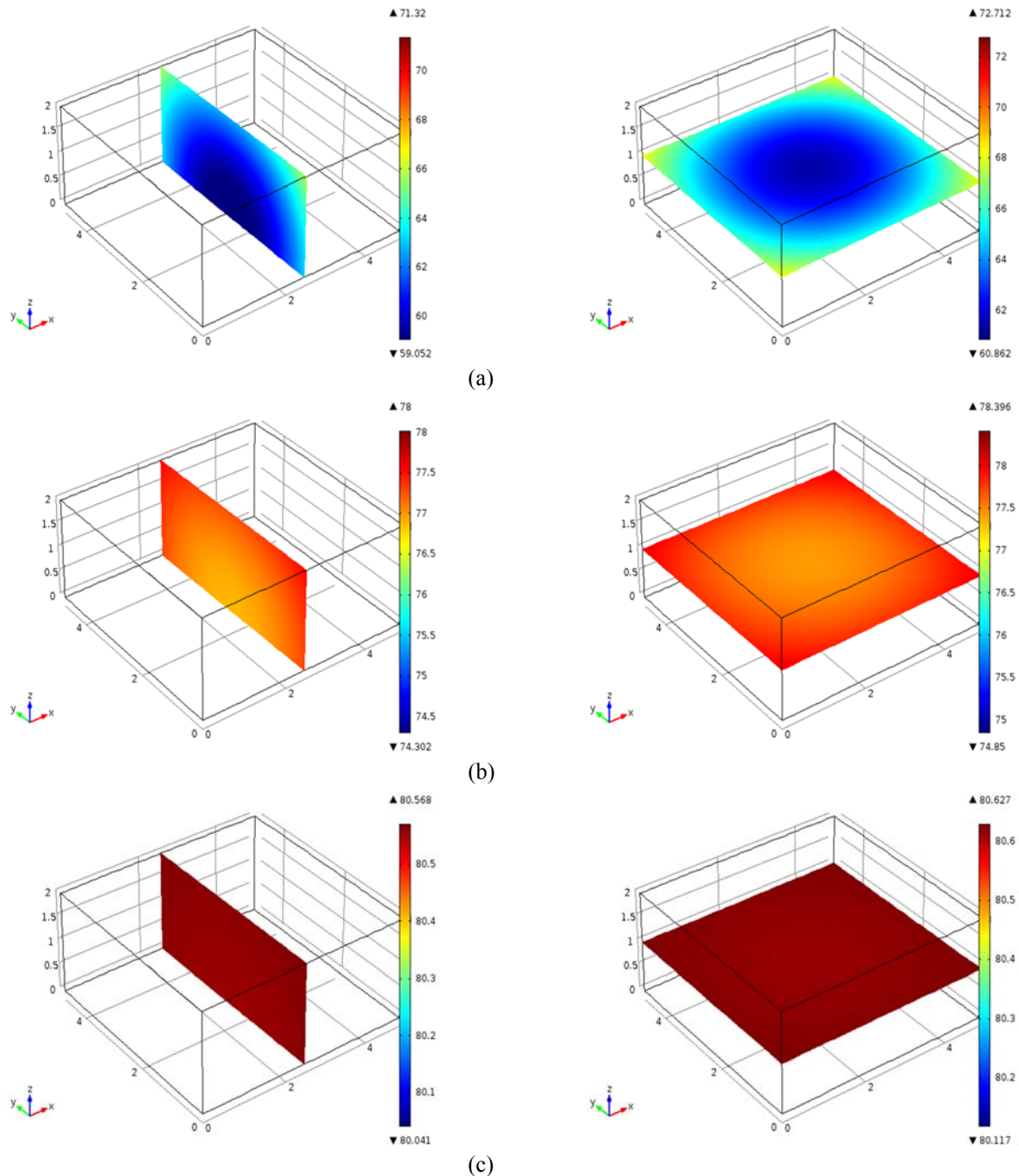


Fig.5. Temperature distribution inside the material (a-1800 s, b-3600 s, c-7200 s)

The amount of liquid transferred by diffusion to the surface during this period is less than the amount of liquid evaporated from the surface. The liquid film layer on the surface continues to decrease until the surface is completely dry at second critical point (0.27 MR). The moisture content continues to decrease after this point. This period is called the second falling rate period. Different parameters, which affect the drying process such as temperature and velocity of air, initial moisture contents of product, were investigated by numerical model.

And the predicted results are also compared with the Midilli model giving the best results (see Fig.7). It can be seen from the Figs.7-8, drying is speeded up either by increasing the average heat and mass transfer coefficients, or by increasing drying air velocity and temperature. When the drying air temperature is high, the temperature rise of the product is great. The product dries more rapidly due to the large difference between its temperature and that of the drying air.

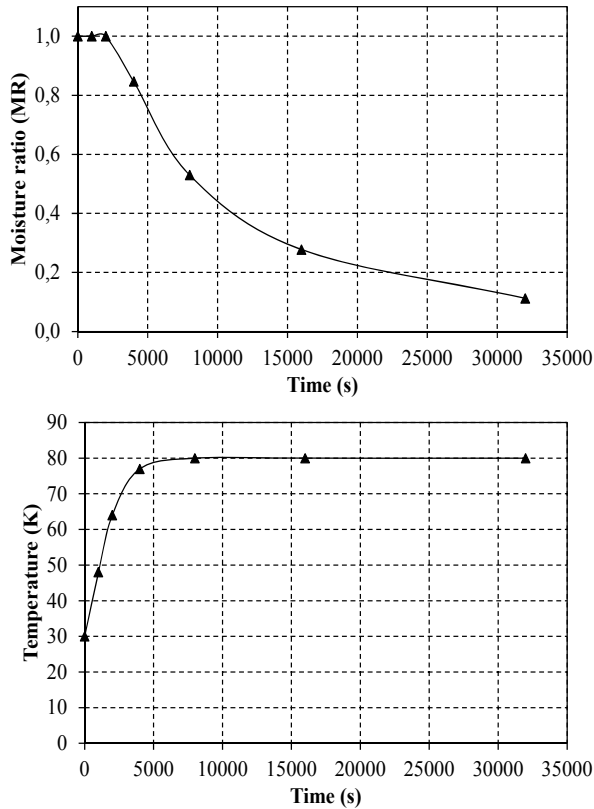


Fig.6. Temperature and moisture ratio values during drying

The changes in the moisture ratios and central temperatures of the product with different initial moisture contents (on wet basis) are also given in Fig.7. When the initial moisture content is high, the temperature rise is relatively slow and drying takes long time, because the higher moisture content needs much more heat for evaporation from the product.

CONCLUSIONS

In this study, the drying process of a three-dimensional model was numerically investigated. The numerical model considers simultaneous heat and mass transfer through the moist porous material. Five surfaces of the food product were assumed to be in contact with hot air. For validation, the present numerical model was compared with two different numerical and experimental studies in the literature. The predicted numerical results of the model agree well with the results in literature. Numerical modelling offers us the advantage of observing the conditions in advance. So, the developed numerical model is a

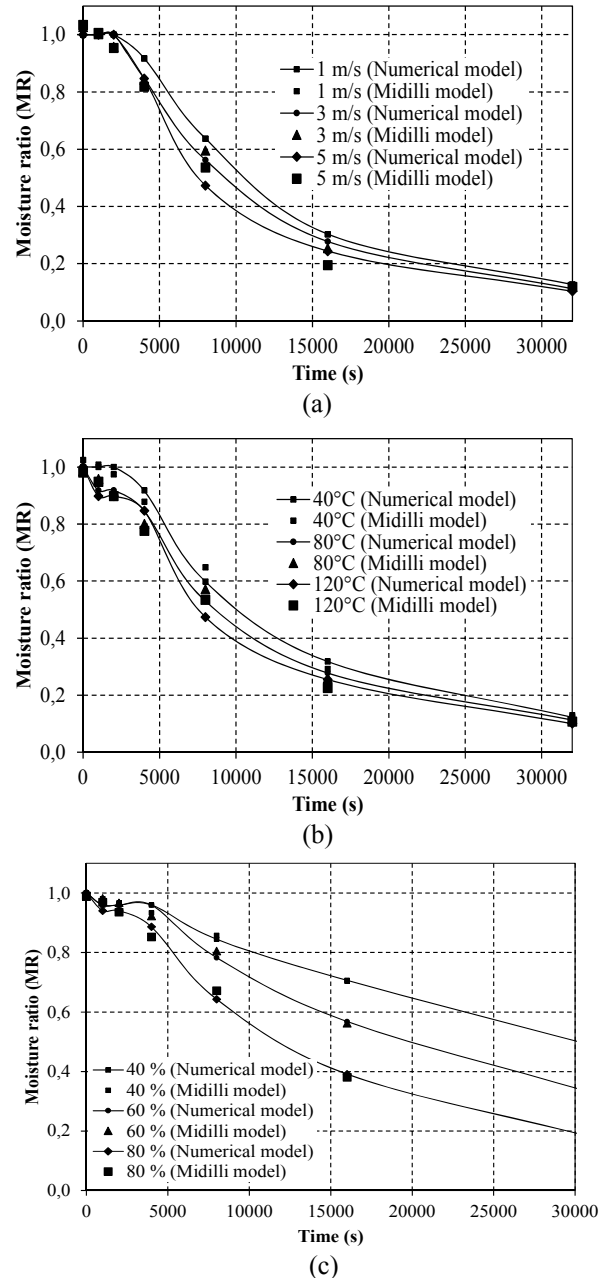


Fig.7. Moisture variation of different drying conditions (a-80°C, 40% ; b- 3 m/s, 40%; c- 80°C, 3 m/s)

powerful tool for evaluation of the drying behaviour of food products and dryer performance for given thermo-economic constraints.

Moisture ratio data were also applied into 5 different thin-layer drying models, and statistical analysis was performed. According to the statistical indicators, Midilli model well describe the thin layer drying kinetics of the apple at investigated conditions. Finally, a parametric analysis is presented to demonstrate that the numerical model

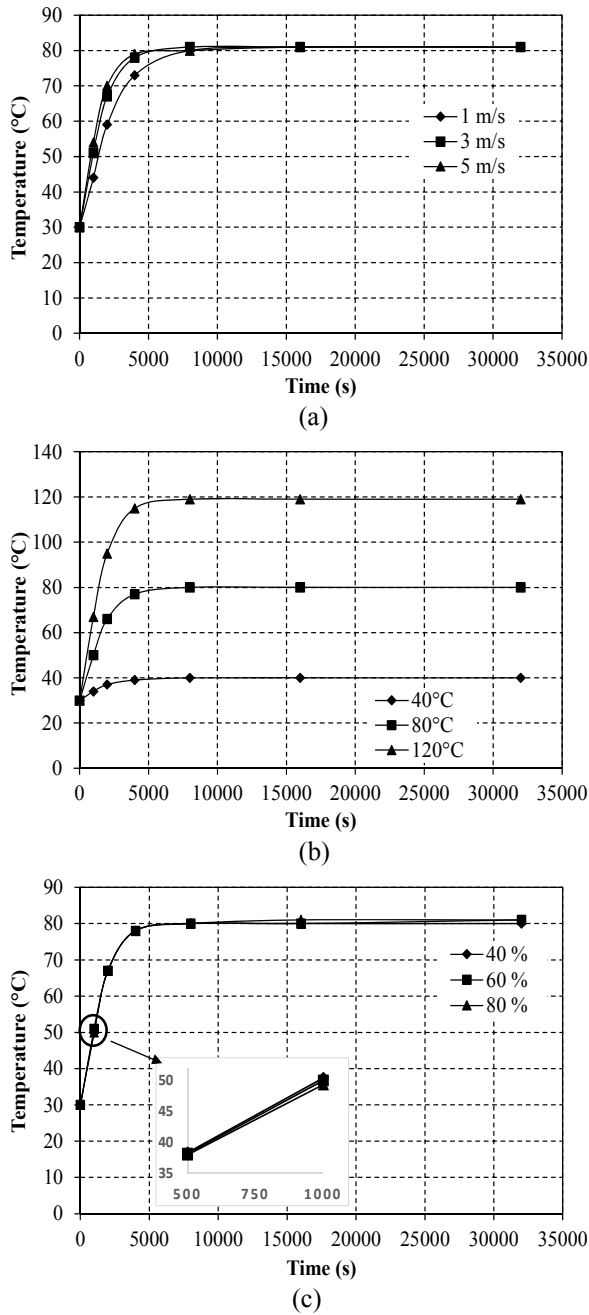


Fig.8. Temperature variation of different drying conditions (a-80°C, 40% ; b- 3 m/s, 40%; c- 80°C, 3 m/s)

can be used for modelling, optimization, estimation, monitoring and control of drying processes.

For this purpose, different parameters, which affect the drying process such as temperature, initial moisture contents, velocity, dimension, depth and time, were investigated.

Numerical modelling provides sufficient information to ensure that food products are dried under optimum conditions without deformation, deterioration or loss of vitamins. And, the results of the numerical study also contribute to better

understanding of the drying process for industrial and academic users.

NOMENCLATURE

- B - width, m;
- c_p - specific heat, J/kgK;
- D_{AB} - diffusion coefficient, m^2/s ;
- H - height, m;
- h_T - heat transfer coefficient, W/m^2K ;
- h_M - mass transfer coefficient, m/s;
- k - thermal conductivity, W/mK;
- L - length, m;
- L_k - characteristic length, m;
- M - moisture content, kg water/kg dry solid;
- MR - moisture ratio, %;
- Nu - Nusselt number,-;
- Pr - Prandtl number,-;
- Re - Reynolds number,-;
- Sc - Schmidt number,-;
- Sh - Sherwood number,-;
- T - temperature, K;
- t - time, s;
- u - air velocity, m/s.

Greek symbols

- α - thermal diffusivity, m^2/s ;
- ν - viscosity, m^2/s ;
- ρ - density, kg/m^3 .

Subscripts

- e - equilibrium
- b,0 - initial condition

REFERENCES

- [1] A. Avci, M. Can. The analysis of the drying process on unsteady forced convection in thin films of ink. *Applied Thermal Engineering* **19**, 641-657 (1999).
- [2] W.K. Lewis. The rate of drying of solid materials. *J. Ind. Eng. Chem.* **13** (5), 427-432 (1921).
- [3] S.M. Henderson, S. Pabis. Grain drying theory. II. Temperature effects on drying coefficients. *J. Agr. Eng. Resource* **6**, 169-174 (1961).
- [4] Y.I. Sharaf-Eldeen, J.L. Blaisdell, M.Y. Hamdy. A model for ear corn drying. *Trans. ASAE* **23**, 1261-1271 (1980).
- [5] C.Y. Wang, R.P. Sing. A single layer drying equation for rough rice. *Am. Soc. Agr. Eng.*, St. Joseph, MI, **78**, 3001 (1978).
- [6] I. Dincer, S. Dost. An analytical model for moisture diffusion in solid objects during drying. *Drying Technol.* **13** (1-2): 425-435 (1995).
- [7] A. Midilli, H. Kucuk, Z. Yapar. A new model for single-layer drying. *Drying Technol.*, **20**, 1503-1513 (2002).

- [8] S.M.A. Rahman, M.R. Islam, A.S. Mujumdar. A study of coupled heat and mass transfer in composite food products during convective drying. *Drying Technol*, **25** (7-8): 1359-1368 (2007).
- [9] Y.Q. Wang, M. Zhang, A.S. Mujumdar. Convective drying kinetics and physical properties of silver carp (*hypophthalmichthys molitrix*) fillets. *Journal of Aquatic Food Product Technology* **20** (4): 361-378 (2011).
- [10] A.M.N. Vega, B. Sturm, W. Hofacker. Simulation of the convective drying process with automatic control of surface temperature. *Journal of Food Engineering* **170**, 16-23 (2016).
- [11] C.V. Bezerra, L.H.M. Silva, D.F. Corrêa, A.M.C. Rodrigues. A modeling study for moisture diffusivities and moisture transfer coefficients in drying of passion fruit peel. *International Journal of Heat and Mass Transfer* **85**, 750-755 (2015).
- [12] M. U. Ateeque, R.K. Mishra, V.P. Chandramohan, P. Talukdar. Numerical modeling of convective drying of food with spatially dependent transfer coefficient in a turbulent flow field. *International Journal of Thermal Sciences* **78**, 145-157 (2014).
- [13] R.A. Lemus-Mondaca, C.E. Zambra, A. Vega-Gálvez, N.O. Moraga. Coupled 3D heat and mass transfer model for numerical analysis of drying process in papaya slices. *Journal of Food Engineering* **116**, 109-117 (2013).
- [14] M.M. Hussain, I. Dincer. Numerical simulation of two-dimensional heat and moisture transfer during drying of a rectangular object. *Numerical Heat Transfer, Part A: Application: An International Journal of Computation and Methodology* **43**, (8), 867-878 (2003).
- [15] A. Kaya, O. Aydın, I. Dincer. Numerical modeling of heat and mass transfer during forced convection drying of rectangular moist objects. *International Journal of Heat and Mass Transfer* **49**, 3094-3103 (2006).
- [16] D. Kim, G. Son, S. Kim. Numerical analysis of convective drying of a moving moist object. *International Journal of Heat and Mass Transfer* **99**, 86-94 (2016).
- [17] A.B. Etemoglu, M. Can, A. Avci, E. Pulat. Theoretical study of combined heat and mass transfer process during paper drying. *Heat Mass Transfer* **41**, 419-427 (2005).
- [18] A.B. Etemoglu, Y. Ulcay, M. Can, A. Avci. Mathematical modelling of combined diffusion of heat and mass transfer through fabrics. *Fibers and Polymers* **10** (2): 252-259 (2009).
- [19] M.T. Harchegani, M.G. Varnamkhasti, D.S.M. Ghanbarian, M. Tohidi. Dehydration characteristics and mathematical modelling of lemon slices drying undergoing oven treatment. *Heat Mass Transfer* **52**, 281-289 (2016).
- [20] M. Aghbashlo, S. Hosseinpour, A.S. Mujumdar. Application of artificial neural networks (ANNs) in drying technology: A comprehensive review. *Drying Technology* **33**, 1397-1462 (2015).
- [21] Y.A. Cengel. *Heat and Mass Transfer: A Practical Approach*. McGraw-Hill Education Pvt Limited, third edition, 879 pages (2007).
- [22] M.A. Karim, M.N.A. Hawlader. Mathematical modelling and experimental investigation of tropical fruits drying. *International Journal of Heat and Mass Transfer* **48**, 4914-4925(2005).
- [23] R Younsi, D. Kocaefe, Y. Kocaefe. Three dimensional Simulation of Heat and Moisture Transfer in Wood. *Applied Thermal Engineering* **26**, 1274-1285 (2006).
- [24] E. Barati, J.A. Esfahani. A new solution approach for simultaneous heat and mass transfer during convective drying of mango. *Journal of Food Engineering* **102**, (4), 302-309 (2011).
- [25] C.V. Bezerra, L.H.M. Silva, D.F. Corrêa, A.M.C. Rodrigues. A modeling study for moisture diffusivities and moisture transfer coefficients in drying of passion fruit peel. *International Journal of Heat and Mass Transfer* **85**, 750-755 (2015).
- [26] M. Aversa, S. Curcio, V. Calabro, G. Iorio. An analysis of the transport phenomena occurring during food drying process. *Journal of Food Engineering* **78**, (3), 922-932 (2007).
- [27] H.T. Sabarez. Computational modelling of the transport phenomena occurring during convective drying of prunes. *Journal of Food Engineering* **111**, (2), 279-288 (2012).
- [28] Comsol Multiphysics 5.3. Heat Transfer Model Library, Heat Transfer Module User's Guide. *Chemical Reaction Engineering Module User's Guide* (2017).
- [29] W.C. Chiang, J.N. Petersen. Experimental Measurement of Temperature and Moisture Profiles During Apple Drying. *Drying Technology* **5**, (1), 25-49 (1987).

Study on mechanical behaviour of agar gel in compression mode

Hao Yu^{1,2}, Jinghu Yu^{1,2*}, Minmin Zhan^{1,2}

¹School of Mechanical Engineering, Jiangnan University Wuxi, Jiangsu 214122, China

²Jiangsu Province Key Laboratory of Advanced Food Manufacturing Equipment and Technology, Wuxi, Jiangsu 214122, China

Gels were widely used in food industry as food material or additives, the deformation of gels not only affect the design of the processing equipment, but also affect the formulation and optimization of this kind food materials. In this study, Stress relaxation and strain relaxation experiment were conducted aimed at the sample of gel concentration of 2.5%, 5% and 7.5% with a texture analyzer. Based on the experimental data, utilizing Kelvin and Maxwell model as basal model, established the four-element model that predict the mechanical behaviour of gels. Experimental results and theoretical models show that: the equilibrium stress of gels was positively correlated with gel concentration; four-element model can accurately describe the mechanical behaviour of food with different concentrations of agar gels and water in the compression, The mechanical model is of important significance for optimization not only in processing technology of food materials with different amounts of gels but also in packaging and shipping process.

Keywords: agar gels, compression velocity, stress relaxation, four-element model

INTRODUCTION

In the food industry, agar gels are commonly used as thickeners, coagulants, and stabilizers in various foods such as pastries, jelly and candies. As a kind of food additive, the agar gel will affect the texture and taste of the food, thus affecting the consumer's choice tendency. Therefore, the research on the mechanical properties of the agar gel is of great significance to the development of the food industry [1, 2].

Gel refers to the colloidal system dispersed phase particles connected to each other to form a network of semi-solid material formed in the gel system, the original dispersion medium filled in the network structure of the gap. The sol loses its original fluidity after gelling and gains elasticity, strength and yield values. For the mechanical properties of gels, lots of researches have been done by scholars. Forte et al. [3] studied the compression and wire-cutting characteristics of gelatin based on the strain rate, and established the fracture model of gels; Shokrieh M M et al. [4] studied the relationship between reinforced polymers and compressive strain rates and proposed a micromechanical model based on strain rate changes. Ma et al [5] studied the influence of agar solution concentration, pH, ionic strength, Na⁺, K⁺ Composition on the agar gel texture

characteristics; Liu Shilin et al [6] discussed the factors affecting the agar gel strength and relaxation characteristics, and on the basis of analysis to research the gel mechanism. At present, scholars focus on the strain rate-related model of the gel mechanics, and the strain rate is constantly changing during the actual processing and storage. Some scholars focus on the relationship between the mechanical properties of the gel and the chemical composition. The relationship between the mechanical properties of the gel and the test parameters has not been studied.

In this paper, the mechanical properties of agar gel with different concentrations under different compression rates were studied by means of a texture analyser. Then the stress relaxation properties of the gel were obtained in the elastic range. The stress relaxation curve was obtained by using the four-element model. The curve has a good fit with the experiment data. The research is of great significance in the study of food texture and the guidance of food processing technology, product quality control and so on.

MATERIALS AND METHODS

Material preparation

(1) Material

Agar powder: food grade, Fujian LvQi Food Colloid Co., Ltd. production, 200 g /bag.

(2) Instruments and equipment

* To whom all correspondence should be sent:
jhyu@jiangnan.edu.cn

Texture analyzer: TMS-pro, the United States FTC company; HH-4A digital constant temperature water bath, Jiangsu Jingda; electronic balance; thermometer; beaker.

(3) Preparation

Take 200ml of distilled water with a beaker and heat it to 95 °C in a constant temperature water bath, replenish the evaporated water in the heating process, weigh a certain amount of agar powder, weigh (m), pour into distilled water at 95 °C and stir 5 min after cooling, poured into a cylindrical mold at about 65 °C cooled to room temperature, placed in a 4 °C oven for 20h.

Experimental methods

Respectively, the concentration of 2.5%, 5.0%, 7.5% agar gel preparation, prepared as a cylindrical sample; TA11 universal cylindrical probe (diameter 25.4 mm; length 35.0 mm) experiments at room temperature, the main parameters are as follows:

(1) Uniaxial compression test

Test temperature: room temperature (28 °C); speed before test: 20.0 mm / min; test speed: 1.0 mm / min, 10.0 mm / min,

(2) Stress relaxation test

Test temperature: room temperature (28 °C); pretest speed: 20.0 mm / min; test speed: 10.0 mm / min; constant strain 0.15; stress relaxation time: 30 min.

The above compression experiments and stress relaxation experiments were performed on cylindrical, agar-gel samples of $\phi 22 \times 17$ mm. Before each test, silicone oil was uniformly applied to the contact surfaces of the probe and the sample so as to minimize the effect of friction on the compression. The effect of the experiment [7], each sample measured 3 times, and finally take the arithmetic mean.

EXPERIMENTAL RESULTS AND DISCUSSION

Uniaxial compression

Assuming that the agar gel volume does not change during compression, the true compressive stress σ_T and the true strain ε_T are in the following relationship:

$$\sigma_T = \frac{F(H_0 - \Delta H)}{\pi R^2 H_0} \tag{1}$$

$$\varepsilon_T = -\ln\left(1 - \frac{\Delta H}{H_0}\right) \tag{2}$$

Where:

F - compressive force of loading;

H_0 - initial height of the experimental sample;

ΔH - compression distance;

R - radius of the experimental sample;

According to the above formula, the real stress σ_T and true strain ε_T of the agar gel in the compression process can be calculated by combining the compressive force F and the compression ΔH collected during the experiment of the texture analyzer.

Fig.1 shows the compressive stress-strain curves of agar gels at 2.5%, 5.0% and 7.5% concentrations at different strain rates (mean calculations for all curves and fitting completed in Origin 9.0). It can be seen that the compression process of colloids can be divided into a linear elastic phase, a non-linear phase of deterioration and a fracture phase. During the elastic phase, the compressive stress of the colloid is less than its critical value, and the stress-strain curve is nearly a straight line. In the nonlinear phase, the damage evolution begins to occur in the material. With the continuous increase of compressive stress, the crack continuously expands and the material stiffness continuously. When the stress reaches the maximum bearing stress, the colloid shows obvious rupture damage. At this moment, the stress drops rapidly. The highest point of the curve is the rupture stress and rupture strain corresponding to the colloid.

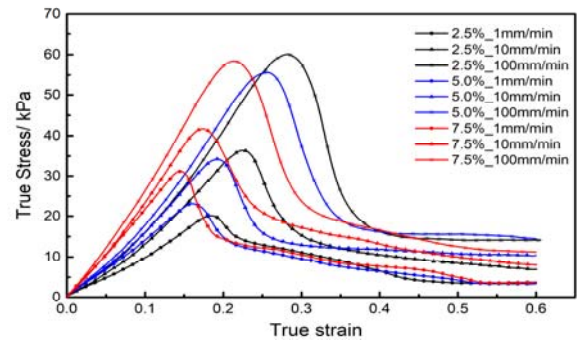


Fig.1. Stress-strain curves of agar gels in various concentrations

At a certain compression speed v_c , the strain rate of the colloid:

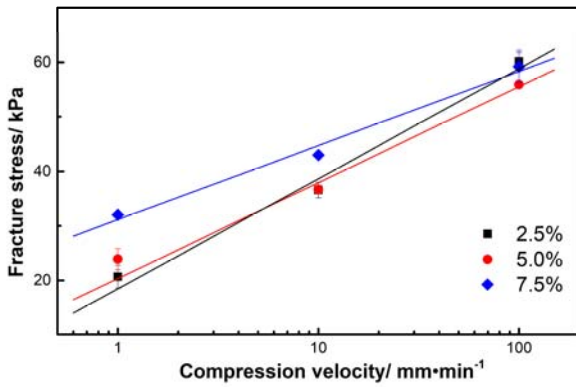
$$\dot{\varepsilon} = \frac{v_c}{H(t)} \tag{3}$$

$$H(t) = H_0 - v_c \cdot t \tag{4}$$

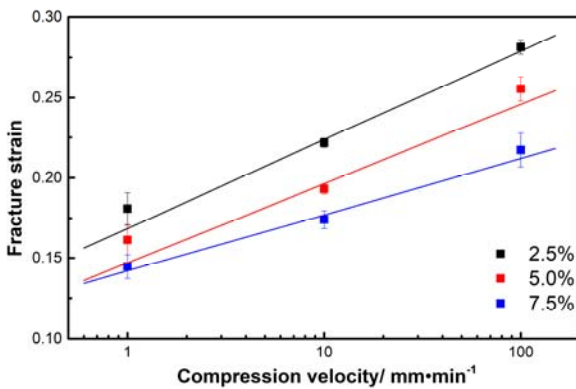
Eq.(3) shows that when the compression rate is a constant, as the sample height decreases, the strain rate of the compression process becomes larger and larger. In the dynamic loading process, due to the stress acting time is very short, there is not enough time to crack development, cannot

reach the energy required for material rupture, it must be higher stress, strain conditions to rupture failure, showing strain rate effect.

Fig.2 shows the fracture stress and strain curves of the colloid at different compression rates. For the compression rate, we use logarithmic coordinates. From the experimental results, the failure stress and failure strain are not only affected by the concentration of colloids, but also depend on the compression speed. As the compression speed increases, the damage stress and failure strain of the colloid are improved. This result is consistent with that of Gamonpilas [8, 9] and Haman [10] et al. It is noteworthy that with the increase of compression speed, the effect of colloidal concentration on fracture stress is getting smaller and smaller; on the contrary, colloids have more and more influence on fracture strain.



(a) fracture stress

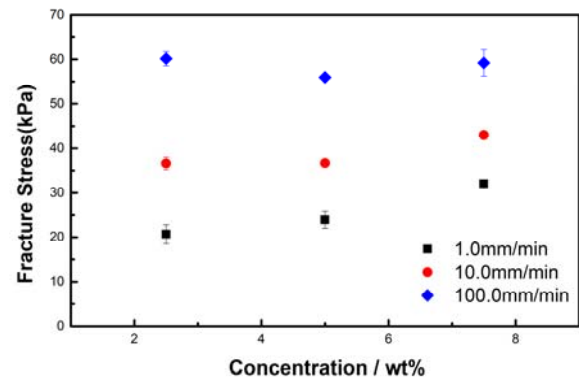


(b) fracture strain

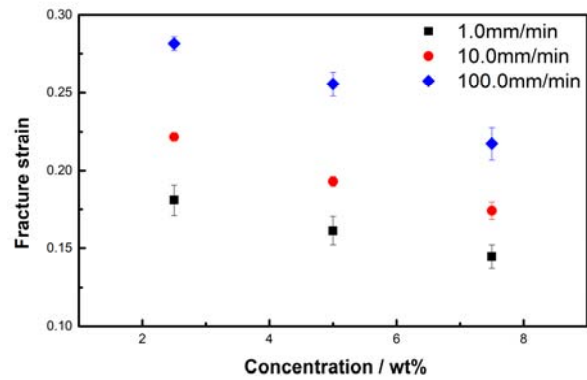
Fig.2. Fracture strength of gels with various compression velocity

Fig.3 shows the relationship between rupture stress and rupture strain and colloidal concentration in the compression process. As the concentration increases, the proportion of dispersoid in the mixture system increases, which leads to the deterioration of the colloidal fluidity. At this time,

the inherent toughness effect of the material is more and more. Therefore, at the same compression speed, the colloidal rupture strain decreases with increasing concentration. It can be predicted that even when the concentration reaches a certain level, the colloidal polymer will break even in brittle form. From the experimental results, when the compression speed reaches 100.0 mm / min, the rupture stress of the three concentrations of colloids are 60.16 kPa, 55.95 kPa and 59.22 kPa, respectively. Compared with the case of low compression rate, the effect of stress is weakened. Fig.4 shows the breakdown of 5.0% and 7.5% agarose gels at a compression rate of 10.0 mm / min. It can be seen from the figure that 5.0% colloidal fluidity is good and can be compressed during compression. It is clearly observed that the material is extruded (the red frame indicates the outline of the colloidal body); for the 7.5% colloid, the fracture of the material occurs at a lower strain rate due to its reduced fluidity and earlier crack growth during compression (Black curve indicates crack).

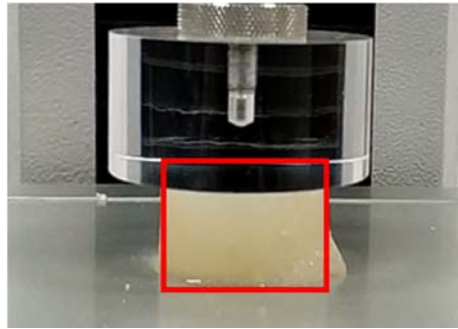


(a) fracture stress

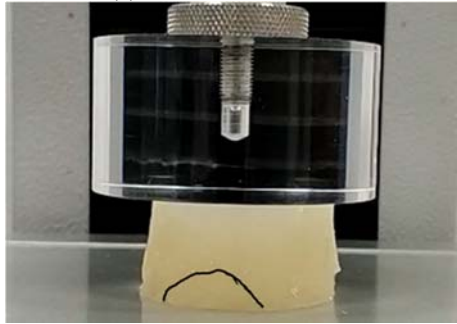


(b) fracture strain

Fig.3. Fracture strength of gel with various concentrations



(a) Concentration 5.0%



(b) Concentration 7.5%

Fig.4. Fracture situation of gels with various concentrations at 10.0mm/min compression velocity

Stress relaxation

Stress relaxation refers to the constant temperature and deformation, stress gradually decay with increasing time. For the colloidal polymer, under the action of external force, the polymer chain is forced to move, resulting in internal stress; in the segment reaches a new equilibrium, the internal stress gradually eliminated. Compared with the linear polymer, the stress of the crosslinked polymer only decays to a certain value σ_∞ without falling to zero.

This paper intends to use the four-element model as shown in Fig.5 for an approximate description of the stress relaxation behavior of agar gel. It consists of two Maxwell models in parallel with a spring unit that is designed for cross-linked polymers, Can make internal stress will not drop to zero.

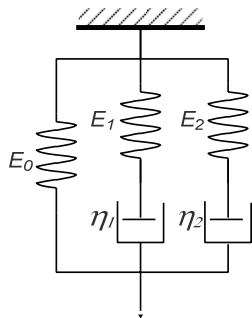


Fig.5. Schematic diagram of four-element model

In the case of constant strain $d\varepsilon/dt = 0$, the stress in the four-element system is distributed to three elements, at this time the equation of motion is:

$$\sigma(t) = \varepsilon_0 E_0 + \varepsilon_0 E_1 e^{-t/\tau_1} + \varepsilon_0 E_2 e^{-t/\tau_2} \quad (5)$$

Where:

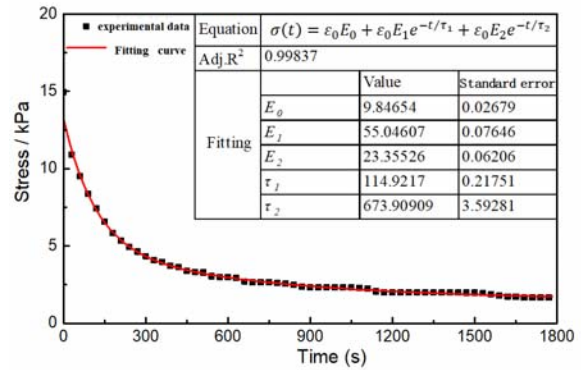
$\sigma(t)$ - relaxation stress;

ε_0 - the initial strain;

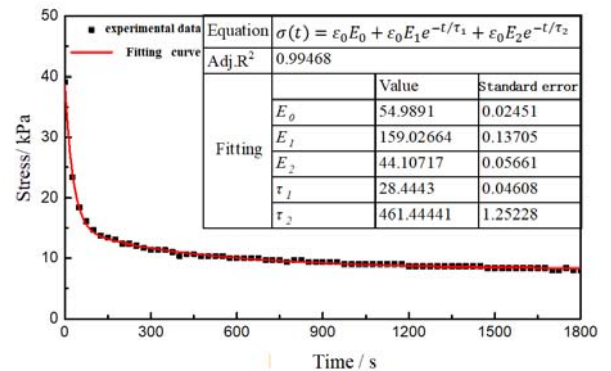
E_i - the spring modulus of the corresponding unit;

η_i -viscosity of the viscous kettle in the corresponding cell;

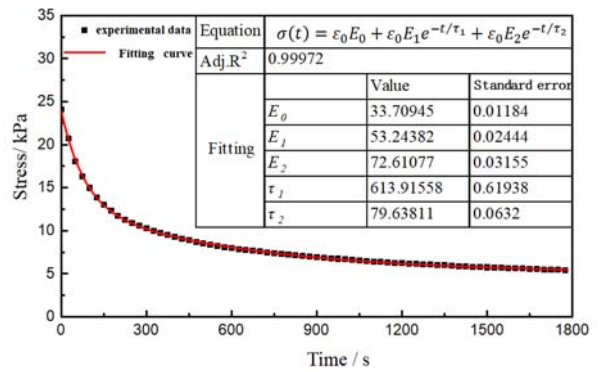
$\tau_i = \eta_i/E_i$ -the relaxation time of the ith unit.



(a) Concentration 2.5%



(b) Concentration 5.0%



(c) Concentration 7.5%

Fig.6. Stress relaxation curves and fitting results of gals at 0.15 strain

Based on the elastic range of the agar gel obtained by the compression experiment, the stress relaxation curve of the agar gel can be obtained by keeping the compression probe stationary in this elastic range. Agar gel stress relaxation curves were obtained using a texture analyzer maintaining strain agar at 2.5%, 5.0% and 7.5% at strain rates of 0.15 at different compression rates. Fig.6 shows the experimental data collected at a compression rate of 10.0 mm / min and the fitted results of the fit were customized by Origin using equation (5).

From the fitting results, the coefficient of determination R^2 is above 0.99, indicating a good fitting effect; from the characteristics of the curve, the stress balance value was positively correlated with the concentration of colloids, the colloidal concentration is higher, the balance of stress relaxation achieved. The value is bigger.

The relaxation time t is defined as the time required for the stress to decrease to 0.368 times the initial stress $\sigma(0)$, and the relaxation time of the three concentrations of colloid is calculated: $t_{2.5\%} = 248.04$, $t_{5.0\%} = 469.4$, $t_{7.5\%} = 102.7$. The concentration of 5.0% of the longest relaxation time of the colloid, the slowest downward trend in stress; 7.5% of the colloidal stress decreased the fastest, in the shortest possible time to reach equilibrium value.

CONCLUSIONS

In this paper, different concentrations of agar gel compression and stress relaxation experiments, the following conclusions:

1. Agar gel is divided into linear elastic phase, non-linear phase and fracture phase in the compression process, and the rupture strength (rupture stress and rupture strain) of gel are affected by concentration and compression rate.

2. Both the rupture stress and the rupture strain of agar gel increase with the increase of the compression rate. However, under the same compression rate, the higher the concentration of colloid, the poorer the fluidity is, the smaller the corresponding rupture strain is. However, There is no clear correspondence between stress and concentration at high compression rates.

3. The defined four-element model can well describe the stress relaxation behavior of agar gel; the higher the concentration, the greater the equilibrium stress, while the relaxation time and concentration have no obvious corresponding relationship.

REFERENCES

- [1] Morris E R, Nisginari K, Rinaudo M. Gelation of gellan – A review. *Food Hydrocolloids*, **28**(2), 373-411 (2012).
- [2] Barrangou L M , Drake M A , Daubert C R , et al. Sensory texture related to large-strain rheological properties of agarglycerol gels as a model food[J]. *Journal of Texture Studies*, 2010, 37(3):241-262.
- [3] Forte A E, D'amico F, Charalambides M N, et al. Modelling and experimental characterisation of the rate dependent fracture properties of gelatine gels. *Food Hydrocolloids* **46**(26), 180-190 (2015).
- [4] Shokrieh M M, Mosalmani R, Omidi M J. Strain rate dependent micromechanical modeling of reinforced polymers with carbon nanotubes[J]. *Journal of Composite Materials*, 2013, 48(27):3381-3393.
- [5] Yun Ma, Yuling Yang, et al. Study on the Texture Properties of Agar Gel. *Food and Fermentation Industries* **33**(9), 24-27 (2007).
- [6] Shilin Liu, Feng Zhu, et al. Study on the Intensity and Relaxation Properties of Agar. *Food Industry Technology* **13**, (2017).
- [7] Charalambides M N, Goh S M, Lim S L, et al. The analysis of the frictional effect on stress - strain data from uniaxial compression of cheese. *Journal of Materials Science* **36**(9), 2313-2321 (2001).
- [8] Gamonpilas C, Charalambides M N, Williams J G, et al. Predicting the Mechanical Behaviour of Starch Gels through Inverse Analysis of Indentation Data. *Applied Rheology* **20** (3), 33283 (2010).
- [9] Goh S M, Charalambides M N, Williams J G. On the mechanics of wire cutting of cheese. *Engineering Fracture Mechanics* **72** (6), 931-946 (2005).
- [10] Hamann D D , Junhua Z , Daubert C R , et al. Analysis of compression, tension and torsion for testing food gel fracture properties[J]. *Journal of Texture Studies*, 2010, 37(6):620-639.

Energy efficiency of impulse drying regimes of beetroot

M. G. Georgieva*, At. I. Tashev, D. G. Atanasov, V. Zh. Georgiev

University of Food Technologies, Department of Industrial Heat Engineering, 26 Maritza Blvd., 4000 Plovdiv, Bulgaria

An experimental research of impulse convective drying regimes of beetroot has been done. The experiments have been grouped in two series according to the periods of heating and cooling. The first group consisted of symmetric experiments with equal periods of heating and cooling, and the second one of asymmetric experiments with a heating period that is two times longer. The temperature of the air during the heating period for both groups was 60°C. The energy consumption for each of the experiments has been determined and compared to the same consumption at the continuous regime. The influence of impulse duration on heat consumption has been analyzed. A saving of energy up to 22% was registered when compared to the continuous drying mode.

Keywords: Drying, beetroot, impulse regimes, specific energy consumption

INTRODUCTION

The drying of foodstuffs is an important and widely used method for preserving [4]. Fresh fruits and vegetables are very perishable due to their high water content of over 80% and putrefaction processes [7, 5, 11]. Drying of food is also important for reducing the weight and volume of the products and for an easier storage and transportation [6]. A relatively high drying rate and high capacity are observed in convective drying.

Beetroot contains valuable active compounds such as carotenoids, polyphenols, flavonoids, saponins and others. Dried beetroot can be consumed in the form of chips or after preparation as a component of instant food, tea, powder in bakery and food supplements [4, 1]. It also can be used in various forms as a red food colorant [4].

The quality of the final dried product is also an important criterion. Drying reflects in changing the properties of the products: discoloring, aroma loss, textural changes, nutritive value and shape. Higher drying temperature reduces the drying time but may result in poor product quality, cracking, deformation or collapse as well as leads to higher energy consumption. Improving energy efficiency in the drying process of food products will support global energy development. Lower temperatures reduce the drying rate and extend the duration of the process [3].

In recent years, new technologies have been developed, and their aim is to improve quality, to reduce the energy consumption, to reduce the harmful impact on the environment and to improve

the safety of foodstuffs [8]. Intermittent drying is one of the technical solutions for this, as it reduces the effective drying time, improves the product quality [3], reduces the energy consumption and non-enzymatic browning [10]. Yang et al. have been reaching the same conclusion, using a heat pump [10]. Intermittent drying is one of the promising solutions for improving the energy efficiency and the product quality without increasing the capital cost of the drier. It is a drying method where drying conditions are variable in time. This can be achieved by the heat supply regimes, varying the airflow rate, air temperature, humidity, or operating pressure. According to Kumar et al. [3] intermittent drying can also be achieved by changing the way energy has been delivered (convection, conduction, radiation or microwave). Intensification of the moisture transfer from the center to the surface of the sample during tempering period has been achieved by the intermittent drying [3, 10]. The drying rate over a constant temperature period is faster than that during the heating period and slower than that during the cooling period. The reasons for this are the directions of the moisture and temperature gradients [10].

Kumar et al. [3] have submitted a possible classification for organizing the impulse drying. [3] A combination of convective drying with intermittent application of ultrasound, infrared heating and microwave has been considered. [3] The proposed classification by Yang et al. consists of 4 categories [10].

The improvement of the energy efficiency and the quality of food products can be achieved by a combination of convective drying and microwave pulse (using microwaves in a convection dryer)

* To whom all correspondence should be sent:
ait79@mail.bg

according to Kumar et al [2]. Experimental investigations with apple slices (from Granny Smith kind apples with a disc thickness of 10mm and a diameter of 40 mm) have been conducted. The air temperature has been 60°C. Periods of microwave influence for 20s and convective drying for 80s have been alternated. A multiphase porous media model has been proposed, and it has been validated by comparison with the experimental results. By this model the moisture content and the temperature field after each heating and tempering period has been investigated [2].

Silva et al. [8] have conducted an experimental investigation intermittent convective drying for whole pears (the kind of Rocha). The investigation has been conducted at two temperatures (40°C and 50°C) and two air velocities (1.28 m/s and 2.66 m/s). From the conducting experiments has been established that the air temperature has higher influence on the drying kinetics, compared to that of the air velocity. Also, shorter drying periods with high relative humidity on supplied air and two temperature levels lead to longer drying period, but to improved organoleptic characteristics, productivity and energy savings [8].

Da Silva et al. [9] compared the experimental results of convective drying of whole bananas in continuous and periodic regimes for 8 hours. The impulse regimes have been symmetrical with the duration of the heating and cooling periods of 0.5h, 1h and 2h. During the heating period, the temperature was 70°C, air velocity was 0.55 m/s, and during the relaxation period, the product has been placed in a desiccator at an ambient temperature of 30°C. After comparing the regimes at the end of the process, the moisture content at a continuous regime has been 0.42, and at the periodical with period of 1h it has been 0.14. The time and the energy consumption for drying have been reduced and the quality of the final product has been increased as a result of the intermittent. Increasing the time for intermittent from 0.5 hours to 2 hours has increased the drying rate [9].

In the literature, an intermittency ratio α is defined as the ratio of the time of the relaxation period to the total time (the sum of the heating and relaxation periods). [3, 9] Yang et al. define it as the ratio of the time of the heating period to the total time [10].

Yang et al. have conducted a comparative simulation study on different intermittent heat pump dryings on Chinese cabbage seeds [10]. The experimental parameters they applied have been: initial moisture content 30% (d.b.), temperature

40°C in heating period, relative humidity 40%, airflow velocity 1m/s, drying time in a range to 1200s. At $\alpha=1/3$ (for intermittent drying), the energy consumed has been 51.9% of that in the continuous drying regime, respectively the energy saving has been 48.1% [10].

Comparing with a continuous process, the energy saving increases with the increase of the intermittency ratio α . A comparison between the improving energy efficiency and the product quality in different impulse regimes also have been done [3].

Aim of the work: The aim of this study is to experimentally determine the optimum impulse regimes for convective drying of beetroot.

MATERIALS AND METHODS

Sample preparation

The process of drying in a thick layer of red beetroot (*Beta vulgaris* ssp. *vulgaris* var. *vulgaris*), has been studied. Beetroots of “Pablo F1” variety were cultivated in a field situated close to Plovdiv (Bulgaria). Roots have been stored at room temperature until use.

The red beetroots of similar size were washed and peeled. Roots were cut into 10 mm cubes by using of a cutter equipped with a knife moving perpendicularly to a horizontal base. The base was covered with thick rubber. The knife of the cutter is a grid with dimensions 10x10 mm.

Drying process

A convective dryer was used to dry red beetroots. It is installed in the Department of Industrial Heat Engineering, University of Food Technologies - Plovdiv.

The process of drying in a thick layer of red beetroot “Pablo F1” variety, has been studied. The red beet was cut into cubes of size 10x10x10 mm.

A dryer was designed and constructed considering the general requirements for drying resulting from pulsed provision of heat. Fig.1 is a schematic diagram of a drying stand which consists of the following basic elements: 1- centrifugal fan, 2 - air ducts, 3 - electric heater, 4 - drying chamber, 5- two-channel regulator MS8111PWM3S, 6 - two-channel microprocessor-based timer MS8203 2Ch, 7- autotransformer, 8- combined sensor “Vektor1” and W – wattmeter.

The drying chamber is in the form of a parallelepiped with dimensions 120x120x160 mm. The centrifugal fan is of the type AV50 / ATII with a power of 50 W and a volumetric flow rate

200m³/h. The electric heater is made of 3 spiral coils with a maximum total power of 2700 W . The ducts have a square cross section with dimensions 50x50 mm. The air ducts, the drying chamber and the electric heater are insulated with aeroflex with a thickness 15mm.

The dryer is equipped with two-channel regulator MS8111PWM3S.Pt100.0, 0 – 200.0°C, 220V with two sensors ST.Pt100.A1.n60.d5.k1500Si-3W to monitor the temperatures before the drying chamber and the ambient air. For the scope of accurately controlling the heat impulse, the system is equipped with two-channel microprocessor-based timer MS8203 2Ch. The relative humidity of the outer air is monitored using a combined sensor “Vektor1”, which reports periodically at an interval of 60 s.

The air is sucked in by the fan, is heated by the electric heater, and then enters the drying chamber. The exhaust air is not regenerated.

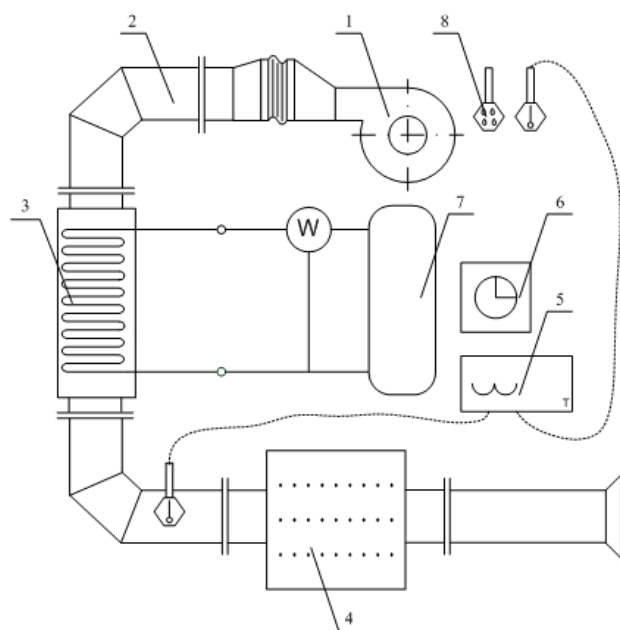


Fig.1. Scheme of the convective dryer

1- centrifugal fan, 2 - air ducts, 3 - electric heater, 4 - Drying chamber, 5 - two-channel regulator MS8111PWM3S, 6 - Two-channel microprocessor-based timer MS8203 2Ch, 7 - autotransformer, 8- combined sensor “Vektor1” and W – wattmeter.

The operating parameters in the drying chamber were: the inlet air temperature during the heating period was 60°C, relative humidity of the air $\phi = 50\%$, air velocity was 2.2 m/s. The loading on the drying chamber was $G/F = 9 \text{ kg/m}^2$.

The experiments were organized in the following three groups.

1st group - continuous modes;

2nd group - symmetric impulse modes: 3+3, 6+6 and 9+9 min;

3rd group - asymmetrical impulse modes are: 3+1.5; 6+3 and 9+4.5 min.

The organization of impulse symmetric and asymmetric modes was automatically made by switching on and off electric heaters by two-channel microprocessor-based timer MS8203 2Ch. The air temperature during the cooling period was 24 °C (ambient temperature).

The energy consumption for each of the experiments was compared to a continuous experiment under the same conditions (amount of evaporated water and ambient temperature).

For each experiment, a drying curve was constructed $U=f(\tau)$. The drying time ($\Delta\tau$) is determined, as it corresponds to the same initial and final humidity and the same amount of evaporated water.

The total dry matter has been determined by gravimetric method with loss of mass on drying. The sample has been dried in an atmospheric oven at $135 \pm 2^\circ\text{C}$. It has been periodically weighed until reaching the constant mass. The mass of the product has been measured by an analytical balance with accuracy of 0.0001 grams.

The total amount of energy consumed for each experiment was measured by a digital multimer with a basic error $\pm 0.01\%$.

Investigation of the kinetics of the drying process

On the basis of experimental data, the drying curves have been drawn Eq.(1).

$$U=f(\tau) \quad (1)$$

From drying curves, the drying rate curves have been drawn by graphical differentiation Eq.(2).

$$\frac{dU}{d\tau} = f(U) \quad (2)$$

where:

U - moisture content,% - kg water/kg drying base;

τ - drying time, min

The drying rate in the first period is described by the Eq.(3):

$$-\frac{dU}{d\tau} = C = const. \quad (3)$$

At the approximation of the drying curve during the second drying period with a straight line (the Fisher's method), the drying rate is described by the Eq.(4):

$$-\frac{dU}{d\tau} = K_c(U - U_p) \quad (4)$$

where: K_c - drying coefficient, %/min;
 U_p - equilibrium moisture content, %. [12]

RESULTS AND DISCUSSION

Tab.1 presents the results for the final energy consumption for all experiments that were conducted. It can be seen that for all experiments in the group of symmetric regimes there is a significant decrease in the energy consumption for drying compared to that of the continuous mode. The highest energy savings (22.6%) was obtained for the mode 3+3.

Table 1. Energy consumption

Regime	Energy consumption, kWh	Energy Reduction,%
continuous	1.99	-
3+1.5	1.966	1.2
6+3	1.969	1.1
9+4.5	1.809	9.1
continuous	1.789	0
3+3	1.384	22.6
6+6	1.424	20.4
9+9	1.533	14.3

There is a slight decrease in energy consumption (about 1%) compared to the continuous mode in the 3+1.5 and 6+3 modes from the group of the asymmetrical modes. Higher energy savings (9.1%) are obtained only in the 9+4.5 mode. In general, it is seen that the application of asymmetric regimes does not lead to substantial energy savings, while increasing the drying time (up to 60 minutes). For this reason, their application to this product and under these conditions is inappropriate.

The reason for the energy savings in impulse drying is the fact that during the cooling period of the product the directions of the temperature and humidity gradient coincide. This results in the reduction of the diffusion resistance and easier movement of the moisture to the periphery of the product. The reason for the differences observed in the energy consumption, for the two groups, is the

ratio of durations of the heating and cooling periods. The drying curves for the two groups of experiments are shown in Fig.2 and Fig.3.

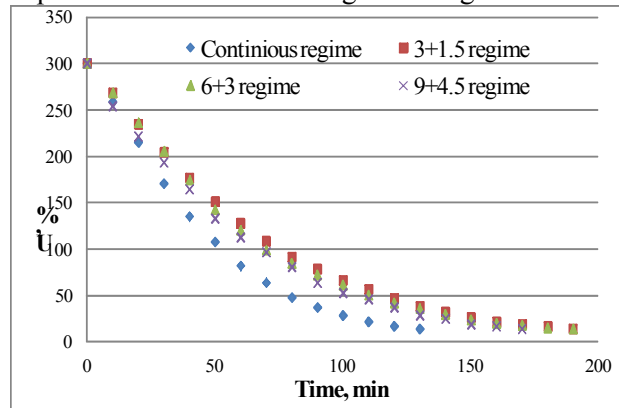


Fig.2. Drying curves for asymmetrical regimes

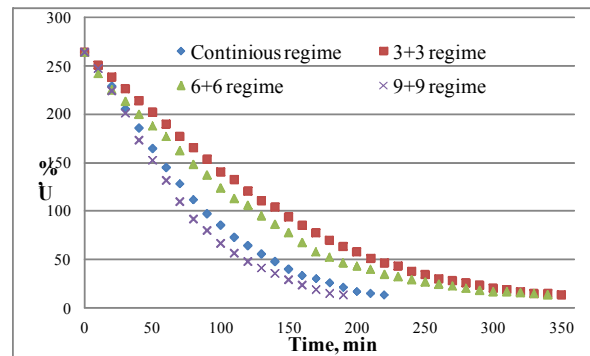


Fig.3. Drying curves for symmetrical regimes

For the group of symmetric regimes, the longest drying time is required for 3+3 mode, followed by 6+6 mode, 350 and 340 minutes, respectively. In 9+9 mode, there is a significant reduction in drying time of up to 190 minutes, which is even 30 minutes less than in continuous mode.

Fig.4 to 7 show the drying rate curves for a second period for the experiments from the group of symmetrical modes and the continuous mode with which they were compared.

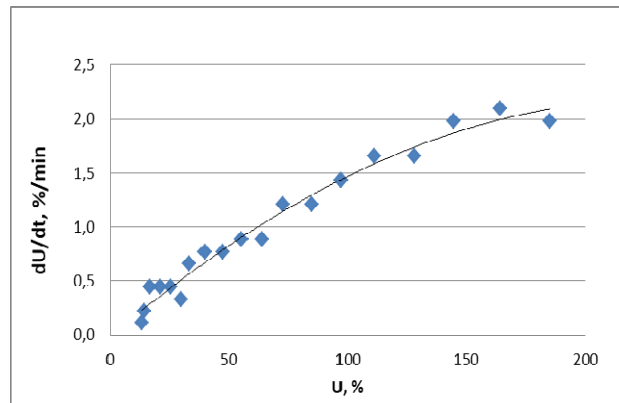


Fig.4. Drying rate curve for the second drying period for the continuous regime

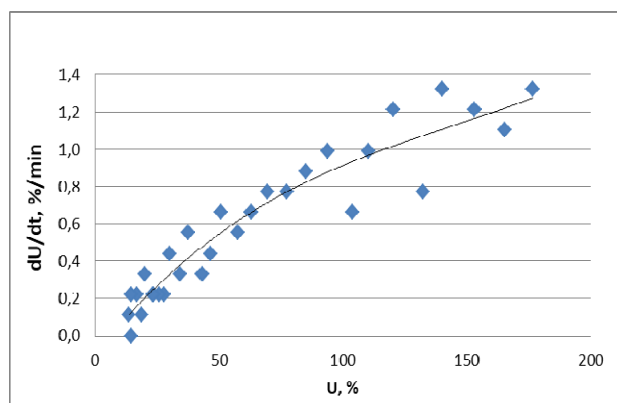


Fig.5. Drying rate curve for the second drying period for the 3+3 regime

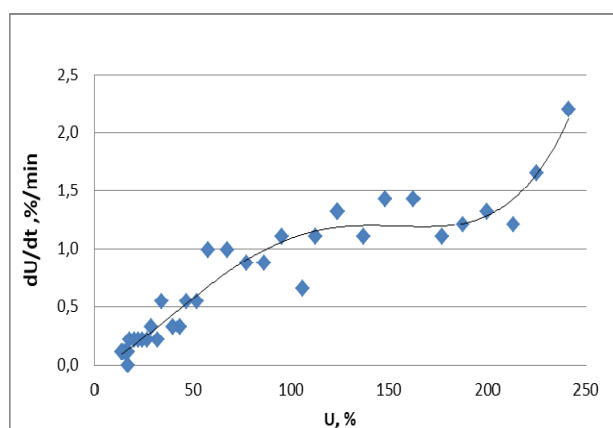


Fig.6. Drying rate curve for the second drying period for the 6+6 regime

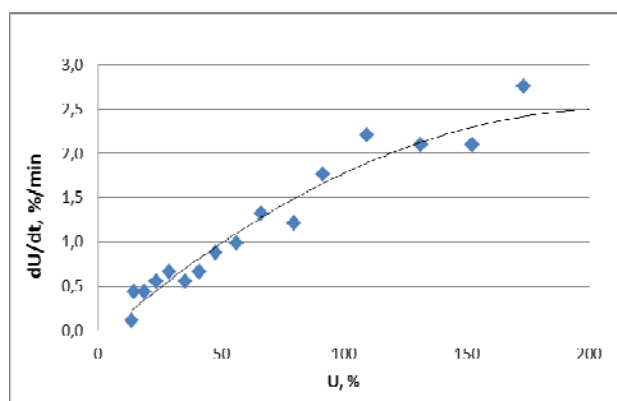


Fig.7. Drying rate curve for the second drying period for the 9+9 regime

It can be seen, from the impulse mode graphs, that there is a significant dispersion of the points due to impulse heat supply.

Tab.2 shows the values of the drying rate for the first period (C , %/min) and the drying coefficient for the second period (K , %/min), calculated on the basis of the drying curves by Fisher's method.

Table 2. The drying rate for the first period and the drying coefficient for a second period

Regime	C , %/min	K , %/min
Continuous	1.9559	0.0309
3+3	1.2241	0.0184
6+6	1.3242	0.0191
9+9	2.2241	0.038

CONCLUSIONS

There is a significant reduction in the energy consumption for drying compared to the continuous mode for all the experiments from the group of symmetrical regimes. Energy savings are in the range from 14.3 to 22.6%.

The energy savings are of lowest number for the group of asymmetric regimes. The energy consumption is comparable to that of continuous drying. This makes the applying of these regimes inappropriate, from an energy point of view.

There is a tendency to decrease the drying time by increasing the impulse duration within the range studied for the symmetrical modes.

The highest values of the of drying rate for the first period and the drying coefficient for the second period are obtained for the 9+9 symmetric mode.

NOMENCLATURE

- α - intermittency ratio, -;
- C - drying rate in the first period, %/min;
- G/F - loading on the drying chamber, kg/m²;
- K_c - drying rate in the second period, %/min
- U - moisture content, % - kg, water/kg drying base;
- U_p - equilibrium moisture content, %;
- φ - relative humidity, %;
- τ - drying time, min.

Subscripts

$d.b.$ - drying base.

REFERENCES

- [1] Adam Figiel. Drying kinetics and quality of beetroots dehydrated by combination of convective and vacuum-microwave methods. *Journal of Food Engineering* **98**, 461–470 (2010).
- [2] C. Kumar, M.U.H. Joardder, T.W. Farrell, M.A. Karim. Multiphase porous media model for intermittent microwave convective drying

- (IMCD) of food. *International Journal of Thermal Sciences* **104**, 304-314 (2016).
- [3] Chandan Kumar, M.A. Karim, Mohammad U.H. Joardder. Intermittent drying of food products: A critical review. *Journal of Food Engineering* **121**, 48–57 (2014).
- [4] Oana-Viorela Nistor, Liliana Seremet (Ceclu), Doina Georgeta Andronoiu, Ludmila Rudi, Elisabeta Botez. Influence of different drying methods on the physicochemical properties of red beetroot (*Beta vulgaris* L. var. *Cylindra*). *Food Chemistry* **236**, 59–67 (2017).
- [5] Pabis S., Jaros M. The first period of convection drying of vegetables and the effect of shape-dependent shrinkage. *Biosyst. Eng.*, **81**, 201 – 211 (2002).
- [6] R. Sivakumar, R. Saravanan, A. Elaya Perumal, S. Iniyar. Fluidized bed drying of some agroproducts – A review. *Renewable and Sustainable Energy Reviews* **61**, 280–301 (2016).
- [7] Stefan J. Kowalski, Joanna M. Lechtańska. Drying of red beetroot after osmotic pretreatment: Kinetics and quality considerations. *Chemical and Process Engineering* **36 (3)**, 345-354 (2015).
- [8] Vítor Silva, Jose J. Costa, A. Rui Figueiredo, Joao Nunes, Catarina Nunes, Tania I.B. Ribeiro, Bruno Pereira. Study of three-stage intermittent drying of pears considering shrinkage and variable diffusion coefficient. *Journal of Food Engineering* **180**, 77-86 (2016).
- [9] Wilton Pereira da Silva, Andréa Fernandes Rodrigues, Cleide Maria D.P.S. e Silva, Deise Souza de Castro, Josivanda Palmeira Gomes. Comparison between continuous and intermittent drying of whole bananas using empirical and diffusion models to describe the processes. *Journal of Food Engineering* **166**, 230–236 (2015).
- [10] Zhao Yang, Enlong Zhu, Zongsheng Zhu, Juan Wang, Siyuan Li. A comparative study on intermittent heat pump drying process of Chinese cabbage (*Brassica campestris* L.ssp) seeds. *Food and Bioprocess Processing* **91**, 381-388 (2013).
- [11] A. S. Mujumdar (ed.). Handbook of Industrial Drying, Third Edition, Taylor & Francis Group, New York, 2007.
- [12] M. Minchev. Drying equipment. UFT Academic Publishing House, Plovdiv, 2012 (in Bulgarian).

BIOTECHNOLOGIES

Application possibilities of open-source software for microbiological analyses

A. M. Danev^{1*}, R. N. Gabrova¹, T. Yaneva-Marinova², A. I. Angelov²

¹University of Food Technologies - Plovdiv, Dept. of Computer systems and technologies, 26 Maritza Boulevard, 4020 Plovdiv, Bulgaria

² University of Food Technologies - Plovdiv, Dept. of Biotechnology, 26 Maritza Boulevard, 4020 Plovdiv, Bulgaria

The main purpose of this paper is to present an approach for automatic microbiological analysis and in particular counting colonies using an open-source software for digital image processing. An open-source computer program called ImageJ is used for developing an algorithm for automatic detection and counting of lactic acid bacterial colonies grown in *MRS* agar. In comparison with commonly used techniques for manually counting of bacterial colonies and the expensive apparatus for microbiological analyses which provide this functionality, the algorithm presented in this paper gives an opportunity for fast, accurate and widely available technique for counting of bacterial colonies in agar medium. A comparative analysis between the proposed algorithm and well known *ImageJ* plugins for semi-automatic counting of bacterial colonies is made. The plugins that are tested are based on implemented in *ImageJ* methods for digital image processing. However, they do not provide a way for separating merged colonies. The results show that in comparison with the other *ImageJ* plugins with high average percentage (obtained after counting lactic acid bacterial colonies), the proposed algorithm achieves better accuracy with lower average percentage error.

Keywords: Open-source software, digital image processing, ImageJ, microbiological analysis, bacterial colonies counting

INTRODUCTION

Various microbiological analyses take a significant part in the food industry and modern technologies for food production and quality evaluation of raw materials. There are a different specialized apparatus and modern machines for performing microbiological analyses but they are too expensive and they can't be used freely by the wide audience. Such a highly specific and expensive apparatuses can be only used in special laboratories.

One of the most commonly used microbiological analysis is counting of bacterial colonies and determination the total microbial count in the sample. In order to perform such kind of analysis a sample with micro-organisms must be taken from the tested raw material or directly from a specific food. Then the sample is placed in a Petri dish called "Agar plate" filled with the culture medium for the specific microorganism. The agar plate can be used either to estimate the concentration of organisms in a liquid culture or the number of that culture in a suitably diluted sample. The micro-organisms contained in the sample begin to grow and multiply under the appropriate conditions forming genetically identical colonies. The colonies differ in shape, size and color depending on the specific microbiological culture. Different colonies can be formed on a single agar

plate. That is why it is important to recognize them and to know the exact number of all colonies grown in each agar plate.

The number of the formed colonies can be counted either manually or by using expensive apparatus with specialized application software for automatic bacterial recognition and using special freely available software applications for PC or smartphones. A brief overview for available free software products for microbiological analyses and in particular bacterial colonies counter applications is made in 2017 [1]. These freely available applications provide a fast and effortless way for enumeration of bacterial colonies, but the results are rather unsatisfactory in comparison to the traditional manual counting.

COMPUTER SOFTWARE FOR BACTERIAL COLONIES COUNTING USING DIGITAL IMAGE PROCESSING TECHNIQUES

Digital image processing is a technology widely used in computer science. Image processing takes a significant part in computer vision and pattern recognition. In brief, image processing using computer systems and applications is a method for performing some operations on an original image taken by a conventional camera, for example, in order to extract useful information needed for a specific analysis. There are various types of computer software applications for image processing as they differ in functionalities, accessibility and price.

* To whom all correspondence should be sent:
angel_danev_bg@abv.bg

Open-source software for digital image analyses – *imagej*

ImageJ is an open-source computer program for digital image processing which provides a lot of functionalities for processing ordinary images taken by a camera as well as scientific multidimensional images. The program is written in objective-oriented programming language *Java* and it is inspired by NIH Image which is a precursor of *ImageJ* [2 and 3]. Because *ImageJ* is written in *Java* the program is platform independent which can be run on any computer with *Java* 1.8 or later virtual machine installed. *ImageJ* has downloadable distributions available for Windows, Mac OS X and Linux. The program can work with the following file formats: TIFF, JPEG, PNG, GIF, BMP, DICOM, PGM, and FITS. Also other formats can be opened with the aid of special free plugins. Because of the fact that *ImageJ* is an open-source software, there are plenty of plugins, macros and extensions freely available for downloading and performing wide variety of tasks in different topics. Different useful programs and plugins for digital image processing based on *ImageJ* functionalities are developed in order to facilitate researchers working in the field of microbiological analyses [6, 11, 12, 13, 18, 19]. *Cell Counter* [15] is an *ImageJ* plugin for manual counting of bacterial colonies, based on simple interface. The plugin counts when the user clicks on the colonies in the image. There are plugins, such as: *Colony Counter* [16], *Colony Blob Count Tool* [17], *ColonyCountJ* [14] based on *ImageJ* functionalities for semi-automatically counting of cells and bacterial colonies.

ImageJ has a large user community which can be useful when a developer get involved with some problems and wants to implement new ideas. *ImageJ* is a powerful tool for fast image processing and the main purpose of the program is to serve on scientific community. A lot of scientific researches from different topics such as biomedical [3] and microbiological analyses, have been made based on the use of the functionality of *ImageJ*. In 2006 a new method based on image analysis using *ImageJ* for determining cyanobacterial biomass by CLSM in stratified benthic sediments are proposed [5]. In 2007 a different approach [7] of using *ImageJ* as an open-source software for digital image processing is presented. In [7] a quantitative analysis for histological staining and fluorescence using *ImageJ* is performed.

ImageJ has relatively easy to use and intuitive interface shown in Fig.1. After launching the program a main screen appears containing a well-

ordered menu bar and a tool bar with the commonly used tools for drawing and editing graphical objects.

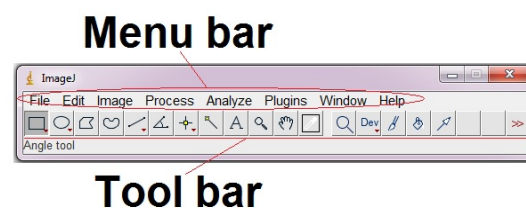


Fig.1. *ImageJ* graphic user interface

As an open-source software for digital image processing *ImageJ* provides various functionalities and plugins for different digital image transformations such as basic image editing tools; filtering algorithms like Mean, Median, Gaussian Blur, Minimum, Maximum, Variance filtering and thresholding on both 8-bit grayscale and RGB color images; tools for pattern recognition; possibilities for automating tasks and creating custom tools using macros; ability for implementing *ImageJ* class library in a different projects such as applets, servlets or applications where image processing is needed; tools for creating, editing and measuring tree types of selections such as rectangular, elliptical or irregular area selections; algorithms for image enhancement like edge detection, smoothing and sharpening; ability for adjustment brightness and contrast of the image; spatial operations such as crop, scale, rotate, resize, flip horizontally and vertically and so on. Some of the most significant functionalities of *ImageJ* are the various types of tools for image analyses such as areas measurements, standard deviation, mean, min and max of entire image or specific selection; tools for lengths and angles measurements using real world measurements units like millimeters. *ImageJ* gives the ability for different color processing in RGB and HSV color space and generating histograms.

Algorithm for automatic counting of bacterial colonies using *ImageJ*

Using some of the functionalities provided by *ImageJ* an algorithm for automatic counting of lactic acid bacterial colonies is developed. The workflow of the algorithm is shown on Fig.2. The algorithm is implemented in *ImageJ* as an additional macro.

For the proper operation of the algorithm a circular region of interest (ROI) is used. The diameter of the ROI is automatically pre-calculated according to the diameter of the agar plates that have been used. Once the ROI is set to appropriate

dimension and position a function provided by *ImageJ* is used for saving the ROI as a template and for future automatic using without the need to be calculated again.

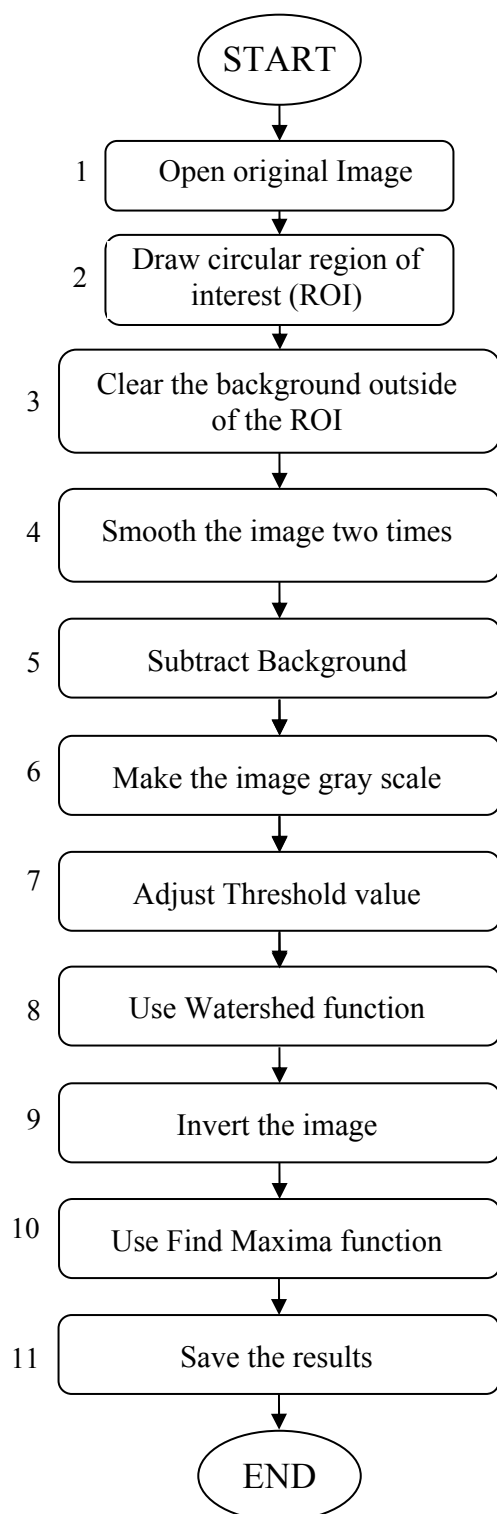


Fig.2. Workflow of the algorithm

During the analyses all agar plates are photographed using smartphone with 13mp camera under the same conditions such as: exactly the same

height between camera lens and the agar plate surface; all agar plates are positioned in the exact same spot on the background surface to ensure the exact positioning of the ROI used later.

The result from execution of some steps from the workflow diagram are shown on Fig.3. Some of the algorithm steps are not shown because the result can't be seen. After the analysis is complete, the results are saved in a text file from where they can be used to plot graphic or to perform some other operations on them.

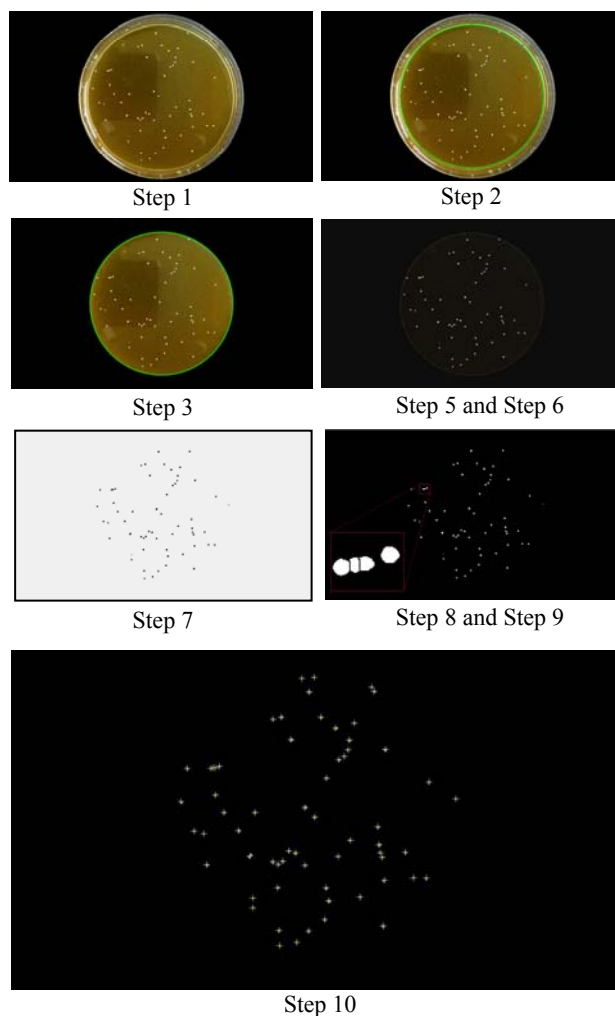


Fig.3. Result images after algorithm steps

Important steps from the algorithm presented above are adjusting the threshold value, using watershed function and using an *ImageJ* function called “Find Maxima”. *ImageJ* provides several popular algorithms for thresholding and for the purpose of this study a default thresholding algorithm is used which is a variation of the IsoData algorithm [8]. The required threshold value must be selected manually to achieve the best results. Using watershed function provided by *ImageJ* library is an essential step in the algorithm

for counting of bacterial colonies. The source code of the macro is shown on Fig. 4.

```
run("ROI Manager...");
roiManager("Open","D:\\BacterialColonies\\ROI\\ROI_1.roi");
roiManager("Select", 0);
setBackground(0, 0, 0);
run("Clear Outside");
run("Smooth");
run("Smooth");
run("Subtract Background...", "rolling=12");
run("8-bit");
setAutoThreshold("Default dark");
setOption("BlackBackground", false);
run("Convert to Mask");
run("Watershed");
run("Invert");
run("Find Maxima...", "noise=145
output=Count");
resultLabel = getResultLabel(nResults-1);
results table
count = getResult("Count");
str = resultLabel + ", " + count;
File.append(str, "D:\\Results\\Results.txt");
close();
```

Fig.4. Source code of the macro

Watershed segmentation is an algorithm for automatically separating particles touching each other. It is a common situation in the process of counting bacterial colonies to have several colonies overlapping each other. It is easy for the human eye to distinguish and count such overlapped group of colonies, but in terms of computer vision and object recognition things are different. This problem is shown on Fig.5. On the first image (on the left) the original image is shown where it is easy for the naked eye to differentiate tree overlapped colonies and one separated from the others. On the second image (the middle one) the same group colonies is shown but after thresholding the image. Here it is not so obvious how much colonies are overlapped. On the right image the overlapped colonies are separated using watershed function and it is easy for a computer program to precisely counting the exact number of overlapped colonies.



Fig.5. Using watershed function

Another important step in the algorithm for counting bacterial colonies is using the function called “Find Maxima” provided by *ImageJ* library. This function determines the local maxima in the selected region from the image, or in the entire image and then creates a binary image or one segmented particle per maximum, marked [9]. As an output type a *Point Selection* option is used which leads to tagging every object different from the background. In the example shown on Fig. 3 the objects representing the colonies are in white color and the background is in black color. As a result of using “Find Maxima” function, each object (colony) from the image is marked with “+” sign (Fig.3 Step 10).

RESULTS

The proposed algorithm for counting of bacterial colonies developed using the open-source software *ImageJ* provides a fast way for microbiological and biotechnological analyses. It doesn’t need special apparatus or any additional experimental settings for receiving the primary data, because using a smartphone camera for taking pictures is easy, quick and cheap way for getting the initial information from the objects under control.

For the purpose of this study photos of agar plates with colonies formed by lactic acid bacteria - *Lactobacillus plantarum* strain *BOM2* in an 8-hour fermentation process (under 37°C) of 6% oat suspension are analyzed. The bacteria have developed and formed colonies in the culture medium *Lactobacillus* MRS agar. Each of the photos is taken with a regular smartphone camera under a daylight. The total number of colonies in each agar plate can range from a few tens to few hundreds depending on the type of the dilution of the bacterial suspension prior to spreading them on the agar plates, and on the time for which the bacteria developed. According to the general rules for enumeration of bacterial colonies the total number of colonies on each agar plate must range from 30 to 300 [10]. For the purpose of this study and in order to determine the accuracy of the suggested algorithm, several agar plates with more than 300 colonies are included in the experimental results, but they can’t be used for performing accurate microbiological analyses. On the other hand, the colonies may differ in their size. As an example, some photos (nine) of the analyzed agar plates with different number of colonies and size are shown in Fig.6.

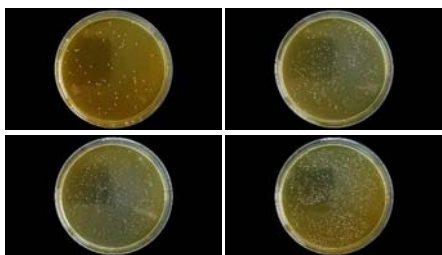


Fig.6. Agar plates with different total number of colonies

The total number of bacterial colonies for each of the analyzed agar plates is counted once manually and then automatically using a computer software with the algorithm described above. The analyzed agar plates, shown in Fig.7, are ordered according to the rate of dilution and the time, and the result data after manually and automatically counting is shown on Fig.8. For each group one, two or three agar plates (samples) with different total number of bacterial colonies are analyzed. The percentage error is calculated by Eq.(1) and it varies between 0.94% and 3.44%.

$$\text{Percent error} = \frac{N_{mc} - N_{ac}}{N_{mc}} * 100 \quad (1)$$

where:

N_{mc} - total number of colonies counted manually;

N_{ac} - total number of colonies counted automatically;

Tab.1 shows the average results for each group of samples which have been transformed in order to achieve appropriate results for plotting a growth curve.

The main purpose of counting the total number of bacterial colonies in agar plates is to plot the growth curve of microbial population. It is shown on Fig.9. The microbial growth curve is a graphical representation of changes in cell counts, biomass, or other suitable microbial growth indicator for a given microorganism in a suitable medium. The curve can also be used for determination of the growth phases which are – Lag phase, Exponential phase, stationary phase and phase of extinction.

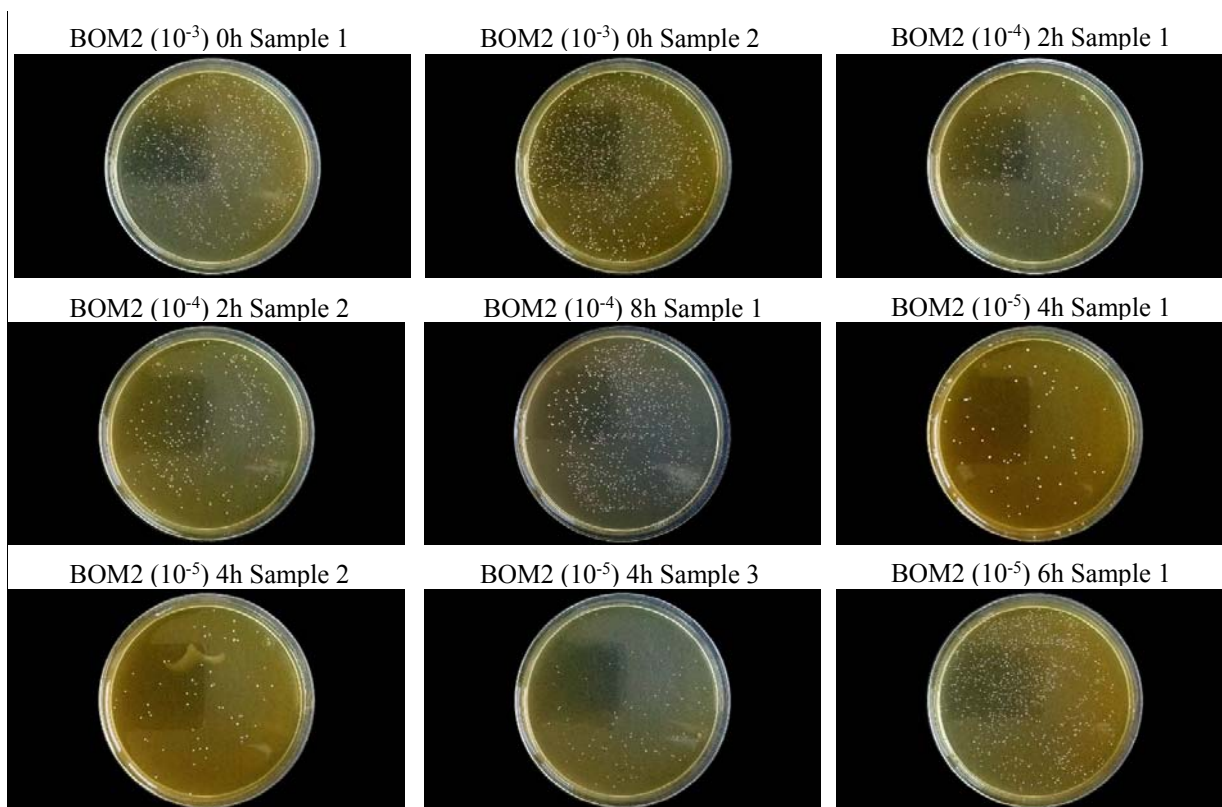


Fig.7. Analyzed agar plates ordered according to the rate of dilution and the time

Table 1. Results according to automatic counting of colonies formed by *Lactobacillus plantarum* strain BOM2 in an 8-hour fermentation process (under 37 °C) of 6% oat suspension

10 ⁷ CFU/ml	0h	2h	4h	6h	8h
<i>Lactobacillus plantarum</i> , BOM2	1,4000	2,8450	7,5666	11,6100	13,7500

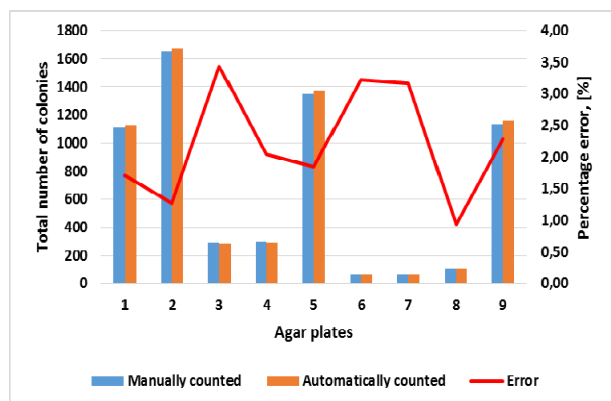


Fig.8. Graphic representation of results data and percent error

As it can be seen from Fig.8 the biggest percentage error is about 3.4% and the smallest percentage error is about 1%. The average error for this set of tested samples is about 2.2%. Therefore, the proposed algorithm can be successfully used for counting lactic acid bacterial colonies grown in *MRS* agar.

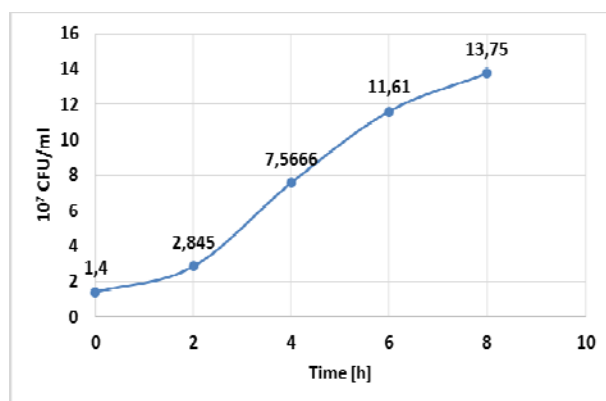


Fig.9. Growth curve of *Lactobacillus plantarum* BOM2 population

With respect to different *ImageJ* plugins and approaches for automatically counting of bacterial colonies, a comparative analysis of our own approach is made. The results achieved after using *Colony Counter* and *Colony Blob Count Tool* plugins are shown respectively in Tab.2 and Tab.3.

As it can be seen from Tab.2 the relative error (25.37) is very high and *Colony Counter* plugin can not be used for automatically counting lactic acid bacterial colonies strain *BOM2* grown in *MRS* agar. The plugin do not provide a functionalities for separating and counting merged colonies and for setting a region of interest.

The relative error after counting lactic acid bacterial colonies using *Colony Blob Count Tool* is 16.84%. This macro achieves better results than the plugin *Colony Counter*, but have some problems. To achieve these results the user have to pre-set

specific settings manually, depending on the sample being tested. Also, the user must know in advance the exact area (in pixels) of the smallest and the biggest colonies in the image. This leads to performing additional manual steps with *ImageJ* functionalities for measuring. This macro does not provide a functionalities for separating merged colonies. A result image after automatically counting lactic acid bacterial colonies using *Colony Blob Count Tool* is shown on Fig. 10.

Table 2. Results after counting with *Colony Counter*

Sample №	Manual Counting	ImageJ Colony Counter
BOM2 (10-3) 0h Sample 1	1108	865
BOM2 (10-3) 0h Sample 2	1653	929
BOM2 (10-4) 2h Sample 1	291	277
BOM2 (10-4) 2h Sample 2	294	286
BOM2 (10-5) 4h Sample 1	62	79
BOM2 (10-5) 4h Sample 2	63	83
BOM2 (10-5) 4h Sample 3	107	107
BOM2 (10-4) 8h Sample 1	1350	1180
BOM2 (10-5) 6h Sample 1	1135	1030
SUM	6063	4836
ΔA = Absolute Error [number of colonies]:	0	1227,00
Relative error [%]:		25,37

Table 3. Results after counting with *Colony Blob Count Tool*

Sample №	Manual Counting	ImageJ Colony Blob Count
BOM2 (10-3) 0h Sample 1	1108	870
BOM2 (10-3) 0h Sample 2	1653	1360
BOM2 (10-4) 2h Sample 1	291	270
BOM2 (10-4) 2h Sample 2	294	282
BOM2 (10-5) 4h Sample 1	62	54
BOM2 (10-5) 4h Sample 2	63	61
BOM2 (10-5) 4h Sample 3	107	110
BOM2 (10-4) 8h Sample 1	1350	1124
BOM2 (10-5) 6h Sample 1	1135	925
SUM	3302	2826
ΔA = Absolute Error [number of colonies]:	0	476,00
Relative error [%]:		16,84

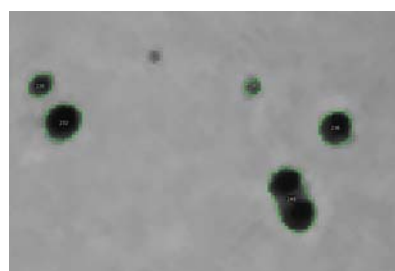


Fig.10. Result image after counting bacterial colonies with the macro *Colony Blob Count Tool*

The tested *ImageJ* plugins can be considered as programs for semi-automatic counting of bacterial colonies, because of the fact that the user have to perform additional steps using some of the *ImageJ* functionalities in order to evaluate the exact area of the colonies grown in the agar.

CONCLUSIONS

An algorithm for automatic counting of bacterial colonies in agar plates using freely available and open-source computer software for digital image processing is developed. The algorithm is based on build-in functionalities and tools in the program *ImageJ* and provides an approach for fast and accurate counting of bacterial colonies for the purpose of microbiological and biotechnological analyses. Several agar plates with different total amount of colonies formed by lactic acid bacteria *Lactobacillus plantarum* strain *BOM2* and *Lactobacillus MRS* agar medium are analyzed in order to evaluate the accuracy of proposed algorithm. The total number of colonies for each agar plate is counted in two ways – manually and automatically using algorithm implemented in open-source software as a macro. The results obtained from the manual counting and from the macro are compared and a percentage error is calculated. The obtained results and the analyses that have been performed lead to conclusion that the presented algorithm can be successfully used to determine the total number of bacterial colonies in the processes of microbiological and biotechnological analyses.

The algorithm mentioned in this paper for automatic counting of bacterial colonies can be implemented as a useful smartphone application in the future work.

REFERENCES

- [1] Danev A. M., R. Gabrova, „Open-source software products for microbiological analyses. A mini review“, Scientific works of University of Food Technologies, 64(1), (2017).
- [2] Schneider, C. A.; Rasband, W. S. & Eliceiri, K. W. "NIH Image to ImageJ: 25 years of image analysis". *Nature methods*, **9(7)**, 671-675, (2012), PMID 22930834.
- [3] Schindelin, J., Rueden, C. T. & Hiner, M. C. et al. (2015), "The ImageJ ecosystem: An open platform for biomedical image analysis", *Molecular Reproduction and Development*, ISSN: 1098-2795 (Online), PMID 26153368.
- [4] Silva A. F., G. CarvalhoEmail, A. Oehmen, M. Lousada-Ferreira, A. van Nieuwenhuijzen, M. A. M. Reis, M. T. B. Crespo, "Microbial population analysis of nutrient removal-related organisms in membrane bioreactors". *Applied Microbiology and Biotechnology* **93(5)**, 2171–2180 (2012).
- [5] A. Sole, J. Mas, I. Esteve, "A new method based on image analysis for determining cyanobacterial biomass by CLSM in stratified benthic sediments". *Ultramicrosc.* **107**, 669–673, (2007).
- [6] T. J. Collins, "ImageJ for microscopy". *BioTechniques* **43(1)**, 25-30 (2007).
- [7] Jensen E.C., "Quantitative analysis of histological staining and fluorescence using ImageJ". *The Anatomical Record* **296**, 378–381, (2013).
- [8] Ridler, TW & Calvard, S, "Picture thresholding using an iterative selection method". *IEEE Trans. on Systems, Man & Cyber.* **8**, 630-632, (1978).
- [9] Edelstein A., N. Amodaj, K. Hoover, R. Vale, Nico Stuurman. Computer control of microscopes using µManager. *Curr Protoc Mol Biol*, Chapter 14:Unit 14.20, 2010, doi:10.1002/0471142727.mb1420s92
- [10] Denkova Z. R., R. S. Denkova, V. B. Yanakieva, I. N. Dobrev, „Food microbiology. Exercise Guide“, UFT Academic Publishing House of, Plovdiv, (in Bulgarian), (2015).
- [11] Masala G. L., U. Bottigli, A. Brunetti, M. Carpinelli, N. Diaz, P. L. Fiori, B. Golosio, P. Oliva and G. Stegel, "Automatic cell colony counting by region-growing approach", *IL NUOVO CIMENTO*, (2007), DOI 10.1393/ncc/i2007-10273-3.
- [12] Choudhry P. (2016) „High-Throughput Method for Automated Colony and Cell Counting by Digital Image Analysis Based on Edge Detection“. *PLoS ONE* 11(2): e0148469. doi:10.1371/journal.pone.0148469.
- [13] Ivan V. Grishagin, "Automatic cell counting with ImageJ", *Anal. Biochemistry* 473 (2015) 63–65.
- [14] Maurya D.K. (2017) "ColonyCountJ: A User-Friendly Image J Add-on Program for Quantification of Different Colony Parameters in Clonogenic Assay", *J ClinToxicol* 7: 358. doi:10.4172/2161-0495.1000358.
- [15] Kurt De Vos, University of Sheffield, Academic Neurology, [www] Available from: <https://imagej.nih.gov/ij/plugins/cell-counter.html>, Accessed on: 17.11.2018;
- [16] Vieira B., University of Lisbon, Colony Counter, [www] Available on: <https://imagej.nih.gov/ij/plugins/colony-counter.html>, [Accessed on: 06.12.2018].
- [17] ImageJ-macros, Colony Blob Count Tool, [www] Available on: http://dev.mri.cnr.fr/projects/imagej-macros/wiki/Colony_Blob_Count_Tool, [Accessed on: 06.12.2018].
- [18] Heras J., C. Domínguez, E. Mata, C. Larrea, V. Pascual C. Lozano, C. Torres, M. Zarazaga, GelJ – a tool for analyzing DNA fingerprint gel images, *BMC Bioinformatics* (2015), <https://doi.org/10.1186/s12859-015-0703-0>
- [19] Alonso CA, C. Domínguez, J. Heras, E. Mata, V. Pascual, C. Torres, M. Zarazaga, Antibioqramj: A tool for analysing images from disk diffusion tests, *Comput Methods Programs Biomed.* (2017) 143:159-169, doi: 10.1016/j.cmpb.2017.03.010

Study on driving mechanical model of microcapsules based on fluid-structure interaction in intestinal tract

Xiao Li^{1,2}, Jinghu Yu^{1,2*}

¹School of Mechanical Engineering, Jiangnan University Wuxi, Jiangsu 214122, China

²Jiangsu Province Key Laboratory of Advanced Food Manufacturing Equipment and Technology, Wuxi, Jiangsu 214122, China

The research of the active capsule endoscopy in the digestive tract is current hotspot. However, the difficult control of capsule endoscope restricts its further application. In this paper, stress of Capsule in a viscous liquid environment was analysed theoretically and the mechanical model of Capsule with different sizes of round and oval head shapes was established. Based on the drive model, the dynamic characteristics of the magnetic drive capsule with different shapes in the gut traveling was studied under the action of Fluid-structure Interaction. With COMSOL Multiphysics bidirectional Fluid-structure interaction module, the relationship of the capsule exercise stress with the gut dynamic viscosity, the capsule size and capsule shape was analysed. Based on the standard k - epsilon turbulence model, the intestinal fluid model and the intestinal wall model were created. With the different created model of capsule, intestinal fluid and intestinal wall, the multiple factors and levels of numerical simulations were carried out. The results were listed as follows: 1) At the same level of dynamic viscosity and intestinal wall dimension parameters, oval head capsule driving resistance decreased about 9.3-16.3% compared to that of circular capsule. 2) The stress model of the capsule could be used as an active control model in the intestinal diagnosis and treatment of magnetic displacement active capsule endoscope, which is of great significance to the application of the capsule endoscope.

Keywords: Fluid-structure interaction, microcapsule endoscopy, intestinal tract, driving mechanical model

INTRODUCTION

The microcapsule robot has a broad development prospect in the medical field as the new digestive tract medical device. The drive mode of capsule endoscope driven by external magnetic field mainly includes the rotary magnetic field control and the permeability control of quasi-static magnetic field control. At present, the problems of inaccurate localization and low attitude control accuracy of capsule robots are the shackles of the development of microcapsules. Tan Renjia et al. [1] established a Ciarletta hyperelastic resistance model for the critical sliding resistance of quasi-static interaction between magnetic-driven capsule endoscopy and intestinal tract. The results showed that the ratio of endoscopy diameter to intestinal tube diameter (R/r) had a significant effect on sliding resistance. The friction force of the head of the capsule was less than 1%. Li Chuanguo et al. [1] proposed an inchworm-like capsule robot which can achieve axial and radial expansion. It uses DC motor to control and clamp the

oil bag to achieve peristalsis. Its maximum radial output force is 150 g, and its complete peristaltic step distance is 9.5 mm. Zhang Yu et al. [1] in viscous Newtonian fluid environment, the liquid resistance moment of petal-shaped and cylindrical side-wall rotary capsule robot was analyzed in the pipeline. The cylindrical side-wall tiles in the four capsule structures showed large eccentricity e_s , which reflected good driving effect. The intestinal wall was defaulted to be rigid body in the model. Chi Minglu et al. established the space magnetic moment model of the universal rotating magnetic vector, improved the slip angle and horizontal angle of the magnetic precession petal capsule endoscope, improved the non-contact driving performance, and had a significant effect on reducing the distortion of the intestinal tract when the capsule turned.

In this study, a force model of capsule motion in viscous resistance fluid environment of elastic intestinal tract was established for a permeable capsule robot with elliptical and circular head shell shapes. Two kinds of capsules with different shapes were numerically simulated under different viscous fluid environments with different dynamic

* To whom all correspondence should be sent:

jhyu@jiangnan.edu.cn

viscosities and intestinal diameters. The stress distribution of the permeable capsule under the interaction of the elastic intestinal wall and viscous fluid and the influence of the capsule on the fluid and intestinal tract were analyzed. The theoretical basis was provided for the shape optimization and accurate positioning of the magnetic-driven capsule robot in viscous and elastic intestinal environments.

STRESS ANALYSIS OF CAPSULE

The mechanical model of the capsule in the liquid intestinal fluid environment can be approximated as the force model of moving objects in the liquid pipeline [1]. The resistance to motion of the capsule F_d is mainly divided into two parts: fluid dynamic pressure F_p and viscous resistance of fluid F_f , namely:

$$F_d = F_p + F_f \quad (1)$$

Head impact resistance

When the capsule is moving in the intestinal flow field, v_r is the axial relative motion velocity of the capsule robot and the fluid in the intestinal tract and dS is the head surface unit of the capsule shown as Fig.1 below. The axial force that fluid impact on the head of the capsule is F_p :

$$F_p = \int_{\Omega} dF_{p1} \quad (2)$$

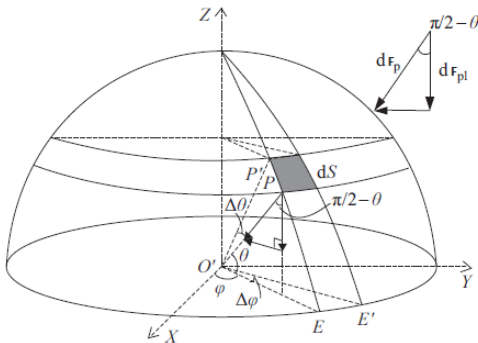


Fig.1. Schematic diagram of force element on the head of capsule

And:

$$df_{p1} = \sigma_c(\theta) \cdot \vec{n} \cdot dS \quad (3)$$

\vec{n} - unit normal vector to the center.

$\sigma_c(\theta)$ - impact stress of unit body is subjected to fluid, which can be known from the fluid dynamics:

$$\sigma_c(\theta) = \rho v_r^2 \sin^2 \theta \quad (4)$$

To the unit surface dS :

$$dS = R^2 \sin \theta d\theta d\varphi \quad (5)$$

The formula Eq.(3), (4) and (5) are introduced into Eq.(2):

$$F_p = \int_0^{2\pi} \int_0^{\alpha} R^2 \rho v_r^2 \sin^4 \theta d\theta d\varphi \quad (6)$$

where:

θ - Angle between the unit method (pointing to the center O) and the XOY Plane, -;

R - radius of capsule head, m;

ρ - fluid density, kg/m³;

φ - the Angle between the unit surface normal vector and the XOZ Plane, -;

v_r - the axial average velocity of the fluid relative capsule, m/s.

Viscous resistance

The viscosity of the intestinal fluid is not negligible [5], Viscous resistance of capsule head is F_{f1} , resistance of the middle cylinder is F_{f2} , F_f is viscous resistance of the fluid in the capsule movement:

$$F_f = F_{f1} + F_{f2} \quad (7)$$

(1) Viscous resistance of capsule head

For the intestinal wall head unit dS , there is a corresponding resistance unit dF_{f1} :

$$dF_{f_1} = \frac{\mu v_t \cos \theta}{h(\theta)} dS \quad (8)$$

$h(\theta)$ is the distance from the inner wall of the intestinal tract, as a function of θ .

For the sphere:

$$h(\theta) = H - R \cos \theta \quad (9)$$

References Eq.(2) include:

$$F_{f_1} = \int_{\Omega} dF_{f_1} \quad (10)$$

Bring Eq.(9) back to the above formula and integrate:

$$F_{f_1} = \int_0^{2\pi} \int_0^{\alpha} \frac{\mu v_t R^2 \sin^2 \theta \cos \theta}{H - R \cos \theta} d\theta d\varphi \quad (11)$$

(2) Viscous resistance of column

The viscous resistance between the capsule and the intestine can be considered as the model of viscous resistance between two parallel plates. According to the calculation formula of viscous resistance:

$$F_{f_2} = \mu A \frac{v_r}{h} \quad (12)$$

A is the contact area of capsule side and liquid:

$$A = \pi R(l - 2R) \quad (13)$$

So:

$$F_{f_2} = \mu \pi R(l - 2R) \frac{v_r}{H} \quad (14)$$

v_r - the axial average velocity of the fluid

relative to the capsule, m/s;

R - the spherical radius of the capsule, m;

l - length of the capsule, m;

H - average distance between capsule wall and intestinal wall, m;

μ - dynamic viscosity of the intestinal fluid, $Pa \cdot s$.

NUMERICAL SIMULATION MODEL

Considering the coupling effect of human intestinal wall elastomers on intestinal fluid motion, the COMSOL Multiphysics bidirectional Fluid-structure interaction module was used to simulate the drive of the capsule [5]. Flow field was set as $k - \epsilon$ turbulence transient model. The intestinal model parameters were set as: Length: $l = 200\text{mm}$, Width: $B = 25\text{mm}$, Intestinal wall thickness: $b = 2\text{mm}$. The intestinal material model USES hyperelastic material. In order to reduce the stress concentration distortion caused by fixed constraints at both ends, the distance between the ends of the capsule and the outlet of the fluid was set as $L_0 = 35\text{mm}$, The physical field control grid is used to improve the grid quality to eliminate the boundary effect.

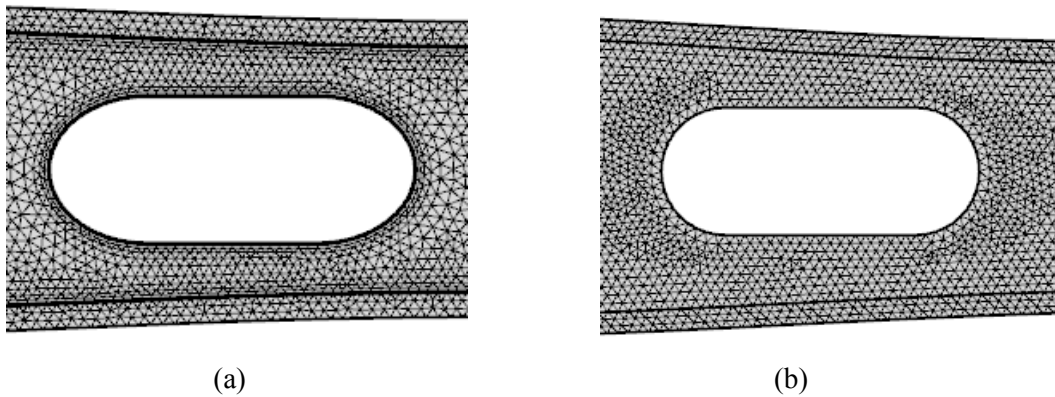


Fig.2. Model grid division $\mu = 5.3, D = 22.1$ (a) Elliptical (b) Circle

The left and right sides of the intestinal wall model are set as fixed end constraints, and the speed of the capsule moving wall was set as $v = 20\text{mm/s}$.

The average of the flow velocity $\bar{v}_n = 20\text{mm/s}$.

Stress monitoring points were inserted into the

middle head and middle of the capsule shell in order to fully detect the force of the outer wall of the capsule. The von-mises stress value σ_m which obtained by the probe were main evaluation parameters of the force of the capsule [5].

NUMERICAL SIMULATION

The kinetic viscosity of the intestinal fluid μ and the intestinal tract size D , each of the two parameters takes two levels which are used for coupling field simulation:

Table 1. Parameter values of each factor

Intestinal fluid dynamic viscosity	Intestinal size	Shape of capsule
μ / mPa·s	D / mm	S / -
5.3	22.1	Circle (C)
20.7	24.5	Ellipse (E)

There are few parameters in this numerical simulation **Error! Reference source not found.** Dynamic viscosity parameters and intestinal size parameters only set two parameter levels, so there is no orthogonal numerical simulation. According to the experimental group combination matching model listed below, 8 groups of prepared capsule intestinal

models were imported into COMSOL. The stress probe is inserted at the designated monitoring point and is solved. The transient solver adopts full coupling automatic (Newton) nonlinear method. The value of Relative tolerance is to be determined to 0.001. The damping factor was restored to 0.75 to ensure the efficiency of the solution.

Table 2. Parameter configuration of the experimental group

FACTOR	μ $\times 10^{-3}$ Pa·s	D mm	S -
NO.1	5.3	22.1	C
NO.2	5.3	22.1	E
NO.3	5.3	24.5	C
NO.4	5.3	24.5	E
NO.5	20.7	22.1	C
NO.6	20.7	22.1	E
NO.7	20.7	24.5	C
NO.8	20.7	24.5	E

INTERPRETATION OF RESULT

The numerical simulation results of 4 sets of

endoscope parameters at $D = 22.1$ mm were selected [8]. The distribution of stress distribution and the distribution of the flow velocity field of intestinal fluid are shown as Fig.3.

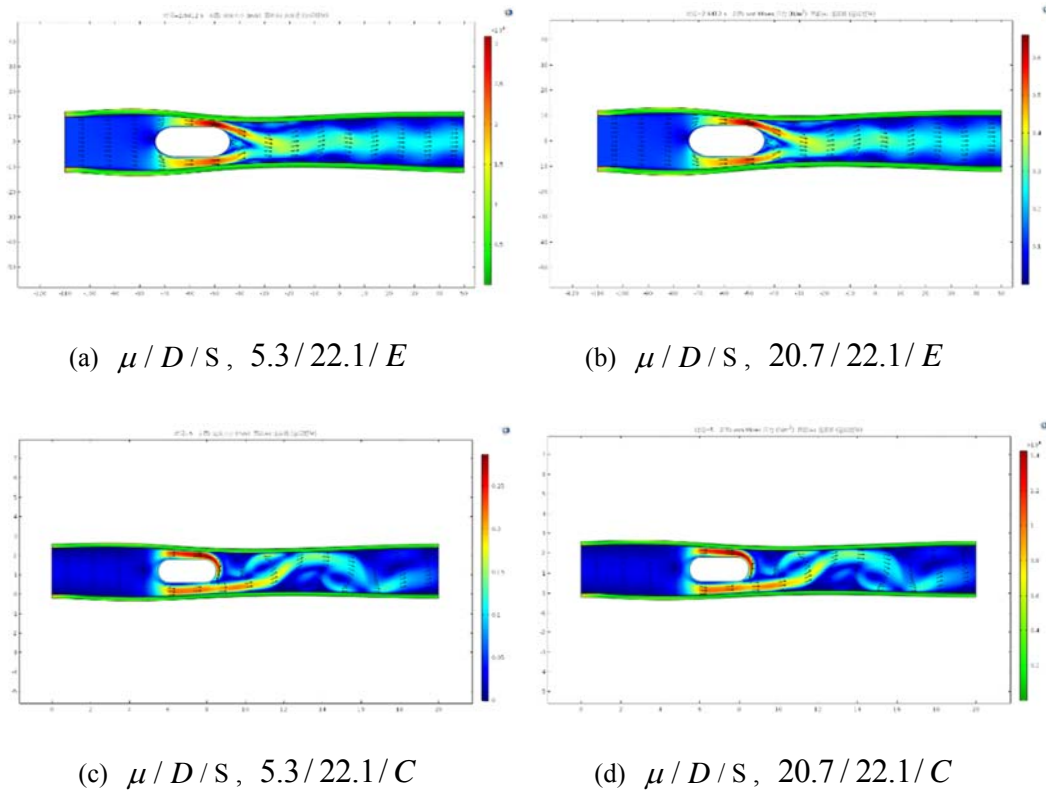


Fig.3. Velocity distribution and intestinal stress cloud diagram of the same intestinal size ($D=22.1\text{mm}$) under $t=3.0\text{s}$

The results showed that the maximum velocity was found near the capsule at low viscosity: $\mu = 5.3$ and $\mu = 20.7$. The velocity of the third second is respectively $v = 0.315\text{m/s(E)}$ and $v = 0.310\text{m/s(C)}$, Maximum stress in the model wall are 7.75kPa(E) and 9.07kPa(C) which mainly happens near the fixed

end of the entrance. This indicates that there is still gravitational concentration at the fixed end. Another thing to note is that, group 2 and 6 of elliptic shapes formed a stable wake. In contrast, group 1 and 5 of the round capsule showed a more obvious disturbance.

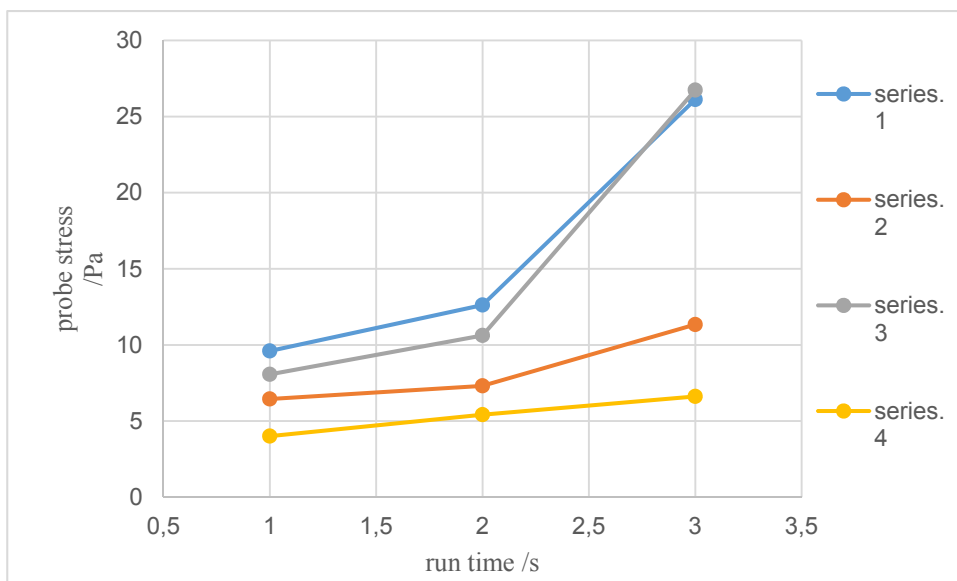


Fig.4. Stress of capsule head $\mu = 5.3 \times 10^{-3} \text{ Pa} \cdot \text{s}$

Table 3. The stress value of the head probe $\mu = 5.3 \times 10^{-3} \text{ Pa} \cdot \text{s}$, σ_t / Pa

GROUP	1	2	3	4
T=1S	9.605	6.450	8.070	4.010
T=2S	12.617	7.310	10.620	5.420
T=3S	26.12	11.340	26.740	6.620

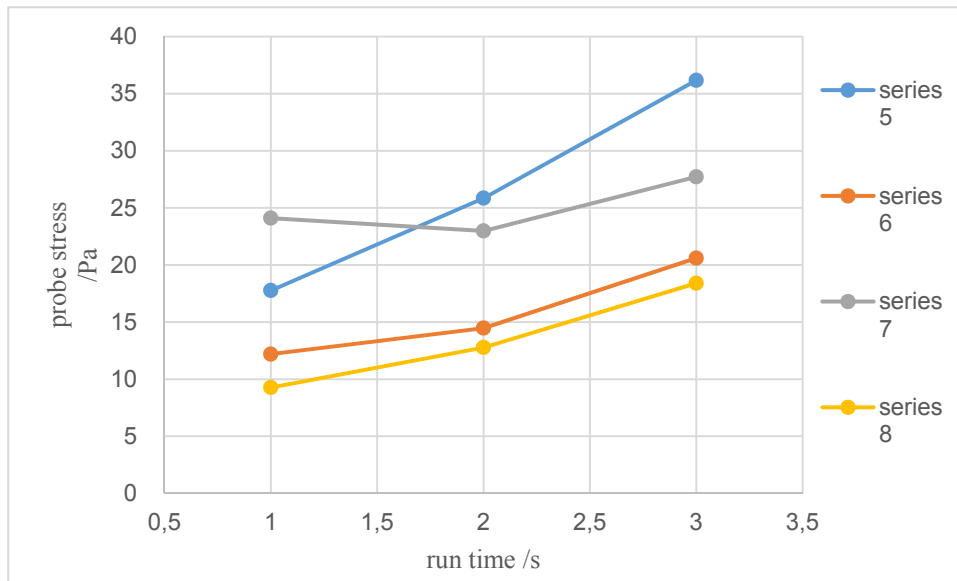


Fig.5. Stress of capsule head $\mu = 20.7 \times 10^{-3} \text{ Pa} \cdot \text{s}$

The stress distribution of the index points of each group in 3s was measured and the results were grouped according to the shape of the capsule (Fig.4, 5). The results showed that the movement stress of the capsule was higher when the viscosity was higher. In the level of the dynamic viscosity parameter $\mu = 20.7 \times 10^{-3} \text{ Pa} \cdot \text{s}$. Series 3, 4 represents the

elliptical head stress within the different sizes of the intestinal tract, the stress mean 19.21Pa is lower than the circular head 21.17 Pa, which represents a 9.3% lower than that of the series 1, 2 in 3s, and the head stress is 16.3% lower than the stress under the level of $\mu = 5.3 \times 10^{-3} \text{ Pa} \cdot \text{s}$.

Table 4. The stress value of the head probe $\mu = 20.7 \times 10^{-3} \text{ Pa} \cdot \text{s}$, σ_t / Pa

GROUP	1	2	3	4
T=1S	17.760	12.190	24.097	9.270
T=2S	25.850	14.470	22.972	12.770
T=3S	36.170	20.600	27.717	18.400

CONCLUSIONS

In this numerical simulation, the dynamic force model of active capsule robot in viscous fluid of human intestinal environment was analyzed

theoretically. The Comsol Multiphysics module was used to simulate the fluid solid coupling in different environments for capsule movement. The results showed that:

- (1) Under different dynamic viscosities and

intestinal diameters, the average stress on the monitoring point of the head of the elliptical head capsule is low, and the maximum stress on the intestinal wall is low, which indicates that the head shape of the elliptical head capsule has better stress distribution and intestinal comfort under the fluid-solid coupling environment.

(2) The stress changes of capsules in 3 seconds are more gentle when they move in liquid environment with high motion viscosity. Under the same capsule size, the larger the intestinal diameter, the lower the stress on the capsule head. The force calculation value of capsule is slightly lower than that of simulation. It is necessary to further study the influence of intestinal expansion factors on capsule movement under coupling state.

(3) The shape of the capsule head disturbs the flow field distribution of the low dynamic viscous fluid. The maximum flow velocity of the two capsules is almost the same (1.5%), but the flow field distribution shows that the elliptical capsule head exhibits motion stability at low speed and straight line motion.

REFERENCES

- [1] Minglu C , Yongshun Z . Research on spatial steering magnetic moment for petal-shaped capsule robot. *Journal of Huazhong University of Science & Technology*, (2018).
- [2] Yamazaki A , Sendoh M , Ishiyama K , et al. Three-dimensional analysis of swimming properties of a spiral-type magnetic micro-machine. *Sensors and Actuators A (Physical)* 105(1), 103-108(2003).
- [3] Zhang Y, Zhang Y. Driving characteristics of petal-shaped capsule robot in viscous fluid. *Modern Machinery*, (2017).
- [4] Tan R, Liu H, Li H, et al. Research on the critical sliding resistance on the quasi-static interaction between the capsule robot and the small intestine. *robot* 36(6), 704-710(2014).
- [5] Sendoh M, Ishiyama K, Arai K I. Fabrication of magnetic actuator for use in a capsule endoscope. *IEEE Transactions on Magnetics*39(5), 3232-3234(2003).
- [6] Chuan-Guo L I, Yan G Z, Wang K D, et al. Development of Micro-Robot for the Active Exploration of the Gastrointestinal Track. *Measurement & Control Technology*, (2010).
- [7] R Tan , H Liu, LI Hongyi, Y Wang, et al. Dynamics Analysis of the Start Motion of a Capsule Robot. *Information and control* 44(5), 552-556(2015).
- [8] Chen B, Yang P, Chen S, et al. Study on mechanical properties of biomimetic interventional micro robot operating in artificial artery. *China Mechanical Engineering* 20(14), 1712-1716(2010).
- [9] Bolotnik N N, Nunuparov A M, Chashchukhin V G. Capsule-type vibration-driven robot with an electromagnetic actuator and an opposing spring: Dynamics and control of motion. *Journal of Computer & Systems Sciences International* 55(6), 986-1000(2016).

Antitumor activity of orthogonal array designed extracts from different part of *Hedyotis diffusa* on human hepatocellular carcinoma HepG2

Yunlan Li^{1,2*}, Hongyan Zhou¹, Yulian Xu¹, Lin Niu¹, PuGuo¹, Lanlan Miao¹, Qingshan Li^{1,2*}

¹School of Pharmaceutical Science, Shanxi Medical University, Taiyuan 030001, P. R. China, Yun-lan Li:

²Shanxi University of Chinese Medicine, Key Laboratory of Innovative Drug for the Treatment of Serious Diseases Basing on the Chronic Inflammation

Hedyotis diffusa, the widely applied traditional Chinese medicine have shown the inhibitive effects on different tumor cells. But the problems about how to extract antitumor products and which part was the principal anticancer extracts, are still unclear. Our current study determined the antitumor activity of extracts from different part of *Hedyotis diffusa* on HepG2 by MTT assay and optimized the extractive conditions by orthogonal array. After choosing the right solvent of water, the index component of p-coumaric acid in *Hedyotis diffusa* was detected by HPLC method to reflect extraction efficiencies. Then the optimal extractive conditions were got through orthogonal array design and different parts of *Hedyotis diffusa* were tested by MTT assay. The results showed that fruit of *Hedyotis diffusa* not only characterized as the highest extraction efficiency of p-coumaric acid but also the highest cell inhibition rate. While the root of *Hedyotis diffusa* showed both the lower extraction efficiency and cell inhibition rate. *Hedyotis Diffusa* aqueous extraction from fruit, herb, stem, leaf and roots all showed anticancer activity on HepG2. Different part of *H. diffusa* showed inhibition on HepG2 with a dose-dependent manner, and fruit showed higher inhibition rate, followed by Herb, then the root showed the lowest inhibition ratio. Fruit not only showed highest extraction efficiency of p-coumaric acid but also showed highest cell inhibition rate, probably because the active substance of fruit loss less because of its hard shell protection.

Keywords: Antitumor activity, orthogonal array, *Hedyotis diffusa*, human hepatocellular carcinoma HepG2

INTRODUCTION

Herba *Hedyotis diffusa* (*H. diffusa*), the dried herb of *Oldenlandia diffusa* (*Willd.*) Roxb (Family Rubiaceae), is officially listed in the Chinese Pharmacopoeia [1]. The herb mainly growing in the south of mainland China is regarded as the traditional herbal medicine for heat-clearing, detoxification and diuresis [2]. It was widely applied in the treatment of inflammations such as appendicitis, urethritis and bronchitis, due to its antibacterial activity. Then, the herb has gained increasingly attention to its usage as an antitumor herb, such as therapy in liver, lung, colon, brain, pancreas and other cancers [3]. Recently there are more and more researches about inhibitive effects of *H. diffusa* on different tumor cells [4,5]. But the problem about how to extract would have higher antitumor activity and which part of *H. diffusa* was the most effective on antitumor activity, are still unclear. Orthogonal array design (DAD) as a chemometric method for the optimization of extraction condition was adopted in this paper, which was based on three factors and four levels (L_93^4). Before all the works, the optimum solvent of water was chosen. *p*-coumaric acid for one of the active ingredients in *H. diffusa*, according to pharmacological research, showed anti-tumor and anti-cardiovascular effects [6]. What's more,

p-coumaric acid has good stability which was naturally could be chosen as an index component of extraction process to reflect extraction efficiency and detected by High Performance Liquid Chromatography (HPLC) method.

3-(4,5-dimethylthiazol-2-yl)-2,5-diphenyltetrazolium (MTT) test has been widely used as a rapid and sensitive method for screening anticancer drugs. Which extraction from different part of *H. diffusa*, such as herbs, roots, fruits, stems and leaves, has higher inhibition rate of HepG2 were tested by MTT method. All the work aimed at elucidating the different antitumor activity in different part of herb, are very important for the use of this herbal medicine.

EXPERIMENTAL

Plant materials, Chemicals and reagents

The *H. diffusa* and adulterant of Herba *Hedyotis Corymbosae* were collected from different places and all herbs were authenticated by the expert from Shan Xi Food and Drug Administration. The herbs were collected from Guangxi province and its lot number was 20111108. The adulterant was from Fuzhou city of Fujian province and its lot number was 20111026. The thin-layer plates of silica gel G was obtained from Qingdao Haiyang Chemical Co. Ltd. The standard *H. diffusa* and *p*-coumaric acid were

* To whom all correspondence should be sent:
liyulanr@163.com

purchased from Chinese food and Drug Testing Institute (Bingjing, China). The purity of *p*-coumaric acid was over 99% by HPLC-PDA analysis. Stock solution of *p*-coumaric acid was prepared in deionized water, stored at 4 °C, and freshly diluted to the desired concentrations before using. Other HPLC-grade for methanol and phosphoric acid were obtained from Tianjin Siyou Co. Ltd. (Tianjin, China). Water used for extraction was double-distilled water and deionized water was used for HPLC analysis. HepG2 cell line was obtained from the Cell Bank of the Chinese Academy of Sciences (Shanghai, China). Cell culture media Dulbecco's modified Eagle's medium (DMEM), fetal bovine serum (FBS) and phosphate buffer saline (PBS) were obtained from Solarbio (Beijing, China). The other chemicals used, such as 3-[4,5- dimethylthiazol-2-yl]-2,5-diphenyltetrazoliumbro-mide (MTT), trypsin and dimethyl sulfoxide (DMSO) were purchased from Sigma Aldrich Chemical (St. Louis, MO).

TLC identification

Weighting dried and powdered samples (1 g) of *H. diffusa* and extracting with 10 mL ethanol under refluxing for 30 min. Then the hot extraction was filtered and ethanol was used to dissolve the residue after drying, from which we could get test solvent. At the same time, we could get the control medicinal solvent with same method. According to TLC experiment, take prepared solvent 5 μ L and identified simultaneously in the same thin layer plate. The mobile phase was a mixed solvent of ether (30 – 60 °C) : toluene : ethylacetate : Glacial acetic acid (20 : 40 : 14 : 1, v / v / v / v) and sprayed with 10 % sulfuric acid ethanol solution after unrolling. Then the layer was heated in 110 °C until the spots were clear.

HPLC analysis

HPLC analysis was carried out using an Agilent 1200 system (Agilent, California, America). Chromatographic separation of *p*-coumaric and other components were achieved on a Agilent TC-C18 column (4.6 \times 250 mm, 5 μ m) protected by a SHIMADZU LC C18 guard column (4.6 \times 10mm, 5 μ m). The mobile phase for HPLC analysis consisted of methanol / 0.1 % aqueous solution of phosphoric acid (30 : 70, v /v, pH 3.0) with a flow rate of 1.0 mL / min. The sample volume of 20 μ L was injected. The detection wavelength was determined by UV-visible spectrophotometry detection and diode array detector (DAD). The

purity of *p*-coumaric acid was also determined by HPLC-DAD analysis. When detected the purity of *p*-coumaric acid, we investigated the exclusive of chromatographic peaks. Then system suitability was studied by detecting the peak difference of *p*-coumaric acid, *H. diffusa* extraction and adulterant extraction. The component was confirmed from their retention times. For analyzing the concentration of *p*-coumaric acid in extract, a calibration curve was obtained based on the relationship of the concentration of *p*-coumaric acid and the peak-area of the chromophore by linear regression. The intra-day and inter-day repeatability were investigated for consecutive three days at the optimized extraction condition for samples. Standard addition test was performed to determine recoveries of *p*-coumaric acid. In this assay, the standard of *p*-coumaric acid was added to the samples with known content. The resultant samples were analyzed using the developed HPLC method mentioned above. The experiments were repeated three times for every sample. The precision of the method was evaluated with six sequential runs of sample solution. The ratio of measured and known amounts was used to calculate the recovery.

Orthogonal assay design

Before all the studies, different solvent (water, methanol and ethanol) were firstly investigated. OAD with a three-factor interaction is an efficient testing strategy in this study. The three factors including the volume of water, extraction time and the times of decoction and their level values were designated in Tab.1.

Table 1. Factors and levels of the orthogonal array design L9 (3⁴) matrix

A(Volume of water)	Factors	
	B (Extraction time (h))	C(Times of decoction)
30-fold	1	1
40-fold	2	2
50-fold	3	3

The three-factor, three-level OAD for each factor, which were fixed in the probable working range, was selected to evaluate the extraction ratio of *p*-coumaric acid. Nine experiments were performed in order to estimate the best conditions for the extraction efficiency. Single factors including the volume of water, extraction time and the times of decoction were studied to provide a basis for OAD.

Extraction preparation of *H. diffusa*

Dried and powdered samples of *H. diffusa* were placed in flask and weighed accurately. Then the herb was refluxed by water. After cooling naturally, weighed flask again and made up loss reduction with double - distilled water. The supernate was filtered through a 0.45 μm filter to directly inject into HPLC system for *p*-coumaric acid analysis. Then the extraction was evaporated to test the cell viability.

Cell culture and Cell viability assay

HepG2 cells were cultured in DMEM supplemented with 10% (v/v) heat-inactivated FBS and 1% (v/v) antibiotic/antimycotic mixture in a humidified incubator aerated with 5% CO_2 at 37°C. When cells reached 70–80% confluence, they were trypsinized, counted, and seeded in 96-well culture plates at a concentration of 5×10^6 cells / well. After cultured for 24 h, the medium was replaced by DMEM medium supplemented with 2% FBS containing various doses of dry extraction. After incubation for the length of time indicated, MTT was added (final concentration 0.5 mg/mL) and kept incubating for 4 h. The formazan crystals were dissolved in 100 μL of DMSO and the plates were read at 570 nm with a microplate reader (Thermo Scientific, USA).

RESULTS AND DISCUSSIONS

Authenticate of herb

The results of TLC were showed in Fig.1.

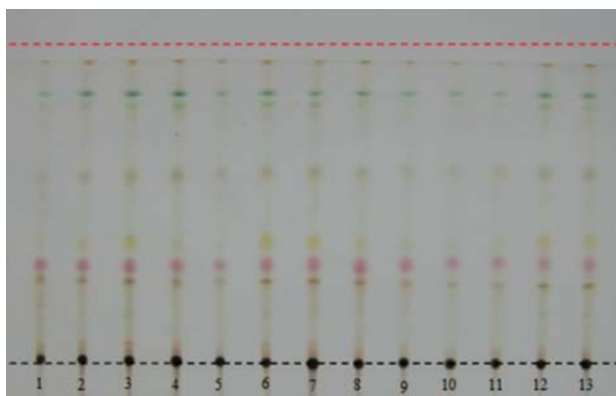


Fig.1. Identified result of TLC. 1 was standard *H. diffusa* 2 -13 was the sample *H. diffusa* of difference batches. The mobile phase was a mixed solvent of toluol (30~60°C) -petroleum ether - ethyl acetate - glacial acetic acid (20 : 40 : 14 : 1), color developing agent was 10% sulfuric acid and ethanol solution.

After investigating the effect of difference of mobile phase, producers of thin layer plate, spotting way, evolving temperature and relative humidity (result not show), we found that the band of samples corresponding to standard *H. diffusa* was clearly observed and well separated from other components.

Result of HPLC analysis

A reversed-phase mode was used in HPLC for the separation of *p*-coumaric acid and other components for convenience of handling samples. In the proposed method, the separation was tested on C18 column and the flow rate was set at 1.0 mL/min at 25°C. With UV full wavelength scanning from 200 to 400nm, the wavelength of 224nm and 308nm simulated the optimum chromatogram (Fig.2a). When thinking about the end absorption at 224nm, 308nm was chosen as detection wavelength. The purity of *p*-coumaric acid was over 99.0% by HPLC-DAD analysis (Fig.2b).

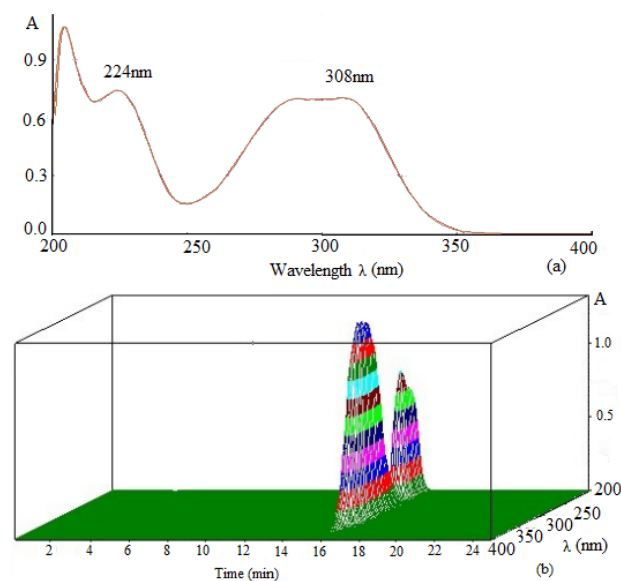


Fig.2. UV wavelength scanning. (a) Measurement results of detecting wavelength by UV spectra of UV-visible spectrophotometry detection. (b) Purity of *p*-coumaric acid showed in 3D chromatogram by HPLC-PAD detection.

Under the chromatographic condition mentioned above, *p*-coumaric acid and other components could be separated in the chromatograms ($R > 1.5$) completely, and there was no interference with the chromatographic peak of *p*-coumaric acid. Meanwhile, *Herba Hedyotis Corymbosae* which is the adulterants of *H. diffusa* was also investigated,

and there was no corresponding chromatographic peak of *p*-coumaric acid (Fig.3).

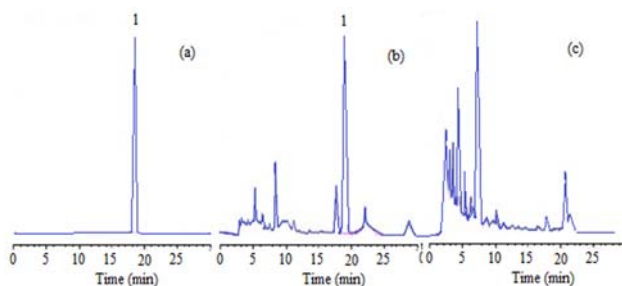


Fig.3. Represent chromatograms of *p*-coumaric acid (a) standard solutions of *p*-coumaric acid (32.29 μ g/ml); 1, *p*-coumaric acid. $t_R = 18.327$ min; (b) extracted sample (Jiangxi province, 20111023); (c) adulterant of *Herba Hedyotidis Corymbosae*.

The selected HPLC method was of higher specificity. The analytical regression curve of *p*-coumaric acid was $A = 153.39 C - 91.59$, and its linearity was in the concentration range of 4.04 to 64.58 μ g/mL with a correlation coefficient of 0.9999, where C (μ g/mL) was the concentration of *p*-coumaric acid determined, and A was the peak area. The intra-day and inter-day precision was determined by a sample solution of *p*-coumaric acid under the selected chromatography conditions, and the RSD was taken as a measure of the intra- and inter-day precisions, which were less than 0.1 and 0.5%, respectively. The recoveries of the investigated components ranged from 98.1% to 103.2%, and their RSD values were less than 1.8%. Considering the results of the recovery test, the method is accurate. In order to improve the chromatographic separation and make the peak shape better, an appropriate volume of phosphoric acid was added to the mobile phase. The effect of the pH value of mobile phase on the separation and peak areas of *p*-coumaric acid in the range of 3.5–7.5 was investigated. It was found that pH lower than 6.0 brought a serious tailing of peaks.

Result analysis of OAD

In order to achieve the higher extraction efficiency of *p*-coumaric acid, primary single factor experiments about extraction solvent, extraction method, the effect of extraction time, times of decoction, volume of solvent added in medicines were performed before OAD experiments. The results showed that the inhibitory rate of the aqueous extraction on HepG2 cells was higher than that of methanol and ethanol extractions. The cell inhibitory rate of aqueous

extraction was 28.3%, while the cell inhibitory rate of methanol and ethanol were 6.2% and 12.9%, respectively. Overall, the water was chosen as the solvent to extract. Then the reflux was chosen as an extraction method for its higher extraction rate of *p*-coumaric acid (0.87mg/g) than ultrasound (0.42mg/g). The Fig.4a showed the effect of extraction time under different conditions by changing the time from 0.5 to 3 hours, when the extraction time increased, the extraction rate of *p*-coumaric acid was improved and got to highest (1.27mg/g) at 2 h. So the extraction time of 1, 2 and 3 hour was investigated in OAD. Times at four different values (1, 2, 3 and 4) were evaluated to optimize the extraction process (Fig.4b). The extraction rate of *p*-coumaric acid increased when increasing the extraction times. The efficiency of *p*-coumaric acid increased a little at 3 times, so the extraction time of 1, 2 and 3 was investigated in OAD. The effect of the volume of water added in extraction of *H.diffusa* efficiency was shown in (Fig.4c).

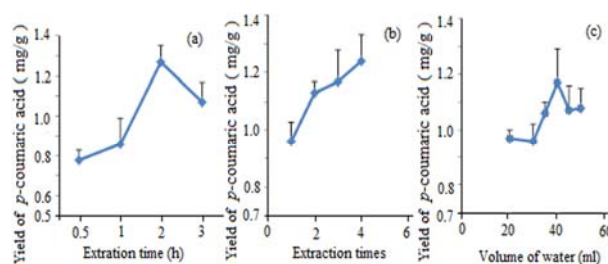


Fig.4. The results of primary single factor experiments. (a) the effect of extraction time, the highest extraction rate of *p*-coumaric acid (1.27mg/g) was got at 2h. (b) the effect of extraction times, theyield of *p*-coumaric acid was 1.17 mg/g at 3 times and 1.24 mg/g at 4 times.(c) the effect of volume of water, the maximum yield of *p*-coumaric acid value (1.17 mg/g) at 40 ml of water.

It was inferred that the extraction rate of the *p*-coumaric acid increased with the increased volume of water added from 20 to 50 mL and attained the maximum yield of *p*-coumaric acid value (1.17mg/g) near 40 mL of water. The volume of water of 30, 40 and 50 mL was investigated in OAD. Since each individual extraction in OAD optimization represented multivariant combination, other factors may contribute much to the extraction efficiency. Therefore, unlike in the univariant optimization, the individual extraction cannot simply mirror the change of factors.

Finally the three factors including volume of water added in medicines, extraction time and times

of extraction were studied in OAD. Three individual factors and their level values are designated in Tab.1. The orthogonal test results of three factors were shown in Tab.2, which helpful to obtain the optimized extraction conditions.

Table 2. Orthogonal array design matrix $L_9(3^4)$ and experimental results

No.	Annotation	Factor				Peak area	Yield of <i>p</i> -coumaric acid(mg/g)
		A	B	C	D		
1	30-fold of water,1h,1time	1	1	1	1	2573.4	0.9803
2	30-fold of water,1h,1time	1	2	2	2	2789.6	1.0625
3	30-fold of water,1h,1time	1	3	3	3	2873.2	1.0943
4	30-fold of water,1h,1time	2	1	2	3	2768.3	1.0545
5	30-fold of water,1h,1time	2	2	3	1	2168.2	0.8261
6	30-fold of water,1h,1time	2	3	1	2	3352.5	1.2771
7	30-fold of water,1h,1time	3	1	3	2	3055.5	1.1636
8	30-fold of water,1h,1time	3	2	1	3	2812.6	1.0713
9	30-fold of water,1h,1time	3	3	2	1	3898.2	1.4845
k1 ^a		1.0457	1.0661	1.1096	1.0970		
k2		1.0526	0.9867	1.2005	1.1677		
k3		1.2398	1.2853	1.0280	1.0734		

^aThe mean values of yield for the factors at each level with standard deviation.

Table 3. ANOVA analysis of four parameters for extraction efficiency

Source	Sum of Squares (SS)	Degrees of freedom (df)	F-ratio	$F_{0.05}$	$F_{0.01}$	Significance
A	0.0729	2	5.1702	19	99	>0.1
B	0.1438	2	10.1915	19	99	<0.1
C	0.0447	2	3.1702	19	99	>0.1
D	0.0141	2		19	99	

Tab.3 shows the relationship between the extraction yields of *p* - coumaric acid and the three variables. From which, it could be inferred that the Factor B (extraction time) is the most significant factor according to the R values, while the Factor A (volume of water added in medicines) is the insignificant one compared with the others. With the direct observation analysis from the results, the optimal extraction condition combination for *p*-coumaric acid was A3-B3-C2. Considering the Factor C (times of decoction) is little influence on extraction efficiency, and error will be increased with more times of extraction. So the optimum values of factors were: 1 times of decoction, the 50mL of water added in medicines, and extraction time 3h.

Determination results of extraction efficiency in *H.diffusa*

The different part of *H. diffusa* was extracted by optimized extraction condition in OAD, which was

50 mL water added in medicine to extract 3 h and 1 times. After detecting by HPLC method, the result (Tab.4) showed that there are maximum amount of *p* - coumaric acid (1.66 mg/g) in fruit, followed by leaves (1.53mg/g), while the root showed the lowest content of *p* - coumaric acid (0.86 mg / g). All of them were statistically significant ($p < 0.05$).

Table 4. Determination results of *p*-coumaric acid in *H. diffusa*

	Peak areas	Yield of <i>p</i> -coumaric acid (mg/g)	Mean (mg/g)
Fruit	3604	1.39	1.66
	4493	1.73	
	4799	1.85	
Leaves	4453	1.72	1.53
	3984	1.54	
	3477	1.34	
Herb	2544	0.98	1.14
	3106	1.20	
	3248	1.25	
Stems	2426	0.94	1.05
	2552	0.98	
	3161	1.22	
Root	1950	0.75	0.86
	2515	0.97	
	2225	0.86	

Annotation: the concentration of standard *p* - coumaric acid was 4.04 $\mu\text{g/mL}$, and the peak area was 518.4, Yield of *p* - coumaric acid (mg/g) = amount of the target *p*-coumaric acid /sample mass.

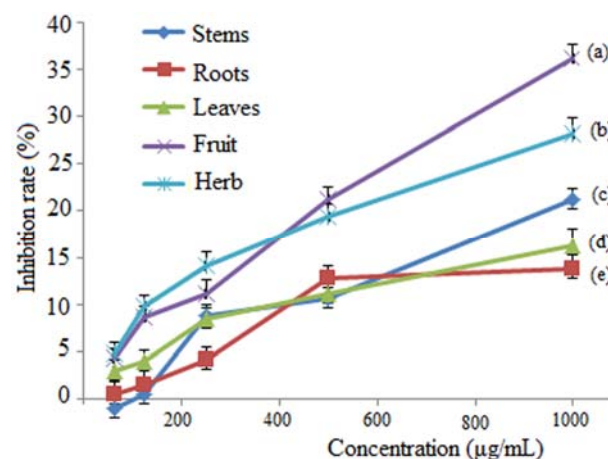


Fig.5. Result of cell viability assay, (a) result of fruit extraction (b) result of herb extraction (c) result of herb stem (d) result of leave (e) result of root

Result of cell viability assay

The Fig.5 showed the results of MTT assay, and the HepG2 cells were treated with water extractives from *H.diffusa* whose consistency were 62.5, 125, 250, 500 and 1000 $\mu\text{g/mL}$. As was shown in Fig.5,

different part of *H. diffusa* has different degrees of inhibition on HepG2 with a dose - dependent manner. The fruit showed the highest inhibition rate (36.18 ± 1.89) %, followed by herb (28.27 ± 1.14) %, then the root showed the lowest inhibition ratio (13.68 ± 1.67) %.

CONCLUSIONS

In this paper, the antitumor activity of extracts from different part of *H. diffusa* on HepG2 was investigated. The water was chosen as extraction solvent for its higher cell inhibitory rates. Based on this, water extraction condition of *H. diffusa* was optimal by OAD and the index component was detected by HPLC to reflect extraction efficiencies. The result showed that when the weight of herb was 1g, we got the optimal extract conditions which were 50 - fold of water, 1 times and 3h for each decoction. In the present study, *p* - coumaric acid showed good linear relationships ($r = 0.9999$) in the investigated concentration range from 4.04 to 64.58 $\mu\text{g/mL}$. The test solution also had a good repeatability ($\text{RSD} = 3.6\%$, $n = 6$) and good stability for 72 h. The recoveries, measured at six concentration levels, varied from 98.1 to 103.6%. The results of content determination showed that there are maximum amount of *p* - coumaric acid (1.66mg/g) in fruit, followed by leaves (1.53mg/g), while the root showed the lowest content of *p* - coumaric acid. Results of cell viability assay showed that different part of *H. diffusa* showed inhibition on HepG2 with a dose - dependent manner, and fruit showed higher inhibition rate (36.18 ± 1.89) %, followed by Herb (28.27 ± 1.14) %, then the root showed the lowest inhibition ratio (13.68 ± 1.67) %. We found that fruit not only showed highest extraction efficiency of *p* - coumaric acid but also showed highest cell inhibition rate. Our suppositions were the active substance of fruit loss less because of its hard shell protection. While the extraction efficiency and cell inhibition rate were not fully correspond, we think there are various antitumor constituents in *H. diffusa*, we just chose *p* - coumaric acid as an index component to reflect extraction efficiency of water extraction. As for root, it had lower extraction efficiency and cell inhibition rate. We think the poor growth environment determines the result. All of those will be the basis for further experiments.

ACKNOWLEDGEMENTS

Financial supports funded by the Shanxi Key Laboratory of Innovative Drug for the Treatment of Serious Diseases Basing on the Chronic Inflammation (Shanxi University of Chinese Medicine, Program for the Natural Science Foundation of Shanxi Province (No. 2014011027-1), the Fund for Shanxi Key Subjects Construction (FSKSC), the Fund for Shanxi Key Subjects Construction, Program for Science and Technology of Shanxi Province (No. 20130313021-9), the Top Science and Technology Innovation Teams of Higher Learning Institutions of Shanxi Province, the Program for the Top Young and Middle-aged Innovative Talents of Higher Learning Institutions of Shanxi Province (2015), Foundation of Young Academic Leader in Shanxi Province, Medicine of Shanxi Province comprehensive development and utilization of collaborative innovation center (2017-JYXT-18) are gratefully acknowledged.

ABBREVIATIONS

H. diffusa - *H. diffusa*;
TLC - thin-layer chromatography;
DAD - diode array detector;
OAD - orthogonal array design;
RSD - relative standard deviation;
DMEM - Dulbecco's modified Eagle's medium;
PBS - phosphate buffer saline;
MTT - 3-(4,5-dimethylthiazol-2-yl)-2,5-diphenyltetrazolium;
HPLC- High Performance Liquid Chromatography;

REFERENCES

- [1] China Pharmacopoeia Committee (2010) Pharmacopoeia of the People's Republic of China (Ed). China Chemical Industry Press, Beijing.
- [2] Gupta S, Zhang D, Yi J, Shao J. *J. Herb. Pharmacother* **4**, 21–33 (2004).
- [3] Shi Y, Wang CH, Gong XG. Apoptosis-inducing effects of two anthraquinones from *Hedyotis diffusa* Willd. *Biol Pharm Bull* **31**, 1075-1078 (2008).
- [4] Lee HZ, Bau DT, Kuo CL. Clarification of the phenotypic characteristics and anti-tumor activity of *Hedyotis diffusa*. *Am J Chin Med* **39**, 201-213 (2011).
- [5] Wang JH, Shu LH, Yang LL, Zhang M. 2-Hydroxy-3-methylanthraquinone from *Hedyotis diffusa* WILLD Induces Apoptosis via Alteration of Fas/FasL and Activation of Caspase-8 in

- Human Leukemic THP-1 Cells. *ARCH MED RES* **42**, 577-583 (2011).
- [6] Liu K, Yan LQ, Guo C, Guo XJ. Estimation of p-coumaric acid as metabolite of E-6-O-p-coumaroyl asandoside methyl ester in rat plasma by HPLC and its application to a pharmacokinetic study. *J Chromatogr B* **831**, 303-306 (2006).
- [7] Ahmad R, Ali AM, Israf DA, Ismail NH, Shaari K, NH. Lajis, *Life Sci* **76**, 1953-1964 (2005).
- [8] Burns JJ, Zhao LJ, Taylor EW, Spelman K. The influence of traditional herbal formulas on cytokine activity. *Toxicology* **278**, 140-159 (2010).
- [9] Ganbold M, Barker J, Ma R, Jones L, Carew M. Cytotoxicity and bioavailability studies on a decoction of *Oldenlandia diffusa* and its fractions separated by HPLC. *J Ethnopharmacol* **131**, 396-403 (2010).
- [10] Lin M, Lin JM, Wei LH, Xu W, Hong ZF, Cai QY. *Hedyotis diffusa* Willd extract inhibits Ht-29 Cell proliferation via cell cycle arrest. *Expther med* **4**, 307-310 (2012).
- [11] Li G, Zhou T, Liu L, Chen J, Zhao Z, Peng Y, Li P, Gao N. Ezrin phosphorylation/ down-regulation contributes to ursolic acid-mediated cell death in human leukemia cells. *Blood Cancer J*, **3**, 1-10 (2013).
- [12] Willimott S, Barker J, Lucy A. Jones, Elizabeth I, Opara. Apoptotic effect of *Oldenlandia diffusa* on the leukaemic cell line HL60 and human lymphocytes. *J Ethnopharmacol*, **114**, 290-299 (2011).
- [13] Xu GH, Kim YH, Chi SW, Choo SJ, Ryoo IJ, Ahn JS, Yoo ID. Evaluation of human neutrophil elastase inhibitory effect of iridoid glycosides from *Hedyotis diffusa*. *Bioorg Med Chem Lett* **20**, 513-515 (2010).
- [14] Zhong GS, Guo XF, Zhang SH, Zhen YS. Optimization of the assembly efficiency for lidamycin chromophore bound to its apoprotein: a case study using orthogonal assay. *Biomed Environ Sic* **24** (6), 602-607 (2011).
- [15] Siti L, Abd K, Harisum Y, Razauden MZ. Potential anti-dengue medicinal plants: a review. *J Nat Med*. **67**, 677-689 (2013).
- [16] Wei Y, Niu L, Liu X, Zhou H, Dong H, Kong D, Li Y, Li Q. Spectroscopic studies and molecular docking on the interaction of organotin antitumor compound bis [2,4-difluoro-N-(hydroxy(κ O)benzamidato(κ O)]diphenyltin(IV) with human cytochrome P450 3A4 protease. *Spectrochimica Acta Part A: Molecular and Biomolecular Spectroscopy*, 163, 154-161, 2016.

Interaction ability of metallic dibutyltin antitumor drug DPDCT with human liver isoenzyme CYP3A4 which metabolized exogenous substances

Yunlan Li^{1,2*}, Ying Wei¹, Xiaoqing Ji¹, Dan Wang¹, Xiaozhi Qiao¹, Qingshan Li^{1,2*}

¹School of Pharmaceutical Science, Shanxi Medical University, Taiyuan 030001, P. R. China, Yun-lan Li:

²Shanxi University of Chinese Medicine, Key Laboratory of Innovative Drug for the Treatment of Serious Diseases Basing on the Chronic Inflammation

Bis[2,4-dichlor-N-(hydroxy-κ-O)benzamido-κ-O]diphenyltin(IV) (DPDCT), which was one of our novel patent organotin compounds with high antitumor activity and relatively low toxicity, may be the inhibitor of human CYP3A4 protease. In this research, DPDCT was synthesized and characterized by elemental analysis, IR, ¹H, ¹³C, ¹¹⁹Sn, NMR spectroscopic techniques, etc. The binding interaction between DPDCT and CYP3A4 was investigated by UV-vis absorption, fluorescence quenching, synchronous fluorescence, three-dimensional fluorescence, circular dichroism and molecular docking technique. The UV absorption spectra of CYP3A4 was changed with the increasing of DPDCT, the enhancement of absorption of CYP3A4 is most probably due to the formation of ground state complex from the inter-molecular interactions. The quenching rate constants and binding constants for DPDCT with CYP3A4 was determined at 298 K and 310 K, which were decreased with the increase of the temperature, showing a static quenching procedure. The apparent binding constants K_b of CYP3A4 with DPDCT at 298 K and 310 K were 3.46×10^4 and 7.59×10^3 , respectively. The number of binding site (n) were 0.87 and 1.46, respectively. The thermodynamic parameters enthalpy change (ΔH) and entropy change (ΔS) of the DPDCT-CYP3A4 complex were negative, which suggested that their interaction was mainly hydrogen bonding and van der Waals force. Gibbs free energy (ΔG) was negative, which showed the binding of DPDCT-CYP3A4 was a spontaneous process. Synchronous fluorescence and circular dichroism spectra indicated that the conformation of CYP3A4 was changed by DPDCT. The Molecular docking was used to study the interaction orientation between DPDCT and human CYP3A4 protein. The results indicated that DPDCT interacted with a panel of amino acids in the active sites of CYP3A4 protein mainly through formation of hydrogen bond. Furthermore, the predicted binding model of DPDCT into CYP3A4 appeared to adopt an orientation with interactions among Ser119.

Keywords: Dibutyltin drug DPDCT, human liver isoenzyme CYP3A4, interaction, conformational change

INTRODUCTION

Organotin (IV) compounds have received significant attentions for their potential biological activities [1]. Our research group synthesized and structurally analyzed a potential organotin candidate, bis[2,4-dichlor-N-(hydroxy-κ-O)benzamido-κ-O] diphenyltin(IV) (DPDCT), which exhibited the strong antitumor activity against seven human cancer cell lines including HepG-2, SHSY5Y, HEC-1-B, EC, T24, HeLa and A549 along with human liver HL-7702, a human normal hepatocytes cell [2]. In this paper, the new compound DPDCT had 2,4-dichlorophenyl groups instead of the 2,4-difluorophenyl groups of bis[2,4-difluoro-N-(hydroxy-κ-O)benzamido-κ-O]diphenyltin(IV) (DFDPT) which had seen in the previous published paper [3]. We have designed and developed the dichloro derivative as an extension to the work previously developed with the difluoro derivative. Because DFDPT had weaker antitumor activity among our synthetic organotin compounds, we want to synthesize the more meaningful antitumor compound compared

with the published DFDPT for developing a new type of potential anticancer agents, which guide us to investigate the relationship about the structure, antitumor activity and the inhibition effect on the key isoenzyme CYP3A4.

Cytochrome P450 (CYP) proteins are the most significant proteins in liver. They have many important physiological functions. The great anticancer activity of DPDCT may be relevant to the inhibition effect on the key isoenzyme CYP3A [4], which could cause the change of metabolism. A crucial fraction of the CYP family is CYP3A4, which composes up to 30% of the total liver CYP enzyme pool in humans [4-7]. The binding to CYP3A4 could affect their properties, such as absorption, distribution, metabolism, excretion, stability and toxicity. Furthermore, it has been demonstrated that the conformation of CYP3A4 will be changed upon binding with DPDCT in this paper, and the spectra change appeared to affect the secondary and tertiary structure of CYP3A4 and their biological function. The structure of DPDCT is shown in Fig.1 (a) and the structure of CYP3A4 protease is shown in Fig.1 (b), which is divided into two regions, namely α helix and β fold region.

* To whom all correspondence should be sent:
liyulanrr@163.com

Heme is the binding site of oxygen and substrate in the oxidation reaction. Central iron atom of heme is the non-covalent binding form in the CYP3A4 molecule.

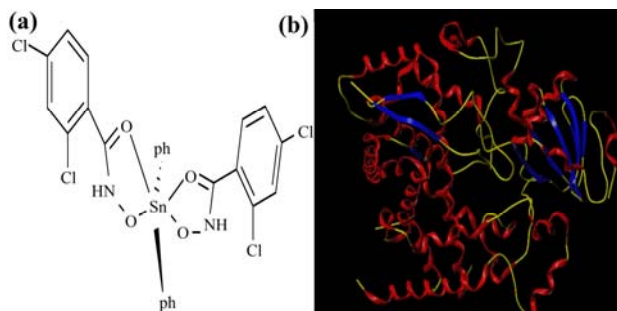


Fig.1. Structure of DPDCT and CYP3A4 protease. (a) DPDCT (b) CYP3A4 protease

Up to now, many methods have been used for the investigate the complex-protein interaction, such as NMR, UV-Vis spectrophotometry, FT-IR, fluorescence, CD and molecular docking and so on [8-12]. Among these methods, fluorescence spectroscopy has a variety of superior advantages over other techniques because of its high sensitivity, rapidity and ease of implementation. Fluorescence spectroscopy is an effective method to reveal the interaction between small molecules and proteins [13]. In this paper, we have studied the interaction of DPDCT with CYP3A4 protein by the fluorescence quenching method. The binding constants were obtained at different temperatures in the medium of PBS (pH 7.4) buffer solution. The binding site and main sorts of binding forces have been suggested. In addition, the conformational changes of CYP3A4 protein were discussed on the basis of UV-visible spectroscopy, synchronous fluorescence (SF), CD and three-dimensional spectroscopy[14-17]. Molecular docking can be used to study the metabolic behavior of the compounds through docking the compounds into the activity sites of drug-metabolizing enzymes. In addition, understanding the interaction of DPDCT with CYP3A4 protein could contribute to the clinical employment of the organotin compounds and the relief of the organotin pollutant. Therefore, the aim of the present study is to determine the binding of DPDCT towards the activity cavity of CYP3A4 protein. Through these data, it may help us find more particular information regarding their metabolism in the human body, and give us a better understanding for its biological action [18,19].

EXPERIMENTAL

Synthesis of DPDCT

Di-phenyltin dichloride (0.344 g, 1.0 mmol) was added to an anhydrous methanol solution (20 mL) of 2, 4-di-chlorbenzohydroxamic acid (0.412 g, 2.0 mmol) and potassium hydroxide (0.112 g, 2.0 mmol). The solution was stirred at room temperature per overnight. Water (20 mL) was added and a white precipitate was formed. Then filtrate and vacuum dry. Yield: 82%; m.p.133-135°C. Calcd (%) for C₂₆H₁₈N₂O₄Cl₄Sn: C, 45.68; H, 2.64; N, 4.10. Found (%): C, 45.52; H, 2.90; N, 4.01. IR: ν = (N-H) 3211 (s), ν = (CO/NC) 1593 (s), 1520 (w), (N-O) 919 (s), (Sn-C) 557 (m), (Sn-O) 523 (m), 448 (s) cm⁻¹. ¹H NMR (CDCl₃): δ = 10.08 (s, br, 2H, NH), 7.98 ~ 7.15 (m, 16H, Harom) ppm. ¹³C NMR (CD₃OD): δ = 175.8 (CO); 161.1, 150.4, 134.5-126.8, 110.5, 105.7 (Carom) ppm. ¹¹⁹Sn NMR (CDCl₃): δ = -339.8, -427.1 ppm. ESI-MS, m/z = 681.9 [M]⁺.

UV-vis absorption studies

The UV-vis absorption spectra can be usually used to determine the structural change of biomacromolecules. The results from UV-vis absorption spectra are usually in agreement with CD measurements which are useful tools to study the interaction conformation. The concentration of CYP3A4 was constant (5×10^{-9} mol·L⁻¹) while varying the compound DPDCT concentration (0, 0.5×10^{-5} , 1×10^{-5} , 1.5×10^{-5} , 2×10^{-5} , 2.5×10^{-5} , 3×10^{-5} , 3.5×10^{-5} and 4×10^{-5} mol·L⁻¹). We measured scan curves in the range of 280 nm to 350 nm at 310K.

Fluorescence quenching spectra

The emission wavelength was performed from 300 nm to 400 nm. The excitation wavelength was at 280 nm. The concentration of CYP3A4 was constant (5×10^{-9} mol·L⁻¹) while varying the compound DPDCT concentration (0, 0.5×10^{-5} , 1×10^{-5} , 1.5×10^{-5} , 2×10^{-5} , 2.5×10^{-5} , 3×10^{-5} , 3.5×10^{-5} and 4×10^{-5} mol·L⁻¹). The excitation and emission band widths were 5nm. Fluorescence spectra were recorded (n = 3 replicates) on LS-55 fluorophotometer (Perkin Elmer, USA) equipped with a 150 W Xenon lamp, a HH-2 waterbath (Changzhou Guohua Electric Appliance Co. Ltd, Changzhou, China) and 1.0 cm quartz cells. Then we measured fluorescence quenching spectra.

Synchronous fluorescence

In order to investigate the structural change of CYP3A4 in the presence of DPDCT, we measured synchronous fluorescence spectra of CYP3A4. In this method, $\Delta\lambda$ stands for the value of the difference between excitation and emission wavelengths. When $\Delta\lambda$ is 15 nm or 60 nm, the synchronous fluorescence spectroscopy just shows the spectroscopic behavior of Tyr residue or Trp residue of proteins, separately. Therefore, synchronous fluorescence spectra of CYP3A4 ($1 \times 10^{-8} \text{ mol} \cdot \text{L}^{-1}$) with complex DPDCT ($0, 0.5 \times 10^{-5}, 1 \times 10^{-5}, 1.5 \times 10^{-5}, 2 \times 10^{-5}, 2.5 \times 10^{-5}, 3 \times 10^{-5}, 3.5 \times 10^{-5}$ and $4 \times 10^{-5} \text{ mol} \cdot \text{L}^{-1}$, respectively) at $\Delta\lambda = 15 \text{ nm}$ and $\Delta\lambda = 60 \text{ nm}$ were recorded on LS-55 fluorescence spectrophotometer.

Energy transfer

Fluorescence resonance energy transfer (FRET) is a reliable method for studying protein-ligand interaction and evaluation of the distance between the ligand and tryptophan residues of the protein. In the method, the absorption spectrum of DPDCT ($5 \times 10^{-9} \text{ mol} \cdot \text{L}^{-1}$) was recorded in the range of 300-500 nm. Then, the overlap of the UV h the absorption spectrum of DPDCT with the fluorescence emission spectrum of CYP3A4 ($5 \times 10^{-9} \text{ mol} \cdot \text{L}^{-1}$) was used to calculate the energy transfer.

Three-dimensional fluorescence

It is well known that three-dimensional fluorescence can provide more detailed information about the conformational changes of proteins. The maximum emission wavelength and the fluorescence intensity of the residues have a close relation to the polarity of their micro-environment. By comparing the three-dimensional fluorescence spectral changes of CYP3A4 protein in the absence and presence of DPDCT, we can investigate the conformational and micro-environmental changes of CYP3A4. In this research, the three-dimensional fluorescence spectroscopies of CYP3A4 protein ($5 \times 10^{-9} \text{ mol} \cdot \text{L}^{-1}$) treated with DPDCT (0 and $3 \times 10^{-5} \text{ mol} \cdot \text{L}^{-1}$) were measured on F-320 fluorophotometer (Tianjin Gangdong Sci. & Tech. Development Co. Ltd., Tianjin, China). The emission wavelength was recorded between 320 nm and 450 nm with an increment of 10 nm. The excitation wavelength was performed between 200 and 300 nm with an increment of 10 nm. The

photomultiplier tubes (PMT) voltage was set at 700 V. The scan speed was set at 12000 nm/min.

CD measurements

CD is a powerful tool in elucidating the modifications of the secondary structure of biopolymers as a result of interaction with small molecules. CD measurements were recorded on a MOS - 450 spectropolarimeter at room temperature under constant nitrogen flush. Quartz cells have pathlength and volume of 0.1 cm and 400 μl , respectively. The acquisition duration was 0.5 s and the scan step was 1 nm in the range of 200-250 nm of scan repeat 3 times. The CD measurements of CYP3A4 constant ($5 \times 10^{-9} \text{ mol} \cdot \text{L}^{-1}$) in the absence and presence of the varying DPDCT concentration ($0, 1 \times 10^{-5}, 2 \times 10^{-5}$ and $3 \times 10^{-5} \text{ mol} \cdot \text{L}^{-1}$). Appropriate blank ran under the same conditions, it was subtracted from the sample spectra.

Molecular docking

The structure of cytochrome P450 CYP3A4 was obtained from Protein Data Bank (<http://www.rcsb.org/pdb>) and PDB code was 4K9W. The two-dimensional structure of DPDCT with standard bond lengths and angles was drawn using Sybyl-X 2.0. The chains of B, C and D of 4K9W were eliminated. Minimization of molecular energy was carried out with the Tripos force field. The most stable conformation was searched using the Powell conjugate gradient algorithm with a convergence criterion of 0.001 kcal/mol. The limit of energy gradient was 0.05 kcal/mol \AA . The compound partial charges were calculated using Gasteiger-Huckel method. CYP3A4 was carried out with the AMBER 7FF99 force field. The protein partial charges were calculated using AMBER method. The docking process was performed with Surflex-Dock (within Sybyl-X 2.0, Tripos international). Docking of ligands into the catalytic domain of the CYP3A4 model was carried out using Surflex-Dock. The top 20 ranked ligands are flexible compounds that can adopt a multitude of conformations within the CYP3A4 active site.

RESULTS AND DISCUSSIONS

Structure characterization

Comparing with the free ligand of the FT-IR spectra, the broad band O-H absorption of 2479 cm^{-1} was absent, because of the deprotonation and coordination. The absorption band of C=O from

1598 cm^{-1} and 1562 cm^{-1} in the free ligand to 1593 cm^{-1} and 1520 cm^{-1} indicated this group occurred coordination. The absorption band of N-O was 901 cm^{-1} in the free ligand and 919 cm^{-1} in the complex. In the complex, the Sn-C absorption was exhibited 557 cm^{-1} , the Sn-O absorption were exhibited 523 cm^{-1} and 448 cm^{-1} . In the ^1H NMR spectrum, DPDCT showed the expected resonances. It exhibited resonances in the range of 7.98-7.15 ppm. ^{13}C NMR spectrum exhibited the C=O signal around the tin atom and the phenyl carbon signal. ^{119}Sn NMR spectra showed the same-type organotin resonance at -339.8 and -427.1 ppm.

UV-Vis spectral measurements

The UV-Vis absorption spectra of CYP3A4 in the presence of increasing concentration of DPDCT (0, 0.5×10^{-5} , 1×10^{-5} , 1.5×10^{-5} , 2×10^{-5} , 2.5×10^{-5} , 3×10^{-5} , 3.5×10^{-5} and 4×10^{-5} $\text{mol} \cdot \text{L}^{-1}$) are measured at stimulated physiological condition. In presence of increasing concentration of DPDCT, the absorption spectra of pure CYP3A4 gradually increases. Fig.2. shows the absorption spectra of CYP3A4 and CYP3A4 in the presence of increasing concentration of DPDCT.

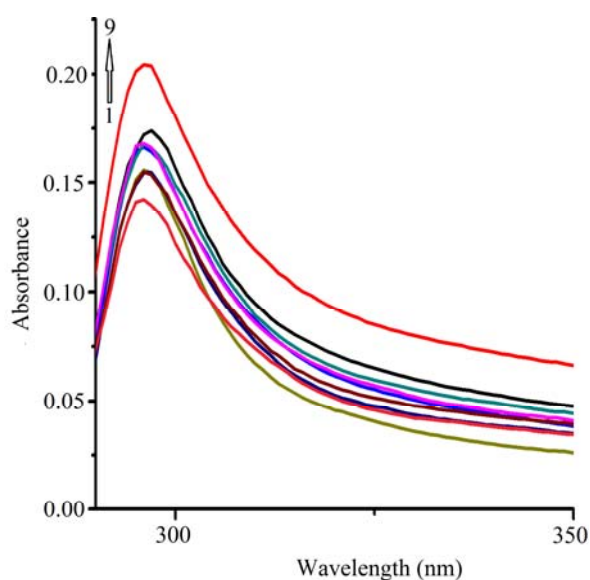


Fig.2. UV-vis spectra of CYP3A4 protein (5×10^{-9} $\text{mol} \cdot \text{L}^{-1}$) in the absence and in the presence of increasing DPDCT concentrations in pH 7.4 PBS buffer. From 1 to 9 lines, concentrations of DPDCT were: 0, 0.5×10^{-5} , 1×10^{-5} , 1.5×10^{-5} , 2×10^{-5} , 2.5×10^{-5} , 3×10^{-5} , 3.5×10^{-5} and 4×10^{-5} $\text{mol} \cdot \text{L}^{-1}$, respectively.

From the Fig.2, it can be observed that the intensity increases significantly as the quencher concentration increased. The increase in intensity can be attributed to the formation of the ground state complex between CYP3A4 protein and DPDCT, as CYP3A4 molecules get absorbed on the surface of DPDCT. As the concentration of DPDCT used possesses negligible absorbance in the region of absorption spectra of CYP3A4, the enhancement of absorption of CYP3A4 is most probably due to the formation of ground state complex from the inter-molecular interactions [20].

Fluorescence quenching results

1. The value of quenching constant

As is well known, the intrinsic fluorescence of CYP3A4, which comes from tryptophan (Trp), tyrosine (Tyr) and phenylalanine (Phe) residues, is often used to be an endogenous fluorescent probe to study the conformational change of CYP3A4 in the binding process of CYP3A4 with compounds. However, Trp residue has the strongest fluorescence intensity and is the most sensitive to the changes in the micro-environment. The fluorescence quenching of protein can be divided into three quenching mechanisms. The static quenching caused by forming ground-state complex of protein with quenchers, the dynamic quenching caused by the collision of protein and quenchers, and combined dynamic and static quenching caused both collision and complex formation with the same quencher, respectively. In the case of the static quenching, the value of quenching constant (K_{sv}) decreased with the increase of temperature due to higher temperature resulting in the decrease of the complex stability. In contrast, for the dynamic quenching process, the value of K_{sv} increased with the increase of temperature due to higher temperature resulting in larger diffusion coefficient and promotes electron transfer [21,22]. In order to research the binding of CYP3A4 protein to DPDCT, the fluorescence spectra were recorded from 300 nm to 400 nm upon excitation at 280 nm. Fig.3. showed the fluorescence spectrum of CYP3A4 in the absence and presence of different DPDCT concentrations at 298 K and 310 K. The fluorescent intensity of CYP3A4 protein decreased regularly with increasing concentration of DPDCT, while the maximum emission wavelength was almost not changed, suggested that a change in the surrounding environment of the fluorophores due to binding interaction with DPDCT and the binding region of DPDCT is the vicinity of Trp residues

since a distant event cannot cause its fluorescence quenching.

The fluorescence quenching data were analyzed by the well-known Sterne-Volmer equation [23,24]:

$$\frac{F_0}{F} = 1 + K_{sv} [Q] = 1 + K_q \tau_0 [Q] \quad (1)$$

where, F_0 and F are the fluorescence emission intensities in the absence and presence of quencher, respectively; K_q is the quenching rate constant, K_{sv} is the Stern–Volmer quenching constant which measures the efficiency of quenching; $[Q]$ is the concentration of the DPDCT, τ_0 is the average lifetime of fluorophore in the absence of quencher and its value is considered to be fluorophore 10^{-8} s. The Stern–Volmer equation was applied to determine K_{sv} by linear of a plot of F_0/F versus $[Q]$. The Stern-Volmer plots of the quenching of CYP3A4 protein fluorescence quenched by DPDCT at different temperatures were shown in Fig.4 (a) and (b). The Stern-Volmer quenching constants K_{sv} and K_q at different temperatures were obtained and listed in Tab.1.

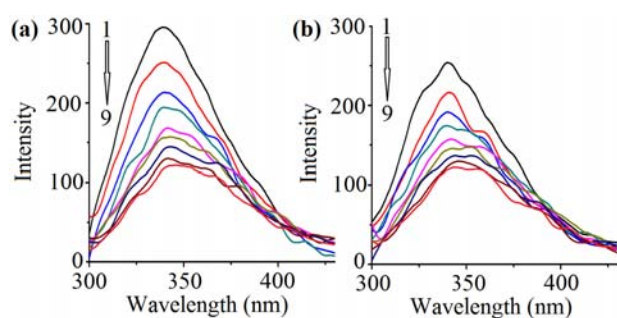


Fig.3. Fluorescence emission spectra of CYP3A4 protein ($5 \times 10^{-9} \text{ mol} \cdot \text{L}^{-1}$) in the absence and in the presence of increasing DPDCT concentrations in pH 7.4 PBS buffer. (a). $T = 298 \text{ K}$. (b). $T = 310 \text{ K}$. From 1 to 9 lines, concentrations of DPDCT were: 0, 0.5×10^{-5} , 1×10^{-5} , 1.5×10^{-5} , 2×10^{-5} , 2.5×10^{-5} , 3×10^{-5} , 3.5×10^{-5} and $4 \times 10^{-5} \text{ mol} \cdot \text{L}^{-1}$, respectively. $\lambda_{\text{ex}} = 280 \text{ nm}$.

Table 1. Quenching constants of CYP3A4 protein with DPDCT at different temperatures

T (K)	K_{sv} (L mol^{-1})	K_q ($\text{L mol}^{-1} \text{ s}^{-1}$)	R^2
298	3.56×10^4	3.56×10^{12}	0.996
310	2.59×10^4	2.59×10^{12}	0.995

A plot of (F_0/F) versus $[Q]$ yields straight line in case of single fluorophore. The plots showed good linear relationships within the investigated concentrations ($R^2 = 0.996$ at 298 K and $R^2 = 0.995$

at 310 K). Linear fittings of the experimental data obtained afford K_{sv} and K_q . K_{sv} is the $3.56 \times 10^4 \text{ L mol}^{-1}$ at 298 K and the $2.59 \times 10^4 \text{ L mol}^{-1}$ at 310 K. Tab.1 shows that K_{sv} values were inversely correlated with temperatures, which suggested that the fluorescence quenching of CYP3A4 was initiated by the formation of ground-state complex. For dynamic quenching, the maximum scattering collision quenching constant of various quenchers is $2.0 \times 10^{10} \text{ L mol}^{-1} \text{ s}^{-1}$. The results showed that the value of K_q was much greater than 2.0×10^{10} which indicated that the probable quenching mechanism of fluorescence of CYP3A4 by DPDCT is not caused by dynamic collision but from the formation of a complex.

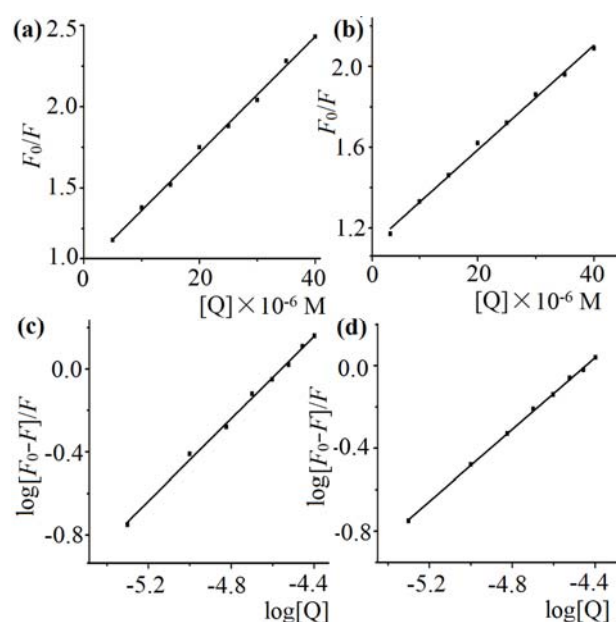


Fig.4. Stern – Volmer plots of CYP3A4 protein ($5 \times 10^{-9} \text{ mol} \cdot \text{L}^{-1}$) quenched by DPDCT at different temperatures. (a). $T = 298 \text{ K}$. (b). $T = 310 \text{ K}$. A plot of $\log[(F_0 - F) / F]$ vs $\log [Q]$ of DPDCT with CYP3A4 protein ($5 \times 10^{-9} \text{ mol} \cdot \text{L}^{-1}$) at different temperatures. (c). $T = 298 \text{ K}$. (d). $T = 310 \text{ K}$. $\lambda_{\text{ex}} = 280 \text{ nm}$

2. Binding constants and binding sites

When small molecules bind independently to a set of equivalent sites on a macromolecule, the equilibrium between free and bound molecules is given by the following equation [25]:

$$\log \frac{F_0 - F}{F} = \log K_b + n \log [Q] \quad (2)$$

where K_b and n are the binding constant and the number of binding sites, respectively. Thus, the K_b and n values can be obtained from the intercept and slope values of the plot of $\log [(F_0-F)/F]$ against $\log[Q]$ as in Fig.4.(c) and (d). The plots showed good linear relationships within the investigated concentrations ($R^2 = 0.9900$ at 298 K and $R^2 = 0.9990$ at 310 K). The values of K_b and n for the DPDCT-CYP3A4 system at 298K were estimated to be 3.46×10^4 and 0.99. The values of K_b and n for the DPDCT-CYP3A4 system at 310K were estimated to be 7.59×10^3 and 0.87, respectively. The values of n are roughly equal to 1.

Table 2. The binding constants and the number of binding sites of CYP3A4 protein with DPDCT at two different temperatures

T (K)	K_b (L mol ⁻¹)	n	R^2
298	3.46×10^4	0.99	0.9900
310	7.59×10^3	0.87	0.9990

Tab.2 gives the corresponding calculated results. The results showed that K_b were decreased with the increasing temperature, which may hint the formation of an unstable complex in the binding reaction. The complex would be partly decomposed with the increasing temperature, therefore, the K_b decreased. Furthermore, the values of n were approximately equal to 1, manifesting the existence of just a single binding site in CYP3A4 protein towards DPDCT. The previous compound DFDPT which has the 2,4-difluorophenyl groups had the apparent binding constants K_b of CYP3A4 at 298 K and 310 K of 2.51×10^7 and 3.09×10^5 . So the diversity of substituent 2,4-dichlorophenyl groups instead of the 2,4-difluorophenyl groups of bis [2,4-difluoro-N-(hydroxy-κO)benzamidato-κO]diphenyltin(IV) shows the strong discrepancy in the binding intensity. The fluorinated group of DFDPT has the impressive interaction with CYP3A4 than the chlorinated group of the organotin antitumor compound DPDCT.

Thermodynamic analysis of binding mode

There are mainly four types of noncovalent interactions that could play a role in ligand binding to proteins. They are hydrogen bonds, van der Waals forces, electrostatic, and hydrophobic interactions, respectively. The model of interaction can be summarized as : (1) $\Delta H > 0$ and $\Delta S > 0$, hydrophobic forces; (2) $\Delta H < 0$ and $\Delta S < 0$, van der Waals interactions and hydrogen bonds; (3) $\Delta H < 0$ and $\Delta S > 0$, electrostatic interaction. The thermodynamic parameters including ΔH , ΔS and ΔG can be calculated from the Van't Hoff equation :

$$\Delta G = -RT \ln K \quad (3)$$

$$\ln \frac{K_2}{K_1} = \left(\frac{1}{T_1} - \frac{1}{T_2} \right) \frac{\Delta H}{R} \quad (4)$$

$$\Delta S = \frac{\Delta H - \Delta G}{T} \quad (5)$$

Where K_1 and K_2 are the binding constants at corresponding temperature (T_1 and T_2), and R is the gas constant. The temperatures used were 298 and 310 K. ΔH , ΔS and ΔG are enthalpy change, entropy change and free energy change, respectively. The free energy change ΔG is estimated from the Eq. (5). Tab.3 shows the values of ΔH and ΔS obtained for the binding site from the slopes and ordinates at the linear Van't Hoff .

Table 3. Thermodynamic parameters of the interaction between DPDCT and CYP3A4

T (K)	ΔH (kJ mol ⁻¹)	ΔS (J K ⁻¹)	ΔG (kJ mol ⁻¹)
298	-97.01	-238.66	-25.89
310	-97.01	-238.65	-23.03

From Tab.3, it can be seen that the negative sign for free energy ΔG means that the interaction process is spontaneous. $\Delta H < 0$ indicated the formation of DPDCT-CYP3A4 coordination was exothermic. Therefore, both ΔH and ΔS are negative value indicated that both hydrogen bond and van der Waals forces play the major role in the interaction of DPDCT and CYP3A4 protein.

Characteristics of synchronous fluorescence spectra

Unlike the steady-state fluorescence spectra, synchronous fluorescence spectroscopy can provide the characteristic information about the microenvironment in a vicinity of disparate chromophores. When setting the scanning intervals ($\Delta \lambda = \lambda_{\text{emi}} - \lambda_{\text{exc}}$) of 15 and 60 nm, the characteristic information of the Tyr and Trp residues can be obtained. The research results had demonstrated that the shift of the maximum emission wavelength represents the alteration of the polarity of the microenvironment surrounding Tyr or Trp residues and the red shift of the maximum emission wavelength indicates that the hydrophobicity surrounding Tyr or Trp residue decreases and the stretching extent of the peptide chain increases [26]. The effect of DPDCT on the synchronous fluorescence spectrum of CYP3A4 protein was showed in Fig.5. Analyzing the Fig.5 (a), the tyrosine residues fluorescence emission was

blue-shift, it demonstrated the microenvironment of the tyrosine residues had been changed in the direction of increasing the hydrophobicity of the microenvironment. From Fig.5 (b), it was observed that the maximum emission wavelength of the tryptophan residues was red-shifted with the increasing concentration of DPDCT. It demonstrated the microenvironment of the tryptophan residues had been changed in the direction of reducing the hydrophobicity of the microenvironment.

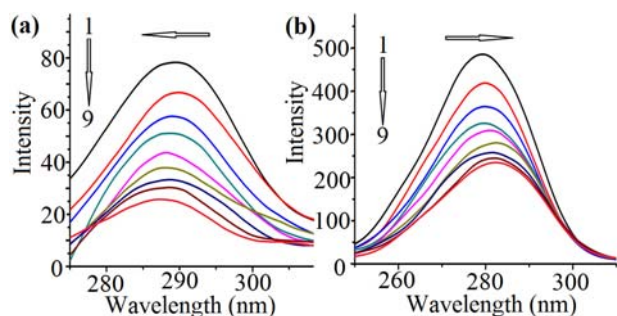


Fig.5. Synchronous fluorescence spectra of CYP3A4 protein ($1 \times 10^{-8} \text{ mol} \cdot \text{L}^{-1}$) in the absence and presence of DPDCT. A. the wavelength difference $\Delta\lambda = 15 \text{ nm}$. B. the wavelength difference $\Delta\lambda = 60 \text{ nm}$. [DPDCT] 1→9: 0, 0.5×10^{-5} , 1×10^{-5} , 1.5×10^{-5} , 2×10^{-5} , 2.5×10^{-5} , 3×10^{-5} , 3.5×10^{-5} and $4 \times 10^{-5} \text{ mol} \cdot \text{L}^{-1}$, respectively.

Energy transfer

According to Forster non-radioactive energy transfer theory, the energy transfer will happen under the following conditions: (a) the donor can produce fluorescence light, (b) there is significant overlap between fluorescence emission spectrum of the donor and UV absorption spectrum of the acceptor and (c) the distance between the donor and the acceptor is lower than 8nm. The fluorescence spectrum of CYP3A4 and the absorption spectrum of DPDCT is shown in Fig.6. The energy transfer efficiency E is defined by the following equation:

$$E = \frac{R_0^6}{(R_0^6 + r^6)} = 1 - \frac{F}{F_0}$$

where r is the distance between the acceptor and the donor, and R_0 is the Forster critical distance, at which 50% of the excitation energy is transferred to the acceptor. F and F_0 are the fluorescence intensities of CYP3A4 in the presence and absence of DPDCT. R_0 can be calculated from donor emission and acceptor absorption spectra using the Forster formula, that is the following equation:

$$R_0^6 = 8.8 \times 10^{-28} k^2 N^{-3} \Phi J$$

where k_2 is the spatial orientation factor of the dipole ($k_2=2/3$); N , the refractive index of the medium ($N=1.336$); Φ , the fluorescence quantum yield of the donor ($\Phi=0.118$); and J is the overlap integral of the fluorescence emission spectrum of the donor and the absorption spectrum of the acceptor J is given by:

$$J = \sum F(\lambda)\varepsilon(\lambda)\lambda^4 \Delta\lambda / \sum F(\lambda)\Delta\lambda$$

where $F(\lambda)$ is the fluorescence intensity of the fluorescent donor of wavelength λ ; $\varepsilon(\lambda)$ and is the molar absorption coefficient of the acceptor at wavelength λ . We have obtained that $J=9.43 \times 10^{-20} \text{ cm}^6 \text{ Lmol}^{-1}$, $R_0^6 = 2.60 \times 10^{-45} \text{ cm}^6$, the energy can transfer from CYP3A4 to DPDCT with high probability and the distance obtained by FRET with higher accuracy.

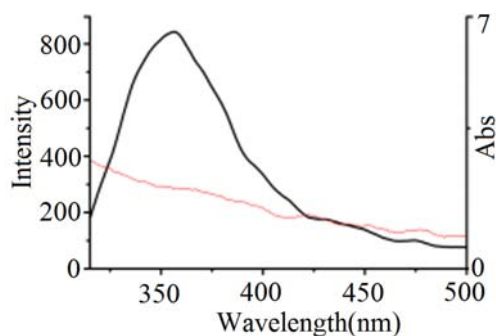


Fig.6. The fluorescence spectrum of CYP3A4 and the absorption spectrum of DPDCT

3D fluorescence spectroscopy

Three-dimensional (3D) fluorescence spectroscopy has become a popular fluorescence analysis technique in recent years. It is well known that three-dimensional fluorescence spectrum can provide more detailed information about the change of the configuration of proteins. By comparing the 3D fluorescence spectroscopy changes of CYP3A4 protein in the absence and presence of DPDCT, we can investigate the conformational and microenvironmental changes of CYP3A4. The contour maps of CYP3A4 and CYP3A4-DPDCT system were shown in Fig.7 and Table 4. In Fig.7, peak A ($\lambda_{\text{ex}}=230\text{nm}$, $\lambda_{\text{em}}=320\text{nm}$) exhibited the fluorescence characteristic of polypeptide backbone structures, and Peak B ($\lambda_{\text{ex}}=280 \text{ nm}$, $\lambda_{\text{em}}=330\text{nm}$) was the characteristic spectroscopy of tryptophan and

tyrosine residues. Fig.7 presents the contour maps of CYP3A4 and DPDCT–CYP3A4.

Table 4. The characteristic parameters of three dimensional fluorescence spectra of CYP3A4 and CYP3A4-DPDCT system

Fluorescence peak A		Fluorescence peak B	
Peak position $\lambda_{\text{ex}}/\lambda_{\text{em}}$ (nm/nm)	Intensity F	Peak position $\lambda_{\text{ex}}/\lambda_{\text{em}}$ (nm/nm)	Intensity F
230/325.0	218.2	280/331.8	2040.8
230/329.6	116.4	280/332.4	1466.4

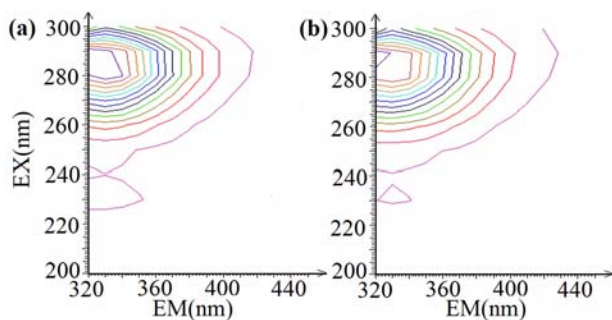


Fig.7. Three-dimensional fluorescence contour maps of CYP3A4 and CYP3A4 - DPDCT system. (a). CYP3A4 ($5 \times 10^{-9} \text{ mol} \cdot \text{L}^{-1}$) (b). CYP3A4-DPDCT (DPDCT: $3 \times 10^{-5} \text{ mol} \cdot \text{L}^{-1}$)

From Tab.4, we found the intensity of peak A was decreased and the emission wavelength was shifted, which implied that the peptide strand structure of CYP3A4 was changed. And, the intensity of peak B was decreased and the emission wavelength was shifted, which demonstrated that the microenvironment of Trp and Tyr residues had been changed. The decrease of the intensity of the peak A and peak B in combination with the fluorescence emission spectra indicated that the binding of DPDCT with CYP3A4 causes slight unfolding of the polypeptide chain of CYP3A4 and conformational change of CYP3A4. This suggests that the binding of DPDCT–CYP3A4 induced some microenvironmental and conformational changes in CYP3A4, and a complex between them may have been formed [27].

Circular dichroism spectroscopy

The CD spectra of CYP3A4 protein in the absence and presence of DPDCT were shown in Fig.8.

The results revealed that there was a band at near 220 nm, which exhibited a typical shape of α -helix secondary structure. The intensities of band slightly decreased with the addition of DPDCT along with the slightly blue shift of the peak at near 220 nm, which indicating that the CYP3A4 still

retained its secondary α -helix structure and α -helix content of CYP3A4 was decreased after DPDCT binding to CYP3A4.

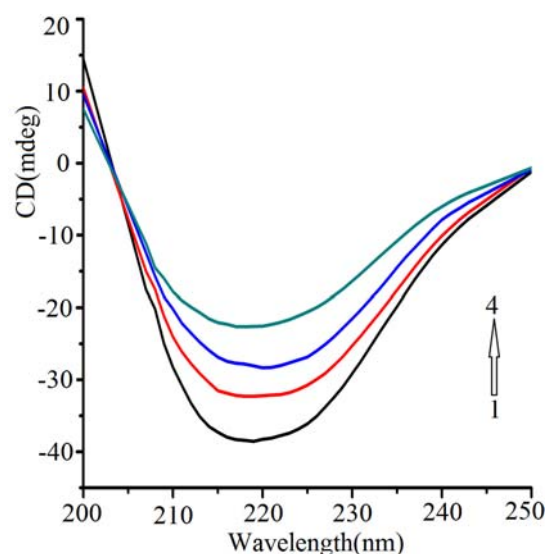


Fig.8. Circular dichroism of CYP3A4 protein ($5 \times 10^{-9} \text{ mol} \cdot \text{L}^{-1}$) and DPDCT in PBS buffer (pH 7.4, from 1→4, concentrations of DPDCT were: 0, 1×10^{-5} , 2×10^{-5} and $3 \times 10^{-5} \text{ mol} \cdot \text{L}^{-1}$, respectively)

Molecular docking

In the field of molecular modeling, molecular docking is a useful method which predicted the preferred orientation of a small molecule to biomacromolecule when bound to each other to form a stable complex and the strength of association between molecules using scoring functions. The molecular docking technique is a fascinating method to study the interaction between drugs and CYP3A4. The binding orientation of DPDCT on CYP3A4 protein were shown in Fig.9(a) which indicated that DPDCT binded to CYP3A4 internal structure. In the Fig.9(b), red link represented the connection bonds of oxygen atom, and blue link represented the connection bonds of nitrogen atom. From our docking results, DPDCT might bind Ser119 of CYP3A4, which thus affects the combination of DPDCT and CYP3A4. DPDCT enters into the cavity of CYP3A4 via hydrogen bonds. There are hydrogen bonds between DPDCT and residues Ser119 (distance, 2.53 and 2.26 Å). The next step, we want to use the CYP3A4 mutant to verify the connection bonds by a variety of spectroscopy techniques.

Compared with the previous compound which has the 2,4-difluorophenyl groups, DPDCT enters into the cavity of CYP3A4 through one hydrogen bonding (Ser119). But the previous compound

connected the cavity of CYP3A4 by three hydrogen bonding (Arg105, Ser119 and Thr309). It testified DPDCT had the weaker binding constants.

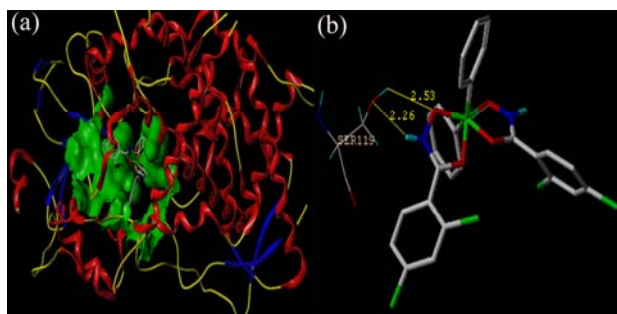


Fig.9. The docking of DPDCT into the activity of CYP3A4 protein. (a). The binding orientation of DPDCT with CYP3A4 (b).Structural details of the interaction between DPDCT and CYP3A4.

CONCLUSIONS

Compared with the published DFDPT, the DPDCT is the more meaningful antitumor compound. The IC_{50} value of DPDCT against human HEC-1-B cell lines was $5.12 \mu\text{mol}\cdot\text{L}^{-1}$, while the IC_{50} values of the DFDPT was $12.30 \mu\text{mol}\cdot\text{L}^{-1}$ by MTT assay according to the standard procedures. In the human SHSY-5Y cell lines, the IC_{50} values of DPDCT is $8.20 \mu\text{mol}\cdot\text{L}^{-1}$, while the DFDPT has the antitumor activity of IC_{50} values of $12.88 \mu\text{mol}\cdot\text{L}^{-1}$. In the human T24, HepG-2 and Hela cells, the new compound DPDCT also had higher antitumor activity than the published DFDPT. The DPDCT is the higher-activity compound which lay the foundation for further design and structure optimization to synthesis the more impressive antitumor activity compound. In this work, we used different approaches to explore the interactions between DPDCT and CYP3A4 under physiological conditions. The experimental results showed that DPDCT quenches the fluorescence of CYP3A4 by a static quenching mechanism. Experimental results from the quantitative analysis of circular dichroism, three dimensional fluorescence studies and synchronous fluorescence spectrum demonstrated that the binding of DPDCT to CYP3A4 protein induced some micro-environmental and conformational change of CYP3A4. Our study is expected to provide important protein into the interaction of the physiologically protein with DPDCT, facilitating further investigation on the pharmacological behavior of DPDCT. This type investigation on drug-protein interaction assumes importance in life

sciences, chemistry and clinical medicine. Identifying the molecular targets for the beneficial or detrimental effects of small-molecule drugs is an important and currently unmet challenge.

ACKNOWLEDGEMENTS

Financial supports funded by the Shanxi Key Laboratory of Innovative Drug for the Treatment of Serious Diseases Basing on the Chronic Inflammation (Shanxi University of Chinese Medicine, the Fund for Shanxi Key Subjects Construction (FSKSC), the Fund for Shanxi Key Subjects Construction, the Top Science and Technology Innovation Teams of Higher Learning Institutions of Shanxi Province, the Program for the Top Young and Middle-aged Innovative Talents of Higher Learning Institutions of Shanxi Province (2015), Foundation of Young Academic Leader in Shanxi Province, Medicine of Shanxi Province comprehensive development and utilization of collaborative innovation center (2017-JYXT-18) are gratefully acknowledged.

REFERENCES

- [1] Chaoqun Y, Jiali Zhang, Taigang Liang, Qingshan Li. Diorganotin(IV) complexes with 4-nitro-N-phthaloyl-glycine: Synthesis, characterization, antitumor activity and DNA- binding studies. *Biomed Pharmacother.* 2015, 71, 119-127.
- [2] Y. Li, Z. Wang, P. Guo, L. Tang, R. Ge, S. Ban, Q. Chai, L. Niu, Q. Li. Diorganotin (IV) derivatives of substituted N-hydroxybenzamidates with selective cytotoxicity in vitro and potent antitumor activity in vivo. *Inorg Biochem.* 2014, 133, 1-7.
- [3] Y. Wei, L. Niu, X. Liu, H. Zhou, H. Dong, D. Kong, Y. Li, Q. Li. Spectroscopic Studies and Molecular Docking on the Interaction of Organotin Antitumor Compound Bis[2,4-difluoro-N-(hydroxy-κ^O)benzamidato-κ^O] diphenyltin(IV) with Human Cytochrome P450 3A4 Protease[J]. *Spectroc. Acta Part A: Molec. and Biomolecular Spec.*, 2016, 163, 154-161.
- [4] S. Shityakov, I. Puskas, N. Roewer, C. Forster, J. Broscheit. Three-dimensional quantitative structure- activity relationship and docking studies in a series of anthocyanin derivatives as cytochrome P450 3A4 inhibitors. *Adv Appl Bioinform Chem.* 2014, 7, 11-21.
- [5] Y. Zhang, Y. Li, Q. Li. Inhibition of Cytochrome P450 3A in Rat Liver by the Diorganotin (IV) Compound di-n-Butyl-di-(4-chlorobenzohydroxamato)tin (IV) and Its Probable Mechanism. *Molecules.* 2012, 17, 10994-11009.

- [6] Yunlan Li, Yang Li, Xiaoqiang Niu, Linjin Jie, Xianmei Shang, Jianping Guo, Qingshan Li. Synthesis and antitumor activity of a new mixed-ligand complex di-n-butyl-(4-Journal of Ichlorobenzohydroxamato) tin(IV) chloride. *Inorg Biochem* 2008, **102**, 1731-1735.
- [7] Yunlan Li, Pu Guo, Niu Lin, Qingshan Li. Pharmacokinetics of di-phenyl-di-(2,4-dichlorobenzohydroxamato) tin(IV): A new metal-based candidate with promising antitumor activity in rats. *Inorgan. Chimica Acta*. 2014, **423**, 235-241.
- [8] B. Geng, X. Liu, Y. Tian, J. Ye, H. Li, J. Wu. Investigation on the interaction between endocrine disruptor triphenyltin with human serum albumin. *Spectrochim Acta A Mol Biomol Spectrosc.* 2014, **120**, 512-516.
- [9] N. Shahabadi, S. Hadidi. Molecular modeling and spectroscopic studies on the interaction of the chiral drug venlafaxine hydrochloride with bovine serum albumin. *Spectrochim Acta A Mol Biomol Spectrosc.* 2014, **122**, 100-106.
- [10] R. Revathi, A. Rameshkumar, T. Sivasudha. Spectroscopic investigations on the interactions of AgTiO₂ nanoparticles with lysozyme and its influence on the binding of lysozyme with drug molecule. *Spectrochim Acta A Mol Biomol Spectrosc.* **152** 2016, 192-198.
- [11] P. Kalaivani, R. Prabhakaran, F. Dallemer, E. Vaishnavi, P. Poornima, V. Vijaya Padma, R. Renganathan, K. Natarajan. Synthesis, structural characterization, DNA/Protein binding and in vitro cytotoxicity of isomeric ruthenium carbonyl complexes. *Organomet Chem.* 2014, **762**, 67-80.
- [12] Anil K. Singh, Abera Asefa. A fluorescence study of differently substituted 3-styrylindoles and their interaction with bovine serum albumin. *Luminescence.* 2009, **24**, 123-130.
- [13] Abdulilah Dawoud. Bani-Yaseen. Spectrofluorimetric study on the interaction between antimicrobial drug sulfamethazine and bovine serum albumin. *Lumin.* 2011, **131**, 1042-1047.
- [14] S. Bi, T. Zhao, H. Zhou, Y. Wang, Z. Li. Probing the interactions of bromchlorbuterol-HCl and phenylethanolamine A with HSA by multi-spectroscopic and molecular docking technique. *Chem. Thermodynamics*, 2016, **97**, 113-121.
- [15] A. Hao, X. Guo, Q. Wu, Y. Sun, C. Cong, W. Liu. Exploring the interactions between polyethyleneimine modified fluorescent carbon dots and bovine serum albumin by spectroscopic methods. *Luminescence*, 2016, **170**, 90-96.
- [16] Gongke Wang, Ye Chen, Changling Yan, Yan Lu. Study on the interaction between gold nanoparticles and papain by spectroscopic methods. *J. of Luminescence*, 2015, **157**, 229-234.
- [17] Swarup Roy, Tapan Kumar Das. Interactions of biosynthesized gold nanoparticles with BSA and CTDNA: A multi-spectroscopic approach. *Polyhedron*, 2016, **115**, 111-118.
- [18] Z. Sun, H. Xu, Y. Cao, F. Wang, W. Mi. Elucidating the interaction of propofol and serum albumin by spectroscopic and docking methods. *Molecular Liquids*, 2016, **219**, 405-410.
- [19] M. Kumari, J. K. Maurya, M. Tasleem, P. Singh, R. Patel. Probing HSA-ionic liquid interactions by spectroscopic and molecular docking methods. *Photochemistry and photobiology B: Biology*, 2014, **138**, 27-35.
- [20] Suman Das, Sultana Parveen, Ankur Bikash Pradhan. An insight into the interaction of phenanthridine dyes with polyriboadenylic acid: Spectroscopic and thermodynamic approach. *Spectrochimica Acta Part A: Molecular and Biomolecular Spectroscopy*, 2013, **138**, 356-366.
- [21] M. Poór, G. Matisz, S. Kunsági-Máté, D. Derdák, L. Sente, B. Lemli. Fluorescence spectroscopic investigation of the interaction of citrinin with native and chemically modified cyclodextrins. *J. of Lumin.*, 2016, **172**, 23-28.
- [22] P. Fan, Lu Wan, Y. Shang, J. Wang, Y. Liu, X. Sun, C. Chen. Spectroscopic investigation of the interaction of water-soluble azocalix [4] arenes with bovine serum albumin. *Bioorganic Chemistry*, 2015, **58**, 88-95.
- [23] T. Hu, Y. Liu. Probing the interaction of cefodizime with human serum albumin using multi-spectroscopic and molecular docking techniques. *J. of Pharm. & Biom. Analysis*, 2015, **107**, 325-332.
- [24] L. Lai, C. Lin, Z. Xu, X. Han, F. Tian, P. Mei, D. Li, Y. GeX, F. Jiang, Y. Zhang, Y. Liu. Spectroscopic studies on the interactions between CdTe quantum dots coated with different ligands and human serum albumin. *Spectrochim. Acta Part A: Molec. & Biom. Spec.*, 2012, **97**, 366-376.
- [25] L. Tian, X. Hu, Z. Liu, S. Liu. Studies on the interaction of heparin with lysozyme by multi-spectroscopic techniques and atomic force microscopy. *Spectrochim. Acta Part A: Molecular & Biomolecular Spectroscopy*, 2016, **154**, 27-32.
- [26] Q. Wang, C. Huang, M. Jiang, Y. Zhu, J. Wang, J. Chen, J. Shi. Binding interaction of atorvastatin with bovine serum albumin: Spectroscopic methods and molecular docking. *Spectrochimica Acta Part A: Molecular and Biomolecular Spectroscopy*, 2015, **156**, 155-163.
- [27] V. D. Suryawanshi, Laxman S. Walekar, A. H. Gore, P. V. Anbhule. Spectroscopic analysis on the binding interaction of biologically active pyrimidine derivative with bovine serum albumin. *Pharm. Analysis*, 2016, **6**, 56-63.

BULGARIAN CHEMICAL COMMUNICATIONS

Instructions about Preparation of Manuscripts

General remarks: Manuscripts are submitted in English by e-mail or by mail (in duplicate). The text must be typed double-spaced, on A4 format paper using Times New Roman font size 12, normal character spacing. The manuscript should not exceed 15 pages (about 3500 words), including photographs, tables, drawings, formulae, etc. Authors are requested to use margins of 3 cm on all sides. For mail submission hard copies, made by a clearly legible duplication process, are requested. Manuscripts should be subdivided into labelled sections, e.g. **Introduction, Experimental, Results and Discussion, etc.**

The title page comprises headline, author's names and affiliations, abstract and key words.

Attention is drawn to the following:

a) **The title** of the manuscript should reflect concisely the purpose and findings of the work. Abbreviations, symbols, chemical formulas, references and footnotes should be avoided. If indispensable, abbreviations and formulas should be given in parentheses immediately after the respective full form.

b) **The author's** first and middle name initials, and family name in full should be given, followed by the address (or addresses) of the contributing laboratory (laboratories). **The affiliation** of the author(s) should be listed in detail (no abbreviations!). The author to whom correspondence and/or inquiries should be sent should be indicated by asterisk (*).

The abstract should be self-explanatory and intelligible without any references to the text and containing not more than 250 words. It should be followed by key words (not more than six).

References should be numbered sequentially in the order, in which they are cited in the text. The numbers in the text should be enclosed in brackets [2], [5, 6], [9–12], etc., set on the text line. References, typed with double spacing, are to be listed in numerical order on a separate sheet. All references are to be given in Latin letters. The names of the authors are given without inversion. Titles of journals must be abbreviated according to Chemical Abstracts and given in italics, the volume is typed in bold, the initial page is given and the year in parentheses. Attention is drawn to the following conventions:

a) The names of all authors of a certain publications should be given. The use of "*et al.*" in

the list of references is not acceptable.

b) Only the initials of the first and middle names should be given.

In the manuscripts, the reference to author(s) of cited works should be made without giving initials, e.g. "Bush and Smith [7] pioneered...". If the reference carries the names of three or more authors it should be quoted as "Bush *et al.* [7]", if Bush is the first author, or as "Bush and co-workers [7]", if Bush is the senior author.

Footnotes should be reduced to a minimum. Each footnote should be typed double-spaced at the bottom of the page, on which its subject is first mentioned.

Tables are numbered with Arabic numerals on the left-hand top. Each table should be referred to in the text. Column headings should be as short as possible but they must define units unambiguously. The units are to be separated from the preceding symbols by a comma or brackets.

Note: The following format should be used when figures, equations, *etc.* are referred to the text (followed by the respective numbers): Fig., Eqns., Table, Scheme.

Schemes and figures. Each manuscript (hard copy) should contain or be accompanied by the respective illustrative material as well as by the respective figure captions in a separate file (sheet). As far as presentation of units is concerned, SI units are to be used. However, some non-SI units are also acceptable, such as °C, ml, l, etc.

The author(s) name(s), the title of the manuscript, the number of drawings, photographs, diagrams, etc., should be written in black pencil on the back of the illustrative material (hard copies) in accordance with the list enclosed. Avoid using more than 6 (12 for reviews, respectively) figures in the manuscript. Since most of the illustrative materials are to be presented as 8-cm wide pictures, attention should be paid that all axis titles, numerals, legend(s) and texts are legible.

The authors are asked to submit **the final text** (after the manuscript has been accepted for publication) in electronic form either by e-mail or mail on a 3.5" diskette (CD) using a PC Word-processor. The main text, list of references, tables and figure captions should be saved in separate files (as *.rtf or *.doc) with clearly identifiable file names. It is essential that the name and version of

the word-processing program and the format of the text files is clearly indicated. It is recommended that the pictures are presented in *.tif, *.jpg, *.cdr or *.bmp format, the equations are written using "Equation Editor" and chemical reaction schemes are written using ISIS Draw or ChemDraw programme.

The authors are required to submit the final text with a list of three individuals and their e-mail addresses that can be considered by the Editors as potential reviewers. Please, note that the reviewers should be outside the authors' own institution or organization. The Editorial Board of the journal is not obliged to accept these proposals.

EXAMPLES FOR PRESENTATION OF REFERENCES

REFERENCES

1. D. S. Newsome, *Catal. Rev.–Sci. Eng.*, **21**, 275 (1980).
2. C.-H. Lin, C.-Y. Hsu, *J. Chem. Soc. Chem. Commun.*, 1479 (1992).
3. R. G. Parr, W. Yang, *Density Functional Theory of Atoms and Molecules*, Oxford Univ. Press, New York, 1989.
4. V. Ponec, G. C. Bond, *Catalysis by Metals and Alloys (Stud. Surf. Sci. Catal., vol. 95)*, Elsevier, Amsterdam, 1995.
5. G. Kadinov, S. Todorova, A. Palazov, in: *New Frontiers in Catalysis (Proc. 10th Int. Congr. Catal., Budapest, 1992)*, L. Guzzi, F. Solymosi, P. Tetenyi (eds.), Akademiai Kiado, Budapest, 1993, Part C, p. 2817.
6. G. L. C. Maire, F. Garin, in: *Catalysis. Science and Technology*, J. R. Anderson, M. Boudart (eds), vol. 6, Springer-Verlag, Berlin, 1984, p. 161.
7. D. Pocknell, *GB Patent 2 207 355* (1949).
8. G. Angelov, PhD Thesis, UCTM, Sofia, 2001.
9. JCPDS International Center for Diffraction Data, *Power Diffraction File*, Swarthmore, PA, 1991.
10. *CA* **127**, 184 762q (1998).
11. P. Hou, H. Wise, *J. Catal.*, in press.
12. M. Sinev, private communication.
13. <http://www.chemweb.com/alchem/articles/1051611477211.html>.

CONTENTS

SOLAR AND HYBRID THERMAL SYSTEMS

<i>G. Saktashova, A. Aliuly, Ye. Belyayev, M. Mohanraj, R. M. Singh</i> , Numerical heat transfer simulation of solar-geothermal hybrid source heat pump in Kazakhstan climates	7
<i>Jinkang Wang, Xu Ji, Qiang Wang, Rongkang Fan, Guoliang Li, Ming Li</i> , Electrical and thermal output characteristics investigation on a solar trough concentrating PV/T system.....	14
<i>M. Nikolaeva-Dimitrova, M. Stoyanova, Pl. Ivanov, K. Tchonkova, R. Stoykov</i> , Investigation of thermal behaviour of innovative Water Flow Glazing modular unit	21
<i>M. Trayanova, V. Hristov, R. Atanassova, E. Haslinger, O. Plank, S. Wyhlidal, A. Benderev</i> , Potential of corrosion and/or deposition of solid phases in the thermal waters in the region of Sofia Valley, Bulgaria, depending on their chemical composition.....	28
<i>T. S. O. Morais, C. H. C. Tsuha</i> , In-situ measurements of the soil thermal properties for energy foundation applications in São Paulo, Brazil.....	34

ENERGY EFFICIENCY

<i>A. F. Altun, M. Kılıç</i> , An investigation of the ammonia adsorption performance on different adsorbents for cooling applications	45
<i>A. S. Askarova, S. A. Bolegenova, A. G. Georgiev, S. A. Bolegenova, V. Yu. Maximov, R. K. Manatbayev, A. B. Yergaliyeva, A. O. Nugymanova, Zh. T. Baizhuma</i> , The use of a new “clean” technology for burning low-grade coal in on boilers of Kazakhstan TPPs ..	53
<i>A. S. Askarova, S. A. Bolegenova, V. Yu. Maximov, S. A. Bolegenova, A. O. Nugymanova, M. T. Beketayeva, Sh. S. Ospanova, R.K. Manatbayev</i> , The computational study of heat and mass transfer processes at combustion of pulverized Kazakh coal in real conditions of energy objects	61
<i>A. S. Askarova, S. A. Bolegenova, V. Yu. Maximov, S. A. Bolegenova, Sh. S. Ospanova, M. T. Beketayeva, A. O. Nugymanova, N. V. Pilipenko, Zh. K. Shortanbayeva, K. S. Baktybekov, A.B. Syzdykov</i> , Investigation of the different Reynolds numbers influence on the atomization and combustion processes of liquid fuel	68
<i>Bo Cao, Weijie Cui, Irsa Rasheed, Yixue Chen</i> , Atmospheric dispersion modelling and radiological safety analysis for a hypothetical accident of liquid-fuel thorium molten salt reactor (TMSR-LF)	78
<i>E. O. Kucuk, M. Kılıç</i> , Simulation and thermodynamic analysis of a regenerative and recuperative organic Rankine cycle	86

<i>K. Saka, Evaluation of mass flowing with COP for triple effect absorption refrigeration system</i>	96
<i>M. Kılıç, Comparative performance analysis of a two-bed adsorption cooling system with adsorption of different adsorbates on silica-gel</i>	102
<i>M. Lalošević, M. Komatina, B. Živković, M. Miloš, Reducing CO2 concentration in city centres with green roofs implementation: Case study Belgrade, Serbia</i>	111
<i>R. Tamašauskas, P. Bruzgevičius, J. Šadauskienė, D. Nikolic, Energy efficiency of wind power plants, Case of Lithuania</i>	120

MATERIALS SCIENCE

<i>A. A. Genbach, D. Yu. Bondartsev, I. K. Iliev, Modelling of capillary coatings and heat exchange surfaces of elements of thermal power plants</i>	133
<i>B. K. Kenzhaliev, V. G. Mironov, G.T. Shilov, Zh. B. Ilmaliev, D. K. Yermekov, The study of the effect of chromium boron (crb2) hardening additive on the developed pg-z40 surfacing powder</i>	140
<i>B. Ongar, I. K. Iliev, Numerical simulation of the coal dust process to the emission of nitrogen oxides</i>	146
<i>Bo Cao, Irsa Rasheed, Growth mechanism and photoluminescence property of flower-like ZnO by hydrothermal method</i>	153
<i>C. Dulucleanu, T. L. Severin, A. Potorac, L. Irimescu, Critical points in solid-state phase transformation of a steel with 0.087% C and 0.511% Mn, determined through dilatometric analyses</i>	158
<i>L. Costiuc, L. Baltas, S. Patachia, M. Tiorean, A. Lunguleasa, Influence of reprocessing by melt-mixing and thermo-formation of polyolefin fractions, separated from wastes, on their calorific power</i>	165
<i>S. N. Rabadzhiyska, L. P. Kolaklieva, T. M. Cholakova, R. D. Kakanakov, V. Chitanov, P. K. Stefanov, G. B. Atanasova, K. T. Balashev, B. S. Rangelov, S. B. Atanasova, Multilayer CrN/TiN coatings deposited at low temperatures by unbalanced magnetron sputtering for implant applications</i>	172
<i>Ş. Patat, A. Ülgen, S. Yıldız, A. R. Türkmen, T. Öztürk, Wood derived hard carbon anode material for low-cost sodium-ion batteries towards practical application for grid energy Storage</i>	181
<i>T. L. Severin, A. Potorac, C. Dulucleanu, L. Irimescu, Mathematical modelling concerning the influence of chemical composition upon hardness of cadmium telluride crystal - Part 2</i>	187
<i>T. M. Cholakova, L. P. Kolaklieva, R. D. Kakanakov, V. A. Chitanov, B. S. Rangelov, S. Atanasova-Vladimirova, P. K. Stefanov, G. B. Atanasova, K. T. Balashev, Effect of the heat treatment on mechanical and structural properties of CrTiAlN coatings deposited at low temperature</i>	197
<i>V. A. Chitanov, L. P. Kolaklieva, T. M. Cholakova, R. D. Kakanakov, Investigation of triple Cr-Ti-based nitride coatings depending on the graded transition layers</i>	205

FOOD ENGINEERING AND TECHNOLOGIES

<i>B. Turkan, A.S. Canbolat, A.B. Etemoglu, 3-D simulation of simultaneous heat and mass transfer of apple</i>	215
<i>Hao Yu, Jinghu Yu, Minmin Zhan, Study on mechanical behaviour of agar gel in compression mode</i>	225
<i>M. G. Georgieva, At. I. Tashev, D. G. Atanasov, V. Zh. Georgiev, Energy efficiency of impulse drying regimes of beetroot</i>	230

BIOTECHNOLOGIES

<i>A. M. Danev, R. N. Gabrova, T. Yaneva-Marinova, A. I. Angelov, Application possibilities of open-source software for microbiological analyses</i>	239
<i>Xiao Li, Jinghu Yu, Study on driving mechanical model of microcapsules based on fluid-structure interaction in intestinal tract</i>	246
<i>Yunlan Li, Hongyan Zhou, Yulian Xu, Lin Niu, PuGuo, Lanlan Miao, Qingshan Li, Antitumor activity of orthogonal array designed extracts from different part of <i>hedyotis diffusa</i> on human hepatocellular carcinoma hepG2</i>	253
<i>Yunlan Li, Ying Wei, Xiaoqing Ji, Dan Wang, Xiaozhi Qiao, Qingshan Li, Interaction ability of metallic dibutyltin antitumor drug DPDCT with human liver isoenzyme CYP3A4 which metabolized exogenous substances</i>	260

Company Data

Company Name: "GEO SIS" LTD.
Main Office: 47 Kuklensko Shousse blvd, Plovdiv, Bulgaria
Phone; e-mail: + (359) 89 579 8726; office@geosis.bg
Unified Identity Code: 115 812 318

"GEO SIS" Ltd.- Plovdiv city has been registered at the Plovdiv District Court under the number N° 7340/ 27.10.2003 with Court Decision number N° 3547/ 2003.

The General Manager of the company - engineer Ognyan Perov Pekov, has long-term experience as a professional and manager.

Field of work

The company is a specialized organization for design and construction of air-conditioning systems, using renewable energy sources - groundwater and earth powered batteries.

The field of work of the company is directed to building and construction of power efficient and power saving systems.

During the realization of the projects and the installation activities the company aims at enforcing all the requirements of the Energy Efficiency Law and the accompanied regulations and subdelegated Bulgarian legislations.

Major activities:

- design, construction and maintenance of industrial and domestic air-conditioning and heat pump installations;
- design, construction and maintenance of industrial and domestic conventional air-conditioning installations and ventilation systems;
- prophylaxis, service and repair of existing air-conditioning and ventilation systems;
- design, construction and prophylaxis of specific air-conditioning and ventilation installations.

Our main goal, care and responsibility is to offer final technical optimal solutions for heating and air-conditioning.

The managing and the executive personnel of the company consist of highly qualified professionals with a great professional experience.